Taylor, B., Huchon, P., Klaus, A., et al., 1999
Proceedings of the Ocean Drilling Program, Initial Reports Volume 180

6. SITE 1109[1]

Shipboard Scientific Party[2]

SITE 1109

Hole 1109A (APC):
9°30.390′S, 151°34.388′E; 2210.9 mbsl
0–9.50 mbsf cored; 9.96 m recovered (105%)
Hole 1109B (APC):
9°30.396′S, 151°34.391′E; 2211.1 mbsl
0–14.80 mbsf cored; 15.14 m recovered (102%)
Hole 1109C (APC/XCB):
9°30.392′S, 151°34.390′E; 2211.0 mbsl
0–375.70 mbsf cored; 323.11 m recovered (86%)
Hole 1109D (RCB):
9°30.380′S, 151°34.355′E; 2211.0 mbsl
0–352.80 mbsf drilled without coring; 352.80–802.00 m cored; 299.87 m recovered (67%)

Site 1109 is located on the Woodlark Rise, 11 km north of a major south-dipping normal fault system that is antithetic to the low-angle fault dipping north from Moresby Seamount. The site was positioned to cross a sequence boundary and an angular unconformity at about 350 and 770 mbsf, respectively, beneath which a lower stratified sequence, interpreted to be prerift forearc basin sediments, dips northward at ~10°.

Four holes were drilled at Site 1109: two short APC holes (1109A and 1109B), one APC/XCB (1109C), and one RCB (1109D). These allowed coring to a total depth of 802 mbsf, complete logging above 786 mbsf with the triple combo geophysical tool, logging two intervals (112–351 and 376–786 mbsf) with the FMS-sonic tools, and conducting a well seismic tool-vertical seismic profile (WST-VSP) with nine receiver locations from 378 to 460 mbsf. The following description uses unit boundaries derived from integrated core-log data interpretation.

[1] Examples of how to reference the whole or part of this volume.
[2] Shipboard Scientific Party addresses.

Ms 180IR–106

Data from Site 1109 show a record of progressive subsidence (from subaerial to lagoonal, then shallow marine and deep water) over a period from latest Miocene to late Pleistocene. These data provide the information to fulfill one of our primary objectives: to determine the sedimentology, biostratigraphy, and vertical motion history of the syn-rift sediments on the hanging wall margin to the Moresby low-angle normal fault.

A second objective, to determine the nature of the forearc basin sequence beneath the rift-onset angular unconformity, was thwarted by the unexpected presence of a massive dolerite with ophitic texture from 773 to 802 mbsf, overlain to 730 mbsf by a conglomerate of dolerite7 and some basalt cobbles in an altered clayey silty matrix with nonrecovered interbeds likely similar to the overlying unit. The dolerite has seismic velocities of 5–6 $km \cdot s^{-1}$. Culminations observed on reflection seismic sections to be developed locally on the erosional unconformity—previously interpreted as reefs—may be volcanic constructions.

From 713 to 730 mbsf, a very altered, clay-rich siltstone and fine-grained sandstone were recovered, including goethite concretions. A nonmarine, swampy setting is inferred. These sediments contain scattered basalt/dolerite clasts that logging data indicate were derived from discrete conglomerate intercalations. The oogonia of charophyte algae present in Sample 180-1109D-39R-CC indicate a locally freshwater environment at the top of this unit.

We envision deposition in a lagoonal setting of the silty claystone and clayey siltstone encountered between 672 and 713 mbsf. Shell, plant, and wood fragments are common to abundant. The lagoon was alternately brackish and, as indicated by the presence of dolomite, hypersaline. This unit has high natural gamma ray and porosity (45%–50%), low magnetic susceptibility, and velocities ~2 $km \cdot s^{-1}$.

The first (lower Pliocene: NN13 and N19/20) sediments deposited in a shallow-marine (<150 m water depth) environment occur at 588–664 mbsf and are mixed carbonate-siliciclastic rocks. From 599 to 672 mbsf the lithology consists dominantly of well-cemented, 30%–40% porosity, sandy bioclastic packstone/grainstone. A lower limestone section (643–672 mbsf) with high resistivity (3 Ωm), has low natural gamma ray, 40–80 wt% calcium carbonate, and average velocities of 2.5–3.0 $km \cdot s^{-1}$. An upper sandstone section with lower resistivity (<2 Ωm), has high natural gamma ray, 20–30 wt% calcium carbonate, and average velocities of 2.0–2.5 $km \cdot s^{-1}$. Above this is an interval (570–599 mbsf) of calcareous (bioclastic) sandstone with 40–50 wt% calcium carbonate and 45%–50% porosity. The entire sequence reflects relatively shallow-water sediments derived from both volcanic-related and neritic carbonate source materials that accumulated before 4 Ma at >70 m/m.y.

A succession of clay-rich siltstones and silty claystones, interlayered with thin (1–10 cm) medium- to fine-grained sandstones, at 390–570 mbsf was rapidly deposited (312 m/m.y.) in upper bathyal (150–500 m) water depths until ~3.35 Ma. Porosity increases (to 60%) as calcium carbonate decreases (to 25 wt%) upsection to ~480 mbsf, whereas velocities steadily decrease from 2.0 to 1.8 $km \cdot s^{-1}$ up the unit, and magnetic susceptibilities are constantly low above 540 mbsf. These are hemipelagic carbonate muds with turbiditic sand interbeds from a dominantly unaltered basalt-andesite volcanic source with minor neritic carbonates, deposited on a well-oxygenated and extensively bioturbated slope.

Above 380 mbsf, significantly greater magnetic susceptibilities that continue to 83 mbsf correspond to the influx of clays and silts from an additional source terrane, characterized by altered calc-alkaline volcani-

clastic material and metamorphic detritus with mixed-layer, and probably smectite, clays. Between 330 and 390 mbsf (~3.07–3.35 Ma) the silty claystone is nearly devoid of sandy interbeds. The lower portion (up to 353 mbsf) has a high frequency of layers with unaltered volcaniclastics. The section from 295 to 330 mbsf was deposited at 69 m/m.y. between 2.57 and 3.07 Ma. Seismic reflection data show that this compressed section is part of a conformable slope sequence that substantially thickens downslope toward the rift basin to the south (i.e., there is a regional "onlap" relationship of flat basin turbidites laterally continuous with conformable slope deposits).

The margin continued to subside with an accumulation rate of 66 m/m.y. between 3.07 and 1.95 Ma (295–255 mbsf), and above 285 mbsf was at middle bathyal (500–2000 m) water depths. Distal silt-clay bioturbated turbidites with volcanic, terrigenous, and biogenic components rapidly onlapped the margin (225 m/m.y.) from 1.95 Ma until 1.0 Ma (~42 mbsf). These include a significant component of reworked slope sediments, as evidenced by dominantly upper Pliocene biota in the younger section. Volcaniclastic sands are most frequent from ~100 to 170 mbsf. Silt to coarse-grained sand interbeds are common from 170 to 247 mbsf, including a poorly recovered sand from 218 to 233 mbsf. These sands are remarkable for their high thorium and potassium contents, producing high natural gamma-ray counts, and lower porosities (40%–50%) and higher velocities (2 $km \cdot s^{-1}$) than adjacent intervals (60%–70% and 1.7 $km \cdot s^{-1}$, respectively).

Between 1.0 and 0.46 Ma the site was relatively sediment starved and/or intermittently eroded (the site is located in a submarine valley), with net accumulation rates of 21 m/m.y. of calcareous clayey silt and silty clay with some thin volcanic ash layers. Since 0.46 Ma, nannofossil-rich, calcareous sand, silt, and clay with volcaniclastic sand and volcanic ash, were deposited at 67 m/m.y. Only the surface sediment has a lower bathyal (>2 km) benthic fauna.

Extensional deformation is very weak throughout the section, except for minor normal faults at about 260 and 360 mbsf and normal shear zones at 678–685 mbsf and in the dolerite. A folded region at 36–55 mbsf is interpreted as a slump.

Velocities linearly increase with depth from 1.5 $km \cdot s^{-1}$ at the surface to 1.9 $km \cdot s^{-1}$ at 520 mbsf, and then more rapidly to 2.2 $km \cdot s^{-1}$ at 590 mbsf with the increasing calcium carbonate. Velocities increase to 3–4 $km \cdot s^{-1}$ and are more variable in the bioclastic sandstones and limestones between 590 and 672 mbsf, and then return to 2 $km \cdot s^{-1}$ in the lagoonal sequence below that. Porosity decreases downward, but the usual negative exponential decay is interrupted at two levels (160–280 and 350–540 mbsf) where the higher porosity reflects undercompaction correlated with periods of high sedimentation rates (225–312 m/m.y.). The thermal conductivity generally mirrors the porosity-depth profile and ranges from 0.78 to 1.5 $W \cdot m^{-1} \cdot °C^{-1}$, except for the dolerite, which shows values up to 2 $W \cdot m^{-1} \cdot °C^{-1}$. Six temperature measurements down to 170 mbsf define a linear thermal gradient of 31 $°C \cdot km^{-1}$ and, when combined with an average thermal conductivity of 0.9 $W \cdot m^{-1} \cdot °C^{-1}$ over this interval, a heat flow of 28 $mW \cdot m^{-2}$.

Although their number rapidly decreases with depth, bacteria are present in all samples obtained down to 746 mbsf. Total populations and numbers of dividing and divided cells show obvious relationships to the sediment geochemistry. Pore-water constituent profiles show that carbonate diagenesis occurs at shallow depth (above 100 mbsf),

aided by the bacterial decomposition of organic matter. Diagenetic transformation of pre-existing detrital clay minerals occurs to 300 mbsf. Bacterial activity further downhole is evidenced by deep-seated (430–550 mbsf) ammonia and alkalinity submaxima (the latter likely because of increased CO_2 production). Of note is a generally increasing pH downhole, from 7.8 to greater than 8.6. Pore-water composition also reflects the alteration of volcanic components, formation of authigenic clay minerals, silica diagenesis, and diffusion of elements above the shell-rich and freshwater units below 672 mbsf. A crossover of Ca and Mg profiles, as often observed above igneous sills, occurs at 661 mbsf.

Headspace gas analyses show a typical methane profile, with concentrations increasing rapidly at 100 mbsf from ~5 to ~6000 ppm, then remaining between 1000 and 10,000 ppm down to 600 mbsf. Methane content begins to decrease below 600 mbsf, reaching 5 ppm by 720 mbsf. The only other hydrocarbon detected was C_2, but it remained below 3.2 ppm throughout the entire cored section. The C_1/C_2 ratios did not drop below 1000, and organic carbon was generally <1% throughout the core.

OPERATIONS

Transit to Site 1109 (ACE-9A)

An APC/XCB coring assembly was fit together during the transit to Site 1109 in dynamic positioning (DP) mode. The ship speed was ~4 nmi/hr during the 1.5 hr the pipe was out of the water. At 1130 hr on 24 June we reduced speed to <1 nmi/hr and began lowering the drill pipe to the seafloor. A beacon was deployed at Site 1109 (proposed site ACE-9A) at 1315 hr on 24 June 1998.

Hole 1109A

The 3.5 kHz depth recorder indicated a seafloor depth of 2214 meters below sea level (mbsl). Hole 1109A was spudded with the advanced piston corer (APC) at 1630 hr on 24 June with the bit at 2210.9 mbsl. The core was virtually full, making an exact seafloor depth difficult to determine. However, there was no evidence of mud on the piston head, and brown sediment inferred to be seafloor material was evident at the top; therefore, the seafloor was defined to be at 2210.9 mbsl. Recovery was 9.96 m, or 104.8% (Tables T1, T2). To ensure we obtained the uppermost seafloor sediments, we decided to spud another hole.

T1. Site 1109 coring summary, p. 226.

T2. Site 1109 coring summary by section, p. 229.

Hole 1109B

Without offsetting the ship, we spudded Hole 1109B at 1715 hr with the bit at 2206.9 mbsl. Core 1H recovered 5.28 m; therefore, the seafloor was calculated to be at 2211.1 mbsl. This confirmed that Hole 1109A had indeed recovered nearly the entire mudline. We took a second APC core, which extended down to 14.8 meters below seafloor (mbsf). Total recovery was 15.14 m (102.3%). These cores were primarily intended to provide whole-round samples for high-resolution microbiological and interstitial water (IW) chemistry studies. Hole 1109B ended when the bit was pulled clear of the seafloor at 1830 hr on 24 June.

Hole 1109C

Again without offset, we spudded Hole 1109C at 1900 hr. Core 1H was taken with the bit at 2208.9 mbsl and recovered 7.37 m, indicating a seafloor depth of 2211.0 mbsl. The APC coring continued through Core 11H (102.4 mbsf), which required 60,000 lb to pull the barrel out of the formation. APC core recovery was 107.55 m (105%). Cores 3H through 11H were oriented with the tensor tool and Adara temperature tool measurements were taken while obtaining Cores 3H, 5H, 7H, 9H, and 11H.

We began extended core barrel (XCB) coring with Core 12X, using soft formation cutting shoes through Core 37X at 346.6 mbsf. A single Davis-Villinger temperature probe (DVTP) measurement was taken after Core 18X (169.7 mbsf). The probe tip was recovered with a very slight bend in it.

While removing the cutting shoe from Core 36X on the rig floor, the threaded connection of the shoe fractured. We suspected that the failure was caused by overheating during drilling and subsequent quenching in seawater. This prompted us to switch to hard formation cutting shoes beginning with Core 38X because the Core 37X barrel had already been deployed. We wanted to continue XCB coring before switching to rotary core barrel (RCB) because of the excellent XCB core recovery (99.3% for the day). A second cutting-shoe failure occurred while cutting Core 40X and when recovered on the rig floor, the lower part of the cutting shoe was missing. We then attempted to advance a half core to see if we could push the junk to the side of the hole, but this attempt was not successful. Erratic torque and an abraded core cutting shoe indicated that we were pushing the broken parts of the cutting shoe tip downhole and coring operations ceased at 375.7 mbsf. Pieces of the broken cutting shoe were recovered in Core 41X once it was split. The bit was pulled clear of the seafloor at 0430 hr on 27 June and the hole officially ended at 0800 hr when the bit cleared the rig floor. Combined APC/XCB recovery for the hole was 323.11 m (86%).

Hole 1109D

We then converted to an RCB coring assembly, including a $9\frac{7}{8}$-in bit, a mechanical bit release, and an additional stand of drill collars. After lowering the pipe to the seafloor, we spudded Hole 1109D at 1245 hr on 27 June. Seafloor was established as 2211.1 mbsl. We drilled without coring (using an RCB center bit) to a depth of 352.8 mbsf. The drilling took 12.25 hr at an average rate of penetration (ROP) of 28.8 m/hr. We then swept the hole clean with sepiolite mud and recovered the center bit, and at 0145 hr on 28 June we started RCB coring at 352.8 mbsf. This allowed an overlap of ~23 m with the cores from Hole 1109C. We continued through Core 35R to 676.4 mbsf with few problems. Sepiolite mud pills (30 bbl) were circulated every third core as a precautionary measure, and hole conditions remained good with no fill on connections, relatively constant torque, and no overpull or drag. The formation appeared to be quite variable, which affected core recovery and penetration rates. Coring continued through Core 45R (772.9 mbsf). In this interval, we began to experience some fill (2–3 m) between connections. As a result, we increased the 30-bbl mud sweeps to every core. Recovery dropped off from the 54.9% of the day before to 47.3%, and ROP dropped from 12.9 m/hr to 3.9 m/hr while coring in a conglomerate. No hole stability problems were encountered until after

cutting Core 46R (777.6 mbsf). While pulling off bottom, the driller noted high pump pressure and high torque, indicating a portion of the hole had caved in from above. After pulling the pipe back to 762.8 mbsf with 50,000 lb overpull, the hole was swept with 30 bbl of sepiolite. High pump pressure was once again noted when we retrieved the core barrel, and a second 30-bbl sepiolite pill was circulated. After retrieving the core barrel, a bit deplugger was deployed to clear the bit throat. Drilling parameters returned to normal, and coring proceeded through Core 51R in hard and massive dolerite to a total depth of 802.0 mbsf. Recovery was exceptional in this portion of the hole (88.9%); however, penetration rates were extremely slow (1.5–2.0 m/hr). Although the science party wanted to penetrate below the dolerite into the inferred forearc sequence below, coring was terminated because there was no indication that we were approaching the bottom of the dolerite.

After sweeping the hole with 40 bbl of sepiolite mud, a short wiper trip was made in the lower (problematic) portion of the hole. The bit was backreamed to 762.8 mbsf with 40,000–50,000 lb overpull before circulation could be established. Upon running the pipe back to the bottom of the hole, the bit encountered fill at 784.8 mbsf, indicating that we had lost the lowermost ~17 m of the hole. We decided not to spend the time to clean out the bottom of the hole. Another 30-bbl sepiolite mud sweep and two wireline runs were made to release the bit. The hole was displaced with 217 bbl of sepiolite mud, and the pipe was pulled up to 98.8 mbsf in preparation for logging.

After rigging up for logging, the triple combo with the temperature-logging tool (TLT) was assembled and lowered down the pipe. The tool suite was able to pass several tight spots between 326.8 and 376.8 mbsf to eventually reach 782.8 mbsf. Excellent logs were recovered over nearly the entire hole to the bottom of the pipe. However, the caliper data indicated that the tight spots between 326.8 and 376.8 mbsf had narrowed to about the tool diameter of 4 in (10.16 cm). After the triple combo was rigged down, we assembled the Formation MicroScanner (FMS)-sonic tool and ran it into the hole. Because of the constrictions, this tool could not be lowered past 349.8 mbsf; therefore, we logged up from that point. Once the FMS-sonic tool was out of the hole, the logging sheaves were pulled aside and the drill string (without the bit) was lowered through the constrictions to 377.8 mbsf. A second run of the FMS-sonic tool was made from 775.8 mbsf up to just below the end of the drill pipe.

The final logging run was with the well seismic tool (WST) to obtain a vertical seismic profile (VSP). Because of the light weight of this tool, it had to be lowered very slowly down the pipe. We tried pumping the tool down, but this did not help and actually made the tool appear lighter because of the pump-off effect from the oil saver. Eventually, we were able to work the tool down to 460.3 mbsf (82.5 m below the end of the pipe). The VSP was conducted at nine different depths with 7–12 shots at each level. All of the logging runs obtained quality data.

After the WST was retrieved and we were rigged down from logging, we filled the hole with 80 bbl of heavy mud. The pipe was then raised to 127.8 mbsf, and the hole was plugged with cement (15 bbl). The drill pipe was pulled out of the hole, clearing the seafloor at 1945 hr on 3 July. The positioning beacon was recovered at 2130 hr, and the last thruster was raised when the end of the drill string cleared the rig floor at 0015 hr on 4 July 1998. Once the rig was secured, we began the transit to Site 1110 (proposed site ACE–10A). At Hole 1109D, we cored 449.2 m of section and recovered 299.87 m (67%).

LITHOSTRATIGRAPHY

Introduction

In the succession cored at Site 1109, we recovered ~770 m of sediments and sedimentary rocks above basic igneous rocks, interpreted as overlying a Miocene forearc sequence. Eleven lithostratigraphic units were recognized on the basis of sediment or rock type, grain size, sedimentary structures, color, smear slides, thin sections, bulk mineralogy (X-ray diffraction [XRD]), and carbonate content. In addition, geophysical logs, including FMS data, were used to help reconstruct the lower part of the succession, which had poor recovery by rotary drilling.

The lithostratigraphic units recognized are shown in Figure F1. Unit I is composed of calcareous sand, silt, and clay, with volcaniclastic sand and volcanic ash. This unit is divided into two subunits, based partly on the relative abundance of volcanic ash. Unit II is dominated by greenish gray clay interbedded with abundant volcaniclastic sand. A marked feature is the presence of graded couplets of dark gray, fine-grained volcaniclastic sand overlain by greenish gray silty clay and clayey silt. Unit III comprises clayey silt, and silty clay interbedded with clayey silt, to coarse-grained sand containing volcanic, siliciclastic, and biogenic particles. Unit IV is more lithified and is marked by generally finer grained, greenish clayey siltstone and silty claystone with rare foraminifers. Unit V marks a return to slightly coarser grained sediment, with dark gray siltstones and sandstones with common volcaniclastic material. Unit VI is characterized by a clayey siltstone and silty claystone with subordinate thin beds of sandstone/siltstone. Unit VII exhibits a sharp change to coarser grained bioclastic sandstones and limestone (i.e., packstone and grainstone). Beneath this, Unit VIII exhibits an additional major change to dark colored silty clay and clayey siltstone with common plant material and shells. Unit IX is characterized by clayey siltstone and volcaniclastic sandstone that is highly altered and contains goethite concretions. In Unit X, conglomerate containing pebbles of variolitic basalt and dolerite was recovered. The conglomerate lies unconformably above basement dominated locally by dolerite (Unit XI; see "Igneous and Metamorphic Petrology," p. 35).

F1. Lithologic logs of successions at Site 1109, p. 84.

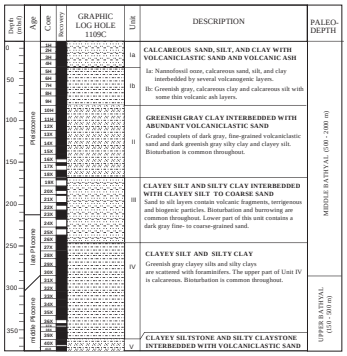

Lithostratigraphic Unit I

Description: calcareous sand, silt, and clay with volcaniclastic sand and volcanic ash
Interval: Core 180-1109A-1H; Cores 180-1109B-1H and 2H; and Cores 180-1109C-1H through 9H
Depth: 0–9.50 mbsf (Hole 1109A); 0–14.80 mbsf (Hole 1109B); and 0–83.40 mbsf (Hole 1109C)
Age: early Pleistocene–?Holocene

All of Unit I was recovered in Hole 1109C. However, the uppermost few meters of the unit were also cored in Holes 1109A and 1109B. These three cores include a number of distinctive marker horizons, notably two individual thin beds of volcanic ash (each ~2 cm thick), calcareous sand, greenish silt layers, and a bed of volcaniclastic sand that together allow a precise correlation between the three holes (Fig. F2; see also "Composite Depths," p. 79), confirming that a complete succession was recovered.

F2. Correlation of successions in Core 180-1109A-1H with cores from Holes 1109B and 1109C, p. 86.

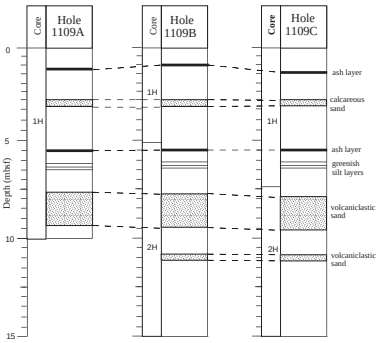

The Unit I succession is composed of the following main types of unconsolidated sediment: nannofossil ooze, calcareous clay, calcareous silt, volcaniclastic silt and sand (with rare granules), and volcanic ash. The volcanic ash layers are best displayed in Core 180-1109C-3H from 16.90 to 26.40 mbsf but occur sporadically throughout the whole of Unit I.

Nannofossil ooze, calcareous sand, silt, and clay, interbedded with a small number of volcanogenic layers, are abundant in the upper part of the succession, and defined as Subunit IA.

Subunit IA

Interval: Core 180-1109A-1H; Cores 180-1109B-1H and 2H; and Cores 180-1109C-1H through 4H
Depth: 0–9.5 mbsf (Hole 1109A); 0–14.8 mbsf (Hole 1109B); and 0–35.9 mbsf (Hole 1109C)

By contrast, the lower part of Unit I is mainly clayey silt and silty clay, with only rare volcanic ash layers; this interval is defined as Subunit IB.

Subunit IB

Interval: Cores 180-1109C-5H through 9H
Depth: 35.9–83.4 mbsf

Similar sediments occur in both Subunits IA and IB and for this reason are described together (as individual lithologies) below:

Foraminifer-Bearing Nannofossil Ooze

Nannofossil oozes rich in clay are present only in the uppermost part of Subunit IA. These sediments range in color from brown (10YR 6/4–6/2), in the uppermost 14.5-cm-thick oxidized interval, to greenish (dominantly 5GY 5/2) beneath this interval. The nannofossil ooze is rich in planktonic foraminifer tests and clay. Determinations of calcium carbonate indicate values ranging from 47–68 wt% in Subunit IA and from 15–67 wt% in Subunit IB (see **"Organic Geochemistry,"** p. 59).

Calcareous Clay

This clay forms a minor constituent of Subunit IA and a major constituent of Subunit IB. The calcareous clay occurs as repeated intervals up to several tens of centimeters thick (e.g., Section 180-1109A-1H-5). Sulfide mottling is ubiquitous. Individual mottles are typically up to several centimeters in size; some follow lithologic boundaries, whereas many occur independently of lithologic variation.

Calcareous Silt

This silt is a minor constituent of Subunit IA and a major constituent of Subunit IB. The silt commonly forms alternating very thin beds (<3 cm) more or less rich in planktonic foraminifers and siliciclastic sand grains (e.g., Section 180-1109C-3H-2). A number of thin foraminifer-rich beds exhibit sharp bases, normal grading, and diffuse tops, passing into nannofossil-rich clays (Fig. **F3**). Locally, small blebs of volcanic glass occur.

Smear-slide analysis shows that the silt is clay rich and contains quartz, plagioclase, rare accessory minerals (e.g., biotite or pyroxene), and variable amounts of fine-grained volcanic glass particles (**"Site**

F3. Graded, calcareous silt beds characterized by sharp, basal contacts, **p. 87.**

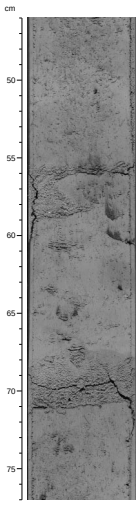

1109 Smear Slides," p. 115). Bioclasts are present as ubiquitous calcareous nannofossils, together with sponge spicules, scattered radiolarians, and diatoms. Radiolarians and diatoms are most abundant in several of the most volcanic-glass-rich layers. XRD analysis shows that the silts consist mainly of calcite, quartz, and plagioclase (Table T3).

T3. X-ray diffraction analysis of thin sections, p. 246.

Carbonate Sand

Carbonate sand occurs sporadically as a minor constituent in Subunit IA. The sand forms relatively coarse-grained, white, granular layers, passing up into fine-grained sand and silt in isolated beds as thick as 25 cm. For example, two beds in intervals 180-1109C-4H-1, 0–28 and 57–61 cm, are composed of coarse granules with abundant fragments of calcareous algae (e.g., *Halimeda* sp.), planktonic and benthic foraminifers, and shell fragments (Fig. F4).

F4. Graded, sharp-based gravel bed with shell fragments and bioclastic detritus, p. 88.

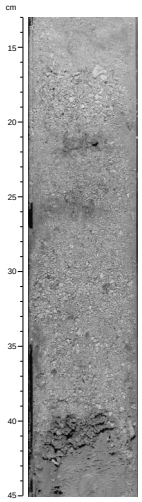

Volcanic Ash and Volcaniclastic Sediment

Discrete ash-fall layers, present in both Subunit IA and Subunit IB, are recognized by their mostly sharp bases (Fig. F5), often bioturbated tops, normal grading, and high content of pyroclastic components. Glass-rich layers are light gray to dark gray, and 0.5–12.5 cm thick. The ash layers are dominated by fresh (i.e., not devitrified) colorless, platy to bubble wall shards that make up 80%–95% of individual layers (Fig. F6). Shards with tubular vesicles and pumice are generally rare. The shards are commonly only a few micrometers thick but range from ~50 to ~300 µm in size. Carbonate and detrital components are minor constituents of ash layers. In addition, Pleistocene ash layers contain less than 10% of co-genetic phenocrysts (i.e., biotite, plagioclase, quartz, amphibole, and clinopyroxene). The ash is most abundant in Subunit IA above 40 mbsf, decreasing downward. Ash persists as sporadic thin layers in Subunit IB (e.g., Sections 180-1109C-5H-5, 5H-7, 6H-2, and 6H-7).

F5. Sharp-based volcanic ash bed, p. 89.

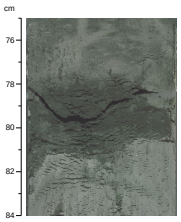

Individual volcaniclastic sediment beds are generally <15 cm thick, but the locally reach 35 cm (interval 180-1109C-3H-7, 34–68 cm). The grain size of the volcanic-ash-rich sediment ranges up to coarse-grained sand with rare granules and pebbles of pumice. Smear-slide analysis confirmed that the volcaniclastic layers are rich in volcanic glass (e.g., Sample 180-1109C-2H-6, 49–53 cm; "Site 1109 Smear Slides," p. 115). This is mainly composed of colorless volcanic glass in the form of platy shards and bubble wall shards and is inferred to be of rhyolitic composition.

The volcaniclastic sand beds exhibit sharp bases, normal grading, planar-laminated upper parts, and diffuse tops, passing up into clay-rich silt (Fig. F7). Some beds are structureless (e.g., Core 2H). In addition, wavy lamination was rarely observed (e.g., intervals 180-1109C-2H-7, 36–37 and 47–49 cm). Also, small (<2 mm) shell fragments are commonly observed, mainly in the upper parts of beds.

F6. Volcanic ash with nondevitrified, colorless, platy to bubble-walled shards, p. 90.

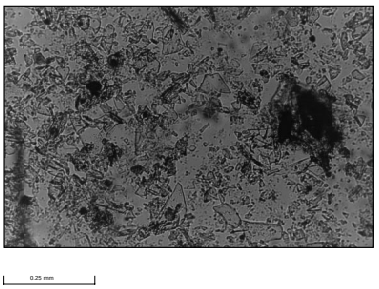

Silt occurs, both forming the upper parts of graded sand beds and as separate, thin (several centimeters) beds of silt grading up into silty clay and clay. This silt is locally sandy (e.g., Core 2H), with dark volcanic glass fragments scattered throughout. Occasional discrete thin layers of volcanic ash, composed of silt-sized particles, were also observed, commonly including a relatively high clay content.

In addition, several thin, very coarse grained volcaniclastic layers were noted throughout Subunit IB. Sandy gravel occurs mainly in the upper levels of this subunit as a few beds up to several tens of centimeters thick (e.g., Section 180-1109B-1H-3). Also, a concentration of pum-

ice fragments up to several centimeters in size in the interval 180-1109C-5H-4, 73–83 cm, is probably related to a specific volcanic event.

Deformed Interval within Subunit IB

From 36 to 55 mbsf, the sediments are markedly deformed. Bedding ranges from subhorizontal to angles of up to 60°, or rarely 90° (e.g., interval 180-1109C-5H-2, 120–150 cm). Apparent folds with a limb spacing of up to 50 cm were observed (e.g., Section 180-1109C-6H-4; Fig. F8). Some beds are strongly disrupted by layer-parallel extension generating a boudinlike fabric. No penetrative fabric is developed. Further details are given in "Structural Geology," p. 38.

Interpretation

Unit I is interpreted as a dominantly deep-water, middle-bathyal (500–2000 m; see "Biostratigraphy," p. 43) hemipelagic succession of calcareous silts and clays interspersed with clastic intervals of several different origins. Only the surface sediment has a lower bathyal (>2000 m) benthic fauna representative of the present water depth (2211 m) at the site.

The thin-bedded calcareous clays and silts were mainly redeposited by low-density turbidity currents. The rare, white carbonate sands are interpreted as derived from neritic shallow-water carbonates (i.e., mainly algal deposits) that were also deposited by turbidity currents. Paleontological data indicate Unit 1B sediments accumulated at ~200 m/m.y. prior to 1 Ma, whereas Unit 1A sediments accumulated at 21 m/m.y. to 0.46 Ma and 67 m/m.y. thereafter (see "Biostratigraphy," p. 43).

The volcaniclastic intervals are interpreted to be the result of contemporaneous volcanism for which volcanoes of the Trobriand Arc or those within Dawson Strait are the probable source (see "Depositional History," p. 31). The well-sorted volcanic ash layers are interpreted as primary pyroclastic airfall deposits, with minimal mixing with other constituents. By contrast, the relatively rare volcaniclastic sand layers are of epiclastic origin and were redeposited by turbidity currents.

Deformed Interval

Several arguments in favor of either a primary origin, or one by drilling disturbance, can be considered.

Drilling disturbance (APC): (1) the deformation is highly incoherent such that individual lithologic units cannot always be recognized on both limbs of individual "folds;" (2) some, but not all, of the deformation is focused within several millimeters of the core liner, suggesting that at least some coring-related disturbance is present; and (3) seismic data for Site 1109 imply that the sedimentary succession is nearly flat lying, although minor faults are imaged on seismic profiles in the vicinity (see "Drill Sites," p. 2, in the "Leg 180 Summary" chapter), and normal faults were observed deeper in the succession at Site 1109 (see "Structural Geology," p. 38).

Primary origin: (1) Many of the structures are sharply truncated at the edges of cores without disruption, suggesting they are considerably larger than the core diameter; (2) the structures occur within high-recovery APC cores, and are not restricted to the upper or lower parts where drilling disturbance is anticipated; and (3) similar deformation features were not observed above or below the discrete deformed interval. Paleontological evidence shows that reworking of biota is signifi-

F7. Beds of normally graded volcaniclastic silt with sharp bases, p. 91.

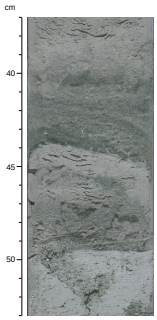

F8. Contorted clay-rich silt and silty clay beds of deformed interval, p. 92.

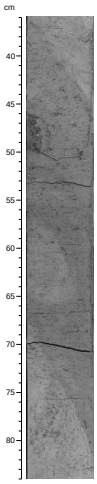

cant in the deformed interval, but no zonal markers are deleted or duplicated (see "Biostratigraphy," p. 43).

Unfortunately, the disturbed interval is too shallow to be imaged by FMS data, which could have conclusively differentiated between the alternative origins. On balance, a primary origin is preferred, suggesting that the seafloor experienced a phase of sediment instability, probably leading to sediment redeposition as a slump that was perhaps triggered by faulting at depth.

Lithostratigraphic Unit II

Description: greenish gray clay interbedded with abundant volcaniclastic sand
Interval: Cores 180-1109C-10H through 18X
Depth: 83.40–169.70 mbsf
Age: early Pleistocene

Unit II is characterized by repeated normal-graded beds of volcaniclastic sand, silt, silty clay, clayey silt, and clay, together with rare carbonate packstone and volcanic ash. Unit II corresponds to an interval of relatively high magnetic susceptibility (see "Physical Properties," p. 61). This unit is the first to be covered by geophysical and FMS logs (see "Downhole Measurements," p. 69).

The top two cores of this unit (10H and 11H) were recovered by APC, whereas the remaining seven cores (12X through 18X) were obtained using the XCB. Visual inspection indicates that the APC cores are undisturbed, whereas the XCB cores become progressively more disturbed downward. Cores 10H, 11H, 12X, and 13X were recorded as moderately disturbed; Core 15X as moderately disturbed; Core 16X and 17X as highly disturbed, and finally Core 18X was logged as drilling biscuits. Notably, no marked change was observed in the appearance of similar lithologies in the lower, APC, and the following upper, XCB cores, confirming that the lithologies described below from XCB cores are primary and not the result of drilling disturbance.

Clay and Silty Clay, with Rare Silt and Sand Partings

Most of the clay and silty clay occurs within the upper parts of thin-graded beds (couplets) as described below. However, structureless clay is also locally present in intervals as thick as tens of centimeters. The sand is homogenous, or occurs as very thin beds. Compared to Unit I, levels of calcium carbonate are much lower (2.8–31 wt%). In general, the more clay-rich zones are more calcareous (10–31 wt%), whereas siltstones are less calcareous (~10 wt%; see "Organic Geochemistry," p. 59).

Fine Sand–Silt–Silty Clay Graded Couplets

An ubiquitous feature of Unit II is the occurrence of repeated greenish colored couplets of fine-grained sand, grading progressively upward into silt and silty clay, and finally into clay. The sands, and silts are slightly darker in color (5Y 4/1–5/1) than the clay and silty clay (5GY 5/1–7/1).

The bases of individual couplets are sharp, locally with evidence of slight scouring sediments beneath. Rhythmic couplets dominate all but one of the cores recovered from Unit II. The clays and silty clays forming the upper parts of individual couplets are markedly bioturbated, as

indicated by *Chondrites* burrows, whereas the sands and silts are commonly less bioturbated (Fig. F9). For example, 25 couplets occur in Core 10H. Because these couplets are from APC cores (with complete recovery), a primary (i.e., not drill disturbed) origin is certain. Core 12X, the first XCB core, contains 52 couplets, individually ranging from 1–3 cm to 10–20 cm, with an average thickness of ~10 cm. The fact that these couplets recovered by XCB are effectively identical with those observed in the overlying two APC cores confirms that they are of primary origin.

Smear-slide analysis of the fine-grained sands and silts reveals the presence of quartz, muscovite, clay (unidentified), volcanic rock fragments, volcanic glass, rare pyroxene, planktonic foraminifers, nannofossils, rare radiolarians, carbonate, and opaque grains (see "Site 1109 Smear Slides," p. 115). In addition, XRD analysis indicates the presence of calcite, chlorite, quartz, plagioclase, augite, illite, and amphibole. Indeed, the XRD data indicate a marked change at the top of Unit II with the appearance of ferromagnesian minerals (augite and amphibole) and clays of mixed-layer type (not identified in detail).

Volcaniclastic Silt, Sand, and Granules

The regular couplets are interrupted from 150.5 to 151.9 mbsf by a single interval of greenish gray silty sand interbedded with three very thin to thin volcaniclastic sand beds (each 1–4 cm thick; Section 17X-1). Each of these thin sand beds exhibits a sharp base, and normal grading from sandy silt at the base to very fine silty clay at the top. An interval of sandy silt, 0.9 cm thick, directly beneath (Section 17X-2), comprises sandy silt with volcanic granules. Bioturbation is ubiquitous, with sulfide-rich burrow infills. Smear-slide analysis shows the presence of quartz, biotite, pyroxene, clay (unidentified), volcanic rock fragments, volcanic glass, planktonic foraminifers, rare siliceous spicules, and pyrite.

Very thin (<3 cm) volcanic ash beds are very rare. Beds exhibit sharp bases composed of fine- to medium-grained sand, grading up to silt (e.g., interval 180-1109C-13X-1, 90–95 cm). These ash layers are seen in smear slides to include colorless, acidic volcanic glass, together with some co-genetic phenocrysts ("Site 1109 Smear Slides," p. 115; see Fig. F10). The glass is similar to that found disseminated within the graded couplets described above.

Calcareous Sand (Packstone)

Two graded carbonate beds (12 and 10 cm thick) were observed in Section 13X-3 (e.g., Fig. F11). Also, a single bed of medium-grained packstone, 30 cm thick, was observed in the interval 180-1109C-14X-1, 0–30 cm. This carbonate sand contains abundant calcareous algae, planktonic foraminifers, and shell fragments. The sand is bioturbated throughout with burrows infilled by sandy silt imparting an overall dark gray color. A calcium carbonate analysis yielded a value of 85 wt% (see "Organic Geochemistry," p. 59). In addition, a single clast of carbonate packstone was recovered from interval 180-1109C-11H-1, 0–7 cm.

F9. Graded volcaniclastic silt and sand with abundant burrows, p. 93.

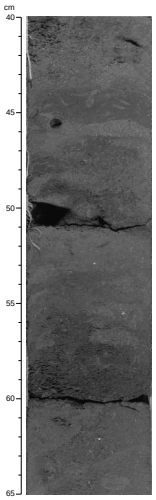

F10. Smear slide of volcaniclastic sand, p. 94.

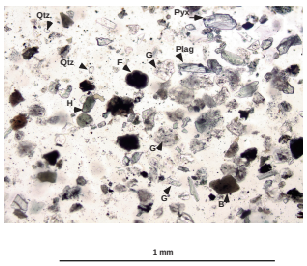

F11. Amalgamated calcareous and volcaniclastic turbidites, p. 95.

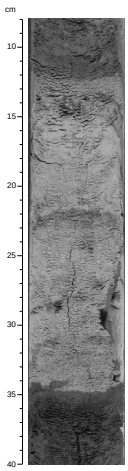

Interpretation

Unit II, of early Pleistocene age, is a rhythmic succession of volcaniclastic sand-silt and silt-clay couplets: these are interpreted as repeated deposits from low-density turbidity currents in deep water (500–2000 m; middle bathyal). Sedimentation rates were very high, estimated as 225 m/m.y. (see "Biostratigraphy," p. 43). The remarkably uniform thickness and grain-size variation of the couplets, without thicker bedded and coarser grained turbidites, could have several possible explanations. These include (1) the fine pyroclastic material was derived from a relatively remote source that accumulated upslope and was then redeposited by turbidity currents and (2) frequent triggering of turbidity currents by volcano-tectonic events or glacioeustatic-related processes. The single interval of more thickly bedded and coarser grained silt, sand, and granules (Core 18X) is viewed as rare deposits from high-density turbidity currents.

In addition, the provenance of a few beds was from a shallow-water origin, as shown by the presence of the rare packstones with calcareous algal and shell fragments. The co-occurrence of common planktonic foraminifers indicates mixing of neritic and pelagic sediment before the final deposition of the packstones as calcareous turbidity current deposits (i.e., as calciturbidites). The volcanic glass in the rare ash layers and admixed with the volcaniclastic turbidity current deposits is of similar acidic (rhyolitic) origin, suggestive of derivation from the Trobriand volcanic arc or volcanoes in the Dawson Strait area as it is for Unit I higher in the succession.

The geophysical and FMS logs confirm that Unit II is composed of alternations of more or less clay- and sand-rich intervals (see "Log Unit L2," p. 71). Thin, graded sand beds are well imaged by the FMS and marked by sharp bases and diffuse tops. The geophysical logs (e.g., gamma ray) indicate the presence of a few sand layers from 156 to 161 mbsf that were not recovered by coring. A carbonate-rich horizon also exists around 161 mbsf that may correspond to one of the thin calciturbidites observed in the cores. Dips of 5°–8° mainly to the south-southwest are common lower in this unit (see "Downhole Measurements," p. 69). This dip might reflect the paleoslope at the time of deposition but is more likely to record postdepositional tilting toward the depocenter of the Woodlark rift basin.

In addition, specific variations in log response (e.g., in the gamma log and photoelectric logs) can be interpreted to indicate the presence of several repeated, discrete cycles (156–161 and 192–200 mbsf) each beginning with calcareous sediment (0.4–2.0 m thick), followed by sand (1.0–4.0 m thick), then clay (up to 5.0 m thick). These cycles could indicate cyclical sedimentation controlled by glacioeustatic sea-level change in the source area, with warmer, wetter interglacial periods being marked by enhanced continental weathering and runoff; alternatively, they could reflect tectonic-controlled events.

Lithostratigraphic Unit III

Description: clayey silt and silty clay interbedded with clayey silt to coarse sand
Interval: Cores 180-1109C-19X through 26X
Depth: 169.70–246.70 mbsf
Age: late Pliocene to early Pleistocene

Unit III is composed of clayey silt and silty clay, with subordinate sand and rare calcareous intervals. Relative to the surrounding units, the recovery was greatly reduced, probably reflecting the difficulty of XCB coring indurated, but unlithified, sediments (see "Operations," p. 4). The recovered sediment was markedly affected by drilling (see "Core Descriptions" contents list). Recovery was low in two cores (24X and 25X), from which mainly unconsolidated medium- to fine-grained sand was recovered, but this interval can be documented using geophysical and FMS logs.

Silty Clay

Greenish gray (5GY 4/1–5/1) silty clay is the dominant sediment type in Unit III. The silty clays are extensively burrowed throughout (mainly *Chondrites*). Smear slides reveal the presence of quartz, feldspar, volcanic glass, carbonate grains, foraminifers, radiolarians, nannofossils, and sponge spicules (see "Site 1109 Smear Slides," p. 115).

Clayey Silt

Clayey silts are very common as normal-graded, thin to very thin beds (<5 cm) and laminae (<1 cm thick), with small-scale burrowing, especially toward the top of individual thin beds. The clayey silt is slightly darker in color than the interbedded silty clay (5GY 5/1 and 6/1). In places, the clayey silt contains scattered sand grains commonly concentrated in burrows. Smear slides reveal mainly planktonic foraminifers, nannofossils, clay, and silt.

Sand

Thin beds of sand occur repetitively in some intervals (e.g., three thin beds in Section 21X-2). Such sands are graded and rarely show planar laminae (e.g., Sections 23X-5, 23X-6, and 23X-7), or cross-laminae (interval 180-1109C-23X-4, 10–13 cm). Also, occasional intervals contain beds of clay-rich sand up to several tens of centimeters thick (Sections 20X-1 through 20X-CC; Fig. F12). However, close inspection shows that such sands are not homogeneous but occur in repeated thin beds several centimeters thick.

In addition, a small number of thin beds are marked by sharp, scoured bases overlain by fine- to medium-grained sand, then passing up into clayey silt and silty clay. These coarser grained, graded units are intercalated with the finer grained, graded clayey silts described above. Examples of thicker and coarser graded beds occur at interval 180-1109C-20X-2, 40–45 cm. By contrast, some sand beds are structureless. Near the base of Unit IV, the sand is unusually dark in color (N4) and contains fragments of wood (interval 180-1109C-24X-1, 0–28 cm). At the base of the unit, fine-grained sand with volcanic rock fragments is also common.

In smear slides, the sands are seen to contain variable abundances of quartz, plagioclase, biotite, muscovite, volcanic fragments, volcanic glass, pyrite, carbonate grains, and plant debris ("Site 1109 Smear Slides," p. 115). In addition, XRD analysis revealed variable abundances of calcite, plagioclase, quartz, augite, chlorite, amphibole, and illite (Table T3). This assemblage remains little changed from Unit II (see "Lithostratigraphic Unit II," p. 11). Samples of silty clay and clay-

F12. Sharp-based, graded volcaniclastic sand beds, p. 96.

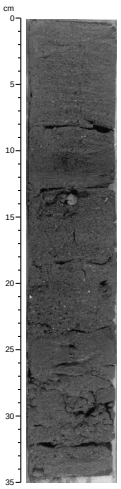

rich silt were found to contain 4–26 wt% calcium carbonate (see "Organic Geochemistry," p. 59).

A thin packstone-wackestone layer was noted in interval 180-1109C-21X-CC, 38–45 cm. This layer consists of alternating grain-supported carbonate (packstone), matrix-dominated (wackestone) carbonate laminae, and thin beds (Fig. F13).

Two thin sections of volcaniclastic sandstone (intervals 180-1109C-21X-1, 40–42 cm, and 26X-CC, 18–20 cm) shed important light on provenance as they contain mixed volcanic, metamorphic, and biogenic components ("Site 1109 Thin Sections"). The volcanic-derived material is variably altered basalt, acidic extrusive rocks, chloritized volcanic glass, zoned plagioclase, quartz, hornblende, and biotite. The metamorphic-derived constituents are polycrystalline quartz, mica schist, and rare serpentinite (Figs. F14, F15). In addition, the bioclastic component includes echinoderm plates, shells, calcareous algae, bryozoans, corals, benthic foraminifers (including rotalines and *Amphistegina*), micritic intraclasts, planktonic foraminifers, phosphatic grains, and pyrite, all set in a micritic matrix.

In addition, a single clast of acidic volcanic rock was noted in interval 180-1109C-22X-1, 0–5 cm.

F13. Parallel-laminated carbonate bed, p. 97.

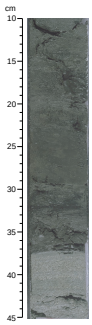

F14. Serpentinite clast surrounded by smaller mineral grains, p. 98.

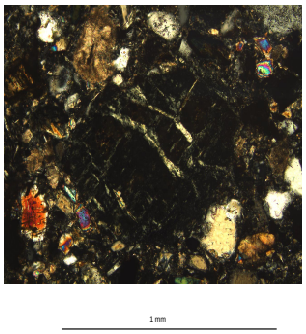

F15. A mica schist grain surrounded by various mineral grains, p. 99.

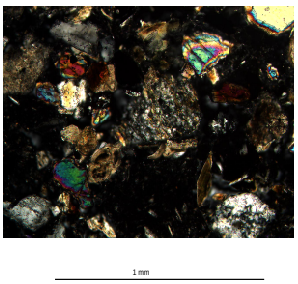

Interpretation

Unit III, of late Pliocene to early Pleistocene age, is interpreted as a deep-water (mid-bathyal 500–2000 m; see "Biostratigraphy," p. 43) succession of pelagic and hemipelagic silty clay interspersed with several types of sediment-gravity-flow deposits. The bottom conditions were continuously aerobic, as shown by the ubiquitous bioturbation (i.e., mainly *Chondrites* and *Zoophycos*). However, the rare occurrence of wood fragments indicates redeposition of terrestrial plant debris by gravity flows.

The background silty clays are interspersed with relatively fine grained, clayey silt deposited from low-density turbidity currents. The sand beds are interpreted as deposits from higher density turbidity currents. Carbonate-rich sands and silts rarely reached the site by redeposition of shallow-water deposits, probably also by turbidity currents. The single clast of acidic volcanic rock is seen as having reached deep water by gravity flow, rather than representing primary pyroclastic lapilli.

The smear-slide analysis revealed that both the fine- and coarse-grained sediments contain variable amounts of fresh plagioclase, quartz, glass, volcanic grains, biotite, and hornblende. The XRD data additionally indicate the presence of a significant amount of mixed-layer-type clays (i.e., probably smectite-chlorite mixed layer) suggesting a distinctive provenance for Unit III.

A relatively coarse grained unit was inferred from 219 to 233 mbsf and was designated as log Unit L2 (see "Downhole Measurements," p. 69). This corresponds to an interval of very limited recovery in Cores 24X and 25X, in which sand, with silt and mud intraclasts, volcanic rock, and wood fragments were recovered. Thin-section study indicated derivation from a source area including evolved arc-type volcanics, metamorphic rocks, and shallow-water carbonates.

Lithostratigraphic Unit IV

Description: clayey silt and silty clay
Interval: Cores 180-1109C-27X through 39X

Depth: 246.7–362.2 mbsf
Age: middle to late Pliocene

Unit IV is dominated by relatively uniform, greenish, clayey silt and silty clay, with scattered planktonic foraminifers. Additional minor lithologies are sporadic volcaniclastic sand and silt, and rare volcanic ash. Recovery was generally good; however, some cores are quite disturbed with the development of drilling biscuits (e.g., Fig. F16). In addition, Unit IV is slightly affected by normal faulting (see "Structural Geology," p. 38). The unit is well documented by both geophysical and FMS logs (see "Downhole Measurements," p. 69).

Details of lithologies follow.

F16. Highly disturbed interval caused by XCB coring, p. 100.

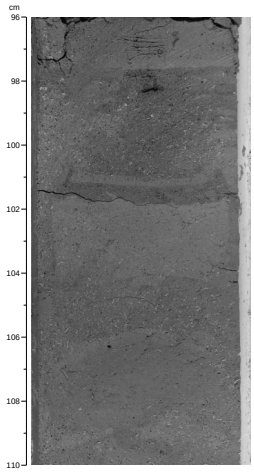

Silty Clay and Clayey Silt

Silty clay and clayey silt, the dominant lithologies, are quite well indurated, with scattered foraminifer tests and detrital grains. Alternating very thin beds are more or less rich in foraminifers. The paler layers are generally richer in calcium carbonate, based on smear-slide analysis. The silty clays are extensively mottled by burrows throughout. *Zoophycos* burrows are generally subordinate to smaller scale *Chondrites* burrows but are rarely conspicuous (e.g., Section 30X-1). Some of the larger *Zoophycos* burrows are infilled with sand grains. Sulfide mottling was commonly observed.

In smear slides, quartz, feldspar, biotite, volcanic glass, opaque grains, pyrite, foraminifers, and nannofossils were observed (see "Site 1109 Smear Slides," p. 115). One thin section indicates the presence of quartz, feldspar chlorite, epidote, pyrite, acidic volcanics, and planktonic foraminifers (interval 180-1109C-28X-1, 4–8 cm) ("Site 1109 Thin Sections"). Analyses of calcium carbonate revealed values of 8.7–39 wt% (see "Organic Geochemistry," p. 59).

XRD analysis indicates the presence of calcite, plagioclase, and quartz in most samples, with, in addition, chlorite, illite, augite, and amphibole appearing near the base of the unit (see Table T3). Unlike Unit III, mixed-layer-type clays were not detected.

Sedimentary structures, other than bioturbation, are rare. Rarely, traces of grading and parallel lamination have survived extensive bioturbation (e.g., Section 27X-5). Also, mainly in the lower part of the unit, thin couplets (<5 cm thick), composed of clayey silt grading into burrowed clay, are preserved.

Sand and Silt

There are infrequent occurrences of thin-bedded sand and silt. These beds are characterized by sharp bases, normal grading, and common occurrences of parallel lamination. In addition, there are sporadic occurrences of coarse- to medium- and fine-grained sand. The sand is mainly present in the upper and lower parts of the unit. Relatively coarse grained sand is present in interval 180-1109C-28X-1, 142–150 cm, and in Cores 31X and 32X. Examples of fine-grained sand are seen in intervals 180-1109C-27X-4, 141–142 and 149–151 cm, as well as in 31X-1, 0–148 cm. Elsewhere, the sand is seen only as disseminated diffuse patches throughout clay and silty clay, with no preserved bedding (e.g., Section 30X-3). Very rarely, convolute lamination was observed in the lower part of the unit (e.g., interval 180-1109C-29X-3, 43–50 cm).

Locally, small shell fragments are also seen within sandy silt (Sections 28X-2 and 32X-5).

In smear slides, the sand is observed to consist mainly of volcaniclastic constituents with particles of colorless volcanic glass, in addition to quartz, plagioclase, biotite, and hornblende, together with particles of organic and inorganic calcite.

Volcanic Ash

Very rarely, concentrations of volcanic glass as thin partings were sufficiently abundant for the interval to be termed volcanic ash in the "barrel sheets" (see the **"Core Descriptions"** contents list; e.g., intervals 180-1109C-30X-1, 106–108 cm; 31X–1, 148–150 cm; and 31X-2, 0–4 cm). Study of smear slides indicates the presence of quartz, biotite, clay, volcanic rock fragments, volcanic class (colorless), hornblende, and minor pyroxene, together with foraminifers, nannofossils, and rare siliceous spicules (see **"Site 1109 Smear Slides,"** p. 115).

Volcanic glass shards are turbid under plane-polarized light and speckly under crossed nicols, suggesting advanced devitrification. Many volcanic glass fragments have diffuse edges. The glass within basaltic lithoclasts is similarly altered. In addition, many individual crystals above 360 mbsf are irregular, internally turbid (due to alteration), with embayed margins, locally gradational to clay. Many of these crystals are subrounded and abraded, in contrast to well-preserved euhedral morphologies below 380 mbsf (see **"Lithostratigraphic Unit VI,"** p. 20).

Interpretation

Unit IV records deep-water hemipelagic calcareous deposition and fine-grained turbidites deposited in upper bathyal depths (150–500 m; Sections 30X through 39X), then mid-bathyal depths (500–2000 m; Sections 27X through 30X) during middle Pliocene to late Pliocene time. Sedimentation rates were initially 160 m./m.y. but decreased to 65–70 m./m.y. (see **"Biostratigraphy,"** p. 43). Bottom-water conditions remained aerobic throughout. Occasional turbidity currents with sand and silt-rich loads reached the depositional site leading to deposition of sand and silt. Sands and silts were subsequently burrowed, such that they are rarely preserved as discrete beds. The sands and silts and the disseminated detrital grains (mainly quartz, plagioclase, biotite, and hornblende) are all of volcaniclastic origin. In contrast to Unit III, volcanic glass is a minor constituent. Rare thin, glass-rich layers are seen as volcanic ash that was reworked by gravity flows and may not record contemporaneous volcanism.

Interpretation of the conventional logs (gamma and porosity) is in keeping with the lithostratigraphy. The sediments are clay rich above 599 mbsf, with peaks in the thorium and potassium logs generally corresponding to rare volcaniclastic sandy layers (~340 mbsf; within log Unit L5; see **"Log Unit L5,"** p. 71). The FMS data reveal more and less clay-rich intervals (e.g., less clay rich at ~250 mbsf) and more sandy layers (e.g., ~341 mbsf). Thin resistive layers on the FMS can in general be correlated with calcareous, sandy parts of turbidites in the cores, although one-to-one correlation is difficult, even where recovery is high, as there is little distinctive bed-thickness variation. Around 305–320 mbsf, dips of 5°–10° to the south-southeast and south-southwest are observed (see **"Downhole Measurements,"** p. 69).

Lithostratigraphic Unit V

Deposition: clayey siltstone and silty claystone interbedded with volcaniclastic sand
Interval: Cores 180-1109C-40X through 41X and Cores 180-1109D-1R through 4R
Depth: 362.2–375.7 mbsf (Hole 1109C) and 352.8–387.6 mbsf (Hole 1109D)
Age: middle Pliocene

A boundary between Unit IV and Unit V was adopted between Cores 180-1109C-39X and 40X, based on the significant appearance of volcaniclastic sand layers in Cores 40X and 41X. In Hole 1109D, Unit V occupies Cores 180-1109D-1R through 4R (see Fig. **F1**). The conventional logs (i.e., gamma) indicate a mainly clay-rich deposit with occasional peaks in the radioactivity logs (i.e., Th) correlating with volcaniclastic intervals observed in the cores. The FMS data for Cores 180-1109D-1R through 4R are not usable because of poor hole conditions.

XCB vs. RCB Coring

Cores down to 375.7 mbsf were recovered by XCB, whereas cores from 352.8 mbsf onward were obtained by RCB. Thus, there was an overlap of ~23 m between the intervals recovered by XCB and those by RCB (from 352.8 to 375.7 mbsf). The recovery by RCB was good to excellent. Note: Correlation of lithologies using physical properties data indicate an offset of ~0.5 m between the values of mbsf quoted for Holes 1109C (APC/XCB) and 1109D (RCB) (see **"Hole-to-Hole Correlation,"** p. 68). The excellent recovery by rotary drilling reflects the relatively uniform, well-cemented calcareous nature of the succession.

Overlap between the parts of the succession recovered by XCB and RCB drilling proved useful in resolving uncertainties as to whether repetitive silt-clay units, ~5 cm thick, were either primary thin beds of more or less clay- and silt-rich composition, or drilling biscuits (a drilling artifact). The controversial silt-clay units are well developed throughout the XCB-cored succession but disappear in the overlapping interval recovered by rotary drilling, effectively proving an origin of the repetitive silt-clay intervals as a drilling artifact. Apparently, the silty clays were more lithified than the clayey silts, and the latter were fluidized by XCB drilling and injected as homogenous silty material every few centimeters to form characteristic drilling biscuits (see Fig. **F16**). Notwithstanding this, occasional graded sand-silt and silt-clay graded beds of primary origin are indeed present within the rotary cores, and these can also be recognized between drilling biscuits in that part of the succession recovered by XCB.

Unit V is characterized by relatively uniform, greenish gray, clayey siltstones and silty claystones interbedded with volcaniclastic silt and sand layers, rare volcanic ash, and quartz-rich sand layers. The core recovery was excellent (>90%); however, cores are disturbed with the development of drilling biscuits (see the **"Core Descriptions"** contents list).

Clayey Siltstone and Silty Claystone

The silty claystone is olive green, calcareous, burrowed, and silty, with scattered detrital sand grains. *Zoophycos* and *Chondrites* burrowing

is commonly present. Calcium carbonate content in the silty claystones of Unit V range from 21 to 32 wt%. By contrast, the volcaniclastic sediments are relatively low in calcium carbonate (<1 wt%; see "Organic Geochemistry," p. 59).

Study of smear slides of the silty claystones indicates the presence of quartz, clay, plagioclase, volcanic glass, pyrite, planktonic foraminifers and nannofossils, inorganic calcite crystals, and scattered siliceous sponge spicules (see "Site 1109 Smear Slides," p. 115). XRD analysis indicates the presence of calcite, plagioclase quartz, illite, chlorite, amphibole, and augite, together with smectite. In addition, alkali feldspar was rarely identified (see Table T3).

Volcaniclastic Sand

Unit V contains seven volcaniclastic beds within Cores 180-1109C-40X through 41X and 58 volcaniclastic layers in Cores 180-1109D-1R through 4R. The thicknesses of these beds range from 1 to 10 cm. The bases of individual volcaniclastic sand beds are mainly sharp and scoured, whereas diffuse tops are common. In places, the bases of individual beds are disrupted by bioturbation (e.g, Fig. F17). Smear-slide analysis reveals a mixture of colorless volcanic glass and sand-sized phenocrysts of amphibole, pyroxene, plagioclase, quartz, and biotite. The volcanic glass grains range from 50 to 300 µm in size. The finer grained glass is mainly composed of platy shards, whereas the coarser material is commonly highly vesicular glass.

A small number of thin sections of volcaniclastic sandstones (see "Site 1109 Thin Sections") reveal the presence of zoned plagioclase, quartz, biotite, pyroxene, hornblende, rare microcline, and basaltic, andesitic, and acidic volcanic grains, also colorless volcanic glass (Fig. F18), all set in a micritic matrix with planktonic foraminifers. Some of the volcaniclastic beds also contain biogenic fragments (e.g., echinoderms). Volcaniclastic grains are also scattered throughout adjacent silty claystone and clayey siltstone. Occasional burrows are filled with volcaniclastic sand.

Volcanic Ash

Unit V contains four volcanic ash layers 1–7 cm thick. An ash layer in Section 180-1109C-41X-1 is composed of almost entirely (>90%) less altered, colorless volcanic glass. The main glass morphologies are platy and bubble wall shards. Highly vesicular glass is rarely observed. The grain size ranges from 100 to 200 µm. In addition, an ash layer in interval 180-1109D-4R-2, 71–72 cm, is characterized by abundant highly vesicular glass (Fig. F19). Phenocrysts of pyroxene, amphibole, biotite, and plagioclase are only rarely observed within the volcanic ash, in contrast with the volcaniclastic sandstone described above.

Interpretation

Unit V, of middle Pliocene age, accumulated in an upper bathyal (150–500 m) setting at a sedimentation rate of ~200 m/m.y. (see "Biostratigraphy," p. 43). Although relatively condensed, this unit is seen to considerably thicken downslope toward the depocenter of the rift basin (see "Drill Sites," p. 2, in the "Leg 180 Summary" chapter). The bioturbated silty clay and clayey siltstones are interpreted as background calcareous hemipelagic and maybe fine-grained turbidite sedi-

F17. Normal-graded sandstone with a sharp, scoured base, p. 101.

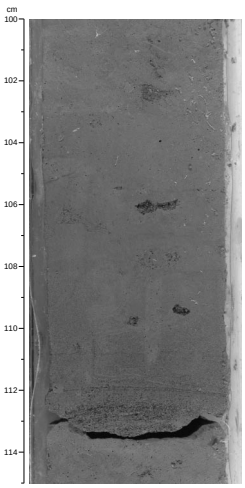

F18. Zoned plagioclase crystals set in siltstone matrix, p. 102.

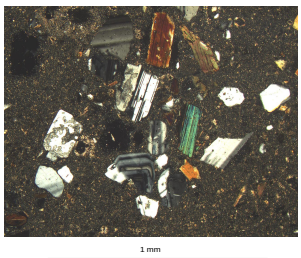

F19. Smear slide dominated by colorless, vesicular glass, p. 103.

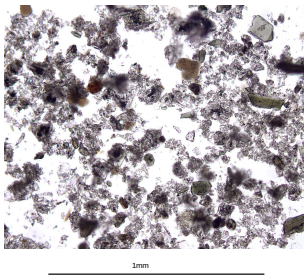

ments on a well-oxygenated seafloor. By contrast, the numerous graded glass-rich sands (with a few ash layers) are seen as volcanic-derived material (i.e., of epiclastic origin) that was redeposited by turbidity currents. They probably relate to a discrete eruptive event in middle Pliocene time, as discussed in the summary section of this chapter. In addition, the volcaniclastic sands are interpreted as epiclastic in origin, and derived from a calc-alkaline arc-type terrain.

The conventional log unit data suggest that Unit VI is relatively fine grained (recognized as log Unit L5; see "Log Unit L5," p. 71); however, this masks the occurrence of discrete thin volcaniclastic beds that characterize Unit V.

Lithostratigraphic Unit VI

Description: clayey siltstone and silty claystone interbedded with clayey siltstone to coarse-grained sandstone
Interval: Cores 180-1109D-5R through 24R
Depth: 387.6–570.4 mbsf
Age: early to middle Pliocene

Unit VI is distinguished from Unit V (see "Lithostratigraphic Unit V," p. 18), by clayey siltstone and silty claystone, with subordinate thin beds of fine- to medium-grained sandstone/siltstone. The unit is the thickest encountered at Site 1109 (~175 m) and is remarkably homogeneous except for a progressive increase in carbonate below 520 mbsf. It is largely equivalent to log Unit L6 (see "Log Unit L6," p. 72). The hole conditions were good throughout this interval, yielding high-quality logs.

Recognition of the boundary between Units V and VI was not straightforward; no marked lithologic change is apparent in the cores for 10 m above and below the boundary picked at the base of Core 4R (387.6 mbsf). However, several lines of evidence suggest that an important boundary does in fact exist around 390 mbsf: (1) In smear slides and thin sections, the bulk composition of the sediment above and below 380 mbsf is similar, derived from a volcanic arc-like provenance. However, volcanic glass, lithic fragments, and individual crystals are less altered below 380 mbsf, and no metamorphic-derived material (e.g. muscovite schist; polycrystalline quartz) or mixed-layer clays are present. (2) Magnetic susceptibility and porosity drop sharply over <5 m (see "Magnetic Susceptibility," p. 48, and "Density and Porosity," p. 62). (3) Significant changes in sediment character are identified on geophysical logs (see "Interpretation," p. 13; also see "Downhole Measurements," p. 69).

Details of the individual sedimentary lithologies present in Unit V follow.

Silty Claystone

The silty claystone is olive green (10Y 6/2), calcareous, and silty, with scattered detrital sand grains. This silty claystone is highly burrowed, commonly with concentrations of medium- to coarse-grained sand within individual relatively large (centimeter-sized) burrows (mainly *Zoophycos*). Elsewhere, *Chondrites* burrowing predominates, giving rise to a weak color mottling. Small shell fragments are rare (interval 180-1109D-7R-3, 10–50 cm).

Determinations of calcium carbonate indicate relatively constant levels above 520 mbsf of 20–30 wt%, increasing to 30–40 wt% below that, with an average of 25–30 wt%. The calcium carbonate abundance generally increases downward (see "Organic Geochemistry," p. 59).

Study of smear slides shows that the silty claystones consist of quartz, clay (unidentified), feldspar, volcanic glass, and pyrite, as well as foraminifers and nannofossils, inorganic calcite crystals, and siliceous sponge spicules (see "Site 1109 Smear Slides," p. 115).

XRD analysis indicates the presence of calcite, plagioclase, and quartz as the dominant constituents of most samples (see Table T3). Amphibole is present in many samples, whereas pyroxene was rarely detected. The clay minerals are dominantly illite, with variable occurrences of chlorite; also, smectite is restricted to high in the unit (above Core 7R). In addition, K-feldspar and aragonite are locally present (see Table T3).

Sandstone and Siltstone

Subordinate, thin to very thin sandstone and siltstone beds, typically <6 cm thick, and rarely more than 10 cm thick, are present throughout the claystone. Where still well preserved, these sandstones exhibit sharp bases, locally with scouring into silty clay beneath (e.g., intervals 180-1109D-11R-3, 68–72 and 87–89 cm; see also Fig. F20). Several of these scour features could be flutes (e.g., interval 180-1109D-7R-3, 79–81 cm). Coarse- to fine-grained, very thin beds and thin laminae of sandstone with sharp bases and tops were rarely observed (Fig. F21). In addition, occasional occurrences of several volcaniclastic, graded beds and laminae were noted. Very rarely, granules of lithic fragments, quartz, and ferromagnesian minerals are present at the base of normal-graded beds (interval 180-1109D-13R-2, 46–47 and 123–124 cm). Typical sandstones are graded over several centimeters and pass up into clayey siltstone and then into silty claystone. Rarely, plane laminations are observed (e.g., interval 180-1109D-9R-3, 20–23 cm).

The sandstone and siltstone are commonly highly burrowed, obscuring original bedding and internal structures. Where intense burrowing has taken place, all intermediaries are seen between intact thin-graded beds (as above) and patches of disseminated sand within claystone (e.g., Section 180-1109D-20R-4). In the lower part of the unit scattered shell fragments, occasional intact small gastropods, and carbonate grains are observed (e.g., Cores 22R through 23R).

In smear slides, the sandstones and clayey siltstones are observed to contain quartz (commonly undulose), fresh plagioclase, biotite, and common green hornblende, together with pyrite, foraminifers, and nannofossils. Pyrite both fills foraminifer tests and occurs as scattered framboids. Some samples contain devitrified volcanic glass. The relative abundance of ferromagnesian grains differs from sandstone to sandstone, with some being relatively richer in biotite or hornblende, respectively ("Site 1109 Smear Slides," p. 115).

Study of thin sections confirmed the presence of the constituents mentioned above ("Site 1109 Thin Sections"). However, the abundance of quartz relative to feldspar was overestimated in the smear-slide analysis, and several of the sandstones are arkoses. Additionally, thin sections revealed the presence of zoned orthoclase, common small devitrified fragments of basic and rare acidic extrusive rocks, rare benthic foraminifers, and shell fragments. Small biotite laths are commonly concentrated in laminae. There is also rare evidence of repetitive

F20. Sharp-based, massive laminae of coarse- to fine-grained sand, p. 104.

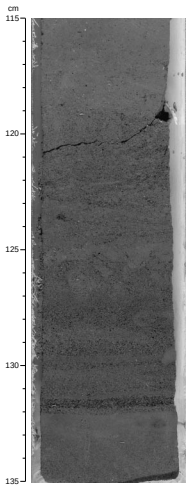

F21. Graded beds and laminae of volcaniclastic sandstone and siltstone, p. 105.

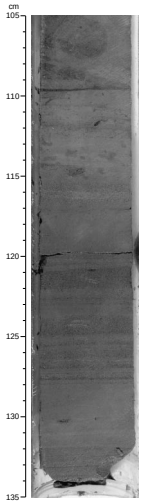

partings with sharp bases and tops, and small-scale ripples (interval 180-1109D-22R-1, 57–60 cm).

Volcanic Ash

Five volcanic ash layers occur between 465 and 485 mbsf. They are mainly composed of colorless acidic glass, but a minor amount of brown glass shards is present as well. Shards in these layers exhibit thin platy and bubble wall morphologies. Most of the glass shards are fresh, with minor signs of devitrification in some places.

Interpretation

This unit can be interpreted with confidence as recovery was excellent (for the "barrel sheets," see the **"Core Descriptions"** contents list). Unit VI, of early to middle Pliocene age (see **"Biostratigraphy,"** p. 43), accumulated as hemipelagic carbonate clay in a quiet upper bathyal setting (150–500 m), interspersed with the occasional arrival of a mainly low- but, rarely, high-density turbidity current. The estimated sedimentation rate, at 312 m/m.y., was relatively high (see **"Biostratigraphy,"** p. 43). The source was dominantly volcanic related (basalt-andesite), but minor amounts of neritic carbonate material (e.g., gastropods) also reached the site of deposition. There is evidence of minor current reworking to produce repetitive lamination and rare small ripples. The seafloor was well oxygenated and was extensively bioturbated, to such an extent as to largely or completely obliterate primary depositional structures, and a slope setting is inferred.

The geophysical logs (e.g., gamma logs) are interpreted to indicate the presence of more and less sandy and clay-rich layers. Carbonate content increases below 500 mbsf, based on the photoelectric log data. On the FMS (static normalized), Unit VI is distinguished by a well-layered structure, with numerous 5- to 10-cm-thick, more resistant layers. These show sharp bases and gradational tops and correlate with the turbidity current deposits seen in the cores. In contrast to the variation in the units above and below, the relatively monotonous log response attests to relatively constant depositional conditions within Unit VI. Bedding is less apparent near the base of the unit (below 505 mbsf).

Lithostratigraphic Unit VII

Description: sandstone, packstone, and grainstone
Interval: Core 180-1109D-25R through Section 35R-4, 74 cm
Depth: 570.4 to 671.8 mbsf
Age: early to middle Pliocene

Unit VII is recognized on the basis of a generally coarser grain size and markedly increased carbonate content, up to 75 wt%, based on chemical analysis (see **"Organic Geochemistry,"** p. 59). The recovery was initially very good (around 80%) but decreased sharply downward to around 10%–25%. This results in considerable uncertainty concerning the identity of the intervals that were not recovered. These deficiencies were largely rectified by the log data, especially the photoelectric log that indicates changes in carbonate content (see **"Downhole Measurements,"** p. 69).

Unit VII consists almost entirely of well-cemented mixed carbonate-siliciclastic rocks. The interval from 599 to 672 mbsf is divided into

three parts: the upper part of the unit was classified as calcareous (bioclastic) sandstone (570–599 mbsf, with 40–50 wt% calcium carbonate); the middle part as slightly calcareous sandstone (599–643 mbsf, with ~20 wt% calcium carbonate); whereas the lower part is bioclastic limestone packstone-grainstone) (643–672 mbsf; 40–80 wt% calcium carbonate).

The intergradational lithologies found in Unit VII follow.

Silt and Sandstone (Predominately Siliciclastic)

Greenish gray (5GY 4/1) calcareous silty sandstone occurs extensively in the upper part of the unit. This sandstone contains ~20–25 wt% calcium carbonate (see "Organic Geochemistry," p. 59). The sandstone varies from fine to medium grained at the top of the unit (Cores 25R-1 through 3), becoming coarser downward (Fig. F22). The sandstone is moderately to strongly burrowed. Large *Zoophycos* burrows are commonly infilled with coarse siliciclastic grains, as observed in overlying units (see "Lithostratigraphic Unit VI," p. 20). The fine- to medium-grained sandstone is mainly well sorted. Planar lamination, cross-lamination, wavy lamination, and herring-bone-type lamination (e.g., Section 34R-6) are developed.

The study of smear slides and a small number of thin sections indicates that many of the sandstone are rich in feldspar, quartz, biotite, hornblende, and pyroxene (in decreasing order of occurrence), together with organic and inorganic calcite and foraminifers ("Site 1109 Thin Sections"). Devitrified volcanic glass and tabular crystals of orthoclase were occasionally observed. In addition, carbonaceous detritus is present (e.g., Core 25R). Thin-section analysis additionally indicated the presence of lithoclasts of basic-acidic igneous rock and rare altered basic glass (e.g., Fig. F23).

XRD analysis reveals the presence of calcite, quartz, plagioclase, amphibole, and illite, with occasional pyroxene and aragonite (Table T3). This composition is little changed from Unit VI, except for the abundant calcite.

Packstone-Grainstone

Most of the mainly calcareous rocks observed (with subordinate volcaniclastic grains, as above) are termed packstones and grainstones. Analyses of calcium carbonate are in the range of 45–75 wt% (see "Organic Geochemistry," p. 59). The carbonate component is seen in smear slides ("Site 1109 Smear Slides," p. 115) and a small number of thin sections ("Site 1109 Thin Sections") to be composed of shell fragments, micritic grains, minor calcite spar, planktonic (and rare benthic) foraminifers, rare echinoderm plates, bryozoans, and nannofossils. The packstone-grainstones are well sorted and cemented by calcite spar. Pyrite occurs as scattered cubes in the matrix and as infills of foraminifer tests. Both planktonic and agglutinating benthic foraminifers were noted. Exceptionally, small angular lithoclasts of plagioclase-hornblende-phyric andesite with a dark unaltered mesostasis were noted, together with very small fragments of altered basalt and isolated olivine crystals (Sample 180-1109D-32R-2, 101–103 cm). The appearance of the plagioclase and amphibole crystals is very similar to that of the scattered grains that occur much more widely throughout this unit.

A number of coarse-grained sand beds of granule- to pebble-size carbonate particles were observed (Fig. F24). For example, paraconglomer-

F22. Volcaniclastic sandstone showing traces of primary bedding, p. 106.

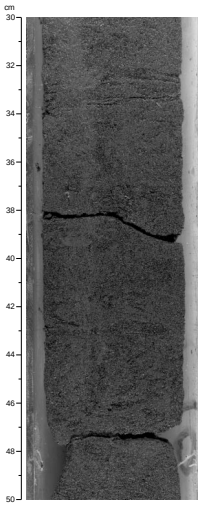

F23. Unaltered basaltic andesite clast set in a wackestone, p. 107.

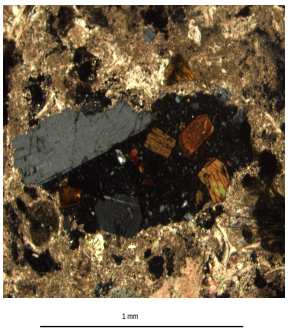

F24. Calcareous rock composed of shell and carbonate fragments, p. 108.

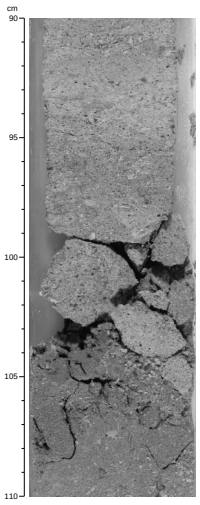

ate in the intervals 180-1109D-27R–1, 8–22 and 65–90 cm, comprises shell fragments, calcite, coral, calcareous green algae (oncolites), calcareous red algae (rhodoliths), echinoderm plates, and detrital grains. The shells are thin and are mainly the remains of bivalves, a few of which are still articulated. Several rugose coral fragments were recovered with an intact calyx (e.g., intervals 180-1109D-29R-4, 4–8 and 37–39 cm; Fig. F25). These coarser bioclastic intervals are poorly sorted and cemented by calcite spar, with admixed siliciclastic grains, as revealed by a smear slide (**"Site 1109 Smear Slides,"** p. 115).

In the upper part of the unit, two pebbles of basalt were recovered (Section 27R-1); also lower in the unit (e.g., intervals 180-1109D-27R-4, 22–23 cm, and 32R-2, 102–103 cm), rare small (<1 cm) well-rounded, altered, basalt pebbles were recovered. In addition, small (<0.3 mm) well-rounded lithic clasts were observed in thin sections (see **"Site 1109 Thin Sections"**).

F25. Cross section of a rugose coral in packstone, **p. 109.**

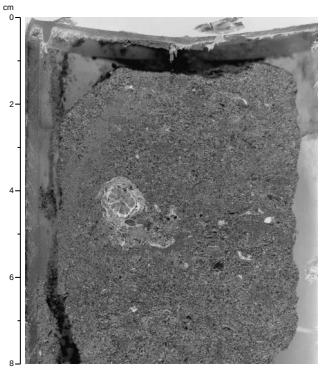

Interpretation

The siliciclastic-carbonate sediments reflect mixing of sediment derived from volcanic-related and neritic carbonate source materials. The sands show evidence of current reworking in a well-oxygenated high-energy environment. Paleontological evidence indicates shallow marine (i.e., neritic; <150 m deposition), based mainly on evidence of benthic foraminifers (see **"Benthic Foraminifers,"** p. 47). The carbonate grains were largely derived from corals and algae, presumably reefal, although we have no evidence of the location, or morphology, of any contemporaneous reefs.

The volcaniclastic components were mainly derived from basic-intermediate composition extrusive igneous rocks, as indicated by the occurrence of small basalt-andesite lithoclasts. The well-rounded shape of many of these clasts suggests that these were reworked and/or eroded before final deposition. In contrast to overlying units, volcanic glass–rich intervals were not observed.

One problematic aspect is the apparently abrupt nature of the change from shallow-water deposition in Unit VII to deep-water (upper bathyal) deposition in Unit VI. This may in part reflect reworking, such that neritic sediments were reworked to water depths of >150 m in the upper part of the unit (without recording the water depth of final deposition).

Interpretation of the geophysical logs, particularly the photoelectric log, reveals additional information on lithologic variation within Unit VII that was not apparent from this generally poorly recovered section (see **"Comparison of Core Data with Results of Downhole Measurements,"** p. 69). The upper part of the unit (599–643 mbsf) contains intervals that on geophysical and FMS logs are interpreted as well-bedded sandstones, and these correlate with volcaniclastic sandstone in the cores. The highest values of calcium carbonate as inferred by the photoelectric log occur in the lower part of the lithostratigraphic unit around 643–675 mbsf. Small peaks in the uranium and potassium logs can be correlated with thin intervals rich in biotite and ferromagnesian minerals (e.g., pyroxene and olivine). Also, rare minerals (e.g., zircon), if present in trace amounts, could influence the log response. The FMS image of the above carbonate-rich interval is highly resistant and "blotchy," interpreted as concentrations of bioclastic material and isolated, angular clasts yielding bright patches.

Lithostratigraphic Unit VIII

Description: dark colored silty claystones and clayey siltstones with shell plant and wood debris
Interval: Sections 180-1109D-35R-4, 74 cm, through 39R-3
Depth: 671.8–708.9 mbsf
Age: undated

Unit VIII is characterized by an abrupt change (i.e., at interval 180-1109D-35R-4, 74 cm) from bioturbated, mixed volcaniclastic-carbonate rocks (sandstone-packstone) to much finer grained, massive calcareous silty claystone. Colors are mainly dark greenish gray (5GY 4/1). Interpretation of the geophysical and FMS log data suggests that the succession contains sand/mud intercalations, although the hole conditions were poor (see "Downhole Measurements," p. 69). For the total unit, bioturbation ranges from absent (e.g., Core 35R) to only very weak, in contrast to all the overlying units. Calcium carbonate varies up to 65 wt% (see "Organic Geochemistry," p. 59).

The lithologies present in Unit VIII follow.

Clayey Siltstone

The most abundant lithology of Unit VIII is greenish calcareous clayey siltstone, with variable abundances of thin shells and plant material (Fig. F26). A weak bedding fabric is defined by subparallel orientation of shell fragments. Monosulfide mottling is occasionally present. The shell fragments are the remains of bivalves and occasional gastropods. They range from isolated to concentrations of fragmented, randomly oriented shells (e.g., intervals 180-1109D-36R-1, 20–23, 43–45, and 87–89 cm). Rarely, shells are still articulated (e.g., interval 180-1109D-36R-6, 0–110 cm). Occasional slightly coarser grained intervals (interval 180-1109D-37R-2, 73–149.5 cm), and rare wavy laminae of sand grains are also present (i.e., interval 180-1109D-39R-3, 49–86 cm).

In smear slides, the clay-rich siltstones are seen to comprise quartz, plagioclase, mica, hornblende, glauconite, possible orthoclase, clay (unidentified), fine-grained basic volcanic rock fragments, and pyrite framboids, together with organic and inorganic calcite, and scattered small foraminifers (including globigerines; see "Planktonic Foraminifers," p. 45).

In addition, XRD analysis of siltstones and one sample of sandstone revealed the presence of plagioclase, pyroxene, quartz, amphibole, smectite, and illite. Smectite appears for the first time since the upper part of Unit V (Table T3).

Silty Claystone

Slightly finer grained intervals of silty claystone also occur (e.g., Section 36R-CC). The silty claystone includes local thin (<3 mm) anastomosing laminae composed of finely divided carbonaceous fragments (lignite; e.g., interval 180-1109D-38R–1, 121–133 cm; Fig. F27).

Sandstone

Sandstones are present as rare intervals up to 40 cm thick (e.g., interval 180-1109D-36R-1, 0–7 cm). These sandstones generally exhibit sharp bases (e.g., interval 180-1109D-38R–1, 7–12 cm) and contain

F26. Silty claystone with shell fragments (without bioturbation), p. 110.

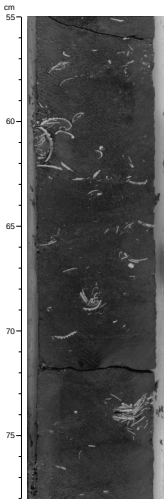

F27. Burrowed silty claystone with local concentrations of shell fragments, p. 111.

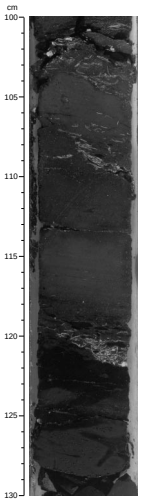

common laminations rich in wood debris (described below). In addition, fine-grained basic rock fragments are present (interval 180-1109D-38R-1, 7–12 cm; see "Site 1109 Thin Sections").

In smear slides ("Site 1109 Smear Slides," p. 115) and a small number of thin sections ("Site 1109 Thin Sections"), the sandstone is arkosic, with angular grains of plagioclase (zoned), quartz (undulose), sericite (i.e., unresolvable mica), biotite, hornblende, rare pyroxene and microcline, organic and inorganic calcite, pyrite, and organic (woody) debris (e.g., Sample 180-1109D-38R-4, 10–14 cm). In addition, common lithoclasts of altered glassy basalt, and rare acidic volcanic rock fragments are observed (e.g. Samples 180-1109D-38R-2, 12–18 cm.

Volcaniclastic Sandstone

A 49-cm-thick dark bluish gray well to moderately sorted, fine-grained volcaniclastic sandstone bed occurs in interval 180-1109D-39R-3, 0–49 cm. A thin section of the sandstone shows it to contain angular grains of quartz, feldspar, clinopyroxene, amphibole, acidic volcanics, glass shards, and rare intraformational siltstone ("Site 1109 Thin Sections"). The glass shards and acidic volcanic fragments are commonly highly altered.

Coal

Terrestrial organic matter ranges from laminae composed of fine-grained plant-derived material (i.e., macerals), to discrete fragments (i.e., woody stems). The plant-rich material is sufficiently diagenetically advanced to be termed lignite (low-grade bituminous coal). Terrestrial matter is well developed (e.g., intervals 180-1109D-37R-2, 65–75 cm, and 38R-2, 10–25 cm) as thinly interlaminated coaly material and claystone (see Fig. F28). Unusually, burrowing has disrupted these coal-claystone laminations.

A number of coaly intervals are composite when examined in detail, being composed of alternations of lignite-dominated laminations, claystone-dominated laminations, and fine-grained sandstone-dominated laminations (i.e., intervals 180-1109D-38R-1, 91.5–133 cm, and 38R-2, 0–99 cm. In one case, such a composite unit indicates a generally fining upward unit (i.e, interval 180-1109D-39R-3, 49–86 cm).

F28. Interlaminated lignite with silty claystone and sandstone laminations, p. 112.

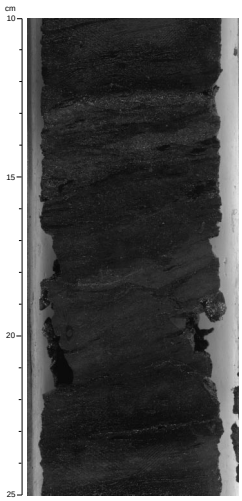

Dolostone

Rare thin intervals were described in the cores as being dominated by small carbonate rhombs. Smear-slide analysis confirms that these carbonate rocks (e.g., interval 180-1109D-37R-1, 7–12 cm) are silt-sized dolomite rhombs with rare quartz, plagioclase, biotite, and accessory minerals.

Interpretation

A number of lines of evidence suggest that Unit VIII accumulated in a marginal lagoonal setting: (1) The sediments are mainly fine grained with abundant clay, suggesting deposition in quiet waters. (2) The shell debris shows little, or no, reworking by currents. (3) Stenohaline (i.e., normal marine salinity) organisms (e.g., corals and echinoderms) are absent, again in contrast to Unit VII. However, the presence of a few benthic foraminifers tolerant of reduced salinities (see "Benthic Fora-

minifers," p. 47) indicates that some connection to the open sea existed. The possibility that the foraminifers were washed in by storms is unlikely as they occur disseminated through fine-grained sediments, and the shell deposits do not include coquina (shell concentrates) characteristic of storm influence. The thin-shelled bivalves and occasional gastropods also may include forms tolerant of reduced, or fluctuating, salinity. (4) The abundant woody material indicates that a copious supply of plant material was available. (5) The near absence of burrowing indicates that the near-surface sediments were characterized by low-oxygen conditions, consistent with a quiet, protected depositional setting. Such conditions would also favor the diagenetic preservation of fine woody and plant material. And (6), the local occurrence of dolostones is indicative of hypersaline conditions. The presence of volcaniclastic sandstone, altered glass, and rare acidic volcanic pebbles is consistent with a marginal, near-land setting.

Interpretation of the log data is hampered by poor hole conditions. However, the FMS images reveal more resistant and less resistant intervals up to several meters thick that are interpreted as sand/mud alternations. In contrast to the underlying units, conglomerate is not imaged (see "Lithostratigraphic Unit IX," p. 27). In addition, on the radioactivity logs, elevated uranium (682–707 mbsf) is interpreted as an indication of anoxic conditions, in keeping with the large amount of reduced organic matter present. Despite the poor hole conditions, the FMS data indicate the presence of sandy and muddy alternations locally, in keeping with the core recovery.

Unit VIII, therefore, is seen as forming in a marginal lagoonal setting subject to salinity fluctuations, ranging from near marine, to locally freshwater, and evaporitic. The nature of any contact between the inferred lagoon and the open sea is unknown, but might have been igneous basement associated with fringing reefs. This setting is suggested by the presence of rare basaltic clasts within Unit VII and by coral in Unit VIII, above. A more detailed scenario is discussed in the concluding section (see "Depositional History," p. 31).

Lithostratigraphic Unit IX

Description: clayey siltstone and sandstone
Interval: Sections 180-1109D-39R-CC through 42R-CC, 30 cm
Depth: 708.9–737.1 mbsf
Age: undated

Unit IX is characterized by a marked change in sediment type, away from the dark-colored organic-rich fine-grained sediment of Unit VIII to a more uniform greenish gray (5G 5/1) clayey siltstone. The recovery was poor, both in amount and quality (see "Core Descriptions" contents list). However, the geophysical and FMS logs indicate that this unit contains a substantial amount of conglomerate that was not cored.

The lithologies observed within the limited core recovery follow.

Clayey Siltstone and Silty Claystone

The dominant lithology is uniformly fine- to medium-grained clayey siltstone, with minor mottling (e.g., interval 180-1109D-42R-2, 75–76 cm). Colors are typically greenish gray (5G 6/2) to orange brown (5Y 5/3 to 5G 5/2). The clayey siltstone generally lacks bedding, although faint layering is seen in places (e.g., Section 41R-3). Minor small-scale burrow-

ing is locally observed (e.g., interval 180-1109D-42R-2, 60–63 cm). In smear slides, the clayey siltstone is seen to contain undulose quartz, feldspar, biotite, clay (unidentified), volcanic rock fragments, accessory minerals, and minor inorganic calcite. In addition, silty claystone was also observed, mainly at the base of the unit. This is vaguely mottled and contains burrows filled with blue-green (5G 6/2) smectite-rich clay, based on XRD analysis (Table T3).

Siltstone-Sandstone

The clayey siltstone is intercalated with several thin intervals of very dark brown, slightly altered coarser grained siltstone and very fine grained sandstone. These sediments are mottled and faintly burrowed, with occasional impressions of rootlets.

Study of smear slides (**"Site 1109 Smear Slides,"** p. 115) indicates the presence of abundant plagioclase, quartz, sericite, volcanic rock fragments, accessory minerals, and iron oxide. Euhedral zoned plagioclase crystals were also noted. Highly altered volcanic rocks and rare, little-altered basaltic clasts are also present. In places, the siltstone to fine-grained sandstone contains ferruginous concretions (see **"Goethite Concretions,"** p. 28).

The XRD analysis confirmed the presence of plagioclase (albite), pyroxene, K-feldspar, quartz, and smectite. A high relative abundance of feldspar and plagioclase (albite) and the presence of smectite was noted in this unit (Table T3).

Goethite Concretions

Several intervals (e.g., intervals 180-1109D-40R-1, 40–80 cm; 40R-CC, 0–20 cm; and 41R-1, 80–150 cm) of clayey siltstone and siltstone (see **"Interpretation,"** p. 29) contain goethite concretions, <1.5 cm in diameter, as confirmed by XRD analysis (Table T3). Some of the concretions are perfectly rounded and densely packed within silty claystone (Fig. F29). When sliced, they are seen to comprise rusty reddish brown iron oxide impregnating host clay-rich siltstone. In other cases, the goethite-rich concretions have a polygonal shape (e.g., Section 41R-1).

F29. Highly altered siltstone and sandstone with goethite concretions, **p. 113.**

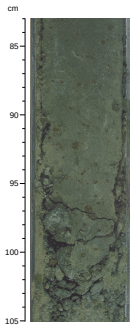

Carbonate Concretions

Several small (<1.5 cm) rounded concretions of fine-grained carbonate were noted within yellowish brown silty clay and clayey silt (i.e., interval 180-1109D-40R-3, 0–100 cm). Several of the concretions exhibit tiny internal radiating calcite veins. Elsewhere, angular fragments of similar carbonate material were noted (i.e., intervals 180-1109D-40R-3, 100–150 cm, and 40R-4, 40–42 cm). In one interval, similar carbonate material was seen to be reworked as angular fragments within clayey siltstone (interval 180-1109D-40R-4, 40–42 cm).

Igneous Clasts (Inferred Conglomerate)

The core catcher of Core 39R contains two pieces of dark gray fine- to medium-grained basic igneous rock (basalt or microdolerite). In addition, a small number of igneous clasts were recovered between sediment. A clast of aphyric basalt was recovered in Sections 39R-CC and 40R-CC. Also, several subrounded to subangular dolerite pebbles were retrieved (i.e., from Sections 39R-CC, 41R-1, 41R-3, and 41R-CC), which

are most likely to be related to conglomerates as inferred from the FMS data. The basaltic clasts generally exhibit fractures infilled with a white, fine-grained alumino-silicate. Similar vein-infilling material was observed within dolerite from Unit XI beneath and identified as the zeolite mineral, natrolite (see "Igneous and Metamorphic Petrology," p. 35).

Interpretation

The greenish gray to orange brown clayey siltstones, silty claystones, and fine-grained sandstones are interpreted as nonmarine deposits in a probable coastal swamp environment (mangrove swamp?). The following lines of evidence support this interpretation: (1) Marine fossils are absent, in contrast to all the overlying units. (2) The sediments include traces of rootlets. (3) The goethite concretions are interpreted as pisoliths, typical of "bog iron ore" (Blatt et al., 1980). The pisoliths presumably developed beneath the sediment surface in a nonmarine setting. (4) Freshwater biota are locally present (i.e., charophytes in Core 39R). (5) The occasional carbonate concretions are similar to caliche. The internal radiating fine cracks are typical of diagenetic growth where volume reduction has taken place. In addition, the local presence of fragments of similar carbonate material probably indicates that some of the caliche was reworked after formation, consistent with a contemporaneous origin. Caliche forms within soils, in areas affected by alternating wet- and dry-season conditions (Easton and Klappa, 1983). However, in this case caliche development was only incipient, as only scattered concretions occur. (6) Smectite is common, based on XRD analysis (see Table T3). Analysis of squeezed pore water indicates a decrease in Mg and increase in Ca, which is attributed to a combination of uptake of Mg to form diagenetic clay minerals and expulsion of Ca related to albitization of feldspar (see "Inorganic Geochemistry," p. 54). Such smectite can form within soils (i.e., pedogenic smectite) affected by an alternating, seasonal wet-dry regime (Bjorlykke, 1983). And (7), the sediments also show evidence of color mottling (e.g., within burrows) that can be interpreted as the result of reduction during diagenesis, again consistent with a swampy setting.

In addition, interpretation of the FMS data suggests that the occasional clasts of basalt recovered from Unit VIII were derived from substantial conglomeratic intercalations similar to those in Unit X (see "Lithostratigraphic Unit X," p. 30). Interpretation is complicated by poor hole conditions, with diameter varying strongly on a meter-by-meter scale (based on FMS caliper data; see "Downhole Measurements," p. 69). This variation itself suggests that highly variable lithologies are present, with the narrow-hole-diameter intervals possibly representing consolidated sand and conglomerate, whereas the wider hole diameters may represent soft silts and muds. Assuming this, the conglomerate wanes, whereas the mud/clay content increases upward.

The highly altered igneous material identified in the sandstones is interpreted as highly altered mesostasis of basaltic rocks. Therefore, it is likely that the conglomerates were dominated by basic igneous rock clasts, as in Unit XI below. The alteration of the grains, especially of feldspars and ferromagnesian crystals, mainly took place during diagenesis, as in typical red-bed formation. The abundance of plagioclase relative to quartz suggests provenance mainly from basic intermediate, rather than acidic, volcanic rocks.

In summary, therefore, Unit IX is seen as having accumulated in a coastal swamplike setting, subject to tropical weathering. The probable depositional setting is discussed in more detail in the depositional history section (see "Depositional History," p. 31). The silty clays, silts, and sands were interbedded with conglomerate, based on interpretation of the log data. The swamp was possibly recharged with river water during seasonal high rainfall, as in coastal Papua New Guinea (PNG) today. The coastal area is seen as backed by an elevated hinterland including basic igneous rocks. Weathering and alteration continued after deposition within a reactive diagenetic setting, characterized by redox-controlled reactions, possibly accelerated during dry-season conditions.

Lithostratigraphic Unit X

Description: igneous-derived conglomerate
Interval: Sections 180-1109D-42R-CC, 30 cm, through 45R-2
Depth: 737.1–772.9 mbsf
Age: undated

Within Core 43R through Section 45R-2, there was minor recovery of conglomerate, individual clasts of basalt, and minor sandstone and claystone. Analysis of FMS data suggests that these lithologies were derived from a major interval of conglomerate ~30 m thick overlying a basement of dolerite rocks (see "Igneous and Metamorphic Petrology," p. 35, and "Downhole Measurements," p. 69). The contact was estimated to lie near 772 mbsf, equivalent to the base of Section 45R-2 (see "Downhole Measurements," p. 69).

Conglomerate occurs in Sections 43R-1, 43R-3, 43R-CC, 44R-1, and 45R-3). The conglomerate recovery in Core 43R is represented by pebbles (from 3 cm × 3 cm to 3 cm × 6 cm) of dark gray basalt. Pebbles in conglomerate from Section 44R-1 are smaller (from 1 cm × 1 cm to 3 cm × 5 cm). The conglomerate is composed of well-rounded pebbles and granules in a matrix of medium- to coarse-grained sandstone. The larger pebbles within the conglomerate exhibit onionskin alteration. In addition, the smaller pebbles, granules, and sand exhibit various stages of reddish oxidation (Fig. F30).

In thin section, the granules and sand are seen to comprise well-rounded grains of altered variolitic basalt and dolerite, altered plagioclase and pyroxene, and rare grains of fine- to medium-grained acidic igneous rocks (i.e., devitrified rhyolite), microcrystalline quartz (devitrified acidic glass), and chloritic grains (altered basic volcanic glass?) cemented by sparry calcite ("Site 1109 Thin Sections;" Fig. F31). XRD analysis of minor silt- and clay-sized material suggests the presence of smectite (see Table T3).

In addition, isolated clasts of basalt and dolerite were recovered from Sections 42R-1, 43R-1, 43R-3, 43R-CC, 44R-1, 45R-1, and 45R-2. The individual clasts recovered range from well rounded to rounded to angular (although the shape of isolated clasts in part may be an artefact of drilling). Also, a number of individual, rounded clasts of very altered sandstone were recovered in Section 44R-1. These are medium grained and include plagioclase and ferromagnesian minerals.

Finally, ~82 cm of clayey siltstone was recovered from within the conglomerate (Section 43R-2). This sediment is structureless, with angular, poorly sorted, sand-sized material and traces of mottling.

F30. Fragments of dolerite and orthoconglomerate, p. 114.

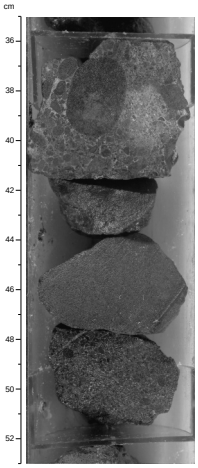

F31. Basaltic grain with microphenocrysts, p. 115.

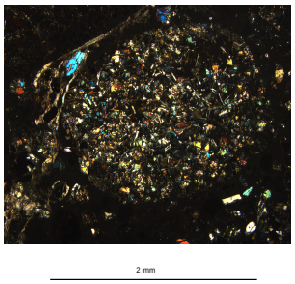

The relation of the recovered conglomerate and clasts and matrix can be correlated with the FMS data. The base of the conglomerate is inferred to be located around 773 mbsf, based on a sharp change from variable to higher and more uniform resistivity. The contact is irregular and probably represents an unconformity. The FMS response of the conglomerate is a "blotchy" resistive image that may correspond to individual rounded clasts (<30 cm thick) within a matrix of low resistivity material that may be sandstone, siltstone, or claystone.

Interpretation

The conglomerates and individual clasts of basalt and sandstone are interpreted to indicate the presence of conglomerate overlying a dolerite basement of inferred intrusive origin (see "Igneous and Metamorphic Petrology," p. 35). Two possibilities for the origin of the conglomerate are that the conglomerates represent beach or fluvial deposits. Several factors favor a fluvial origin: (1) marine fossils (e.g., shells) were not observed; (2) the FMS data indicate the presence of conglomerate throughout Unit X, with finer grained, clastic sediments between the clasts, rather than as a single thick, well-sorted interval, as predicted for a beach unit; and (3) the overlying Unit IX is interpreted as terrestrial, swamp setting with conglomerate deposited away from a shoreline.

In addition, the composition of the clasts indicates a predominant derivation from basaltic and dolerite igneous rocks, with a subordinate additional input from acidic extrusive and possible intrusive rocks that were not otherwise recovered. The material is strongly altered (either subaerially or during diagenesis), as indicated by the abundance of smectite.

Lithostratigraphic Unit XI

Description: dolerite
Interval: Cores 180-1109D-46R through 51R
Depth: 272.9–802.5 mbsf
Age: undated

The lithostratigraphic Unit XI dolerite is described in "Igneous and Metamorphic Petrology," p. 35.

Depositional History

The main results are summarized in a series of figures. A sedimentary log of the succession and the downhole variation in grain size is displayed in Figures F32, F33, and F34. Trends in the sediment composition according to smear-slide data are indicated in Figure F35. Finally, the presence and relative abundance of volcanic ash and volcaniclastic layers are shown in Figure F36.

The depositional history at Site 1109 involves an overall transition from terrestrial to marginal (coastal/lagoonal) to shallow-marine, and then deep-marine (bathyal) accumulation. The succession recovered is sufficiently complete to interpret the depositional history, except for Unit IX, which has to be inferred using logging data. The age of the upper part of the succession is well documented (Units I to VI inclusive). However, Units VIII through X lack diagnostic fossils. For the

F32. Summary of succession cored at Site 1109, p. 116.

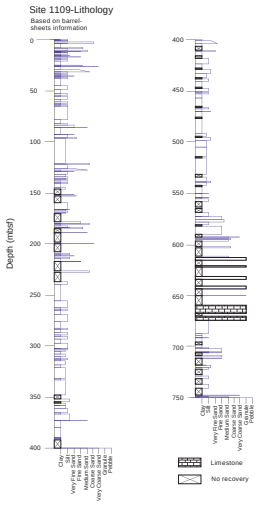

F33. Summary of grain-size trend in Hole 1109C, p. 117.

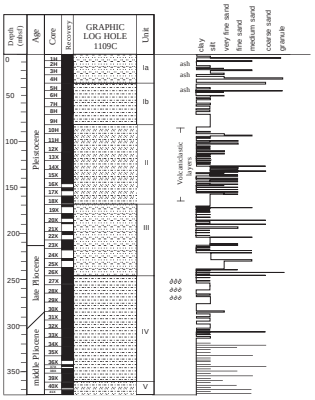

F34. Summary of grain-size trend in Hole 1109D, p. 118.

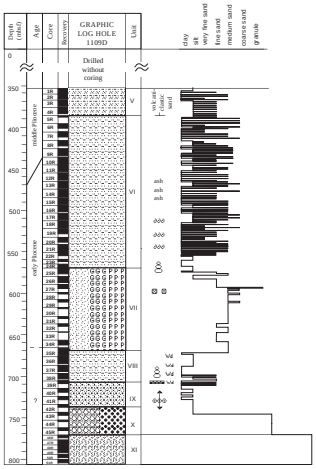

well-dated parts of the succession, rates of deposition were inferred to range from 21 to 312 m/m.y. (see "Biostratigraphy," p. 43).

The overall scenario inferred through time follows.

Forearc Stage (Probably Miocene)

Before the onset of the recorded deposition at Site 1109, the area formed part of the forearc region of the Miocene Trobriand Arc, related to southward subduction of oceanic crust within the Solomon Sea (Lock et al., 1987; Davies et al., 1984). This scenario is discussed more fully in the "Leg 180 Summary" chapter. The volcanic front is inferred to have been located south of Site 1109, in the vicinity of the Moresby Seamount, although Pliocene andesitic volcanoes also existed to the west-northwest and east-northeast of the site in the Amphlett Islands and Egum Atoll (Smith and Milsom, 1984). The outer arc high is located about 100 km to the northeast of Site 1109, which is therefore located in the arc-proximal part of the forearc basin. Forearc basins are expected to be dominated by arc-related volcaniclastic sediments, as suggested by drilling of the Tonga and Izu-Bonin forearc basins (Boe, 1994; Taylor, Fujioka, et al., 1990) and study of well-exposed analogues emplaced on land (e.g., the Late Cretaceous Dras-Kohistan arc complex, Himalayas; Robertson and Degnan, 1994). Trobriand Arc–derived volcaniclastic sedimentary rocks were not observed. This may suggest that the basalt clasts were locally derived from magmatic rocks associated with dolerite emplacement rather than from the Trobriand magmatic arc.

Uplift Phase (Undated)

Before the onset of the recorded deposition at Site 1109, the inferred arc-proximal forearc region was uplifted. Regional seismic analysis and exploratory hydrocarbon drilling indicates that the Cape Vogel area, including the Trobriand depocenter to the northwest of Site 1109, was uplifted and deformed in middle- to late-Miocene time. In the west, the northern and southern margins of this basin were stratigraphically inverted at this stage.

The dolerite at the base of Hole 1109D are low-K tholeiites (see "Igneous and Metamorphic Petrology," p. 35). Following intrusion, the entire magmatic complex was uplifted and subaerially eroded in a tropical climate, and fluvial conglomerates were deposited in a marginal, terrestrial (swampy) setting (Unit IX).

Seismic mapping of the morphology of the erosional unconformity (see the "*Data Report:* Marine Geophysical Surveys of the Woodlark Basin Region" chapter) indicates that Site 1109 is located in a north-south–trending depression that presently deepens to the south (see Fig. F9, p. 18, in the "*Data Report:* Marine Geophysical Surveys of the Woodlark Basin Region" chapter). Beneath the unconformity, the strata forming the southern flank of the forearc basin dip northward at ~10°. The local east-west relief is up to 0.2 s, estimated as 200–250 m (assuming a seismic velocity of the lower section of 2.0–2.5 km·s^{-1}), with a width of around 5 km. The depression is interpreted as a paleovalley, thus explaining the 60 m of terrestrial clastics within Units IX and X at the base of the sedimentary succession as a silt-sand-gravel–filled channel system. The possible direction of flow in this paleovalley is discussed in the "Leg 180 Summary" chapter in the light of the regional paleogeographical setting. Notwithstanding this, Unit X can be interpreted as an aggrading channel-fill succession interbedded with clay, silt, or sand. A

F35. Summary of results of smear-slide analyses, Hole 1109D, p. 119.

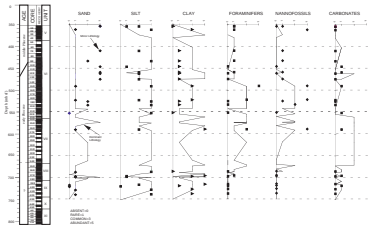

F36. Volcanogenic ash layers and ash thickness per core, Site 1109, p. 121.

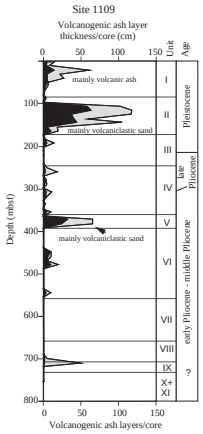

further implication of the textural maturity of the conglomerate is that the hinterland was perhaps of relatively low relief (less than several hundred meters), consistent with only limited emergence of the former forearc region.

The inferred swamp deposits (Unit IX) can be viewed as overbank deposits, with a broad valley of low relief relative to stream courses that were stabilized by dense vegetation. Relief decreased with time, or the base level of erosion rose; hence, the decrease in conglomerate and transition to deposits of Unit VIII. Later, the inferred remanent paleovalley was inundated and became a marine lagoon (Unit VIII) subject to fluctuating salinity ranging from freshwater to hypersaline.

With further subsidence, marine transgression occurred, giving rise to a shallow carbonate-dominated shelf setting (Unit VII). Small highs in the basement of up to several hundred meters (see Fig. **F9,** p. 18, in the "*Data Report:* Marine Geophysical Surveys of the Woodlark Basin Region" chapter) could have existed as small islands at this stage, possibly fringed with coral reefs and thus providing the extrusive igneous and shallow-water carbonate clasts (e.g., coral) observed in Unit VII. No evidence of a barrier (e.g., bar or reef) between the inferred lagoonal and shallow-marine carbonate deposits is preserved at Site 1109D. A possible explanation (assuming that sediment transport was by then to the south) is that the drowned river valley formed a natural inlet that, together with small islands, formed a protected coastal setting without construction of a sedimentary barrier.

Deep-Water Rift Basin Phase (Early–Late Pliocene)

The area continued to subside such that overlying sediments entirely accumulated in deepening water (from upper bathyal to middle and then to lower bathyal). Thick (~180 m), rapid (~300 m/m.y.) deposition of hemipelagic mud, silt, and minor sand turbidites ensued during early to middle Pliocene time (Unit VI). This interval contains relatively unaltered lithoclasts consistent with derivation from the uplifted and rapidly eroding Trobriand forearc region. Sediments at ~380 mbsf correspond to an important boundary between two inferred mega-sequences of differing sediment type and provenance.

There was then an interval marked by an important input of volcaniclastic sand and silt, with abundant finer grained mud and thin-bedded silt turbidites (Unit V). Unit IV records fine-grained calcareous sediments with sporadic turbidity current depositions. Unit III is a succession of pelagic and hemipelagic silty clay interspersed with several types of deep-water (middle bathyal 500–2000 m) sediment-gravity-flow deposits. An interval of sand obtained near the base with poor recovery (Cores 180-1109C-24R and 25R) probably represents an important interval of turbidity current deposition, comprising material from arc-type volcanic, metamorphic, and shallow-water carbonate settings. This was followed by an interval of characteristic volcaniclastic silt and sand turbidites (Unit II), with small (5–10 m) carbonate sand-clay-rich cycles. The probable source of the metamorphic detritus is the D'Entrecasteaux Islands (Davies and Warren, 1988), or southeastern PNG (Davies, l980).

Finally, the Pleistocene (Subunits IA and IB) was marked by additional calcareous nannofossil-rich pelagic deposition, interspersed with volcaniclastic silt, sand turbidites, and volcanic ash (see **"Role of Volcanism,"** p. 34). The entire early Pliocene–Quaternary succession includes sporadic (allodapic) calciturbidites derived from shallow-water carbon-

ate sources. Sedimentation rates apparently decreased markedly to ~21 m/m.y. between 1.0 and 0.46 Ma. Possible explanations include diminished sediment input possibly caused by erection of topographic barriers between the site of deposition and the source area, or slowing of net sediment accumulation owing to enhanced bottom-current activity during Quaternary time.

Role of Volcanism

A total of 48 volcanic ash and 377 volcaniclastic layers were recovered at Site 1109, with a combined total thickness of 10.07 m compared to the total sediment thickness of 772.9 m. The stratigraphic distribution and number of volcanogenic ash layers observed per core, as well as the total thickness of volcanogenic ash layers per core, are shown in Figure F36. Three pronounced maxima are apparent: (1) in the middle Pliocene; (2) in the early Pleistocene; and (3) in the late Pleistocene–?Holocene. These three volcanic episodes are characterized by different transport processes and possibly different sources, as follows:

In the lower Pliocene sequence (Unit VII), ash fallout layers are absent. In Unit VI, five ash fallout layers are present between 465 and 485 mbsf. These are mainly composed of colorless silicic glass, with a minor contribution of brown glass shards. These shards exhibit thin platy and bubble wall morphologies; most are fresh with only minor signs of devitrification.

An important change in the nature of volcanogenic deposition took place in the middle Pliocene where the volcanic material of Unit V (i.e., 352–385 mbsf) is dominantly in the form of volcaniclastic turbidites. Total crystal content is high (up to 50%) relative to the abundance in the inferred ash-fall deposits. Also, volcanic lithoclasts, terrigenous (e.g., metamorphic derived) and bioclastic material are present, indicating an epiclastic origin. In marked contrast, in Unit VI and below most of the glass and phenocrysts are moderately to highly altered.

Three ash-fall layers are present in Unit IV (middle Pliocene), which are characterized by common to abundant vesicle-rich glass shards.

Finally, Pleistocene Units I and II record several volcanic episodes, represented by 33 volcanic ash layers together with four ash-rich turbidites. Primary ash-fall layers, reworked to a variable extent, are predominate in this uppermost interval at Site 1109.

The middle Pliocene and Quaternary glass-rich layers record explosive acidic volcanism, inferred to have been sited in the Trobriand Arc to the south (including Amphetts Islands and Egum Atoll), or eastern PNG including the D'Entrecasteaux Islands (Johnson et al., 1978; Davies et al., 1984). In addition, the epiclastic turbiditic sands clearly originated within the confines of the Woodlark Basin area. Two alternatives are that the glass originated in calc-alkaline volcanism of the Trobriand Arc that is related to southward subduction of oceanic crust from the Solomon Sea (Davies et al., 1984), or from calc-alkaline of eastern Papua and/or peralkaline volcanism of the Dawson Strait area that is attributed to rifting of the Woodlark Basin rift (Smith, 1976; Johnson et al., 1978; Stolz et al., 1993). Eastern Papuan Peninsula has been volcanically active from the middle Miocene to the present day, and there have been eruptions on many of the surrounding islands and in the marine basins (Smith and Milson, 1984). However, these alternatives can only be discriminated following postcruise major and trace element analysis of glass shards and related phenocrysts.

Site 1109, therefore, documents the rift-subsidence history of the Pliocene–Pleistocene Woodlark Basin. Taken as a whole, the sedimentary succession can be (provisionally) subdivided into two megasequences, separated by important changes in lithology, physical properties (e.g., magnetic susceptibility), log units, and seismic character around 370–380 mbsf. The provenance of the lower megasequence was probably mainly from the then emergent Trobriand Arc/forearc. This area formed the proximal part of the Miocene arc/forearc region that was uplifted, eroded, suppled detritus, and later submerged.

By contrast, the provenance of the upper, onlapping megasequence that includes altered calc-alkaline volcaniclastic material, local metamorphic detritus, smectite, and mixed-layer clay was possibly mainly the calc-alkaline volcanic and metamorphic terrains represented by the D'Entrecasteaux Islands and eastern PNG. However, the two possible provenances probably also interfinger to some extent.

IGNEOUS AND METAMORPHIC PETROLOGY

Igneous rocks were initially represented by a conglomerate containing generally highly rounded clasts of glassy basalt and dolerite in a clayey silt matrix with volcaniclastic material or sparry calcite (Fig. **F37**). This conglomerate of lithostratigraphic Unit X, which was recognized in Sections 180-1109D-42R-CC through 45R-3 (see **"Lithostratigraphic Unit X,"** p. 30) and is thought to extend from 737.2 to 772.9 mbsf, is underlain by the dolerite (lithostratigraphic Unit XI), which was first encountered in Section 45R-3 and continued downward to the base of Hole 1109D at ~802 mbsf. This is a compound intrusion, but otherwise extremely homogeneous.

Rounded dolerite clasts from lithostratigraphic Unit X have 1- to 2-mm concentric weathering rings that are interpreted as Fe oxidation penetrating into the clast. This weathering suggests transport and deposition of the clasts into an oxidizing environment. Some clasts near the bottom of the conglomerate unit exhibit red alteration products rimmed by green alteration products (Fig. **F38**). This may represent a change from an oxidizing to a reducing environment. The basaltic clasts are variolitic, with quench crystals of plagioclase and microphenocrysts of olivine (Fig. **F39**), and were probably extruded under water. Alternatively, these glassy rocks may be from the upper contact of the intrusive body although, in this case, we would expect the glass to be less extensive, giving way to microcrystalline material after a centimeter or so.

The topmost samples of dolerite (lithostratigraphic Unit X) have a fine-grained granular texture (Fig. **F40**), suggesting that they come from close to a chilled margin, but this passes rapidly downward into the typical ophitic texture almost ubiquitous in such rocks. Poikilitic plates of augite, ~1 mm in size, enclose numerous plagioclase laths with a length of about half this size (Fig. **F41**). A few percent of opaque iron-titanium oxides are present along with about 5% alteration products that appear to have replaced interstitial glass, although some may pseudomorph original olivine crystals (Fig. **F42**). No entirely unequivocal olivine pseudomorphs were identified.

The massive dolerite (Unit XI), of which 34.93 m was recovered, is extremely homogeneous in terms of mineralogy and texture and, apart from fractures and veins (see **"Structural Geology,"** p. 38), contains no features of note, except toward the bottom of the hole. In Section 180-

F37. Conglomerate with basalt and dolerite clasts, **p. 122.**

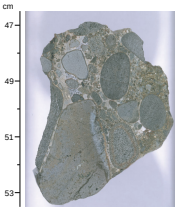

F38. Dolerite clast at the boundary between a dolerite sill and conglomerate unit, **p. 123.**

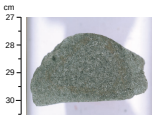

F39. Swallowtail and hopper crystals of plagioclase in variolitic groundmass, **p. 124.**

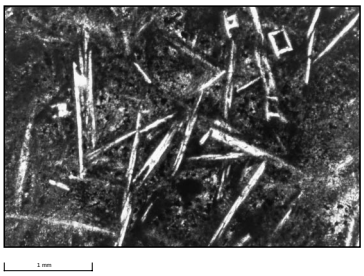

F40. Granular dolerite with altered plagioclase and iron oxides, **p. 125.**

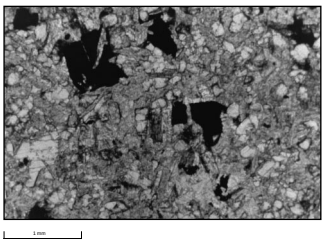

F41. Ophitic dolerite with plagioclase laths in plates of augite, **p. 126.**

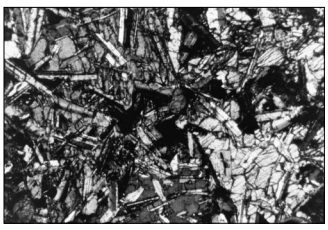

1109D-51R-3 at about 100 cm (799 mbsf), the grain size begins to decrease, suggesting the approach of a lower contact. In Section 180-1109D-51R-4 (at about 20 cm) there is a chilled margin with thin veins of glassy material intruding upward into the fine-grained base of the upper component. This is clear evidence for the intrusion of a second component of the sill, which, in turn, becomes coarser downward to the bottom of the hole. However, material from the lowermost recovery does not attain the ophitic texture seen in the most slowly cooled parts of the dolerite higher up.

Along the contact between the glassy chilled material and the crystalline dolerite, small "pillows" of the glassy material are enveloped in the dolerite, suggesting that the latter was still plastic at the time of the new intrusion (Fig. **F43**).

Fractures include both joints and faults (Figs. **F44, F45**). Pyrite, greigite (XRD identification), tetronatrolite (XRD), cristobalite (XRD), and calcite (identified in thin section) fill these fractures, which are described more comprehensively in **"Structural Geology,"** p. 38.

Chemistry

Variation throughout the Body

The X-ray fluorescence (XRF) analyses (Tables **T4, T5**) of the dolerite confirm its general homogeneity, but show that there is a small systematic variation with depth. The data is plotted against depth in Figure **F46A** and **F46B.** In general, with decreasing depth (i.e., height in the body) MgO falls while Fe_2O_3 rises (seen most clearly in the Fe_2O_3/MgO ratio). This is the pattern to be expected from fractionation of the original magma after emplacement and is seen in countless examples of sill-like bodies worldwide. The upward-increasing pattern is also shown by other incompatible elements, such as Na_2O (marginally), TiO_2, Zr, and Ce (although Zr and Ce both show anomalously low values around the middle of the profile, perhaps not significant because they do not coincide). Ni, like Co, also shows a decrease with height, typical of compatible elements. The more equivocal is Cr, with high values in the middle of the section. At the uppermost end of the range for basaltic rocks, SiO_2 also shows low values around the middle of the profile, reinforcing the indication that there is indeed a difference here.

The lowermost analysis appears to be from a separate magma injection, and the uppermost part of the dolerite is lacking. The former may explain the different position of the lowermost sample in some plots (e.g., Fe_2O_3, Na_2O, and TiO_2) and the fact that these variations are not in concert (Fe_2O_3 is high, whereas Na_2O and TiO_2 are low, in spite of the fact that they are all to some degree incompatible) suggests a slightly different magma batch

Comparisons

Ideally, it should be possible to see from the chemical compositions the tectonic affinities of these rocks (Wilson, 1989), because volcanics from collisional environments tend to be enriched in the large ion lithophile elements (K, Rb, Ba, and Sr) and depleted in high field strength elements (Ti, Zr, etc.). Figures **F47, F48,** and **F49** show the position of this dolerite in the discriminatory diagrams of Pearce et al. (1977), Pearce and Cann (1973), and Pearce (1980), which have been widely used for this type of discrimination. In the TiO_2-K_2O-P_2O_5 dia-

F42. Ophitic dolerite with plagioclase laths in plates of augite with an alteration patch, **p. 127.**

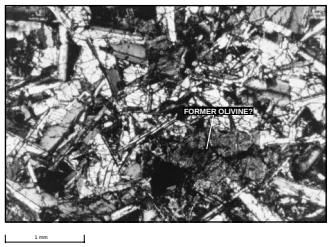

F43. Internal contact between glassy dolerite and crystalline dolerite, **p. 128.**

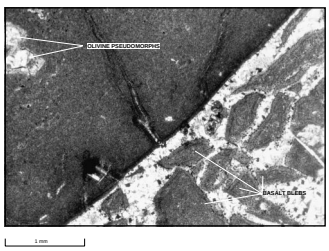

F44. Joint filled with greigite and pyrite within dolerite, **p. 129.**

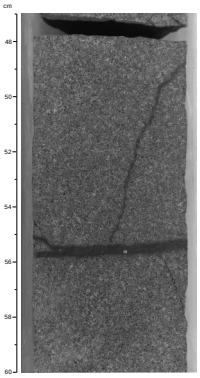

F45. Vein minerals filling a fault in dolerite, **p. 130.**

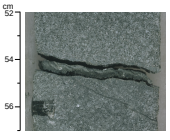

T4. Major element analyses of dolerite by XRF, **p. 248.**

T5. Trace element analyses of dolerite by XRF, **p. 249.**

gram, the dolerite plots clearly in the oceanic basalt field, whereas in the two remaining diagrams it is also in the field of oceanic basalts, although there is substantial overlap with the field of calc-alkali or island-arc tholeiite; therefore, no unequivocal distinction can be drawn. These diagrams do, however, clearly rule out any within-plate basalt affinities for this dolerite. A similar conclusion can be drawn from the Ti-Zr-Sr diagram of Pearce and Cann (not shown here), where the dolerite also plots in the ocean-floor basalt field. In comparison, data from nearby Woodlark Island (Ashley and Flood, 1981) is shown. Both the Hole 1109D dolerite and the data from the Woodlark low-K tholeiites plot in the fields of the low-K tholeiites and are quite distinct from the later high-K, or shoshonitic, rocks from this island. The latter are also included in Figures **F46** and **F47** to show the dramatic compositional difference.

Interpretation

Although the interpretation of this igneous body remains equivocal, our present view is that it is a sill. Arguments against a thick, ponded flow are mainly the lack of any vesicles (which are almost ubiquitous in flows) and also the lack of any flow-top breccia (which could, however, have been eroded away). We cannot, of course, rule out the possibility that we encountered a dike and have been following it down, as dikes are frequently tens of meters thick. The magnetic properties of the dolerite offers some help with this problem.

Regarding the time between the intrusion of the two dolerite components, the evidence outlined above suggests that the first component was still plastic at the time of the new intrusion and, hence, there was no significant time gap between them.

We picture an outcropping sill from which the uppermost part had already been removed. This subsided and became overlain by a deposit of rounded pebbles and boulders derived from the sill with some basalts and sandstones perhaps washed in from elsewhere (see **"Lithostratigraphy,"** p. 7). These are the sediments of lithostratigraphic Unit X, probably derived from a hinterland that had previously been uplifted, as witnessed by the presence of submarine basalts among the clasts. Initial lithologic interpretation of cores just above the conglomerate unit suggests an anoxic, reducing environment. The interpreted transition in weathering from oxidation to reduction in dolerite clasts fits well with subsidence from a subaerial to a lagoonal setting. This scenario suggests that there may be a considerable time difference between the intrusion of the sill and the deposition of its overlying sediments, although this cannot be quantified at the present time.

Low-K basalts, resembling both mid-ocean ridge and arc tholeiite types, are widespread in the Papuan Peninsula-Milne Bay area (e.g., Smith, 1982). These are generally of Cretaceous to Paleocene age. Additional Paleocene volcanics include the Cape Vogel boninites, which are chemically quite distinct from the dolerite discussed here. High-K rocks also occur, although these are appreciably younger, extending up to subrecent. In the Dobu Island area there is a bimodal suite, including transitional basalts and comendites clearly related to the recent extensional tectonics in the Woodlark Basin. At the moment, we can only say that the Hole 1109 dolerite is related either to the low-K tholeiites or to the low-K calc-alkaline basalts. It has no affinities to the high-K rocks or to the basalts and rhyolites (comendites) of the Dobu Island area.

F46. Variation of major and trace elements with depth within dolerite body, **p. 131.**

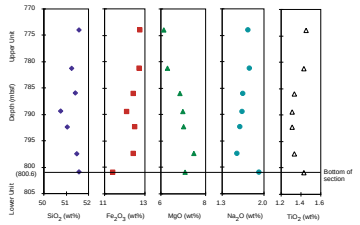

F47. TiO_2-K_2O-P_2O_5 diagram of low-K tholeiites and high-K suite, Hole 1109D, **p. 133.**

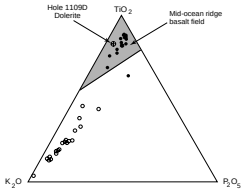

F48. Ti-Zr-Y/3 diagram of low-K tholeiites and high-K suite, Hole 1109D, **p. 134.**

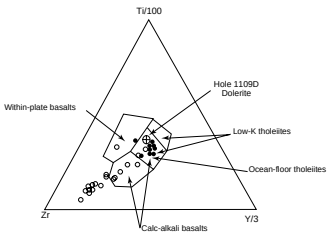

F49. Ti/Y vs. Zr plot showing low-K tholeiites and average value for Hole 1109D dolerite, **p. 135.**

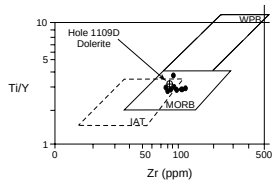

Ashley and Flood (1981) considered that the low-K tholeiites on Woodlark Island were of ocean-ridge affinity and were part of the Papuan ophiolite, which is of Paleocene age. Although it does not seem likely that the Hole 1109D dolerite is part of an ophiolite, radiometric dating will hopefully throw considerable light on this problem.

STRUCTURAL GEOLOGY

Hole 1109C

No evidence for brittle tectonics is recorded in Hole 1109C; however, two types of deformation are locally observed within both unconsolidated and indurated sediments. The three structural domains, which can be distinguished from top to bottom and appear to be controlled by differing lithologic competency, follow.

Structural Domain I

Domain I is represented by unlithified and undeformed sediments of lithostratigraphic Subunit IA identified from Cores 180-1109A-1H through 180-1109C-4H (0–35.9 mbsf) (see "Subunit IA," p. 8).

Structural Domain II

Domain II comprises weakly indurated, massive greenish clay-rich silts of lithostratigraphic Subunit IB (see "Subunit IB," p. 8). In Sections 4H-3 through 9H-7 (29.4–83.6 mbsf), these sediments are deformed into a series of fold structures that are clearly outlined by alternating, variously colored bands. The color variation is probably related to diagenetic processes and does not always indicate primary lithologic changes. However, some of the bands are also marked by changes in grain size, and these are likely to represent deformed bedding.

The geometry of folds can be inferred either by direct observation of core faces or by reconstruction from successively opposing bedding dips within single coherent core intervals.

Both the wavelength and amplitude of folds are typically tens of centimeters in size, when measured along two successive hinge zones and following classical fold criteria (Ramsay and Huber, 1987), as observed in intervals 180-1109C-5H-2, 110–150 cm; 5H-4, 75–120 cm; and 6H-6, 50–90 cm.

The profiles of folds range from large open structures, generally characterized by a flat-lying axial surface (intervals 180-1109C-5H-2, 120–150 cm; 5H-6, 80–90 cm; and 9H-5, 15–35 cm) to tight hinge zones, usually exhibiting moderate to steeply dipping axial planes, in addition to a well-marked fold asymmetry (Sections 5H-3, 5H-4, and 6H-6). Within the entire folded sequence, the sediments generally dip between 30° and 60° (Figs. F50, F51). However, a pronounced shallowing of the bedding attitude is observed in the lowermost part of the domain (Core 9H; 73.9 mbsf), in association with a progressive decrease in fold frequency downward from Cores 5H to 9H. The bedding dip values measured in Domain II are consistent with moderately plunging fold axes.

Most of the geometrical features of the 47-m-thick (36–83 mbsf) folded sequence described above, such as the weak induration of the sediments, or the moderate plunging attitude of the fold axes, are typical of soft-sediment deformation commonly generated either within

F50. Summary of structural features, Hole 1109C, p. 136.

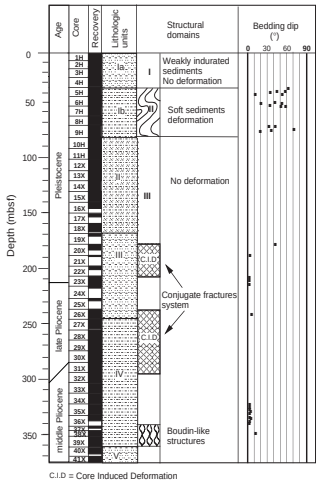

F51. Bedding dips, Hole 1109C, p. 137.

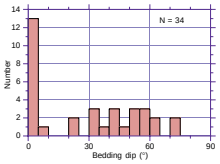

unstable overpressured sedimentary sequences or over active seismogenic submarine areas. Folding, as well as fracturing, could also be generated as core-induced deformations. However, such an explanation is unlikely for the folds in Hole 1109C, mainly because the wavelength of the folds, as measured in a horizontal plane perpendicular to the core axis, is considerably greater than the diameter of the drill bit, and, therefore, the folded interval zone must be of substantial width.

Structural Domain III

Domain III extends from Core 10H (83.4 mbsf) through Core 41X (376.6 mbsf) at the base of Hole 1109C. It comprises well-bedded silt/claystones and minor sandstone alternations, forming lithostratigraphic Units II, III, IV, and V (see "Lithostratigraphy," p. 7). These sediments are horizontal and undisturbed, without evidence of tectonic deformation (Figs. F50, F51).

However, more indurated and dominantly silty sequences occurring from Core 20X (179.3 mbsf) downward are deformed by two types of structures that are confidently attributed to coring disturbance.

The first type of such deformation occurs in the intervals of Cores 20X to 22X (179.3–198.5 mbsf) and 26X to 31X (237.0–294.8 mbsf). It comprises a dense network of open conjugate fractures, dipping at about 45° with respect to the vertical axis of the core. Because most of these fractures typically do not show evidence of displacement and fade away laterally to a tip zone that does not reach the core liner, they are likely to have originated from brittle failure, under vertical maximum stress, and parallel to the drilling axis. However, a few individual fractures cutting the core face at higher angles (~60°) and with a more planar and longer extent (e.g., intervals 180-1109C-28X-2, 100–110 cm, and 29X-3, 120–130 cm) may be in situ fracture/fault surfaces, as confirmed locally by the observation of steeply plunging striations. These structures may account for the inclined features identified in the on board FMS images along the two intervals 2466–2476 meters below rig floor (mbrf) (255–265 mbsf) and 2483–2484 mbrf (272–273 mbsf).

The second type of coring-induced deformation is observed in regular decimeter-sized silt/clay alternations in the interval from Cores 37X to 39X (343.1–362.5 mbsf). Within this interval, clay interbeds systematically form thin depressed zones that separate more resistant dm-thick intervening silt layers, resulting in a core-scale boudinlike pattern that indirectly outlines the general bedding of the cored section. This "pinch and swell" geometry can be assigned to rotation of more competent silty material along clay-rich interlayers that have acted as horizontal layers of decoupling during the drilling process.

Hole 1109D

The structural zonation established in Hole 1109D is dominated by four main domains whose sharp boundaries seem to be closely controlled by lithology. This is supported by good correlation between the lithologic and tectonic logs (Fig. F52).

The section cored is undeformed over most of its length, except along three significant extensional fault zones confined to the top (FZ1), and to the lowermost part (FZ2 and FZ3) of Hole 1109D.

F52. Summary of structural features, Hole 1109D, p. 138.

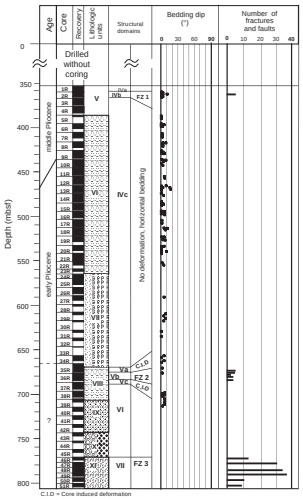

Structural Domain IV

Domain IV occupies the largest part of Hole 1109D, extending ~324 m from Core 1R (352.8 mbsf) to 35R (676.6 mbsf). It mostly corresponds to the sandstones of lithostratigraphic Units V and VI. The consistently flat-lying attitude of bedding has an average dip of 0°–10° (Figs. **F52, F53**).

The only evidence of brittle deformation consists of discrete fault planes that are moderately to steeply inclined and cut Sections 2R-1 and 2R-2 (360.4 mbsf). In Figure **F52,** the latter are referred to as Fault Zone 1 (FZ1). The observed slickenside lineations typify pure dip-slip displacements that are related to extensional strain, according to the offsets identified on core faces (intervals 180-1109D-2R-1, 120–130 cm, and 2R-2, 30–35 cm; Fig. **F54**). In this fault zone, some of the normal faults are arranged as conjugate structures, dipping at 55°, and consistent with a vertical maximum stress (interval 180-1109D-2R-2, 25–65 cm; Fig. **F54**).

Exceptionally, one reverse fault is documented in Section 2R-1, 115–120 cm, from its steplike morphology, but the subsidiary fault array developed in its footwall still shows extensional kinematics (Fig. **F55**). Furthermore, one of the steep fractures present in the footwall of this fault zone is seen to be filled with brown sandy material that passes downward into a 1-cm-thick sandy layer, hence suggesting that some of the brittle faults of FZ1 may have nucleated along earlier open fractures initiated during the deposition of lithostratigraphic Unit V.

Structural Domain V

Domain V represents a deformed zone, ~25–30 m thick, from 671.6–690.5 mbsf (Sections 35R-5 to 37R-3; Fig. **F52**). It comprises an intermediate fault zone (Subdomain Vb) bounded on both sides by drilling-induced disturbed zones (Subdomains Va and Vc).

The top of Subdomain Va is located a few meters below the contact between the sandstones of lithostratigraphic Unit VI and the silty claystones of lithostratigraphic Unit VII. Its base is at the bottom of Section 35R-8 (676.3 mbsf). Its main structural features consist of a network of vertical fractures, 10–40 cm long, that penetrate only half of the thickness of the cores, but which cause the dislocation of the core pieces into elongated fragments.

Subdomain Vb represents an extensional fault zone (FZ2), 7–8 m thick, extending throughout Core 36R (676.4 mbsf). Its structural fabric is dominated by a system of discrete and planar fault planes limiting coherent core pieces, 10–100 cm long. Their average dip is moderate and clusters at ~45° (Fig. **F56**). The entire slickenside population indicates pure dip-slip movements and the indicators of sense of displacement, such as stretched shells (interval 180-1109D-36R-2, 135–140 cm) or steplike morphologies (interval 180-1109D-36R-3, 103–108 cm), consistently indicate extensional faulting.

Subdomain Vc is confined to Core 37R (686.0 mbsf). It is composed of individual pieces of silt/sandstones, a few centimeters long, that probably result from the dislocation of a dominantly sandy interval by drilling-induced rotations along bedding planes, similar to Subdomain IIIb of Hole 1109C discussed in **"Structural Domain III,"** p. 39.

F53. Bedding dips in Hole 1109D, **p. 139.**

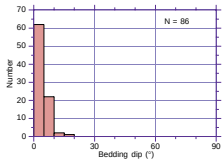

F54. Conjugate planar normal faults, **p. 140.**

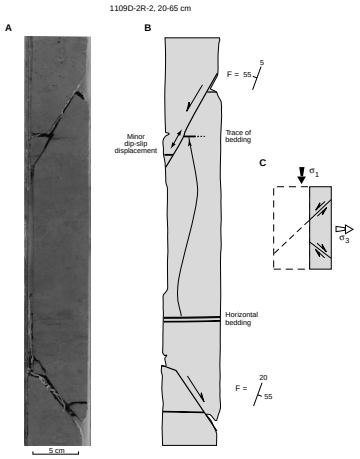

F55. Array of extensional faults in the footwall of a reverse fault, **p. 141.**

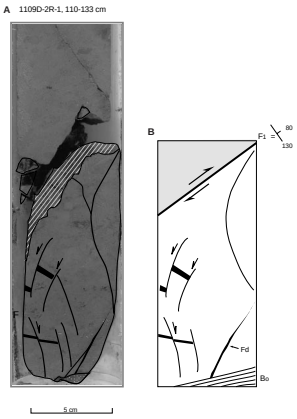

F56. Fault/fracture population in fault zone FZ2, **p. 142.**

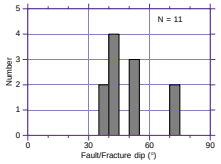

Structural Domain VI

Domain VI includes the lower part of lithostratigraphic Unit VIII down to Unit X (Cores 38R to 45R; 695.6–767.0 mbsf). The almost horizontally layered silt/clay sediments that compose its upper part (Fig. F52), as well as the individual clasts and pebbles involved in its poorly recovered basal part (see "Lithostratigraphy," p. 7), show no evidence of brittle deformation.

Structural Domain VII

Domain VII is represented by a fractured dolerite, ~50 m thick, occurring between Section 45R-3 (766.2 mbsf) and the base of Hole 1109D (802.0 mbsf; Fig. F52). The dolerite is crosscut by a moderately dense network of filled veins and fractures whose mutual spatial and time relationships can be used to constrain the deformational history experienced by the intrusion since its emplacement.

The vein network is infilled with various secondary minerals that were identified by use of hand lenses, microscopic observations, and XRD analyses. They include, in decreasing order of occurrence, greigite (iron sulfide), natrolite mixed with smectite/chlorite, cristobalite mixed with smectite/chlorite, and carbonates. These infilling minerals occur, for the most part, separately and within veins showing specific morphologies. The most common mineral, greigite, is present as a fine-grained dark green material, filling a dense system of thin (1 mm) small veins that propagate through the core at shallow angles (Fig. F57A, F57B). These veins commonly show overlapping tip zones (e.g., intervals 180-1109D-47R-1, 85–90 cm, and 47R-2, 55–60 cm; Fig. F57A). Less numerous, dominantly natrolite- and cristobalite-filled veins form wide (>1 cm), linear fissures 10–100 cm long, which are systematically vertical in position (Sections 48R-1 [782.5 mbsf] and 49R-3 [789.8 mbsf]). Cristobalite-filled veins post date natrolite-filled ones (interval 180-1109D-49R-3, 0–25 cm). Locally, some of the master vertical veins connect via shorter and flat-lying cristobalite/natrolite-filled veins to form extensive small-scale relay ramps, and at some localities, minor steeply dipping greigite-filled veins are laterally offset by shallow cristobalite veins.

The composite vein pattern crosscutting the dolerite intrusion in Hole 1109D can be regarded as extensional fissures that were probably formed during a postmagmatic alteration process, possibly of hydrothermal origin. Given the consistent orientation of the resulting filled fissure network, with two main sets of fissures dipping at right angles, the vein pattern is likely to have originated under horizontal tensile stress perpendicular to the wall of the steep master veins. Such a kinematic arrangement is in agreement with the existence of horizontal-shearing features commonly observed parallel to the subsidiary shallow veinlet system (e.g., intervals 180-1109D-49R-1, 35–40 cm, and 53R-3, 52–57 cm; Fig. F57B). A large number of both steep- and shallow-dipping veins are highly striated as the result of subsequent reactivation as fault planes. Additional (newly formed?) fault surfaces also exist, usually coated by carbonates and more typically by millimeter-sized cubes of pyrite.

The histogram shown in Figure F58A reveals that the fault dip dataset comprises three main peaks around 0°, 20°–30°, and 60°. The frequency of the shallowest fault population increases markedly toward the base of the drilled section, within Cores 49R through 51R. The

F57. Vein network crosscutting dolerite, Hole 1109D, p. 143.

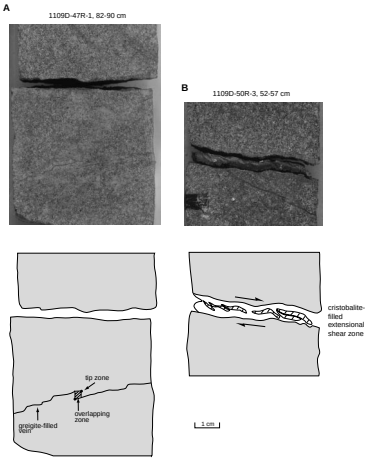

F58. Dip of fault population and fault dip vs. plunge of slickensides, p. 144.

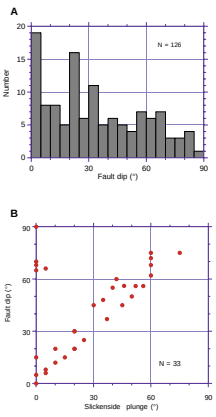

majority of the observed slickensides indicate dip-slip displacement (Fig. F58B). Because clear crosscutting relationships exist between kinematically contrasting faults, it is possible to reconstruct a two-dimensional map view of the overall fault pattern, as shown on the diagram in Figure F59C. Where the structures are observed in larger coherent pieces of core, it is possible to infer the direction of extension with respect to the core reference frame (Fig. F59).

To reorient core structures to true coordinates, an attempt has been made to correlate them with FMS images. Special attention was paid to the two more fractured zones (FZ2 and FZ3) because they contain steeply inclined structures that are more easily identified. The upper limit of FZ2 strictly coincides with a pronounced change in the FMS recording at 2888.5 mbrf (678 mbsf) (see "Log Unit L9," p. 72, "Log Unit L10," p. 72, and "Log Unit L11," p. 72). There we observe a sharp boundary between a relatively poorly layered domain that passes downward into a regularly banded zone about 5 m thick. Within the first meter, these highly conductive layers are closely spaced (interval = <20 cm), and then their frequency diminishes rapidly and disappears below 2893 mbrf (683 mbsf). The structural meaning of the horizontal features seen on FMS images is unclear; no bedding has been observed throughout the corresponding sedimentary core section (Core 36R [676.4 mbsf]). In addition, none of the steep fractures described on cores throughout FZ2 is expressed in the FMS images.

We also note that the structural boundary mentioned above corresponds to an abrupt variation of some physical properties measurements, such as the total natural gamma ray and the porosity, which both increase dramatically close to 675 mbsf, probably in relation to an increase in the clay content (see "Physical Properties," p. 61). That variation suggests a control of the grain size of the sediments on the locus of brittle strain.

The FZ3 is expressed on the FMS images with no specific signature, except in the logged interval 2990.5–2997 mbrf (780–787 mbsf), where it is finely banded with mainly horizontal and closely spaced (<10 cm) conductive horizons. Some of them might be assigned to the greigite-filled vein network, which is particularly well developed in the upper part of the intrusion (Sections 47R-1 and 47R-2; see Fig. F60). A few FMS features with a significant inclination occur in the logged interval 2993–2996 mbrf (783–786 mbsf), but we observe neither the vertical vein-filled system nor the steep fault planes (further coated with pyrite) identified on cores. At this preliminary stage of the work, no clear relationships exist between the FMS images and the core measurements.

Discussion

Relatively little evidence of tectonic deformation is recorded in the sequence drilled at Site 1109 (Fig. F61). This is consistent with the almost continuous and mostly unfaulted character of the sedimentary package imaged by seismic data (see "Vertical Seismic Profile and Depth Conversion," p. 76). The most recent deformation is documented in Hole 1109C by a 20-m-thick folded zone involving weakly indurated sediments of Pleistocene age. Given the general rift tectonic setting of the Woodlark Basin, these soft-sediment structures might result from gravity-driven features generated in response to the instability of the basin floor during a syn- or postdepositional faulting event. However, their in situ origin as a megaslide of unconsolidated and overpressured sediments cannot be ruled out.

F59. Fault/fracture/vein relationships in Section 180-1109D-47R-2, p. 145.

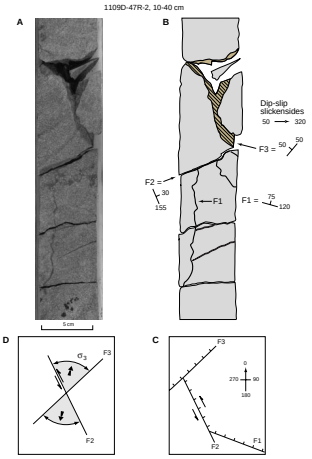

F60. Two-state evolutionary tectonic model for deformation of dolerite, Site 1109, p. 146.

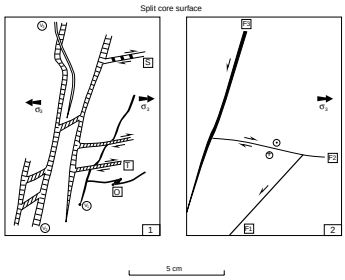

F61. Schematic structural log, Site 1109, p. 147.

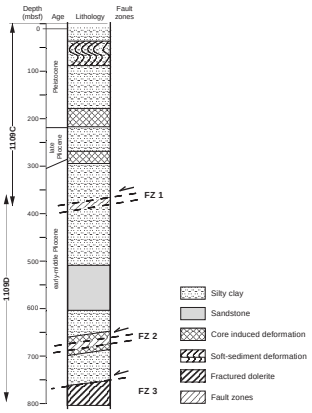

Brittle faulting and fracturing are restricted to the lower part of the cored section along two main deformed zones located at 678–685 mbsf (FZ2) and 773–802 mbsf (FZ3) (Fig. F61). Their locations, close to major lithologic boundaries between lithostratigraphic Units VII/VIII and X/IX, respectively, suggest that variation in lithologic competency was a significant factor in controlling strain. The fracture and fault patterns of FZ1 and FZ2 are quite similar, both resulting from one phase of extension, which is therefore assumed to be post-middle Pliocene in age. However, one should note that the frequency of brittle fractures increases significantly in the dolerite, but that is probably enhanced by the early disruption of the intrusion during a late magmatic hydrothermal process.

BIOSTRATIGRAPHY

Introduction

The nannofossil and foraminiferal biostratigraphy, complicated by numerous turbidites, is shown in Figure F62. Estimates of paleobathymetry were interpreted from assemblages of benthic foraminifers.

F62. Biostratigraphic units and ages for Site 1109, p. 148.

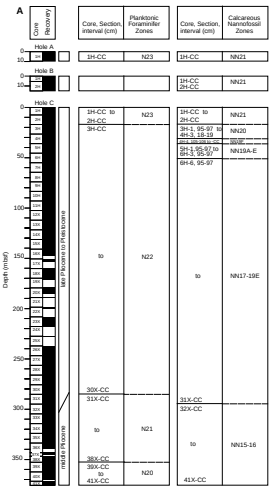

T6. Calcareous nannofossils, Holes 1109A, 1109B, 1109C, 1109D, p. 250.

Calcareous Nannofossils

Abundance and Preservation

Nannofossils are abundant and well preserved in samples from Sections 180-1109A-1H-CC; 180-1109B-1H-CC and 2H-CC; and 180-1109C-1H-CC through 8H-CC. From Cores 180-1109C-9H through 15X, nannofossils range in abundance from few to abundant (mostly common), with generally moderate preservation. Sample 180-1109C-17X-CC contains rare, poorly preserved specimens. Nannofossils in Samples 180-1109C-20X-CC through 41X-CC range from few to abundant (37X-CC is barren), with moderate to good preservation.

In Hole 1109D, nannofossils are mostly abundant from Samples 180-1109D-1R-CC down to 8R-CC, common to abundant from 9R-CC through 26R-CC, and few to abundant in 27R-CC through 35R-CC. Nannofossils are rare in Sample 180-1109D-36R-CC and occur in only trace amounts in 37R-CC. Sediments in Cores 180-1109D-38R through 43R are barren of nannofossils. Scrapings were taken from the sandstones and conglomeratic matrix in Sections 180-1109D-44R-1, 44R-2, 45R-1, and 45R-2; all samples were barren of nannofossils. Preservation is moderate to very good from Samples 180-1109D-1R-CC down to Sample 23R-CC, moderate to poor from Sample 24R-CC to Sample 32R-CC, and poor from Sample 33R-CC to Sample 37R-CC.

Zonation

Calcareous nannofossil zonal assignments for samples taken from Holes 1109A, 1109B, 1109C, and 1109D are shown in Figure F62. A range chart showing the distribution of the index species and other selected species is shown in Table T6A and T6B. This table was prepared during shipboard investigations and does not list all species present in a given sample.

We assign Samples 180-1109A-1H-CC, 180-1109B-1H-CC to 2H-CC, and 180-1109C-1H-CC to 2H-CC to calcareous nannofossil Zone NN21

(late Pleistocene to Holocene) on the basis of the presence of *Emiliania huxleyi*. Samples 180-1109C-3H-1, 95–97 cm, to 4H-3, 18–19 cm, lack *E. huxleyi* and indigenous *Pseudoemiliania lacunosa,* indicating Zone NN20. Sample 180-1109C-4H-4, 105–106 cm, contains the stratigraphic last occurrence (LO) of *P. lacunosa,* which marks the upper boundary of Subzone NN19F. The stratigraphic first occurrence (FO) of *Gephyrocapsa omega* in Sample 180-1109C-4H-CC indicates the lower boundary of Subzone NN19F. Samples 180-1109C-5H-1, 95–97 cm, to 6H-3, 95–97 cm, lack both *G. omega* and *Discoaster brouweri;* this interval is in Subzones NN19A–E. Samples 180-1109C-6H-6, 95–97 cm, through 31X-CC are in Zone NN17 through Subzone 19E, based on lack of *Discoaster surculus*. The LOs of *D. brouweri* and *D. pentaradiatus* (Zone NN18/19 and Zone NN17/18 boundaries, respectively) are not assigned because of large numbers of apparently displaced specimens. *D. surculus* has its LO in Sample 180-1109C-32X-CC (Zone NN16/NN17 boundary).

Martini's (1971) Zone NN16 was subdivided into Subzones 16A and 16B by Rio et al. (1990), based on the LO of *D. tamalis,* a distinctive event in the Mediterranean area where the subdivision was first established. The LO of *D. tamalis* is less distinctive elsewhere. *D. tamalis* is rare throughout its range at Site 1109. We have not subdivided Zone NN16 here because the species is too rare to place the LO with certainty.

The Zone NN15/NN16 boundary is defined by the LO of *Reticulofenestra pseudoumbilica*. The difficulty of determining an accurate position for this boundary, especially in low latitudes where the index species is rare, is well known (see Perch-Nielsen, 1985). The tendency for specimens of this large, robust species to be reworked above its true extinction level is an additional complicating factor. Some biostratigraphers (e.g., Perch-Nielsen, 1985; Siesser and de Kaenel, 1999) have, therefore, recommended using the LO of *Sphenolithus abies/S. neoabies* to approximate this zonal boundary, because *Sphenolithus* spp. become extinct just above the LO of *R. pseudoumbilicus* (Perch-Nielsen, 1985). However, Sphenoliths are present up through Sample 180-1109C-37X-1, 93–95 cm, which is anomalously high in the section when compared to the FO of the foraminifer *Globorotalia tosaensis* and to the Gauss/Gilbert Chron boundary. Therefore, we assign Zone NN15/NN16 undifferentiated down through Sample 180-1109C-41X-CC and from Sample 180-1109D-1R-CC to 23R-2, 21–22 cm.

The Zone NN14/NN15 boundary is defined by the LO of *Amaurolithus tricorniculatus*. This species is often very rare, and we did not find it in any of the samples from this hole. The rarity or absence of this zonal marker has been dealt with elsewhere by either combining Zones NN14 and NN15 into one zone (e.g., Rio et al., 1990) or by using a secondary nannofossil event to approximate the boundary (e.g., Siesser and de Kaenel, 1999). The LO of *A. tricorniculatus* is known to occur just below the last common occurrence (LCO) of *R. pseudoumbilicus* (Siesser and de Kaenel, 1999). Specimens of *R. pseudoumbilicus* decrease in abundance and in overall size rather abruptly at this level. This decrease occurs between Samples 180-1109D-23R-2, 21–22 cm, and 23R-CC in this hole, which approximates the Zone NN14/NN15 boundary.

The first common occurrence (FCO) of *D. asymmetricus* marks the next lower zonal boundary (NN13/NN14). The marker species occurs rarely, but fairly consistently, down to Sample 180-1109D-24R-CC, and we consider that sample to be the base of Zone NN14. Zone NN13 continues down to at least Sample 180-1109D-34R-CC, based on the presence of *Ceratolithus rugosus* in that sample.

Paleoceanography

An unusual oceanographic event may have occurred in the time interval represented between Samples 180-1109C-7H-CC and 8H-3, 94–96 cm. Large specimens of *Braarudosphaera bigelowi* occur in this interval in unusually large numbers (3%–5% of the sediment). Braarudosphaerids are present, although rare, in samples from Sections 180-1109C-8H-1 and 8H-3, but in Sample 180-1109C-7H-CC they are few to common in abundance. Moreover, the braarudosphaerids are abnormally large. Coccoliths of this species are normally less than ~10 µm wide, whereas these specimens average 17 µm in width and range up to 21 µm. We did not find braarudosphaerids in any sample above or below this interval.

Braarudosphaera bigelowi is a long-ranging species (Jurassic to Holocene). In today's oceans it is found only in low-salinity coastal waters (e.g., Gulf of Maine and Gulf of Panama) and rarely in the open ocean (see Siesser et al., 1992). In fossil assemblages, *B. bigelowi* is also found in sediments interpreted as having been deposited in nearshore environments. It is generally assumed that the same environmental control(s) (salinity?) influencing the modern distribution also controlled the occurrence of this species in the past. Thus, it has been difficult to explain the occurrence of the Oligocene "*Braarudosphaera* Chalk" deposited under apparently open-ocean conditions in the South Atlantic and other open-ocean braarudosphaerid-rich layers drilled during Deep Sea Drilling Project/Ocean Drilling Program (DSDP/ODP) cruises. The South Atlantic "*Braarudosphaera* Chalk" is more than 1 m thick in places and may be composed of >90% braarudosphaerid coccoliths.

There has been considerable speculation as to the oceanographic conditions that triggered such enormous blooms of this genus. A low-salinity event, either alone or combined with the availability of selective nutrients, are the solutions most frequently offered (see Parker et al., 1985, and Siesser et al., 1992, for reviews of the *Braarudosphaera* problem). Heavy regional rainfall (Bukry, 1974) increased meltwater from the Antarctic (Bukry, 1978), and various mechanisms for upwelling (Berger, 1979; Parker et al., 1985; Siesser et al., 1992) have all been suggested to explain possible low-salinity episodes in the open ocean.

Because Site 1109 is so close to shore, the possibility of downslope transport from a nearby coastal bay must be considered as a possible explanation for the braarudosphaerid-enriched interval at this site (unlike the South Atlantic and other occurrences of braarudosphaerid-rich sediments, which are long distances from shore). Alternatively, Site 1109 is also probably close enough to shore to have been affected by a period of prolonged rainfall and freshwater runoff during this interval in the late Pliocene, which could have temporarily lowered the salinity of surface water at this site.

Planktonic Foraminifers

Abundance and Preservation

In Holes 1109A, 1109B, and 1109C, planktonic foraminifers were abundant, and their preservation was good in Samples 180-1109A-1H-CC, 180-1109B-1H-CC to 2H-CC, and 180-1109C-1H-CC through 15X-CC, 180-1109C-18X-CC, 19X-CC, 27X-CC through 30X-CC, and 180-

1109C-38X-CC through 41X-CC. Abundance was few to rare and the preservation moderate to poor, or the samples were barren of planktonic species as in Samples 180-1109C-16X-CC, 17X-CC, 20X-CC through 25X-CC, 36X-CC, and 37X-CC.

In Hole 1109D, planktonic foraminifers were abundant and their preservation was good in Samples 180-1109D-1R-CC through 7R-CC, 18R-CC through 24R-CC, and in 26R-CC. Abundance was few to common and the preservation was moderate in Samples 180-1109D-8R-CC through 17R-CC. In Samples 180-1109D-25R-CC and 27R-CC through 34R-CC specimens were rare or few and their preservation was poor, whereas Samples 180-1109D-36R-CC through 39R-CC were barren of planktonic foraminifers.

Zonation

The planktonic foraminiferal zonation for Site 1109 is summarized in Figure F62. Table T7 shows the stratigraphic distribution of species.

T7. Planktonic foraminifers, Holes 1109A, 1109C, 1109D, p. 253.

Samples 180-1109A-1H-CC, 180-1109B-1H-CC to 2H-CC, and 180-1109C-1H-CC to 2H-CC are placed in late Pleistocene–Holocene planktonic foraminiferal Zone N23, based on the occurrence of *Bolliella adamsi* and *Bolliella calida,* whose first appearance datum (FAD) marks the basal zonal boundary.

Sample 180-1109C-2H-CC contains the pink variant of *Globigerinoides ruber,* which disappears from the Pacific at 120 ka; thus, the sample is no younger than that date. Sample 180-1109C-3H-CC, which contains *Globorotalia truncatulinoides* without *G. tosaensis,* lies in the upper part of Zone N22, whereas Samples 180-1109C-4H-CC through 30X-CC, which have the concurrence of those two species, are assigned to the lower part of Zone N22, older than 650 ka. Samples 180-1109C-5H-CC through 8H-CC contain abundant *Globigerinoides fistulosus,* but in the interval between Samples 180-1109C-9H-CC and 29X-CC, rare to few specimens of *G. fistulosus* occur only in Samples 180-1109C-14X-CC, 24X-CC, 26X-CC, and 28X-CC, before continuous downhole distribution sets in at Section 30X-CC. Paleomagnetic data suggests massive displacement of late Pliocene sediment through this interval. The top of Zone N21 is placed below the FO of *G. truncatulinoides* in Sample 180-1109C-30X-CC and the base of Zone N21 is defined by the absence of *Globorotalia tosaensis* (FAD 3.35 Ma) below Sample 180-1109C-38X-CC. Samples 180-1109C-39X-CC through 41X-CC are placed in Zone N20, based on the presence of *Globorotalia crassaformis* in the absence of *G. tosaensis* (early middle Pliocene).

Sample 180-1109D-1R-CC, which contains *Globorotalia tosaensis,* is placed in Zone N21. Samples 180-1109D-2R-CC through 20R-5, 70–72 cm, are assigned to Zone N20, based on the presence of *Globorotalia crassaformis* in the absence of its descendant, *G. tosaensis*. These two species are quite similar in appearance initially. We differentiated *G. tosaensis* by its more circular periphery, gentle curve of the dorsal sutures, and sharp projection of the final chamber from the umbilical area.

Samples 180-1109D-21R-CC through 23R-CC are placed in Zone N20, although *Globorotalia crassaformis* is absent. These samples contain *Pulleniatina,* which undergoes the sinistral to dextral coiling change in Sample 180-1109D-23R-CC that has been dated at 3.95 Ma (562.7 mbsf). The samples below, Samples 180-1109D-24R-CC through 30R-CC, are in either Zone N20, Zone N19, or older, based on the presence of sinistral coiling in *Pulleniatina primalis.* The reduction in plank-

tonic diversity in these samples, as well as those from Samples 180-1109D-31R-CC through 39R-CC, is because of a progressive shallowing to inner neritic facies in which planktonic foraminifers are rarely found.

Benthic Foraminifers

Paleobathymetry

The stratigraphic sequence of assemblages of benthic foraminifers suggests that Site 1109 has subsided progressively from subaerial exposure to its present lower bathyal depth of 2211 m. Some of the species defining the assemblages are given below.

Surface sediments in Sample 180-1109B-1H, 0–1 cm, contained a large agglutinated component that was almost entirely lacking deeper in the section, probably because of decomposition of the organic cement binding the grains. The agglutinated and calcareous taxa found at the surface are

Cyclamina
Recurvoides
Reophax
Rhabdammina
Saccammina
Trochammina
Martinottiella
Ceratobulimina pacifica,
Globocassidulina moluccensis,
Hoeglundina elegans,
Nuttallides umbonifera,
Parrelloides bradyi,
Pseudoparrella exigua, and
Triloculina tricarinata auct.

From Samples 180-1109C-1H-CC through 30X-CC (Pleistocene through late Pliocene) the assemblage is indicative of middle bathyal (500–2000 m) depths and includes

Ceratobulimina pacifica,
Fontbotia wuellerstorfi,
Parrelloides bradyi,
Pseudoparrella exigua, and
Uvigerina asperula.

From Samples 180-1109C-31X-CC through 1109D-26R-CC (middle and late Pliocene) the assemblage is indicative of upper bathyal (150–500 m) depths, with the following species:

Anomalinoides colligerus,
Bolivinita quadrilatera,
Osangularia culter,
Rectobolivina columellaris (striate),
Siphonina tubulosa/australis, and
Uvigerina schwageri.

From Samples 180-1109D-27R-CC through 34R-CC (early Pliocene) a neritic environment (0–150 m) is indicated by the following species:

Amphistegina radiata,
Asterorotalia gaimardi,
Elphidium craticulatum,
Elphidium spp.,

Loxostomina limbata, and
Spiroplectammina arenosuturata.

From Samples 180-1109C-35R-CC through 38R-CC (age undetermined) a brackish water environment is indicated by the presence of abundant ostracodes in Section 35R-CC, as well as the presence of only two types of small benthic foraminifers:

Ammonia beccarii and
Elphidium spp. Gr.

Sample 180-1109D-39R-CC contains no benthic foraminifers, but the oogonia of charophytic algae are present, suggesting a freshwater environment. Sands coated with iron oxide suggest subaerial deposition in Samples 180-1109D-40R-CC through 43R-CC.

Sediment Accumulation Rate

We estimated the sedimentation curve based on nannofossil and foraminifer datum events and magnetic chron and subchron boundaries at Site 1109 (Fig. F63).

PALEOMAGNETISM

The investigation of magnetic properties for sedimentary units at Site 1109 included the measurement of (1) bulk susceptibility of whole core sections, (2) point susceptibility and remanent magnetization of archive-half core sections, and (3) magnetic susceptibility and its anisotropy and remanent magnetization of discrete samples. For igneous rocks from Hole 1109D, magnetic susceptibility and its anisotropy and remanent magnetization were measured for discrete samples. The Tensor tool was used to orient Cores 180-1109C-3H through 11H (Table T8).

Magnetic Susceptibility

Measured values of magnetic susceptibility made on whole core sections as part of the multisensor track (MST) analysis (see "Magnetic Susceptibility," p. 66) and on half core sections as part of the archive multisensor track (AMST) analysis are shown plotted vs. depth in Figure F64A and F64B. In general, susceptibility data from the MST and AMST analyses agreed; differences in magnitude can be attributed to volume differences for the uncorrected data.

Magnetic susceptibility and its anisotropy (AMS) were measured on discrete samples from sedimentary units of Holes 1109C and 1109D. The mean magnetic susceptibility, the degree of anisotropy (P_j) and the shape parameter (T) for the susceptibility ellipsoid (Jelinek, 1981), and the inclination of the maximum and minimum axes of the susceptibility ellipsoid (K_{max} and K_{min}, respectively) are shown vs. depth in Figure F65.

The trend of susceptibility data from discrete samples was consistent with the trends of MST and AMST data on long cores. The very low susceptibilities occurring in the 380–540 mbsf interval suggest that the susceptibility is controlled mainly by paramagnetic minerals. The higher susceptibilities occurring in the 85–380 and 710–750 mbsf intervals,

F63. Age-depth relationship at Site 1109, p. 150.

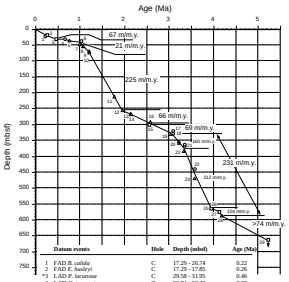

	Datum events	Hole	Depth (mbsf)	Age (Ma)
1	FAD *R. cellula*	C	17.29 - 26.74	0.22
2	FAD *E. huxleyi*	C	17.29 - 17.85	0.26
*3	LAD *P. lacunosa*	C	29.58 - 31.95	0.46
4	LAD *G. tosaensis*	C	26.74 - 36.42	0.65
5	Brunhes/Matuyama	C	36	0.78
6	FAD *G. omega*	C	36.42 - 36.85	0.90
*7	Top Jaramillo	C	47.5 - 48.0	0.99
8	Bottom Jaramillo	C	53.5 - 54.0	1.07
9	Top Cobb	C	74	1.201
10	Bottom Cobb	C	74	1.211
11	Top Olduvai	C	213	1.77
*12	Bottom Olduvai	C	255	1.95
13	Top Reunion	C	266	2.14
14	Bottom Reunion	C	269	2.15
*15	LAD *D. surculus*	C	294.81 - 304.36	2.55
*16	Matuyama/Gauss	C	291	2.58
17	LAD *G. multicornerata*	C	314.23 - 324.02	3.09
*18	LAD *D. altispira*	C	324.02 - 333.83	3.09
*19	Top Kaena	C	331	3.04
20	Top Mammoth	C	355	3.22
		D	358	3.22
*21	FAD *G. tosaensis*	C	362.43 - 369.79	3.35
		D	359.01 - 368.00	3.35
*22	Bottom Mammoth	D	384.5	3.33
23	LAD *G. margaritae*	D	434.70 - 444.49	3.58
24	Gauss/Gilbert	D	470	3.58
*25	LCO *R. pseudoumbilicus*	D	502.51 - 562.71	3.94
*26	S/D *Pulleniatina*	D	>562.71	3.95
27	FCO *D. asymmetricus*	D	571.66 - 576.42	4.13
*28	Top C3n	D	587	4.18
*29	FAD *C. rugosus*	D	>664.29	5.23

* datum used in sedimentation rate calculation

T8. Tensor tool orientation data for cores, Hole 1109C, p. 255.

F64. Comparison of susceptibility data from long core measurements, p. 151.

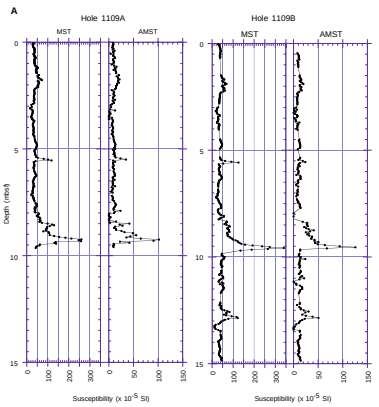

F65. AMS data for discrete samples from Holes 1109C and 1109D, p. 153.

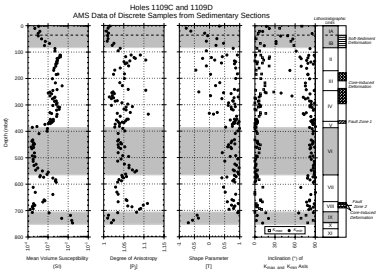

coupled with a similar trend in the remanent intensity data (Fig. **F66B**), suggest that the contribution of ferromagnetic minerals is large in these intervals.

Between 0 and 120 mbsf, P_j values increased from low values around 1.01 to values between 1.05 and 1.1 (Fig. **F65**). Below 120 mbsf, values fluctuated around 1.05 with higher values occurring at ~130, 240, 330, and 550 mbsf, and between 670 and 710 mbsf. Low values between 1.01 and 1.03 were observed at the base of the section below 710 mbsf. The range of P_j values reflected an overall low degree of anisotropy.

Values for the shape parameter (T) from Hole 1109C increased with depth from –0.8 to +0.5 between 0 and 85 mbsf (Fig. **F65**), which corresponded to lithostratigraphic Subunits IA and IB (see **"Subunit IA,"** p. 8, and **"Subunit IB,"** p. 8). Between ~85 and 340 mbsf, T values were scattered with a bias toward values higher than ~0.5. Data from Hole 1109D (below ~350 mbsf) dominantly showed T values above 0.5, which indicated oblate ellipsoids. Negative T values occurred below ~710 mbsf, which indicated prolate ellipsoids.

Inclinations of K_{max} and K_{min} axes are shown in Figure **F65** without structural correction. Structural data indicate horizontal bedding throughout most of Holes 1109C and 1109D, except for the ~35–85 mbsf interval, where bedding dips ranged between ~20° and 70° and were associated with soft-sediment deformation observed in liithostratigraphic Subunit IB (see **"Subunit IB,"** p. 8, and **"Structural Geology,"** p. 38). Most samples between ~85 and 710 mbsf showed very shallow K_{max} axes and subvertical K_{min} axes, with a small change in the inclinations of K_{max} axes corresponding to a larger change in K_{min} axes between 250–260 mbsf. Below 710 mbsf, a marked switch occurred between the inclinations of K_{max} and K_{min} axes; K_{max} axes were subvertical and K_{min} axes were very shallow.

In summary, the AMS of sediments in Holes 1109C and 1109D is characterized by an oblate magnetic fabric with a subvertical K_{min} axis, which is interpreted as a primary fabric related to sediment compaction (Tarling and Hrouda, 1993). Notable are (1) the low mean susceptibilities, (2) the relatively low scatter of all three AMS parameters, (3) a predominance of T values greater than 0.5 indicating an oblate fabric, and (4) the very steep inclinations of K_{min} axes associated with data from the 380–560 mbsf interval, which is a dominantly fine-grained clay-rich unit (see **"Lithostratigraphic Unit VI,"** p. 20). The AMS data for this interval clearly reflect a primary magnetic fabric related to compaction.

Scatter in P_j and T values between 85 and 380 mbsf may be related to variations in the orientation, volume, and grain size of magnetic minerals related to changing provenance and energy of flow (see **"Lithostratigraphy,"** p. 7, and **"Physical Properties,"** p. 61).

The scatter in T values and inclinations of K_{max} and K_{min} axes between 0 and 85 mbsf may be the result of the low degree of compaction suggested by the low P_j values; however, soft-sediment deformation (see **"Lithostratigraphy,"** p. 7) was observed between ~35 and 85 mbsf, which probably contributed to the scatter in the deformed zone.

Magnetic fabrics of samples from altered sediments below 710 mbsf (see **"Lithostratigraphic Unit IX,"** p. 27) showed prolate ellipsoids with subvertical K_{max} axes. The AMS data suggest a vertical alignment of magnetic grains, which may be related to migration of fluids that might have played a role in the alteration of the sediments. The samples were from cores that showed the presence of goethite, based on XRD analysis, occurring as concretions (lithostratigraphic Unit IX; see **"Litho-**

F66. Data from long cores after AF demagnetization, **p. 154.**

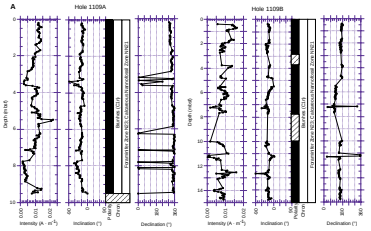

stratigraphic Unit IX," p. 27). The susceptibility of goethite is very low relative to that of magnetite or maghemite (Tarling and Hrouda, 1993), which suggests that goethite probably does not account for the observed high susceptibilities.

Remanent Magnetization

Measurement of remanent magnetization was made on all but the most disturbed archive-half sections from sediment cores. A total of 114 discrete samples from working-half sections of sediment cores were measured.

Demagnetization behavior of discrete samples generally showed two components of magnetization. The soft component, which was removed by 20 mT alternating field (AF) demagnetization, showed directions that were moderately steep to steep downward in XCB cores (Fig. F67A, F67B); RCB cores showed directions associated with the soft component that ranged between shallow to steep downward (Fig. F67C, F67D). The downward directions associated with the soft component probably represent an overprint acquired from the drill string.

Most XCB samples showed stable directions after AF demagnetization at 25 mT (Fig. F67A, F67B); but many samples from RCB cores showed erratic behavior during AF demagnetization with no stable endpoint reached (Fig. F67E).

At Holes 1109A and 1109B, intensities were on the order of 10^{-2} A·m^{-1}, consistent with the intensities observed at Hole 1109C for comparable depths (Fig. F66A, F66B). Intensity of remanent magnetization after AF demagnetization increased sharply from values on the order of 10^{-3} A·m^{-1} to maximum values on the order of 10^{-2} A·m^{-1} at ~85 mbsf; below ~100 mbsf the intensity decreased gradually to values on the order of 10^{-3} A·m^{-1} with a few narrow horizons showing higher values (Fig. F66B). Another abrupt increase in intensity occurred at ~270 mbsf, followed by a gradual decrease to low values on the order of 10^{-5}–10^{-4} A·m^{-1} by ~377 mbsf, below which values remained very low. Between ~540 and 590 mbsf, values increased by about one order of magnitude, after which very low values (10^{-5}–10^{-4} A·m^{-1}) persisted until ~710 mbsf. Below 710 mbsf values increased abruptly up to 10^{-3} to 10^{-2} A·m^{-1}. Intensities of discrete samples were consistent with those from long core data for the same AF demagnetization levels.

Reliable core orientation data from the Tensor tool was limited to two cores (180-1109C-10-H and 11-H). Tensor tool results for the other oriented cores showed a large amount of scatter in data used to determine the mean orientation angle (MTF; see Table T8). Therefore, declinations corrected for core orientation between 84 and 102 mbsf were consistent with the expected declination, but elsewhere Tensor corrected declinations were questionable. Declinations from XCB and RCB cores were highly scattered, which precluded their use for magnetostratigraphic interpretation (Fig.F66B).

The polarity of the remanent magnetization after AF demagnetization at 20 mT for Hole 1109C and at 25 mT for Hole 1109D was determined primarily from the inclinations. Although scatter was relatively high, trends within the inclination data from long cores, corroborated by discrete sample analysis and intensity data, facilitated the polarity interpretation. Only sedimentary sections were used for the magnetostratigraphy.

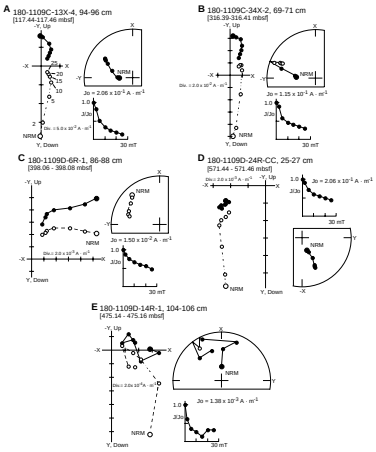

F67. Vector demagnetization plots, stereoplots, and decay of intensity of samples, Site 1109, p. 159.

Magnetostratigraphy

From Holes 1109A and 1109B, only 10 and 15 m, respectively, of sediment were recovered to meet the demand for on ship high resolution sampling. Sediments from these holes recorded part of the Brunhes normal polarity chron, which is consistent with the paleontologic data (Fig. F66A).

Figure F66C shows the variation of inclination with depth at Holes 1109C and 1109D, as well as the polarity zones that are listed in Table T9. Magnetostratigraphic interpretation of the polarity zones described below are consistent with the paleontologic data (see "Biostratigraphy," p. 43).

T9. Polarity zonation in Holes 1109C, 1109D, p. 256.

The transition that occurs at the base of N1 (35.8–36 mbsf) is marked by a decrease in intensity and a rapid change in the polarity of inclination data (Fig. F66D). This boundary represents the Brunhes/Matuyama Chron boundary (0.78 Ma).

The transitions observed between R1-N2 and N2-R2 (47.5–48 mbsf and 53.5–54 mbsf) were marked by a rapid change in polarity and a decrease in intensity (Fig.F66D). These transitions represent the upper and lower boundaries, respectively, of the Jaramillo Subchron (C1r.1n; 0.99–1.07 Ma).

A normal polarity interval occurs between 70.5 and 74 mbsf (N3; Fig. F66C), which probably represents the Cobb Mountain Subchron (C1r.2r.1n; 1.20–1.21 Ma).

The apparent transitions between ~35 and 85 mbsf, described in the preceding paragraphs, occurred in sections where soft-sediment deformation was observed and overturned beds within this interval were noted (see "Structural Geology," p. 38). Correction of the paleomagnetic data for tilted and overturned beds changed the polarity and removed the limited transition data indicated by the inclinations. However, interpretation of precisely which horizons were overturned was not clear, so that correction for tilt was viewed with caution, and tilt-corrected data were not shown in Figure F66A, F66B, F66C, and F66D.

The boundary between R5 and N4 (290–291.5 mbsf) shown in Figure F66C represents the Matuyama/Gauss polarity transition (2.58 Ma).

Mixed polarities were observed between ~213 and 255 mbsf (M1) and again between 266 and 269 mbsf (M2), above the Matuyama/Gauss boundary. These data, which admittedly were from a zone of poor core recovery and were highly scattered, suggest that the Olduvai Subchron (C2n; 1.77–1.95 Ma) and the Reunion Subchron (C2r.1n; 2.14–2.15 Ma), respectively, were recorded at these depths. The magnetostratigraphic interpretation of the Olduvai and Reunion is supported by seismic stratigraphic correlation between Sites 1109 and 1118 (see Fig. F40, p. 74, and "Vertical Seismic Profiling, Depth Conversion, and Site Correlation" p. 28, both in the "Leg 180 Summary" chapter).

The termination of the Kaena Subchron (C2An.1r; 3.04 Ma) occurs at the boundary between N4 and R6 (331 mbsf) in Figure F66C; the beginning of the Kaena (3.11 Ma) is not clearly defined but occurs within M3 (342–353 mbsf), where mixed polarities were observed. This interpretation is consistent with the paleontologic data, which dates the interval between ~314 and 334 mbsf at 3.09 Ma (see "Biostratigraphy," p. 43).

The termination and beginning of the Mammoth Subchron (C2An.2r), the ages of which are 3.22 and 3.33 Ma, respectively, occur at the boundaries between N5-R7 (358 mbsf) and R7-N6 (384.5 mbsf) in Figure F66C; the termination of the Mammoth is found in Hole 1109C at ~355–357 mbsf. Paleontologic data indicate an age of 3.35 Ma

between ~362 and 370 mbsf in Hole 1109C, and between ~359 and 368 mbsf in Hole 1109D, which is reasonably consistent with the magnetostratigraphic interpretation.

The Gauss/Gilbert transition (3.58 Ma) occurs at the boundary between N6 and R8 (470–472 mbsf) in Figure F66C. Paleontologic data places an age of 3.58 Ma at depths between 434.70 and 444.49 mbsf, which is reasonably consistent with the magnetostratigraphic interpretation.

The remainder of Hole 1109D below 472 mbsf spans part of the Gilbert reversed polarity chron (Fig. F66C). Within the Gilbert reversed polarity chron, mixed polarity zone M4 (698–715 mbsf) reflected unreliable data associated with very low intensities.

Igneous Rocks

A total of 43 minicore and cut cube samples were taken from igneous rocks found below 750 mbsf in Hole 1109D. The rocks were identified as dolerite and interpreted as a sill, which was divided into two components based on petrographic observations (see "Igneous and Metamorphic Petrology," p. 35). The boundary between the two components is present at ~20 cm in Section 180-1109D-51R-4 (800.59 mbsf). A fine-grained zone was observed at the base of the upper component between ~800 mbsf (at ~100 cm in Section 180-1109D-51R-3) and the boundary in Section 51R-4. Downward from the boundary, a coarsening of grain size was observed in the lower component (see "Igneous and Metamorphic Petrology," p. 35); however, the coarsest grain size observed in the lower component was finer than that observed in the upper component. At the boundary, a chilled glassy margin with thin veins of glassy material intruded into the upper component, which suggested the intrusion of the lower component into the upper one. Out of 43 samples, five samples were collected from the fine-grained base of the upper component and four from the lower component.

Nineteen minicores were subjected to AF demagnetization up to 30 mT: 17 samples from the upper component, one from the fine-grained base, and one from the lower component. The natural remanent magnetization (NRM) intensity of the samples ranged between 1×10^0 and 4×10^0 A·m^{-1}. A soft component with a steep downward direction was largely removed between 2 and 5 or 10 mT after removal of a viscous component between 0 and 2 mT (Fig. F68A, F68B, F68C, F68D). For most samples, less than 50% of the initial intensity remained after AF demagnetization at 5 mT. The soft component with the steep downward direction was considered a drilling-induced overprint carried by large grains of ferrimagnetic minerals (probably multidomain titanomagnetite). Demagnetization results between 10 and 30 mT generally indicated the presence of two components. Four samples provided a stable component between 20 and 30 mT (Fig. F68, examples shown in B and D), which is referred to as the characteristic remanent magnetization (ChRM). However, isolation of the ChRM in other samples was prevented by a large overlap of coercivities, which was indicated by the curved trajectory of demagnetization results or by unstable magnetic behavior related to a very weak intensity of remanence at high demagnetization steps (Fig. F68, examples shown in A and C).

The ChRM directions of four samples are shown in Figure F68E. Steep upward inclinations (range: –53° to –62°) were indicated for two samples from the upper component and for one sample from the fine-

F68. Demagnetization behavior of samples from dolerite unit, p. 160.

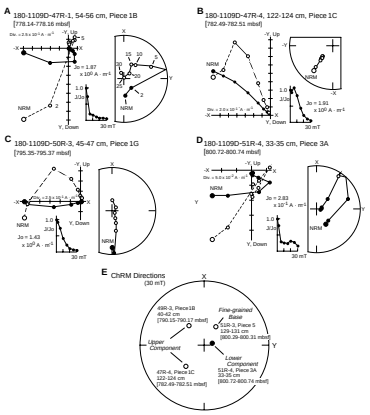

grained base; the one sample from the lower component showed a steep downward direction. The difference in the polarity indicated by the ChRM of these four samples suggests different ages of emplacement between the two components of the sill (or dike). Furthermore, inclinations from all four samples were much steeper than expected for the present site latitude (~18.5°) and were much steeper than those of the sediments overlying the dolerite. The ChRM directions preserved in the dolerite implied a tilting of the sill after emplacement, either as a coherent unit or as fragmented blocks. Tilting of the dolerite may be the result of block rotations related to faulting; many fractures observed in the dolerite were interpreted as faults (see **"Structural Geology,"** p. 38). Block rotation probably preceded the formation of the overlying sedimentary sequences, because structures observed in the sediments indicated no large scale tilting of the sedimentary basin.

The mean susceptibility, the degree of anisotropy (P_j) and the shape parameter (T) for the susceptibility ellipsoid (Jelinek, 1981), and the inclinations of the maximum (K_{max}), intermediate (K_{int}), and minimum (K_{min}) axes of the susceptibility ellipsoid for discrete samples are shown in Figure **F69.** Mean susceptibilities were on the order of 10^{-2} SI, which suggested that ferrimagnetic minerals dominated the susceptibilities. The fine-grained base and the lower component showed relatively weaker susceptibilities than the upper component. The P_j values generally ranged between 1.01 and 1.10, reflecting an overall low degree of anisotropy. Almost all samples showed T values between ~0 and –0.8, indicating prolate ellipsoids that reflect a predominant lineation to the magnetic fabric. The degree of prolateness appeared to increase with increasing values of P_j. Magnetic fabrics of the upper component generally showed steep K_{max} axes with subhorizontal K_{int} and K_{min} axes, whereas horizontal K_{max} axes with vertical K_{min} axes are observed in samples from the fine-grained base and the lower component.

Studies have shown that magnetic lineations in igneous rocks may be either parallel or perpendicular to the flow direction, depending on magma viscosity and flow rate (Tarling and Hrouda, 1993). This suggests that the magnetic fabric of the upper component of the dolerite unit of Hole 1109D may have been controlled by the magma flow.

Interpretation of grain-size variations (see **"Igneous and Metamorphic Petrology,"** p. 35) suggested that the fine-grained base and the lower component underwent rapid cooling near the contact plane, which may have caused the different magnetic fabrics determined for the two components. Magnetic fabrics near a contact plane generally reflect an inward-directed cooling stress, which results in K_{min} axes normal to the contact plane (Tarling and Hrouda, 1993); alternatively, irregular flow of magma near the contact could have caused the difference in the magnetic fabrics determined for the two dolerite components in Hole 1109D.

Because the orientations of the dolerite cores were unknown and the ChRMs implied a tilting of the dolerite unit, directions associated with the magnetic fabrics do not reflect the true flow direction. Postcruise paleomagnetic studies may enable further interpretation of the directions of the magnetic fabrics.

F69. AMS data from dolerite unit in Hole 1109D, **p. 161.**

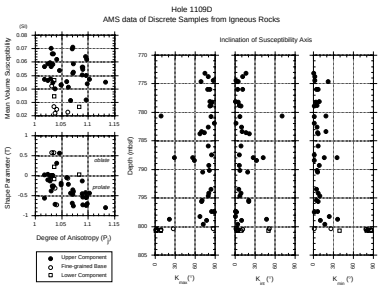

INORGANIC GEOCHEMISTRY

The high-resolution IW sampling program at Site 1109 consisted of a total of 64 IW samples. Eight were collected from the first two cores, one was taken from each subsequent core down to 480 mbsf, and one from every other core until hard rock was encountered, unless core recovery or the composition of the material did not allow it. Except for Core 180-1109D-43R, in which a smaller whole round (7 cm) was taken because of the paucity of material available, the IW yield from whole rounds was always sufficient to permit shipboard analysis of the full suite of constituents and the acquisition of splits for all shore-based scientific interests.

Results

The IW was analyzed for salinity, pH, alkalinity, major cations (Na^+, K^+, Ca^{2+}, and Mg^{2+}) and anions (Cl^- and SO_4^{2-}), SiO_2, NH_4^+, Sr^{2+}, and Li^+. Results of shipboard inorganic chemical analyses are presented in Figure **F70.** The pH measurements made during the alkalinity determination in IW samples are considered to be generally reliable. We believe this to be the case because no significant degassing was observed, as evidenced by a rapid acquisition of a stable initial pH reading during the alkalinity titration (see **"Inorganic Geochemistry,"** p. 23, in the "Explanatory Notes" chapter).

The titration alkalinity profile shows four broadly defined zones. In the first zone, alkalinity rises sharply from ~3.5 mM in the shallowest cores to a maximum of 13.5 mM at 107 mbsf (Table **T10;** Fig. **F70A**) and decreases abruptly over the next 60 mbsf. A gentler negative concentration gradient between 160 and 330 mbsf gives way to another rise to a broad alkalinity submaximum between 375 and 535 mbsf, below which alkalinities are less than 1.5 mM to the bottom of Hole 1109D. The NH_4^+ profile shown in Figure **F70A** crudely parallels that of alkalinity with maxima and minima observed in the same depth ranges. However, the deep-seated NH_4^+ maximum exhibits proportionally much greater concentrations than its alkalinity counterpart. Dissolved SO_4^{2-} is strongly depleted with increasing depth over the first 100 mbsf and mirrors the alkalinity profile down to ~160 mbsf. From 200 to 500 mbsf, SO_4^{2-} remains almost fully depleted except for a few minor excursions to 3.0–4.5 mM. Sulfate appears to be fully depleted in IW recovered from the bottom 300 m of the hole, except possibly in the deepest sample collected immediately above hard rock.

The salinity exhibits a narrow range of 31–35. A systematic and gentle decrease from seawater values occurs down to 480 mbsf. Although a return to a salinity of 34 occurs by 717 mbsf, the deepest IW sample recovered immediately above hard rock displays a significantly lower salinity of 31 (Table **T10**).

The dissolved Na^+ and Cl^- profiles at Site 1109 (Fig. **F70B**) do not covary. Although Na^+ concentrations generally decrease downhole throughout the entire sedimentary column, dissolved Cl^- remains in a tight range of 550–560 mM down to ~550 mbsf. Below this depth, Cl^- increases to 579 mM at 612 mbsf, followed by a decrease to the lowest value (522 mM) in the deepest (745 mbsf) IW sample collected. Dissolved Cl^- measurements made by $AgNO_3$ titration are better constrained than those by ion chromatography (IC) and are deemed more reliable. Excursions occur in Cl^- data from IC on a run-by-run basis,

F70. Interstitial water constituents at Site 1109 with lithostratigraphy, **p. 162.**

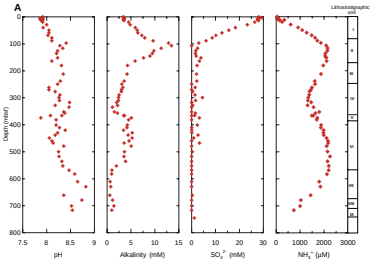

T10. Interstitial water geochemistry, **p. 257.**

with notable divergence of the titration and IC data observed in the first 150 mbsf (Fig. F70A). Dissolved K^+ exhibits large fluctuations downhole between near-seawater values immediately below the mudline to near complete depletion at the bottom of the sedimentary sequence (Fig. F70B). A slight enhancement over seawater is observed in the shallowest sediments, whereas ~40% depletion relative to seawater concentration occurs by 310 mbsf. This trend reverses between 310 and 430 mbsf, below which a strong removal of K^+ from pore fluids is once again observed throughout the deeper sediments.

Dissolved Li^+ (Fig. F70B) exhibits a rather complex profile at Site 1109 and varies over the range of 10–86 µM. An initial minimum coincides with the alkalinity maximum and sulfate minimum. The fine structure of the Li^+ profile appears to correlate with fluctuations of these two parameters down to 150 mbsf. Below this depth however, dissolved Li^+ increases downhole through a series of concentration gradients of different slopes to a maximum at 568 mbsf, the bottom of lithostratigraphic Unit VI (see "Lithostratigraphic Unit VI," p. 20). The Li^+ profile does not appear coupled strongly to that of any other IW constituents in this depth range. A submaximum in Li^+ occurs near 680 mbsf, but concentrations drop dramatically in the two deepest IW samples.

The dissolved Ca^{2+} and Mg^{2+} profiles display four principal zones (Fig. F70C). The first zone, between 0 and 100 mbsf, is characterized by removal of ~90% of the Ca^{2+} and 40% of the Mg^{2+} from the pore water. In the second zone, between ~100 and 300 mbsf, dissolved Ca^{2+} concentrations return to near seawater values, whereas those of Mg^{2+} increase gradually from ~34 to 40 mM. A third zone of relatively constant Ca^{2+} and Mg^{2+} concentrations occurs between ~300 and 470 mbsf. The fourth zone displays a sharp increase in dissolved Ca^{2+} with increasing depth, whereas Mg^{2+} concentrations initially remain little changed (35–40 mM down to ~600 mbsf), before decreasing sharply toward the bottom of the hole. The Sr^{2+} profile is also characterized by four zones that correspond broadly to those noted above for Ca^{2+} and Mg^{2+}. However, the shape of the Sr^{2+} profile is quite different, and the range of concentrations is much wider than those of Ca^{2+} and Mg^{2+} (Fig. F70C). The Sr^{2+} maximum at 661 mbsf is more than 15 times the seawater concentration and occurs at the same depth as the crossover point for the Ca^{2+} and Mg^{2+} profiles.

Dissolved SiO_2 also displays a complex profile (Fig. F70C). Concentrations fall into three broad ranges downhole. In the first 140 mbsf, dissolved SiO_2 remains mostly between 400 and 540 µM. Greater fluctuations are then observed, with several local maxima (461 and 803 µM) and minima (268 and 145 µM) evident between 140 and 500 mbsf. A sharp decrease to ~100 µM SiO_2 occurs over the next 50 m, below which concentrations remain under 250 µM throughout the remainder of the sedimentary column.

Discussion

Changes in the composition of interstitial fluids are particularly useful in fingerprinting diagenetic reactions; even small changes in the composition of the solid phase lead to large changes in fluid compositions because of orders of magnitude higher concentrations of most constituents in the solid phases relative to seawater (Sayles and Manheim, 1975). At Site 1109, the composition of IW reflects the bacterial

oxidation of organic matter, its effect on early diagenesis of biogenic carbonate and silica, and the alteration of volcanic matter and subsequent formation of authigenic clay minerals, as well as transformations of pre-existing detrital minerals.

The bacterially mediated oxidation of organic matter (Claypool and Kaplan, 1974) following the general reaction shown below, is clearly evident in the strong depletion of SO_4^{2-} and concomitant increases in alkalinity and NH_4^+ concentrations (Fig. F70A):

$$1/53(CH_2O)_{106}(NH_3)_{16}(H_3PO_4) + SO_4^{2-} =$$

$$2HCO_3^- + HS^- + 16/53NH_4^+ + 1/53H_3PO_4 + H^+.$$

Although a decrease in pH normally results from the decomposition of organic matter, in the presence of aluminosilicate sediments pH can be buffered at higher values than those observed in carbonate sediments (Ristvet, 1978; Mackenzie et al., 1981). This is consistent with the increase in pH we observed over this depth interval but cannot account for larger increases in pH observed below 500 mbsf in lithostratigraphic Units VI and VII. The latter increase in pH may be attributable to precipitation of $CaCO_3$ cements observed between 580 and 670 mbsf (see "Lithostratigraphy," p. 7, and "Organic Geochemistry," p. 59).

The sharp increase in alkalinity with increasing depth in the shallower sediments (~100 mbsf) induces dissolution and recrystallization of biogenic carbonates (Morse and Mackenzie, 1990). This is reflected in the dissolved Ca^{2+}, Mg^{2+}, and Sr^{2+} profiles and in the initial drop in the Ca/Mg ratio (Fig. F70C). The early diagenesis of carbonates in the upper 100 mbsf of the sediments, in addition to the initial compaction of sediments and concomitant fluid expulsion, likely contributes to the observed decrease in sediment porosity (see Fig. F71).

A second potential source of alkalinity, although generally less important than the oxidation of organic matter, is the alteration of volcanic matter. The following reaction, which describes the alteration of volcanic matter, has been invoked previously to explain alkalinity increases observed in sediments from Sites 998 and 999 in the absence of significant bacterially mediated oxidation of organic matter (Sigurdsson et al., 1997):

$$2.33NaAlSi_3O_8 + 8.64H_2O + 2CO_2 =$$

$$Na_{0.33}Al_{2.33}Si_{3.67}O_{10}(OH)_2 + 2Na^+ + 2HCO_3^- + 3.32H_4SiO_4.$$

Potassium feldspar can be substituted for Na-feldspar in the above equation.

The abundance of ash layers in lithostratigraphic Unit II (see "Lithostratigraphic Unit II," p. 11), especially between 100 and 150 mbsf, likely also produces alkalinity and may contribute to the fine structure of the profile evident in Figure F70A. A small upturn in dissolved SO_4^{2-} between 115 and 152 mbsf, which suggests a reduced rate of microbial activity, is consistent with this interpretation. The second and less pronounced alkalinity maximum observed between ~375 and 480 mbsf exhibits fluctuations that broadly correspond to the abundance of ash layers (see Fig. F36). In this section of the sedimentary col-

F71. Correlation of dissolved SiO_2 and porosity in sediments at Site 1109, p. 165.

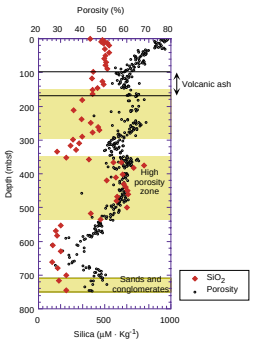

the second broad NH_4^+ maximum, although weathering of mica is also known to release NH_4^+ to solution. The downcore decrease in NH_4^+ below 580 mbsf in the calcite-cemented sandstone of lithostratigraphic Unit VII could reflect a reduced contribution from microbial activity in combination with enhanced alteration and authigenesis of clay minerals. Detrital clay minerals represent a potential NH_4^+ sink through incorporation as a trace cation or by exchange with monovalent alkali cations (Stevenson and Cheng, 1972).

Examination of variations in the Ca/Mg ratio shown in Figure F70C reveals evidence of various sedimentary reactions. The initial decrease over the first 100 mbsf is consistent with a dissolution and recrystallization of biogenic carbonates, accompanied by release of Sr^{2+} to solution throughout sediments of lithostratigraphic Unit I, similar to that observed, for example, at the Great Bahamas Platform sites (Eberli et al., 1997). Between 100 and 300 mbsf, Ca^{2+} and, to a much lesser extent below 180 mbsf, Mg^{2+} are released to solution, as evidenced by an increasing Ca/Mg ratio. Here the source of dissolved Ca^{2+} is likely the alteration of volcanic minerals, especially plagioclase, dispersed throughout the sediments (e.g., Gieskes, 1981, 1983; Gieskes et al., 1982). Microscopy studies show that volcanic glass, lithic fragments, and individual crystals are more abundant above 380 mbsf (see "Lithostratigraphy," p. 7). Formation of authigenic clays that would remove Mg^{2+} does not appear to be an important process in this zone. Rather the presence of common chlorite/smectite mixed-layer clays (see "Lithostratigraphy," p. 7) between ~100 and 200 mbsf suggests diagenetic transformation of pre-existing detrital clay minerals (McDuff and Gieskes, 1976; McDuff, 1981).

The negative K^+ gradient (Fig. F70B) within the 100–200 mbsf interval can be attributed to removal of this constituent from pore fluids by illite formation. A shallower K^+ gradient observed between 200 and 260 mbsf is consistent with the absence of illite in XRD patterns of the bulk sediments (see Table T3). The reappearance of this mineral in several XRD samples taken near 300 mbsf coincides with further depletion of K^+ from the pore water. Below 300 mbsf, increases in dissolved K^+ may be attributed to alteration of K-feldspars found within lithostratigraphic Unit V and, to a lesser extent, in the increasingly calcite-rich sediments of lithostratigraphic Unit VI. Very low abundances of illite, which can act as a sink for this constituent (see "Lithostratigraphy," p. 7), also contribute to the maintenance of elevated dissolved K^+ concentrations. Within this depth interval, little change is observed in the Ca/Mg ratio, which is also consistent with a lack of authigenic clay mineral formation.

There are major changes in the lithology below 570 mbsf. Lithostratigraphic Unit VII is a calcite-rich sandstone in which dissolution of abundant biogenic carbonate components acts as a source of dissolved Ca^{2+}, as reflected in the increasing Ca/Mg ratio (Fig. F70C). However, no significant change in the dissolved Mg^{2+} concentration is observed. Substantially lower porosity and enhanced calcite cementation were observed between 570 and 670 mbsf, an interval in which only a small change in the Ca/Mg ratio and the dissolved Mg^{2+} concentration was noted. The large negative K^+ gradient throughout this interval (Fig. F70B), as well as a sharp drop in dissolved SiO_2 (Fig. F70C), is consistent with the reduced porosity associated with cementation of the sediments. Substantially reduced pore-water yields during squeezing of the

whole rounds of sediments from this portion of Site 1109 also support this inference.

Large changes in the pore-water constituent profiles occur within and below lithostratigraphic Unit VII. A large increase in dissolved Ca^{2+} is observed in the lower portion of this unit, whereas the sharp maximum in the dissolved Sr^{2+} (Fig. F70C) and a Cl^- maximum (Fig. F70A) is near the boundary between lithostratigraphic Units VII and VIII. A Li^+ submaximum (Fig. F70B) is immediately below this boundary. The variations in IW composition beginning in Unit VII and continuing in Unit VIII, interpreted to be lagoonal sediments because of an abundance of shell, plant, and wood fragments, are bounded within a shalelike morphology that apparently minimizes diffusion. The source of dissolved Ca^{2+} and Sr^{2+} here is presumably the dissolution of bioclasts (e.g., aragonitic shells of gastropods; see "Lithostratigraphy," p. 7). The increasing dissolved Ca^{2+} and Cl^- and the sharp uptake of Mg^{2+} below the boundary of lithostratigraphic Units VII and VIII likely reflect diffusive profiles resulting from the alteration of K-feldspars and plagioclase and concomitant formation of the quite pure authigenic smectites observed in XRD samples collected from lithostratigraphic Units VIII and IX (see "Lithostratigraphic Unit VIII," p. 25, and "Lithostratigraphic Unit IX," p. 27).

Dissolved Li^+ and SiO_2 (Fig. F70B, F70C) display variations throughout the sediments that are interpreted to reflect both lithologic and structural variations. In the uppermost sediments, early dissolution of biogenic silica leads to a substantial enrichment of this constituent over seawater. Between 80 and 170 mbsf, however, low-temperature alteration of abundant volcaniclastic turbidites contributes to the dissolved SiO_2 content of the IW. Relatively wide fluctuations in dissolved SiO_2 concentrations below 200 mbsf generally coincide with changes in the porosity of the sediments (Fig. F71) or in substantial mineralogical variations. A submaximum in dissolved SiO_2 at 260 mbsf in the upper portion of lithostratigraphic Unit IV (see "Lithostratigraphic Unit IV," p. 15) coincides with a local porosity maximum (Fig. F71). This is a fault zone containing a conjugate fracture system that likely enhances fluid flow (see "Structural Geology," p. 38, and "Downhole Measurements," p. 69) and where a change in the dissolved Li^+ gradient suggests upward diffusion of Li-enriched pore water from below. The next SiO_2 maximum at 374 mbsf is at the base of a volcaniclastic sand layer (lithostratigraphic Unit V). It is also near another porosity maximum (Fig. F71) and coincides with a change in lithology to more mixed terrigenous, bioclastic, and volcanic material, as well as the onset of a steeper dissolved Li^+ gradient. The drop in dissolved SiO_2 to very low concentrations is at ~550 mbsf near the boundary between lithostratigraphic Units VI and VII (see "Lithostratigraphic Unit VI," p. 20, and "Lithostratigraphic Unit VII,"p. 22). and a sharp decrease in porosity (Fig. F71; see also "Physical Properties," p. 61). The boundary between high and low dissolved SiO_2 concentrations also coincides with the Li^+ maximum. Although calcite cementation of sediments in this interval may contribute to a reduced diffusion of dissolved SiO_2 from above and help maintain higher dissolved Li^+ in the remaining pore fluids, it is

more likely that this chemical composition reflects the uptake of dissolved SiO_2 and the exclusion of dissolved Li^+ during the formation of other silicate minerals.

The lowest dissolved Na^+, Cl^-, and Li^+ concentrations at Site 1109 were measured in IW from Sample 180-1109D-43R-2, 82–89 cm. It was

recovered from lithostratigraphic Unit X, which has a clayey silty matrix and is located slightly above the dolerite of lithostratigraphic Unit XI (see "Lithostratigraphic Unit X," p. 30). These low concentrations may represent the remains of a paleofreshwater signal that is being slowly erased with time by diffusion from overlying saline waters.

Summary

A summary of sedimentary geochemical processes is given in Table T11. The chemical composition of the IW reflects strongly both the influence of ash layers and other volcanic minerals dispersed throughout the sediments and the carbonate dissolution and recrystallization reactions induced by fluid compositional changes derived from the microbial oxidation of organic matter. Other carbonate mineral reactions and those involving silica and transformations of pre-existing detrital clay minerals also contribute to variations observed in pore-water profiles at this site. The inferences regarding geochemical reactions based upon the chemical composition of the IW are substantiated by lithostratigraphic observations, mineralogical identifications (XRD), and changes in the physical properties of the sediment.

T11. Diagenetic reactions in sediments, p. 258.

ORGANIC GEOCHEMISTRY

At Site 1109, the shipboard organic geochemistry consisted of determinations of total organic carbon (TOC), inorganic carbon, total carbon, total nitrogen, and total sulfur in sediments, in addition to the routine hydrocarbon gas safety monitoring procedure. The analytical techniques used are outlined in "Organic Geochemistry," p. 25, in the "Explanatory Notes" chapter.

Volatile Hydrocarbons

Headspace methane concentrations for Site 1109 displayed a typical downhole profile. Very low methane concentrations (~2–4 ppmv) were found between 0 and 100 mbsf. Below this, methane levels increased rapidly and generally remained between 1000 and 10,000 ppmv to 620 mbsf. Subsequently, the methane concentration gradually dropped to 3–6 ppmv below ~710 mbsf (Fig. F72). Ethane (C_2) was the only other hydrocarbon consistently detected, but it remained at very low concentrations (≤3 ppmv) throughout the hole (Table T12; Fig. F72). For this reason, the C_1/C_2 ratio remained high (>1000) throughout the Hole (Fig. F72). The increase in methane below 100 mbsf coincided with the disappearance of sulfate in the pore water (Fig. F70A; also see "Inorganic Geochemistry," p. 54). This, coupled with low concentrations of C_2 and the high C_1/C_2 ratio downhole (>1000), indicates that the gas is of biogenic origin.

F72. C_1, C_2, and C_1/C_2 hydrocarbon profiles, p. 166.

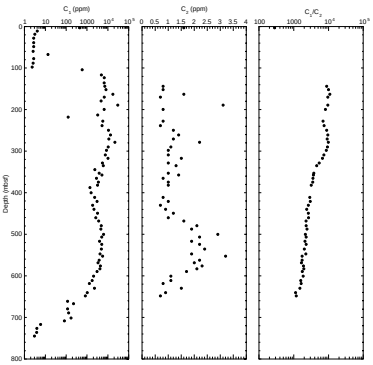

T12. Headspace gas in sediments, p. 259.

$CaCO_3$, Sulfur, Organic Carbon, and Nitrogen

The abundance of $CaCO_3$ was found to correlate well with the lithology (see "Lithostratigraphy," p. 7). The only exception to this is the outlying point at ~160 mbsf that represents a very thin carbonate layer unlike the major lithology of the unit. The sulfur abundance was very low throughout the hole, averaging ~0.16 wt% (Table T13). The organic

T13. Carbon, calcium carbonate, nitrogen, and sulfur contents, p. 261.

carbon content was also low throughout the core, averaging ~0.42 wt%, although peak concentrations of 2.73 and 1.10 wt% were observed at 218 and 702 mbsf, respectively (Fig. F73). These occur in lithostratigraphic Units III and VIII, which were both found to contain wood fragments. The peaks correlate with a high C/N ratio, indicating a terrestrial source. Below 300 mbsf, a gradual transition is seen from a mixed marine and terrigenous source to a dominantly marine source by 500 mbsf. This extends to ~630 mbsf, where there is an abrupt increase in the C/N ratio to >20, indicating terrestrially derived carbon. This change is consistent with the change in the lithologies with lithostratigraphic Units VII and VIII representing successively shallower water deposition. More terrestrial input was experienced downhole (>630 mbsf) through this transition.

F73. $CaCO_3$, organic carbon, and C/N profiles, p. 167.

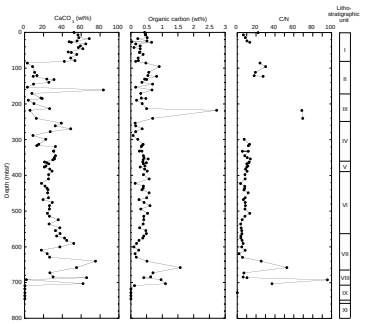

Coal

Two coal samples were collected for analysis from the base of lithostratigraphic Unit VII. These (Samples 180-1109D-38R-1, 130–131 cm, and 38R-2, 82–83 cm) were found to have organic carbon contents of 43.81 and 13.95 wt% and sulfur contents of 6.73 and 7.77 wt%, respectively (Table T13). These data have not been plotted in Figure F73.

MICROBIOLOGY

Samples for microbiological analysis were obtained from Holes 1109B (APC), 1109C (APC/XCB), and 1109D (RCB). Forty-five samples were obtained for direct microscopic examination aboard ship. Fourteen whole-round samples were taken for shore-based microbiological analysis to measure potential bacterial activities and micro-organisms that can be cultured.

T14. Bacteria and dividing and divided cells, p. 263.

Bacteria were present in all samples examined (Table T14; Fig. F74); their numbers decreased rapidly with increasing depth. In the mudline sample (180-1109B-1H-1, 0–1 cm), total bacterial numbers were 3.28 × 10^8 cells/cm^3. The TOC at 0.13 mbsf was 0.44% (see Table T13). Bacterial populations in surficial sediment at Site 1109 are similar to those at other sites with similar overlying water depths and near-surface organic carbon concentrations (see Table T10, p. 125, in the "Site 1108" chapter). Total bacterial populations in the deepest sample analyzed, 746 mbsf, were 1.24 × 10^6 cells/cm^3. Although this represents only 0.4% of the near-surface population, it still represents a substantial bacterial community at considerable depth. The population at this depth is similar to that in the deepest sample yet analyzed for the presence of bacteria, 748 mbsf at Site 997 during Leg 164, which contained 1.8 × 10^6 cells/cm^3 (Wellsbury et al., in press).

F74. Bacterial populations and dividing and divided cells, Holes 1109B, 1109C, and 1109D, p. 168.

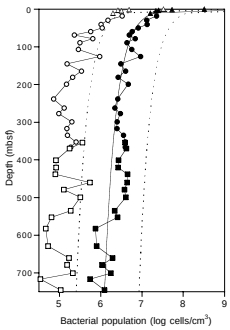

The depth distribution of total bacterial numbers in sediments from Site 1109 conforms to the general model for bacterial populations in deep-sea sediments (Parkes et al., 1994). This hole is only the second time sediments from deeper than 650 mbsf have been microscopically analyzed for the presence of bacteria, and it confirms that bacteria are ubiquitous in deep-marine sediments.

Evidence for continued microbial activity at depth in Site 1109 sediments is provided by geochemical data. Sulfate concentrations in interstitial water decrease rapidly with increasing depth in the uppermost 100 m of sediment, with complete depletion at 106.9 mbsf (see Fig. F70). In contrast, headspace methane concentrations remain low in the

uppermost 100 mbsf (in the range 2–13 ppmv between 10 and 100 mbsf), increasing rapidly to 570 ppmv at 104 mbsf and reaching 4800 ppmv by 116 mbsf (see Table T12).

In addition, subsurface changes in alkalinity and ammonia reflect the continuing action of bacterial processes downhole. The uppermost peak in pore-water ammonia concentrations is associated with a peak in bacterial numbers between 106 and 145 mbsf (Fig. F74) and is clear evidence of organic matter degradation. Deeper in the sediment, between ~430 and 480 mbsf, a secondary alkalinity maximum occurred, reflecting increased CO_2 production; concomitant with this was a second peak in pore-water ammonia between ~450 and 580 mbsf. Once again, this is reflected in a broad zone where bacterial numbers are higher than the general model (Fig. F74). Deeper in the sediment column, the in situ temperature increases; previous research has demonstrated that the bioavailability of organic matter may be affected by such temperature increases, resulting in increases in the concentration of important metabolic intermediates such as acetate (Wellsbury et al., 1997). At Site 1109, the temperature gradient was 31°C·km^{-1} (see "Temperature Measurements," p. 76), which suggests a temperature of 17.5°C around 480 mbsf. Methane concentrations are high at this depth (4748 ppmv at 479 mbsf). Whether this methane production is derived from acetate (which would account for the increase in CO_2) will be investigated further onshore.

It is significant to note that at Site 1109 there is no evidence for lateral fluid flow (see "Temperature Measurements," p. 76), and the presence of the dolerite at 773 mbsf physically prevents any fluid flux upward. Furthermore, ratios of C_1/C_2 indicate that no thermogenic gas production occurs in the sediments at Site 1109 (Table T12; also see "Organic Geochemistry," p. 59). This further substantiates the role of bacteria in controlling geochemical parameters in Site 1109 sediments.

As Holes 1109C (XCB) and 1109D (RCB) both drilled through an overlapping depth interval, they provided an opportunity to compare the effects of RCB and XCB coring on microscopic determinations of bacterial populations. Total bacterial numbers in Samples 180-1109C-38X-5, 0–1 cm (352.6 mbsf); 180-1109D-1R-2, 0–1 cm (354.3 mbsf); 180-1109C-40X-4, 0–1 cm (366.7 mbsf); and 180-1109D-3R-2, 0–1 cm (370.2 mbsf), were not significantly different (see Fig. F74).

PHYSICAL PROPERTIES

Introduction

Four holes (1109A through 1109D) were cored at Site 1109, recovering a composite profile down to a depth of 802 mbsf. Physical properties measurements included MST readings on unsplit cores as well as index properties on discrete samples from split cores. Depending on the induration of the sediment, thermal conductivity was measured from either unconsolidated whole cores or discrete rock slices. Low recovery and fragmentation of core in the deepest part of the recovered succession precluded the use of the MST from Core 180-1109D-43R downward. Both undrained shear strength and unconfined compressive strength were measured in the uppermost 220 mbsf of the succession recovered from Holes 1109B and 1109C.

Density and Porosity

All index properties data are shown in Table T15. Gamma-ray attenuation (GRAPE) density measured on unsplit cores are found to agree well with the bulk sediment density determined from discrete sediment and rock samples from Holes 1109A through 1109C (Figure F75A), but not for the RCB-cored Hole 1109D. A full compilation of GRAPE data is presented with the MST measurement data in ASCII format on the accompanying LDEO CD-ROM.

Bulk density increases gradually from about 1.50 g·cm^{-3} near the seafloor to 1.75 g·cm^{-3} at ~120 mbsf (Fig. F75). Below this interval, density data decrease to values around 1.70 g·cm^{-3} at ~250 mbsf but are characterized by high scatter. This zone (~120–250 mbsf) corresponds to lithostratigraphic Units II and III (see "Lithostratigraphic Unit II," p. 11, and "Lithostratigraphic Unit III," p. 13), and was deposited rapidly (i.e., at rates of ~400 m/m.y.; see "Biostratigraphy," p. 43). From ~250 to 374 mbsf, an almost linear increase in density exists from ~1.50 to 1.80 g·cm^{-3} (Fig. F75A). Below 380 mbsf, the GRAPE data from the RCB-cored Hole 1109D are consistently lower than the bulk density determinations from index properties measurements, although the observed trends of each remain similar. Lower densities from ~340 mbsf to 390 mbsf occur within the predominantly claystones and clayey siltstones of lithostratigraphic Unit V (see "Lithostratigraphic Unit V," p. 18). Density values increase with depth between ~390 and 670 mbsf, ranging from 1.70 to 1.90 g·cm^{-3} (Fig. F75). This interval is within lithostratigraphic Units VI and VII, which are characterized by relatively high sedimentation rates (231 m/m.y.; see "Biostratigraphy," p. 43). Below ~670 mbsf, the density data vary widely within the neritic, lacustrine, lagoonal, and subaerial deposits of lithostratigraphic Units VII to X. These units consist of siltstones and conglomerates. The GRAPE densities range from 1.50 g·cm^{-3} to values greater than 2.20 g·cm^{-3}, the latter of which occur in conglomeratic units containing igneous rock clasts within a calcareous matrix. No GRAPE densities were obtained from the dolerite flows of lithostratigraphic Unit XI because of extensive core fracturing. Laboratory results on discrete samples, however, yielded bulk densities of 1.95–2.00 g·cm^{-3} for the sandstones and grainstones of lithostratigraphic Unit VII and 1.80–2.20 g·cm^{-3} for the underlying lagoonal sediments of lithostratigraphic Unit VIII. Dolerite bulk densities were found to vary between 2.50 and 3.00 g·cm^{-3} (Fig. F75A).

By comparison with bulk densities from the index properties measurements, GRAPE densities were generally found to be 0.2 to 0.3 g·cm^{-3} lower in cores recovered from Hole 1109D (i.e., beneath 380 mbsf in Fig. F75A). This discrepancy most likely relates to the decrease in diameter of the core produced by the RCB technique of drilling. However, correction of the GRAPE density data for the difference in both the core diameter (d_{XCB}/d_{RCB} = 1.15789) and the gamma-ray path length (factor 1.1726; following Boyce, 1976) failed to provide a satisfactory result. An empirical factor of 1.11691 led to a data shift resulting in excellent agreement between the GRAPE and index properties data. However, no theoretical justification can be found for this factor. The uncorrected GRAPE densities from the RCB, presented in Figure F75A, underestimate the bulk densities as determined by the index properties measurements. As a result, the GRAPE bulk sediment density should be used with caution.

T15. Index properties of cores, p. 264.

F75. Bulk density and grain density measurements, p. 169.

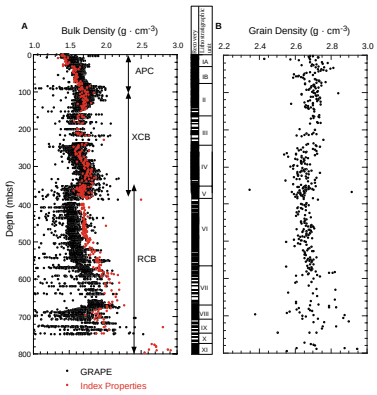

Grain density was found to vary little with depth in the uppermost 380 mbsf, ranging from 2.55 g·cm^{-3} to 2.75 g·cm^{-3} (Fig. F75B). There is an overall but slight decrease in grain density in this interval, apparently independent of either lithology or grain size (Fig. F75). An increase in grain density with depth can be seen below 380 mbsf and may be associated with the higher abundance of volcaniclastic sands within lithostratigraphic Unit VI. Values between 2.65 and 2.75 g·cm^{-3} occur from 380 to 580 mbsf. Below this interval, grain density data are characterized by high scatter and an overall increase to values of up to 2.85 g·cm^{-3}. Carbonate can only partly explain the overall grain density trend, being pertinent for the carbonate increase within the section from 420 to 580 mbsf (see "Organic Geochemistry," p. 59) and with the carbonate-rich packstones and grainstones of lithostratigraphic Unit VII (580–670 mbsf; Fig. F75B). The change in the grain density trend at around 380 mbsf is likely related to a change in provenance, as suggested from clast compositions and paleomagnetic evidence (see "Lithostratigraphy," p. 7, and "Paleomagnetism," p. 48). In the lowermost part of the recovered succession, wide variations in grain density reflect the lagoonal and subaerial deposits of Units IX through XI (Fig. F75B, "Lithostratigraphic Unit IX," p. 27, and "Lithostratigraphic Unit X," p. 30).

Porosity vs. depth strongly reflects bulk density variations, as expected from the method used for determination (see "Index Properties Measurements," p. 31, in the "Explanatory Notes" chapter). As illustrated in Figure F76, the uppermost part of the recovered section shows a strong reduction in pore space from an initial value of nearly 80% at the seafloor to values of 55%–60% at ~130 mbsf. The observed range in porosity corresponds approximately with what is known for the compaction of fine-grained marine sediments (e.g., Brückmann, 1989; Athy, 1930). Porosities are higher than expected in the intervals between ~130–280 mbsf and ~340–540 mbsf (Fig. F76). The first interval has porosities of 60%–68%, and the second has values between 55% and 62%. Similarly, results from anisotropy of magnetic susceptibility (AMS) indicate a smaller amount of uniaxial shortening parallel to the core axis in these intervals than in the overlying units (see "Magnetic Susceptibility," p. 48). High porosity zones, the AMS data, and the undrained shear and unconfined compressive strength are all consistent with the presence of underconsolidation zones within the recovered section. Underconsolidation and possible overpressuring of the anomalous intervals may be a consequence of rapid sedimentation rates (~225–312 m/m.y; see "Sedimentation Accumulation Rate," p. 48) and overlying low-permeability sediments hindering fluid escape from these intervals (Fig. F76). Although no in situ pore pressure or permeability tests have been conducted, this hypothesis is supported by the existence of high-frequency fine-grained sediments at ~105–125 mbsf and 310–340 mbsf above the high-porosity intervals (see "Lithostratigraphy," p. 7). These clay-dominated sediments may well have prevented fluid expulsion from the underlying, rapidly deposited, coarser grained turbidites. The lowermost part of the porosity curve is controlled by the lithology, showing a distinct decrease down to 30%–40% within Units VII and VIII (packstones, siltstones, and claystones) but an increase of up to ~45% in the sandstones and conglomerates of Units IX and X (see "Lithostratigraphic Unit IX," p. 27, and "Lithostratigraphic Unit X," p. 30).

F76. Comparison of porosity with sedimentation rate and grain size distribution, p. 170.

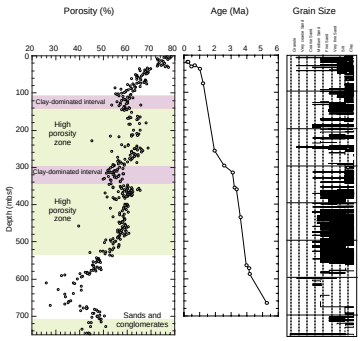

Compressional-Wave Velocity

The *P*-wave velocity was measured using the *P*-wave logger (PWL) on the MST, the PWS1 and PWS2 insertion probe system, and the PWS3 contact probe system. The PWL logging on unsplit core yielded poor quality results; therefore, only the PWS data is presented here. All PWS data can be found in Table T16.

Transverse (i.e., across the core axis) and longitudinal (i.e., along the core axis) *P*-wave velocities were measured from Holes 1109A through 1109D. Below 270 mbsf (i.e., from Core 180-1109C-28X downward), the sediment was well lithified, requiring velocity measurements to be conducted on rock cubes in the x, y, and z directions. Data are presented in Figure F77.

Velocities obtained above 100 mbsf yielded values between ~1500 and 1650 m·s^{-1}, as expected for poorly consolidated marine sediments. The velocities in the x and y (transverse) and z (longitudinal) directions show a linear increase with depth (Fig. F77). At ~560 mbsf, longitudinal velocities increase to ~1900–2050 m·s^{-1}. Below 560 mbsf, a prominent increase in velocity is seen, with values ranging from >2000 m·s^{-1} to almost 3900 m·s^{-1} (shaded area in Fig. F77). These high velocities, particularly those in excess of 3000 m·s^{-1}, correlate strongly with the existence of calcareous and siliceous cements (e.g., at 390 mbsf). In general, the steady increase in carbonate content with depth, from 420 to 480 mbsf (see "Inorganic Geochemistry," p. 54), corresponds to the general increase in velocities with depth. The abrupt increase and scatter in the velocities within the packstones and sandstones of lithostratigraphic Unit VII relates to their carbonate content (see "Lithostratigraphic Unit VII," p. 22). Velocities drop back to values around 2000 m·s^{-1} at a depth of ~680 mbsf and do not exceed 2300 m·s^{-1} within samples from the lagoonal siltstones and sandstones of lithostratigraphic Unit VIII. At the bottom of Hole 1109D, dolerite with velocities of 5000–6000 m·s^{-1} was measured.

Triaxial seismic velocity measurements indicate that the transverse and longitudinal velocities typically differ by <5% (Fig. F78). Nevertheless, there is a considerable amount of scatter within the data shown in Figure F78A and F78B. From 300 to 565 mbsf, the anisotropies are consistently skewed by ~5% toward higher transverse velocities. This interval correlates with the claystones and siltstones of lithostratigraphic Units IV, V, and VI. From ~580 to 700 mbsf, the anisotropy increases to values in excess of 15%, and is associated with the carbonate-rich sandstones, packstones, and grainstones of lithostratigraphic Unit VII and the claystones and siltstones of lithostratigraphic Unit VIII. The scatter within these latter units may be related to carbonate-rich and organic-rich intervals. It is unclear as to why the average transverse velocities should be greater than the longitudinal velocities; however, this effect is observed for claystones, siltstones, sandstones, and conglomerates alike.

Thermal Conductivity

Thermal conductivity on unsplit cores was obtained for all material recovered from Holes 1109A, 1109B, and 1109C. For RCB cores in Hole 1109D, measurements were carried out on discrete samples. Depending on core quality and time available, the number of measurements per core varied from two to six (Table T17). The reported value per measurement is an average of the repeat measurements. For the purpose of com-

T16. Longitudinal and transverse velocities for cores, p. 272.

F77. Site 1109 *P*-wave velocities (x, y, and z), p. 171.

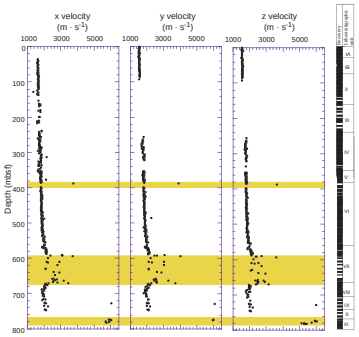

F78. Longitudinal velocity vs. transverse velocity and anisotropy with depth, p. 172.

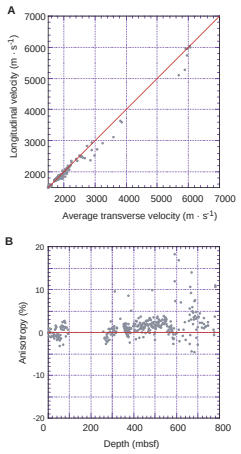

T17. Thermal conductivity values, p. 279.

parison between the two methods (and probes), thermal conductivity was determined on several cores both before and after splitting. The results were consistent and assured confidence in the data sets. This observation is supported indirectly, because no shift in the data is observed at the Hole 1109C–Hole 1109D transition at ~375 mbsf (Fig. F79).

Above 100 mbsf, thermal conductivities are 0.8–1.1 W·m^{-1}·°C (Fig. F79), increasing linearly with depth. From 100 mbsf to nearly 280 mbsf, thermal conductivity is widely scattered (0.7–1.1 W·m^{-1}·°C). This zone corresponds to Units III and IV and, more importantly, to the high porosity zones discussed above. Alternatively, some of the scatter may be related to using the needle probe in cores that are semilithified. In such cores, the coupling between sediment and probe is sometimes compromised (see "Thermal Conductivity," p. 30, in the "Explanatory Notes" chapter). Below 280 mbsf, thermal conductivities appear to follow a linear trend with depth. At ~300 mbsf, typical values are ~1.0 W·m^{-1}·°C, whereas at around 600 mbsf (i.e., the sandstones and packstones of lithostratigraphic Unit VI) an overall increase to ~1.35–1.5 W·m^{-1}·°C is observed. The lagoonal and subaerial deposits underlying Unit VII are thermally less conductive, ranging between 1.0 and 1.15 W·m^{-1}·°C (Fig. F79). This decrease in conductivity corresponds most likely to the inhomogeneous composition of the sediments that contain goethite nodules and clasts of various rock types. Thermal conductivities increase to values between 1.4 and 2.0 W·m^{-1}·°C for the dolerite recovered at the base of Hole 1109D.

F79. Site 1109 thermal conductivity, p. 173.

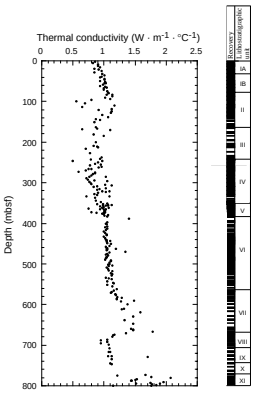

Shear Strength and Compressibility Measurements

Split cores from Holes 1109B and 1109C were used to determine undrained shear strength and unconfined compressive strength using the motorized miniature vane-shear device and the pocket penetrometer, respectively. These strength parameters could not be measured below 220 mbsf because of increasing induration of the sediment. The data are presented in Figure F80, and listed in Table T18.

Undrained shear strength (S_u) shows a slight linear increase with depth, rising from 10 kPa near the seafloor to ~30–40 kPa at 50 mbsf (Fig. F80). This depth range is characterized by the nannofossil-rich calcareous sands of lithostratigraphic Subunit IA. Within the clay-dominated turbidites of lithostratigraphic Subunit IB, the strength increases more rapidly to values up to 125 kPa at ~72 mbsf. From the top of Unit II (83.4 mbsf) downward, strength decreases to values as small as 10 kPa, which can be partially explained by the effects of bioturbation, volcaniclastic enrichment of the sediment, or drilling disturbance of the core.

If the unconfined compressive strength (2 S_u) is compared to the undrained shear results, similar trends can be recognized. A linear increase in strength is observed over the uppermost interval between ~20 and 120 mbsf, with strengths ranging from 30 kPa to more than 200 kPa. Below ~120 mbsf, even the unconfined compressive strength drops to values close to those obtained near the seafloor (Fig. F80). With the exception of the outliers, in the interval below 130 mbsf strength is generally ~40–50 kPa and does not exceed 100 kPa.

From a least-squares linear fit to the strength data, the extrapolated downhole trend was found to vary between 0.30 and 2.57 kPa·m^{-1} (from undrained shear strength, with an average of 1.18 kPa·m^{-1}) and

F80. Site 1109 undrained shear strength and unconfined compressive strength, p. 174.

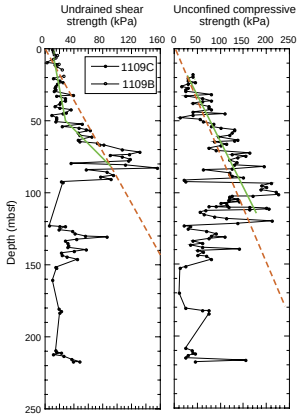

T18. Unconfined compressive and vane shear strengths, p. 291.

1.60 kPa·m^{-1} (based on the pocket penetrometer data). The state of sediment consolidation can be estimated by comparing the range of strengths measured relative to a normally consolidated sediment, expressed as the ratio of undrained strength (S_u) to effective overburden stress (P_0'). The effective overburden stress is calculated using grain and pore-water density and the thickness of the overlying sedimentary succession, if hydrostatic pore-fluid pressures are assumed. Normally consolidated sediments show S_u/P_0' ratios of 0.2 (e.g., Mesri, 1975), as shown by the dashed red line in Figure **F80.** Note that the dashed red line would have a steeper gradient if the pore-fluid pressure were above hydrostatic. However, it can be inferred that the upper part of the sediments, namely lithostratigraphic Units I and II, have undergone normal consolidation. On the other hand, the sediment beneath ~130 mbsf is underconsolidated, as has been suggested from the porosity and bulk density (see discussion in **"Density and Porosity,"** p. 62).

Magnetic Susceptibility

Magnetic susceptibility reflects changes in magnetic mineralogy (e.g., lithologic variations) and was obtained routinely as part of the MST measurement of sediment cores from Holes 1109A through 1109D. The quality of magnetic susceptibility data is a function of reduced core diameter and/or increased disturbance to the core by the drilling process; therefore, it commonly degrades from APC- to XCB- to RCB-cored sections. The full magnetic susceptibility data set can be found as part of the MST compilation in ASCII format on the accompanying LDEO CD-ROM.

The magnetic susceptibility of the recovered section is displayed in Figure **F81** and is compared with grain-size distribution and the remanent magnetic intensity. Because of this compressed scale, only the general trends can be identified. In particular, there exists a first-order difference between the high-amplitude susceptibility within the upper part of the section (80–380 mbsf) and the low-amplitude susceptibility within the middle part of the section (380–540 mbsf). The transition occurs within lithostratigraphic Unit V and marks the first input of metamorphic detritus into the basin. The high-amplitude magnetic susceptibility zone between 80 and 360 mbsf correlates with the presence of high-frequency, fine-grained turbidites. In contrast, the low-amplitude magnetic susceptibility zone (380–540 mbsf) relates to high-frequency turbidites that are characterized by abundant fine to coarse sands. Lithologically, these differing clay- and sand-dominant turbidite units have been termed distal and proximal, respectively (see **"Lithostratigraphy,"** p. 7). Second-order trends are represented by the relatively high amplitude susceptibility variations occurring at the base of lithostratigraphic Unit VI and the transition between lithostratigraphic Units VI and VII (540–600 mbsf), the lagoonal and subaerial deposits on lithostratigraphic Units IX and X, and the dolerite at the base of Hole 1109D (Unit XI; 720–796 mbsf).

At the top of the succession, frequent ash and sand layers interbedded with nannofossil clays correspond with spikes on an otherwise uniform curve. Highly variable but generally increased susceptibilities were obtained from 80 and 170 mbsf, which strongly reflects the increase in volcaniclastic input to the section (i.e., lithostratigraphic Unit II) and possibly the dominance of silts and clays (Fig. **F81A**). Within Units III, IV, and V, no obvious correlation between grain size and susceptibility

F81. Comparison of grain-size distribution and magnetic data, Holes 1109C and 1109D, **p. 175.**

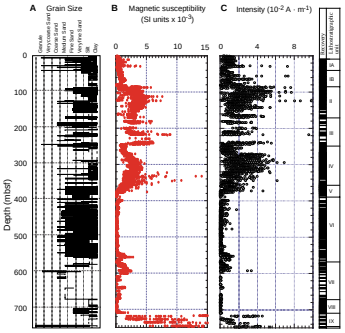

can be found (see "Site 1109 Core Descriptions"). Apparently, some, but not all, of the spikes in the susceptibility curve correlate with the location of coarse-grained sediment. On the other hand, the presence of two high-frequency turbidite intervals (in Units II and V; see "Lithostratigraphic Unit II," p. 11, and "Lithostratigraphic Unit V," p. 18) correspond to relatively high susceptibilities. However, data scatter is more likely related to different sources of material within these sediments, namely metamorphic components and mixed-layer clays (see "Lithostratigraphy," p. 7). Sediments above Unit V consist of clays and silts including components of altered calc-alkaline volcaniclastic material and metamorphic detritus, with smectite and mixed-layer clays. Below ~370 mbsf, magnetic susceptibility is rather uniform and near zero in lithostratigraphic Unit VI. Here, turbiditic sands and muds derived from a dominantly fresh basalt-andesite volcanic source with minor neritic carbonates show little or no alteration, suggesting a major change in provenance.

Unit V is a transitional interval (350–380 mbsf), with both variable grain size and scatter in magnetic susceptibility. The observed relationships imply that the magnetic material derived from the clastic source regions of both the lower uniform and the upper, more susceptible interval appears both in fine- and coarse-grained deposits. The remarkable change at ~370 mbsf is reflected in the results from both the natural gamma ray (NGR) logging data as total gamma ray count (HSGR) (refer to Fig. F88) and the remanent magnetization intensity (see both Fig. F81 and "Paleomagnetism," p. 48). The packstones of lithostratigraphic Unit VII (~560–645 mbsf) show consistently higher magnetic susceptibility compared with the overlying lithostratigraphic units, whereas the underlying claystones are uniformly close to zero. Both the altered siltstones of proposed lagoonal origin (including Fe-rich concretions scattered within; see "Lithostratigraphic Unit VII," p. 22) and the conglomerates with variable clast lithologies exhibit higher susceptibilities, often exceeding 0.015 SI.

By comparing the magnetic susceptibility with the remanent magnetization intensity (see "Remanent Magnetization," p. 50), it is possible to determine if the mineralogy carrying the magnetic remanence is also responsible for the susceptibility. Figure F81 compares the magnetic susceptibility, grain size, and remanent intensity. Within the sequences characterized by a metamorphic clastic component (0–380 mbsf), there exists a direct correlation among the susceptibility, NGR (Fig. F82; also see "Natural Gamma Ray," p. 67), and remanent intensity. We conclude that, in general, the mineralogy controlling the magnetic susceptibility is the same as that controlling the remanent magnetic intensity. Further, the correlation between NGR variations and the magnetic susceptibility suggests that the clays and sands containing radioactive material also are rich in ferromagnesian minerals.

F82. Natural gamma ray and magnetic susceptibility, Holes 1109C and 1109D, p. 176.

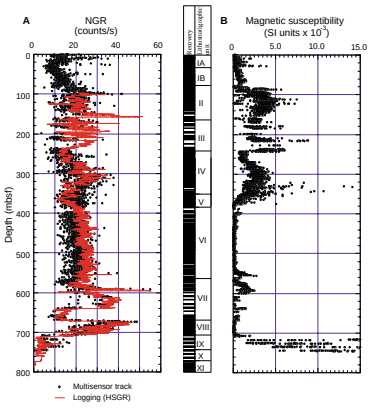

Natural Gamma Ray

The NGR count was recorded on the MST, and a composite log is shown in Figure F82. The full data set can be found as part of the MST compilation in ASCII format on the accompanying LDEO CD-ROM. Superposed on the NGR count is the HSGR logging data. The excellent agreement between the MST gamma-ray data and the logging gamma-ray data supports use of the logged data in regions of poor core recovery. Although there is significant scatter, a number of general trends can be recognized in the data. From the seafloor to 380 mbsf, the NGR

count is remarkably similar in form to the magnetic susceptibility (Fig. F82) and the bulk density (Fig. F75). This same range consists of the high-frequency distal turbidites referred to above. From 380 to 580 mbsf, the NGR count is rather uniform although the absolute level is ~20 counts/s. The local NGR count maxima centered on 140 and 320 mbsf have about the same value. Further, both the majority of the carbonate-rich lithostratigraphic Unit VII and the lagoonal/swamp deposits of lithostratigraphic Unit VIII are associated with high NGR counts.

In general, there is no straightforward relationship between high and low NGR with the presence of clay/silts and sands, respectively. The reason why this simple distinction cannot be made at Site 1109 may be that either the sequences are poorly sorted or that the lithology varies on a rather small scale. The characteristic highs at 80–180 mbsf and 260–370 mbsf (see Fig. F82) do not correspond to obvious lithostratigraphic changes or unit boundaries (Fig. F82). The usual high/low NGR relationship is confounded at Site 1109 by the presence and intermixing of radioactive sands and clays. For example, a ~12-m-thick sand layer interpreted at 219–231 mbsf is marked by a strong NGR peak. This sand layer was not recovered except for minor amounts in the core catcher (for details, see "Lithologic Analysis," p. 70). In contrast, the overlying clay unit (210–219 mbsf) of similar thickness as the sand is characterized by a low NGR count. The abrupt change from variable amounts of radioactive sediment components in the upper part of the succession to a uniformly lower level at ~370 mbsf may correspond to the change in provenance mentioned above (see "Lithostratigraphy," p. 7).

Hole-to-Hole Correlation

An important application of MST measurements is to determine the correlation between multiple holes at this site (see detailed section on "Composite Depths," p. 79). For this purpose, GRAPE density, magnetic susceptibility, and NGR were used to correlate between Holes 1109A, 1109B, and 1109C, and magnetic susceptibility to correlate between Holes 1109C and 1109D. The correlation is based on recognizing characteristic features in the data sets. For example, Figure F83 shows a small, relatively high density, calcareous sand unit at 2.75–3.25 mbsf in the Hole 1109A core. A similar density anomaly exists within the core at Holes 1109B and 1109C, suggesting (1) minimal offset between Holes 1109A and 1109B and (2) a 0.4- to 0.5-m offset between Holes 1109B and 1109C (shaded zone, Fig. F83). Similarly, the magnetic susceptibility contains distinct peaks at 5.2–5.5 mbsf and 9–10 mbsf, and the NGR has a sequence of characteristic peaks at 7.45–10 mbsf and at 10.8–11.5 mbsf (shaded zones; Figs. F84, F85). Unlike the GRAPE density interhole correlation, these data suggest a minimal offset between Holes 1109A and 1109C.

The magnetic susceptibility data were also used to correlate between Holes 1109C and 1109D (Fig. F86). A characteristic arrangement of peaks exist between 355 and 356 mbsf in Hole 1109C cores. This same pattern exists in Hole 1109D but between 355.7 and 356.5 mbsf, suggesting an offset of 0.5 m (shaded zone, Fig. F86).

F83. Correlation between Holes 1109A, 1109B, and 1109C using density data, p. 177.

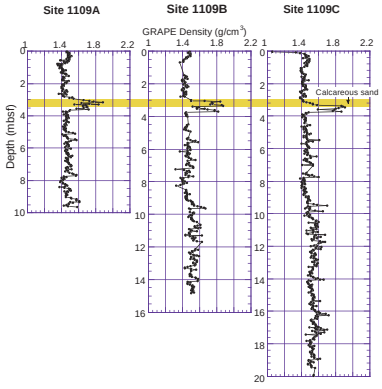

F84. Correlation between Holes 1109A, 1109B, and 1109C using magnetic susceptibility data, p. 178.

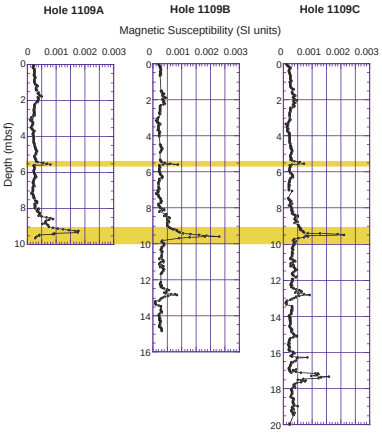

F85. Correlation between Holes 1109A, 1109B, and 1109C using NGR data, p. 179.

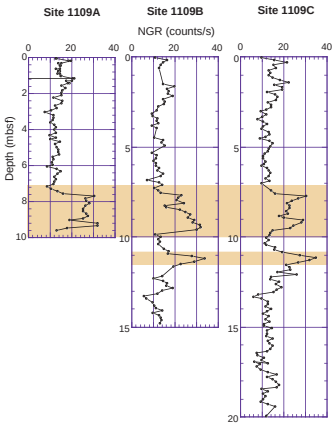

Comparison of Core Data with Results of Downhole Measurements

Physical properties measurements obtained from cores and downhole logging data from Site 1109 provide complementary data sets. Logging data yield denser measurements and fill gaps in areas of low core recovery. Core measurements provide data in areas where logging is effectively precluded by either the drill pipe (above ~120 mbsf) or washouts. It is interesting to note that the volume of rock involved in a downhole logging measurement is on the order of 30 dm^3 (1 cubic foot), whereas that of a physical properties measurement is on the order of 1 cm^3. In addition, physical properties measurements can be directly related to other shipboard core descriptions and measurements. Index properties determinations of bulk density are in good agreement with those from the logging run, although logging data show slightly higher magnitudes (Fig. F87). Significantly, logging data confirm a high-density zone around 219–233 mbsf that was poorly defined by physical properties measurements because of low recovery (see "Log Unit L2," p. 71). Logging data below 680 mbsf indicate very low bulk densities, but data quality in this zone may have been degraded by washouts.

Core physical properties measurements of longitudinal (z-direction) velocity show excellent agreement with data from downhole sonic velocity logs (Fig. F86). Logging data reveal a high-velocity interval between ~220 and ~233 mbsf, coincident with the high-density zone and poor recovery.

DOWNHOLE MEASUREMENTS

Operations

Four logging runs were recorded in Hole 1109D: one triple combo run that logged from a total depth of 786 mbsf to above mudline, two FMS-sonic runs that logged the top and bottom parts of the hole, and a VSP run. "Vertical Seismic Profile and Depth Conversion," p. 76, describes the VSP data and operations, and this section concentrates on the other logging runs.

For the first run, the pipe was raised to 99 mbsf, and the triple combo with dual induction tool (DIT) (see Table T7, p. 74, and Fig. F15, p. 66, both in the "Explanatory Notes" chapter) was lowered downhole. HNGS data were monitored during the descent in the pipe to locate the mudline where the string was stopped for 3 min to provide a depth reference for the TLT. Upon reaching open hole, HNGS and DIT data were logged during the descent (Table T19). The tool had difficulty going down between 350 and 375 mbsf but was finally worked down to nearly total depth (786 mbsf; Table T19). An upward log was then recorded at 300 m/hr. A 7.5-kN (1500 lb) overpull was necessary to pass through the 375–350 mbsf interval. The pipe was then raised to 79 mbsf, and the log was recorded up to 68 m above mudline. The tool string was then lowered again to 141 mbsf for a short, second repeat pass up to 24 mbsf. It was then stopped at the mudline for a few minutes both to run calibrations and to give the TLT data a depth reference.

The caliper log from the lithodensity tool (Fig. F88) revealed four intervals between 330 and 375 mbsf where the borehole diameter was smaller than drill-bit size (25.1 cm [9-⅞ in]). Over one 5-m interval (365–370 mbsf), the hole size was less than 10 cm (4 in). This is thought

F86. Correlation between Holes 1109C and 1109D using magnetic susceptibility data, p. 180.

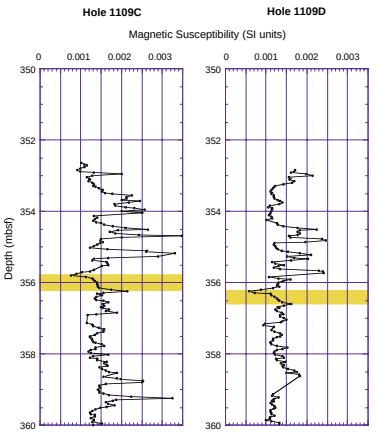

F87. Comparison of physical properties measurements with equivalent downhole logging data, p. 181.

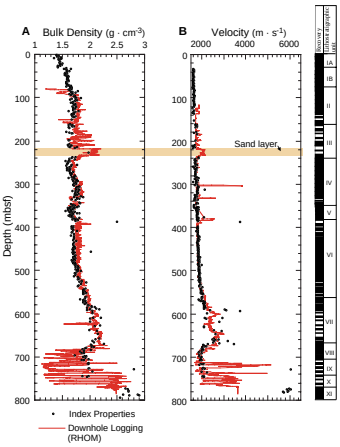

T19. Logging operations, Hole 1109D, p. 295.

F88. Hole 1109D composite log, p. 182.

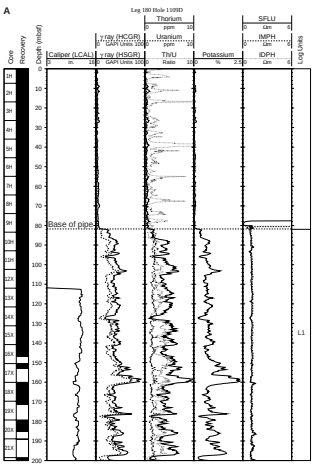

to be caused by clay swelling because it occurs in one of the most clay-rich units of the borehole (see description, "Log Unit L5," p. 71).

For the second run, the pipe was lowered again to 99 mbsf, and the FMS-sonic string (see Table T7, p. 74, and Fig. F1, p. 51, both in the "Explanatory Notes" chapter) was lowered downhole. The string could not pass the 351-mbsf restriction; therefore, the log was run from 351 mbsf up to the bottom of pipe, which was again raised to 79 mbsf (Table T19). The logging speed was 300 m/hr.

After the tools were out of the hole, the pipe was lowered to 381 mbsf (drill-pipe depth) to allow the tools to pass below the 350-mbsf restriction. A second descent was made with the FMS-sonic string. This time, the tool encountered serious drag just below the pipe but was finally worked through and reached the total depth (786 mbsf; Table T19). The upward log was then recorded at 300 m/hr. When the tool reached 344 mbsf, it encountered serious drag that required 9 kN (2000 lb) overpull. The FMS calipers would not close entirely upon reaching the pipe. After multiple opening and closing sequences and washing with circulating fluid, they closed enough for the tool to be dragged inside the pipe up to the rig floor with a slight overpull.

Depth Shifts

The mudline wireline depth (Table T19), which defines the depth shift from meters below rig floor to meters below seafloor, was located by its associated natural gamma-ray decay for the triple combo run (Fig. F89). The depth shift for the first and second FMS-sonic runs were derived by correlating the NGR with that of the triple combo run, respectively, within the 140–170 mbsf (Fig. F90) and 570–600 mbsf (Fig. F91) intervals that were chosen for their large, characteristic variations.

Lithologic Analysis

Generally, natural gamma-ray magnitude is proportional to clay content, but a surprising aspect of the log response in Hole 1109D is that the formations containing the least clay actually exhibit the highest gamma-ray values. One is left to rely upon the relationship between the neutron and density porosity (APLC and DPHI; see "Lithologic Analysis," p. 37, in the "Explanatory Notes" chapter) to discriminate high-clay and low-clay (clean) lithologies.

Also in Hole 1109D, uranium content varies little, and the total gamma ray appears to be controlled mainly by the thorium and potassium contents, which are often correlated.

The log analysis, combined with the results of core analysis, defines 11 logging units (Fig. F92); shows the recurrence of a carbonate to sand to clay sequence; confirms that sonic velocity increases are correlated mostly with increased carbonate content (a result obtained from physical properties measurements; see "Comparison of Core Data with Results of Downhole Measurements," p. 69); and reveals several potential seismic reflectors not recovered in the cores.

Log Unit L1 (82–219 mbsf)

The APLC is larger than the DPHI, which indicates a significant clay content. However there are many short intervals where the two porosity logs converge, indicating thin, clean beds. Three clean intervals are thicker than 1 m: 156–161 mbsf (Fig. F93), 192–200 mbsf, and 209–211

F89. Hole 1109D total gamma ray from the triple combo at mudline after depth shifts, p. 190.

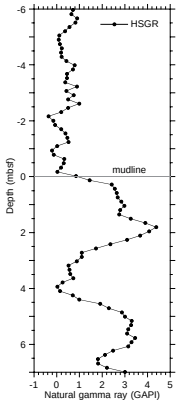

F90. Hole 1109D total gamma ray from the triple combo and FMS-sonic first run after depth shifts, p. 191.

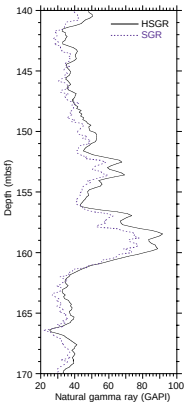

F91. Hole 1109D total gamma ray from the triple combo and FMS-sonic second run after depth shifts, p. 192.

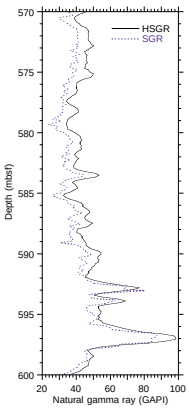

mbsf (Fig. F94). The two upper intervals exhibit the same lithologic sequence, beginning at the bottom with a layer that is carbonate rich as shown by the high photoelectric effect (PEFL) and confirmed by $CaCO_3$ analysis at 161 mbsf (see "$CaCO_3$, Sulfur, Organic Carbon, and Nitrogen," p. 59) and that displays low gamma-ray magnitude and a marked sonic velocity increase. Just above the inferred carbonate is a clean interval with high gamma-ray magnitude interpreted to be a radioactive sandy layer. In the case of the 156–161 mbsf interval, the sandy layer has the highest gamma-ray magnitude in Unit L1 and the second highest gamma-ray magnitude encountered in this borehole. It also coincides with the presence of K-feldspars, as reported in the lithostratigraphy section. The lowest interval shows mainly a low (50%) porosity sandy layer and sonic velocity increase. Another thin bed (<1 m) of low clay content is located at 176 mbsf.

Log Unit L2 (219–234 mbsf)

This is the third thickest clean unit in the borehole and one of the most prominent seismic reflectors at this site, as described in "Vertical Seismic Profile and Depth Conversion," p. 76. It follows the pattern seen in clean intervals in log Unit L1: a thin lower carbonate-rich layer grading into a thick radioactive sandy layer (Fig. F94). The sonic velocity increase is associated with a decrease in porosity, although the velocity peak at the bottom is associated with the higher carbonate content. This unit also exhibits the highest Th/U value in the borehole (Fig. F88), which suggests the presence of volcanic minerals (Shipboard Scientific Party, 1997). This interval was poorly recovered in core and corresponds to an observed increase in grain size (see Fig. F94F and "Lithostratigraphy," p. 7).

Log Unit L3 (234–293 mbsf)

This unit is clay dominated, similar to Unit L1, but has a slightly lower gamma radioactivity and a slightly higher porosity, especially if its greater burial is considered. There are no significantly thick, clean beds in the interval.

Log Unit L4 (293–330 mbsf)

This unit is more compacted than Unit L3 and displays higher gamma-ray magnitude and a thin, clean bed at 305 mbrf (Fig. F95). Thus, it has more affinity with Unit L1. Two sharp peaks of gamma-ray counts at 307 and 315 mbrf (Fig. F95) arise close to where mixed-layer clays were observed (see "Lithostratigraphy," p. 7).

Log Unit L5 (330–390 mbsf)

This unit, like Unit L3, shows lower gamma-ray magnitude and a near absence of clean beds: the only thin clean interval is located at 365 mbsf. Moreover, the divergence between the two porosity curves is consistently large, indicating a completely clay-dominated unit. It also corresponds to the zone where borehole diameter was under drill-bit size (Fig. F88). A change in clay mineralogy may be partly responsible for the differences between this and other zones. In addition, this unit contains a fault zone (Fig. F92) described in "Structural Domain IV," p. 40.

F92. Hole 1109D log units and correlations, p. 193.

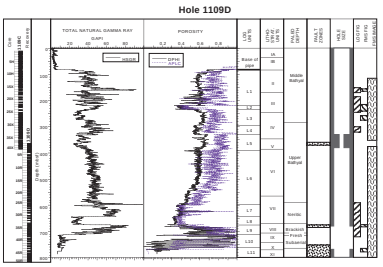

F93. Hole 1109D logs in the 150–170 mbsf interval, p. 194.

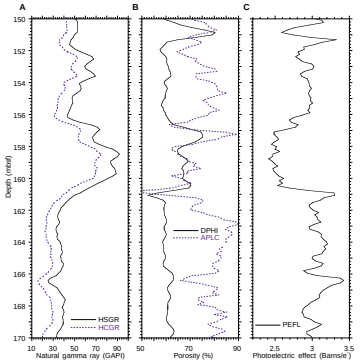

F94. Hole 1109D logs and grain size from core observations in the 185–245 mbsf interval, p. 196.

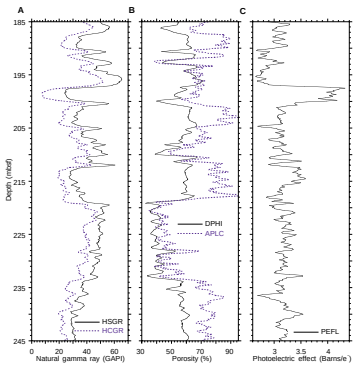

F95. Hole 1109D logs within the 300–320 mbsf clay-rich interval, p. 198.

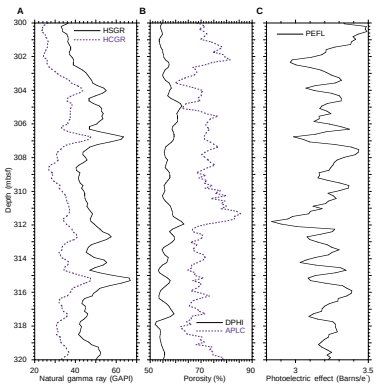

Log Unit L6 (390–599 mbsf)

This unit has some similarity with the top part of Unit L1: high gamma-ray counts, high clay content as shown by the divergence of the two porosity curves, and numerous thin, clean beds located at 415.5, 442, 455.2, 476, 518, 528, 534, 571, and 593 mbsf. Below 500 mbsf, carbonate content increases smoothly as shown by PEFL.

Log Unit L7 (599–643 mbsf)

This unit (Fig. F96) marks a sharp change of trends from Unit L6: gamma-ray counts increase, porosity drops, and the formation is consistently clean. This unit appears to be dominated by radioactive sands as in Unit L2, with some carbonate and clay added to the mixture. In the uppermost part (602 mbsf), a thin layer shows a high carbonate content, as indicated by PEFL and sonic velocity increase.

F96. Hole 1109D logs within the 590–720 mbsf interval, p. 200.

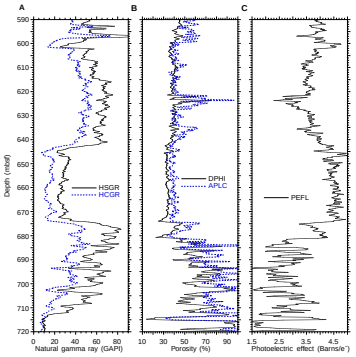

Log Unit L8 (643–673 mbsf)

This is a carbonate-dominated, clean unit with some sand and clay, high PEFL, high sonic velocity, higher resistivity, and very low gamma ray (Fig. F96). Together, Units L8, L7, and the bottom part of L6 seem to repeat the carbonate to sand to clay pattern on a much larger scale than observed above in the hole.

Log Unit L9 (673–714 mbsf)

This unit (Fig. F96) is characterized by high gamma ray counts, low PEFL, and higher uranium content than any other unit. It corresponds very closely to lithostratigraphic Unit VIII. It also corresponds to a zone of thin washouts (Fig. F88).

Log Unit L10 (714–762 mbsf)

This unit is defined by a very sharp drop in gamma-ray radioactivity. It shows alternations of low-resistivity layers that correlate with large washouts, alternating with high-resistivity layers that have similar log response to dolerite in Unit L11 (Fig. F88). Resistive layers are likely to be dolerite conglomerate recovered in core. Washed-out layers are unconsolidated material of low sonic velocity, probably sand, silt, and clay. The contrast between these layers suggests that the boundaries are excellent seismic reflectors.

Log Unit L11 (762–775 mbsf)

This unit is distinguished by a slight increase in gamma ray radioactivity, a hole perfectly in gauge, the highest borehole resistivity, and the lowest porosity, and corresponds to the dolerite of lithostratigraphic Unit XI.

F97. Hole 1109D deviation, p. 202.

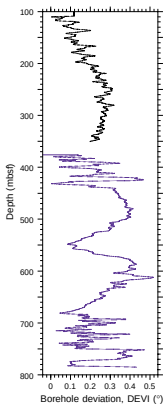

Borehole Geometry, Magnetic Field, and FMS Dynamics

The accelerometer data of the FMS-sonic run show that the hole deviation remains below a half degree (Fig. F97). They also show a more dispersed acceleration magnitude for the upper run than for the lower

one (Fig. F98), which indicates a more irregular tool movement and lower quality raw images, as was observed during logging.

The FMS caliper data reveal periodic enlargement in the 240–330 mbsf and 440–600 mbsf intervals (Fig. F99). The spacing between these washouts corresponds to the core length of ~9.5 m. They are probably caused by the circulation that is maintained when the drill bit progression halts during core retrieval.

During the lower FMS run, the tool string rotated as expected (Fig. F100). However, during the upper run the tool orientation remains remarkably constant: Pad 1 is oriented north and west in the 110–275 mbsf and 280–360 mbsf intervals, respectively. It is particularly interesting to note that despite the 90° rotation of the tool at ~280 mbsf, the orientation of the largest borehole diameter remains north-south, even in the washout intervals. Thus, the borehole is consistently enlarged in the north-south direction. This preferential direction of enlargement, if stress related, would indicate a north-south minimum principal stress direction (i.e., a north-south relative extension).

The magnetometer measurements yield both inclination and magnitude of the total field. These measurements are strongly influenced by the pipe when approaching it. The inclination decreases from –29.9° at the top of the logged section to –30.8° at the bottom (Fig. F101). Both inclination and intensity (Fig. F102) are anomalous in Unit L2 (219–234 mbsf) and in the bottom part of Unit L6 (520–580 mbsf), suggesting the presence of magnetic minerals.

FMS Images

The FMS image interpretation is organized according to log units defined in this chapter from the triple-combo and sonic logs. The FMS image quality is best between ~115 and 350 mbsf in the upper section and between 390 and 778 mbsf in the lower section, with the exception of large, periodic washouts below 680 mbsf. Log Unit L5 was not recorded by the FMS and, thus, is not discussed. Processing steps applied to the images discussed in this section included speed correction, depth shifting (Table T19), and static and dynamic normalization using a 1-m moving window. Statically normalized images were used for recognizing large-scale features and correlating FMS images with the triple combo and sonic logs. Dynamically normalized images were used for interpreting the small-scale structures and textures of individual stratigraphic units. Boundaries between the lithologic units were recognized in the FMS images in several instances, according to changes in either large-scale resistivity and/or small-scale bedding patterns and deformation structures. A preliminary examination of bedding dips revealed shallow 5°–10° dips that range from southeast to southwest throughout most of Hole 1109D (Fig. F103).

Log Unit L1 (82–219 mbsf)

The shallowest interpretable section of FMS data from Hole 1109D begins at 115 mbsf within lithostratigraphic Unit II, which is largely composed of greenish gray clays with abundant volcaniclastic sand interbeds (see "Lithostratigraphic Unit II," p. 11). Large-scale resistivity is relatively uniform as shown in the statically normalized FMS images, as well as in the dual induction resistivity logs. Normally graded, 1-m-thick turbidite units are recognized by resistive, sandy bases that grade upward into more conductive, clayey tops. Carbonate grains

F98. Hole 1109D FMS tool string acceleration, p. 203.

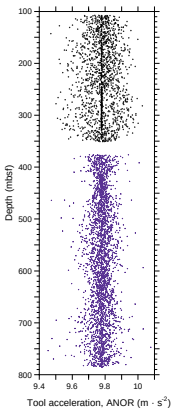

F99. Hole 1109D FMS and HLDS caliper data, p. 204.

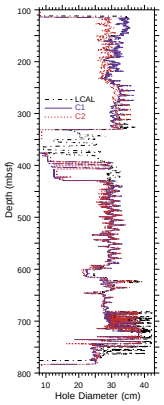

F100. Hole 1109D FMS Pad 1 azimuth with respect to magnetic north, p. 205.

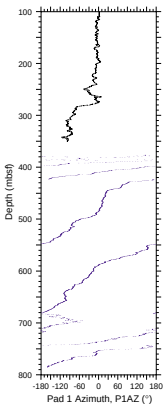

or cementation are also occasionally observed to produce a high-resistivity signature at the base of some turbidites. Thin, 10-cm layers of distinctive, highly resistive sands commonly occur in couplets at the base of these units. Bed boundaries are generally diffuse, which is inferred to be caused by bioturbation, as recognized in the core sections (see "Lithostratigraphic Unit II," p. 11). Bed boundaries dip from 5° to 8° to the south-southeast. South-southwest dips of 5°–8° also are present intermittently in this unit and increase in frequency with depth, suggesting a gradual change in source direction or structure. The base of lithostratigraphic Unit II shows up clearly in the FMS images at 161.5 mbsf as the base of a 4.5-m-thick turbidite unit that is composed of a 1-m-thick basal carbonate sand that fines upward to 157 mbsf (Fig. F104). This unit correlates well with the conventional logs, which display large gamma-ray values over this interval, as well as a sharp spike in the triple combo resistivity curves at 161.5 mbsf. Below this turbidite unit, bed boundaries are more clearly defined, suggesting decreased bioturbation.

Log Unit L2 (219–234 mbsf)

A 15-m-thick highly resistive (possibly carbonate rich) sand is clearly indicated in both the conventional logs and FMS images between 219 and 234 mbsf (Fig. F105). Synthetic seismograms computed from both logs and physical properties measurements show that this layer correlates with a pronounced positive-polarity reflection in the seismic reflection data (see "Vertical Seismic Profile and Depth Conversion," p. 76). The unit is bounded at the top by a thinner, 30-cm highly resistive sandy layer at 219 mbsf and at the bottom by a sandy, carbonate layer at 234 mbsf. The structure and lithologic composition of this unit is relatively homogeneous and contains only minor thin, conductive, clayey layers.

Log Unit L3 (234–293 mbsf)

The top of this unit grades from highly resistive carbonate-rich sands of Unit L2 into clays over an 11-m interval between 234 and 245 mbsf. The base of this interval at 245 mbsf marks the top of litho-stratigraphic Unit IV, which is described as a clayey siltstone and silty claystone (see "Lithostratigraphic Unit IV," p. 15). Below this gradational interval, Unit L3 is characterized by uniformly low resistivity suggested to be caused by increased clay content. The FMS images for this unit display an overall grainy appearance and poorly defined bed boundaries, which correlate with sand and carbonate grains and intense bioturbation observed in the cores (see "Lithostratigraphic Unit IV," p. 15). Between ~255 and 265 mbsf, normally graded beds with diffuse boundaries ranging in thickness from 1 to 1.5 m display a dramatic increase in dip of ~50°–65° to the southwest (Fig. F106). Thin, 10-cm conductive layers at 255 and 265 mbsf are the only distinctive features that bound this interval from the 5°–10° dipping layers that characterize most of Hole 1109D. Relatively steeply dipping (32°) layers also occur between 272 and 273 mbsf to the southeast. Preliminary studies of core samples suggest that the steeply dipping units are the products of normal faulting; however, fractures were not identified in the FMS images (see "Structural Geology," p. 38). Below 282 mbsf, bed boundaries become more distinctive and display a bimodal distribution of southeast and southwest dips of ~5°. A change in bed-form character at 282 mbsf cor-

F101. Hole 1109D magnetic inclination (FINC), p. 206.

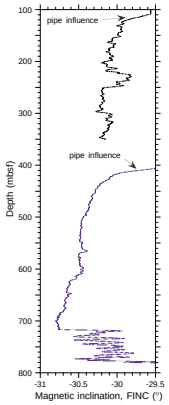

F102. Hole 1109D magnetic intensity (FNOR), p. 207.

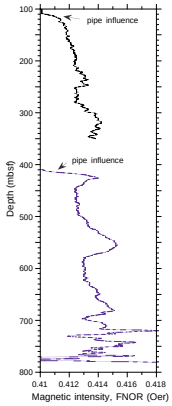

F103. Dip direction histogram interpreted from Hole 1109D FMS images, p. 208.

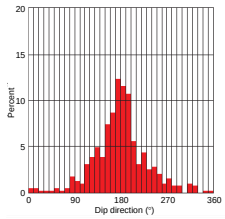

relates closely with the middle bathyal/upper bathyal paleodepth boundary (see "Biostratigraphy," p. 43).

Log Unit L4 (293–330 mbsf)

The upper 10 m of Unit L4 is characterized by overall high resistivity interpreted to indicate increased sand and carbonate content. Bed boundaries are poorly defined throughout most of Unit L4; however, well-defined bed boundaries are present between 305 and 320 mbsf, with dips of 5°–12° that vary from south-southeast to south-southwest.

Log Unit L5 (330–390 mbsf)

Unit L5 is located between the bottom of the upper logged interval and the top of the lower logged interval and was therefore not recorded by the FMS (see "Operations," p. 69).

Log Unit L6 (390–599 mbsf)

Fining-upward turbidite sequences ~1 m in thickness dominate Unit L6 between 390 and 553 mbsf. These turbidite sequences are contained within lithostratigraphic Unit VI, which is a clayey siltstone and silty claystone interbedded with clayey siltstone to coarse sandstone (see "Lithostratigraphic Unit VI," p. 20). Thin, 10-cm, highly resistive layers define the bases of the turbidite units and commonly display wavy bases. Highly resistive basal layers are less common below 510 mbsf, where turbidite boundaries are more poorly defined. The unit possesses an overall mottled texture that increases with depth. Between 553 and 587 mbsf, layering is virtually nonexistent, with the exception of rare 10–20 cm resistive layers.

Log Unit L7 (599–643 mbsf)

The interval between 592 and 621.5 mbsf contains highly disturbed turbidite sequences with resistive bases. A dramatic change in structure occurs between 621.5 and 625 mbsf, where the formation appears to be composed of large (<0.5 m), irregular resistive nodules; whether this is an artifact of poor FMS pad contact with the borehole wall could not be confirmed from the caliper data at this small scale. Between 625 and 647 mbsf, the unit displays a similar, but more homogeneous texture with occasional resistive layers and nodules that appear to be disturbed resistive beds and clasts.

Log Unit L8 (643–673 mbsf)

A massive carbonate-rich unit between 647 and 674.5 mbsf is characterized by high resistivity and a homogeneous distribution of small (<2 cm), angular, randomly oriented resistive fragments that appear to be carbonate clasts, commonly recognized in the cores (see "Interpretation," p. 24, in "Lithostratigraphic Unit VII").

Log Units L9 to L11 (673–775 mbsf)

A single massive turbidite sequence between 674.5 and 681 mbsf is composed of a 15-cm resistive layer and grades upward into clays with a thick, 2-m interval of lenticular, 10-cm-thick clay and silt laminations

F104. Hole 1109D statically normalized FMS image of turbidite unit, p. 209.

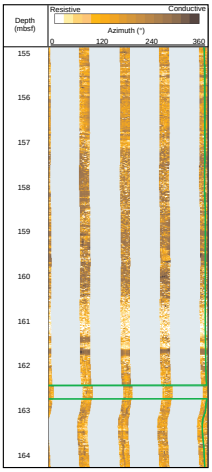

F105. Hole 1109D statically normalized FMS image showing sharp contrast in resistivities, p. 210.

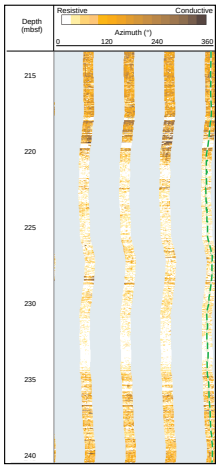

F106. Hole 1109D dynamically normalized FMS image of steeply dipping beds, p. 211.

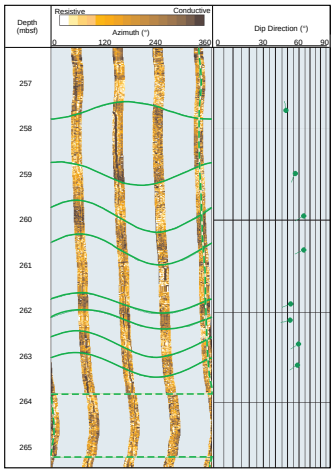

(Fig. F107). Irregular borehole geometry below ~681 mbsf degraded the FMS images, making interpretation difficult except for a few intervals. A highly resistive interval between 715 and 776 mbsf displays a mottled texture with scattered resistive nodules interpreted to be conglomeratic igneous clasts as recognized in the cores (see "Igneous Clasts (Inferred Conglomerate)," p. 28). Massive dolerite underlies the conglomerate at 776.5 mbsf and is characterized by uniformly high resistivity and numerous irregular conductive layers that may indicate flow banding and fractures (Fig. F108). Thin, millimeter-scale conductive features interpreted to be fractures are ubiquitous within the dolerite; however, few of the fractures can be traced confidently from pad to pad.

Temperature Data

The temperature profiles within the pipe and in open hole are shown in Figures F109 and F110. The maximum borehole temperature of 12.5°C is reached at 787 mbsf and is consistent with the near-linear thermal gradient inferred above 170 mbsf (see "Temperature Measurements," p. 76).

TEMPERATURE MEASUREMENTS

In situ thermal measurements were successfully conducted within Hole 1109C using the Adara tool on Cores 180-1109C-3H, 5H, 7H, and 9H at 26.4, 45.4, 64.4, and 83.4 mbsf, respectively (Fig. F111). An additional temperature measurement was obtained before Core 180-1109C-19X using the DVTP at a probe-tip depth of 170.8 mbsf (Fig. F112).

Equilibrium formation temperatures were estimated using the TFIT program for Adara runs and the CONEFIT program for the DVTP run (see "Data Reduction," p. 41, in the "Explanatory Notes" chapter). The estimates of equilibrium temperature used the thermal conductivity determined by core measurements (see "Thermal Conductivity," p. 64), rounded to the nearest 0.1 $W \cdot m^{-1} \cdot °C^{-1}$. Linear regression of the temperatures as a function of depth yields an estimated thermal gradient of $0.031°C \cdot m^{-1}$ ($31°C \cdot km^{-1}$). The intercept was specified to be the mudline temperature (2.6°C). Core measurements suggest an average thermal conductivity of 0.9 $W \cdot m^{-1} \cdot °C^{-1}$ above 170 mbsf (see "Thermal Conductivity," p. 64), yielding a heat flow of 28 $mW \cdot m^{-2}$ (Fig. F113).

VERTICAL SEISMIC PROFILE AND DEPTH CONVERSION

A VSP experiment was carried out during the logging run at Site 1109. The goals of the VSP experiment were to give accurate depth estimations of reflectors identified in the multichannel seismic (MCS) data, thereby allowing correlation of lithostratigraphic units, and to provide parameters with which to improve velocity processing of existing MCS data. A 300-in^3 air gun was used to generate a source signal, which was received in the hole by the WST. The source signal was also recorded on a hydrophone close to the air gun (see "Acquisition Hardware," p. 43, in the "Explanatory Notes" chapter).

As part of the preparation for recording the VSP, the end of the drill pipe was lowered to 380 mbsf to allow logging instruments to pass

F107. Hole 1109D statically and dynamically normalized FMS images of turbidite unit, p. 212.

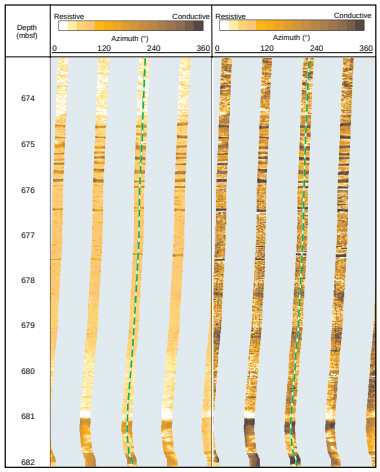

F108. Hole 1109D dynamically normalized FMS image of contact between conglomerate and dolerite, p. 213.

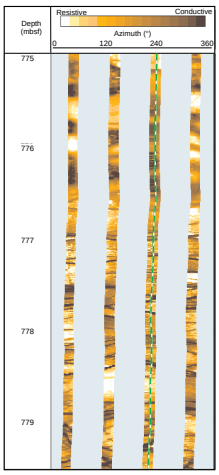

F109. All TLT data from Hole 1109D, p. 214.

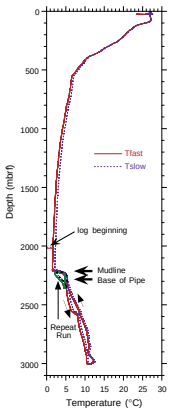

through sections of the hole that had become severely restricted (see "Downhole Measurements," p. 69). Restrictions deeper in the hole prevented the WST from being lowered past 462.4 mbsf. The WST was raised to 459.5 mbsf, at which point the clamping arm was engaged, pushing the instrument against the wall of the hole. By raising the WST in ~10-m intervals, a total of nine clamping stations were occupied. Variations in the clamping interval were a result of the WST not being seated properly or of a better location being found from the caliper log. Before the last two stations, the drill pipe was raised by 20 m. The final station occupied was at 378.1 mbsf. At each station, the air gun was triggered a number of times. Shots that did not have a clear first arrival and showed high noise levels were flagged. Each good shot was stacked, with firing continuing until the stack contained seven shots. Movement of the WST after it had been clamped against the side of the hole was noted at half of the clamping stations. This accounted for a significant percentage of the noise in the signal arriving at the WST.

The Schlumberger MAXIS system was used for preliminary shipboard processing of the VSP. The *P*-wave transit times used to derive interval velocities were picked as the first arrival in the downgoing wavefield at the WST (Table T20). Velocity filtering, wave shape deconvolution, a zero-phase 10- to 60-Hz bandpass filter, and corridor stacking (see "Vertical Seismic Profiling," p. 42, in the "Explanatory Notes" chapter), were applied to the data. Velocity filtering was tried for four stations (3, 5, 7, 9). A five-level velocity filter sufficiently separated the upgoing and downgoing wavefields, leaving five traces that were stacked into a single corridor stack. This stack was found to match very poorly with the migrated MCS data at this location (Fig. F114). Because of the position of the WST low in Hole 1109D, little is seen of the sedimentary section on top of the Miocene forearc basin sequence. A reflector, possibly associated with the top of lithostratigraphic Unit XI (see "Lithostratigraphic Unit XI," p. 31), is seen at ~3.83 s two-way traveltime (TWT), but beyond this, correlations with the MCS data are limited. Further shore-based processing may prove fruitful.

Interval velocities calculated over the depth extent of the VSP experiment are variable (Table T20). Fitting a straight line to the data gives an interval velocity of 1777 m·s^{-1} (Fig. F115). This compares with 1800–1830 m·s^{-1} velocities obtained by logging (see "Downhole Measurements," p. 69) and laboratory measurements (see "Physical Properties," p. 61).

The short depth extent of the VSP makes it unsuitable for the determination of depths to the primary reflectors identified in the MCS data. In order to correlate between seismic traveltime and hole depths, we examined the velocity information available from laboratory measurements and sonic logs to develop a model of the variation of velocity with depth. In this model, sonic velocities measured downhole were used rather than values determined from laboratory measurements, except for 0–84, 336–374, and 707–783 mbsf. In these intervals, log sonic velocities were absent or of poor quality. Because of an offset between the laboratory velocities measured using the PWS3 transducer and those of the PWS1 and PWS2 transducers (see "Compressional-Wave Velocity," p. 64), the consistently 40 m·s^{-1} higher PWS3 (transverse) measurement was used. Where velocities measured using the PWS3 transducer were absent, the vertical velocity measured using the PWS1 transducer was substituted with a +40 m·s^{-1} offset. The resultant velocity-depth function (Fig. F116) was used to create a TWT-to-depth conversion. To confirm the validity of the depth conversion, it was

F110. Hole 1109D borehole TLT data, p. 215.

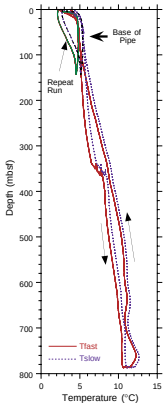

F111. Temperature as a function of time for the Adara temperature runs in Hole 1109C, p. 216.

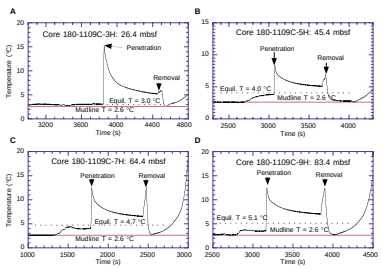

F112. Temperature as a function of time for the DVTP temperature run in Hole 1109C, p. 217.

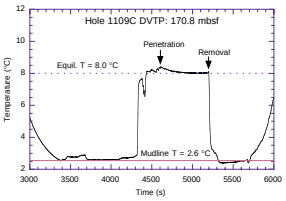

F113. Estimated temperatures as a function of depth and computed thermal gradient, p. 218.

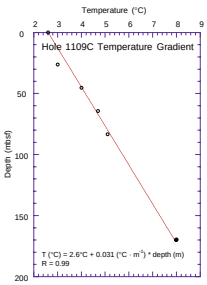

T20. VSP experiment data, p. 296.

compared with VSP check-shot information. The *P*-wave transit time to the WST geophone and depth (Table **T20**) were properly corrected for the geometry of the experiment (see **"Vertical Seismic Profiling,"** p. 42, in the "Explanatory Notes" chapter) to give a direct and absolute tie between TWT and depth. Comparing this to the MCS data, correlates the horizons from TWT to depth. The VSP is limited to depths from 378.1 to 459.5 mbsf; therefore, this comparison was conducted only over a short depth interval. Table **T21** shows that the difference between the VSP depth and that calculated for an equivalent time from the velocity-depth function ranges from –4.13 to 0.85 m, with an average of 2.12 m. Thus, we can predict that depth conversions using our velocity-depth relationship are accurate to ~3 m above 459.5 mbsf. Below this depth, we estimate that the depth conversion has a similar accuracy.

A synthetic seismic trace was generated using velocity and density data from Site 1109. Density data for Site 1109 were compiled from downhole logging measurements and laboratory index measurements. Similar to the compilation of velocity measurements, in situ logging measurements were preferred to laboratory measurements, except where they were absent or of poor quality (0–95 and 680–800 mbsf; Fig. **F117**). A number of synthetic seismic traces were computed following the application of different filtering parameters to the velocity and density data. The preferred synthetic trace was generated by applying to both data sets a 3-m median filter to remove spikes, a 2-m gaussian filter to smooth the data, and an Akima spline to resample the data to 1 m. An Akima spline was used in preference to a simple linear extrapolation because of the variation in measurement interval between the laboratory (meter scale) and downhole (centimeter scale) measurements. A reflection coefficient was subsequently calculated from the two data sets. Using the depth-time relationship derived above, the reflection coefficient was converted from depth to time (Fig. **F118**). A source signal, comprising the first 500 ms of the direct wave from the migrated MCS coinciding with Site 1109, was convolved with the reflection coefficient to give the synthetic seismic trace. Using the depth-time function derived above, both the synthetic trace and a number of migrated MCS traces close to the site were converted to depth (Fig. **F118**).

The match between the synthetic seismic and the MCS data is good above 350 mbsf, with the exception that some amplitude estimates are not accurate. Below this depth, the match becomes poor (Fig. **F118**). Given that above, we have shown our conversion between time and depth is accurate, this indicates that the problem is with the parameters used to generate the synthetic seismic trace. Further work on this problem will include adjusting the filtering parameters of the velocity and density data, as well as experimenting with the source signal. A reflector at 3.8 s TWT, directly above the reflector interpreted as the top of the Miocene forearc sequence (Fig. **F119**), is estimated to be at 740 mbsf at Site 1109. At this depth, there is a 40-m-thick conglomerate unit, underlain by dolerite (see **"Lithostratigraphic Unit X,"** p. 30). Both these units are associated with high *P*-wave velocities and densities (see **"Density and Porosity,"** p. 62, and **"Compressional-Wave Velocity,"** p. 64). At 3.275 s TWT, a prominent doublet reflection is seen (Fig. **F119**). Depth conversion predicts that the top of this reflector occurs at a depth of 243 mbsf. This coincides with a 30-m-thick unit in the logging data that is associated with high velocity and density and interpreted to be a sand layer. We had poor core recovery in this unit, hence, it was poorly represented in laboratory physical properties measure-

F114. VSP corridor stack repeated and placed between multichannel seismic traces, Site 1109, **p. 219.**

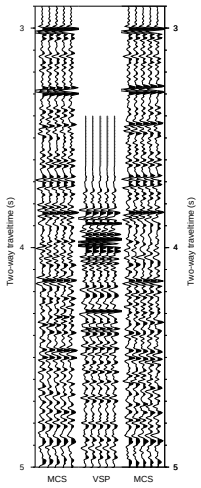

F115. Depth vs. transit time for Site 1109 VSP, **p. 220.**

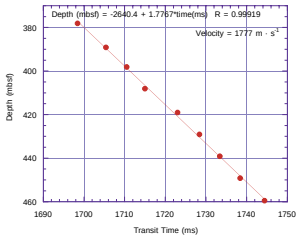

F116. Velocity vs. depth function, Site 1109, **p. 221.**

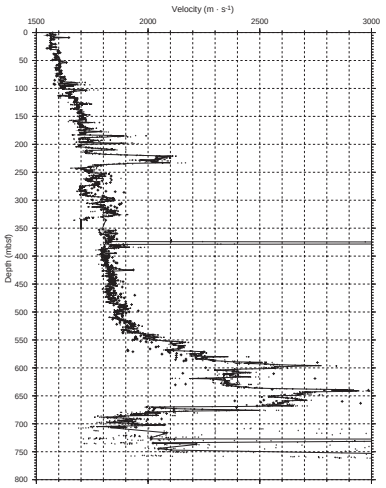

T21. VSP data compared with depth estimates, **p. 297.**

ments and lithostratigraphic descriptions. However, this unit is well reproduced in the synthetic seismic trace. At 3.6 s TWT, a negative polarity event is seen in the MCS data. In the depth-converted section, this event is at ~563 mbsf and coincides with the upper boundary of lithostratigraphic Unit VII, which is characterized by high calcite content (see "Lithostratigraphic Unit VII," p. 22).)

COMPOSITE DEPTHS

Introduction

We established composite depth based on the correlation between Cores 108-1109A-1H, 180-1109B-1H and 2H and 180-1109C-1H and 2H (Table T22). The correlation is based on key beds and magnetic susceptibility curves (Fig. F120).

Correlation

Sediments from 0 to 17 mbsf at Site 1109 have several key beds that enable visual correlation among the three holes. The magnetic susceptibility curves are similar to each other, and 53 peaks (29 positive peaks and 24 negative peaks) were used for correlation. Both key bed and magnetic susceptibility data sets provide consistent correlations (Fig. F120).

Composite Depths

Composite depths were calculated by the following procedure (Table T22):

1. To account for core length expansion in cores having recovery greater than 100%, depths were calculated by (distance from core top) × (cored length) ÷ (core length recovered).
2. The depth differences between correlative horizons in adjacent holes were calculated, and the average of these two or three differences were considered to be the differences in composite section.
3. The differences of composite section were cumulated for derivation of meters composite depth (mcd) for each horizon.

The gap between Cores 180-1109B-1H and 2H and between Cores 180-1109C-1H and 2H were estimated to be 0.14 and 0.24 m, respectively. The top of Cores 180-1109A-1H and 180-1109B-1H were evaluated to be 0.20 and 0.09 m deeper than the top of Core 180-1109C-1H.

F117. Density vs. depth function for Site 1109, p. 222.

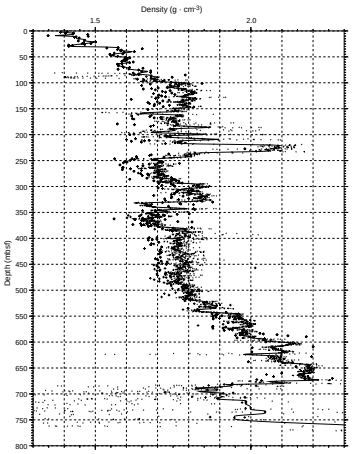

F118. Depth-converted MCS data, synthetic seismic trace, reflection coefficient, and VSP, p. 223.

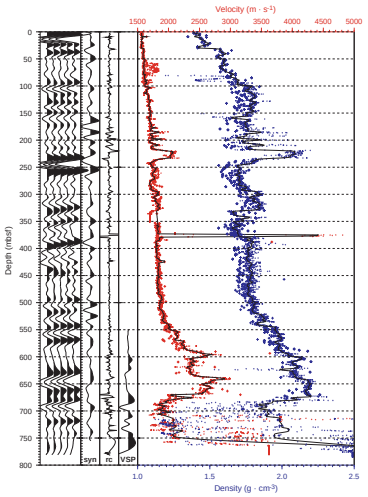

F119. MCS Line EW9510–1366, p. 224.

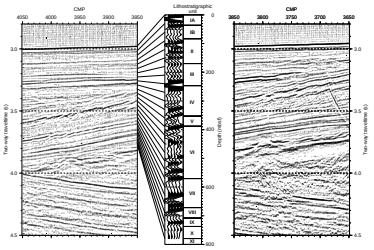

T22. Depths of magnetic susceptibility peaks, p. 298.

F120. Holes 1109A, 1109B, and 1109C correlated by magnetic susceptibility and key beds, p. 225.

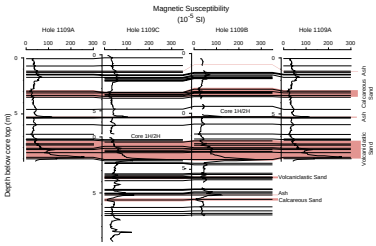

REFERENCES

Ashley, P.M., and Flood, R.H., 1981. Low-K tholeiites and high-K igneous rocks from Woodlark Island, Papua New Guinea. *J. Geol. Soc. Aust.,* 28:227–240.

Athy, L.F., 1930. Density, porosity, and compaction of sedimentary rocks. *AAPG Bull.,* 14:1–24.

Berger, W.H., 1979. Impact of deep-sea drilling on paleoceanography. *In* Talwani, M., Hay, W., and Ryan, W.B.F. (Eds.), *Deep Drilling Results in the Atlantic Ocean: Continental Margins and Paleoenvironment*. Am. Geophys. Union Monogr., Maurice Ewing Ser., 3:297–314.

Bjørlykke, K., 1983. Diagenetic reactions in sandstones. *In* Parker, A., and Sellwood, B.W. (Eds)., *Sediment Diagenesis*. NATO ASI Ser. C, 169–213.

Blatt, H., Middleton, G., and Murray, R., 1980. *Origin of Sedimentary Rocks* (2nd ed.): Englewood Cliffs, NJ (Prentice-Hall).

Bøe, R., 1994. Nature and record of late Miocene mass-flow deposits from the Lau-Tonga forearc basin, Tongan platform (Hole 840B). *In* Hawkins, J., Parson, L., Allan, J., et al., *Proc. ODP, Sci. Results,* 135: College Station, TX (Ocean Drilling Program), 87–100.

Boyce, R.E., 1976. Definitions and laboratory techniques of compressional sound velocity parameters and wet-water content, wet-bulk density, and porosity parameters by gravimetric and gamma-ray attenuation techniques. *In* Schlanger, S.O., Jackson, E.D., et al., *Init. Repts. DSDP,* 33: Washington (U.S. Govt. Printing Office), 931–958.

Brückmann, W., 1989. Typische Kompakationsmuster mariner Sedimente und ihre Modifikation in einem rezenten Akkretionskeil (Barbados Ridge). *Beitr. Geol. Inst. Univ. Tübingen, Rh. A,* 5:1–135.

Bukry, D., 1974. Coccoliths as paleosalinity indicators: evidence from Black Sea. *AAPG Mem.,* 20:335–353.

Bukry, D., 1978. Cenozoic silicoflagellate and coccolith stratigraphy, southeastern Atlantic Ocean, Deep Sea Drilling Project Leg 40. *In* Bolli, H.M., Ryan, W.B.F., et al., *Init. Repts. DSDP,* 40: Washington (U.S. Govt. Printing Office), 635–649.

Claypool, G.E., and Kaplan, I.R., 1974. The origin and distribution of methane in marine sediments. *In* Kaplan, I.R. (Ed.), *Natural Gases in Marine Sediments:* New York (Plenum), 99–139.

Davies, H.L., 1980. Folded thrust fault and associated metamorphics in the Suckling-Dayman massif, Papua New Guinea. *Am. J. Sci.,* 280-A:171–191.

Davies, H.L., and Warren, R.G., 1988. Origin of eclogite-bearing, domed, layered metamorphic complexes ("core complexes") in the D'Entrecasteaux islands, Papua New Guinea. *Tectonics,* 7:1–21.

Davies, H.L., Symonds, P.A., and Ripper, I.D., 1984. Structure and evolution of the southern Solomon Sea region. *BMR J. Aust. Geol. Geophys.,* 9:49–68.

Easton, M., and Klappa, C.F., 1983. Subaerial exposure. *In* Scholle, P.A., Bebout, D.G., and Moore, C.H. (Eds.), *Carbonate Depositional Environments*. AAPG Mem., 33:1–95.

Eberli, G.P., Swart, P.K., Malone, M.J., et al., 1997. *Proc. ODP, Init. Repts.,* 166: College Station, TX (Ocean Drilling Program).

Gieskes, J.M., 1981. Deep-sea drilling interstitial water studies: implications for chemical alteration of the oceanic crust, layers I and II. *In* Warme, J.E., Douglas, R.G., and Winterer, E.L. (Eds.), *The Deep Sea Drilling Project: A Decade of Progress*. Spec. Publ.—Soc. Econ. Paleontol. Mineral., 32:149–167.

Gieskes, J.M., 1983. The chemistry of interstitial waters of deep-sea sediments: interpretation of deep-sea drilling data. *In* Riley, J.P., and Chester, R. (Eds.), *Chemical Oceanography* (Vol. 8): London (Academic), 221–269.

Gieskes, J.M., Elderfield, H., Lawrence, J.R., Johnson, J., Meyers, B., and Campbell, A., 1982. Geochemistry of interstitial waters and sediments, Leg 64, Gulf of California.

In Curray, J.R., Moore, D.G., et al., *Init. Repts. DSDP,* 64 (Pt. 2): Washington (U.S. Govt. Printing Office), 675–694.

Jelinek, V., 1981. Characterization of the magnetic fabric of rocks. *Tectonophysics,* 79:63–67.

Johnson, R.W., Mackenzie, D.E., and Smith, I.E.M., 1978. Volcanic rock associations at volcanic plate boundaries: re-appraisal of the concept using case histories from Papua New Guinea. *Tectonophysics,* 46:197–216.

Lock, J., Davies, H.L., Tiffin, D.L., Murakami, F., and Kisomoto, K., 1987. The Trobriand subduction system in the western Solomon Sea. *Geo-Mar. Lett.,* 7:129–134.

Mackenzie, F.T., Ristvet, B.L., Thorsenson, D.C., Lerman, A., and Leeper, R.H., 1981. Reverse weathering and chemical mass balance in a coastal environment. *In* Reeder, R.J. (Ed.), *Carbonates: Mineralogy and Chemistry:* Chelsea (Mineral Soc. Am.), 97–144.

Martini, E., 1971. Standard Tertiary and Quaternary calcareous nannoplankton zonation. *In* Farinacci, A. (Ed.), *Proc. 2nd Planktonic Conf. Roma:* Rome (Ed. Technosci.), 2:739–777.

McDuff, R.E., 1981. Major cation gradients in DSDP interstitial waters: the role of diffusive exchange between seawater and upper oceanic crust. *Geochim. Cosmochim. Acta,* 45:1705–1713.

McDuff, R.E., and Gieskes, J.M., 1976. Calcium and magnesium profiles in DSDP interstitial waters: diffusion or reaction? *Earth Planet. Sci. Lett.,* 33:1–10.

Mesri, G., 1975. Discussion of new design procedures for stability of soft clays. *J. Geotech. Div., Am. Soc. Civ. Eng.,* 101:409–412.

Morse, J.W. and Mackenzie, F.T. 1990. *Geochemistry of Sedimentary Carbonates:* Amsterdam (Elsevier).

Parker, M.E., Clark, M., and Wise, S.W., Jr., 1985. Calcareous nannofossils of Deep Sea Drilling Project Sites 558 and 563, North Atlantic Ocean: biostratigraphy and the distribution of Oligocene braarudosphaerids. *In* Bougault, H., Cande, S.C., et al., *Init. Repts. DSDP,* 82: Washington (U.S. Govt. Printing Office), 559–589.

Parkes, R.J., Cragg, B.A., Bale, S.J., Getliff, J.M., Goodman, K., Rochelle, P.A., Fry, J.C., Weightman, A.J., and Harvey, S.M., 1994. A deep bacterial biosphere in Pacific Ocean sediments. *Nature,* 371:410–413.

Pearce, J.A., 1980. Geochemical evidence for the genesis and eruptive setting of lavas from Tethyan ophiolites. *In* Panayiotou, A. (Ed.), *Proc. Int. Ophiolite Symp. Cyprus.* Cyprus Geol. Surv., 261–272.

Pearce, J.A., and Cann, J.R., 1973. Tectonic setting of basic volcanic rocks determined using trace element analyses. *Earth Planet. Sci. Lett.,* 19:290–300.

Pearce, T.H., Gorman, B.E., and Birkett, T.C., 1977. The relationship between major element chemistry and tectonic environment of basic and intermediate volcanic rocks. *Earth Planet. Sci. Lett.,* 36:121–132.

Perch-Nielsen, K., 1985. Cenozoic calcareous nannofossils. *In* Bolli, H.M., Saunders, J.B., and Perch-Nielsen, K. (Eds.), *Plankton Stratigraphy:* Cambridge (Cambridge Univ. Press), 427–554.

Ramsay, J.G., and Huber, M.I., 1987. *The Techniques of Modern Structural Geology* (Vol. 2): *Folds and Fractures:* New York (Academic Press).

Rio, D., Raffi, I., and Villa, G., 1990. Pliocene Pleistocene calcareous nannofossil distribution patterns in the Western Mediterranean. *In* Kastens, K.A., Mascle, J., et al., *Proc. ODP, Sci. Results,* 107: College Station, TX (Ocean Drilling Program), 513–533.

Ristvet, B., 1978. Reverse weathering reactions within recent nearshore marine sediments, Kaneohe Bay, Oahu. Test Directorate Field Command, Kirtland AFB, New Mexico.

Robertson, A.H.F., and Degnan, P., 1994. The Dras Arc Complex: lithofacies and reconstruction of a Late Cretaceous oceanic volcanic arc in the Indus Suture Zone, Ladakh Himalaya. *Sediment. Geol.,* 92:117–145.

Sayles, F.L., and Manheim, F., 1975. Interstitial solutions and diagenesis in deeply buried marine sediments: results from the Deep Sea Drilling Project. *Geochim. Cosmochim. Acta,* 39:103–127.

Shipboard Scientific Party, 1997. Site 998. *In* Sigurdsson, H., Leckie, R.M., Acton, G.D., et al., *Proc. ODP, Init. Repts.,* 165: College Station, TX (Ocean Drilling Program), 49–130.

Siesser, W.G., and de Kaenel, E.P., 1999. Neogene calcareous nannofossils: biostratigraphy and paleoclimatology, ODP Leg 161, western Mediterranean. *In* Zahn, R., Comas, M.C., Klaus, A., and Cita-Sironi, M.-B. (Eds.), *Proc. ODP Sci. Results,* 161: College Station, TX (Ocean Drilling Program), 223–237.

Siesser, W.G., Bralower, T.J., and De Carlo, E.H., 1992. Mid-Tertiary *Braarudosphaera*-rich sediments on the Exmouth Plateau. *In* von Rad, U., Haq, B.U., et al., *Proc. ODP, Sci. Results,* 122: College Station, TX (Ocean Drilling Program), 653–663.

Sigurdsson, H., Leckie, R.M., Acton, G.D., et al., 1997. *Proc. ODP, Init. Repts.,* 165: College Station, TX (Ocean Drilling Program).

Smith, I.E., 1976. Peralkaline rhyolites from the D'Entrecasteaux Islands, Papua New Guinea. *In* Johnson, R.W. (Ed.), *Volcanism in Australasia:* Amsterdam (Elsevier), 275–285.

Smith, I.E.M., 1982. Volcanic evolution in eastern Papua. *Tectonophysics,* 87:315–333.

Smith, I.E., and Milsom, J.S., 1984. Late Cenozoic volcanism and extension in eastern Papua. *In* Kokelaar, B.P., and Howells, M.F. (Eds.), *Marginal basin geology: volcanic and associated sedimentary and tectonic processes in modern and ancient marginal basins*. Geol. Soc. Spec. Publ. London, 16:163–171.

Stevenson F.J., and Cheng, C.N., 1972. Organic geochemistry of the Argentine Basin sediments: carbon-nitrogen relationships and Quaternary correlations. *Geochim. Cosmochim. Acta,* 36:653–671.

Stolz, A.J., Davies, G.R., Crawford, A.J., and Smith, I.E.M., 1993. Sr, Nd and Pb isotopic composition of calc-alkaline and peralkaline silicic volcanics from D'Entrecasteaux Islands, Papua New Guinea, and their tectonic significance. *Mineral. Petrol.,* 47:103–126.

Tarling, D.H., and Hrouda, F., 1993. *The Magnetic Anisotropy of Rocks:* London (Chapman and Hall).

Taylor, B., Fujioka, K., et al., 1990. *Proc. ODP, Init. Repts.,* 126: College Station, TX (Ocean Drilling Program).

Wellsbury, P., Goodman, K., Barth, T., Cragg, B.A., Barnes, S.P., and Parkes, R.J., 1997. Deep marine biosphere fueled by increasing organic matter availability during burial and heating. *Nature,* 388:573–576.

Wellsbury, P., Goodman, K., Cragg, B.A., and Parkes, R.J., in press. The geomicrobiology of deep-marine sediments from Blake Ridge containing methane hydrate (Sites 994, 995, and 997). *In* Paull, C.K., Matsumoto, R., Wallace, P., and Dillon, W.P. (Eds.), *Proc. ODP, Sci. Results,* 164: College Station, TX (Ocean Drilling Program).

Wilson, M., 1989. *Igneous Petrogenesis: A Global Tectonic Approach:* London (Unwin Hyman).

Figure F1. Lithologic logs of the successions recovered at Site 1109. (For key to symbols, see Figure F2, p. 52, in the "Explanatory Notes" chapter.) **A.** Upper part of the succession recovered by APC and XCB. Only the surface sample has a lower bathyal (>2000 m) benthic fauna. (Continued on next page.)

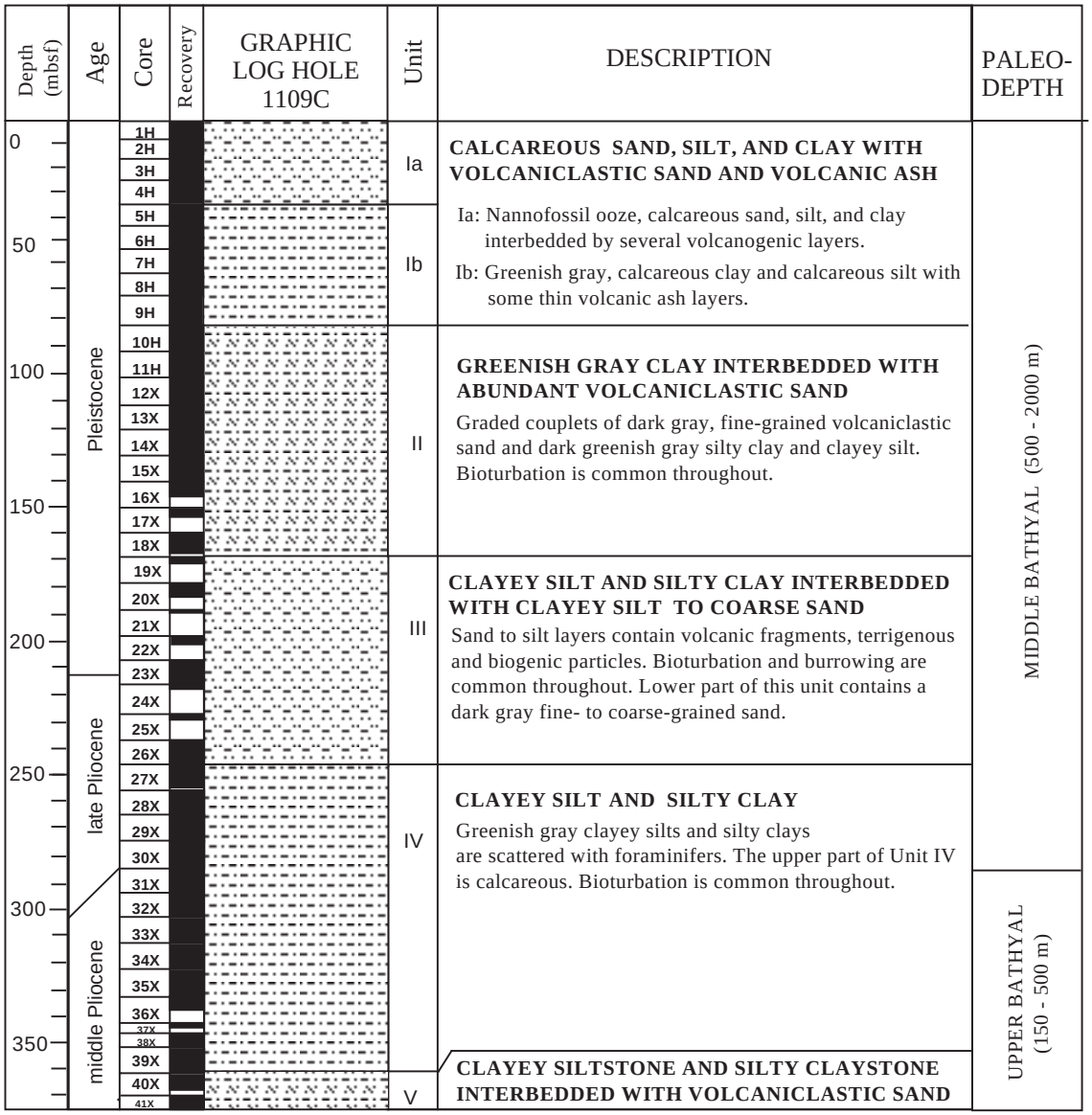

Figure F1 (continued). B. Lower part of the succession recovered by RCB. The water depths estimates are from paleontological evidence.

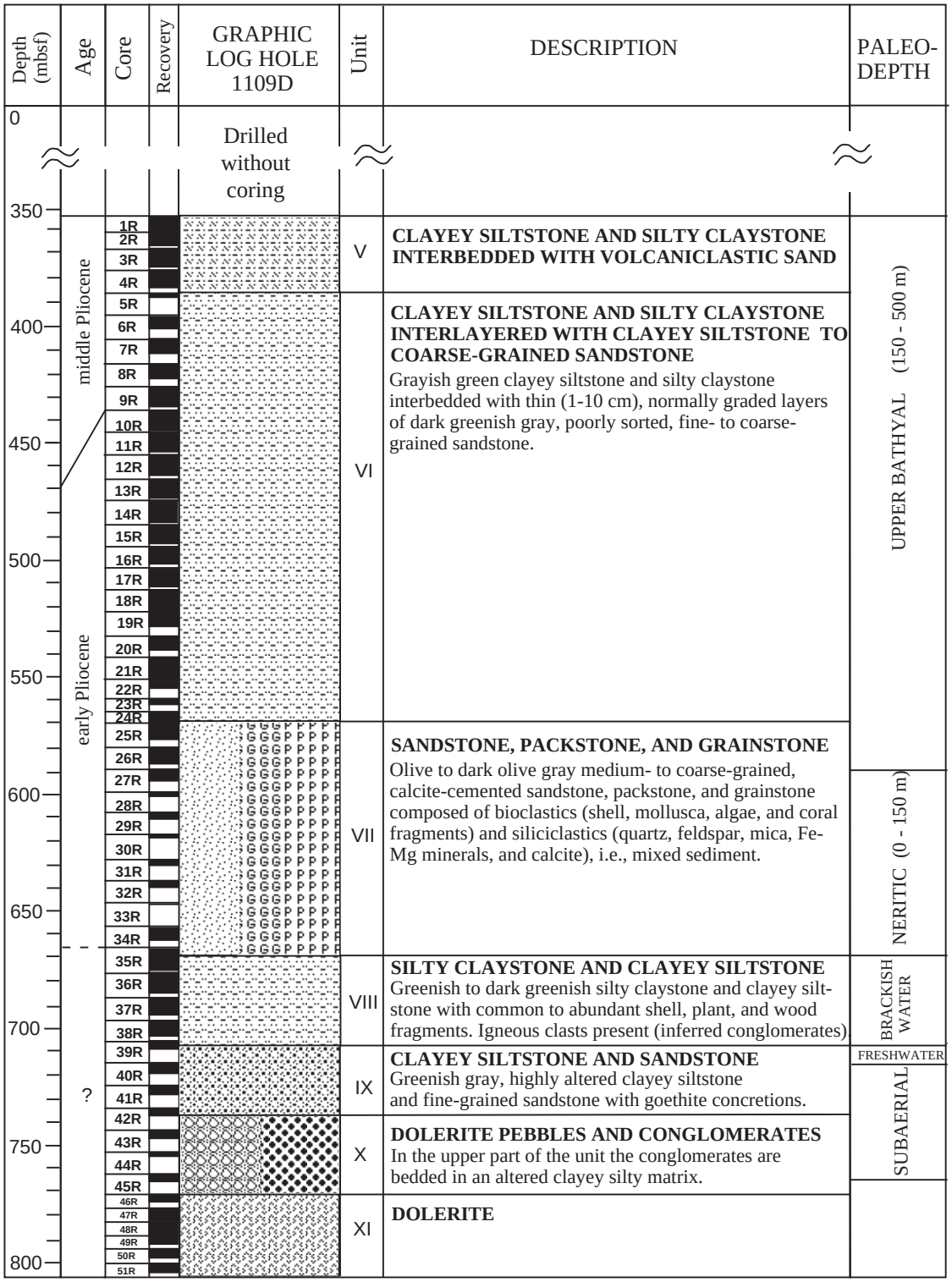

Figure F2. Correlation of the successions recovered in Core 180-1109A-1H with those recovered in Cores 180-1109B-1H and 2H and Core 180-1109C-1H. Detailed correlations based on physical properties and paleomagnetism are included in **"Physical Properties,"** p. 61, **"Paleomagnetism,"** p. 48, and **"Composite Depths,"** p. 79.

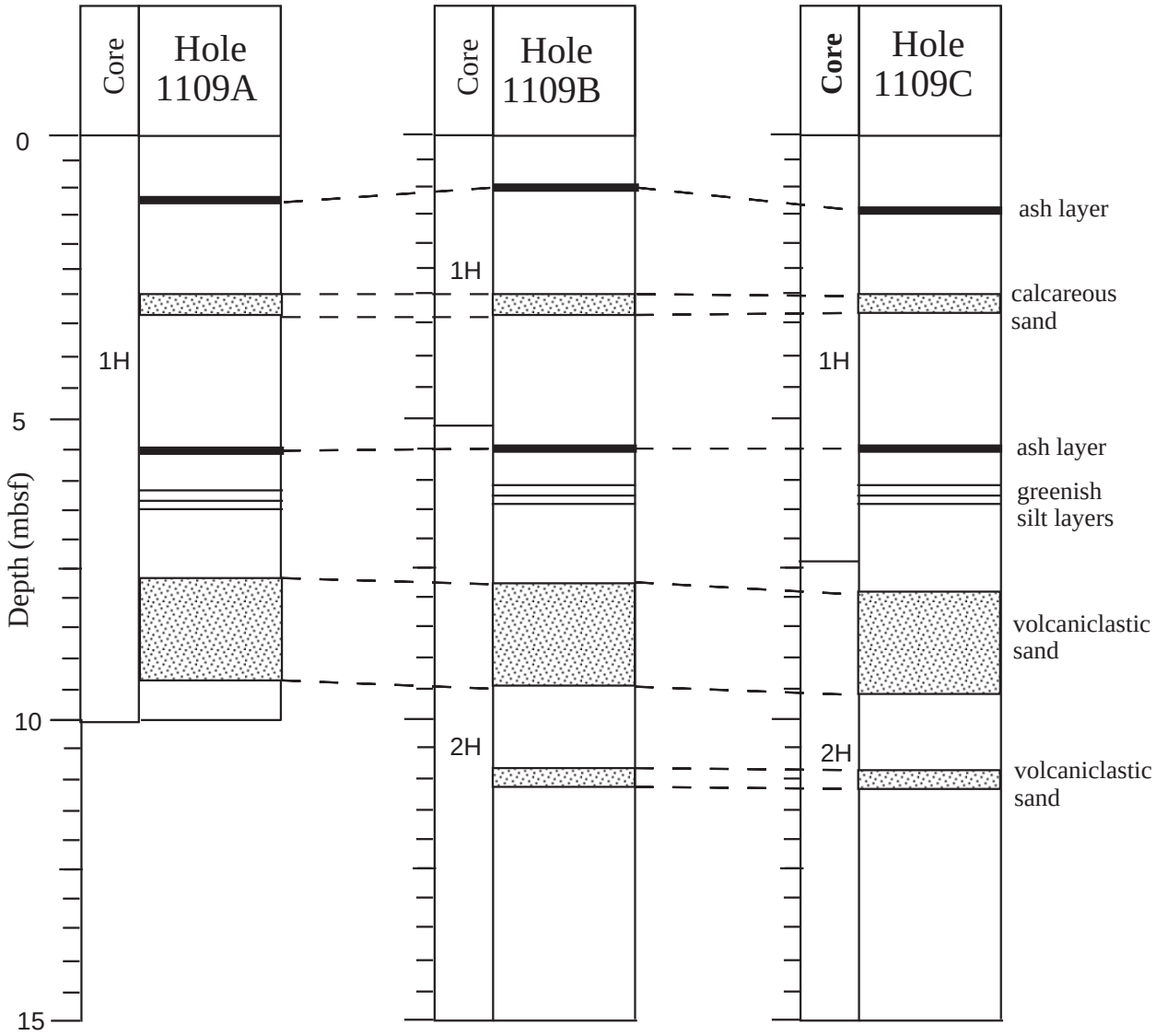

Figure F3. Normally graded, calcareous silt beds (e.g., 68–72 cm) characterized by sharp, basal contacts. These graded beds alternate with nannofossil ooze beds (interval 180-1109C-2H-5, 46–77 cm).

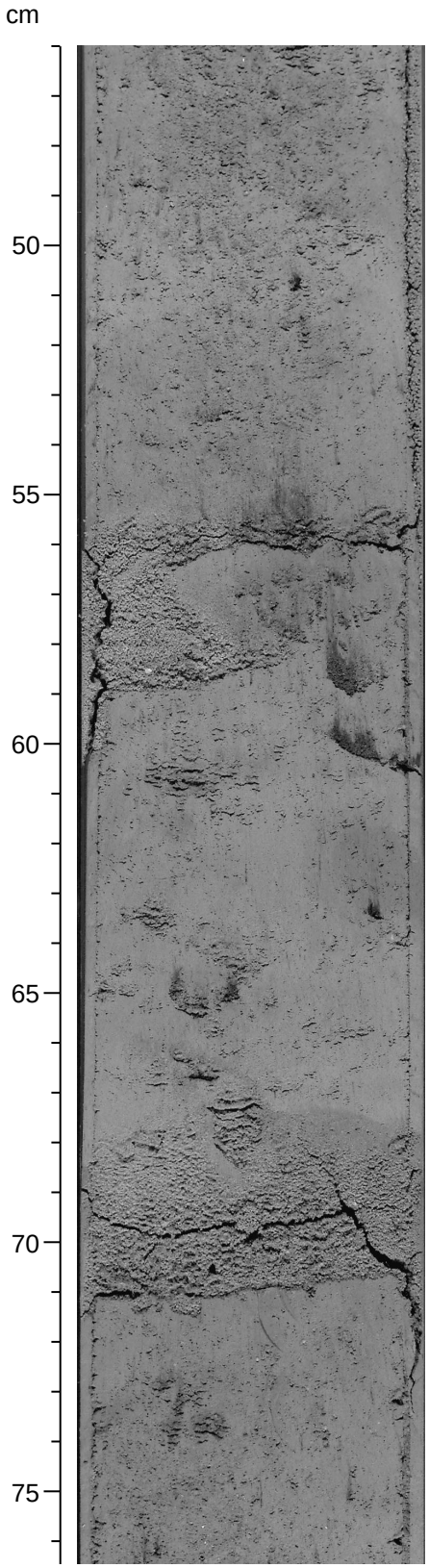

Figure F4. Normally graded, sharp-based gravel bed composed of shell fragments and other bioclastic detritus (33–40 cm) (interval 180-1109B-1H-3, 13–45 cm).

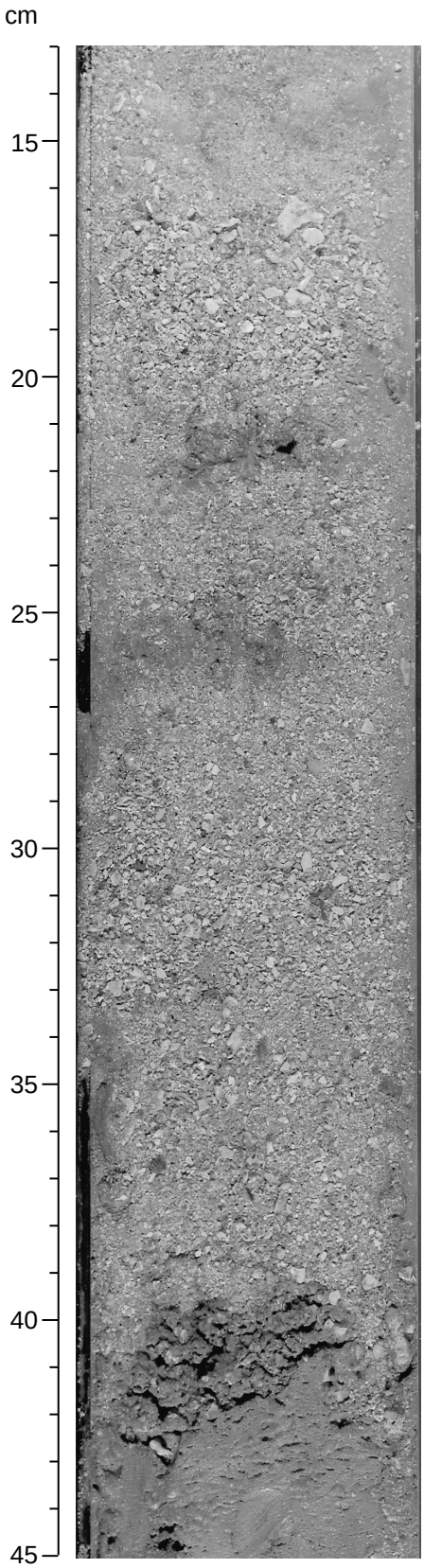

Figure F5. Sharp-based volcanic ash bed composed of >90% colorless glass shards (interval 180-1109C-4H-2, 75–84 cm).

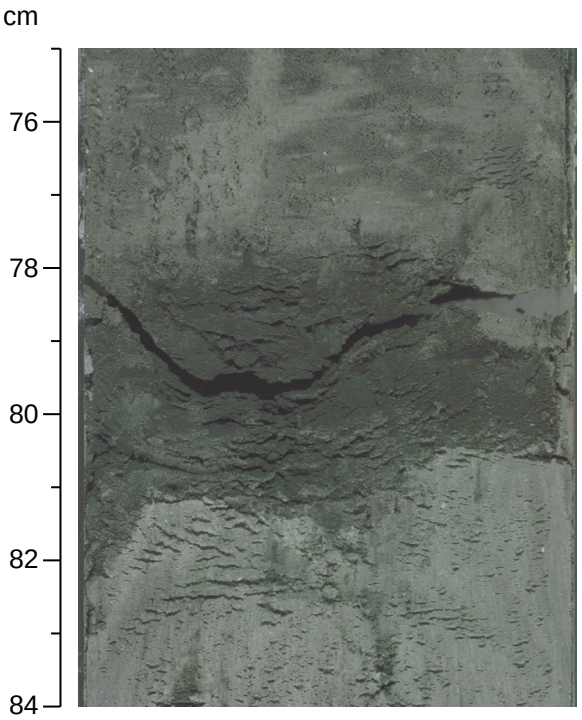

Figure F6. Digital photomicrograph of volcanic ash with nondevitrified, colorless, platy to bubble-walled shards (interval 180-1109A-1H-1, 123–124 cm).

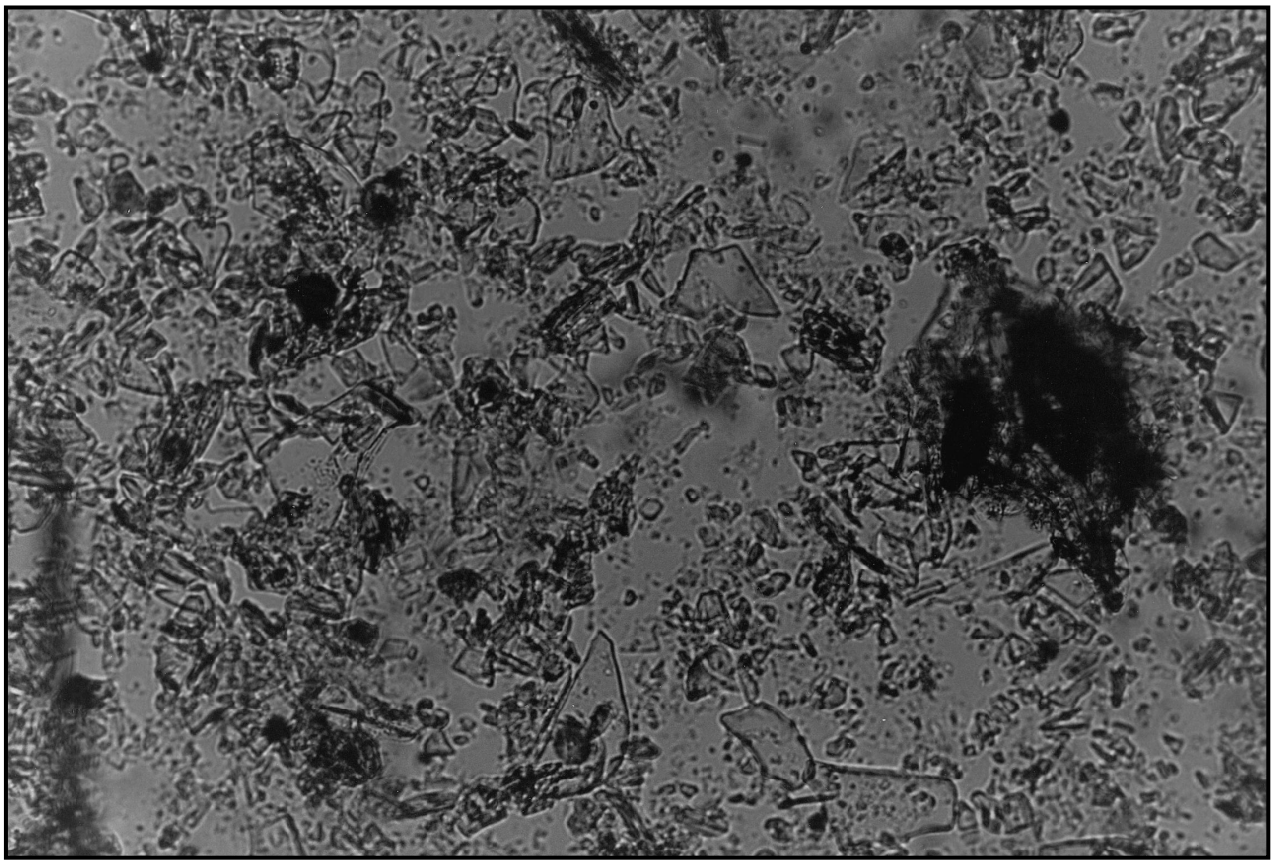

Figure F7. Thin beds of normally graded volcaniclastic silt with sharp bases. These beds alternate with nannofossil ooze (interval 180-1109C-3H-6, 37–53 cm).

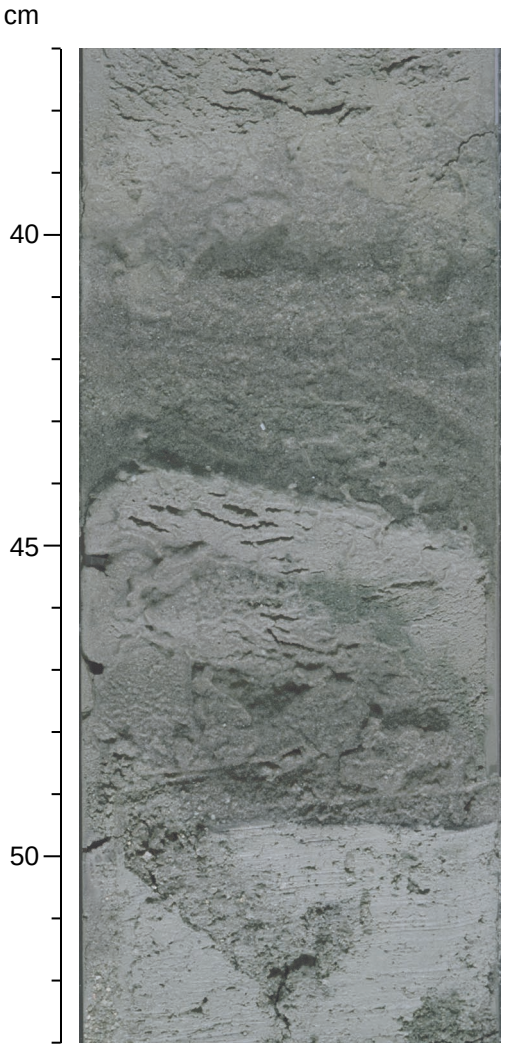

Figure F8. Contorted clay-rich silt and silty clay beds of the deformed interval of Unit I. The deformation is in the form of folds(?) and highly extended and disrupted beds (55–70 cm) (interval 180-1109C-5H-3, 36–84 cm).

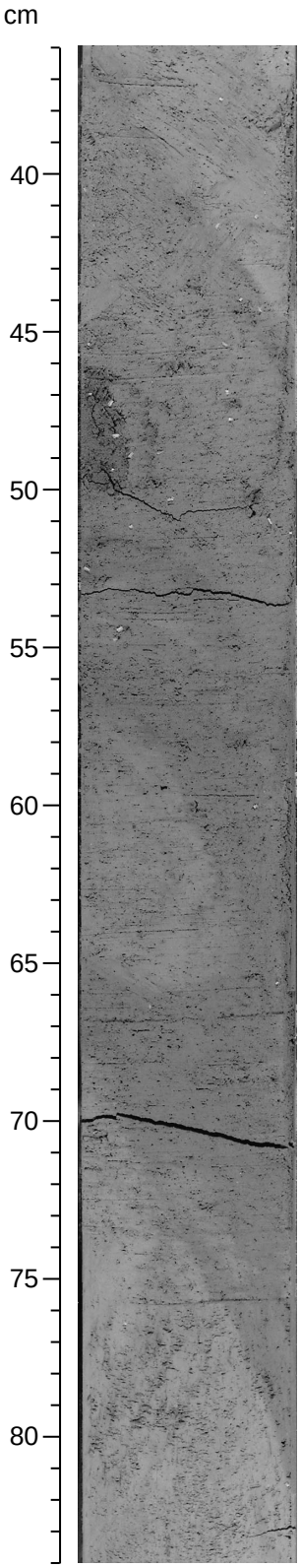

Figure F9. Graded volcaniclastic silt and sand with abundant *Chondrites* burrows (interval 180-1109C-11H-4, 40–65 cm).

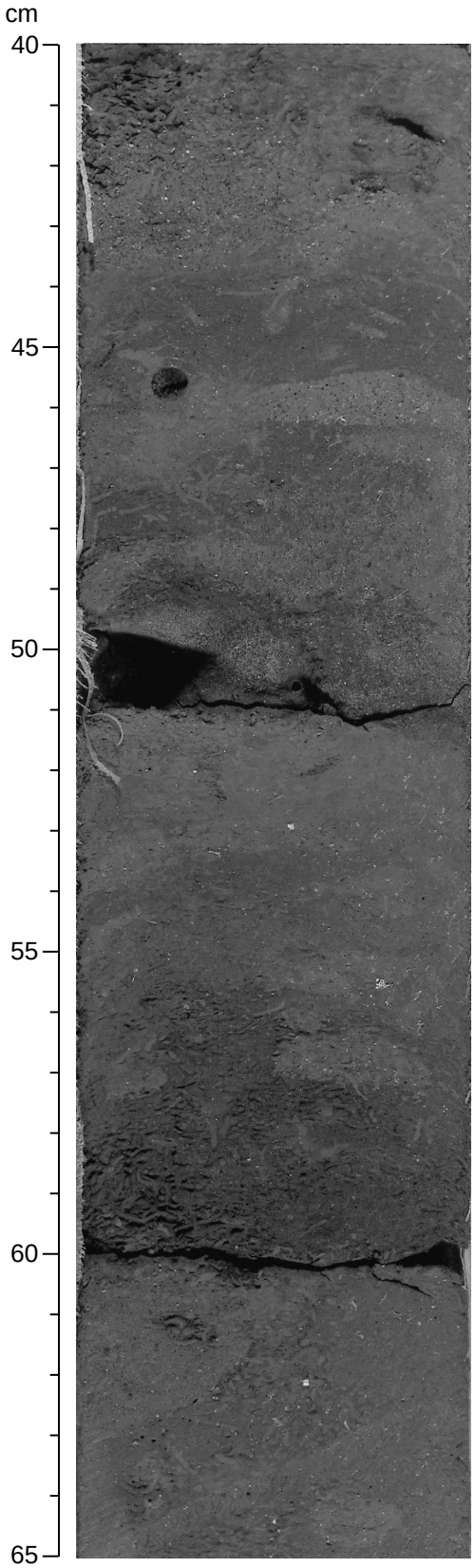

Figure F10. Digital photomicrograph of a smear slide (plane polar) of volcaniclastic sand with common colorless volcanic glass shards (G), rare crystals of quartz (Qtz), plagioclase (Plag), pyroxene (Pyx), biotite (B), hornblende (H), and planktonic foraminifers (F) (Sample 180-1109C-13H-5, 99 cm).

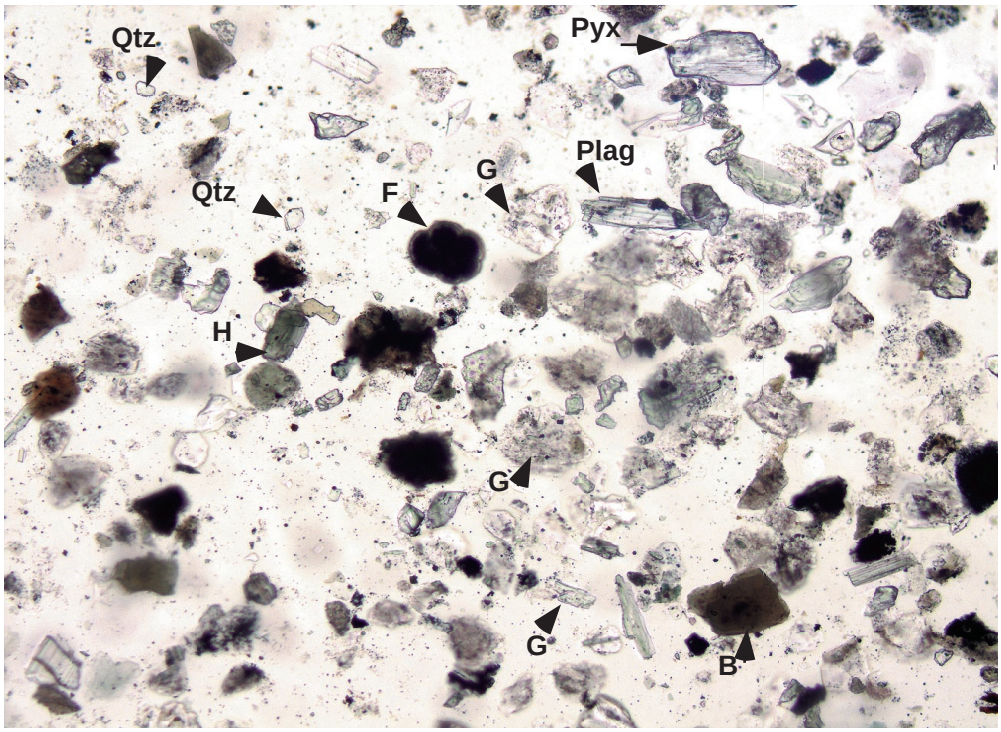

Figure F11. Amalgamated turbidites. Two calcareous turbidites (12–23 and 23–34 cm), with little or no clay between the two beds. The lower carbonate turbidite is amalgamated with the underlying volcaniclastic turbidite (at 34 cm) (interval 180-1109C-13X-3, 8–40 cm).

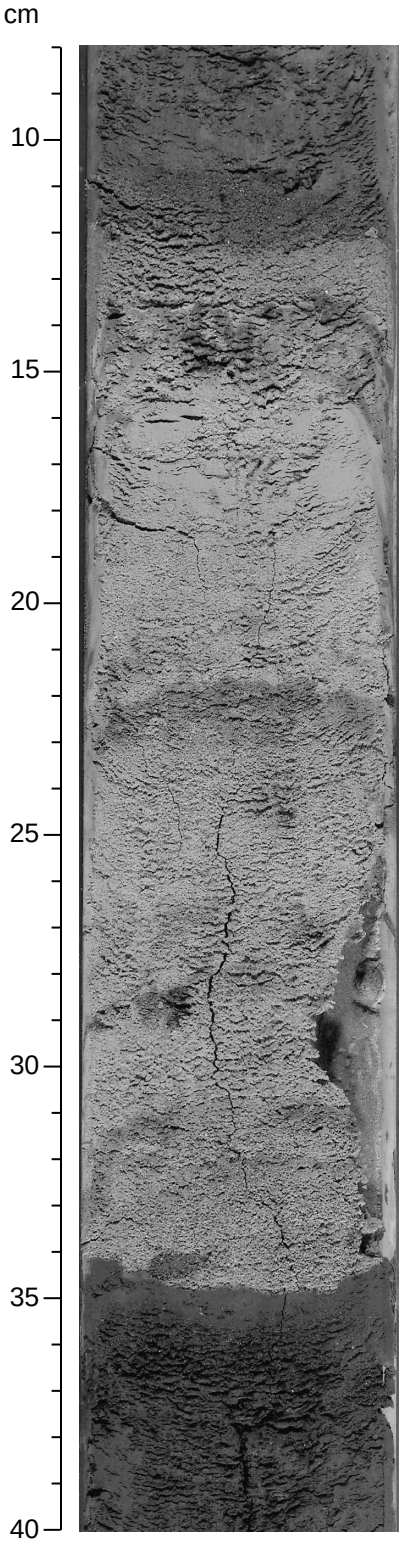

Figure F12. Several sharp-based, graded (coarse to fine grained) volcaniclastic sand beds. The lower part of each bed is massive and coarse grained, whereas the upper part is parallel laminated, or cross laminated, and finer grained (interval 180-1109C-20X-CC, 0–35 cm).

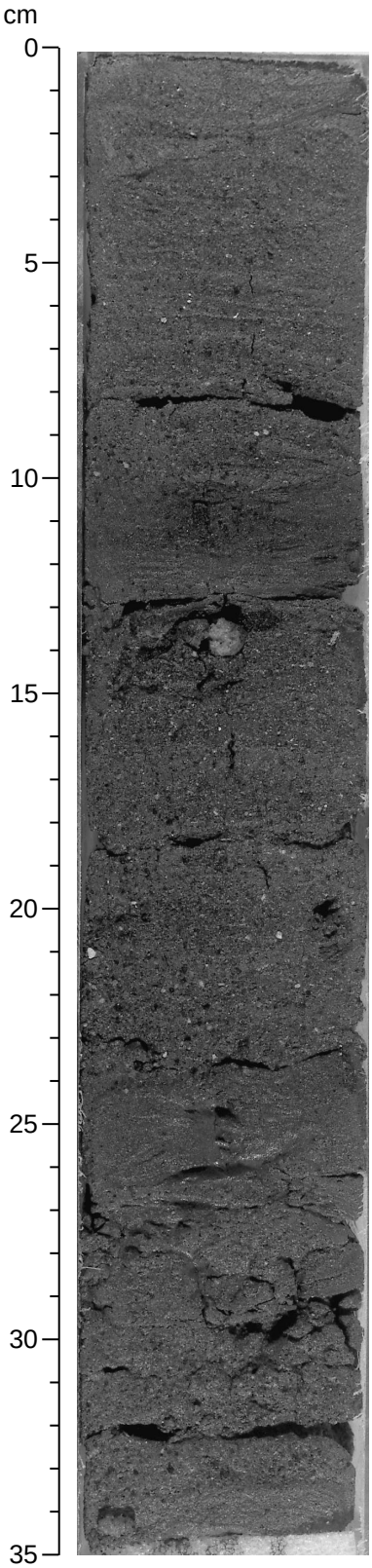

Figure F13. Parallel-laminated carbonate bed (37.5–45 cm). The laminations are composed of grain-supported particles (packstone), alternating with matrix-supported laminae. The upper part (10–37 cm) consists of two normal-graded volcaniclastic sand beds with parallel lamination in their lower part (interval 180-1109C-21X-CC, 10–45 cm).

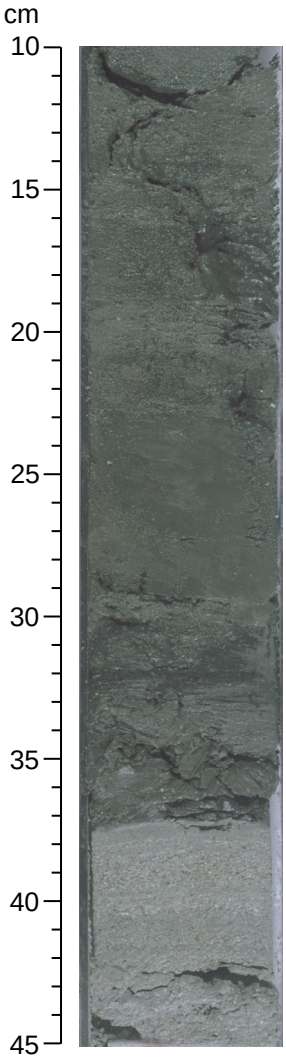

Figure F14. Digital photomicrograph (crossed nicols) of subrounded serpentinite clast surrounded by smaller grains, including feldspar and ferromagnesian minerals (interval 180-1109C-26X-CC, 18–20 cm).

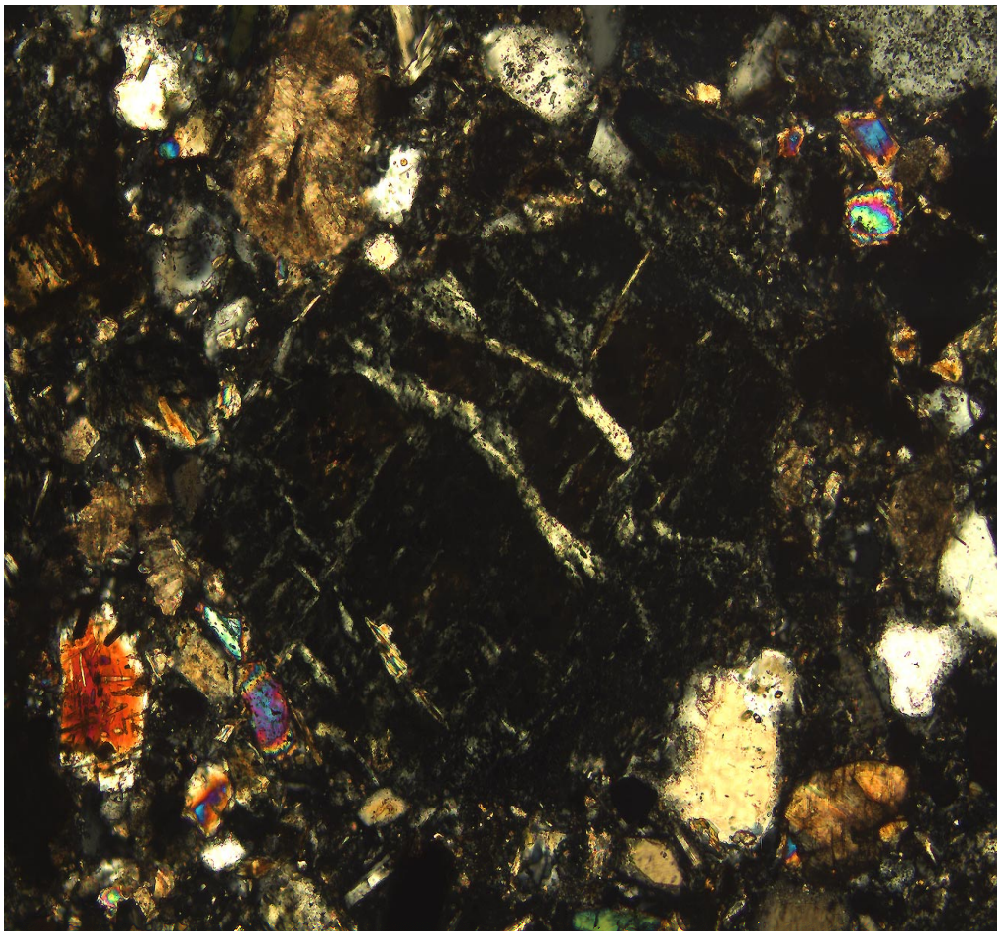

Figure F15. Digital photomicrograph (crossed nicols) of a small subangular grain of mica schist surrounded by various grains, including quartz, feldspar, ferromagnesian minerals, and foraminifers. Note the grain of polycrystalline quartz, bottom right (interval 180-1109C-26X-CC, 18–20 cm).

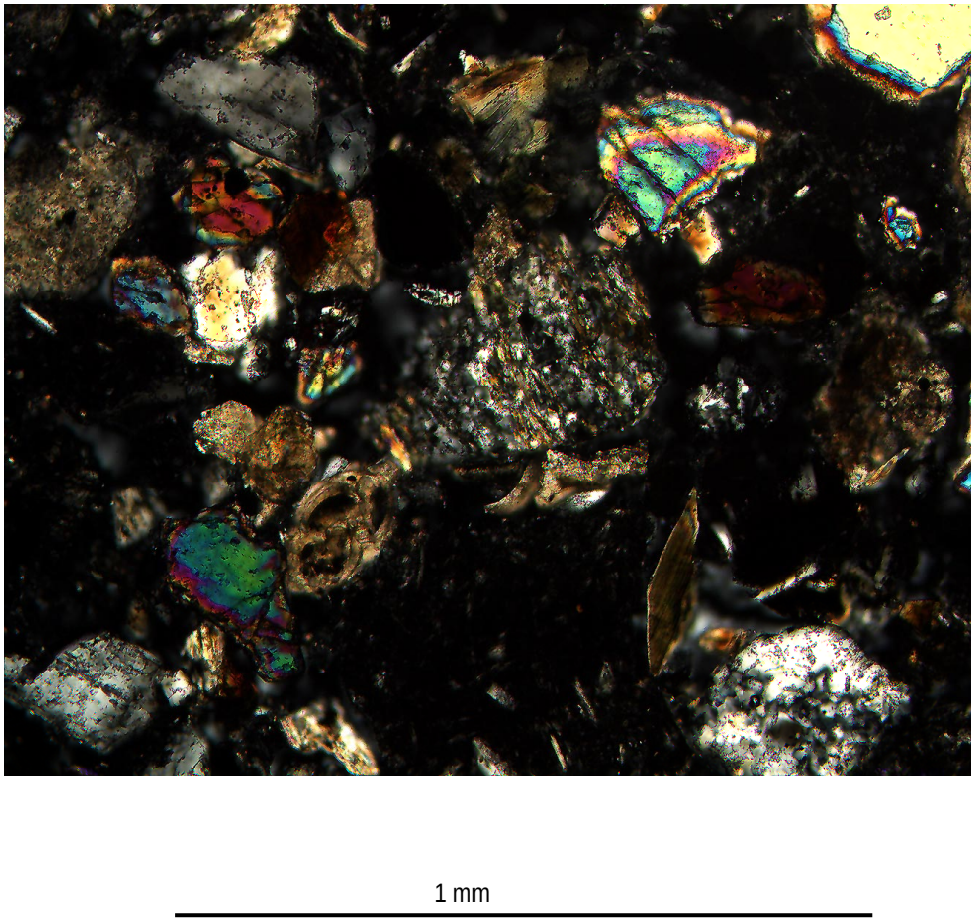

Figure F16. Highly disturbed interval caused by XCB coring. The harder drilling biscuits (e.g., 96–97.5 and 102–105 cm) are composed of fine-grained, indurated silty clays. The biscuits are surrounded by softer, relatively coarser material that was washed in by coring, resulting in "false bedding" (interval 180-1109C-35X-3, 96–110 cm).

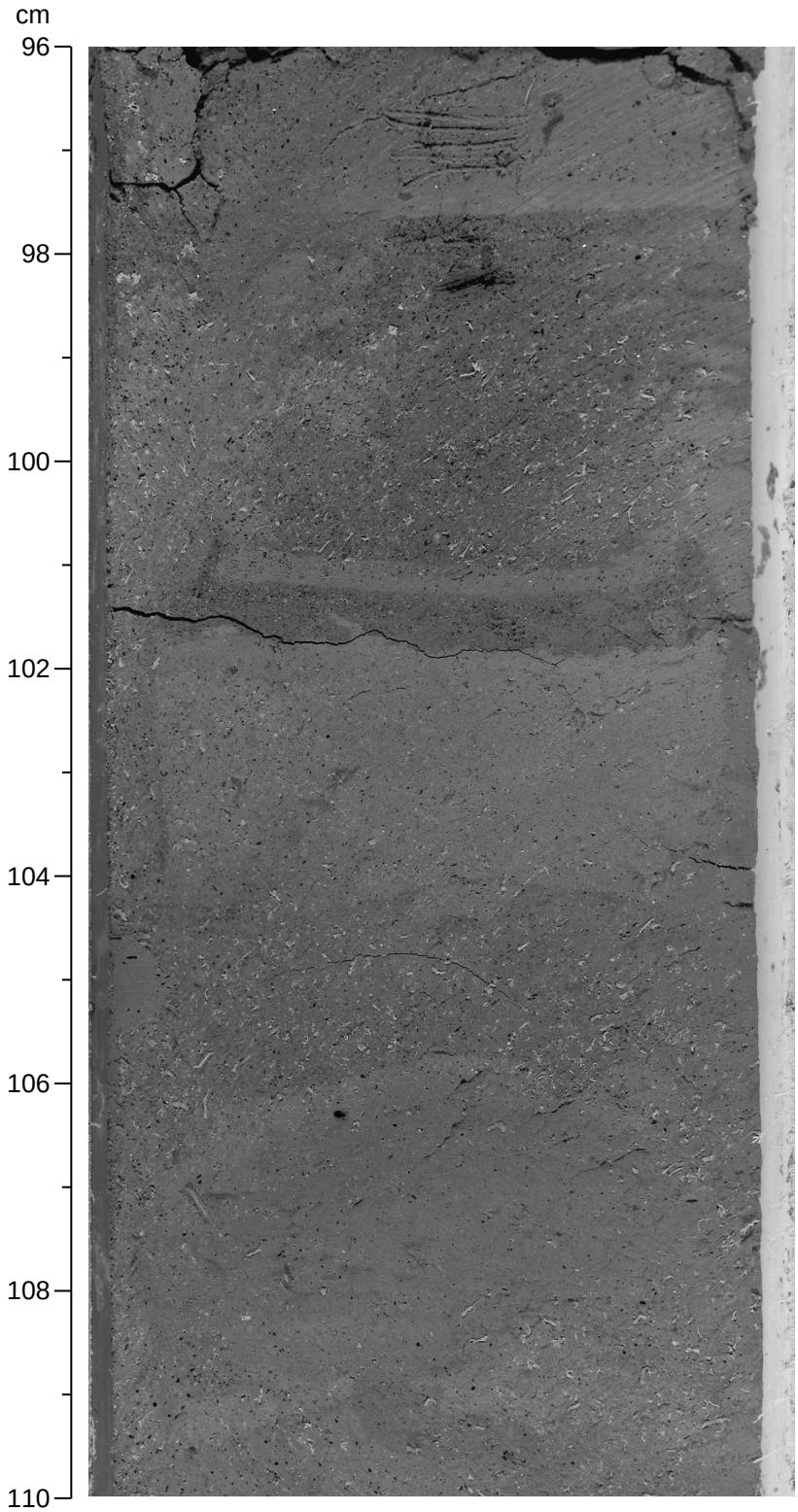

Figure F17. Normal-graded medium- to coarse-grained sandstone with a sharp, scoured base. The upper parts of these beds are highly bioturbated with burrows filled with medium- to coarse-grained sand (interval 180-1109D-2R-2, 100–115 cm).

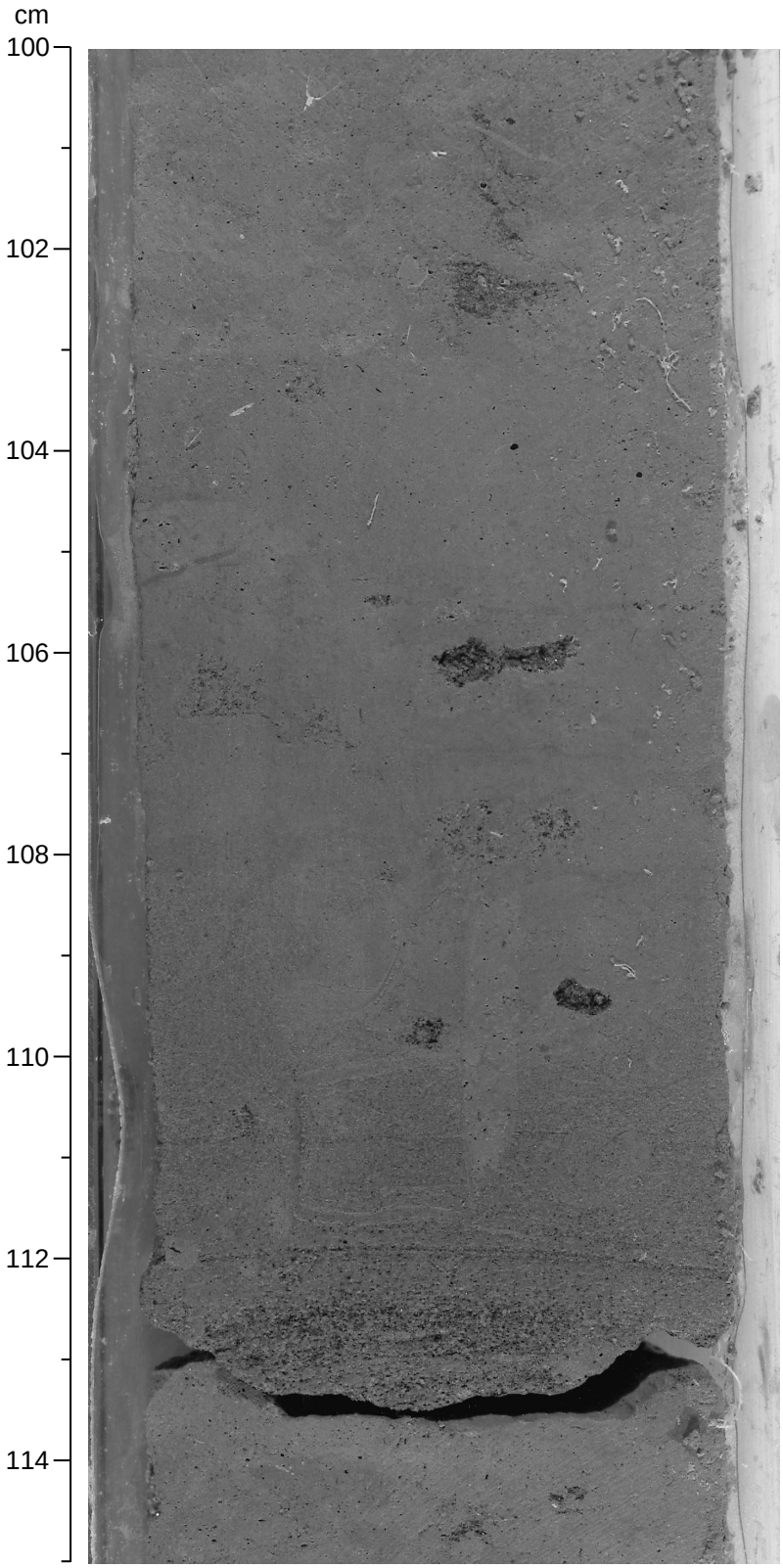

Figure F18. Digital photomicrograph (crossed nicols) of crystals of zoned plagioclase, hornblende, and biotite set in a siltstone matrix. Note the angular grain boundaries and absence of alteration (interval 180-1109C-1R-2, 48–49 cm).

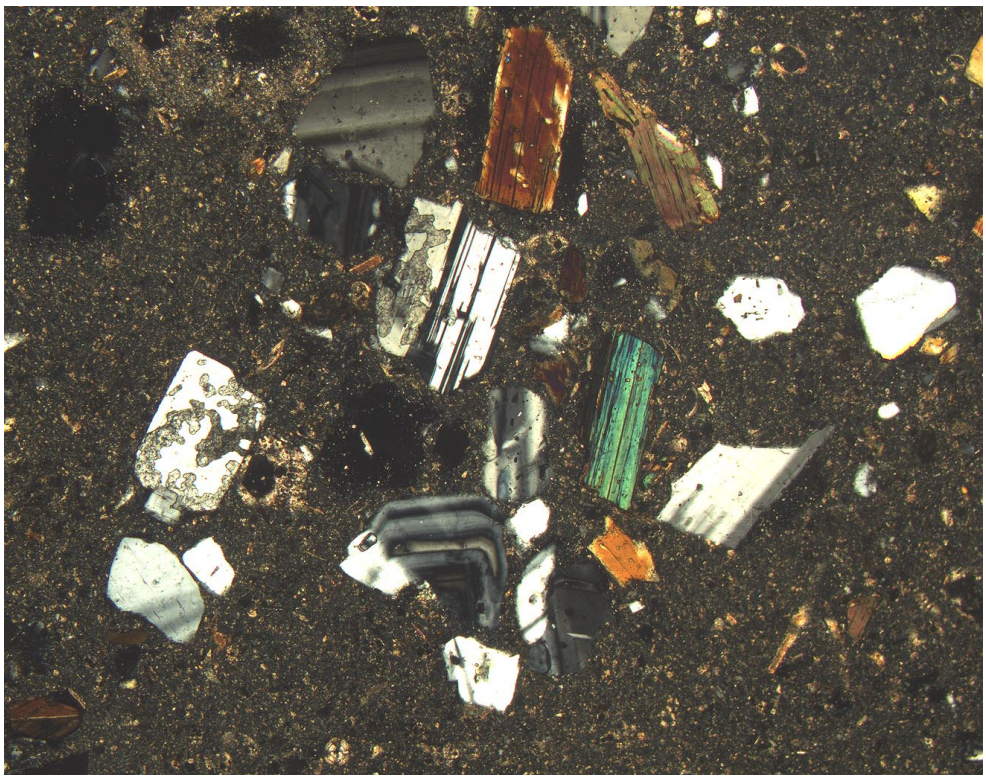

Figure F19. Digital photomicrograph of a smear slide (plane-polarized light) dominated by colorless, highly vesicular glass; rare crystals of biotite and green hornblende are also present (Sample 180-1109C-4R-2, 71 cm).

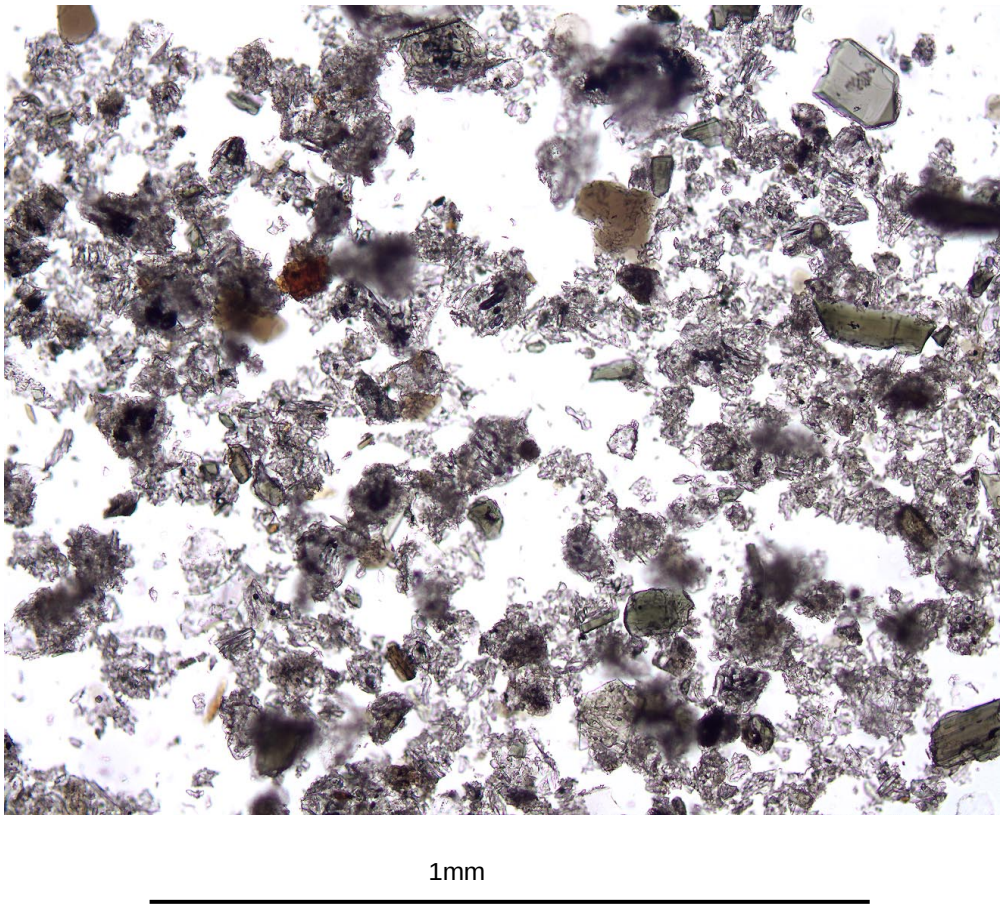

Figure F20. Several sharp-based, massive laminae (127–132 cm), composed of coarse- to fine-grained sand (e.g., 131.5–132 cm). Each of the sand lamina is overlain by a thin clay lamina (interval 180-1109D-21R-4, 115–135 cm).

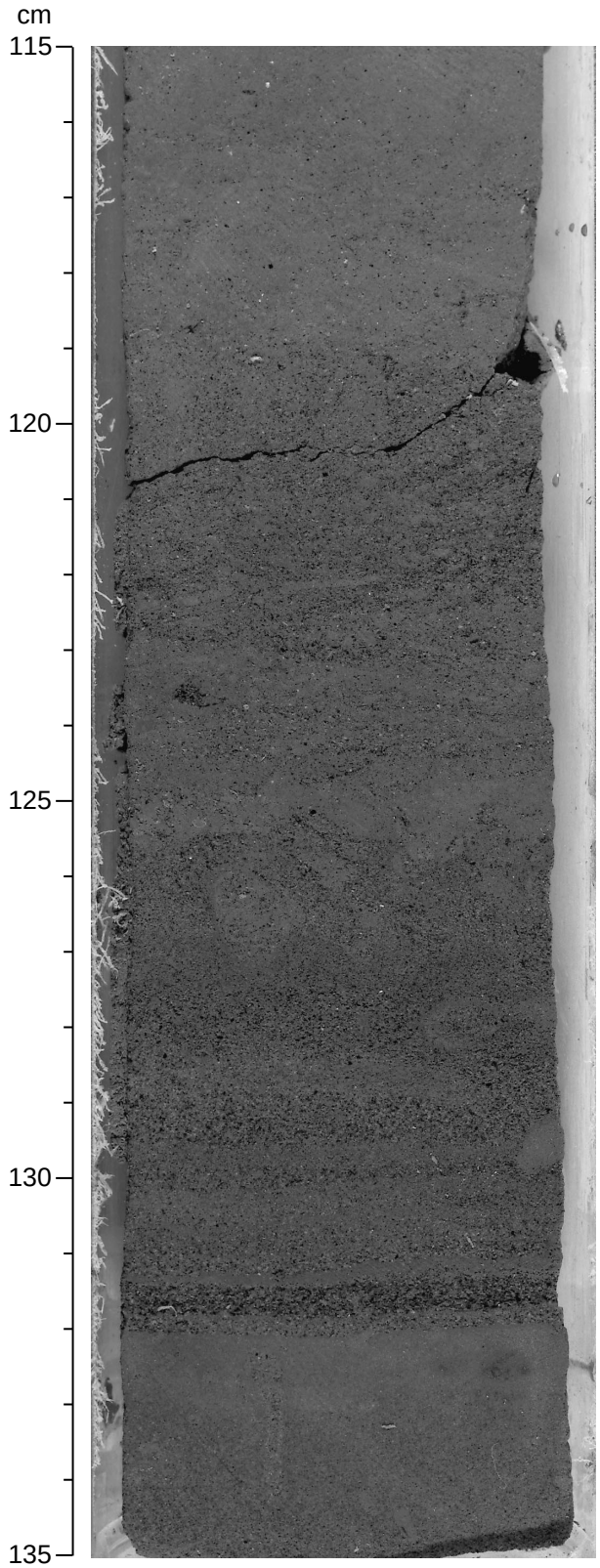

Figure F21. Graded, very thin beds and thin laminae of volcaniclastic medium-fine-grained sandstone and siltstone (interval 180-1109D-10R-1, 105–135 cm).

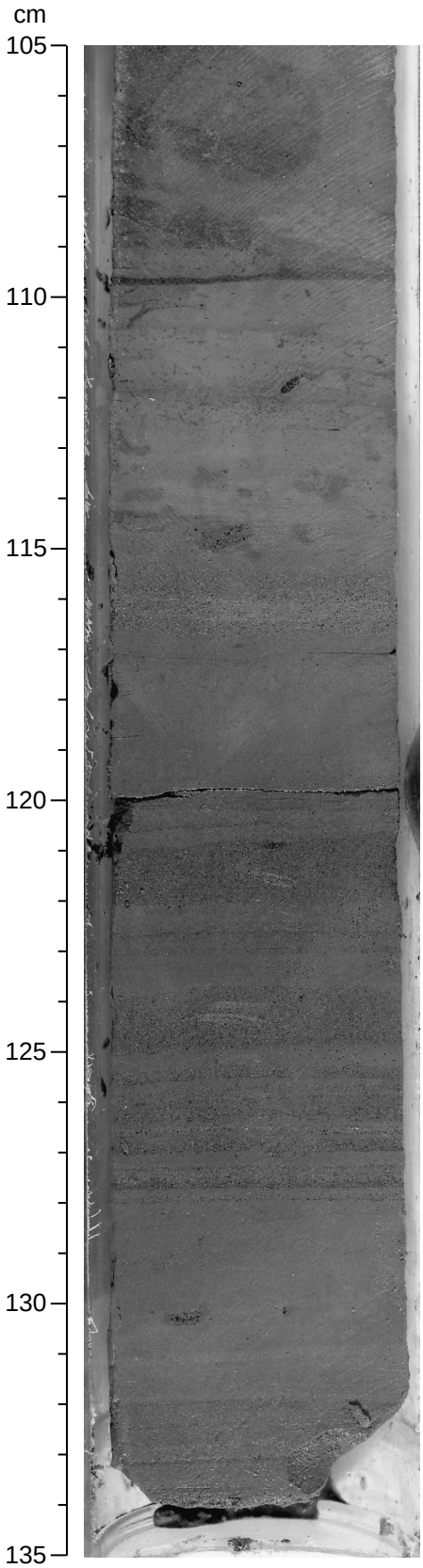

Figure F22. Coarse-grained volcaniclastic sandstone that shows traces of primary bedding (33–34 and 41–43 cm) (interval 180-1109D-29R-2, 30–50 cm).

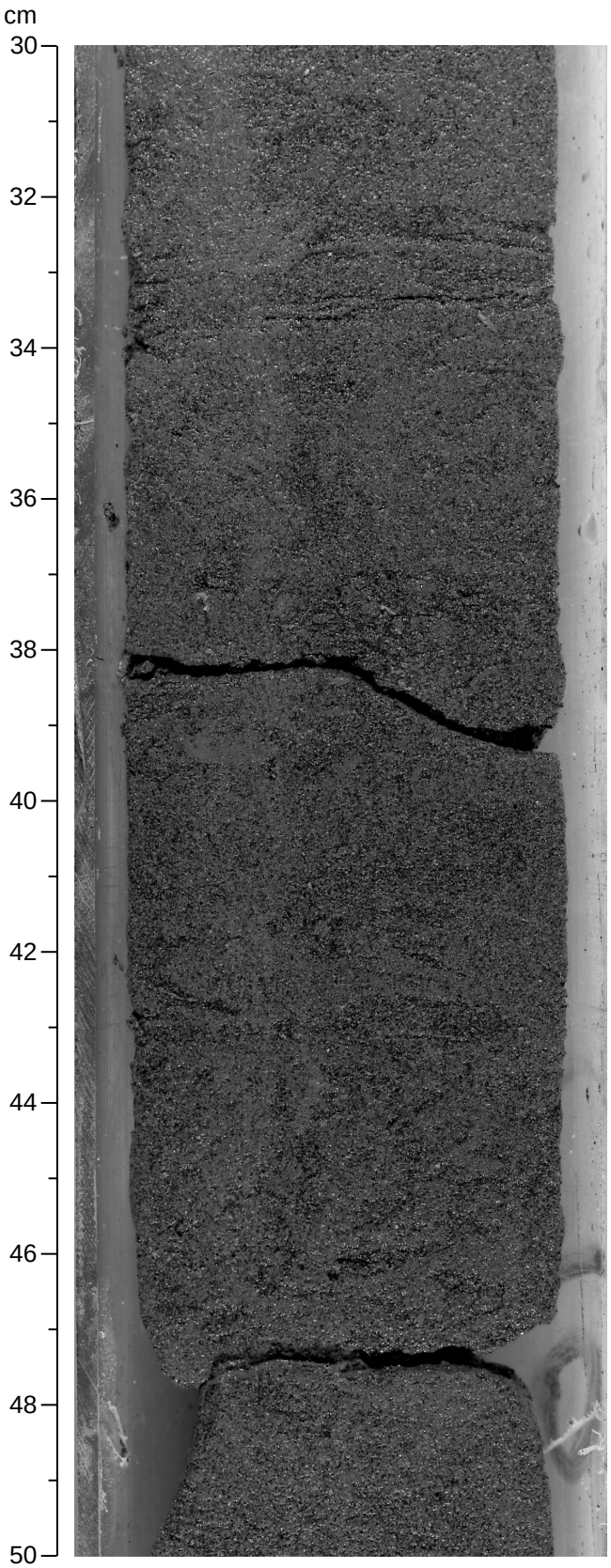

Figure F23. Digital photomicrograph (crossed nicols) of an unaltered basaltic andesite clast with phenocrysts of plagioclase, hornblende, and biotite. The clast is set in a wackestone with rare volcaniclastic grains (interval 180-1109D-32R-2, 101–103 cm).

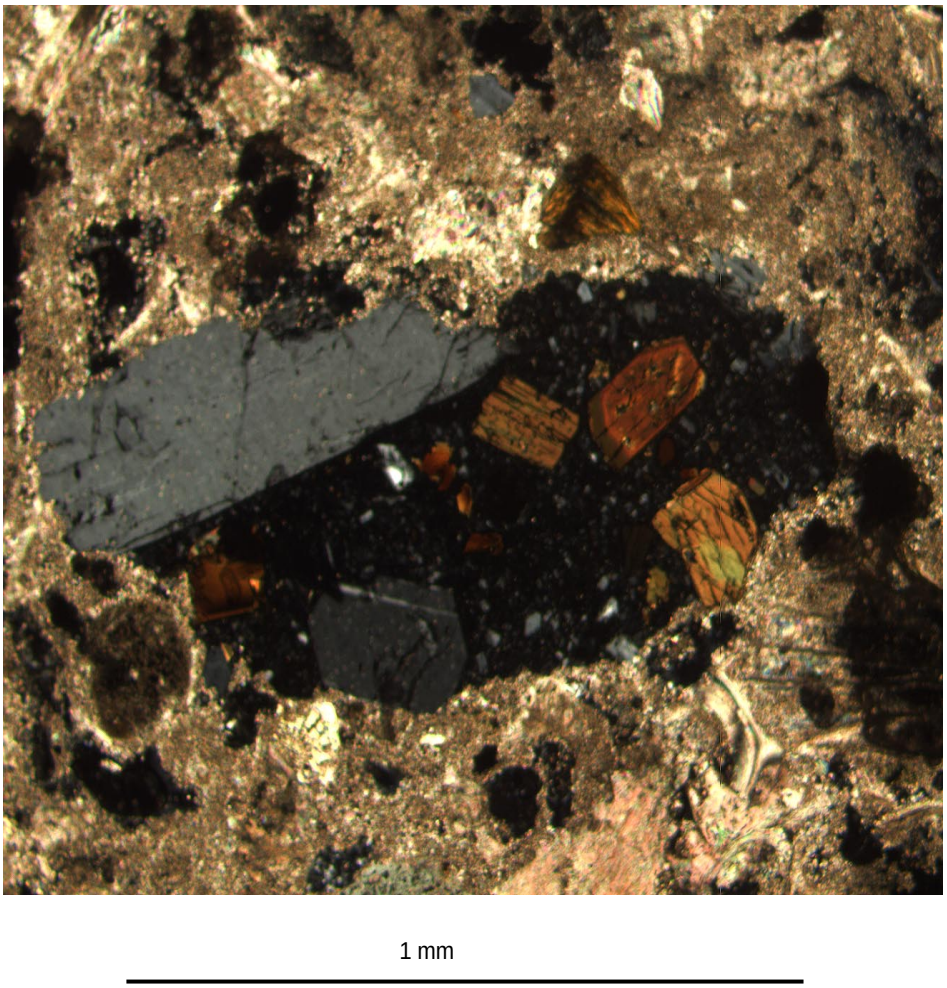

Figure F24. Coarse-grained calcareous rock (packstone) composed mostly of shell and carbonate fragments cemented by calcite (interval 180-1109D-32R-2, 90–110 cm).

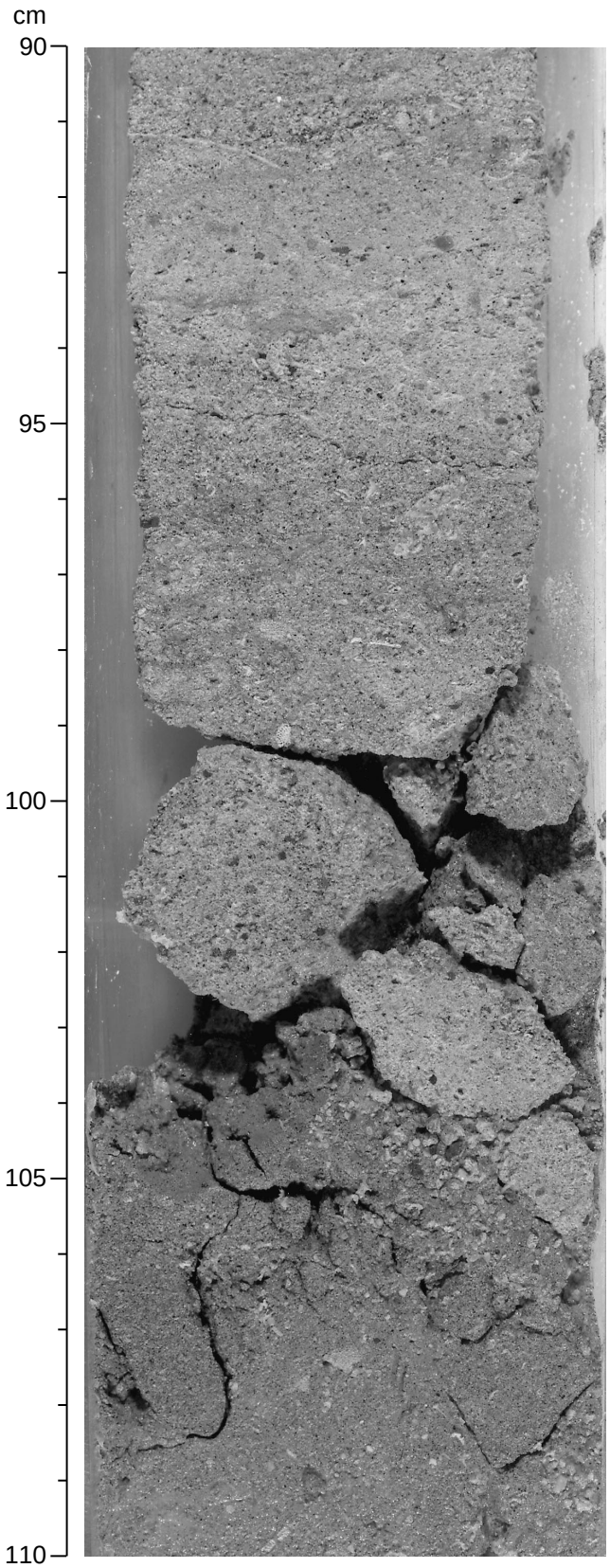

Figure F25. Cross section of a rugose coral. Coral fragments occur in packstone, mainly shell fragments. Note the absence of any obvious diagenetic alteration (interval 180-1109D-27R-4, 0–8 cm).

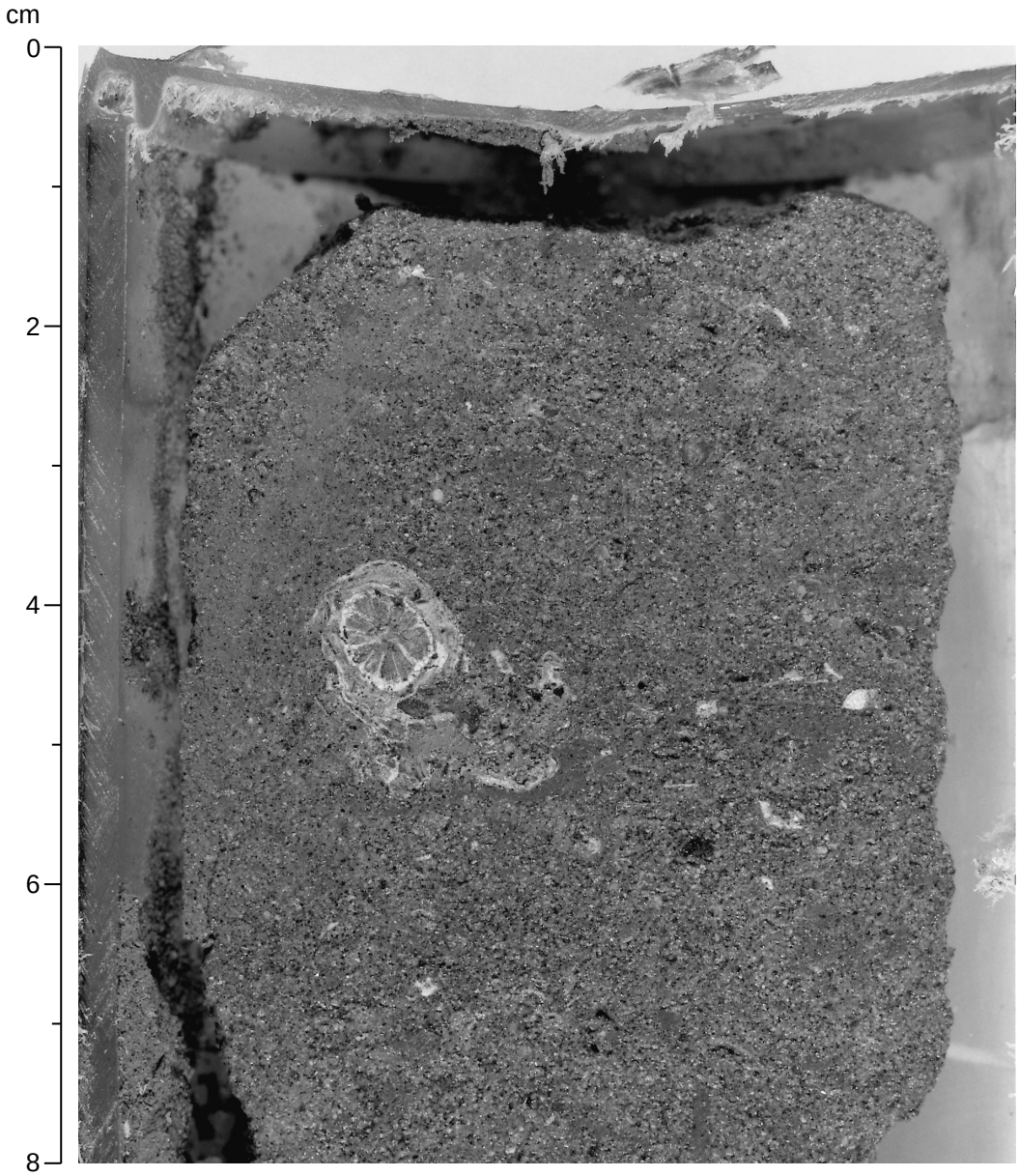

Figure F26. Massive silty claystone with scattered shell fragments, but without bioturbation (interval 180-1109D-36R-4, 55–78 cm).

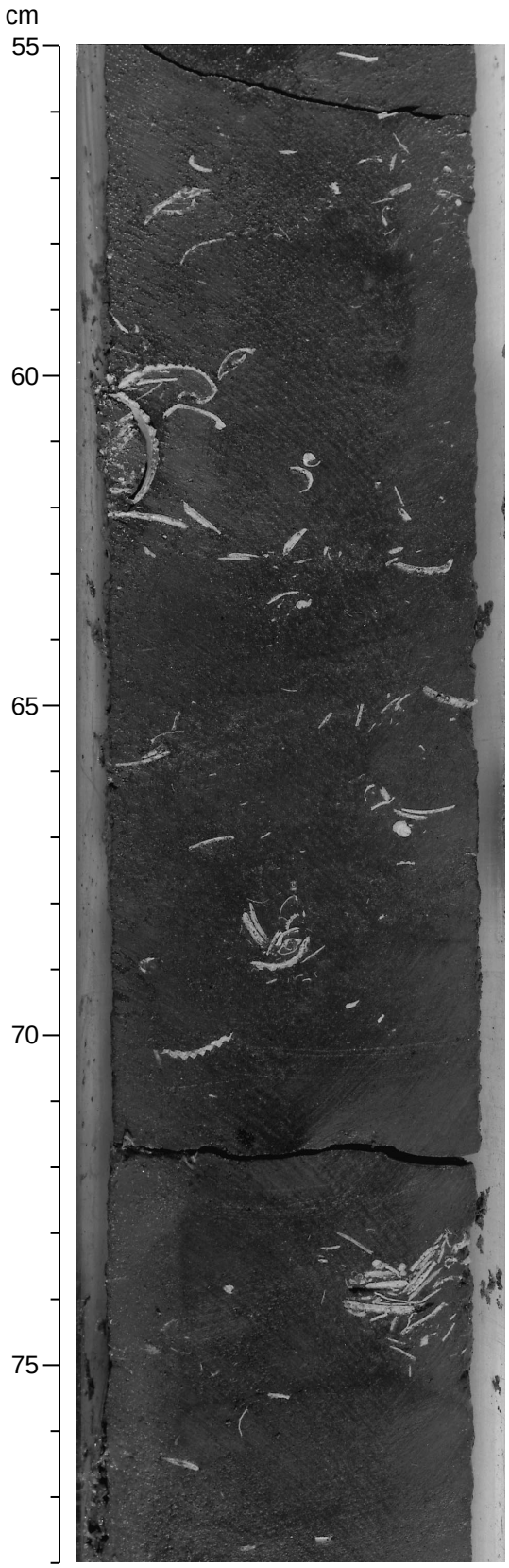

Figure F27. Massive to slightly burrowed silty claystone with localized concentrations of shell fragments (interval 180-1109D-38R-1, 100–130 cm).

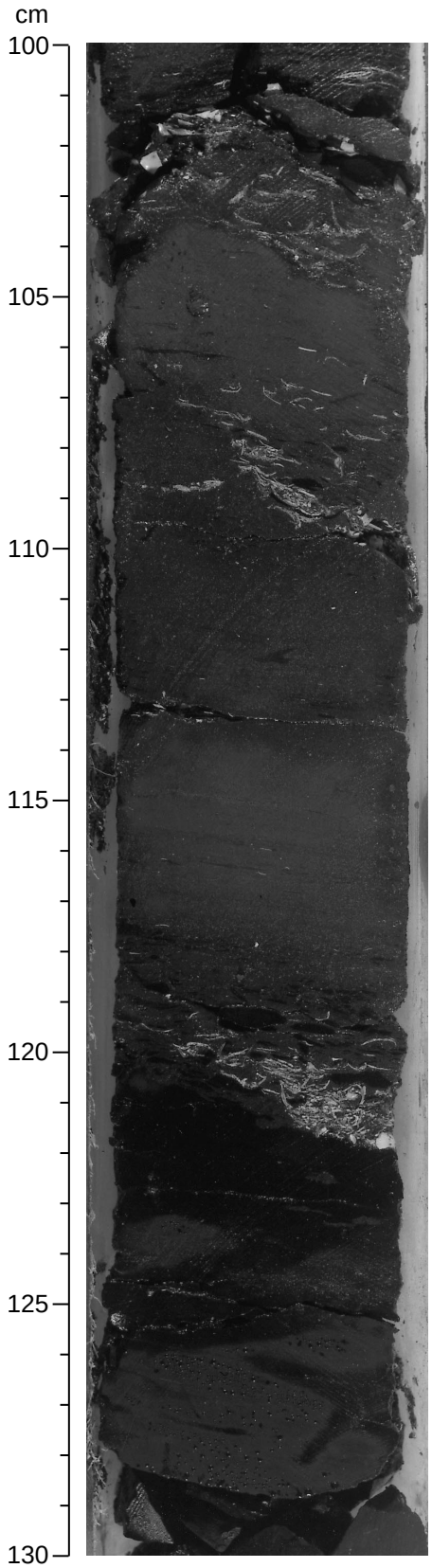

Figure F28. Interlaminated lignite-dominated laminations (very dark at 11.5 cm) with silty claystone and fine-grained sandstone laminations (light color at 13.5 cm) (interval 180-1109D-38R-2, 10–25 cm).

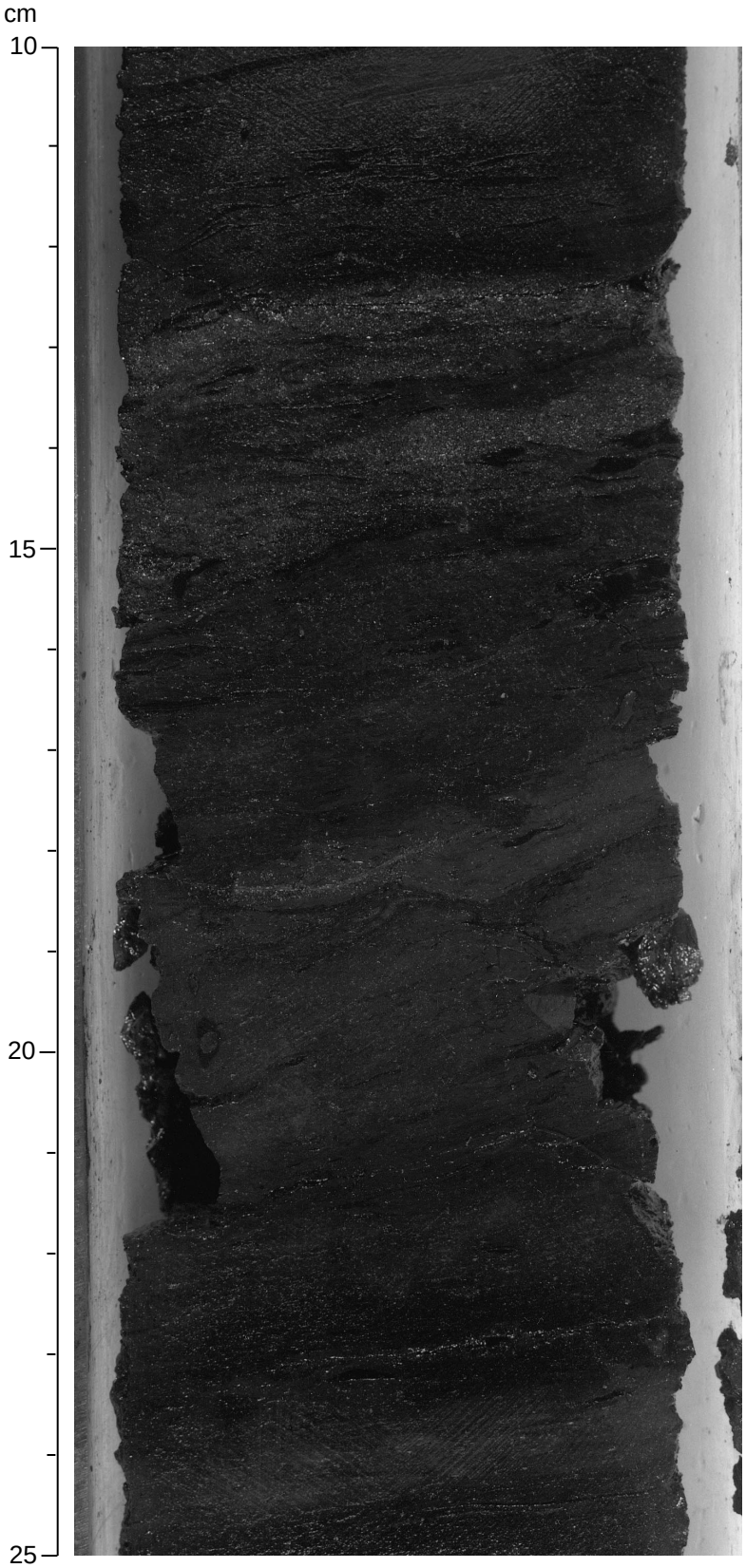

Figure F29. Highly altered, poorly sorted siltstone and fine-grained sandstone with abundant goethite concretions (interval 180-1109D-40R-3, 83–105 cm).

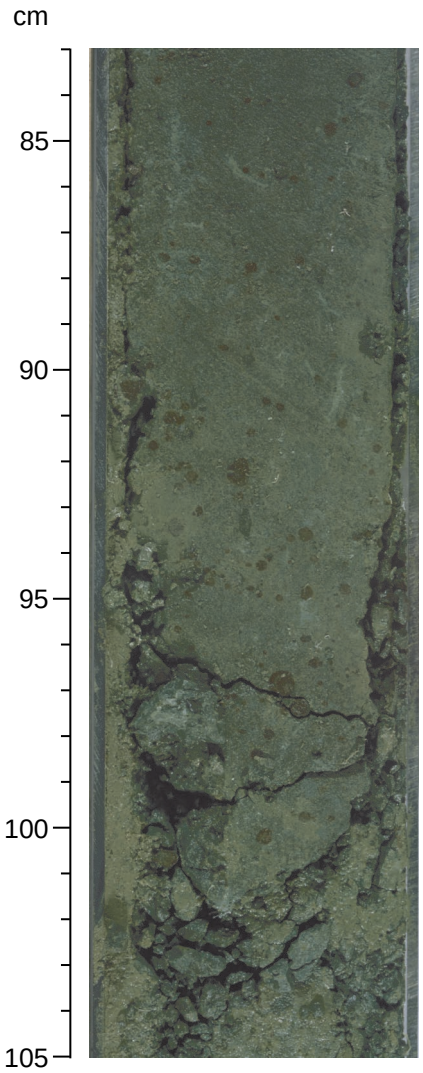

Figure F30. Fragments of dolerite and orthoconglomerate. The conglomerate is made of very well rounded altered basalt and dolerite clasts in a matrix of sandstone (interval 180-1109D-43R-1, 35–53 cm).

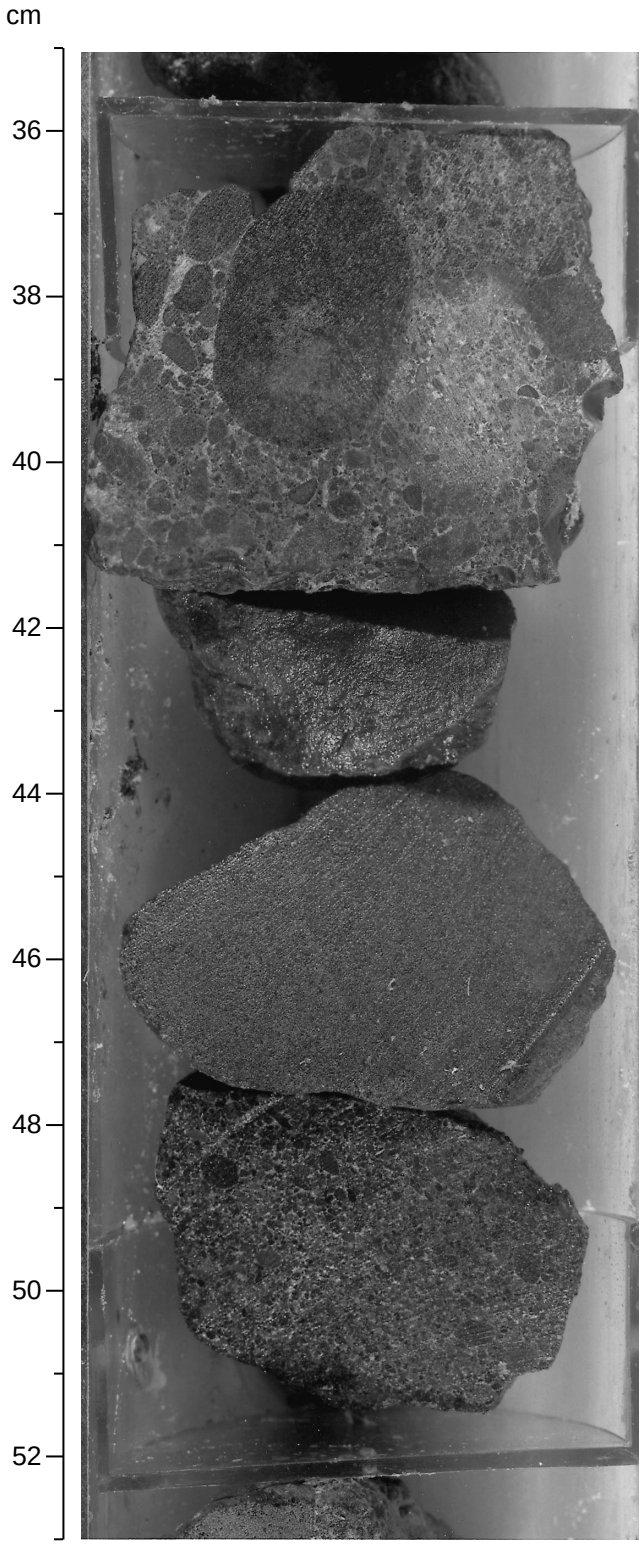

Figure F31. Digital photomicrograph of a well-rounded basaltic grain with plagioclase and pyroxene microphenocrysts set within a matrix of altered sandstone within orthoconglomerate (interval 180-1109D-43R-1, 75–78 cm).

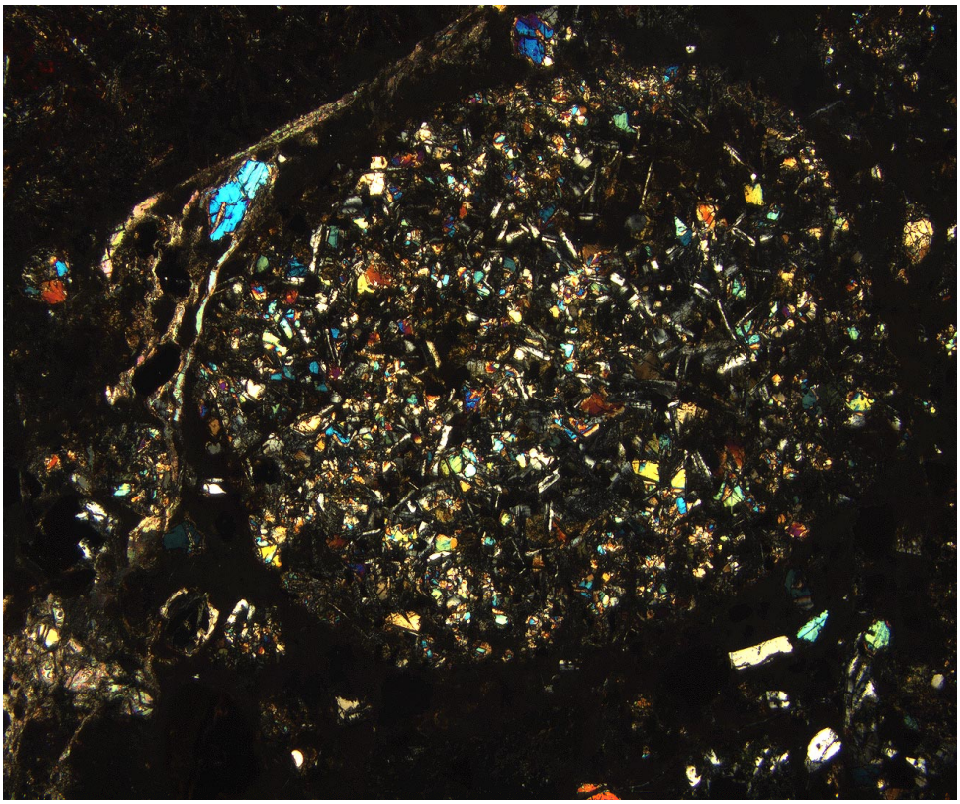

Figure F32. Summary of the sedimentary succession cored at Site 1109, based on the actual recovery and barrel sheets; intervals of nonrecovery are indicated.

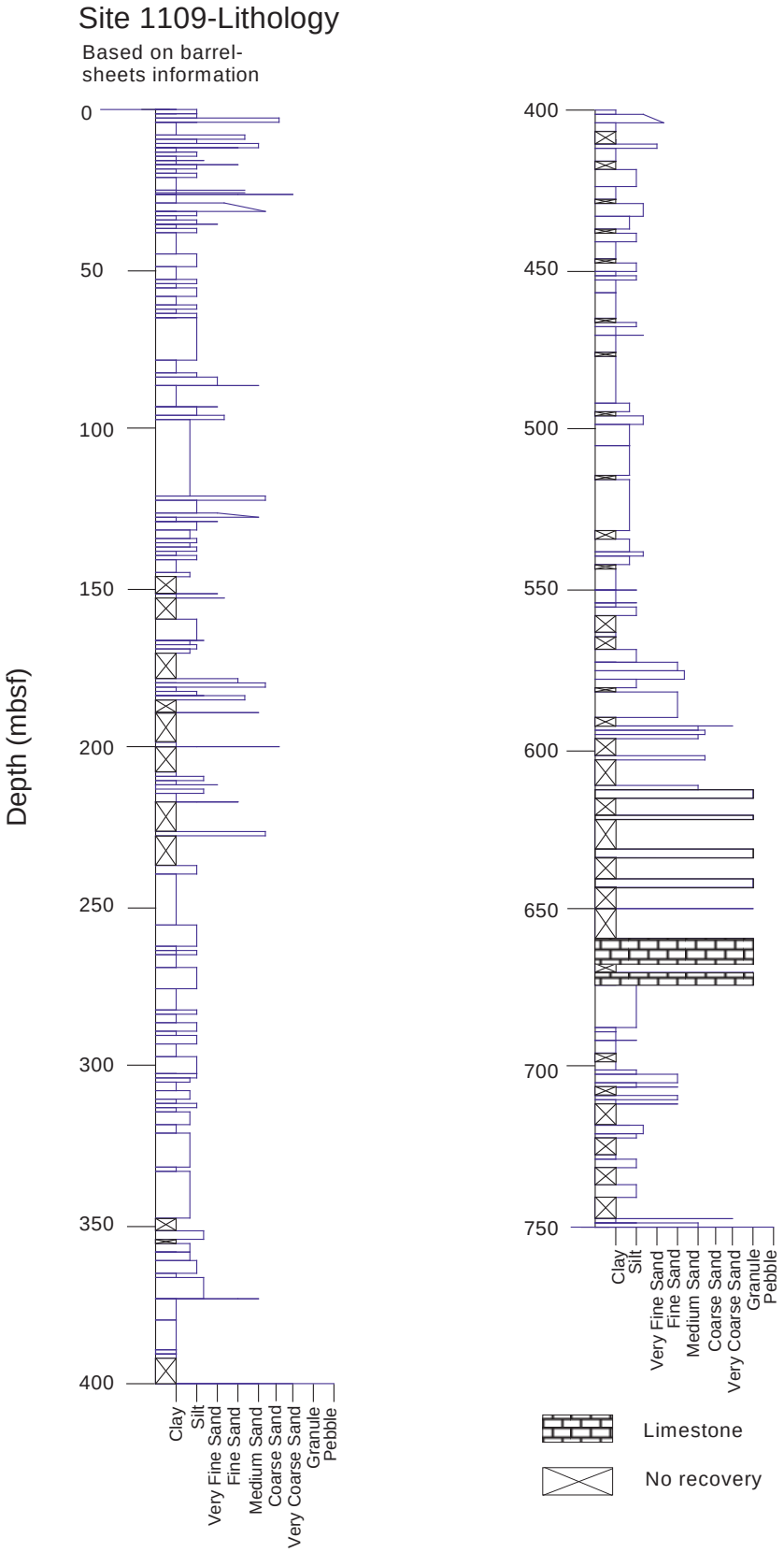

Figure F33. Summary of grain-size trend at Hole 1109C. The plots smooth the original grain-size variation as recorded on the barrel sheets. Note that anomalies may result in areas of low recovery. For key to symbols, see Figure F2, p. 52, in the "Explanatory Notes" chapter.

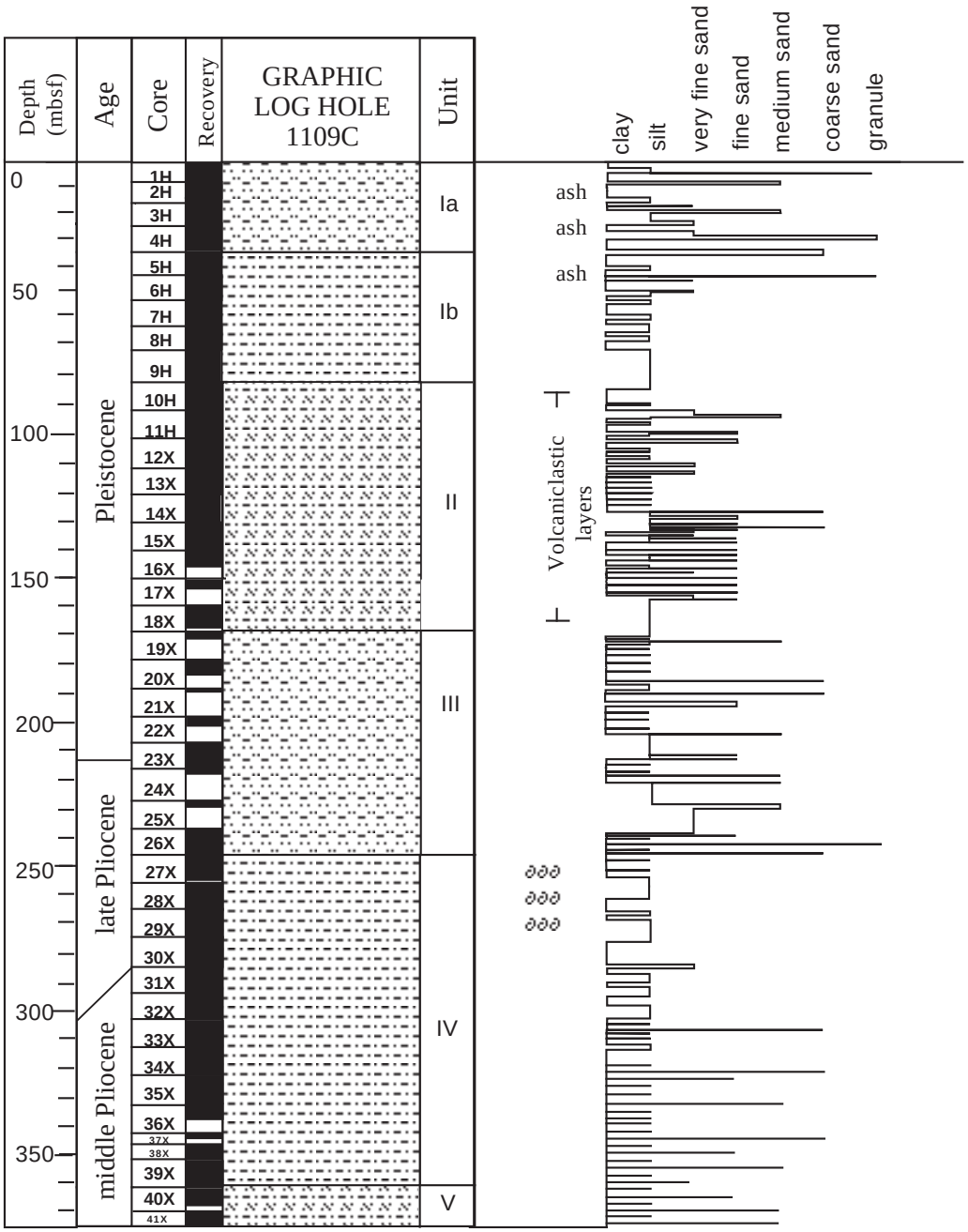

Figure F34. Summary of grain-size trend in Hole 1109D. The plots smooth the original grain-size variation as recorded on the barrel sheets. Note that anomalies may result in areas of low recovery. For key to symbols, see Figure F2, p. 52, in the "Explanatory Notes" chapter.

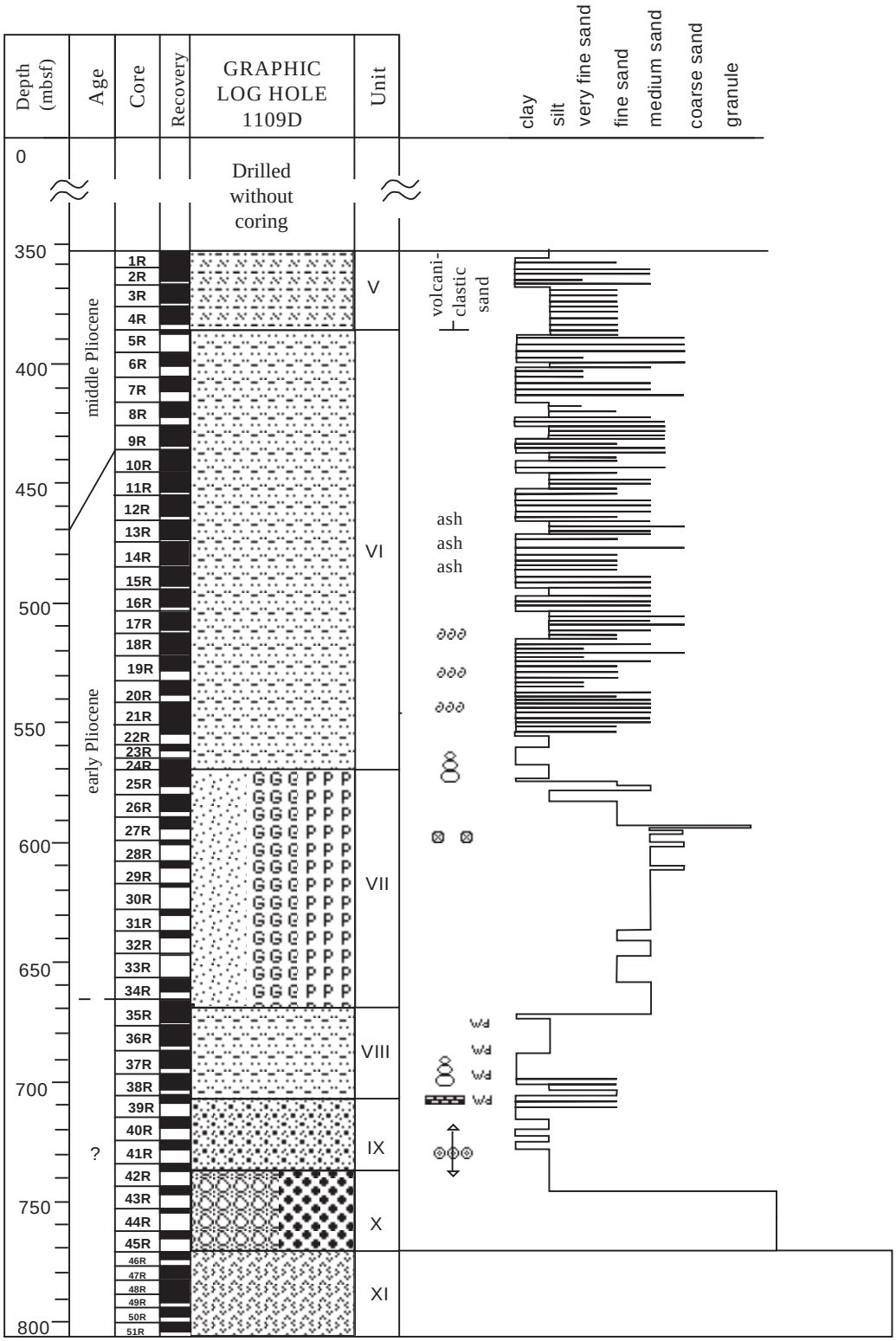

Figure F35. A. Summary of results of smear-slide analyses, Hole 1109D. Individual constituents are plotted against depth. (Continued on next page.)

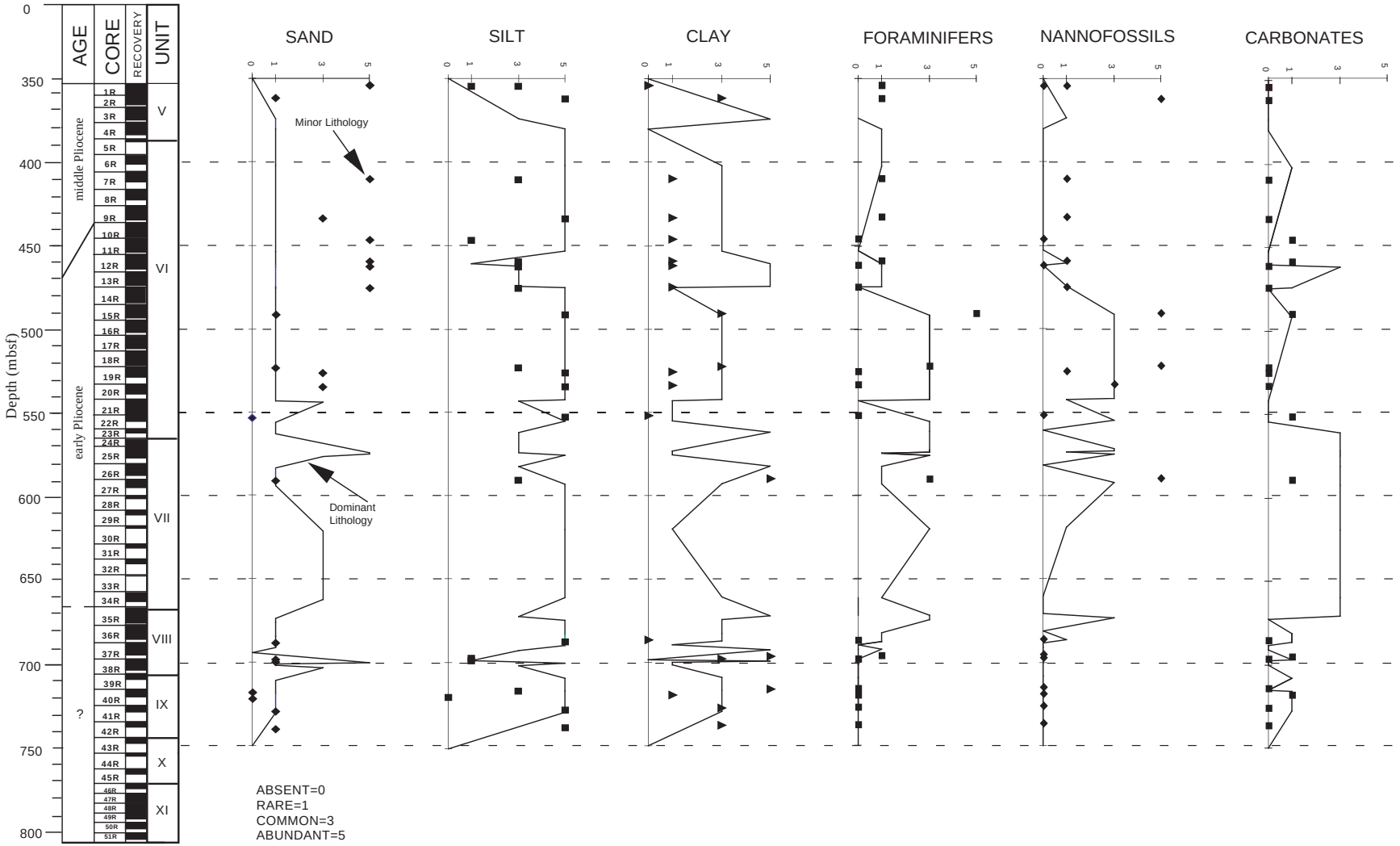

Figure F35 (continued). B. Summary of results of smear-slide analyses, Hole 1109D. Individual constituents are plotted against depth.

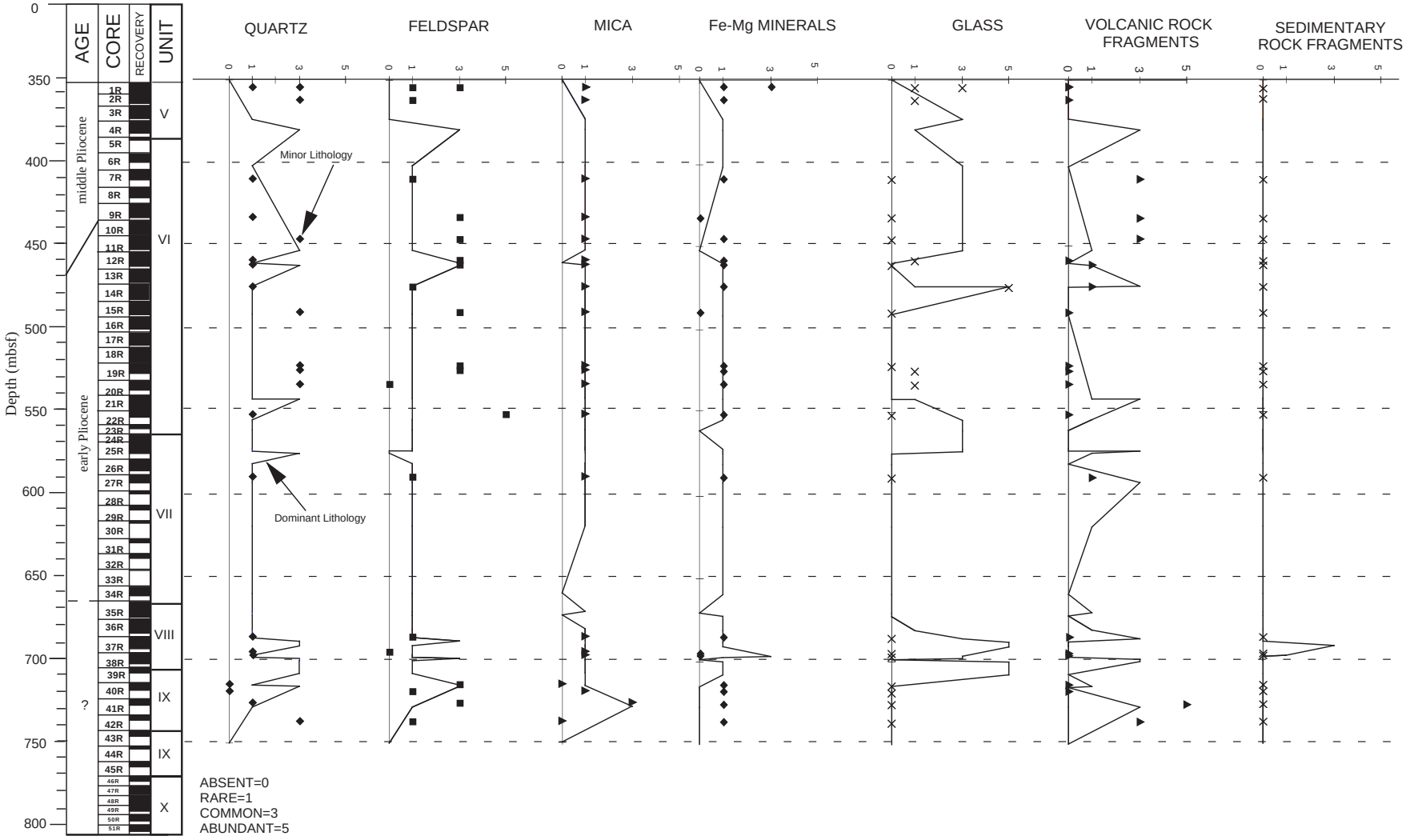

Figure F36. Number of volcanogenic ash layers (black) and total volcanogenic ash thickness per core in centimeters (shaded), Site 1109. Note that the variation may not be representative of the actual recovery within intervals of low recovery.

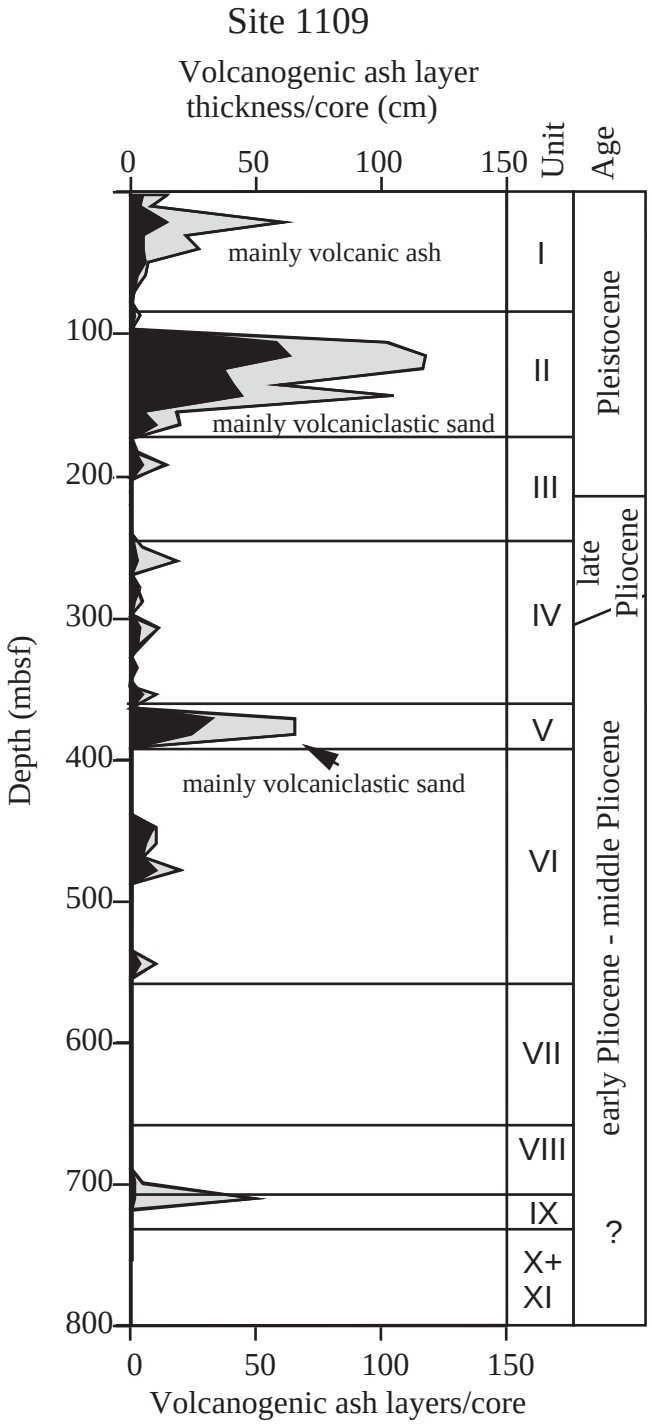

Figure F37. Conglomerate with variably weathered, well-rounded basalt (some of subaqueous origin) and dolerite clasts in a micritic calcite-clayey matrix (interval 180-1109D-45R-1, 46.5–53.5 cm).

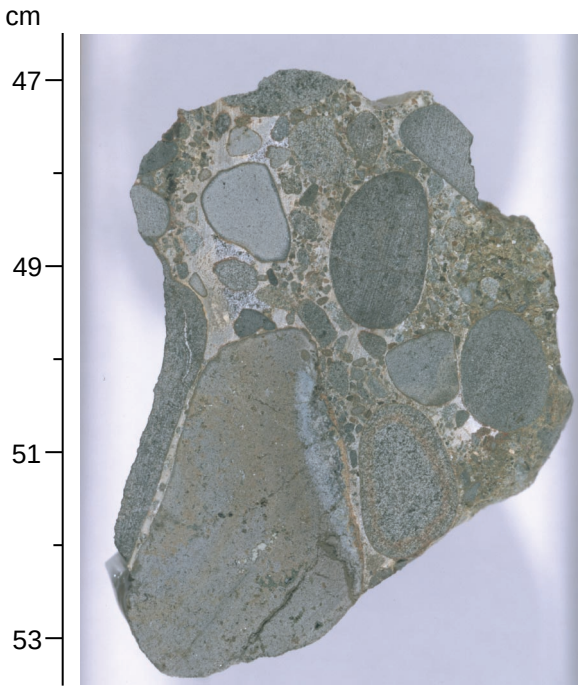

Figure F38. Dolerite clast at the boundary between a dolerite sill and overlying conglomerate unit. Rounded clast has red weathering products rimmed by green (5GY 7/2) weathering products (at right side of clast). This suggests an environmental change from a subaerial (oxidation) to a lagoonal (reduction) setting, in accordance with other observations (interval 180-1109D-45R-3, 27–30.5 cm).

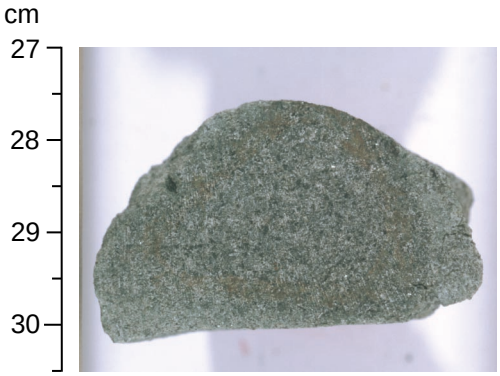

Figure F39. Digital photomicrograph (plane-polarized light) of swallowtail and hopper crystals of plagioclase in a variolitic groundmass (interval 180-1109D-44R-1, 34–41 cm).

Figure F40. Digital photomicrograph (plane-polarized light) of granular dolerite with altered plagioclase and large iron oxides (interval 180-1109D-44R-2, 68–71 cm).

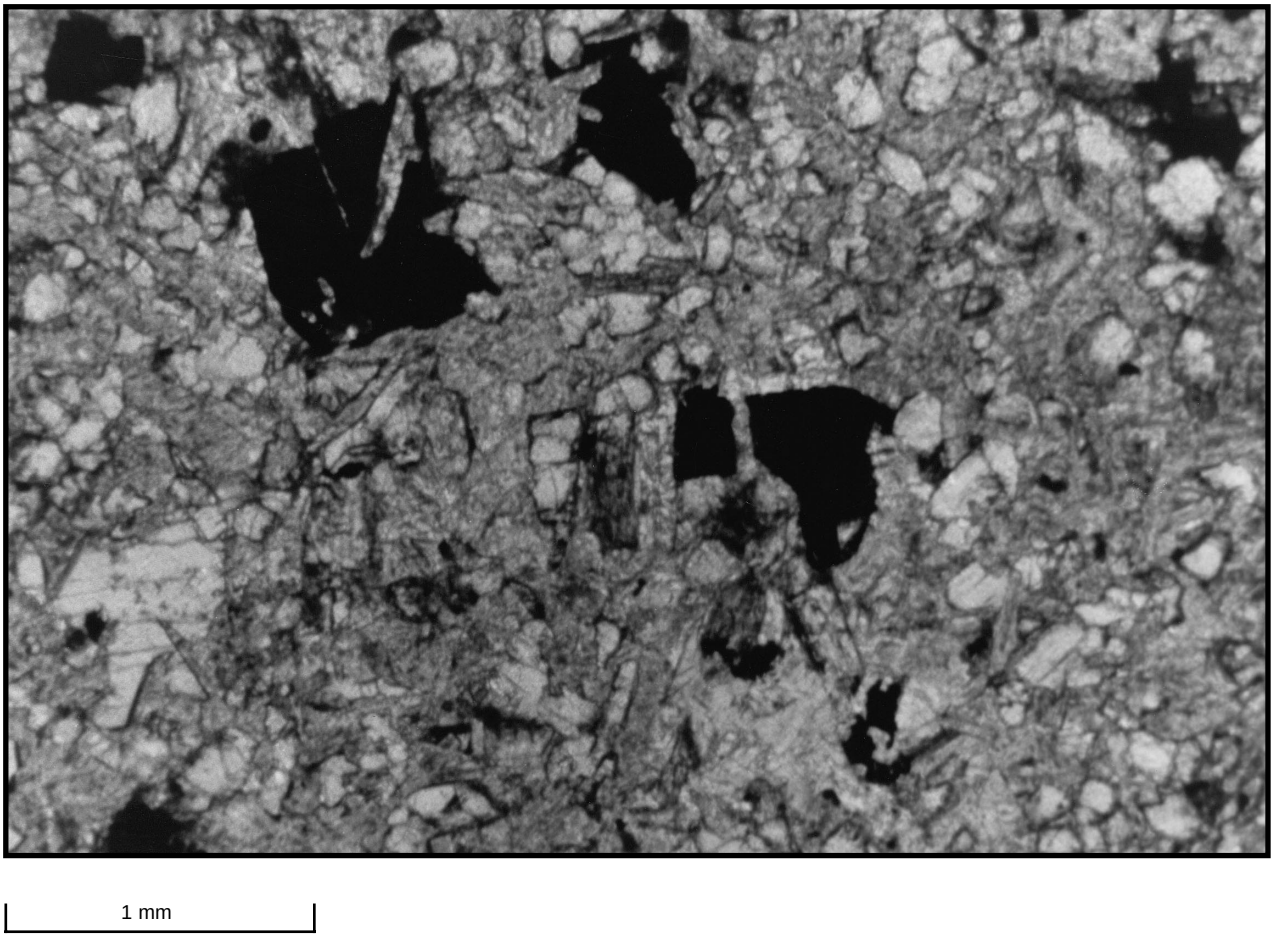

Figure F41. Digital photomicrograph (crossed nicols) of ophitic dolerite with plagioclase laths enclosed in large plates of augite (interval 180-1109D-44R-3, 40–43 cm).

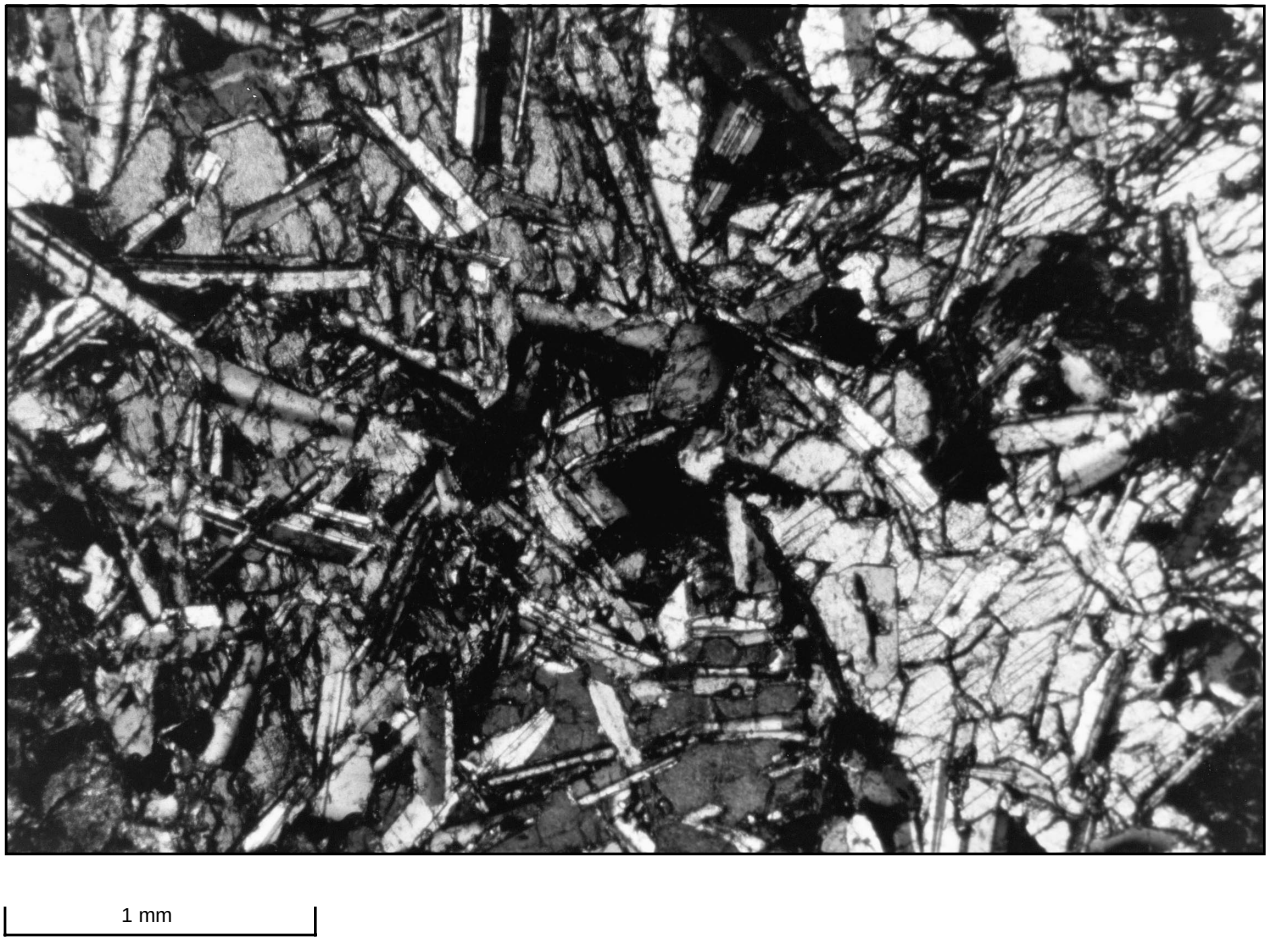

Figure F42. Digital photomicrograph (crossed nicols) of ophitic dolerite with plagioclase laths enclosed in large plates of augite. In the lower center, an alteration patch thought to be after olivine is seen (interval 180-1109D-44R-3, 40–43 cm).

Figure F43. Digital photomicrograph (plane-polarized light) of internal contact in dolerite. Glassy dolerite in top left (with pseudomorphs after olivine microphenocrysts at upper left) intrudes crystalline dolerite (bottom right). Rounded blebs of the intruding rock are incorporated within the crystalline dolerite (plane-polarized light) (interval 180-1109D-51R-4, 22–24 cm).

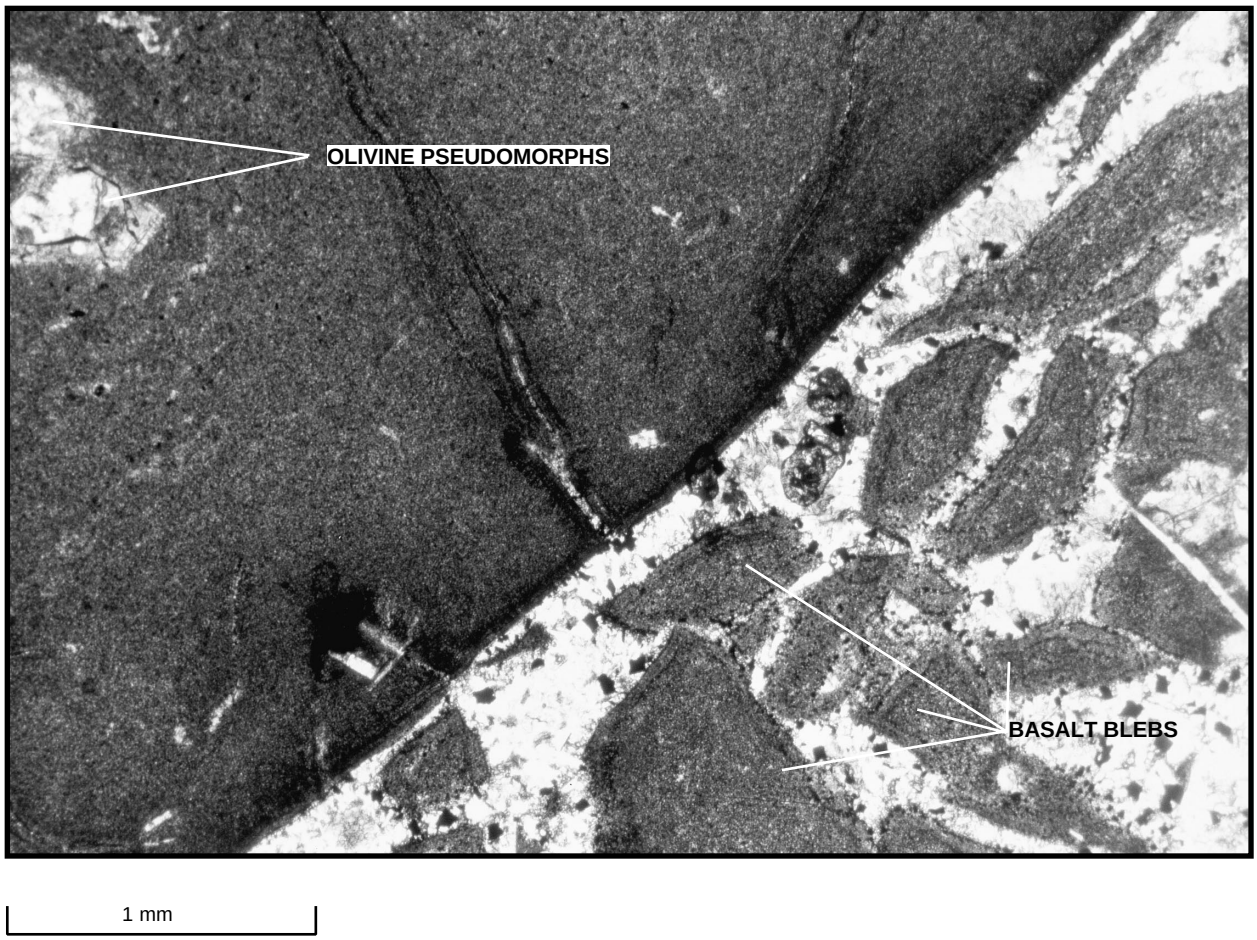

Figure F44. Core split view showing joint (perpendicular to core axis) filled with greigite (black, visually amorphous, identified by XRD) and pyrite within dolerite. Mottling of the dolerite is because of its ophitic texture (interval 180-1109D-45R-3, 47–60 cm).

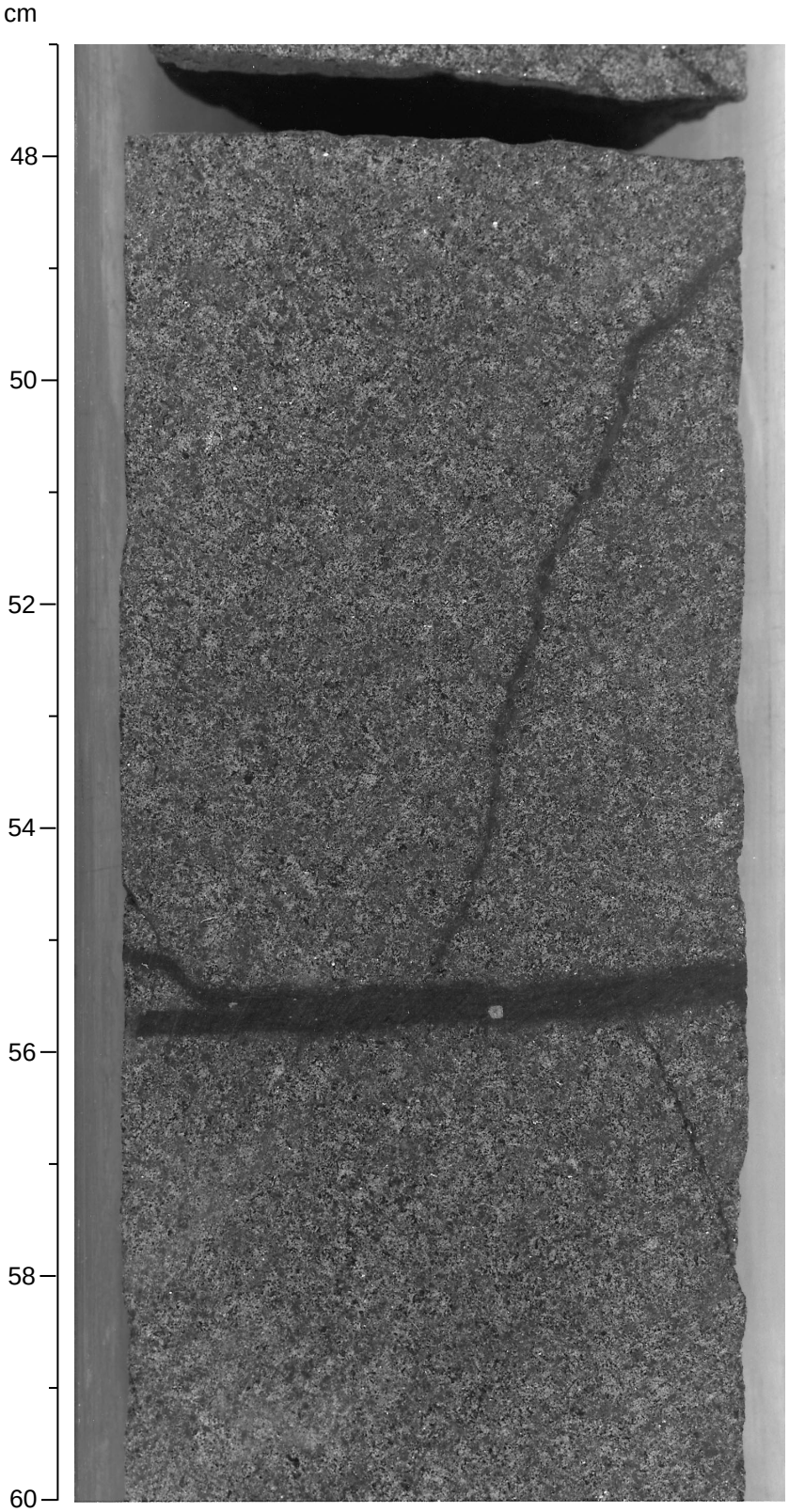

Figure F45. Vein minerals (calcite and chlorite hand specimen identification) filling a fault in dolerite (interval 180-1109D-50R-3, 52–57 cm).

Figure F46. A. Variation with depth of selected elements in the dolerite body. (Continued on next page.)

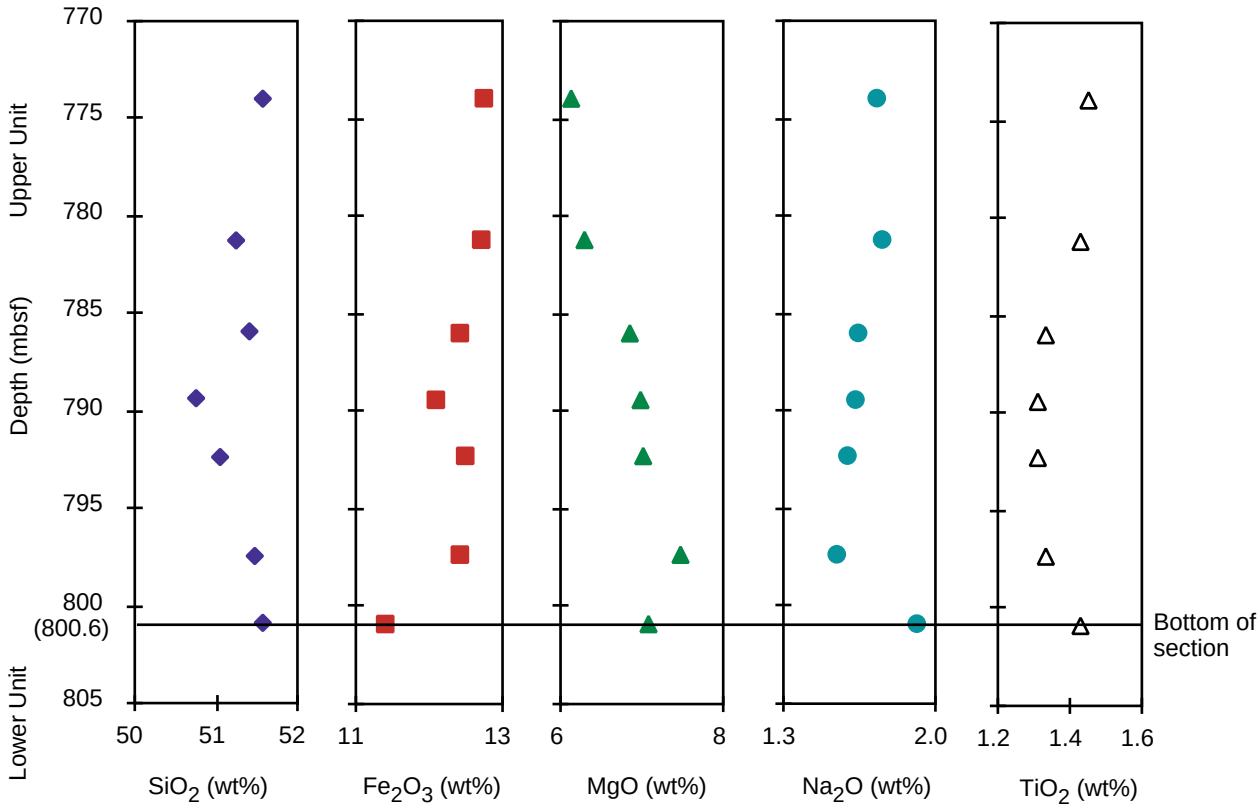

Figure F46 (continued). B. Variation with depth of selected elements in the dolerite body.

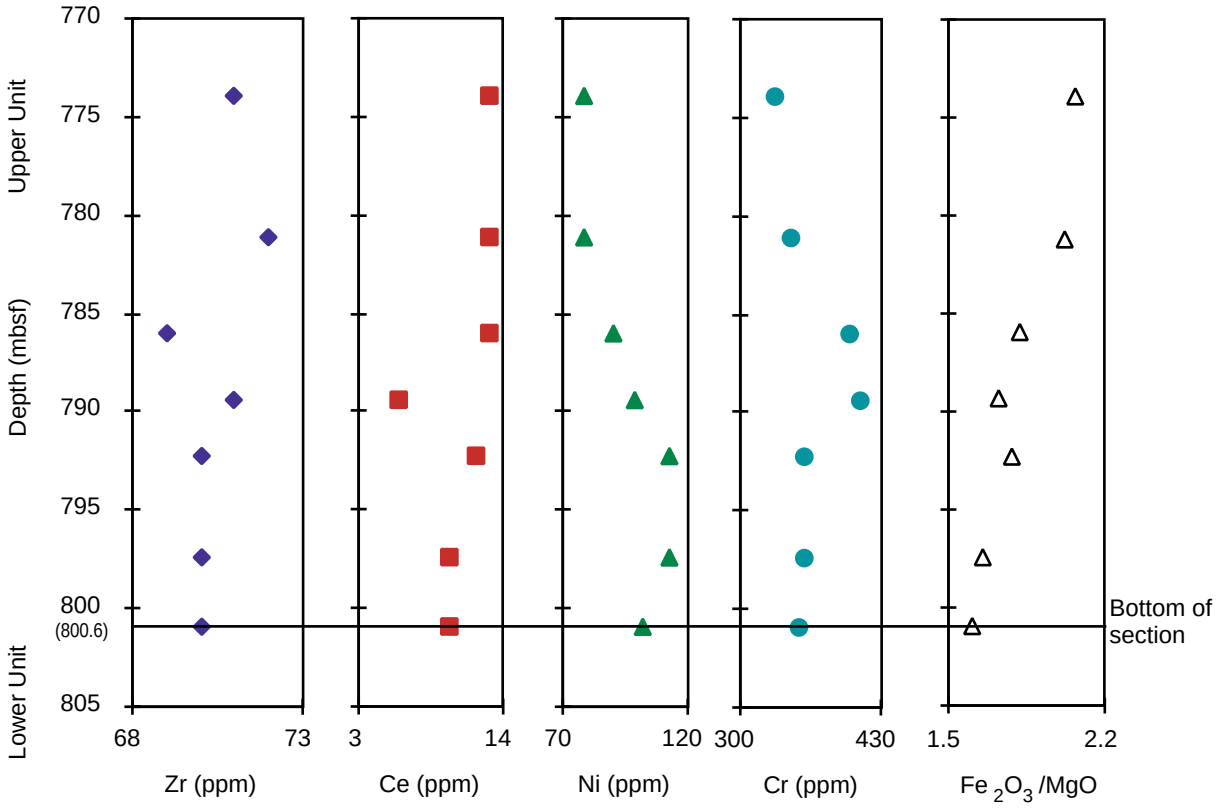

Figure F47. TiO_2-K_2O-P_2O_5 diagram from Pearce et al. (1977) showing Woodlark Island low-K tholeiites (solid circles) and high-K suite (open circles) along with average value for Hole 1109D dolerite. Oceanic basalts plot in the shaded field above the diagonal line in this diagram. Woodlark Island analyses from Ashley and Flood (1981).

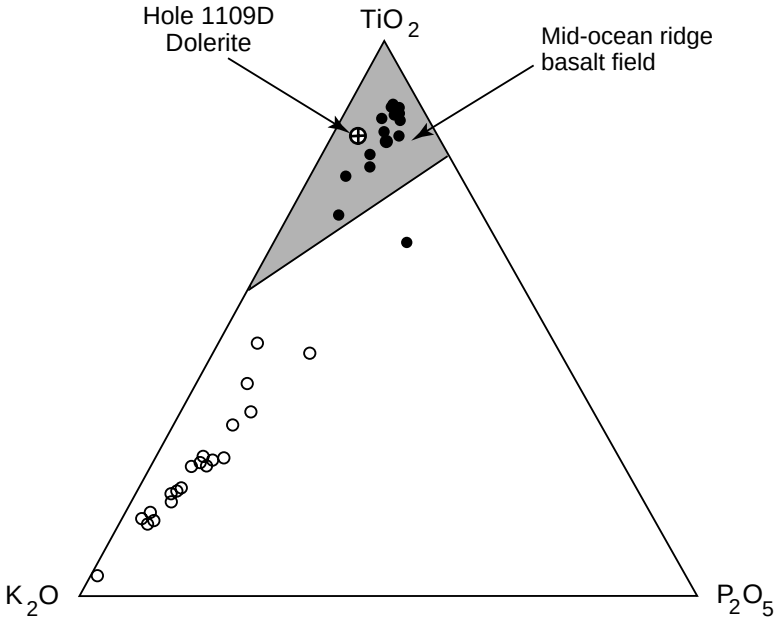

Figure F48. Ti-Zr-Y/3 diagram from Pearce and Cann (1973) showing low-K tholeiites (solid circles) and high-K suite (open circles) of Woodlark Island (Ashley and Flood, 1981) along with the average value for the Hole 1109D dolerite. Fields of high-K tholeiites, "ocean-floor" (= mid-ocean ridge) basalts, calc-alkali basalts, and "within-plate basalts" are shown.

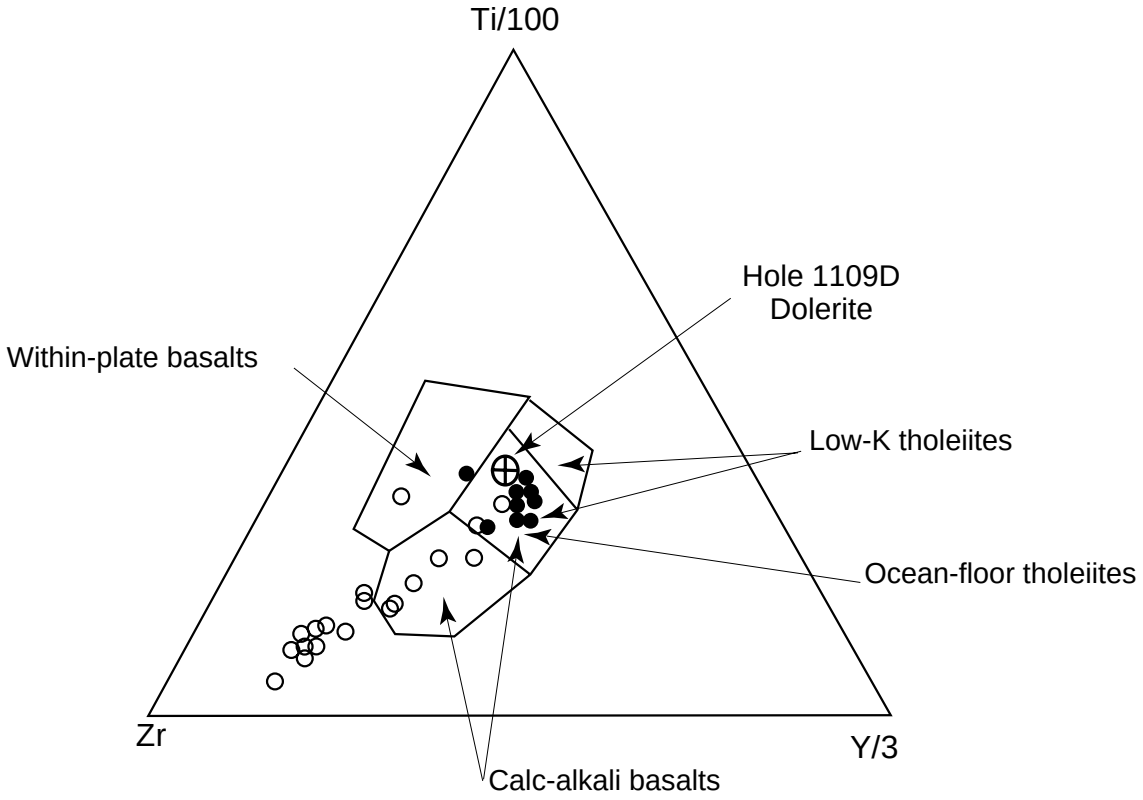

Figure F49. Ti/Y vs. Zr plot from Pearce (1980) showing low-K tholeiites from Woodlark Island (Ashley and Flood, 1981) and the average value for Hole 1109D dolerite. Both sets of data plot in the overlap between the mid-ocean ridge basalt (MORB) field and the island arc tholeiite (IAT) field. WPB = within-plate basalts.

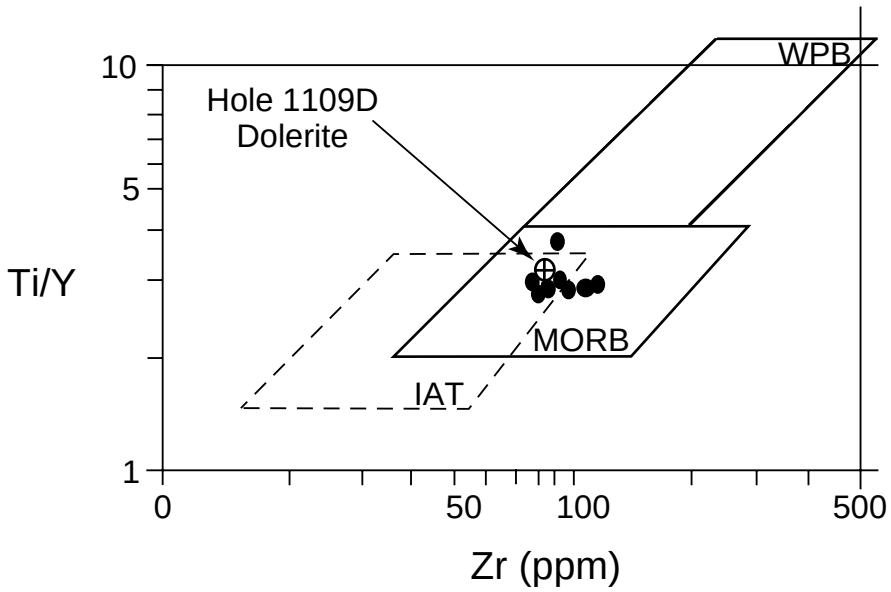

Figure F50. Summary of the main structural features measured in Hole 1109C. For description of lithostratigraphic Units I to V, see "Lithostratigraphy," p. 7. For key to symbols, see Figure F2, p. 52, in the "Explanatory Notes" chapter.

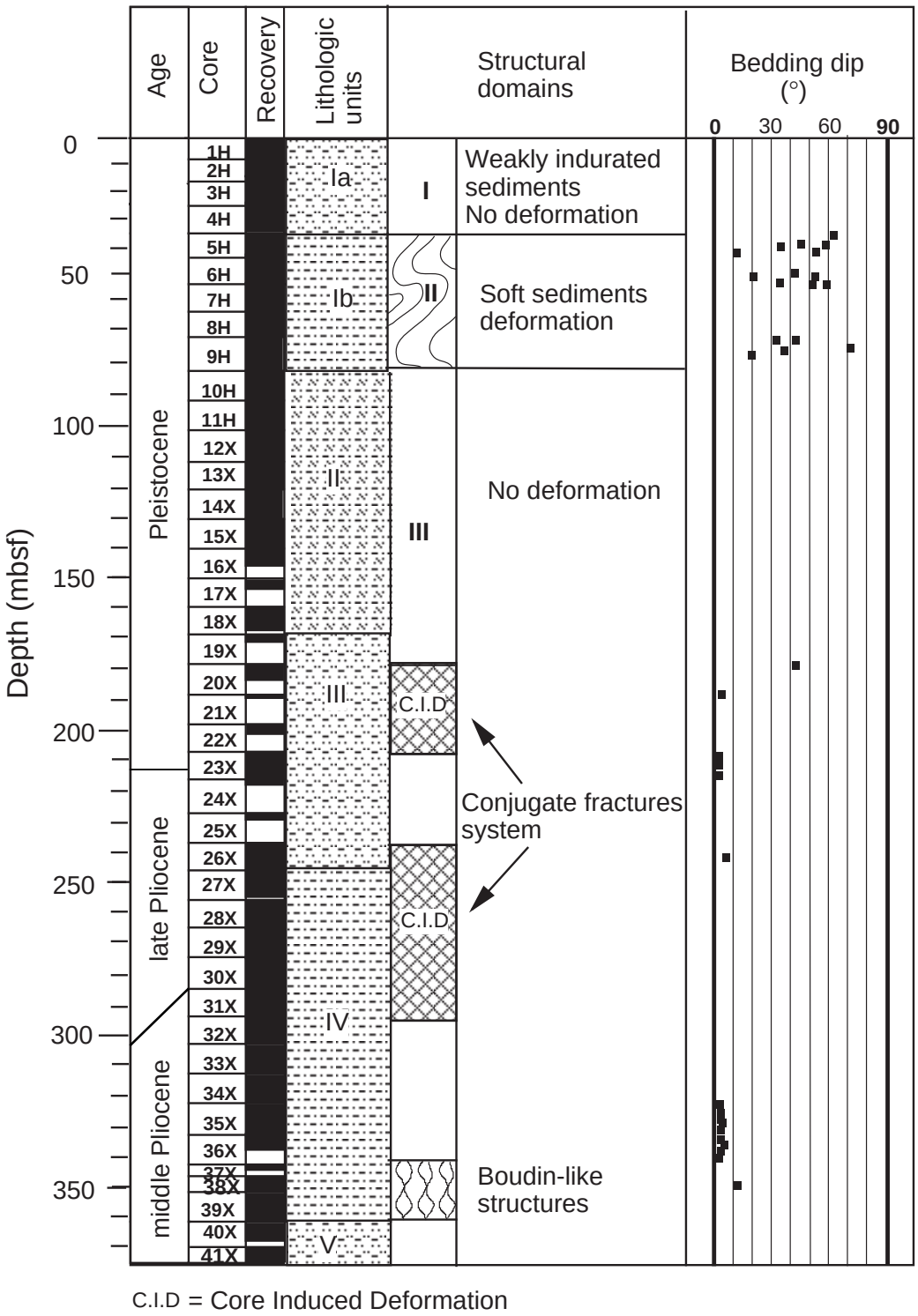

Figure F51. Bedding dips measured in Hole 1109C. N = number of measurements.

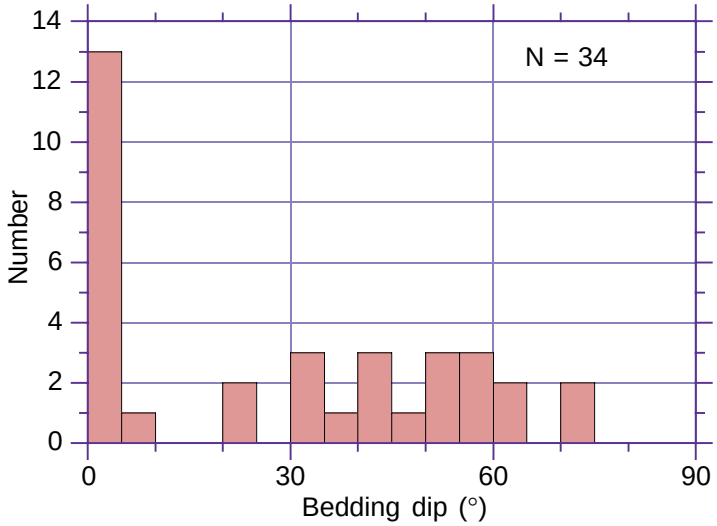

Figure F52. Summary of the main structural features measured in Hole 1109D. For description of lithostratigraphic Units V to XI, see **"Lithostratigraphy,"** p. 7. For key to symbols, see Figure **F2,** p. 52, in the "Explanatory Notes" chapter. FZ1, FZ2, FZ3 = fault zones (see **"Structural Geology,"** p. 38).

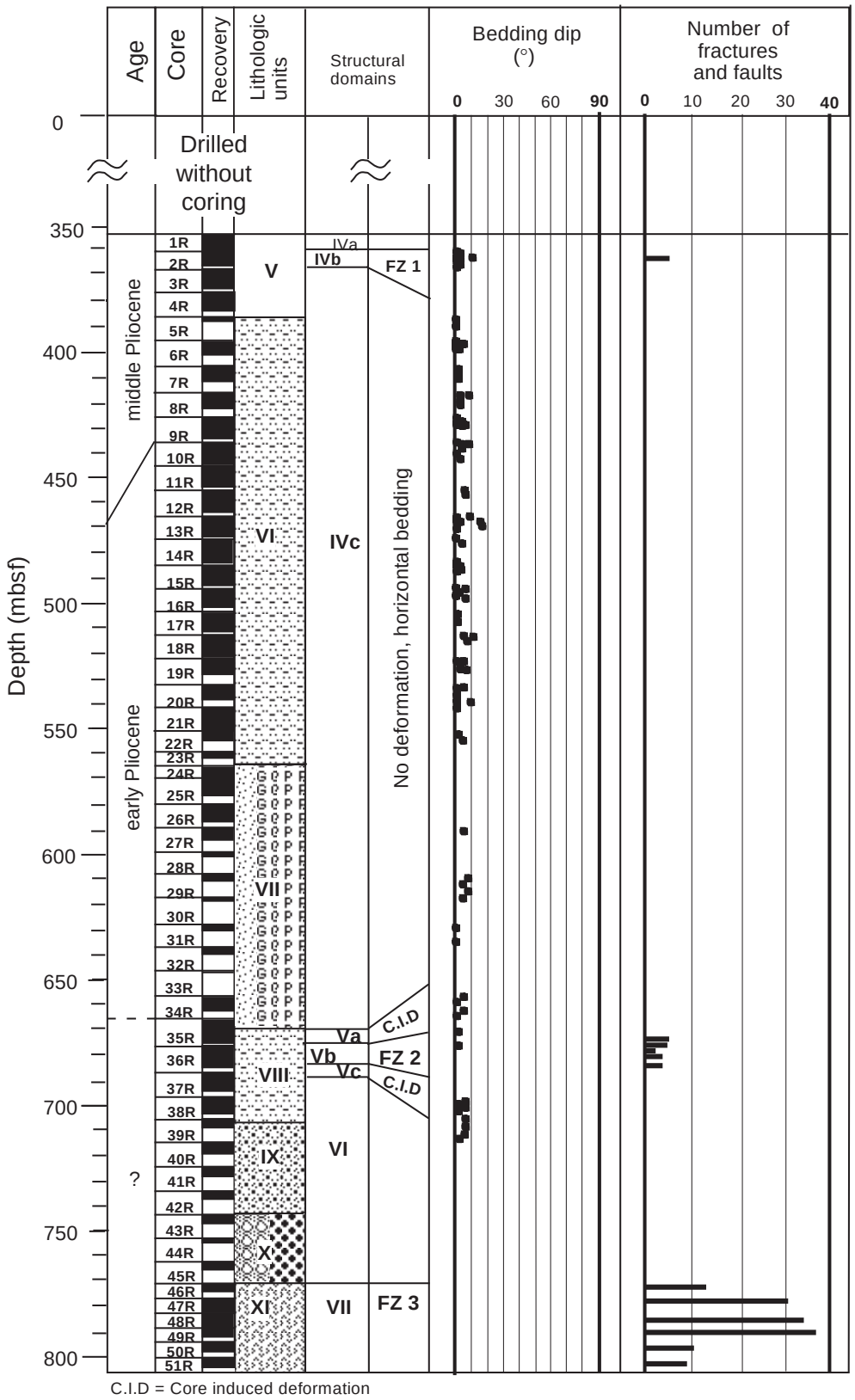

C.I.D = Core induced deformation

Figure F53. Bedding dips measured in Hole 1109D. N = number of measurements.

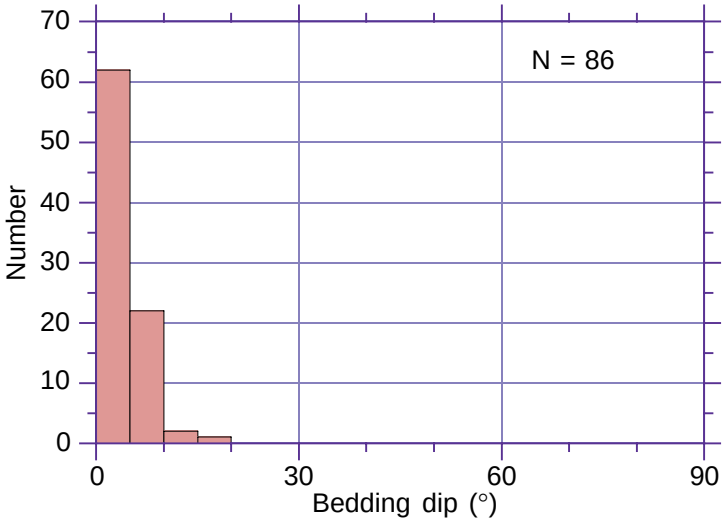

Figure F54. **A.** Example of conjugate planar normal faults moderately inclined at 55° and showing a true dip-slip displacement of about 3 cm (Sample 180-1109D-2R-2, 20–65 cm [360.6 mbsf]). **B.** Sketch of same core section. F = strike and dip of fault (core reference frame). **C.** Reconstruction of the orientation of the vertical maximum stress (σ_1) and horizontal minimum stress (σ_3) from the geometry of the fractures.

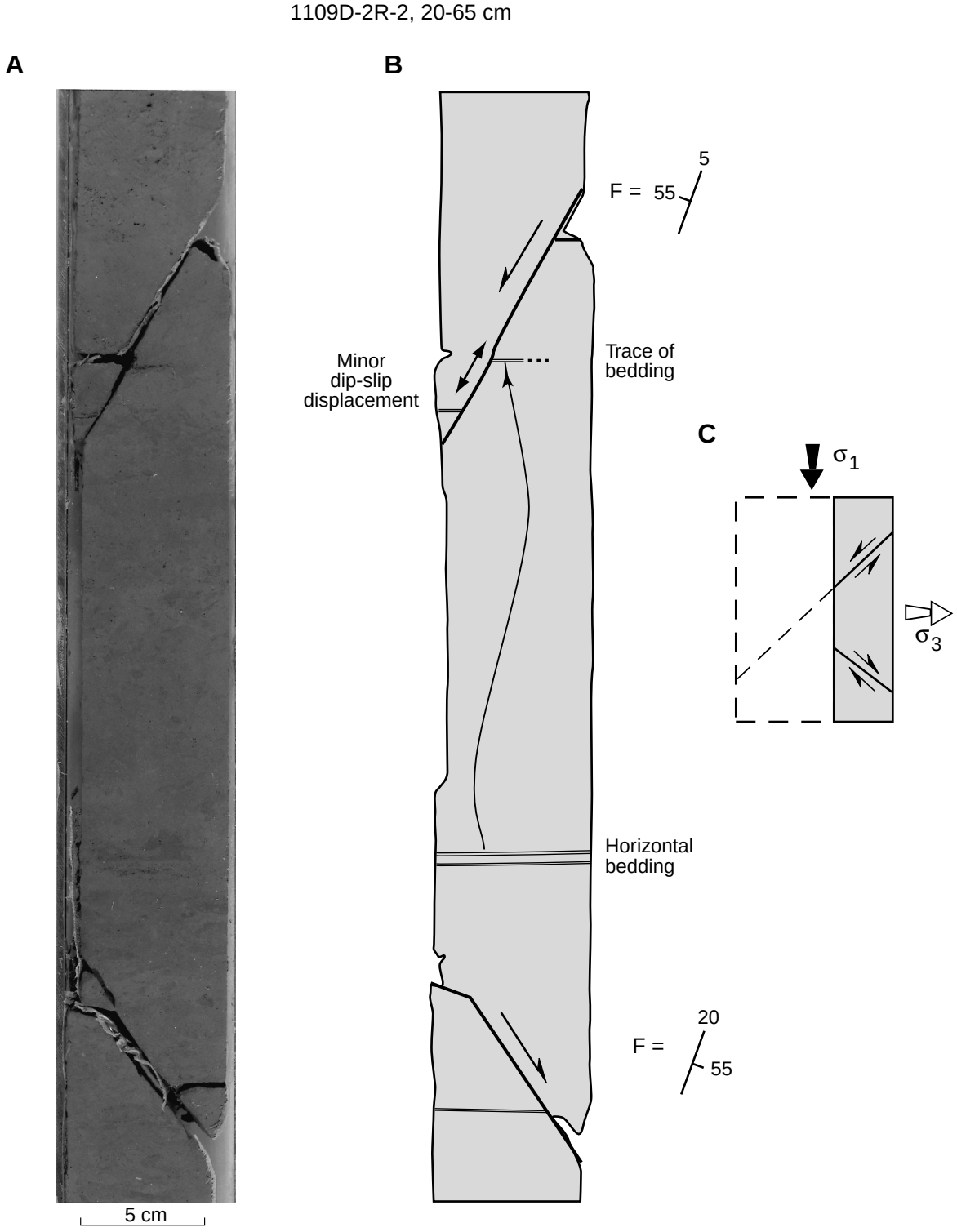

Figure F55. A. Array of minor extensional faults cutting through a millimeter-thick sandy level. **B.** The fault labeled Fd, filled with sand, represents an early syndepositional feature. This composite fault pattern occurs in the footwall of a reverse fault (F1 = strike and dip in core reference frame) identified by the steplike morphology of its surface. Bo = bedding. (Sample 180-1109D-2R-1, 110–133 cm [360.20 mbsf]).

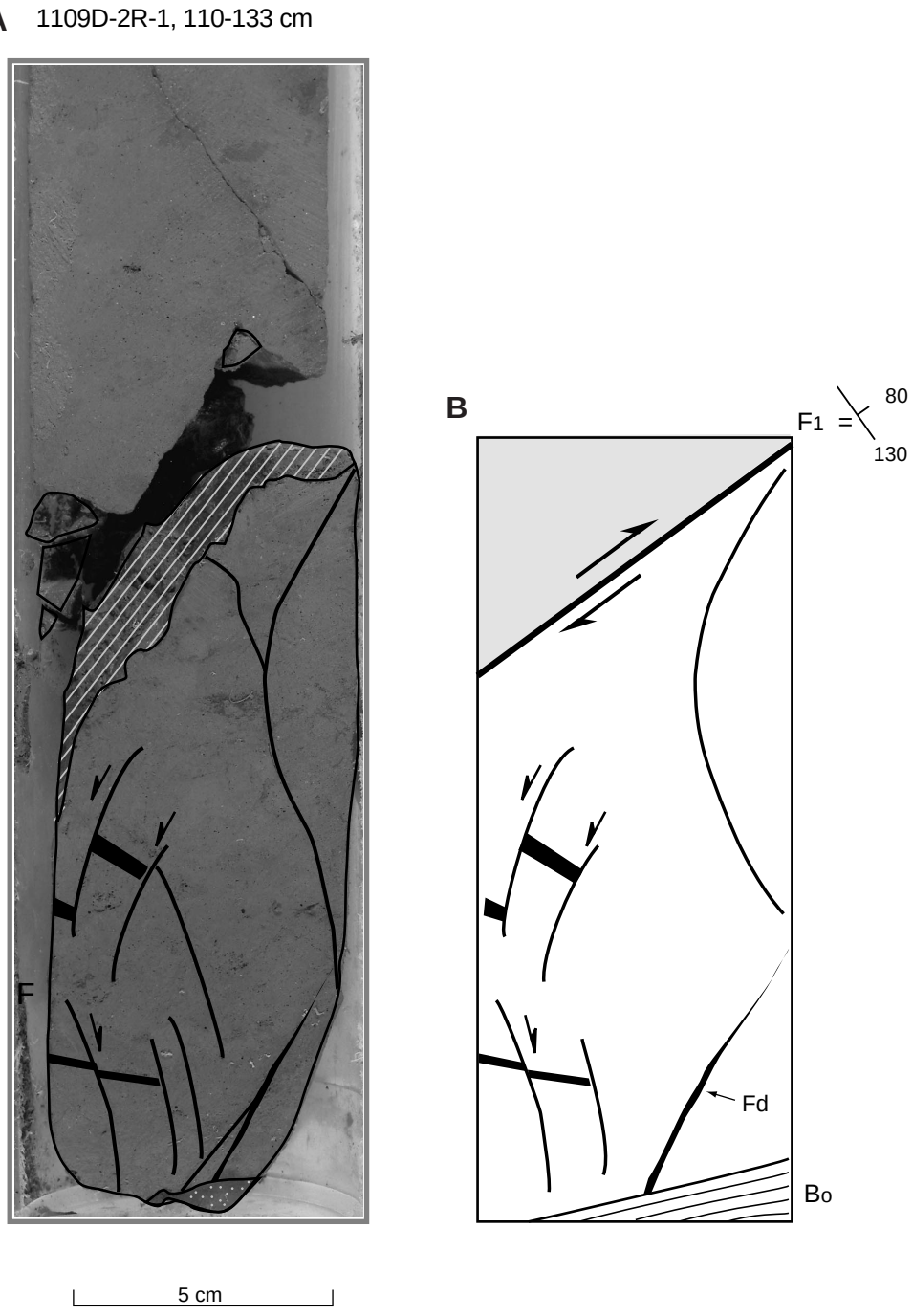

Figure F56. Histogram of the fault/fracture dips measured in the fault zone FZ2 (Hole 1109D). N = number of measurements.

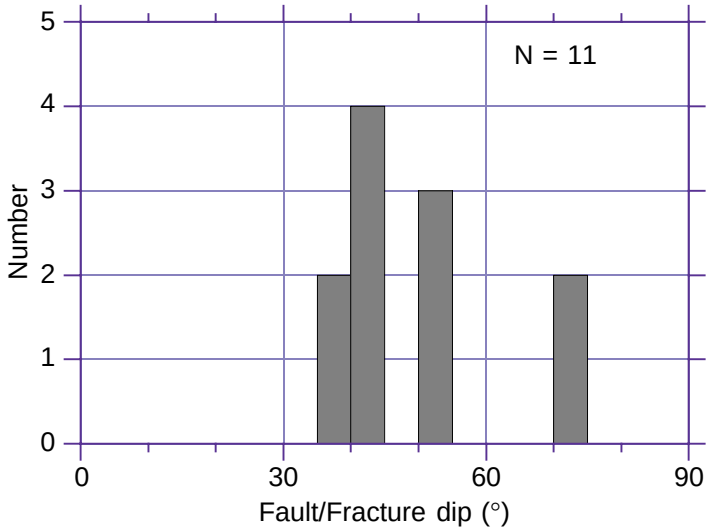

Figure F57. Geometry of the shallow-dipping vein network crosscutting the dolerite in Hole 1109D. **A.** Overlapping tip zone between millimeter-thick greigite-filled veins in Section 180-1109D-47R-1 (777.6 mbsf). **B.** Cristobalite-filled extensional shear zone in Section 180-1109D-50R-3 (794.9 mbsf). The folded shape of the individual veins results from an advanced stage of horizontal shearing.

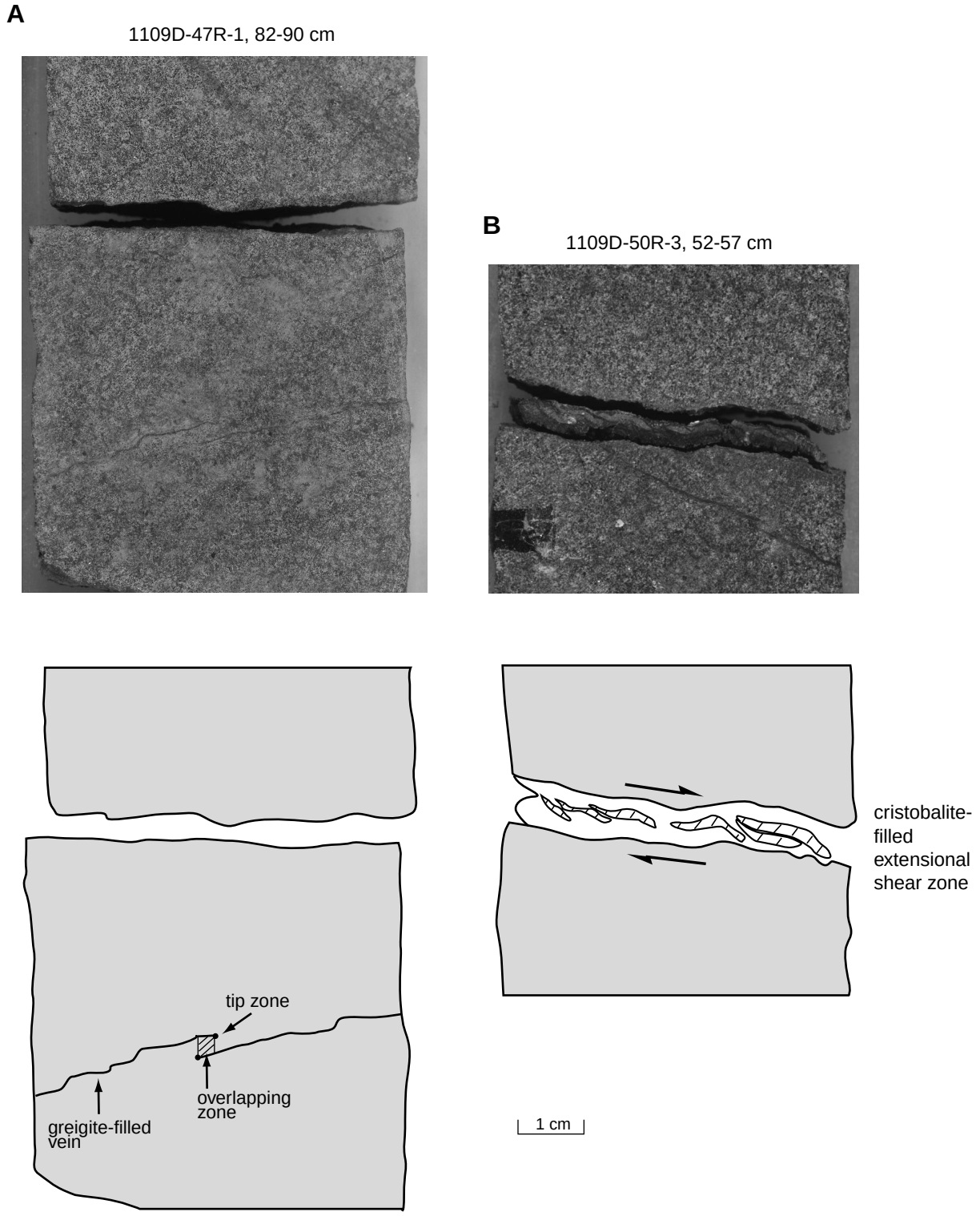

Figure F58. A. Histogram of the fault dips measured in the dolerite (FZ3, Hole 1109D). **B.** Fault dip vs. plunge of the corresponding slickensides in the faulted dolerite (FZ3). The linear correlation is typical of pure dip-slip fault kinematics. N = number of measurements.

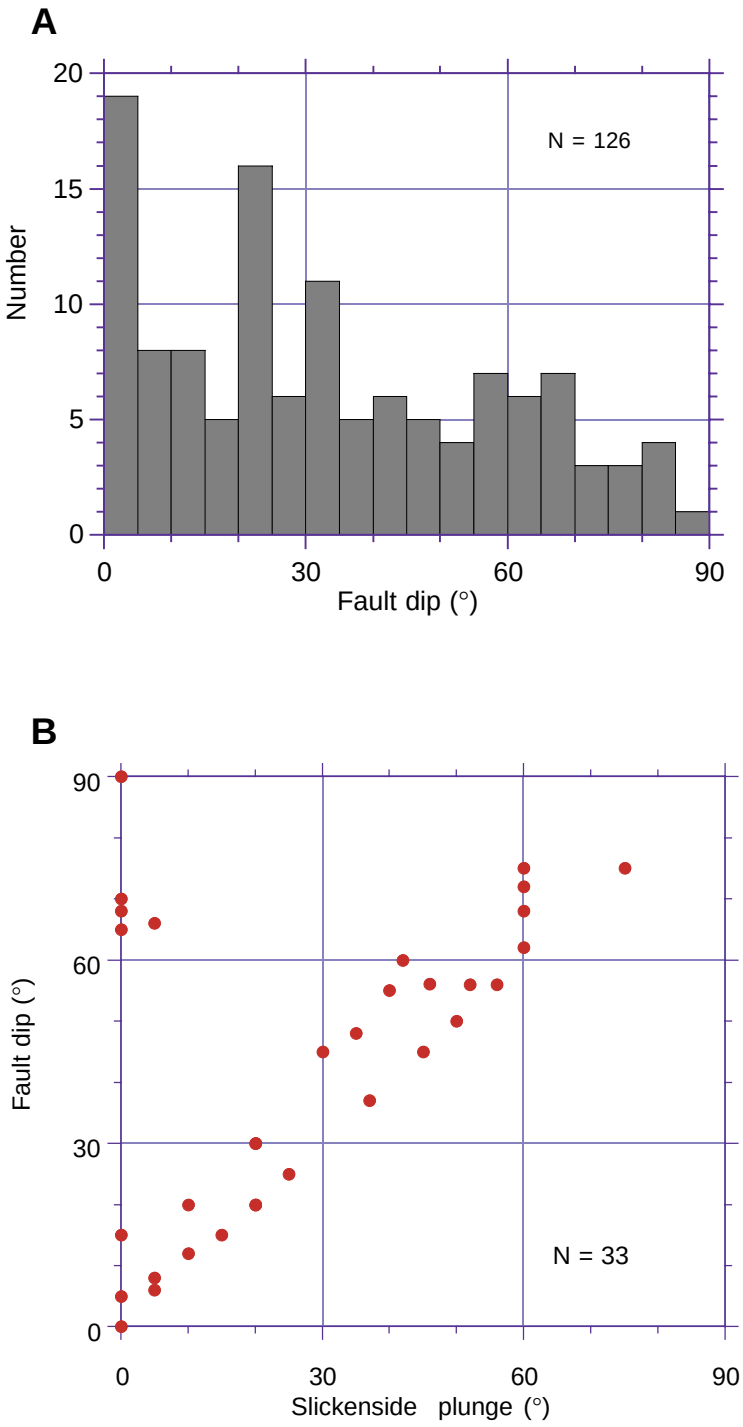

Figure F59. Example of fault/fracture/vein relationships observed in Section 180-1109D-47R-2 (778.7 mbsf). **A.** Core structures (archive half). **B.** Schematic interpretation; F1 and F3, pure dip-slip normal faults; F2, sinistral-normal fault (1, 2, 3, refer to their progressive younger age). **C.** Plane view in the core reference frame. **D.** Interpretation in terms of direction of extension.

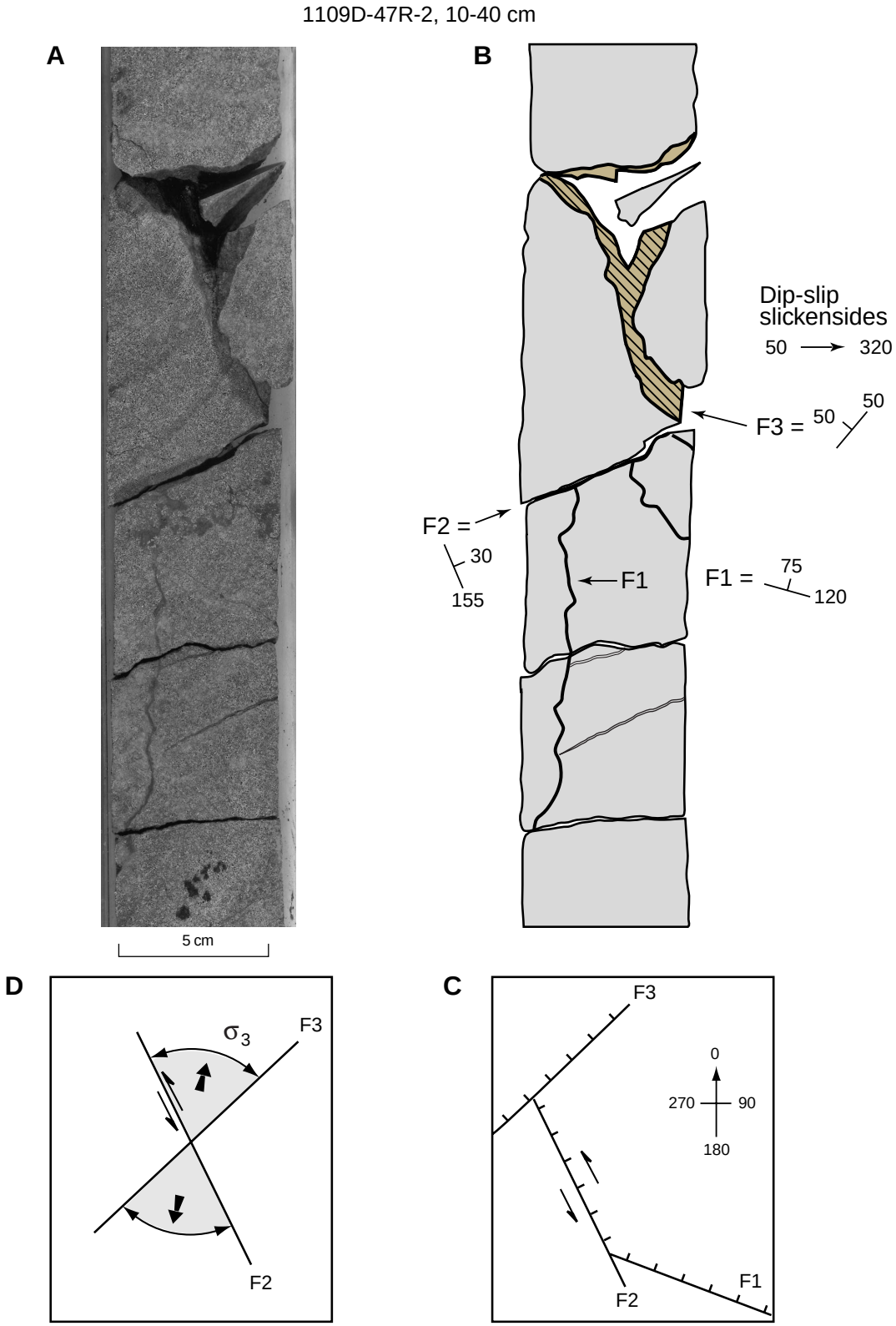

Figure F60. Two-stage evolutionary tectonic model for the postmagmatic brittle structures observed in the dolerite intrusion (Section 180-1109D-47R-2). **1.** Diagram illustrating the crosscutting relationships between successive generations of filled veins emplaced under horizontal tensile conditions (split core surface); V_2, V_3 = young master vertical veins (cristobalite, smectite, and chlorite) at right angles to σ_3; V_1 = early shallow greigite-filled veins. Note evidence for horizontal shearing (S) along shallow V_2-type veins that also act as transfer structures (T) for earlier V_1 veinlets. Overlapping zone (O) between two greigite-filled veinlets. **2.** Geometry of later extensional faulting as deduced from Figure **F59** A and B, p. 145. Note that the two successive events (emplacement of veins and faulting) are both consistent with almost horizontal extension. Symbols: ⊕ = downward motion; ⊙ = upward motion.

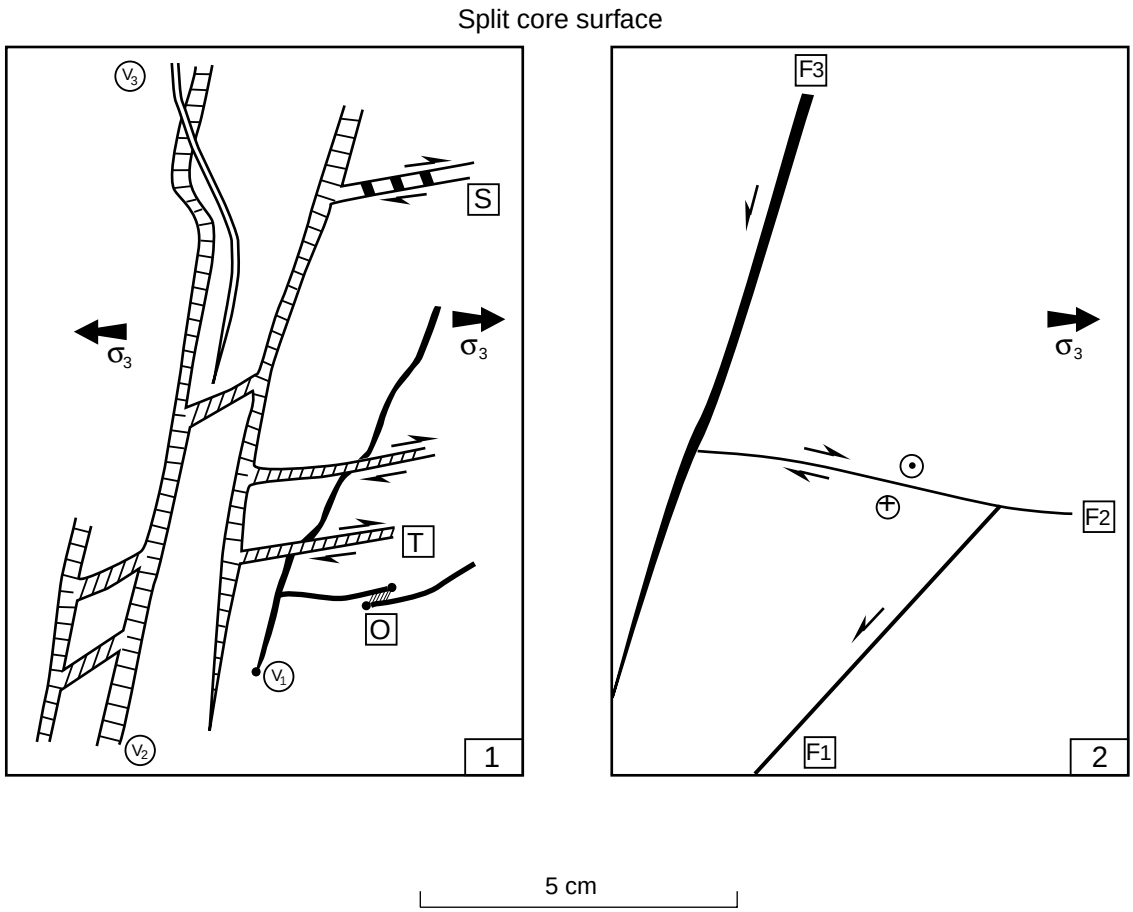

Figure F61. Schematic structural log of Site 1109 (Holes 1109C and 1109D).

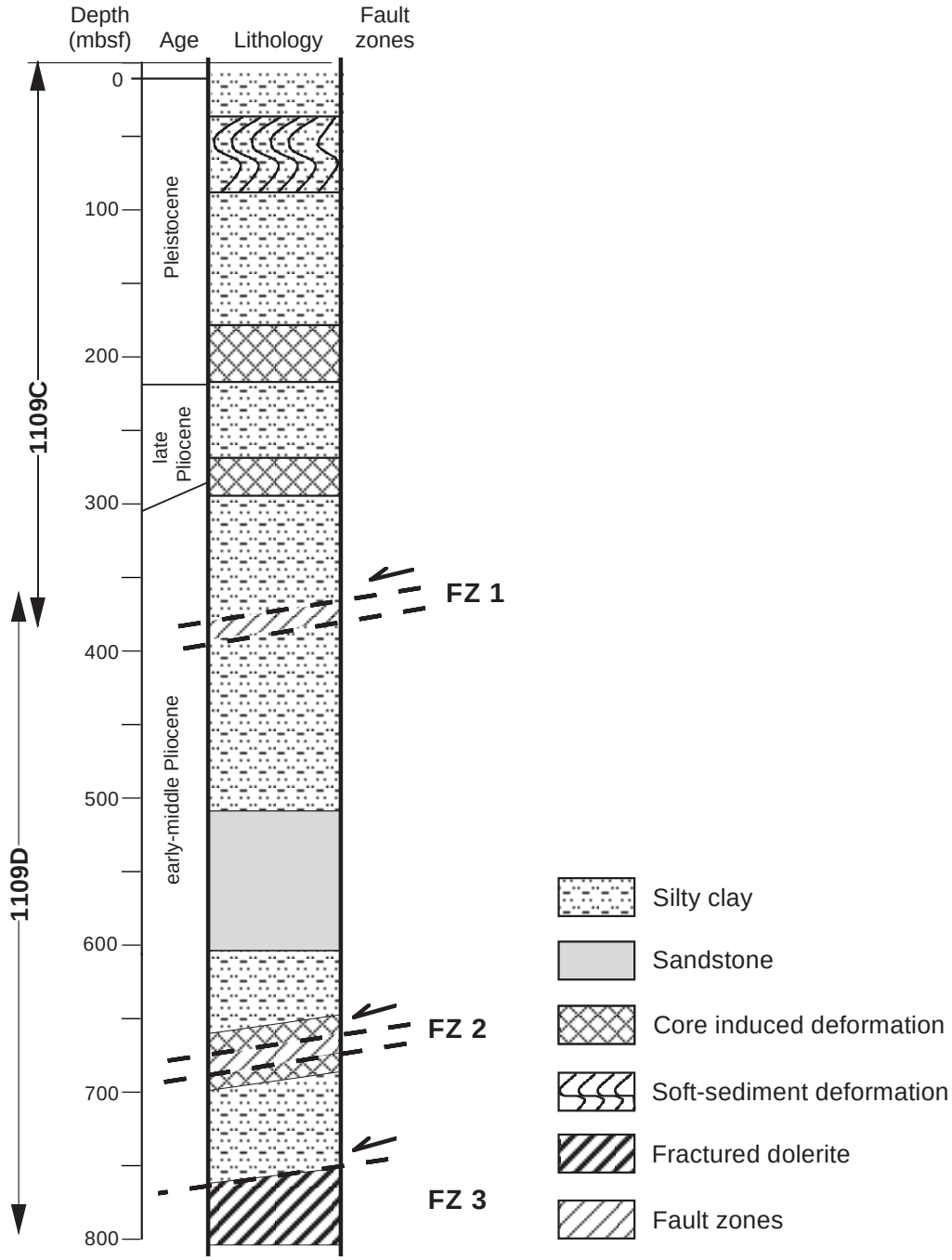

Figure F62. Biostratigraphic units and ages for Site 1109. Dashed lines indicate the true zonal boundary may lie above or below the indicated level. **A.** Holes 1109A, 1109B, and 1109C. (Continued on next page.)

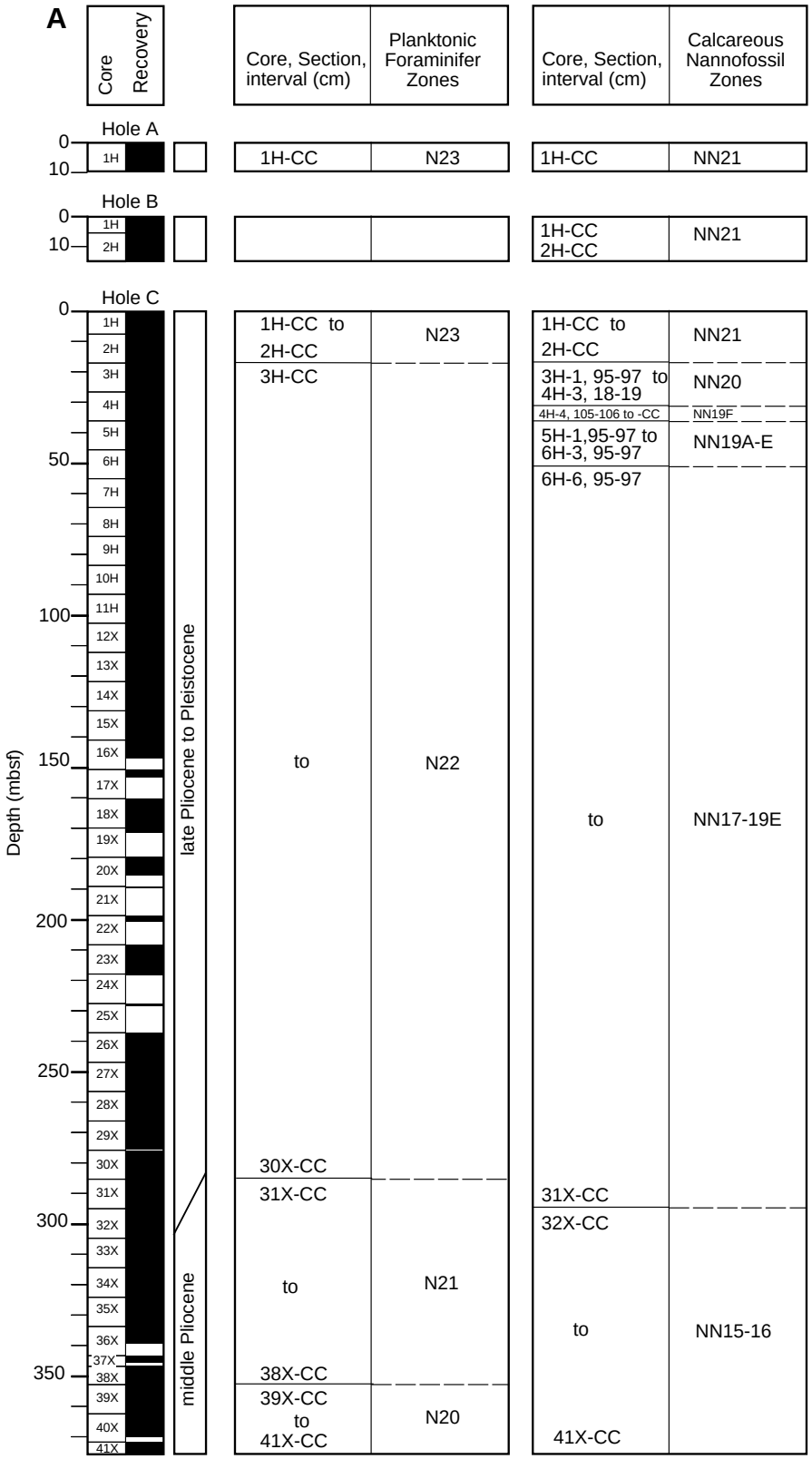

Figure F62 (continued). B. Hole 1109D.

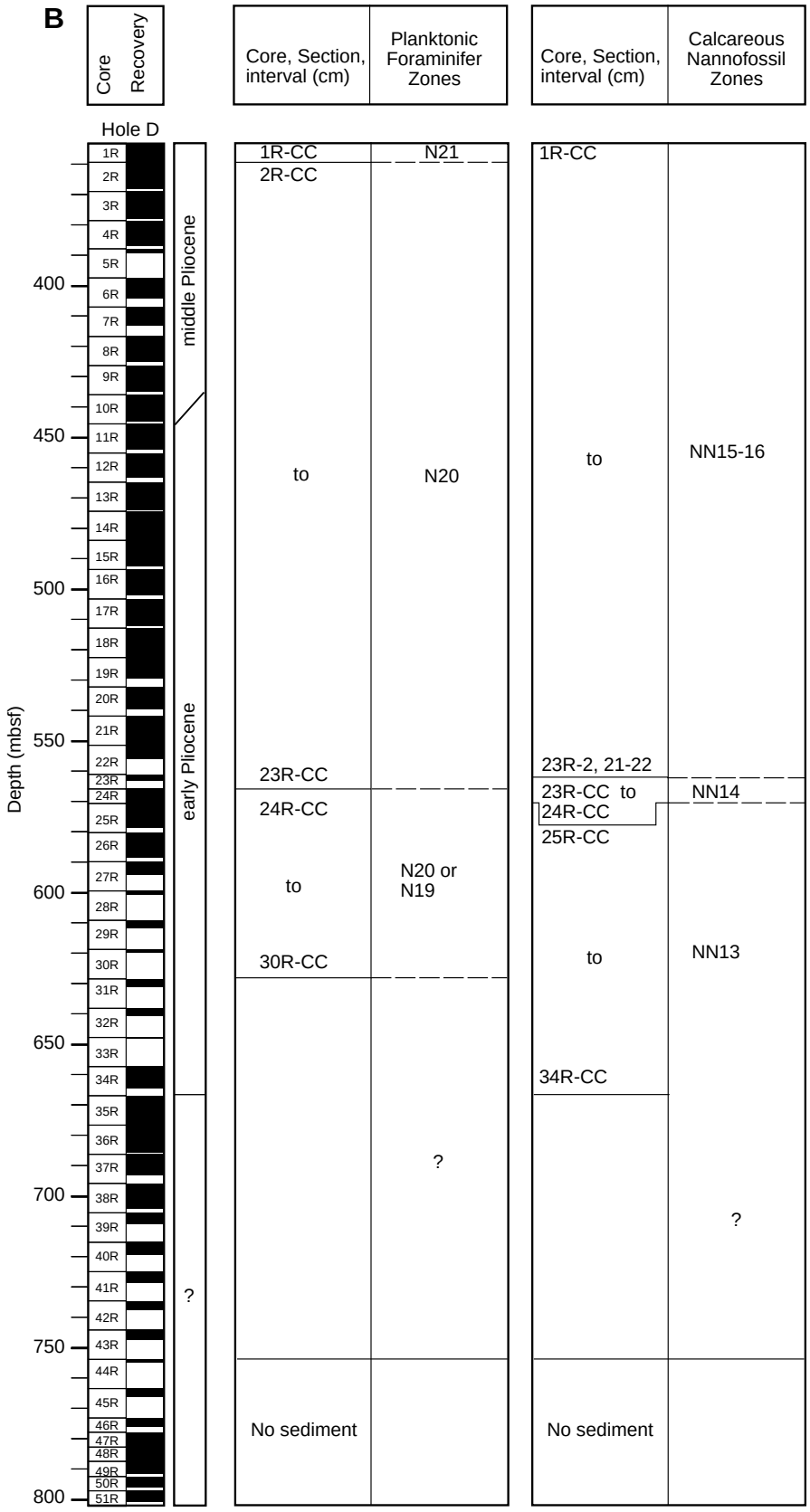

Figure F63. Age-depth relationship at Site 1109, based on nannofossil (square) and planktonic foraminiferal (circle) datum events and magnetic chron and subchron boundaries (triangle). Sediment accumulation rates are estimated in m/m.y.

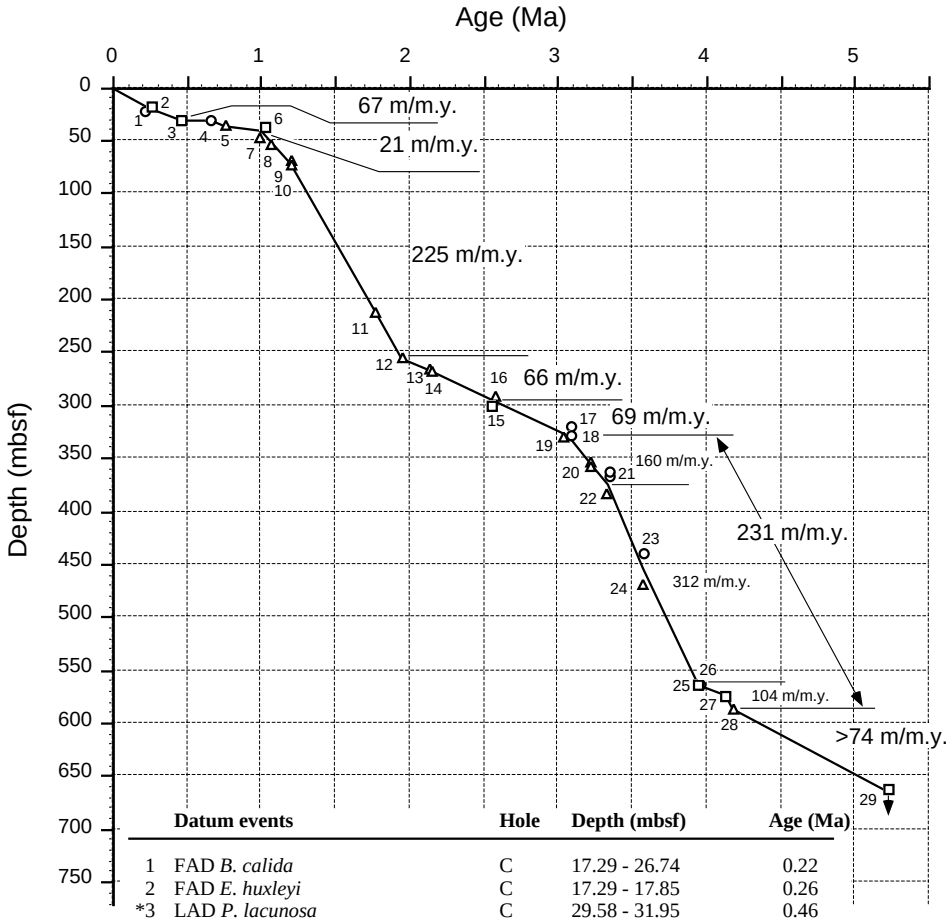

	Datum events	Hole	Depth (mbsf)	Age (Ma)
1	FAD *B. calida*	C	17.29 - 26.74	0.22
2	FAD *E. huxleyi*	C	17.29 - 17.85	0.26
*3	LAD *P. lacunosa*	C	29.58 - 31.95	0.46
4	LAD *G. tosaensis*	C	26.74 - 36.42	0.65
5	Brunhes/Matuyama	C	36	0.78
*6	FAD *G. omega*	C	36.42 - 36.85	1.02
*7	Top Jaramillo	C	47.5 - 48.0	0.99
8	Bottom Jaramillo	C	53.5 - 54.0	1.07
9	Top Cobb	C	70.5	1.201
10	Bottom Cobb	C	74	1.211
11	Top Olduvai	C	213	1.77
*12	Bottom Olduvai	C	255	1.95
13	Top Reunion	C	266	2.14
14	Bottom Reunion	C	269	2.15
*15	LAD *D. surculus*	C	294.81 - 304.36	2.55
*16	Matuyama/Gauss	C	291	2.58
17	LAD *G. multicamerata*	C	314.23 - 324.02	3.09
*18	LAD *D. altispira*	C	324.02 - 333.83	3.09
*19	Top Kaena	C	331	3.04
20	Top Mammoth	C	355	3.22
		D	358	3.22
*21	FAD *G. tosaensis*	C	362.43 - 369.79	3.35
		D	359.01 - 368.00	3.35
*22	Bottom Mammoth	D	384.5	3.33
23	LAD *G. margaritae*	D	434.70 - 444.49	3.58
24	Gauss/Gilbert	D	470	3.58
*25	LCO *R. pseudoumbilicus*	D	562.51 - 562.71	3.94
*26	S/D *Pulleniatina*	D	~562.71	3.95
27	FCO *D. asymmetricus*	D	571.66 - 578.42	4.13
*28	Top C3n	D	587	4.18
*29	FAD *C. rugosus*	D	>664.29	5.23

* datum used in sedimentation rate calculation

Figure F64. Comparison of susceptibility data (uncorrected for volume) from long core measurements using the MST and AMST. **A.** Holes 1109A and 1109B. (Continued on next page.)

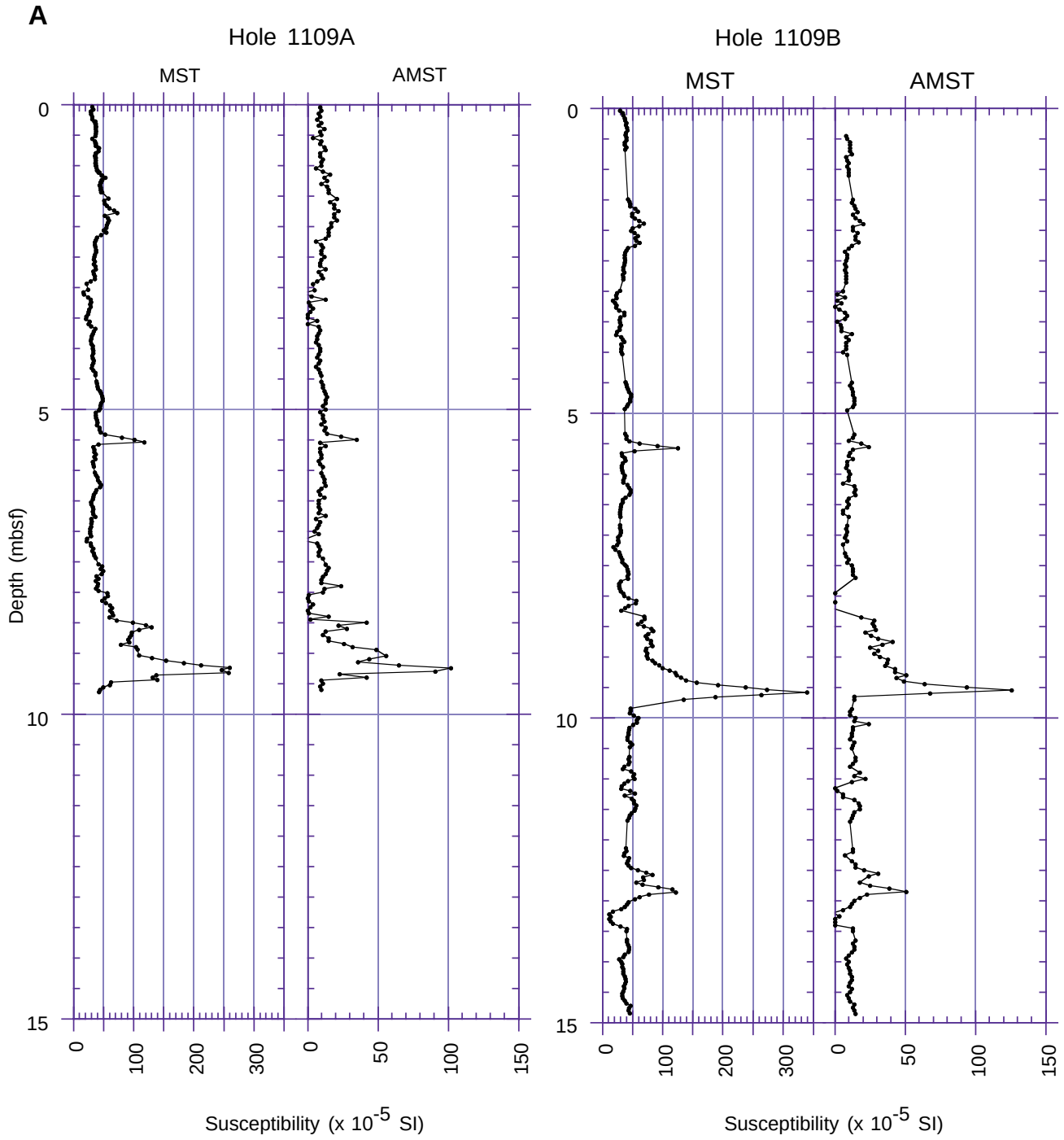

Figure F64 (continued). B. Holes 1109C and 1109D.

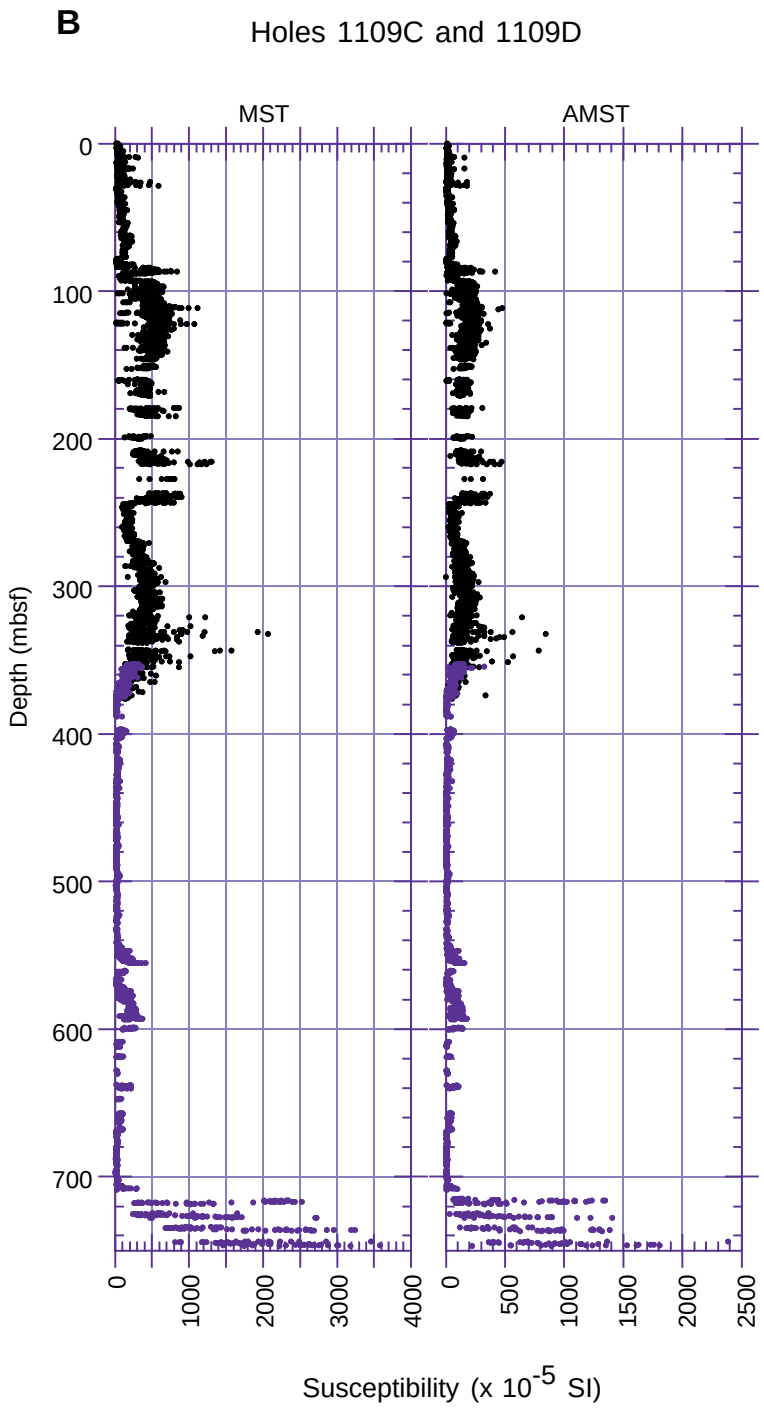

Figure F65. Anisotropy of magnetic susceptibility (AMS) data for discrete samples from Holes 1109C and 1109D. Degree of anisotropy (P_j) and the shape parameter (T) calculated according to Jelinek (1981).

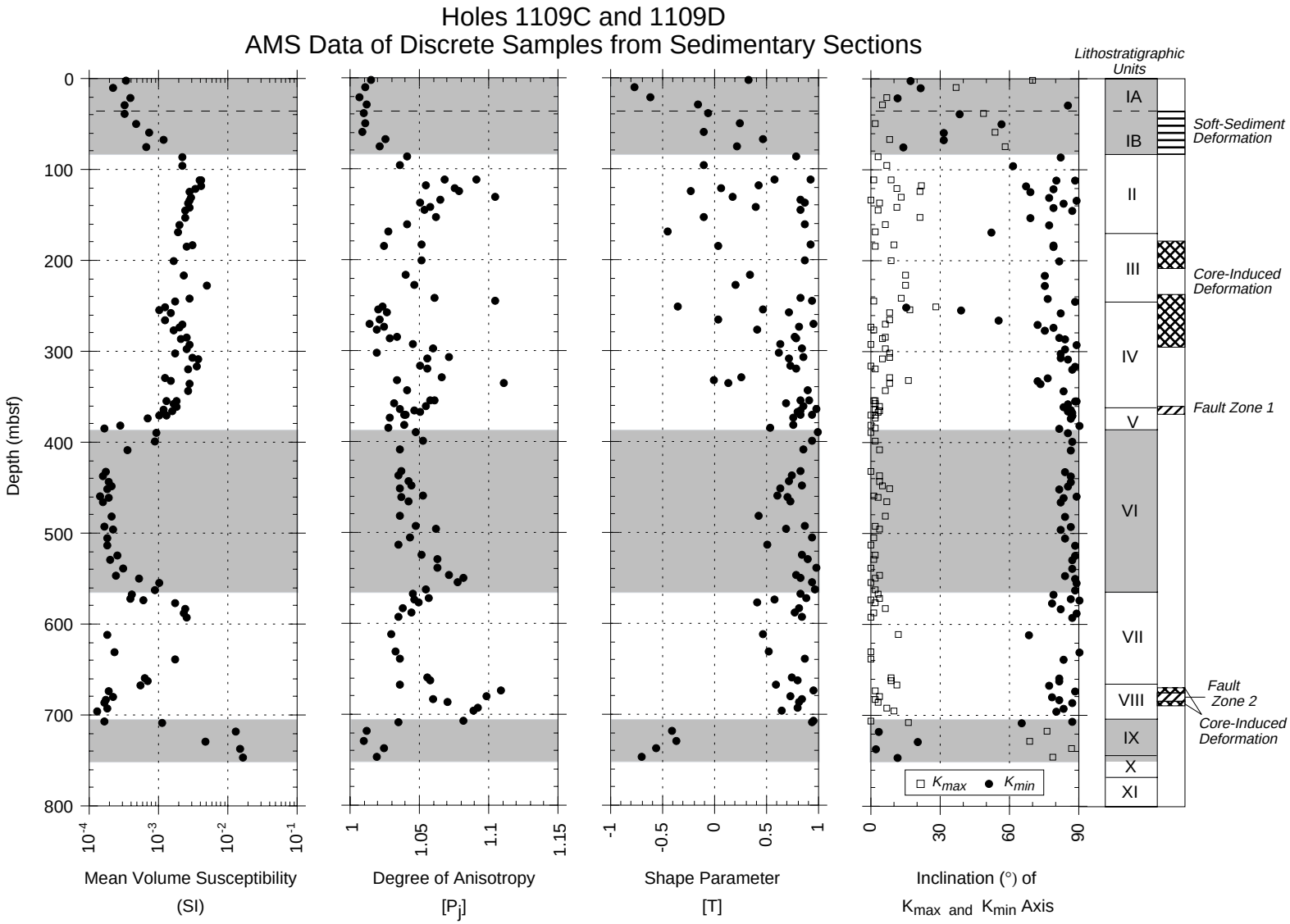

Figure F66. A. Downhole plots of intensity, inclination, declination, magnetostratigraphic interpretation, and paleontologic data. Holes 1109A and 1109B. Data from long cores after AF demagnetization. (Continued on next page.)

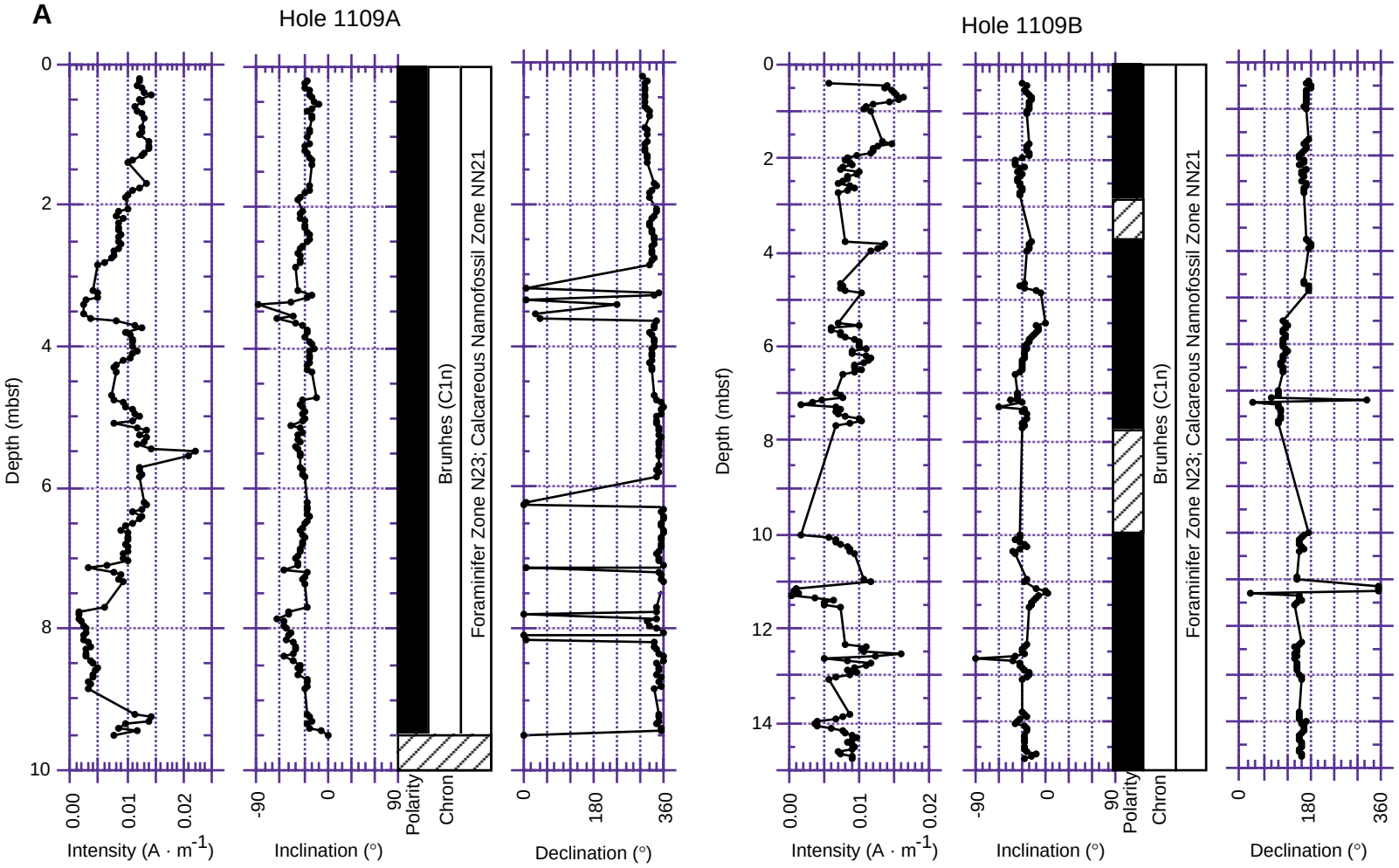

Figure F66 (continued). B. Downhole plots of intensity, inclination, and declination, Holes 1109C and 1109D. Data from long cores and discrete samples after AF demagnetization. Discrete sample data shown as open squares.

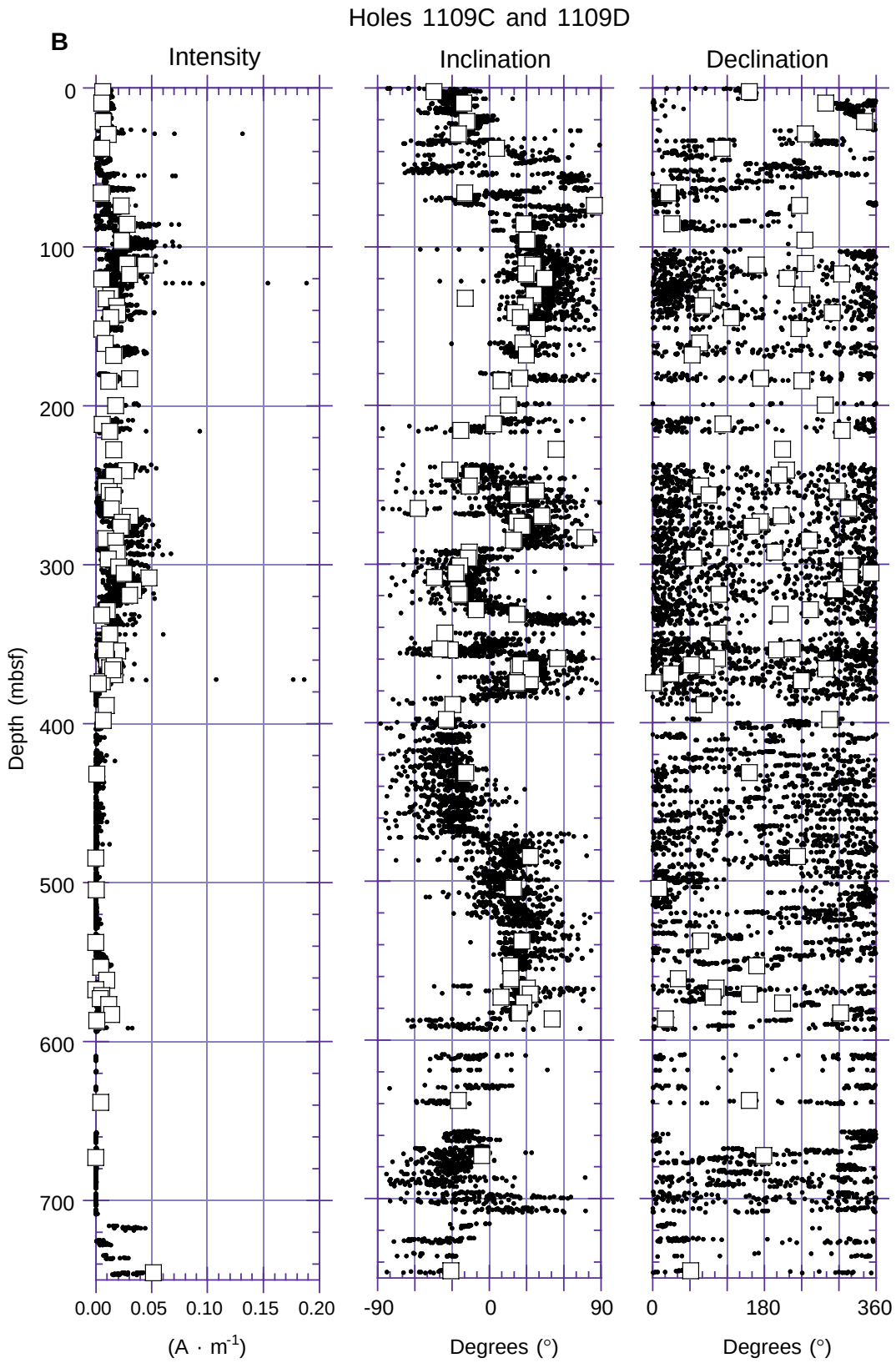

Figure F66 (continued). C. Inclination data from long cores (black points, connected) and from discrete samples (open circles) after AF demagnetization, Holes 1109C and 1109D. Also shown are magnetostratigraphy and biostratigraphy with structural information. Magnetostratigraphy: N or black = normal; R or white = reversed; M or diagonal lines = mixed or no data (see Table T9, p. 256). Chrons: C1n = Brunhes (0.0–0.78 Ma); C1r = upper part of the Matuyama (0.78–1.77 Ma); C1r.1n = Jaramillo (0.99–1.07 Ma); C1r.2r.1n = Cobb Mountain (1.20–1.21 Ma); C2n = Olduvai (1.77–1.95 Ma); C2r.1n = Reunion (2.14–2.15 Ma); C2An.1n = upper part of the Gauss (2.58–3.04 Ma); C2An.2n–1r = Kaena and middle Gauss, undivided (3.04–3.22 Ma); C2An.2r = Mammoth (3.22–3.33 Ma); C2An.3n = lower part of the Gauss (3.33–3.58 Ma); C2Ar = upper part of the Gilbert (3.58–4.18 Ma); C3n = middle part of the Gilbert, undivided (4.18–5.23 Ma). Ages according to Berggren et al. (1995). **(Figure shown on next page.)**

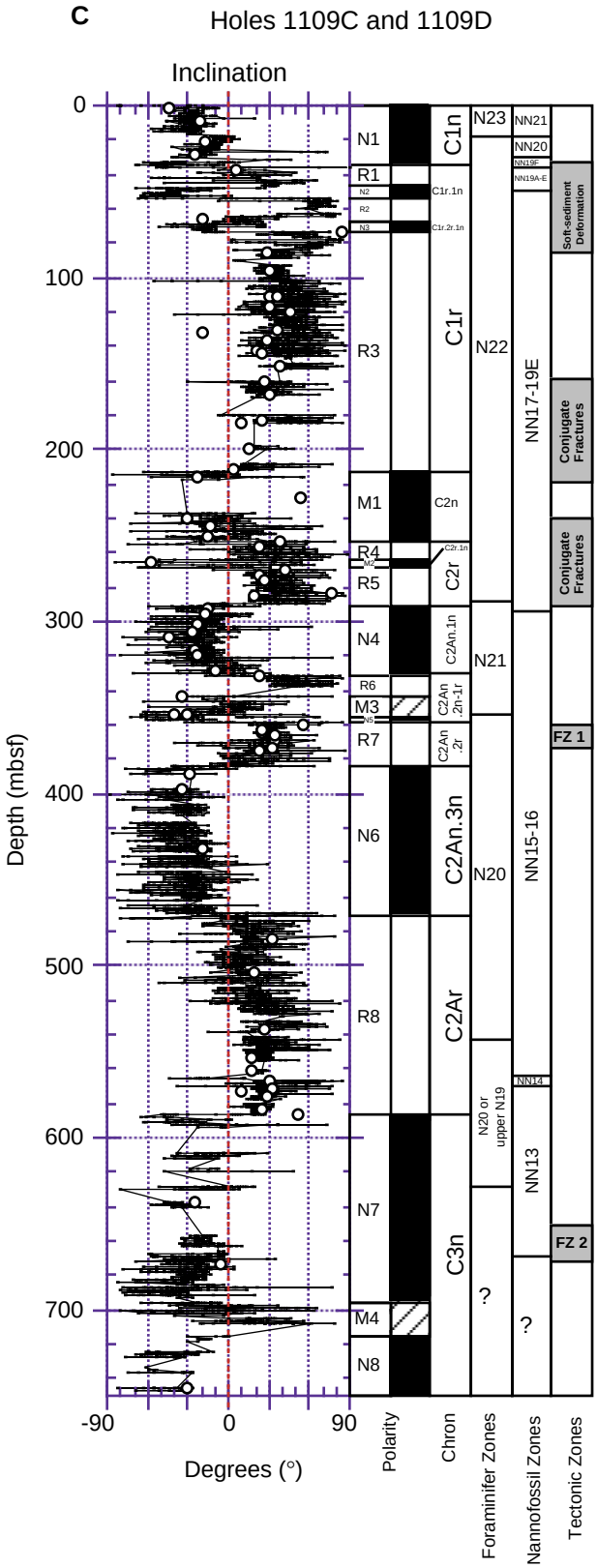
C
Holes 1109C and 1109D
Inclination
Depth (mbsf)
0
100
200
300
400
500
600
700
-90
0
90
Degrees (°)
Polarity
Chron
Foraminifer Zones
Nannofossil Zones
Tectonic Zones
N1
R1
N2
R2
N3
R3
M1
R4
N5
R5
N4
R6
M3
N6
R7
N6
R8
N7
M4
N8
C1n
C1r.1n
C1r.2r.1n
C1r
C2n
C2r.1n
C2r
C2An.1n
C2An .2n-1r
C2An .2r
C2An.3n
C2Ar
C3n
N23
N22
N21
N20
N20 or upper N19
?
NN21
NN20
NN19F
NN19A-E
NN17-19E
NN15-16
NN14
NN13
?
Soft-sediment Deformation
Conjugate Fractures
Conjugate Fractures
FZ 1
FZ 2

Figure F66 (continued). D. Transition data from Hole 1109C. Shaded areas = transition.

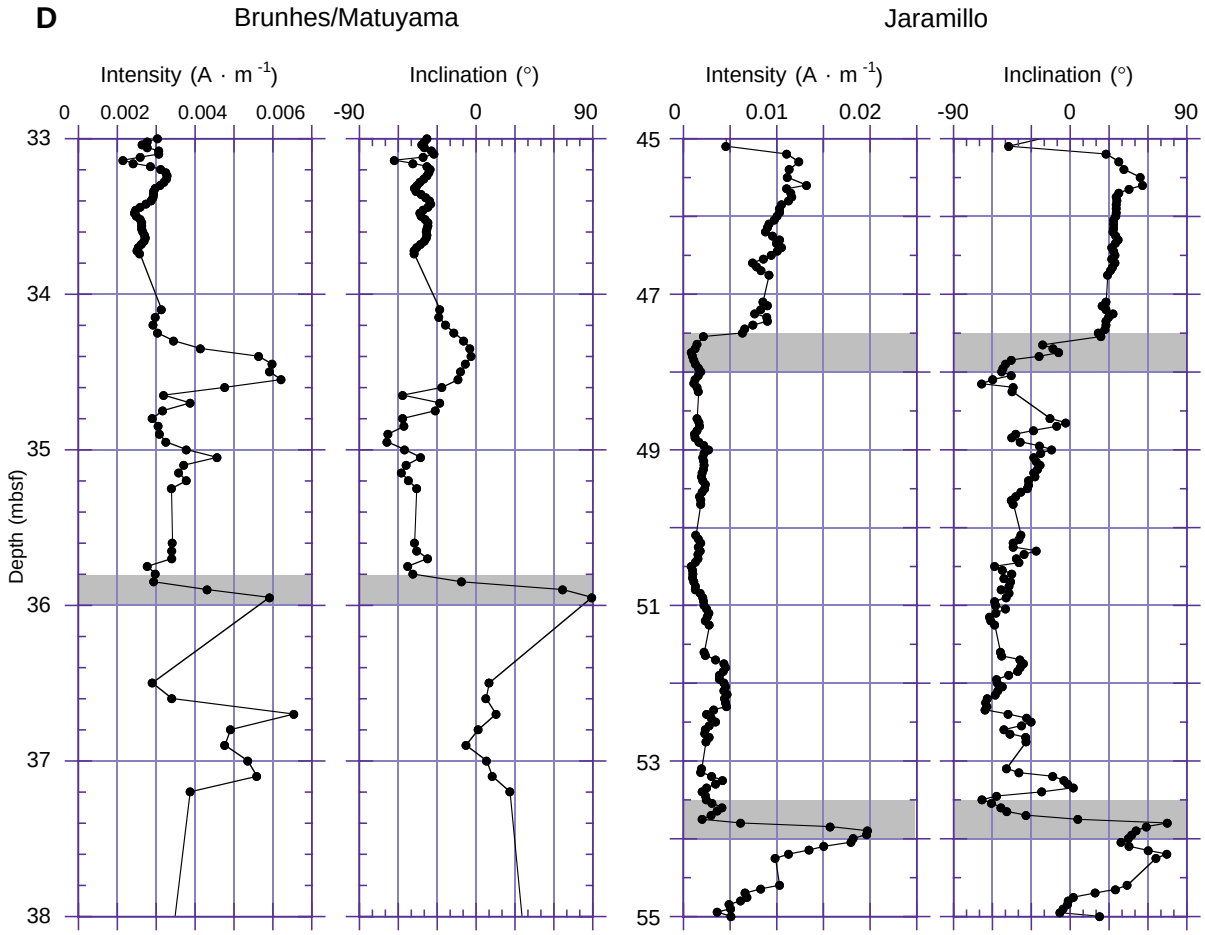

Figure F67. Vector demagnetization plots, stereoplots, and decay of intensity of magnetization (normalized) of discrete samples. **A.** Reversed polarity characteristic remanent magnetization (ChRM). Steep downward overprint. **B.** Normal polarity ChRM. Steep downward overprint. **C.** Normal polarity ChRM. Shallow downward overprint. **D.** Reversed polarity ChRM. Steep downward overprint. **E.** Erratic behavior during AF demagnetization. Vector plots: horizontal component = filled circles; vertical component = open circles. Stereonet plots: lower hemisphere = filled circles; upper hemisphere = open circles; NRM = natural remanent magnetization; Div. = Division; Jo = NRM intensity.

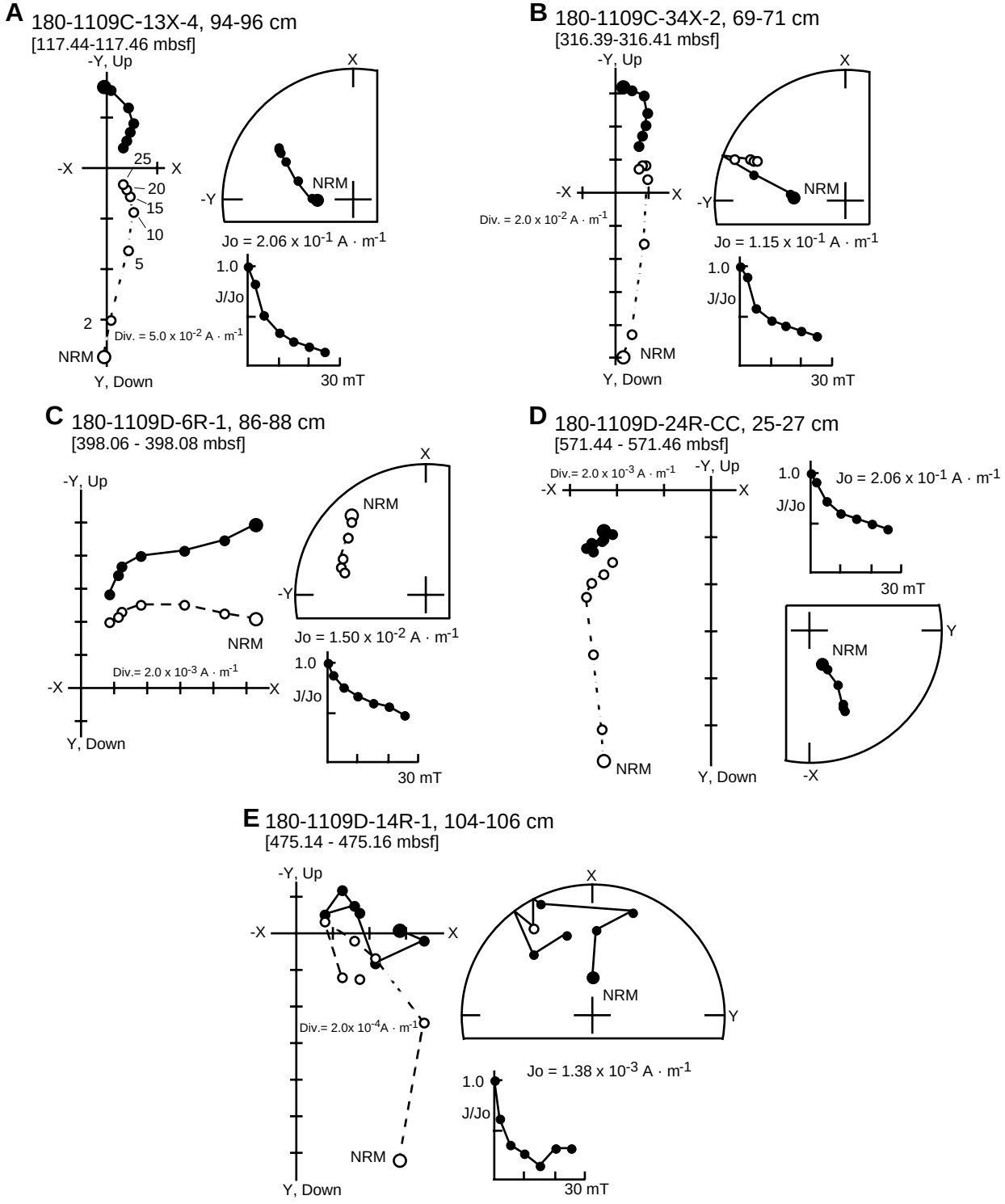

Figure F68. Demagnetization behavior of discrete samples from dolerite unit in Hole 1109D shown in vector plots, stereoplots, and normalized decay of intensity of magnetization. See Figure **F67,** p. 159, for definitions of terms.

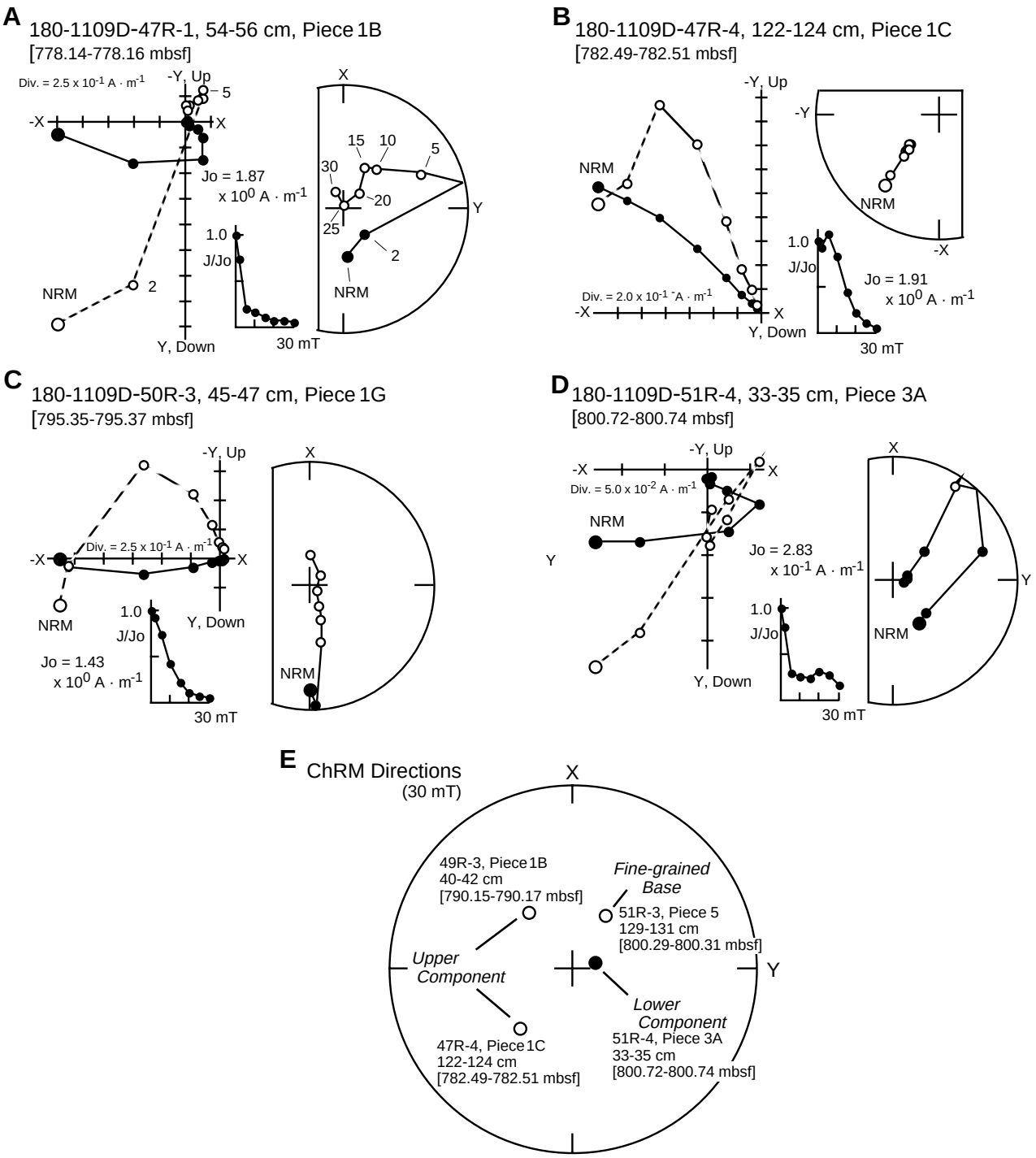

Figure F69. Anisotropy of magnetic susceptibility (AMS) data of discrete samples from dolerite unit (lithostratigraphic Unit XI, see **"Igneous and Metamorphic Petrology,"** p. 35) at Hole 1109D. K_{max}, K_{int}, and K_{min} are the maximum, intermediate, and minimum axes, respectively, of the susceptibility ellipsoid. Degree of anisotropy (P_j) and the shape parameter (T) calculated according to Jelinek (1981).

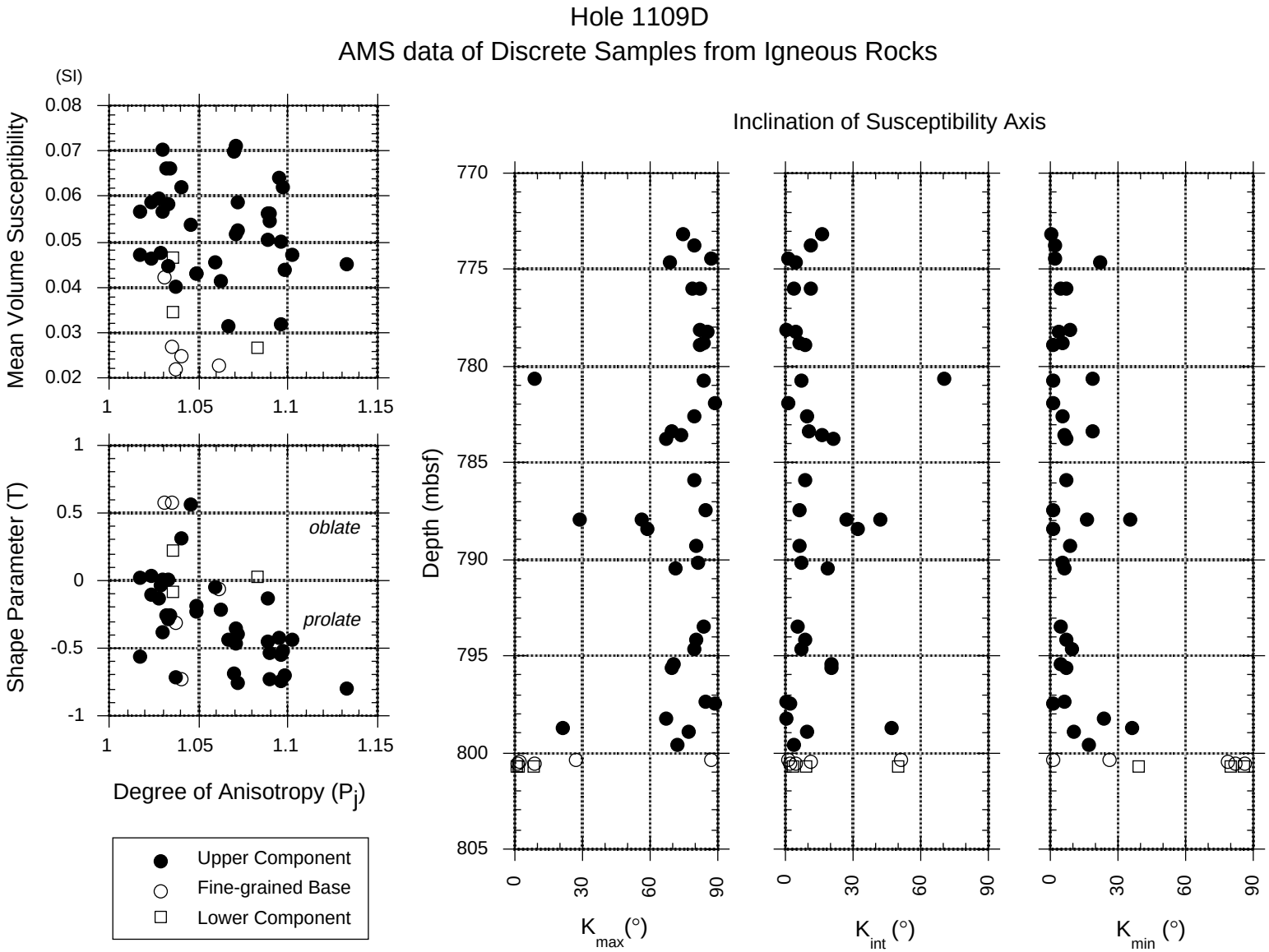

Figure F70. A. Depth profiles of interstitial water constituents at Site 1109, with the lithostratigraphy column at right; pH, alkalinity, SO_4^{2-}, and NH_4^+. (Continued on next two pages.)

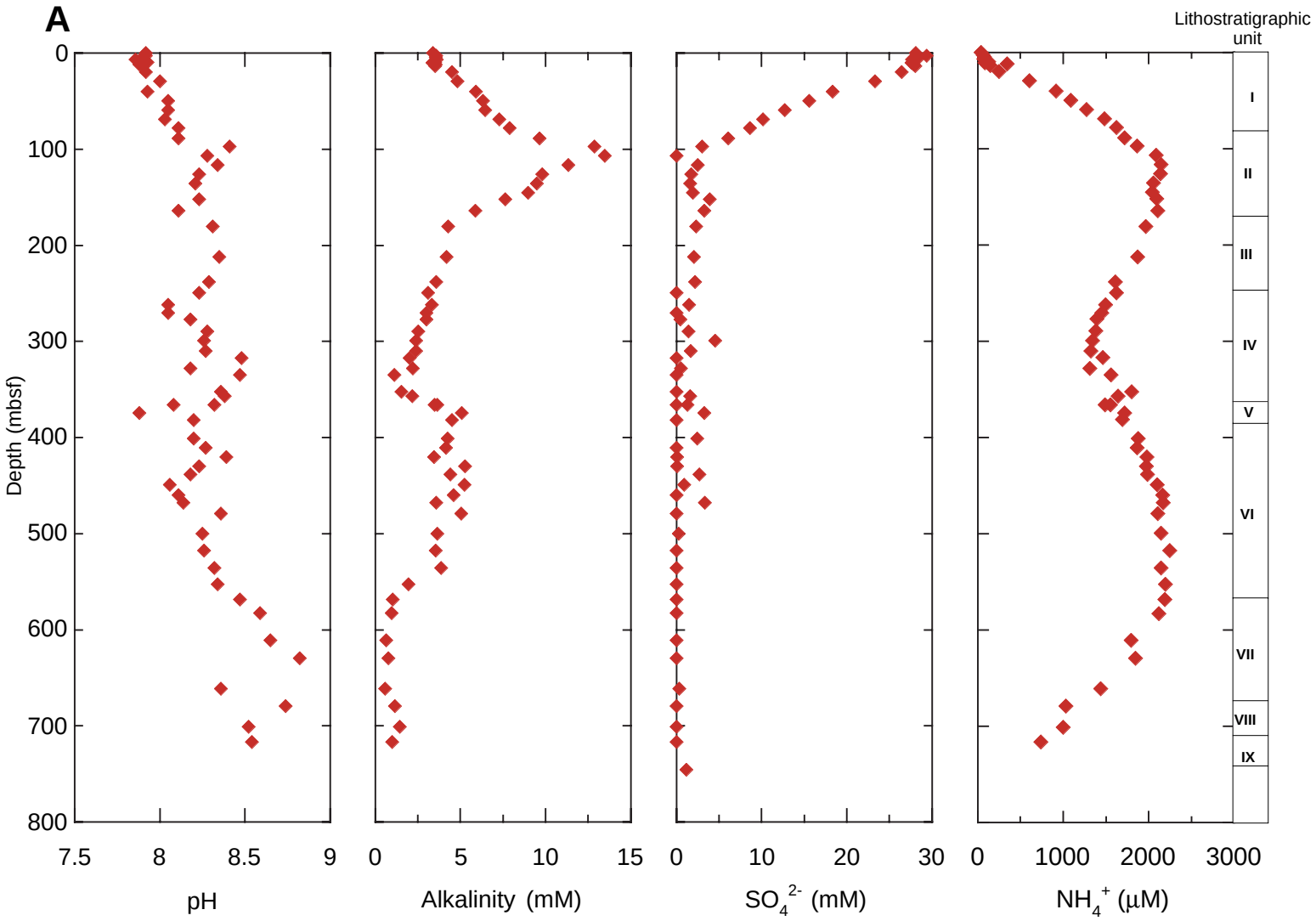

Figure F70 (continued). B. Depth profiles of interstitial water constituents at Site 1109; Na^+, Cl–, K^+, and Li^+. I.C.= chloride by ion chromatography.

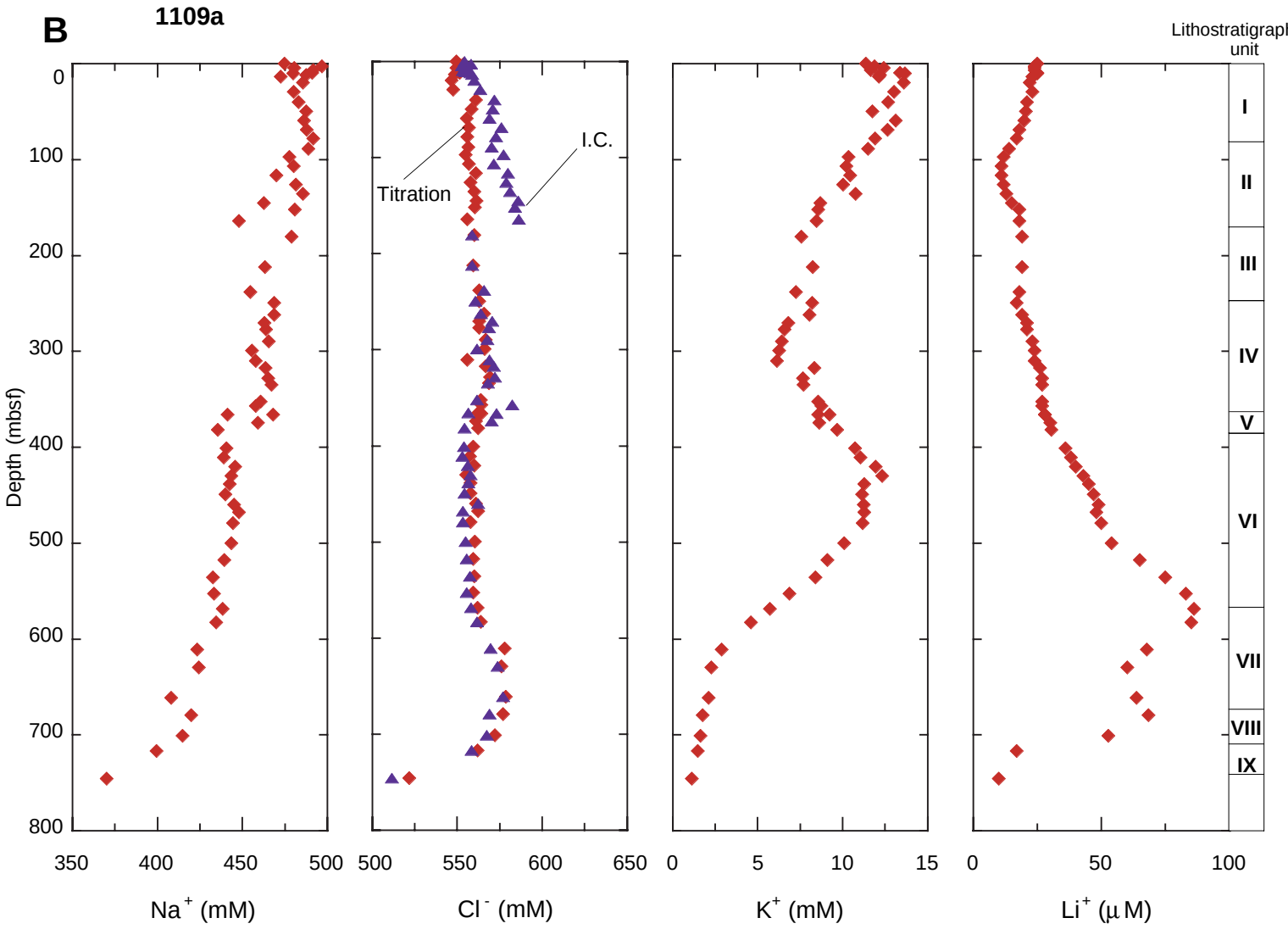

Figure F70 (continued). C. Depth profiles of interstitial water constituents at Site 1109; Ca^{2+} and Mg^{2+}, Sr^{2+}, SiO_2, and Ca/Mg.

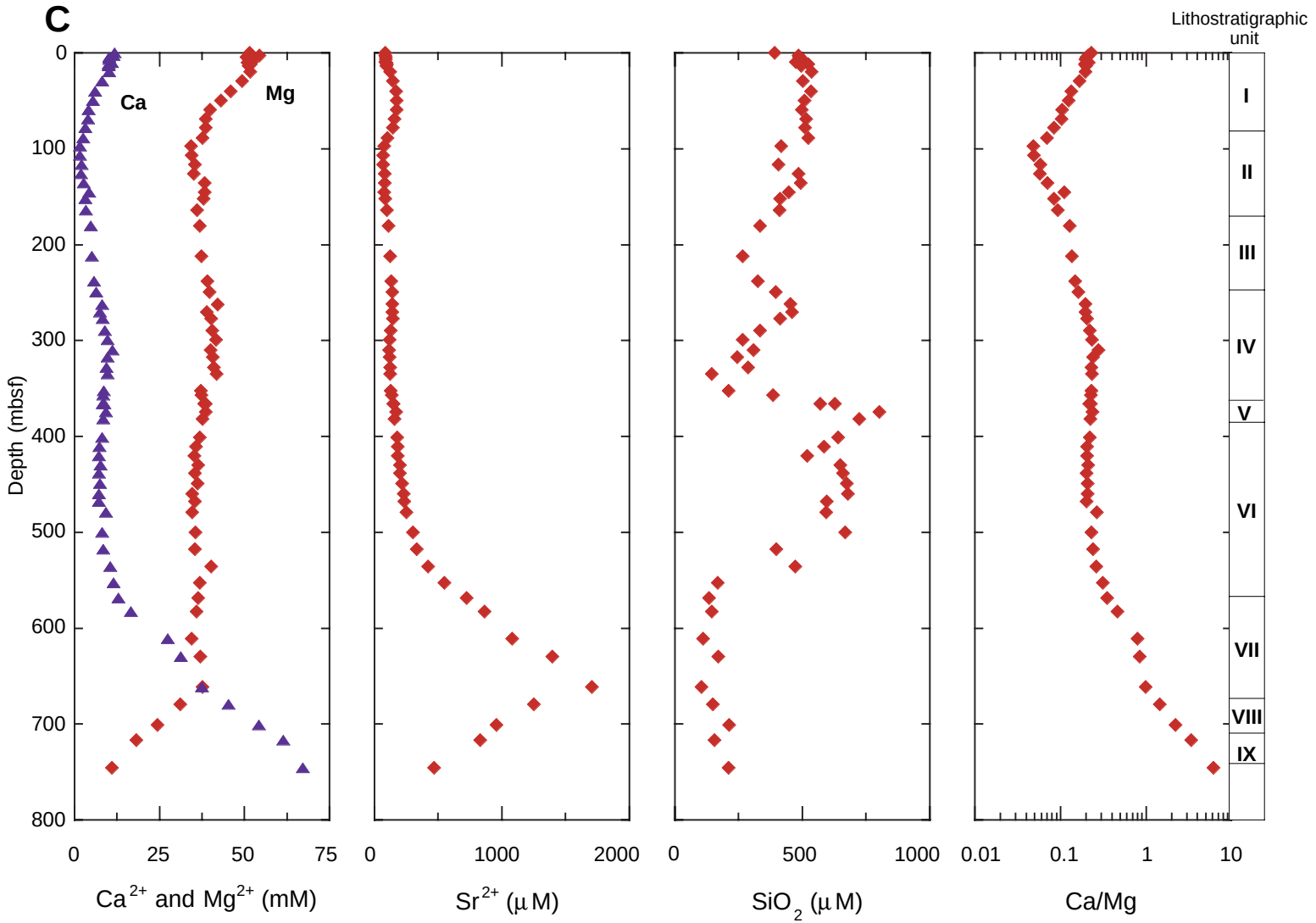

Figure F71. Correlation of dissolved SiO_2 and porosity in sediments at Site 1109. Note the lack of correlation in the first 100 mbsf because of early diagenesis of easily solubilized solid phases containing silica, and an anticorrelation in the volcanic ash-rich interval that provides an important source of this constituent to the pore water. Below 260 mbsf a strong positive correlation exists between porosity and dissolved SiO_2.

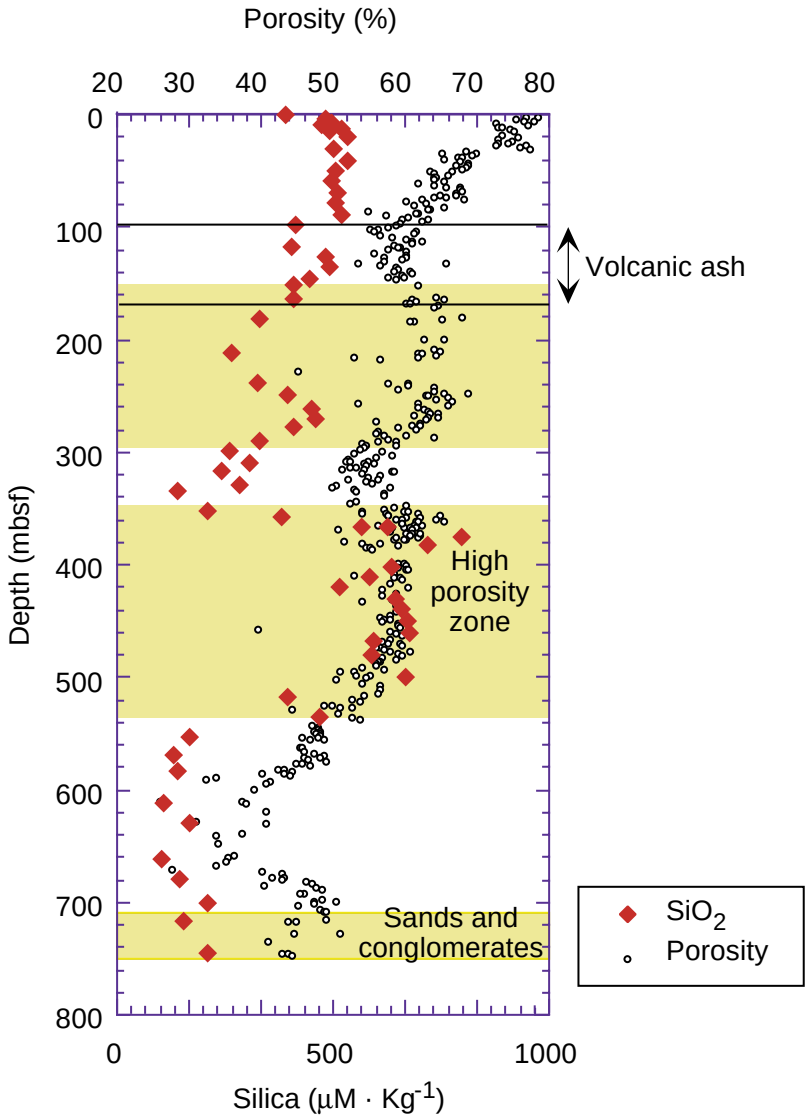

Figure F72. C_1, C_2, and C_1/C_2 hydrocarbon profiles, Site 1109.

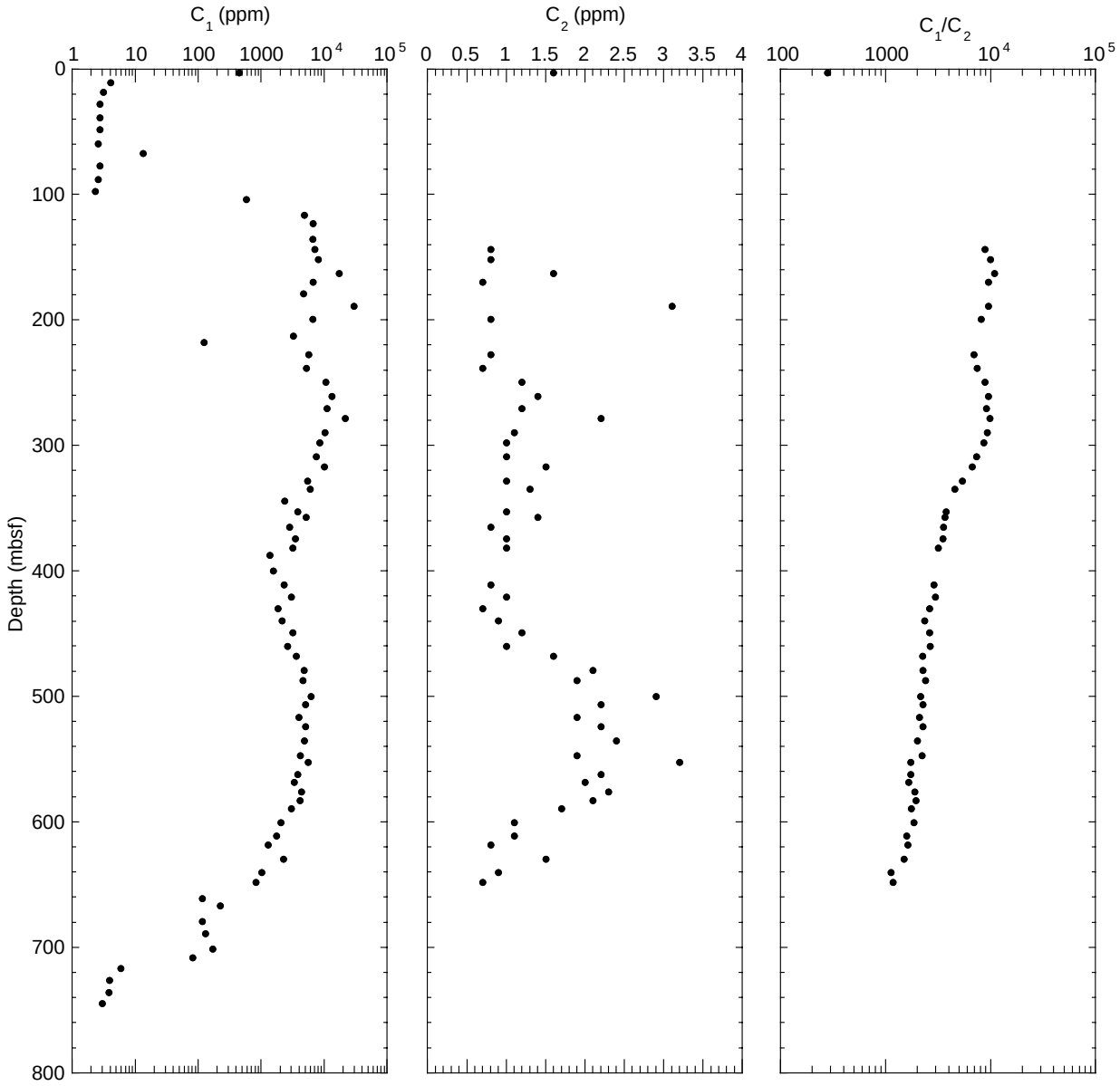

Figure F73. $CaCO_3$, organic carbon, and C/N ratio profiles and lithostratigraphic units, Site 1109.

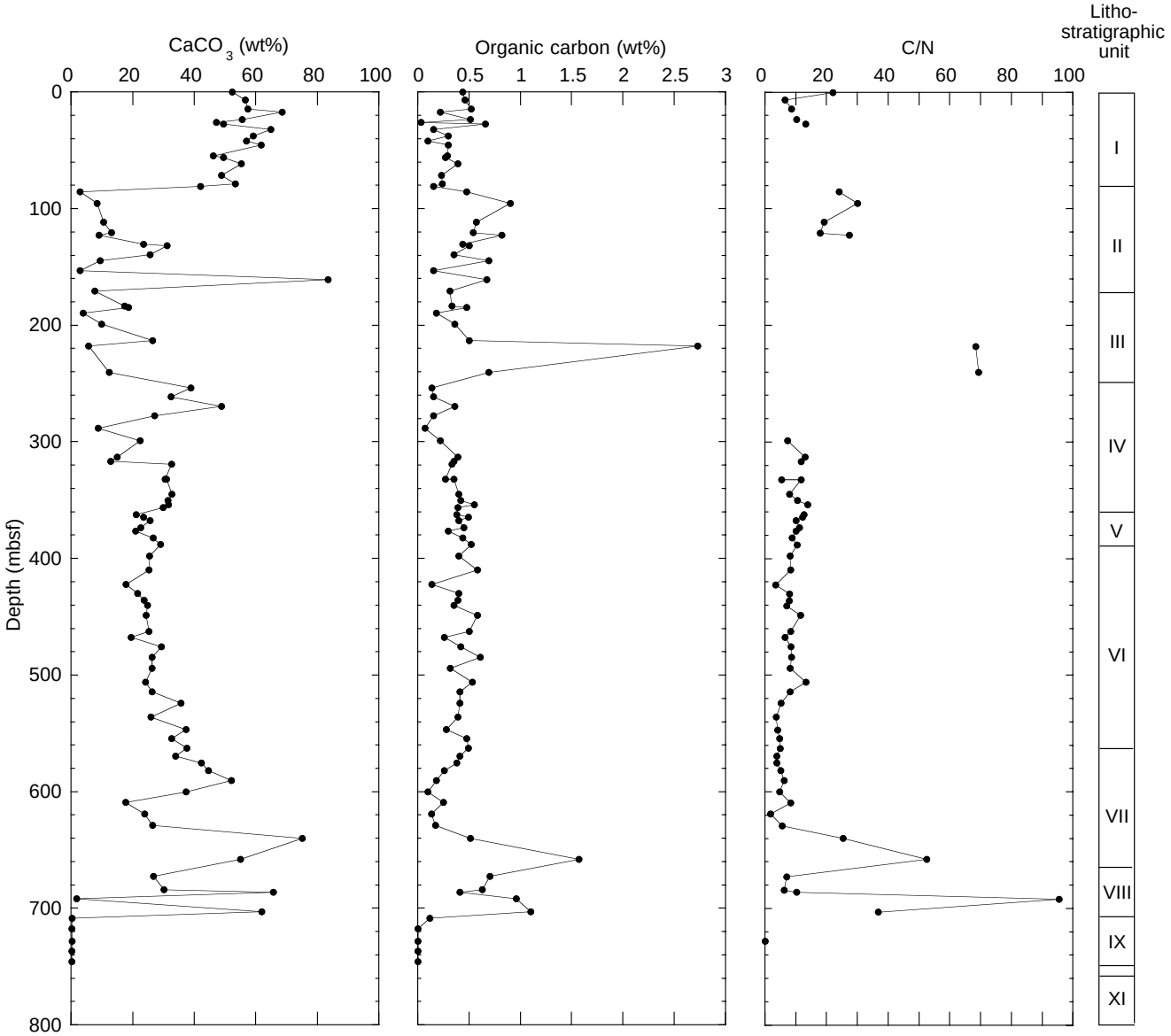

Figure F74. Depth distributions of total bacterial populations (solid symbols) and dividing and divided cells (open symbols) in sediment samples from Holes 1109B (triangles), 1109C (circles), and 1109D (squares). The solid curve represents a general regression line of bacterial numbers vs. depth in deep-sea sediments (Parkes et al., 1994), with 95% upper and lower prediction limits shown by dashed curves.

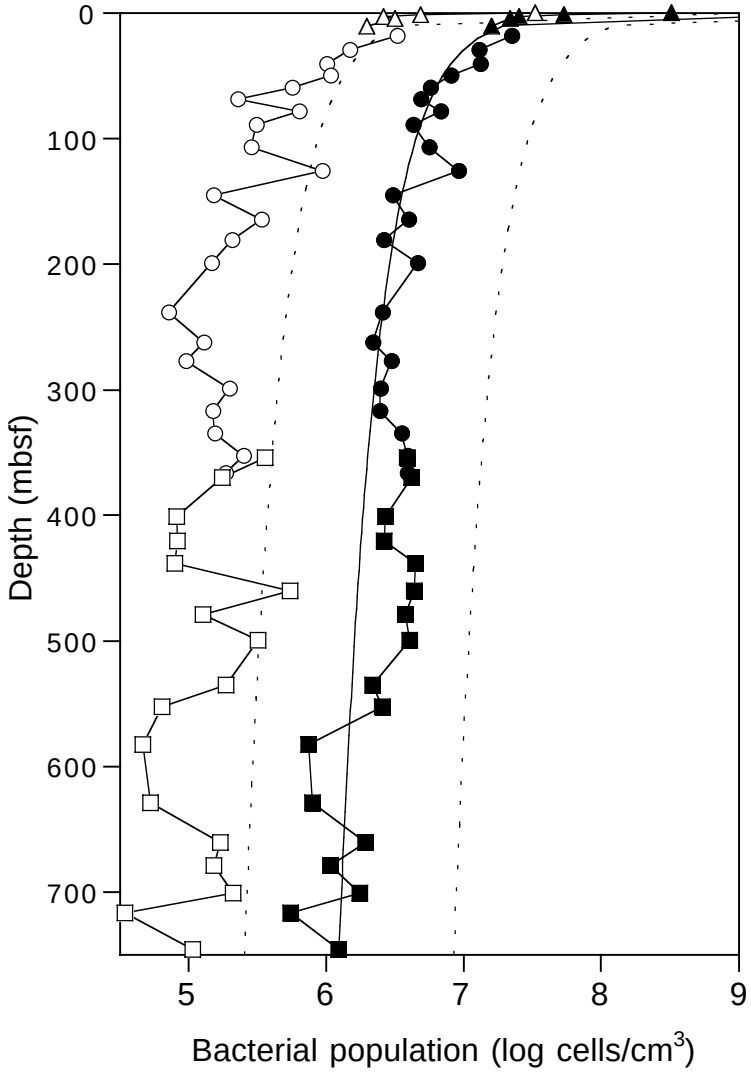

Figure F75. (**A**) Bulk density and (**B**) grain density derived from GRAPE and MAD index property measurements.

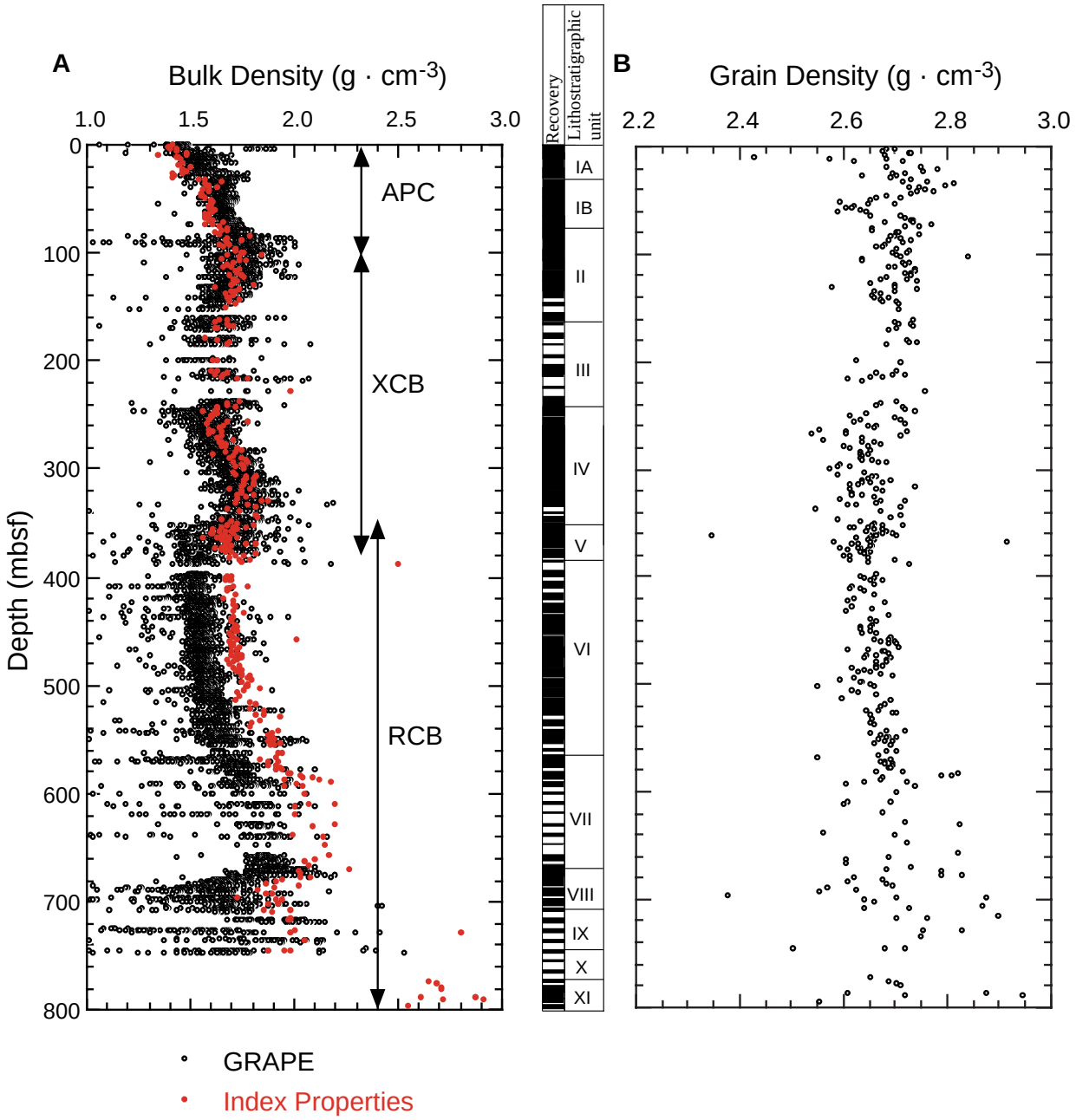

Figure F76. Comparison of porosity, sedimentation rate derived from biostratigraphy data, and grain-size distribution. Highlighted zones represent characteristic lithostratigraphies and porosity behavior; pink/intermediate gray = clay dominated intervals; orange/dark gray = sands and conglomerate; yellow/light gray = high porosity zones.

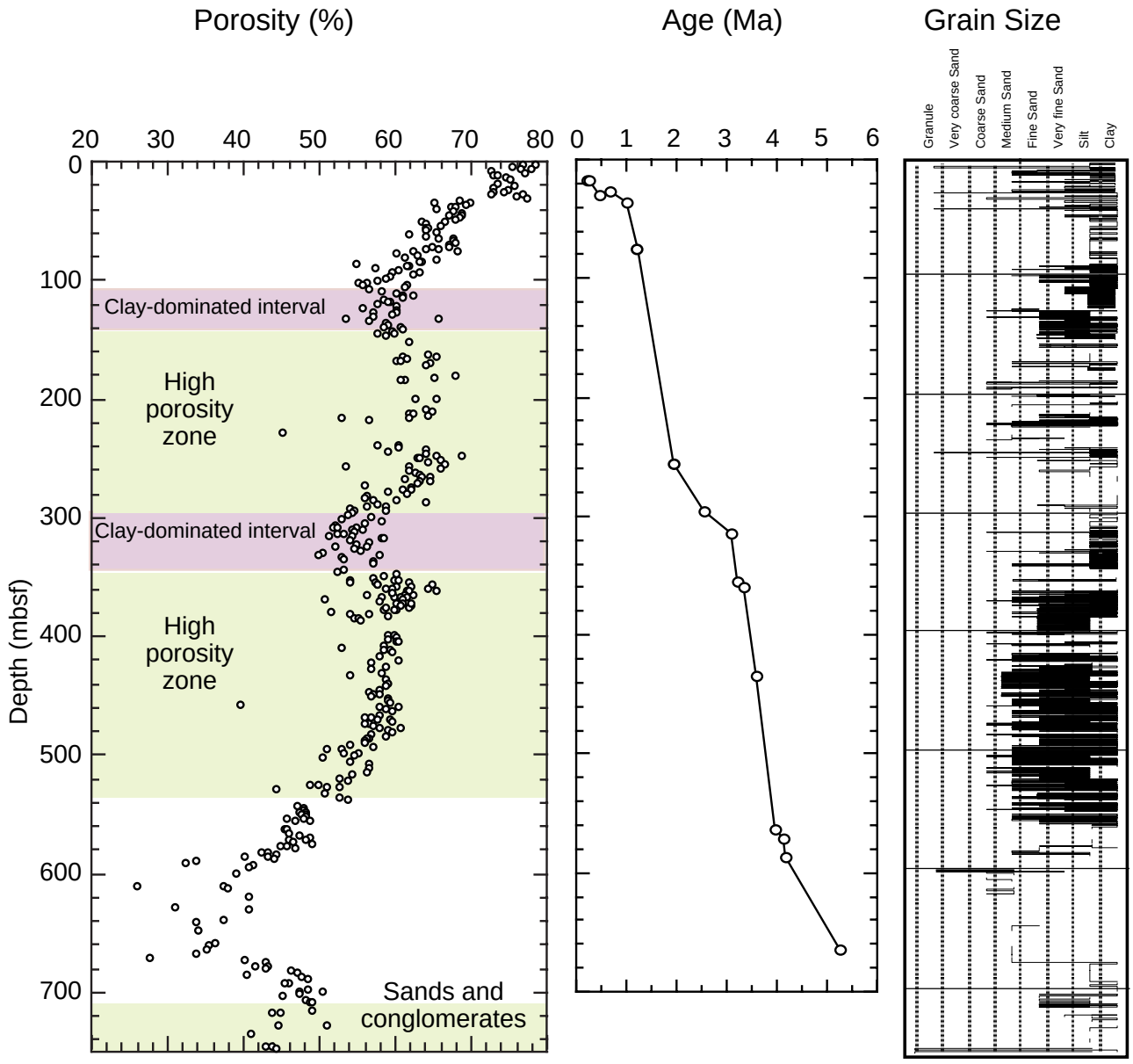

Figure F77. Site 1109 *P*-wave velocities (x, y, and z). Highlighted intervals represent high-velocity zones and correspond to the presence of carbonate cements or igneous rock.

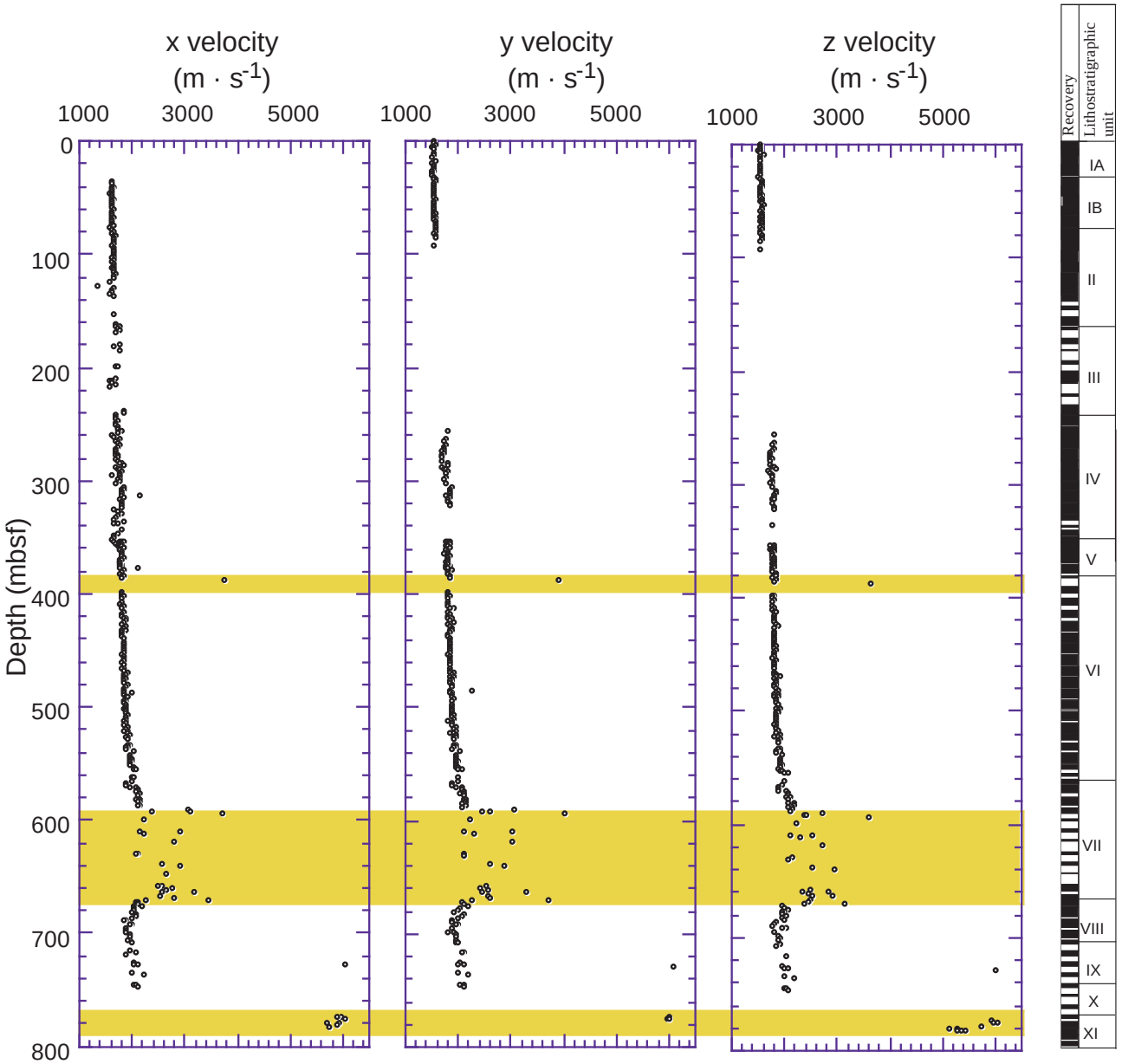

Figure F78. A. Longitudinal velocity vs. average transverse velocity. **B.** *P*-wave anisotropy (for method used, see **"*P*-wave Velocities on Split Cores,"** p. 33, in the "Explanatory Notes" chapter). A positive anisotropy indicates that the transverse velocity is greater than the longitudinal velocity.

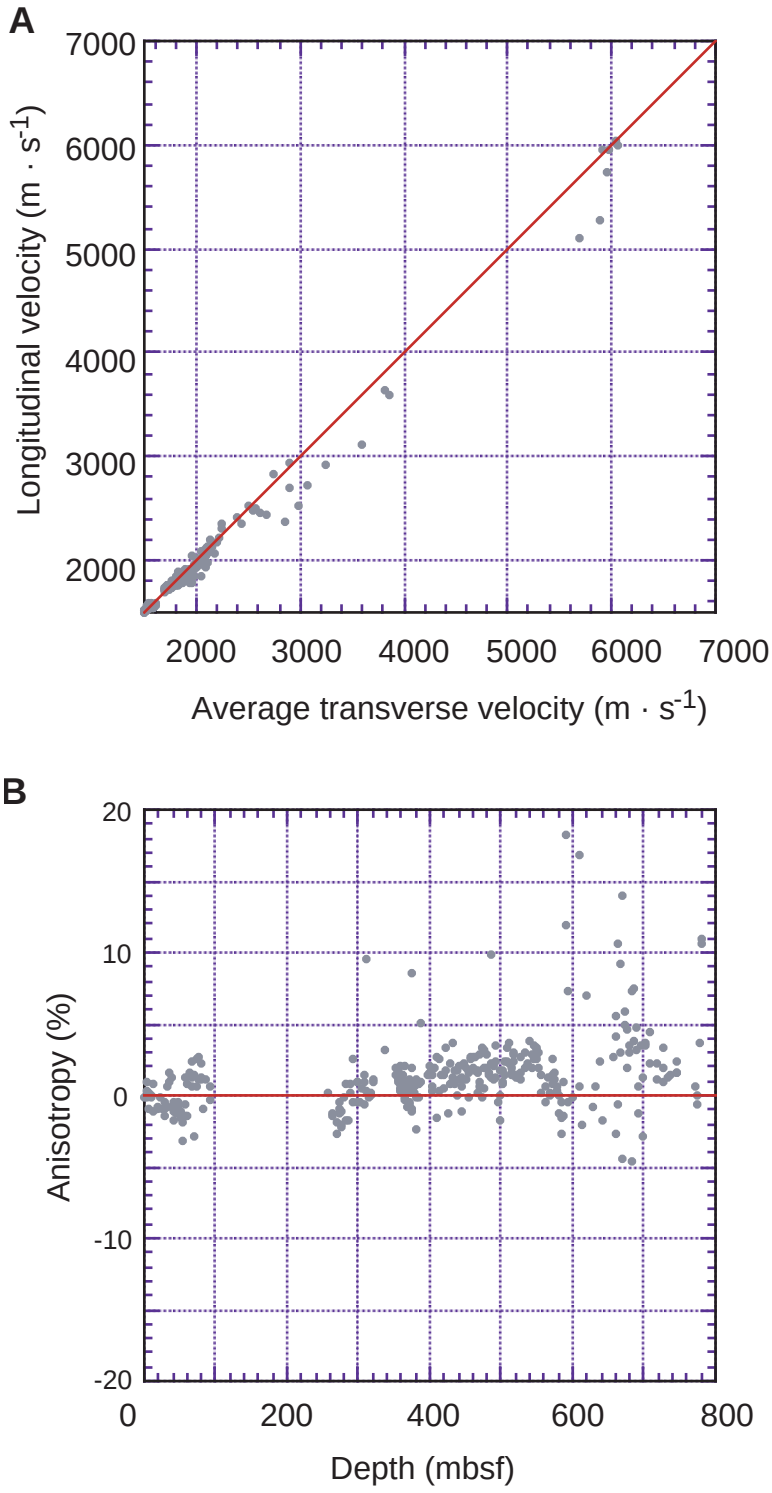

Figure F79. Site 1109 thermal conductivity measurements. Note that all acquired data are presented here, although values of 0.6 $W \cdot m^{-1} \cdot °C^{-1}$ or lower are not trustworthy because they are lower than seawater.

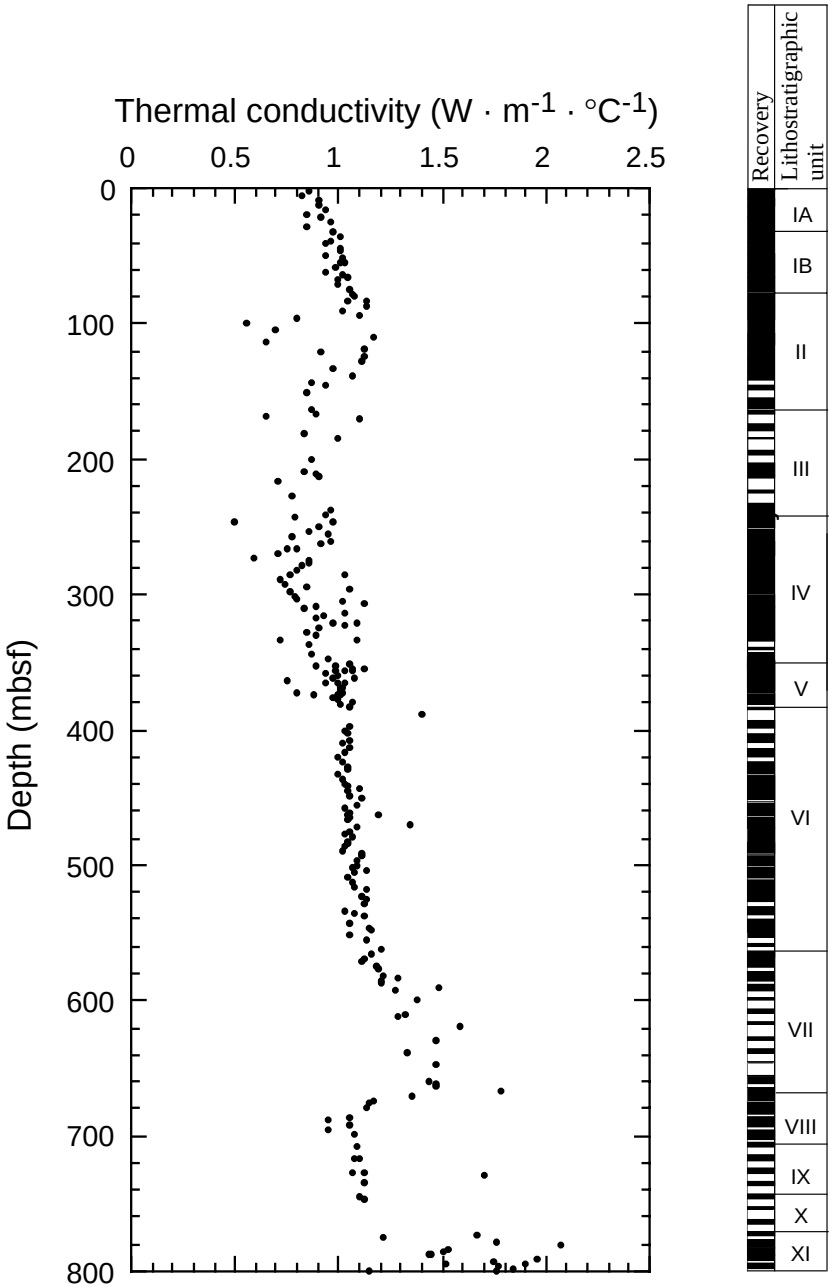

Figure F80. Site 1109 undrained shear strength and unconfined compressive strength results. Solid (green) lines indicate strength gradients, whereas the dashed (red) lines reflect the unconfined compressive strength to overburden stress ratio for normal sediment consolidation: $S_u/P_0 = 0.2$.

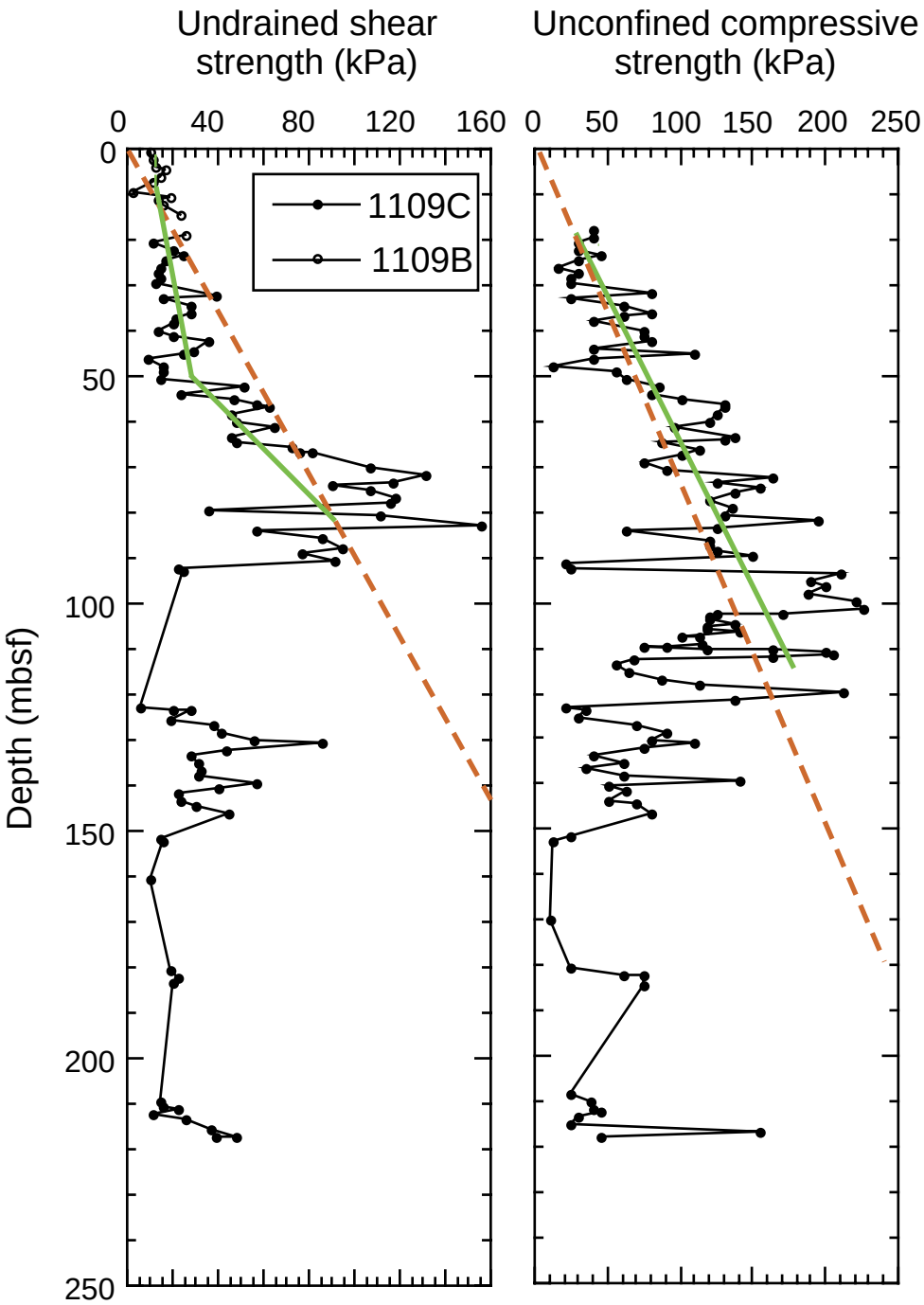

Figure F81. Comparison of (A) grain-size distribution, (B) magnetic susceptibility, and (C) magnetic intensity data, Holes 1109C and 1109D.

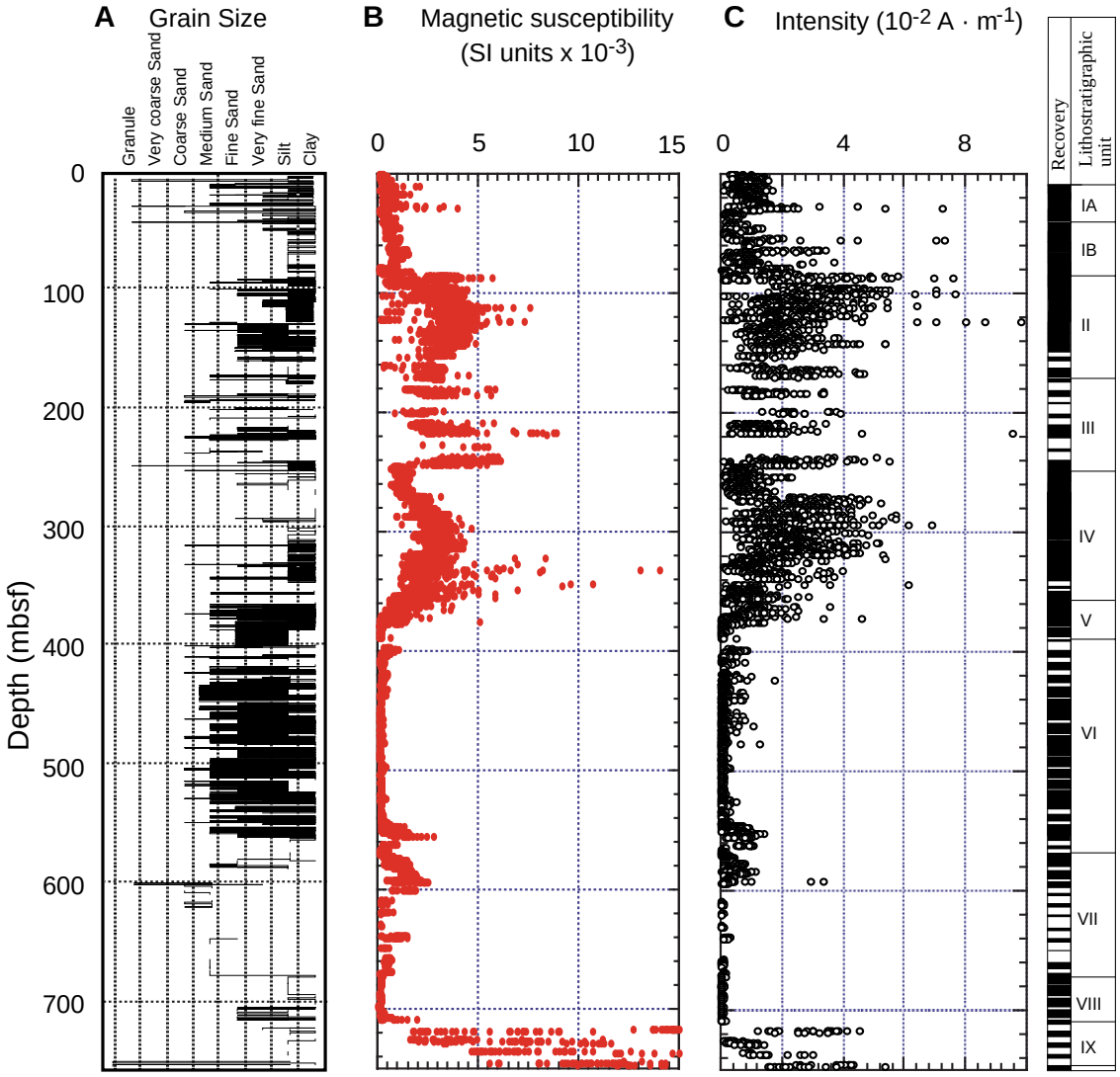

Figure F82. Comparison between **(A)** natural gamma ray and **(B)** magnetic susceptibility data, Holes 1109C and 1109D.

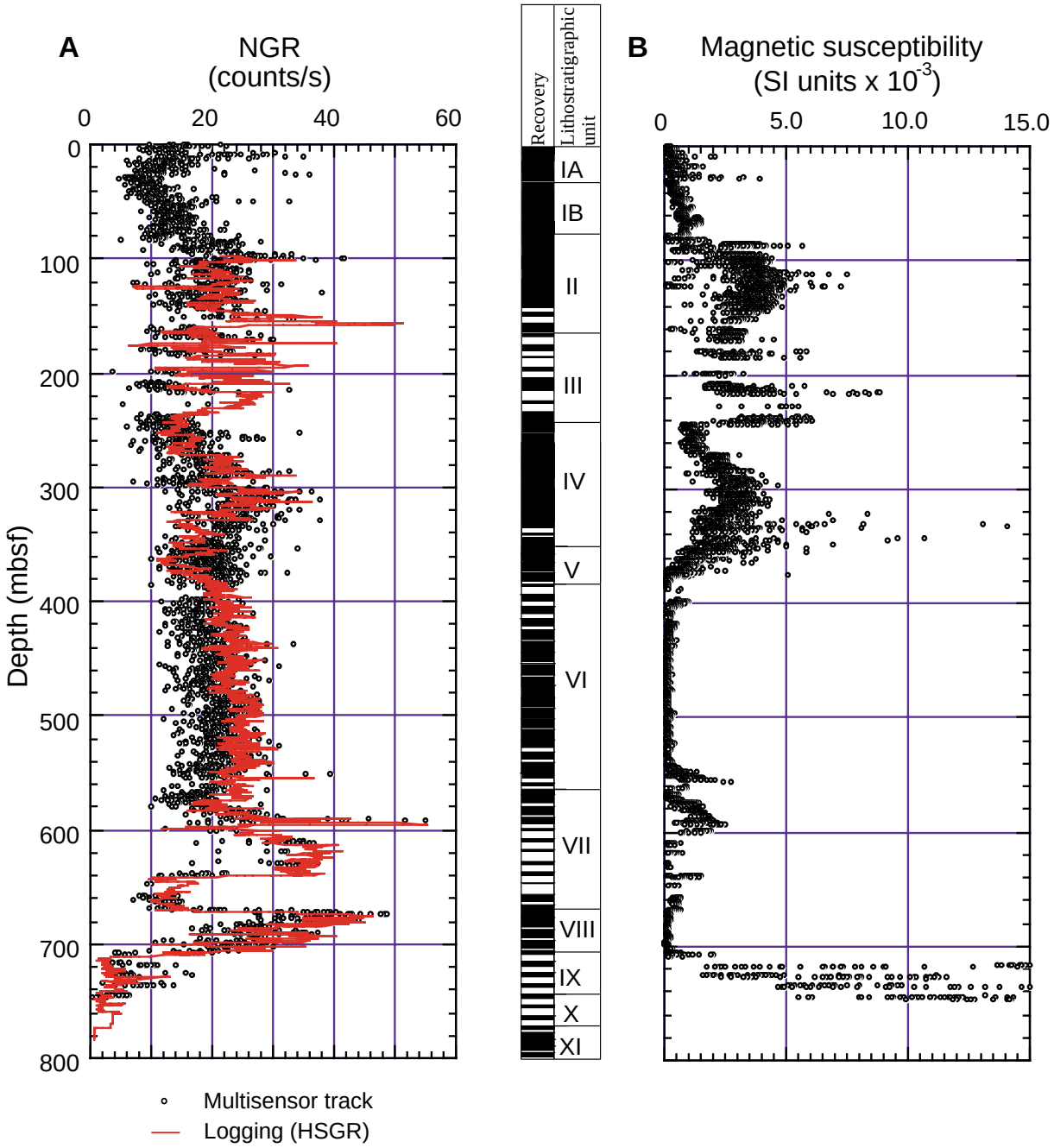

Figure F83. Correlation between Holes 1109A, 1109B, and 1109C using GRAPE density data.

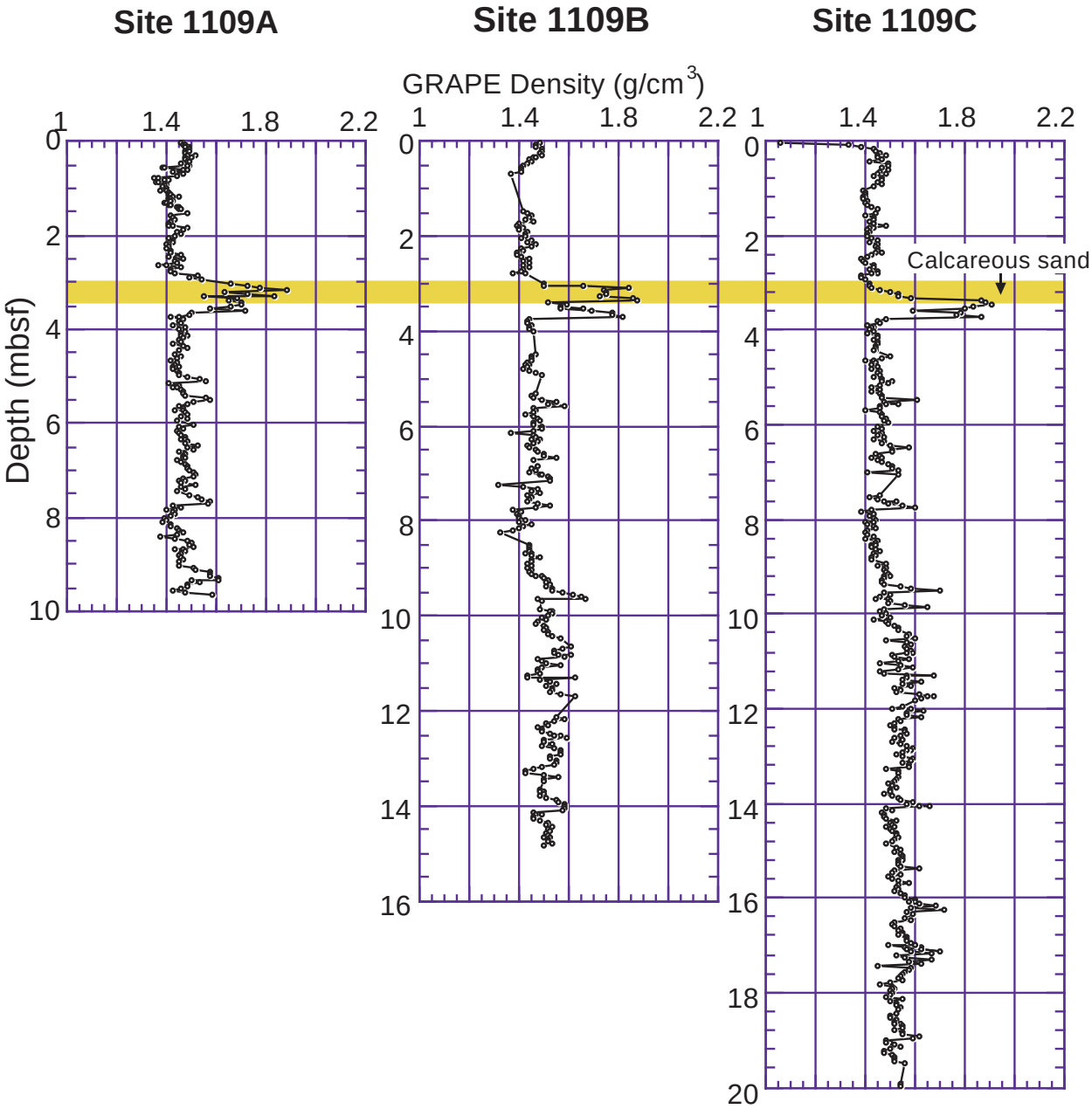

Figure F84. Correlation between Holes 1109A, 1109B, and 1109C using magnetic susceptibility data. Shaded zones identify the susceptibility features used for correlation.

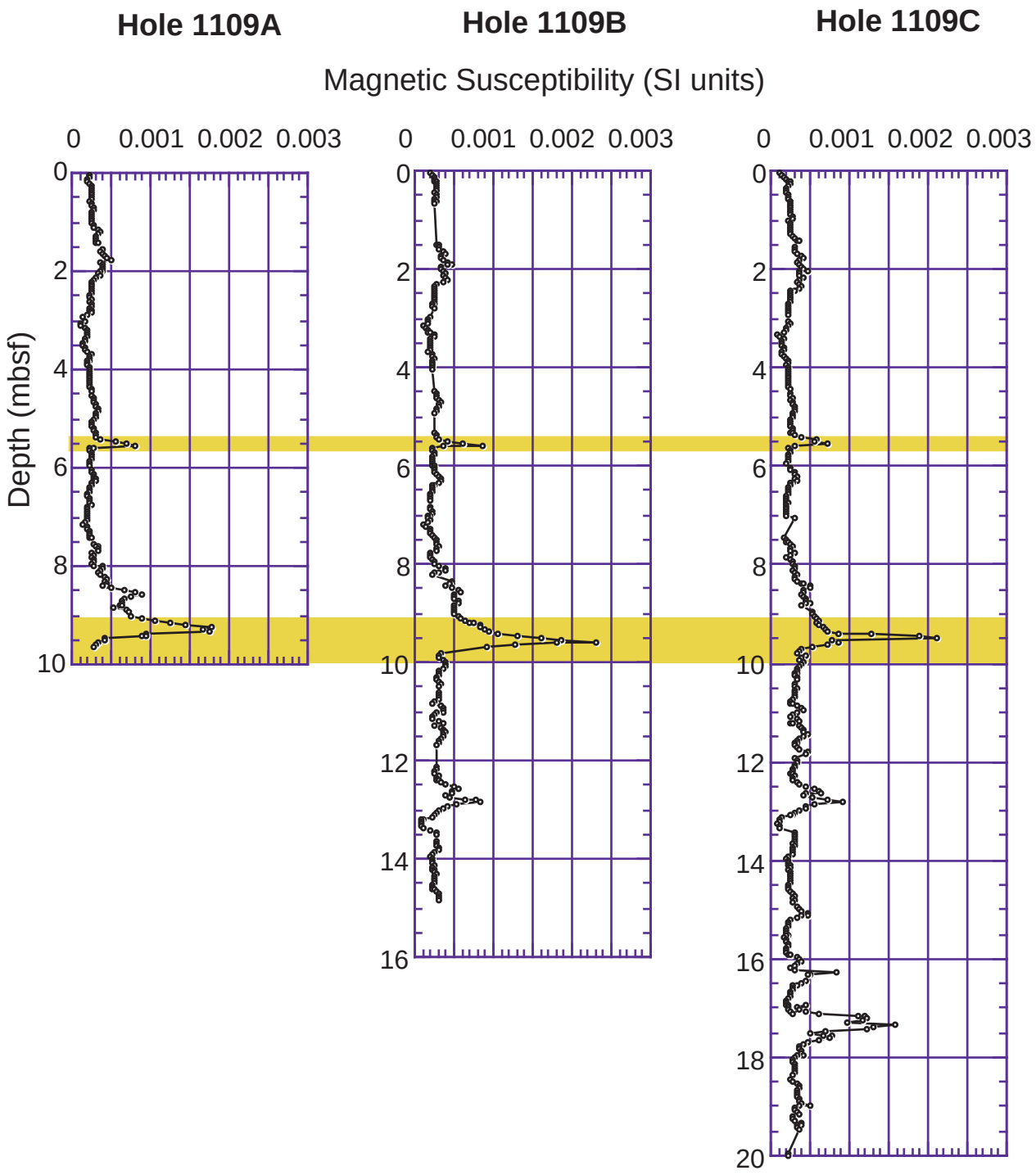

Figure F85. Correlation between Holes 1109A, 1109B, and 1109C using natural gamma ray (NGR) data. Shaded zones identify the NGR features used for correlation.

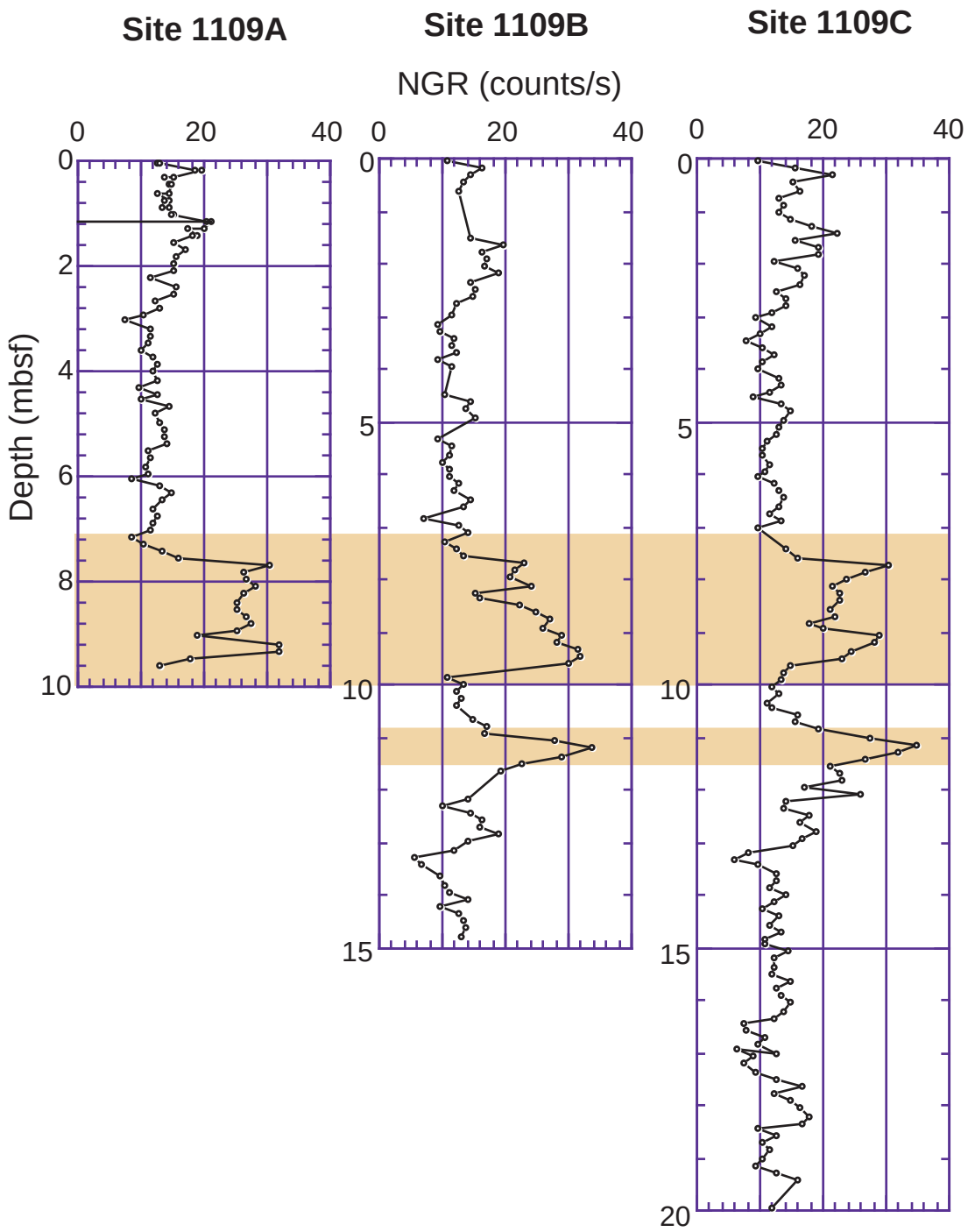

Figure F86. Correlation between Holes 1109C and 1109D using magnetic susceptibility data. Shaded zone identifies the susceptibility features used for correlation.

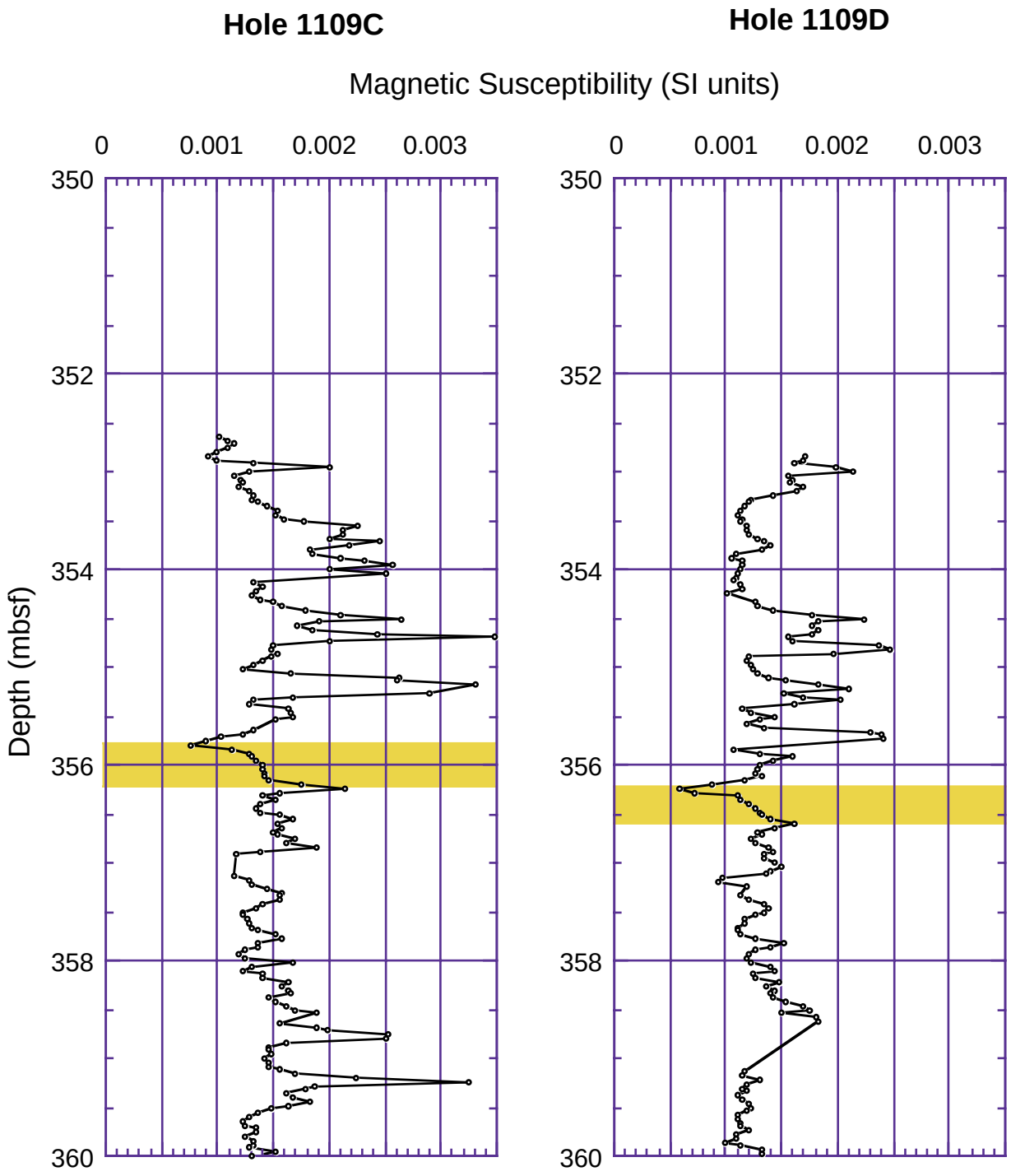

Figure F87. Comparison of physical properties measurements with equivalent downhole logging data, Holes 1109C and 1109D. **A.** Bulk density. **B.** Velocity.

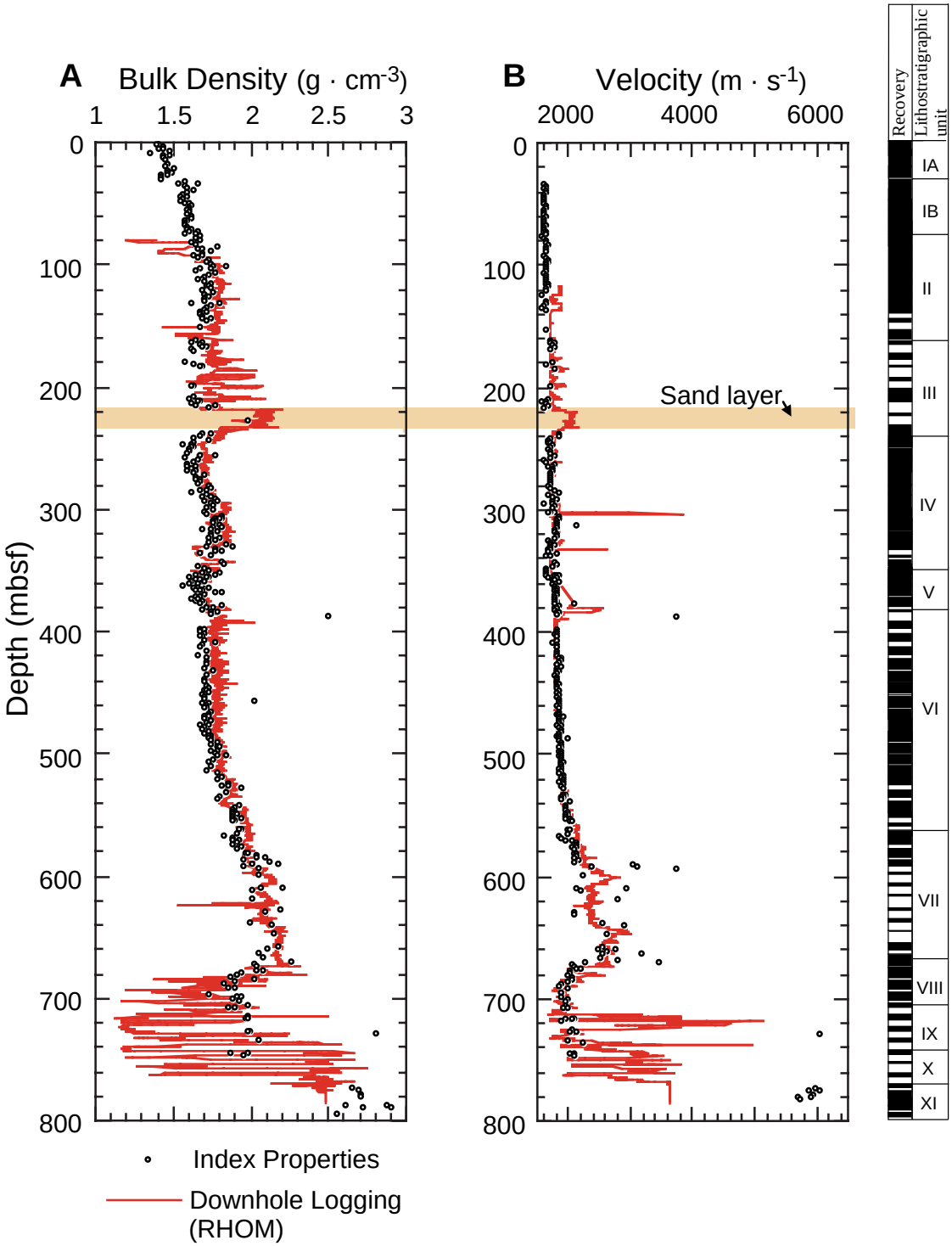

Figure F88. Hole 1109D composite log from 0 to 800 mbsf. **A.** Left to right: (1) core number and recovery intervals for Holes 1109C and 1109D; (2) caliper measurements from the triple combo run (LCAL); (3) total natural gamma ray (HSGR) and total natural gamma ray minus uranium contribution (HCGR); (4) thorium and uranium content and Th/U ratio; (5) potassium content, (6) resistivity from the DIT tool, consisting of deep induction (IDPH), medium induction (IMPH), and shallow spherically focused current (SFLU), and (7) log units. Composite log from 0 to 200 mbsf. To compare other logs at equivalent depth, see Figure **F88B,** p. 186. (Continued on next seven pages.)

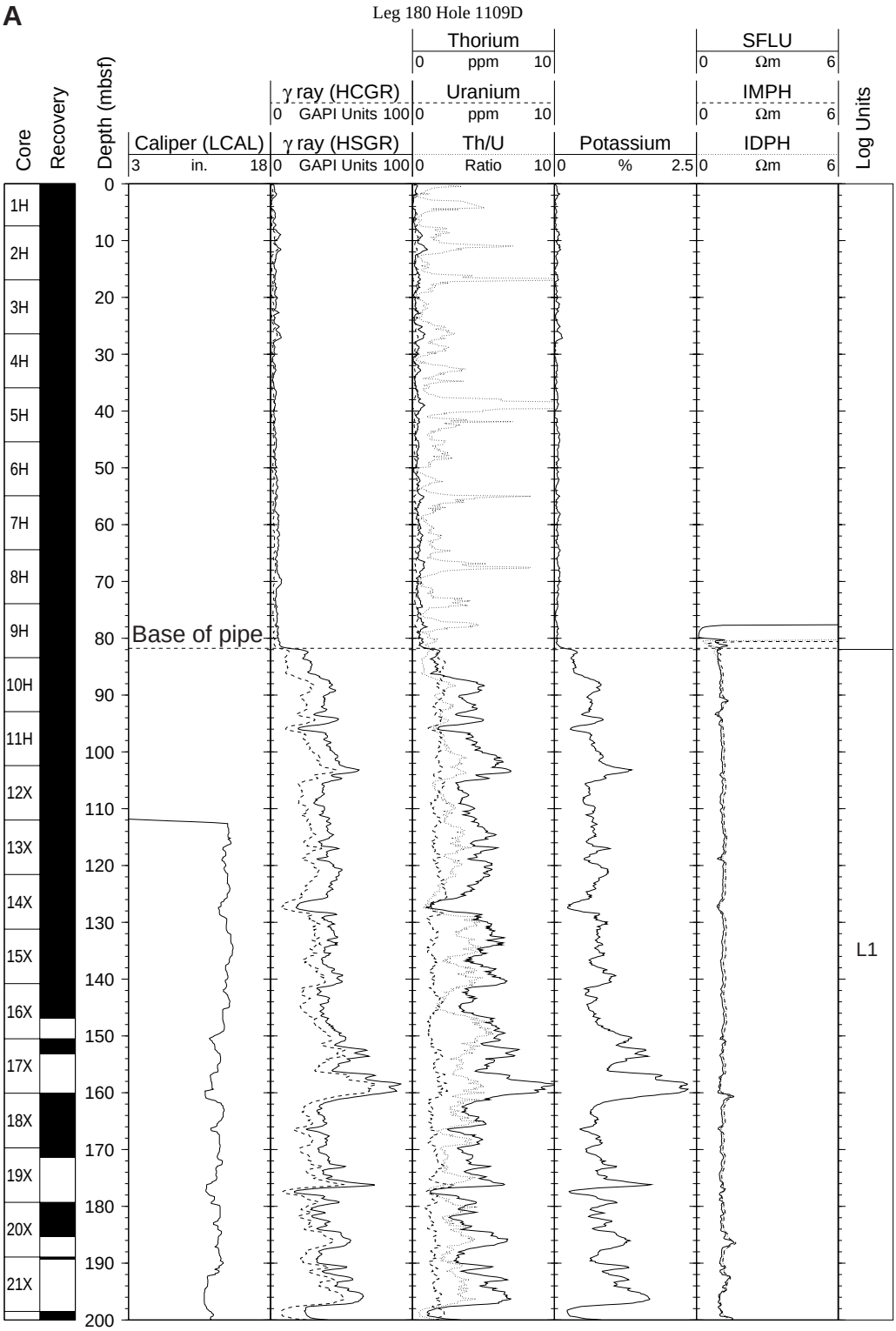

Figure F88 (continued). Composite log from 200 to 400 mbsf. To compare other logs at equivalent depth, see Figure **F88B,** p. 187.

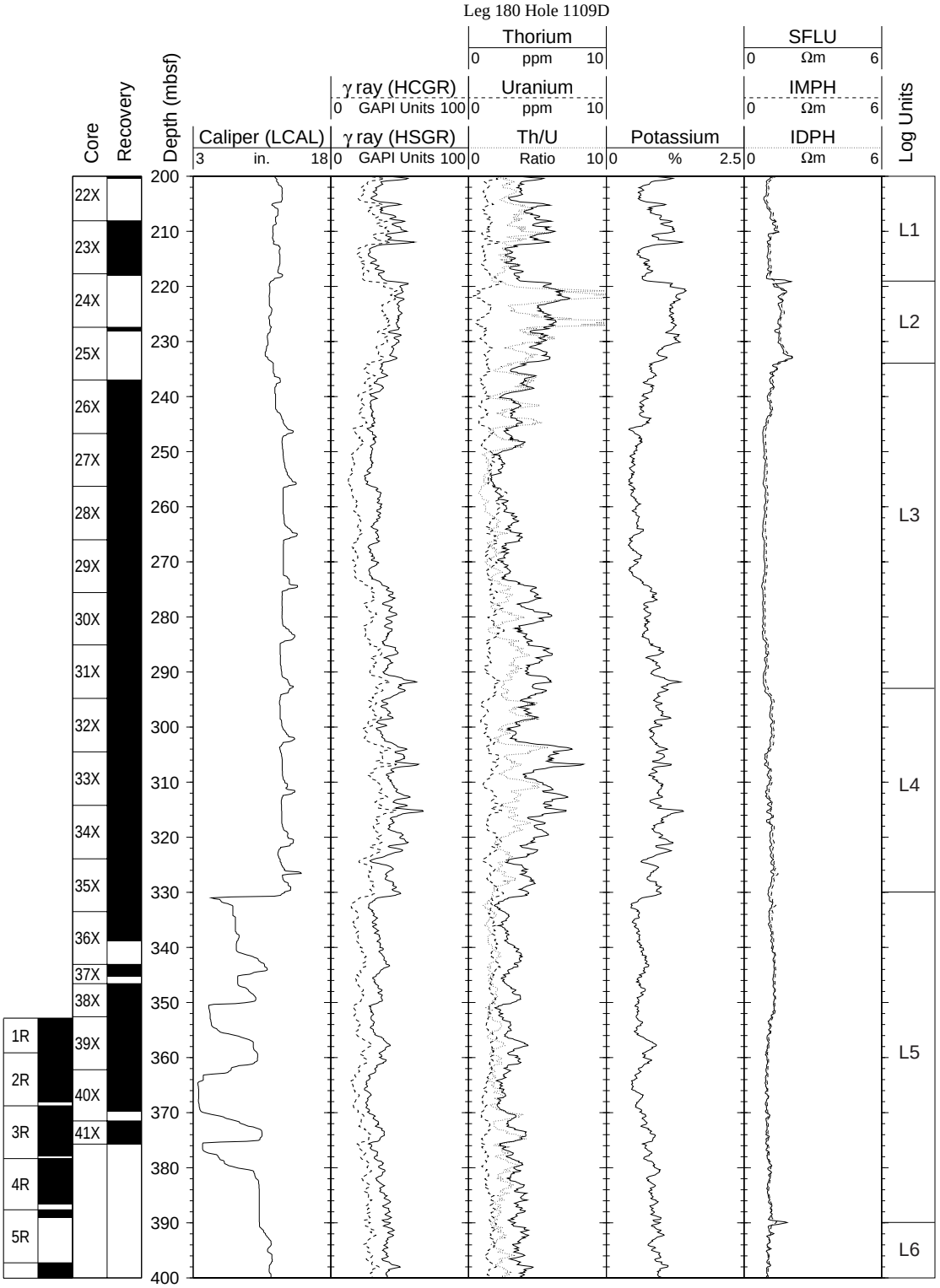

Figure F88 (continued). Composite log from 400 to 600 mbsf. To compare other logs at equivalent depth, see Figure **F88B,** p. 188.

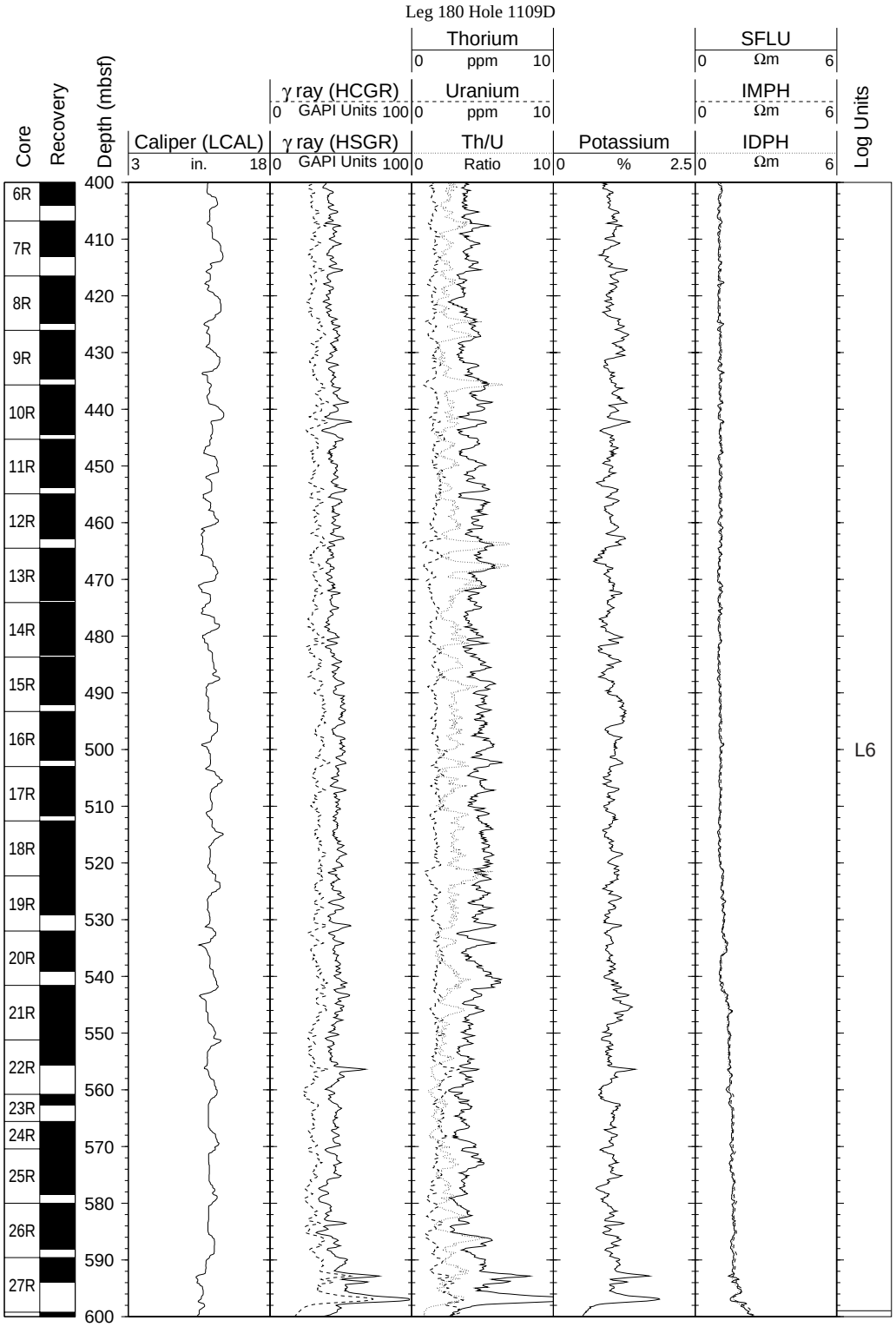

Figure F88 (continued). Composite log from 600 to 800 mbsf. To compare other logs at equivalent depth, see Figure **F88B,** p. 189.

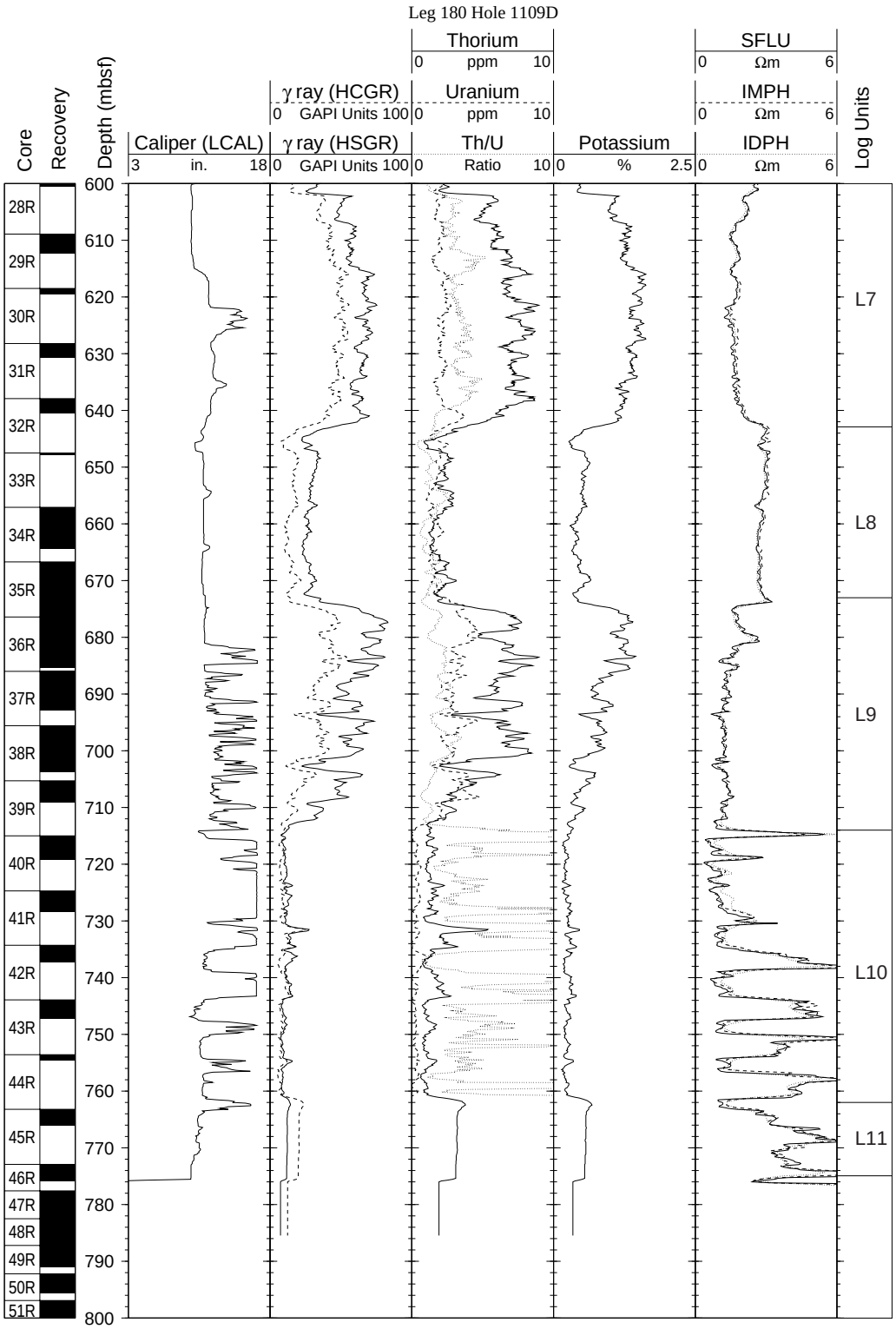

Figure F88 (continued). B. Left to right: (1) core number and recovery intervals for Holes 1109C and 1109D; (2) bulk density (RHOM) from the lithodensity sonde (HLDS) and from measurements on cores; (3) photoelectric effect (PEFL); (4) neutron porosity (APLC), density porosity (DPHI) and porosity from measurements on cores; (5) neutrons capture rate (SIGF); (6) sonic velocity from array sonic tool (DTCO) and from either z axis or, when not available, from average of x and y axis measurements on cores; and (7) log units. Composite log from 0 to 200 mbsf. To compare other logs at equivalent depth, see Figure **F88A,** p. 182.

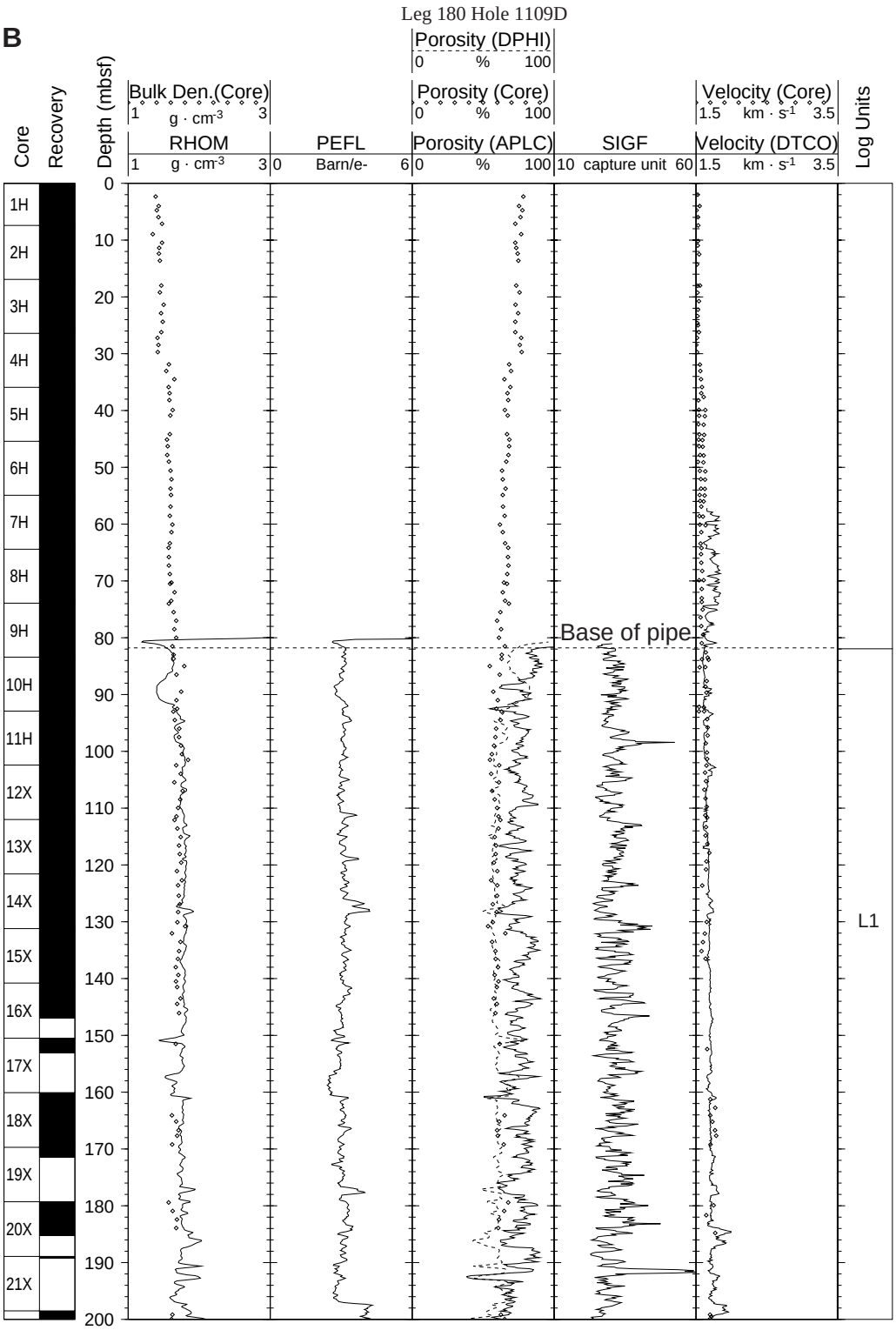

Figure F88 (continued). Composite log from 200 to 400 mbsf. To compare other logs at equivalent depth, see Figure F88A, p. 183.

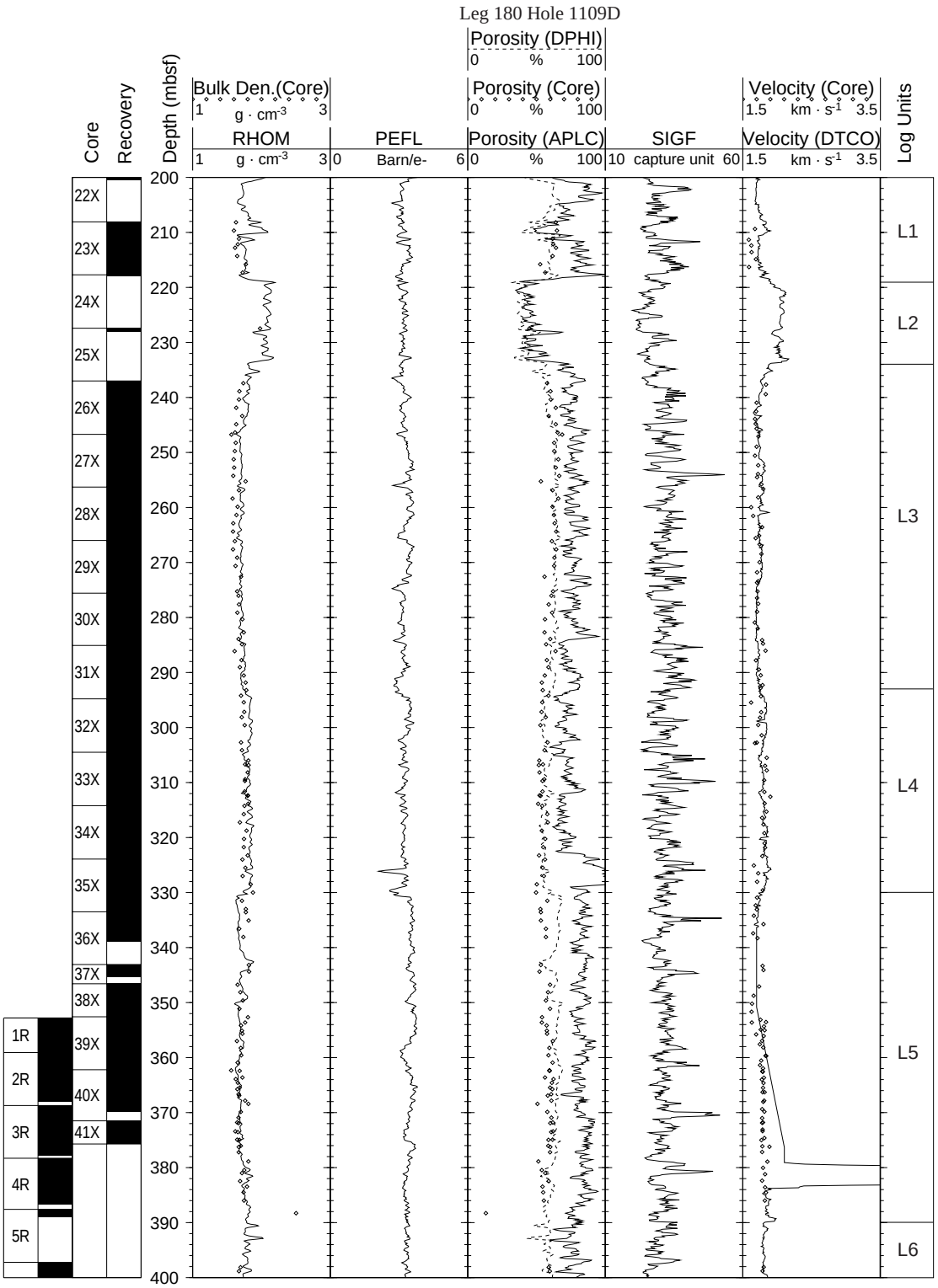

Figure F88 (continued). Composite log from 400 to 600 mbsf. To compare other logs at equivalent depth, see Figure F88A, p. 184.

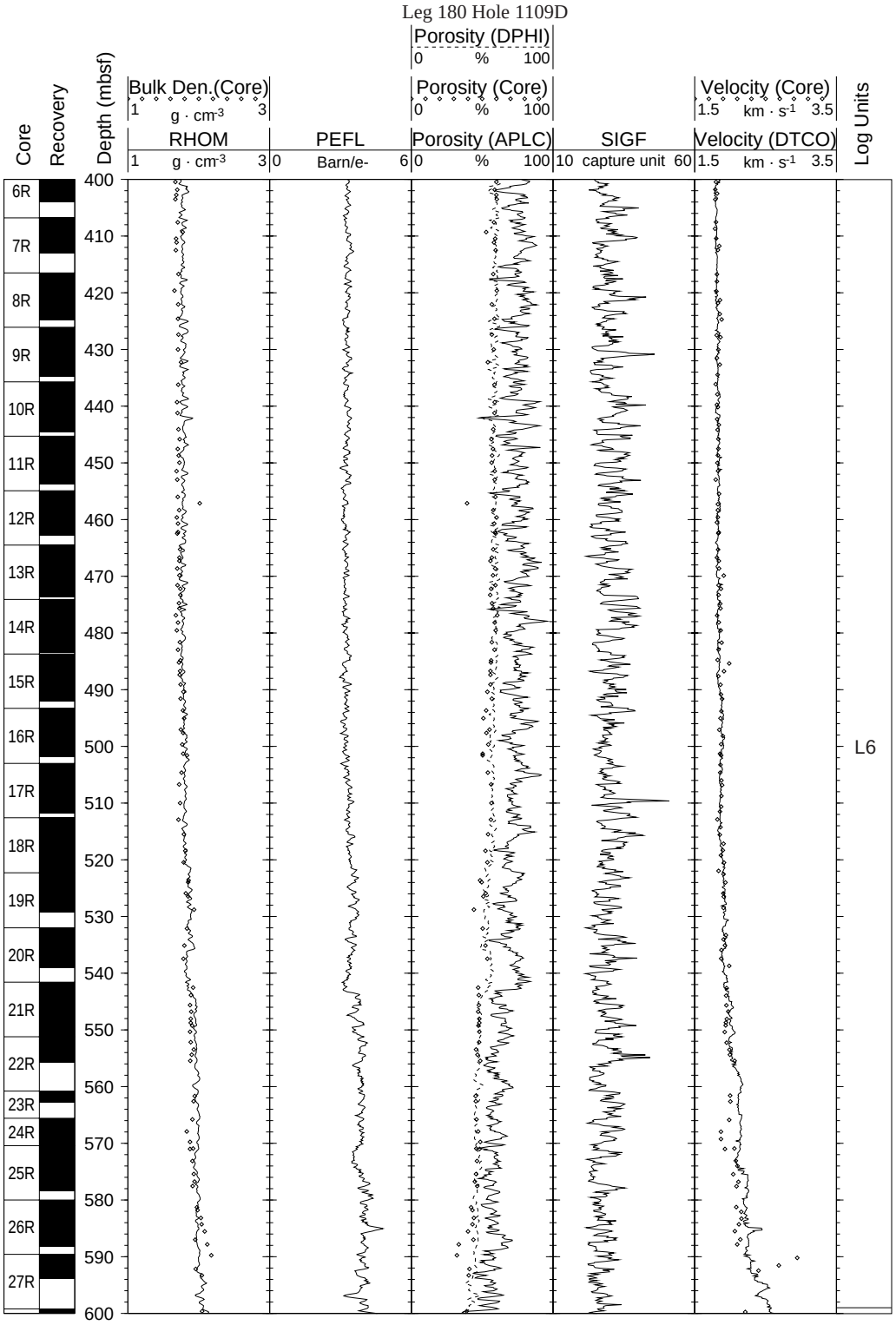

Figure F88 (continued). Composite log from 600 to 800 mbsf. To compare other logs at equivalent depth, see Figure F88A, p. 185.

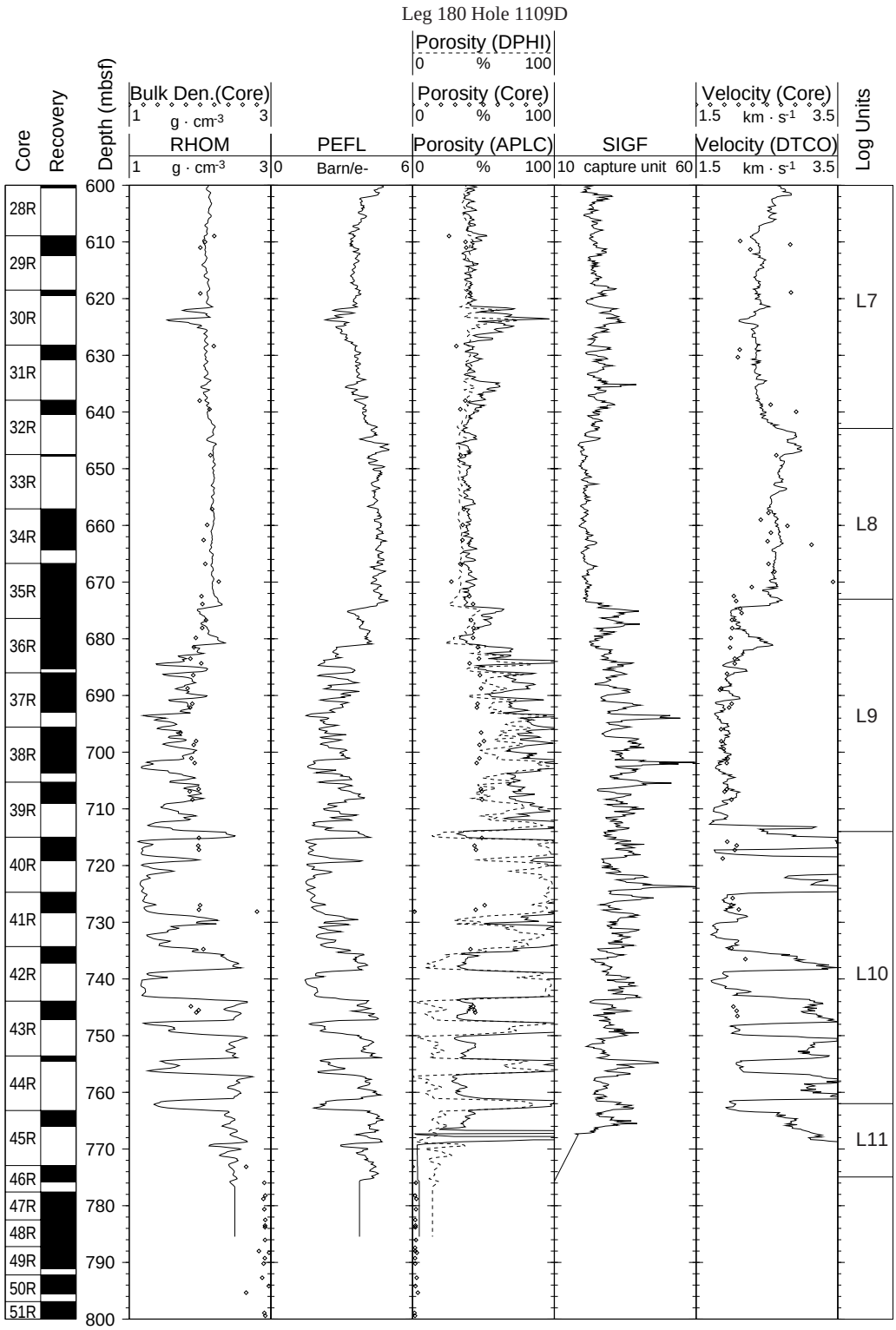

Figure F89. Hole 1109D total gamma ray (HSGR) from the triple combo at the mudline after depth shifts as given in Table T19, p. 295.

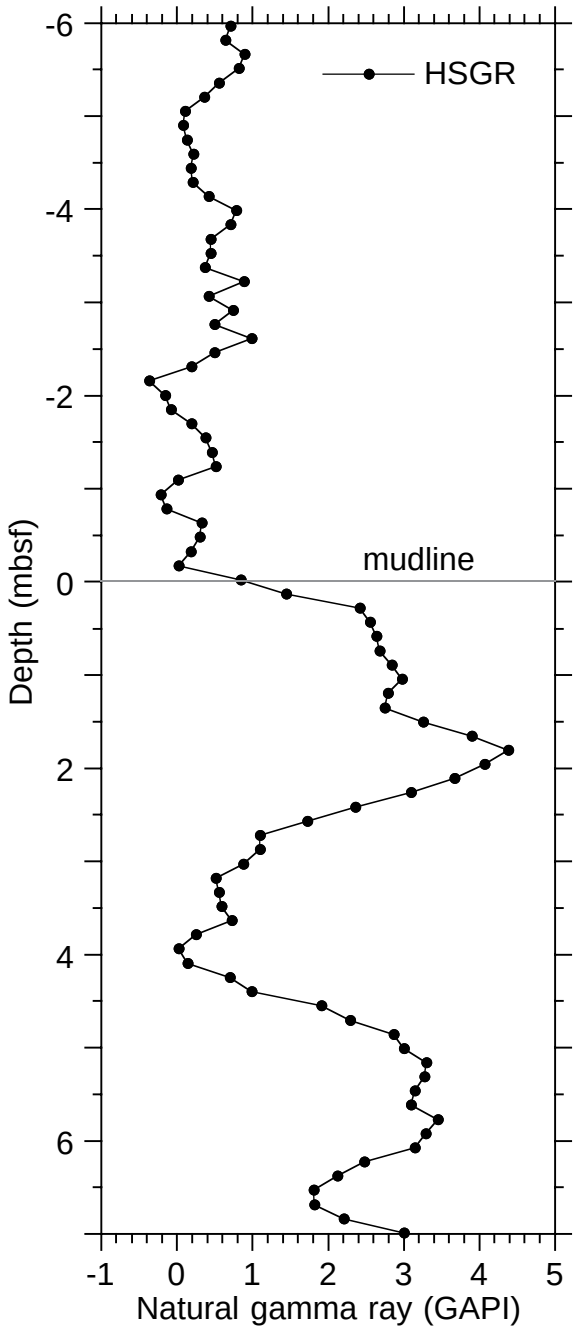

Figure F90. Hole 1109D total gamma ray from the triple combo (HSGR) and FMS sonic string first run (SGR) after depth shifts as given in Table T19, p. 295.

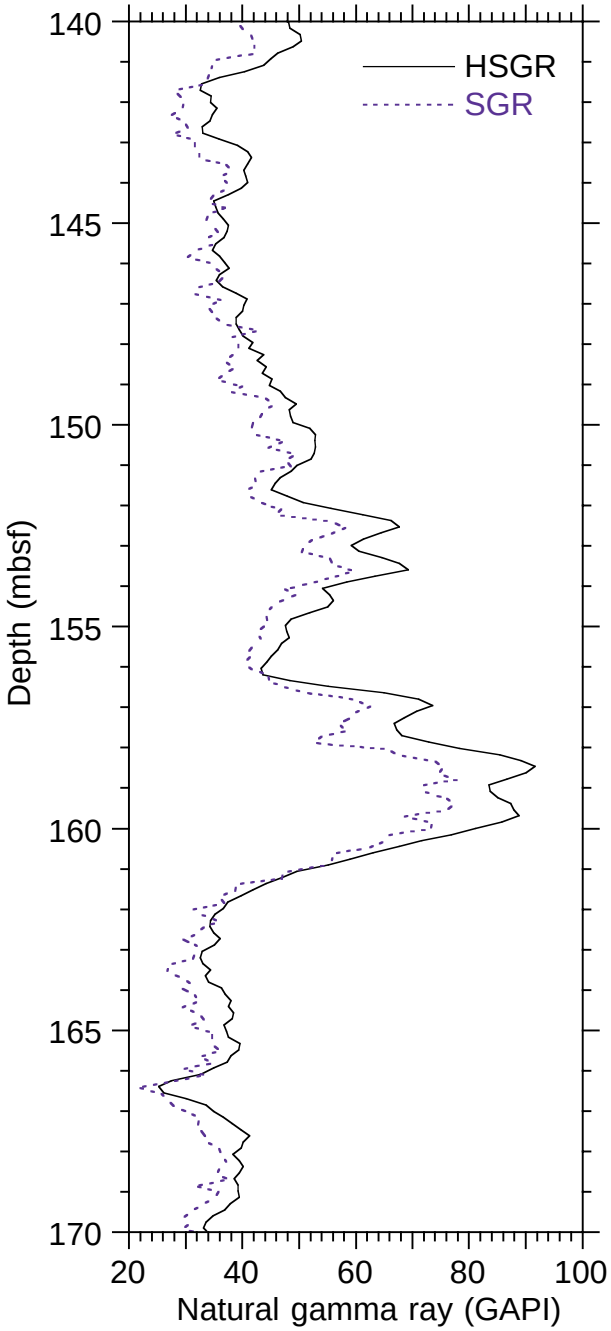

Figure F91. Hole 1109D total gamma ray from the triple combo (HSGR) and FMS sonic string second run (SGR) after depth shifts as given in Table T19, p. 295.

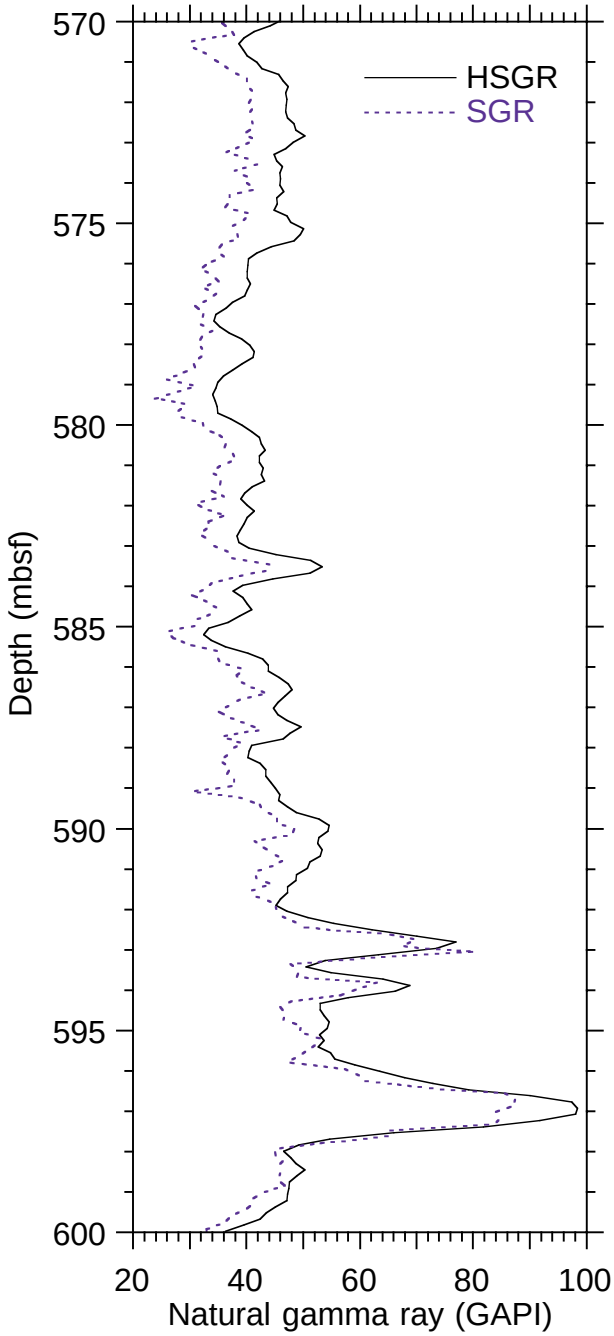

Figure F92. Lithologic units derived from logging response in Hole 1109D and core analysis in Holes 1109C and 1109D. From left to right: core recovery; natural gamma ray (HSGR); density (DPHI) and neutron (APLC) porosity; units defined by the logging response; lithostratigraphic units (defined in **"Lithostratigraphy,"** p. 7); paleodepth (defined in **"Biostratigraphy,"** p. 43); fault zones (defined in **"Structural Geology,"** p. 38); schematic hole size derived from caliper; and intervals corresponding to the detailed logs of Figures **F93,** p. 194; **F94,** p. 196; **F95,** p. 198; **F96,** p. 200; the FMS images of Figures **F104,** p. 209; **F105,** p. 210; **F106,** p. 211; **F107,** p. 212; **F108,** p. 213; and the two FMS runs (Table **T19,** p. 295).

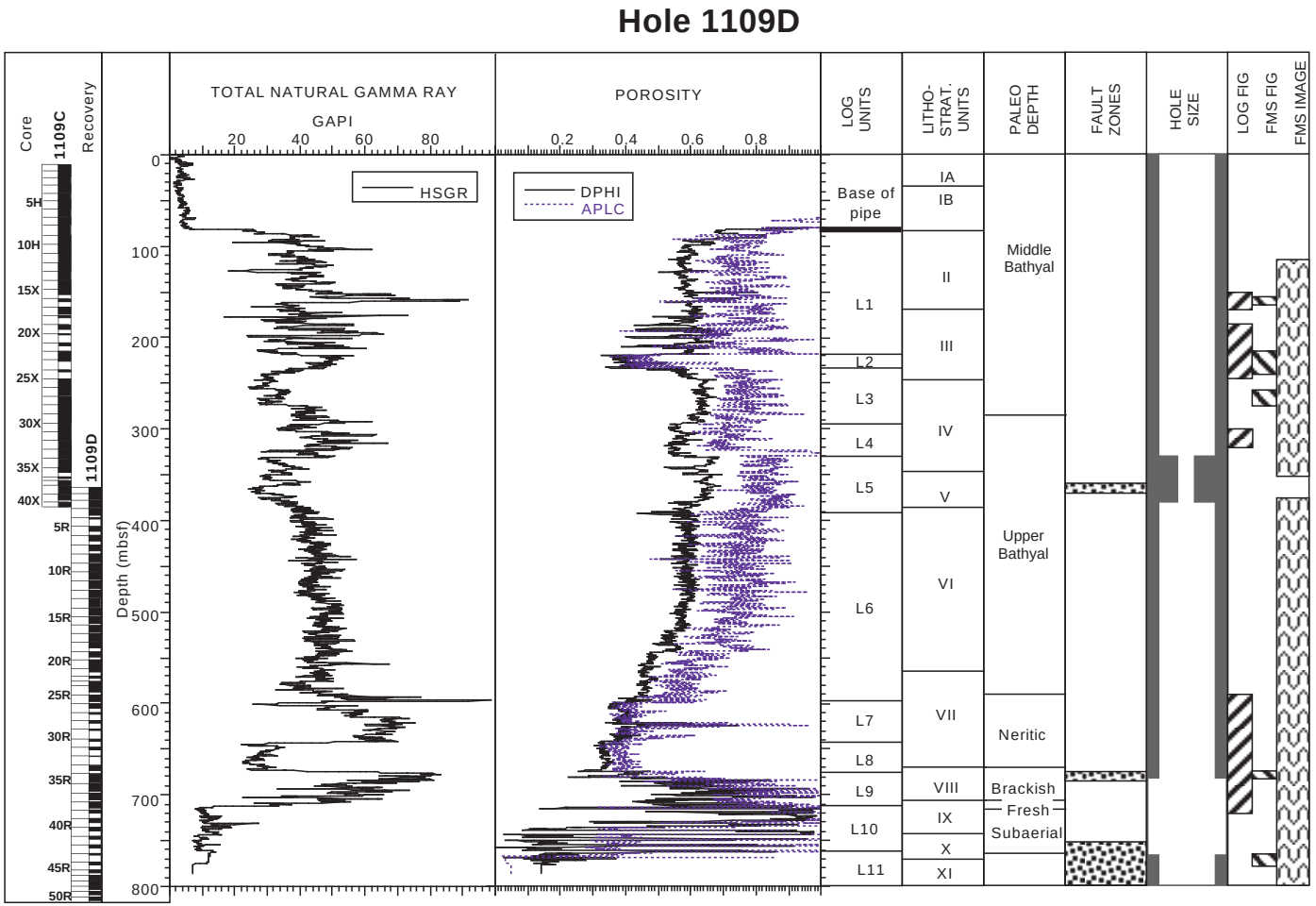

Figure F93. Hole 1109D logs within the 150–170 mbsf interval. **A.** Natural gamma ray (HSGR) and natural gamma ray minus uranium contribution (HCGR). **B.** Neutron (APLC) and density (DPHI) porosity. **C.** Photoelectric effect (PEFL). (Continued on next page.)

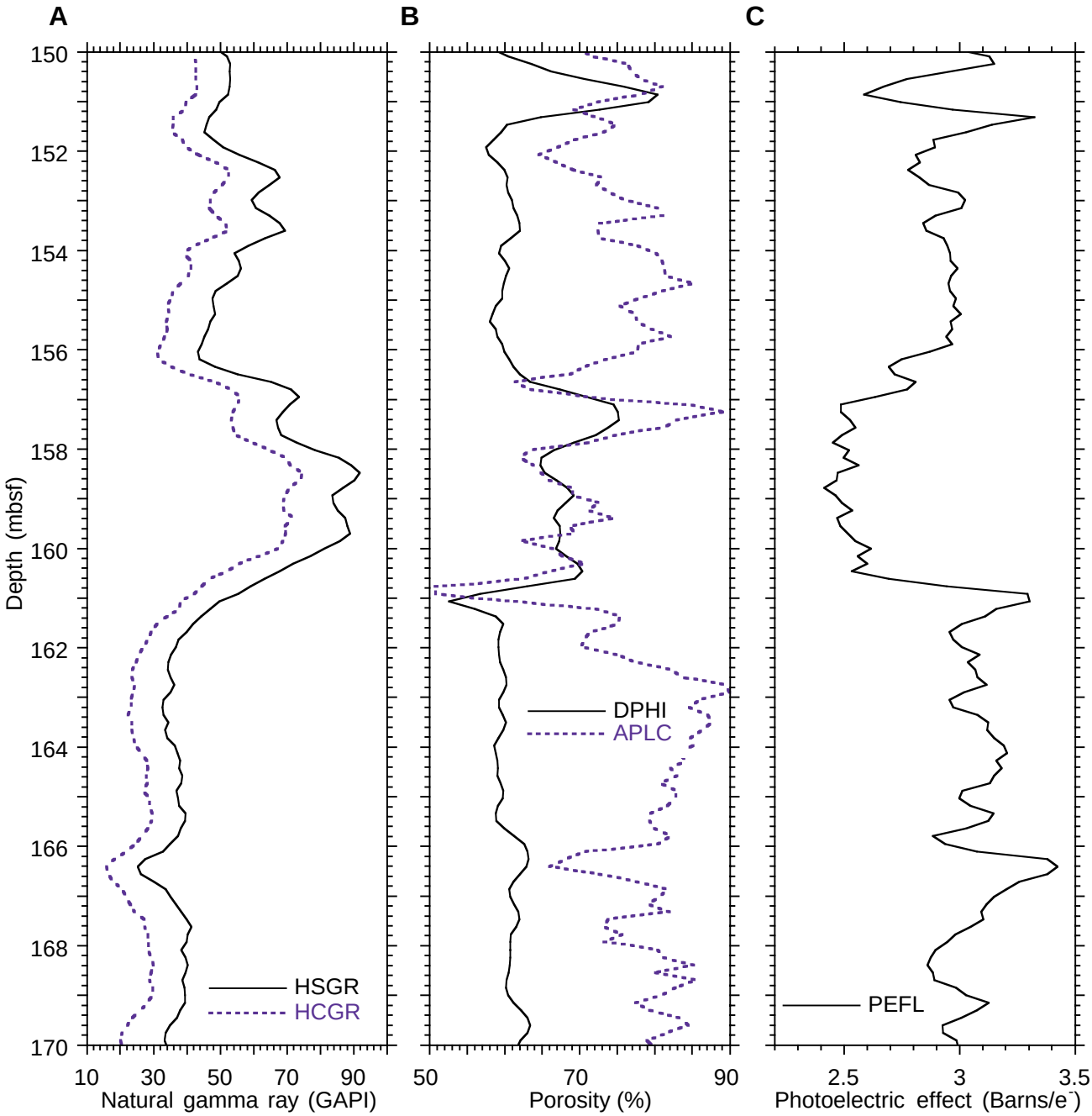

Figure F93 (continued). D. Resistivity from deep (IDPH) and medium (IMPH) induction, and from shallow spherically focused current (SFLU). **E.** Sonic velocity from array sonic tool (DTCO). A carbonate-rich layer at 161 mbsf is overlain by a clean radioactive layer extending from 161 to 158 mbsf.

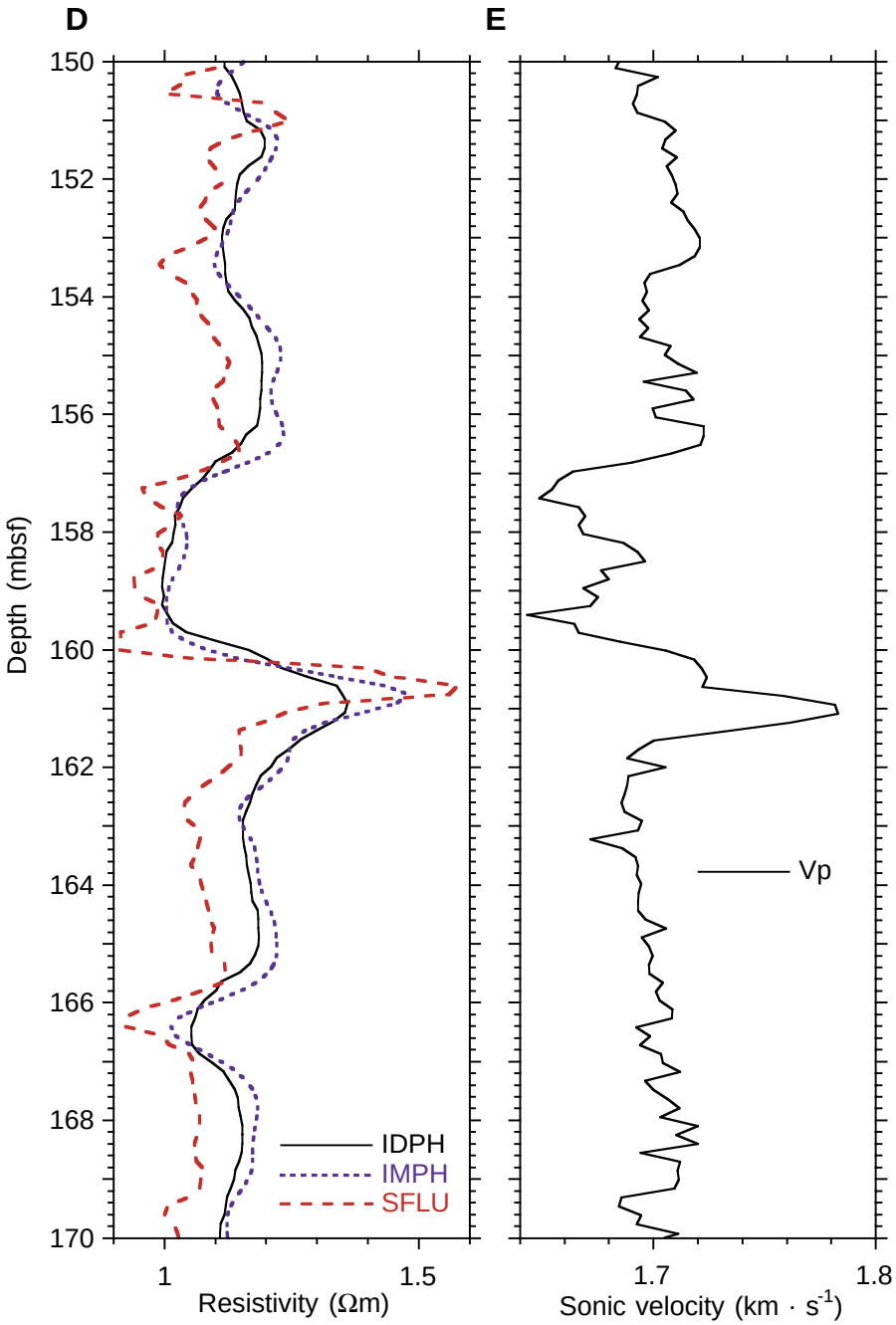

Figure F94. Hole 1109D logs within the 185–245 mbsf interval. **A.** Natural gamma ray (HSGR) and natural gamma ray minus uranium contribution (HCGR). **B.** Neutron (APLC) and density (DPHI) porosity. **C.** Photoelectric effect (PEFL). (Continued on next page).

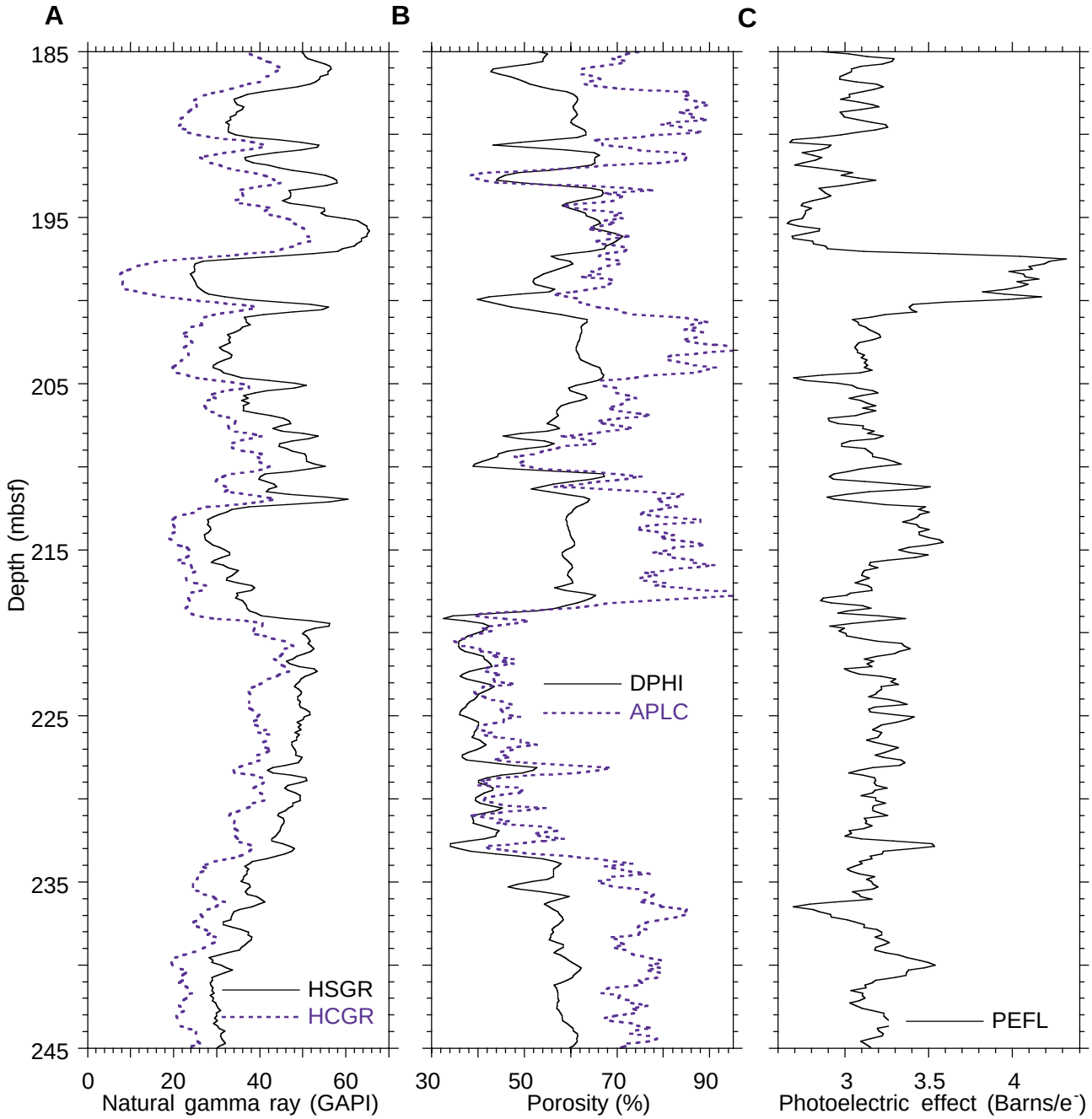

Figure F94 (continued). D. Resistivity from deep (IDPH) and medium (IMPH) induction, and from shallow spherically focused current (SFLU). **E.** Sonic velocity. **F.** Grain size from core observations. A carbonate-rich layer at 201–197 mbsf is overlain by a clean radioactive layer extending from 197 to 193 mbsf. The thick clean layer from 234 to 219 mbsf is defined as Unit L2 and corresponds to high sonic velocity and resistivity and to an increase in grain size observed in core.

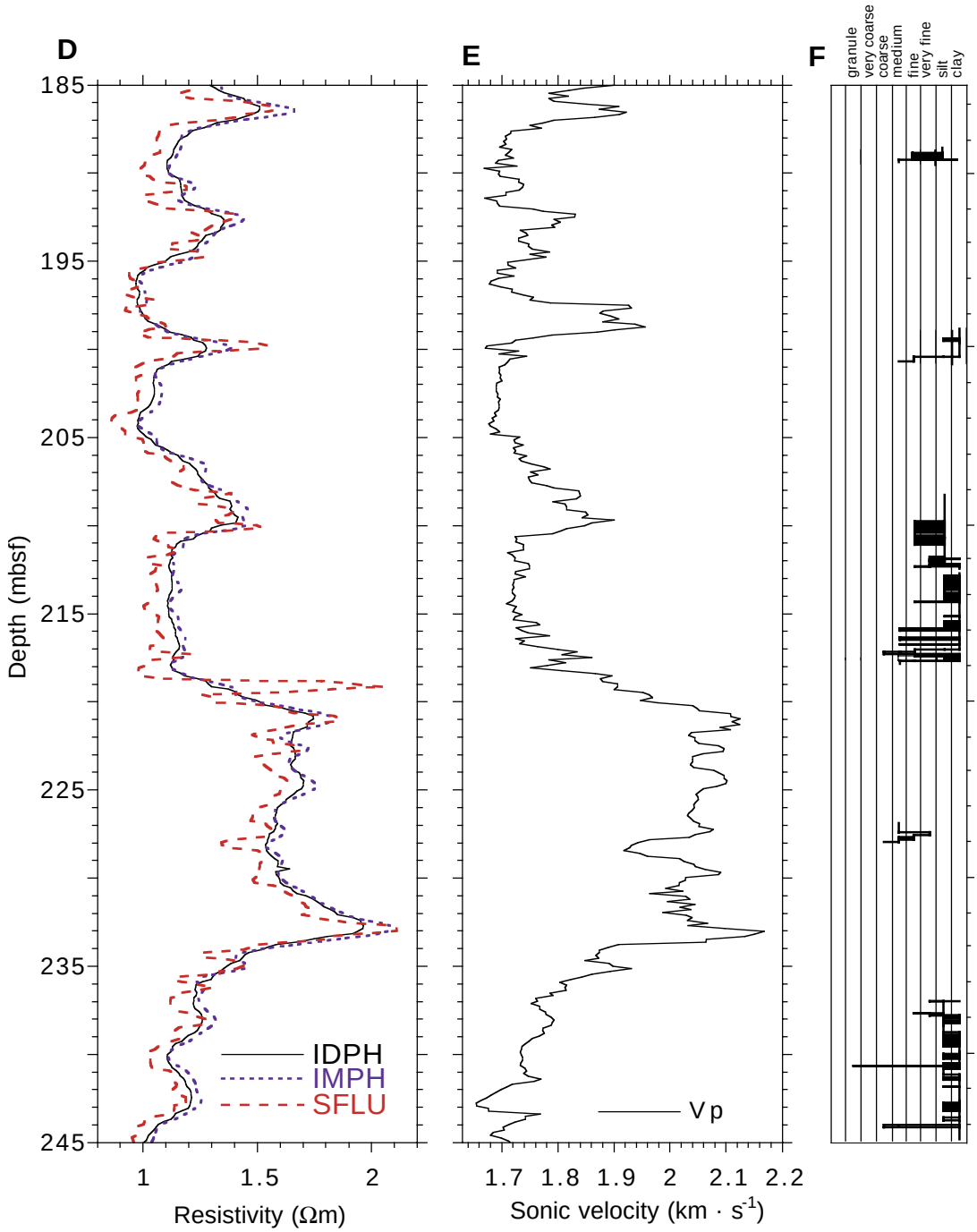

Figure F95. Hole 1109D logs within the 300–320 mbsf clay-rich interval with high gamma-ray values. **A.** Natural gamma ray (HSGR) and natural gamma ray minus uranium contribution (HCGR). **B.** Neutron (APLC) and density (DPHI) porosity. **C.** Photoelectric effect (PEFL). (Continued on next page.)

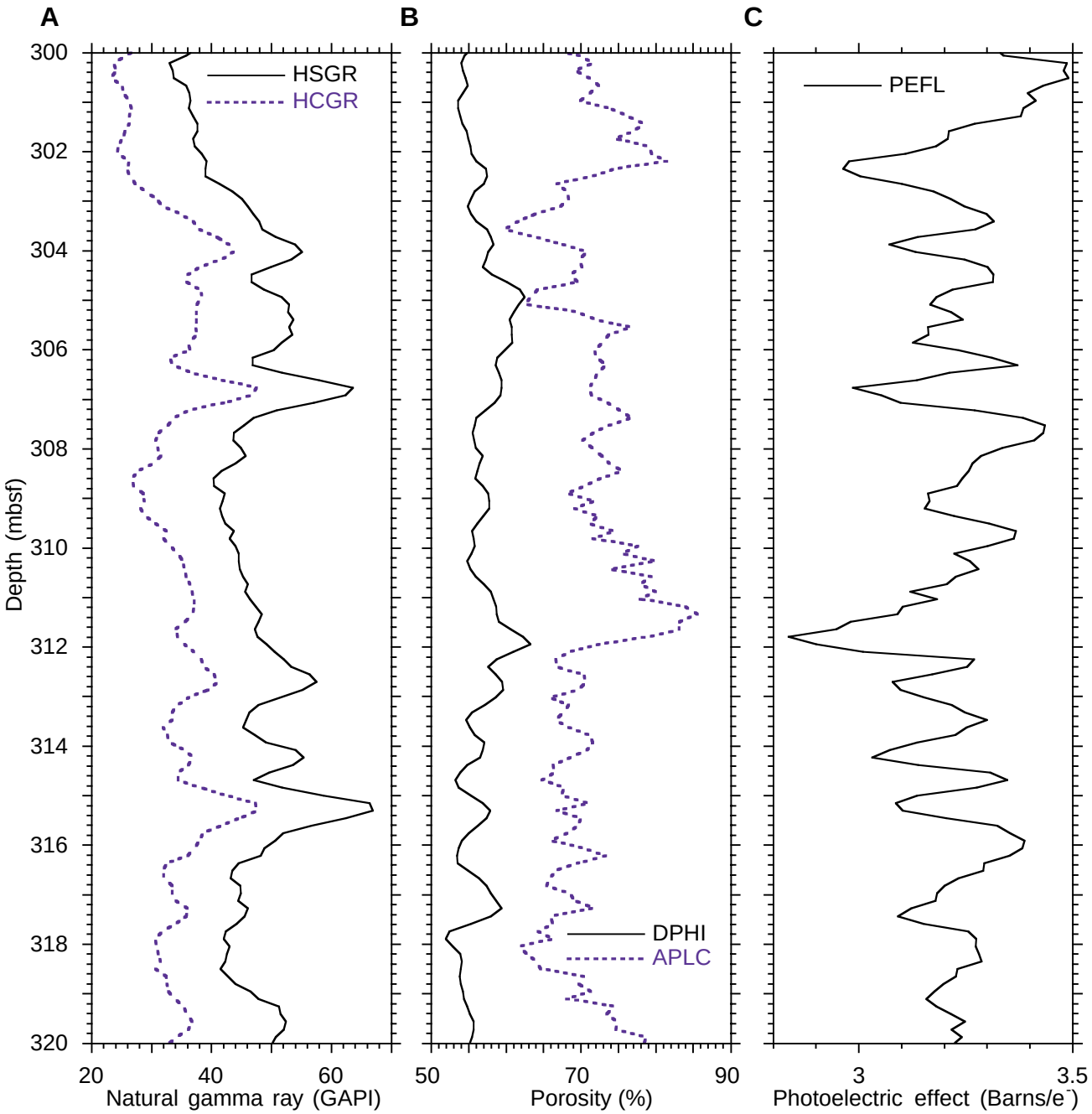

Figure F95 (continued). D. Resistivity from deep (IDPH) and medium (IMPH) induction, and from shallow spherically focused current (SFLU). **E.** Sonic velocity.

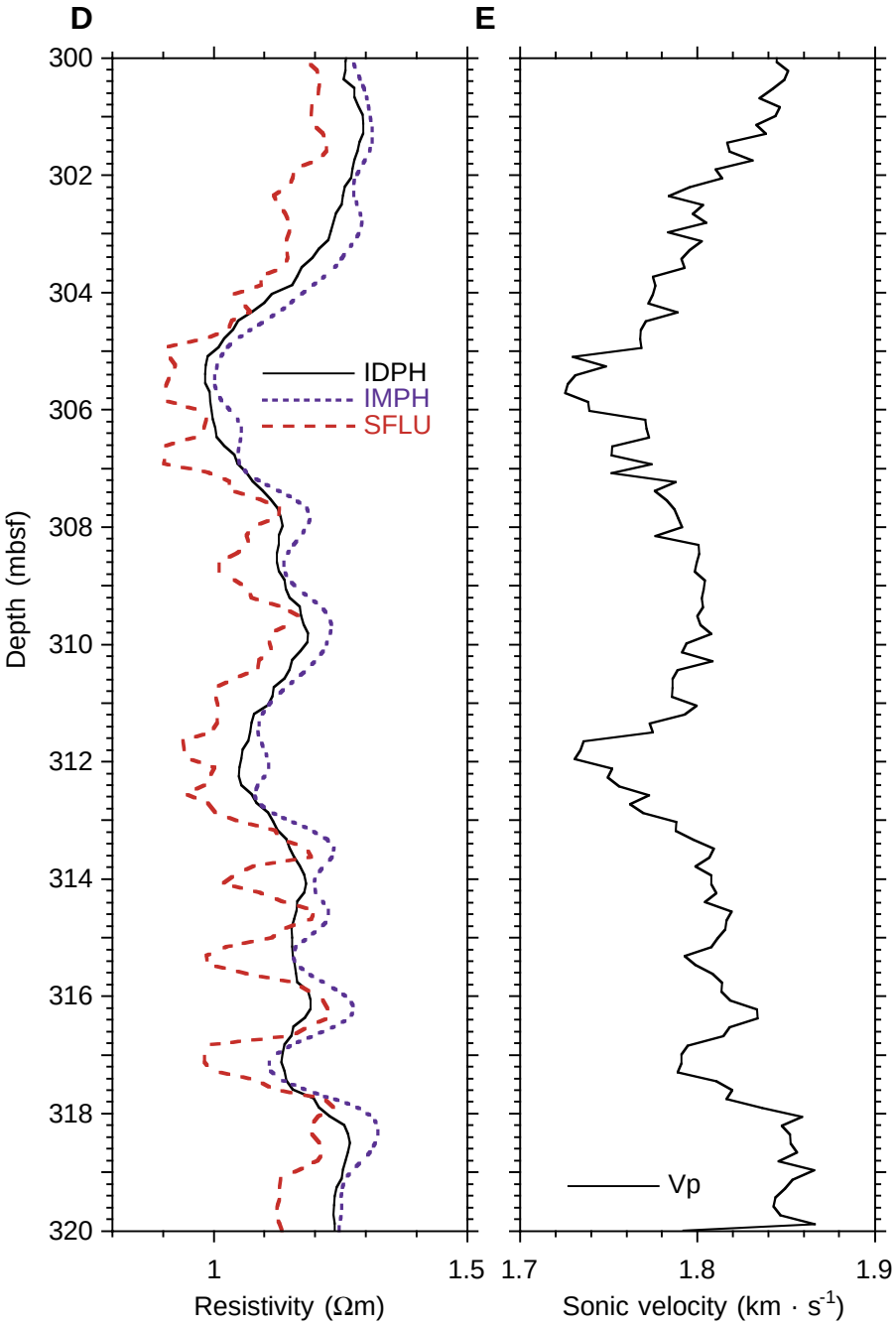

Figure F96. Hole 1109D logs within the 590–720 mbsf interval. **A.** Natural gamma ray (HSGR) and natural gamma ray minus uranium contribution (HCGR). **B.** Neutron (APLC) and density (DPHI) porosity. **C.** Photoelectric effect (PEFL). The clean interval from 673 to 599 mbsf is composed of a carbonate-rich lower unit (Unit L8) and a radioactive sand upper unit (Unit L7). (Continued on next page).

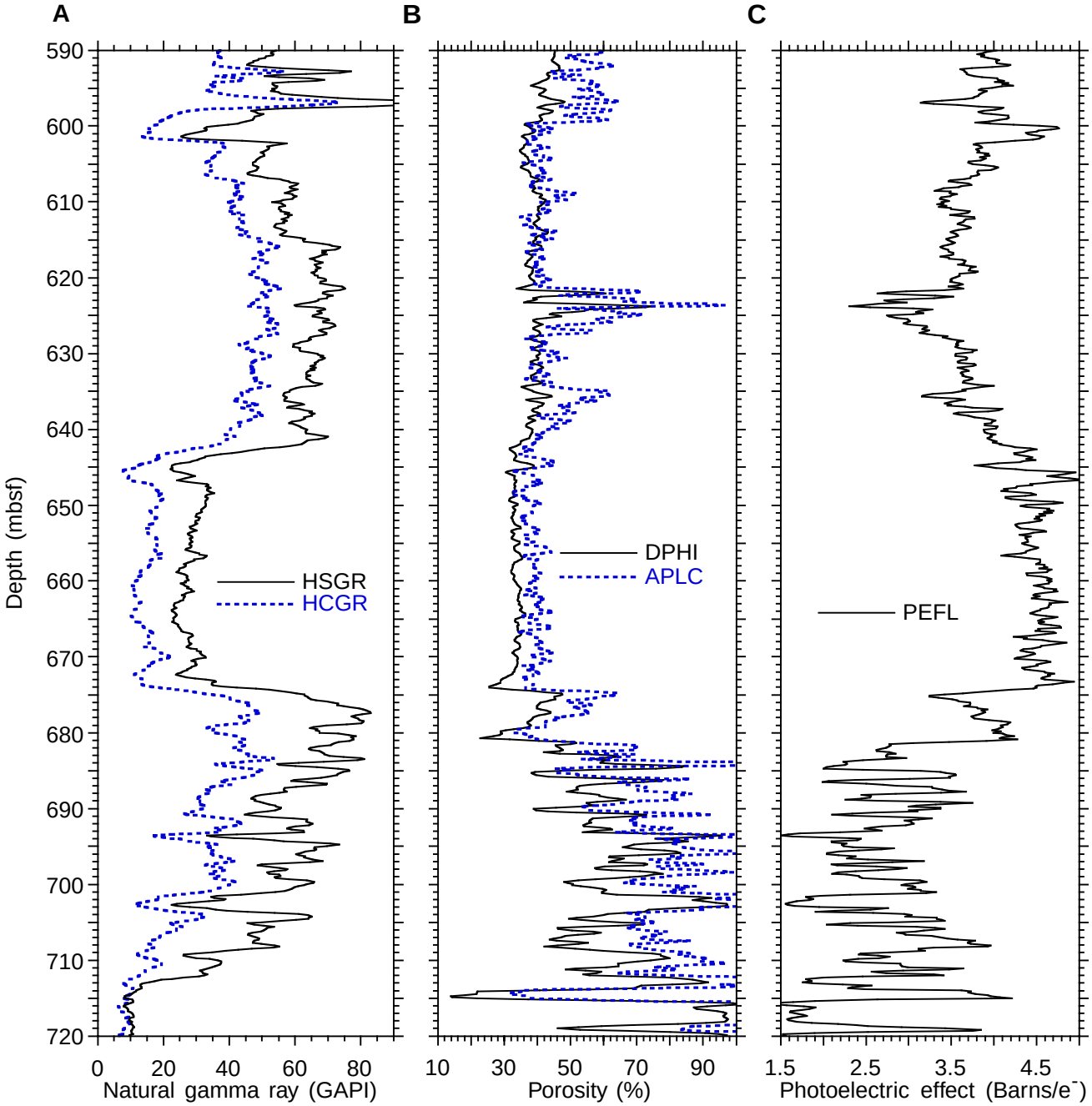

Figure F96 (continued). D. Resistivity from deep (IDPH) and medium (IMPH) induction, and from shallow spherically focused current (SFLU). **E.** Sonic velocity.

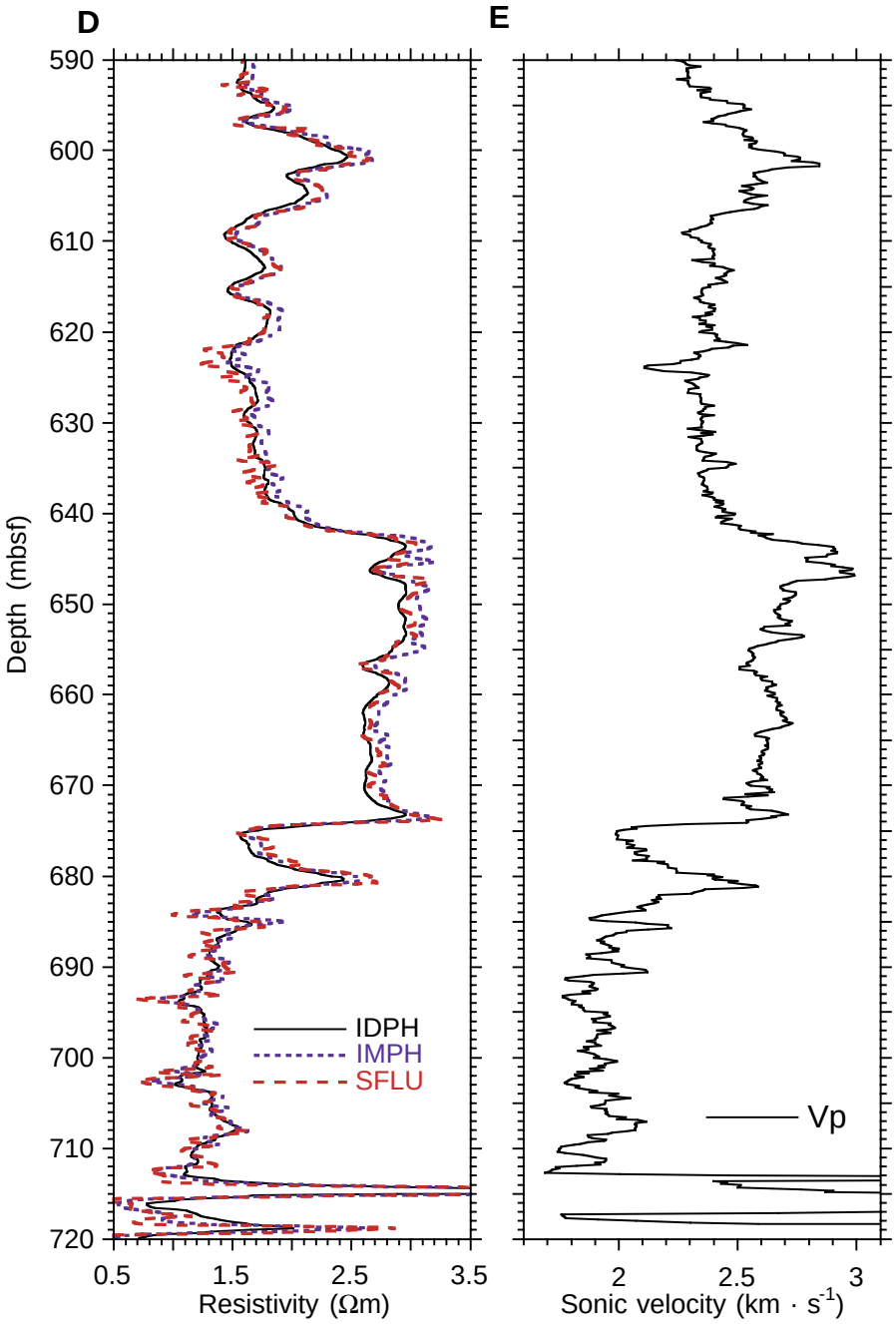

Figure F97. Hole 1109D borehole deviation.

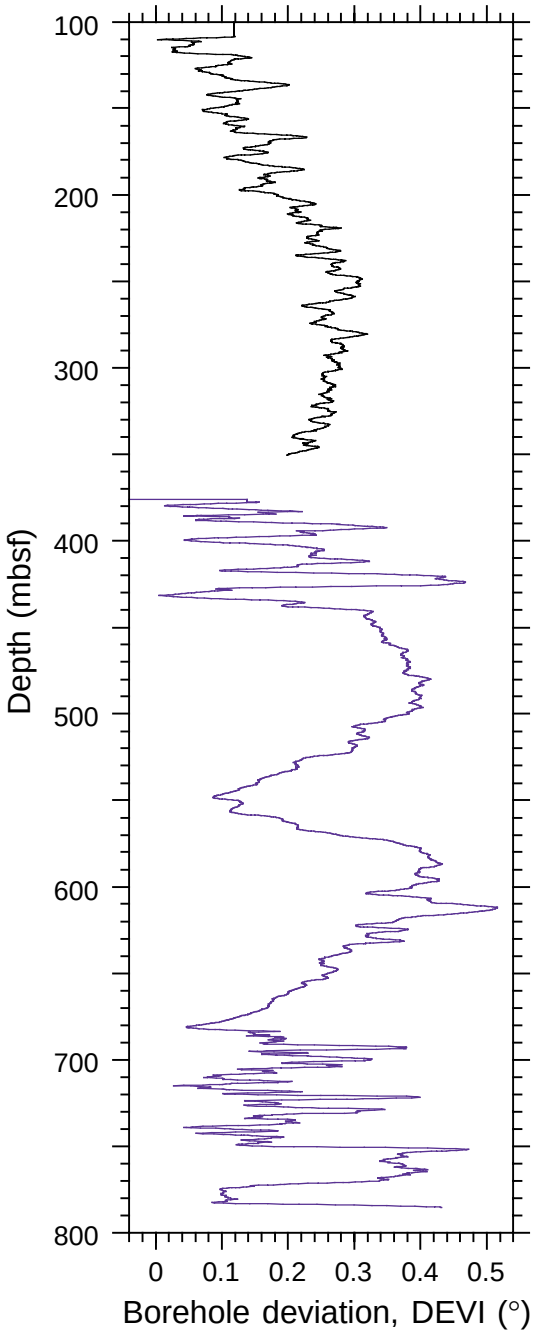

Figure F98. Hole 1109D FMS tool string acceleration.

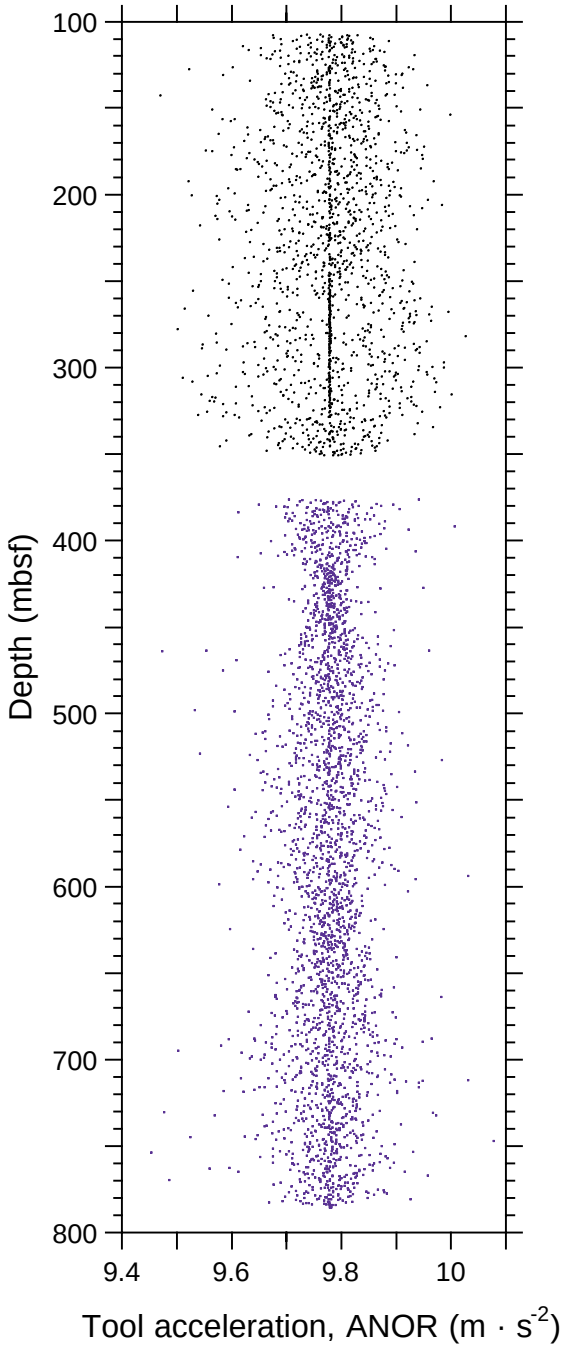

Figure F99. Hole 1109D FMS (C1 and C2) and HLDS (LCAL) caliper data. Note the consistency of the three different passes and the regularly spaced (~9.5 m) washouts that are believed to be caused by the stationary circulation while retrieving the core barrels.

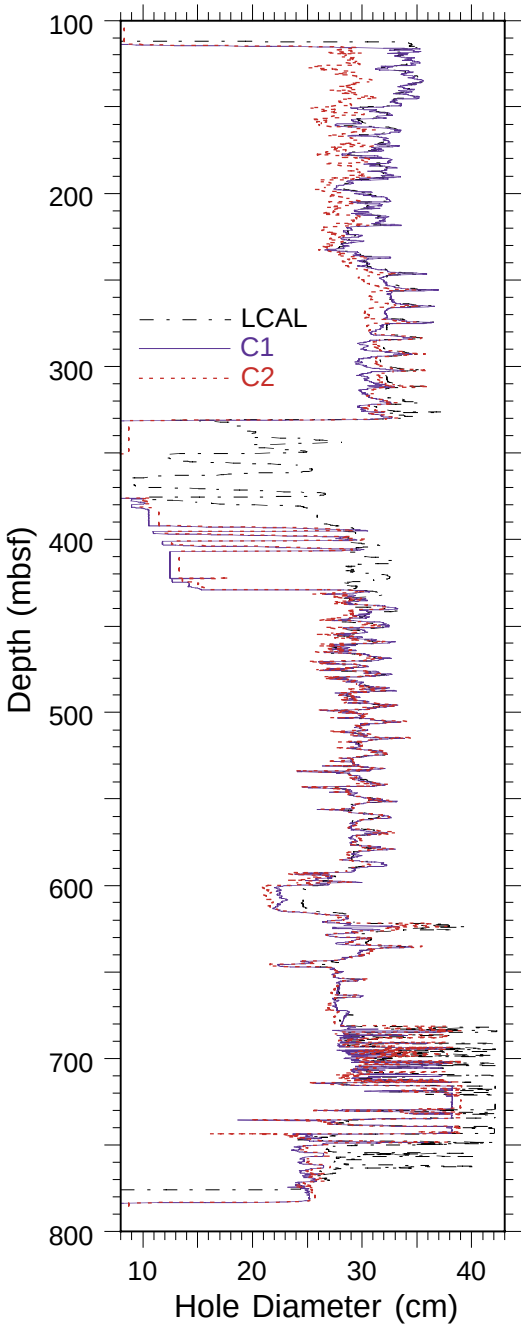

Figure F100. Hole 1109D FMS Pad 1 azimuth (P1AZ) with respect to magnetic north. Note the consistent northward orientation of the largest diameter of the hole in the 300–100 mbsf interval.

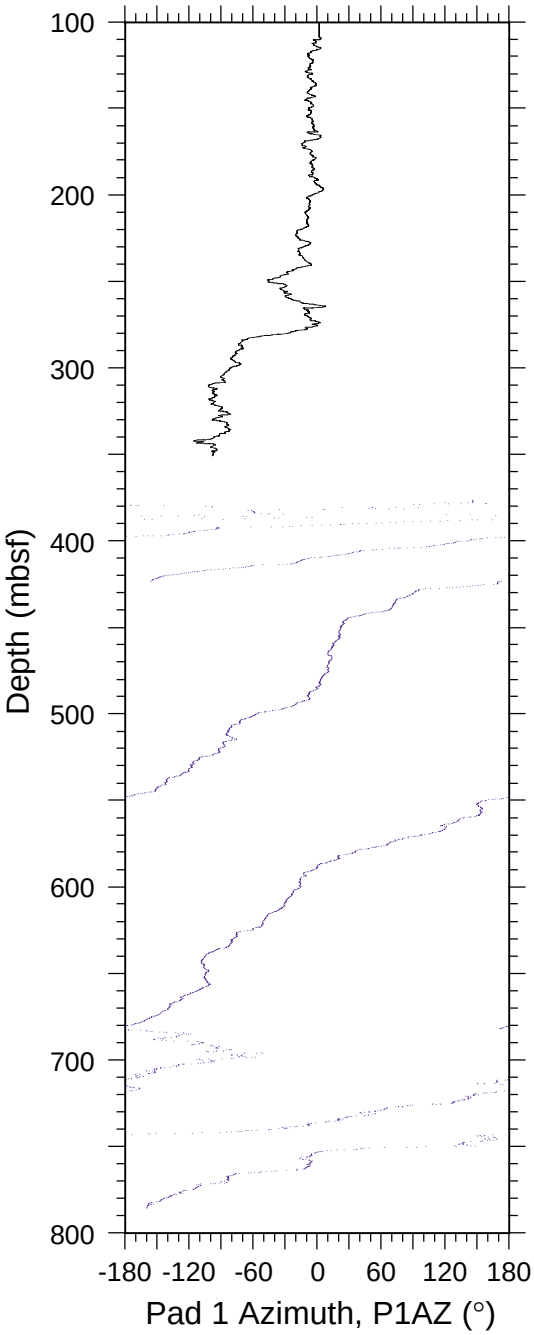

Figure F101. Hole 1109D magnetic inclination (FINC). Note the anomaly associated with Unit L2 (234–219 mbsf).

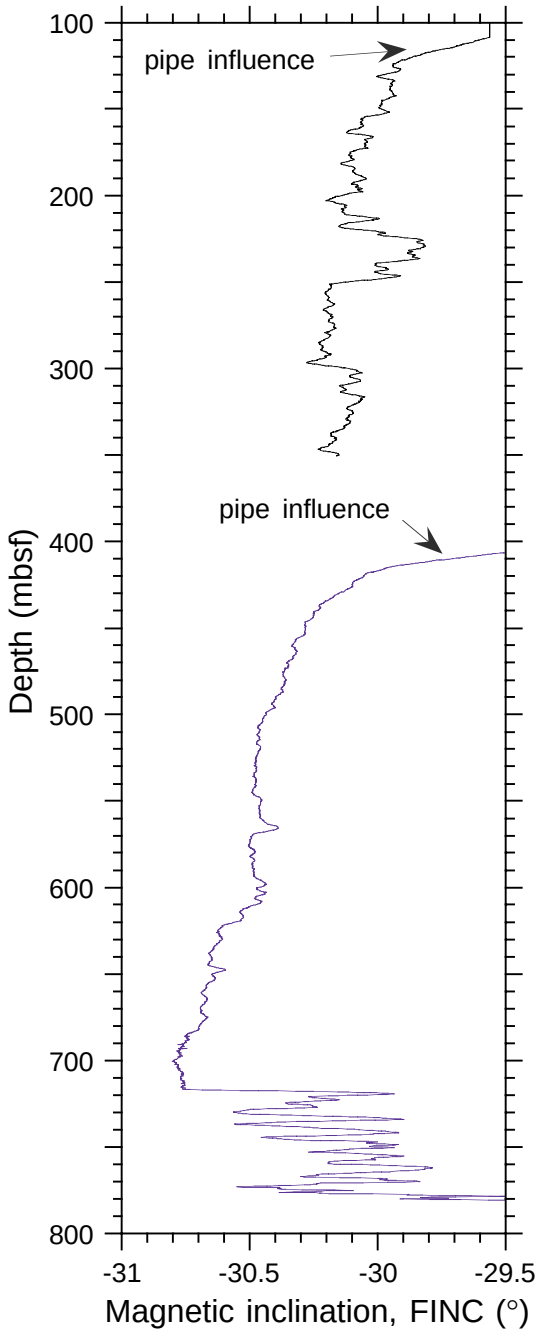

Figure F102. Hole 1109D magnetic intensity (FNOR).

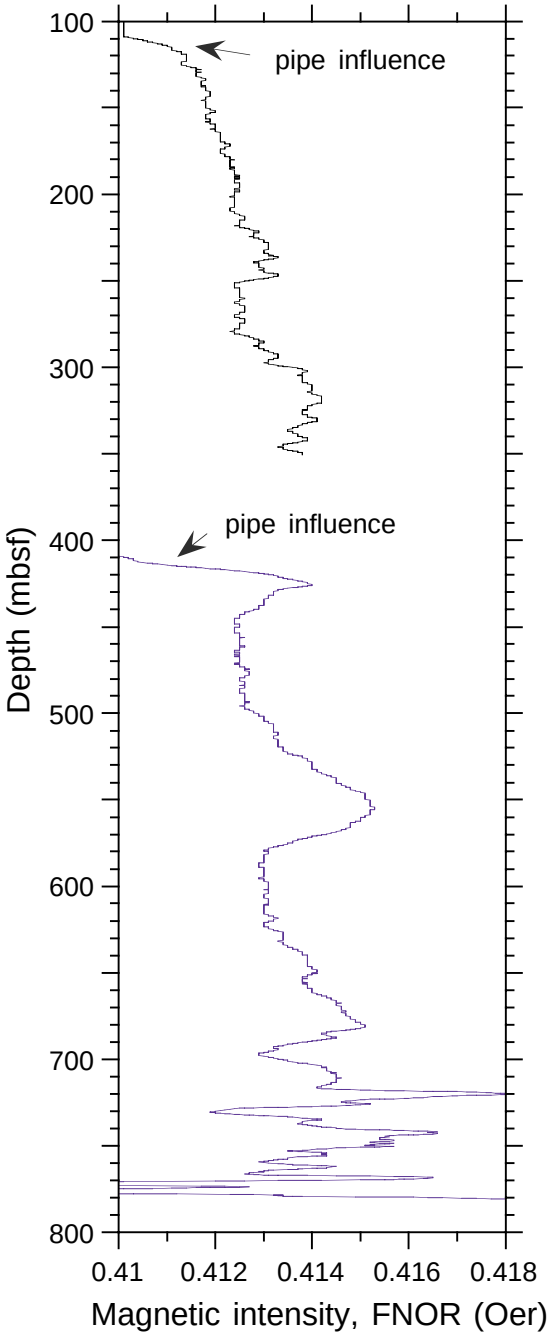

Figure F103. Dip direction histogram that was calculated from dipping beds interpreted from the Hole 1109D FMS images shows that bed dip directions range from south-southeast to south-southwest.

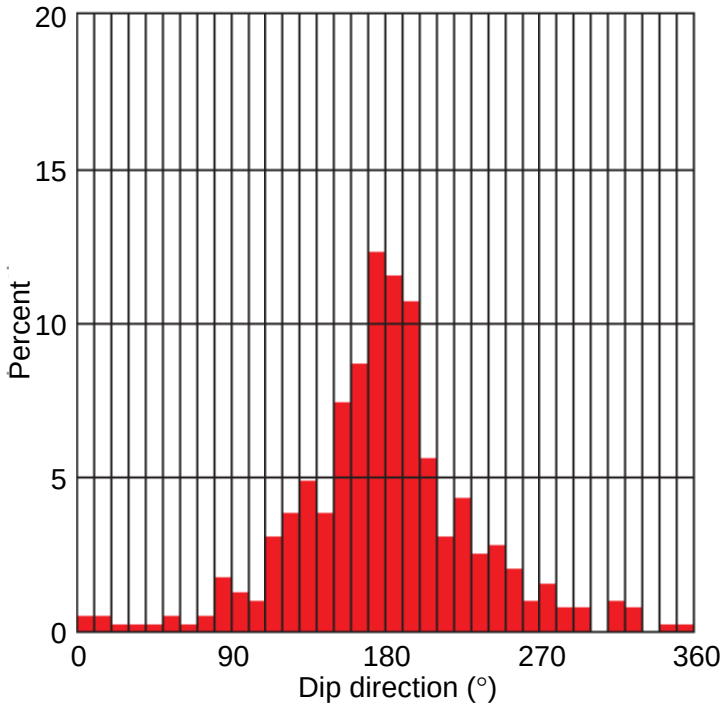

Figure F104. Hole 1109D statically normalized FMS image shows the highly resistive, sandy base of a turbidite unit at 161.5 mbsf that grades upward to more conductive clays at 157 mbsf. The well-defined base of this unit correlates with the lithostratigraphic Unit II/III boundary (see **"Lithostratigraphy,"** p. 7). Vertical scale = 1:40.

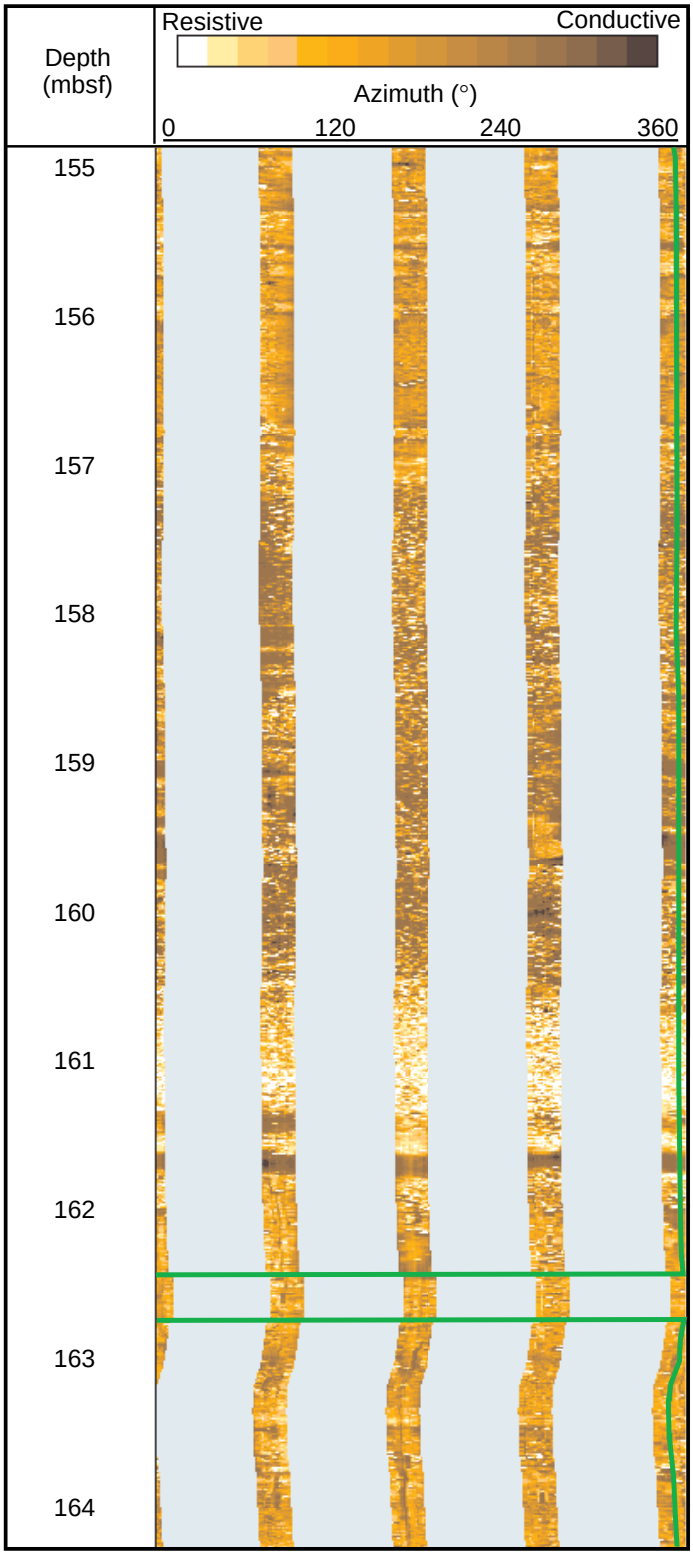

Figure F105. Hole 1109D statically normalized FMS image showing the sharp contrast in resistivity of Unit L2 (219–234 mbsf) relative to the surrounding material, which clearly defines the boundaries of this unit. Vertical scale = 1:120.

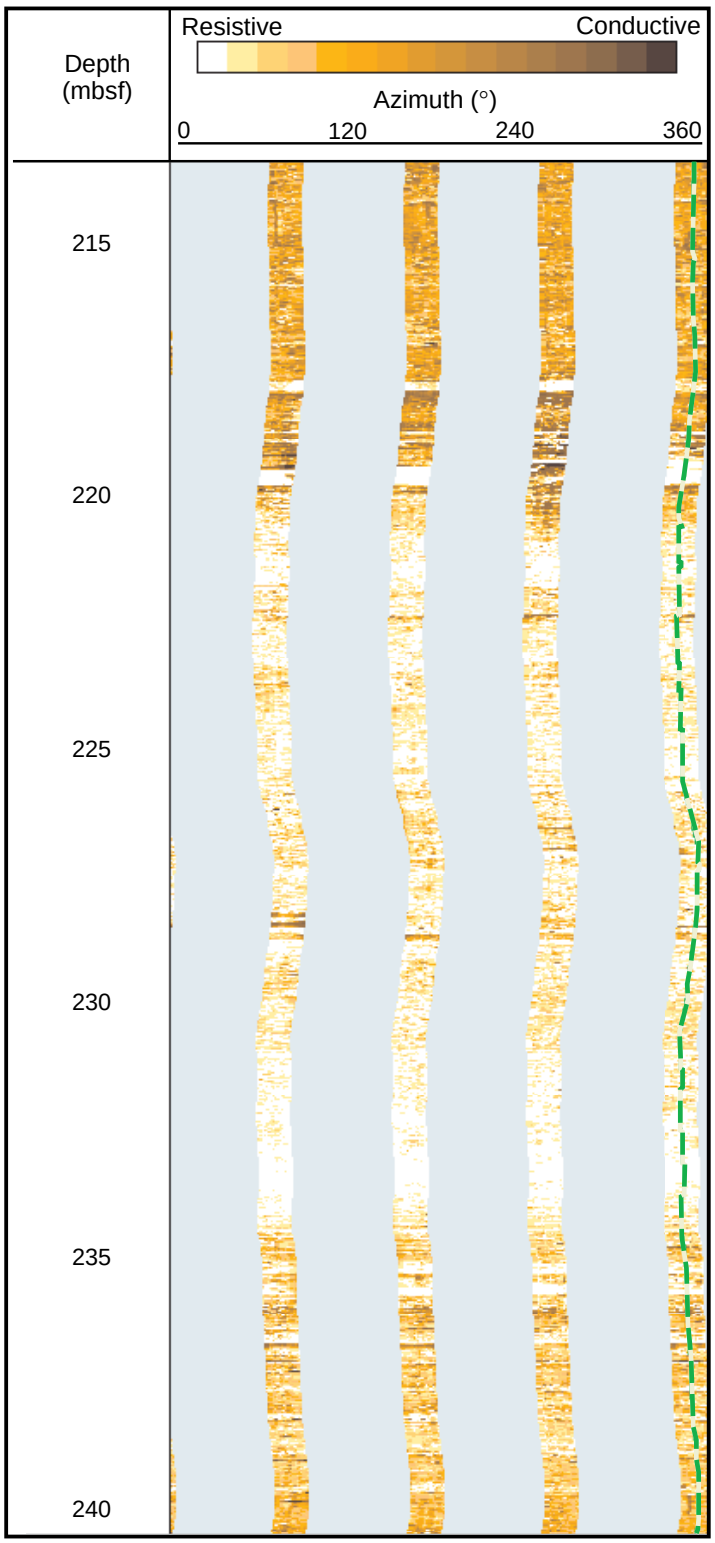

Figure F106. Hole 1109D dynamically normalized FMS image of steep (~50°–65°), southwest-dipping beds located within Unit L3. Tadpole position indicates dip, and tail points toward the dip direction of selected planar features. Vertical scale = 1:40.

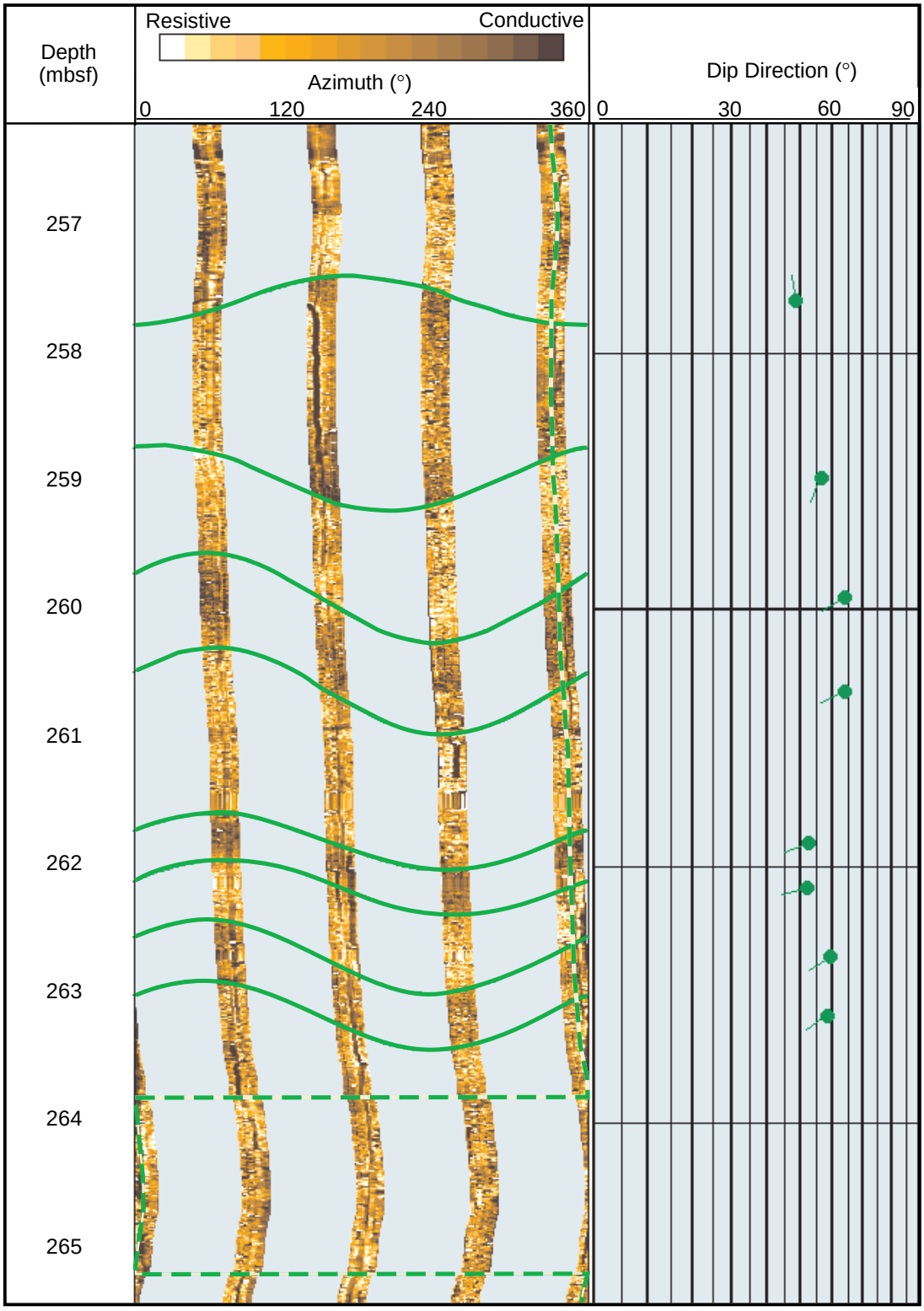

Figure F107. Hole 1109D statically (left) and dynamically (right) normalized FMS images of a single turbidite unit located within Unit L9. The bright resistive layer at 681 mbsf defines the base of the turbidite unit that fines upward to more conductive, clayey thin laminations at ~675 mbsf. Vertical scale = 1:40.

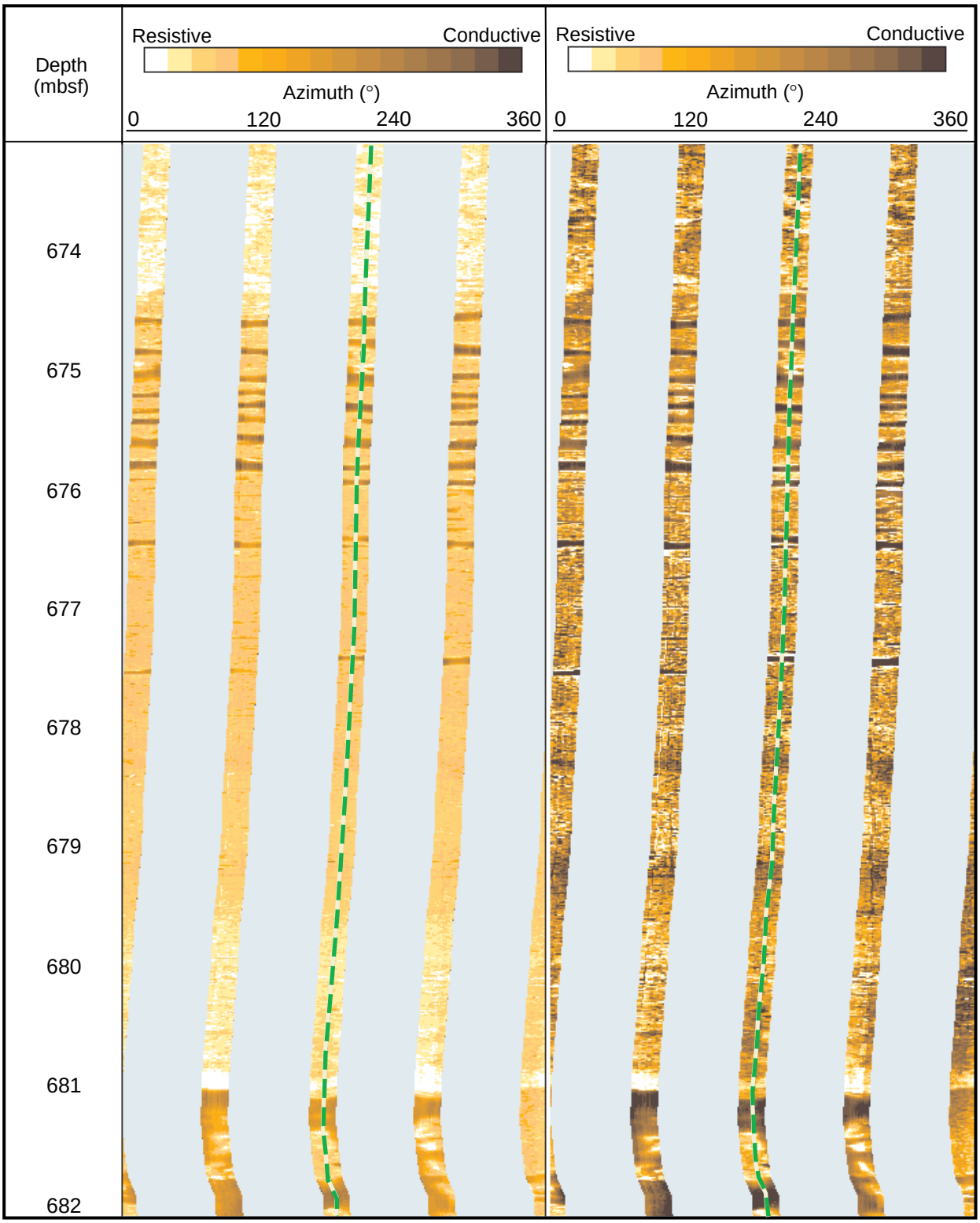

Figure F108. Hole 1109D dynamically normalized FMS image showing the contact between the conglomerate and dolerite at 776.5 mbsf. Large, rounded resistive nodules above 776.5 mbsf represent clasts within a more conductive matrix. Dynamic normalization enhances the numerous fractures located throughout the dolerite. Vertical scale = 1:20.

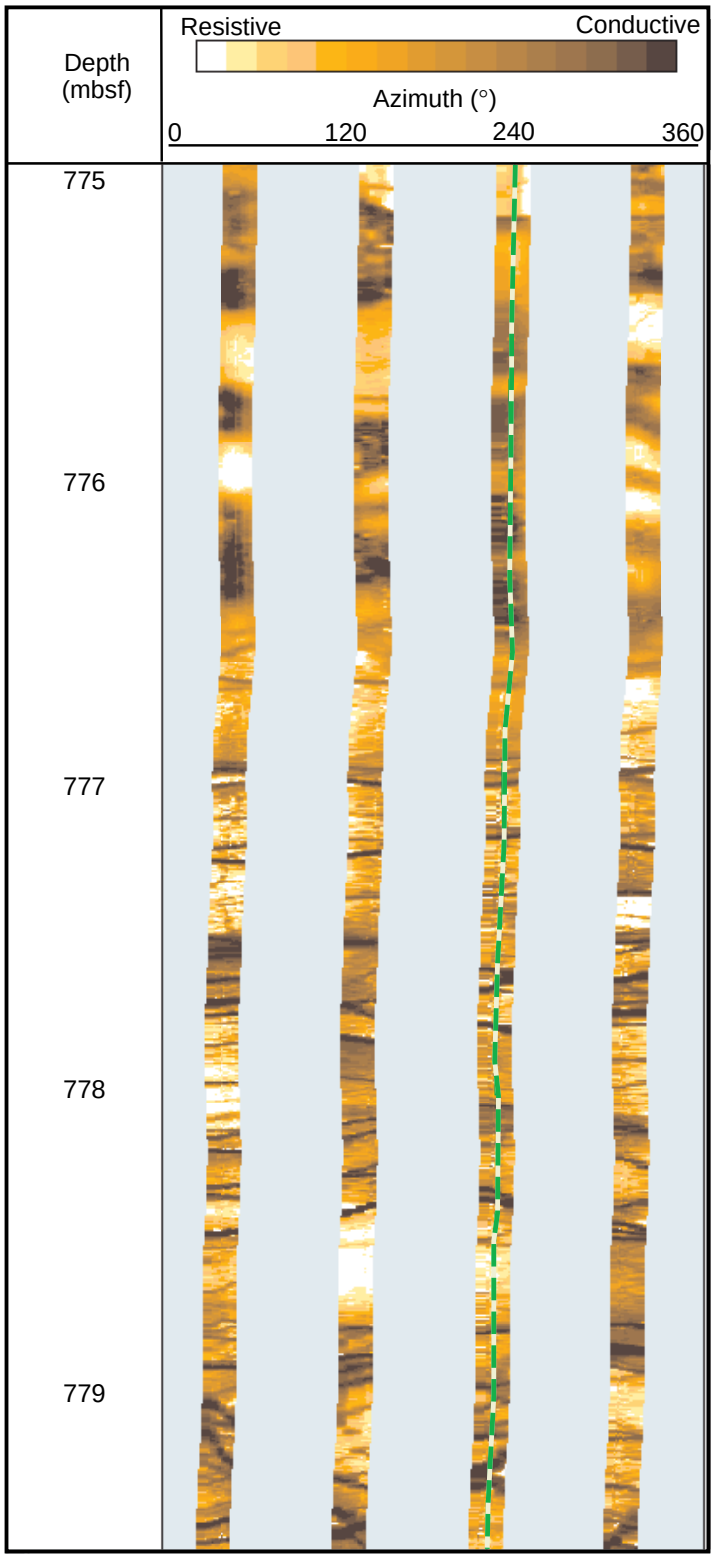

Figure F109. Hole 1109D, all TLT data. T_{fast} and T_{slow} refer to the fast and slow thermistors, respectively. The log started on the way down 200 m above seafloor and continued until the tool reached the rig floor.

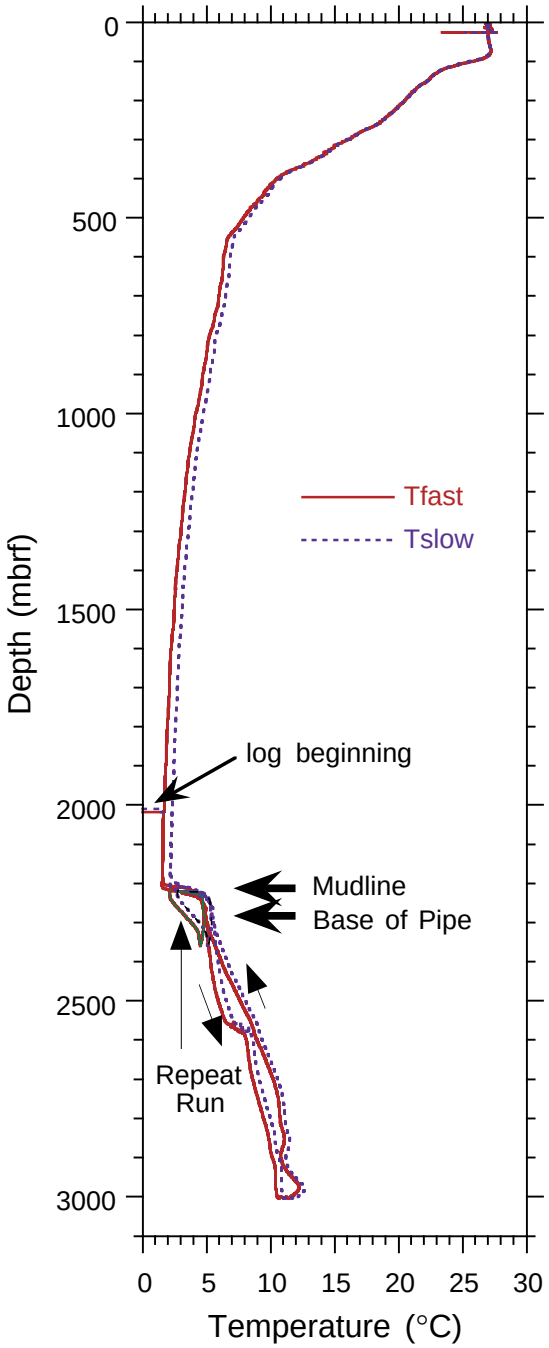

Figure F110. Hole 1109D borehole TLT data. T_{fast} and T_{slow} refer to the fast and slow thermistors, respectively.

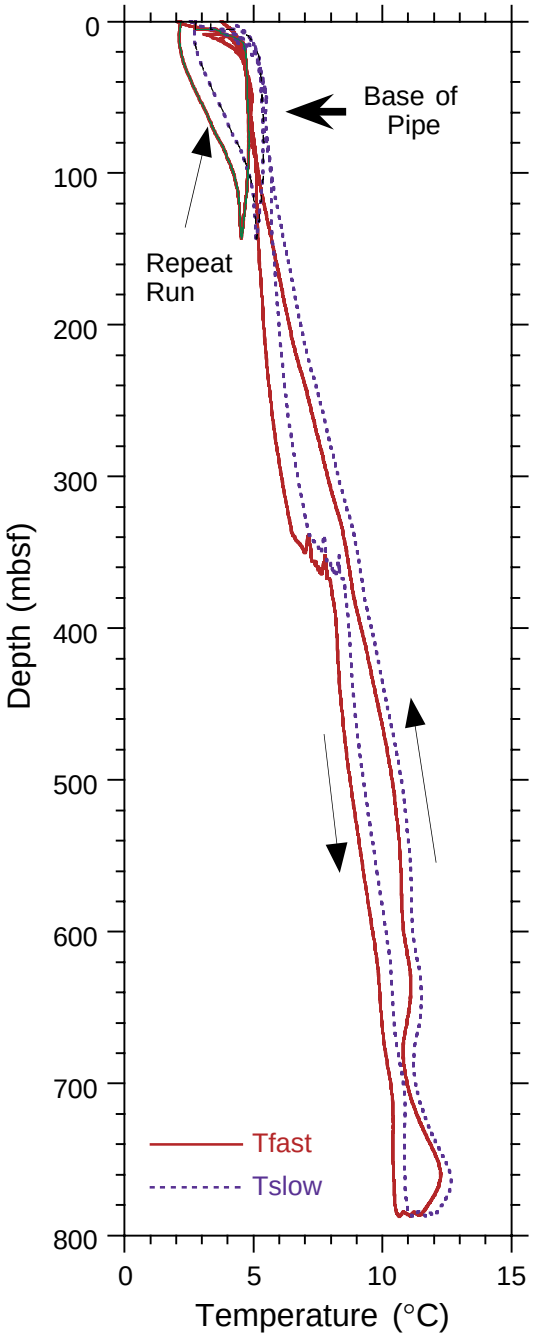

Figure F111. Temperature as a function of time for the Adara temperature runs at (**A**) 26.4 mbsf, (**B**) 45.4 mbsf, (**C**) 64.4 mbsf, and (**D**) 83.4 mbsf. Mudline temperature is marked by a solid line, whereas extrapolated equilibrium temperatures are marked by a dashed line.

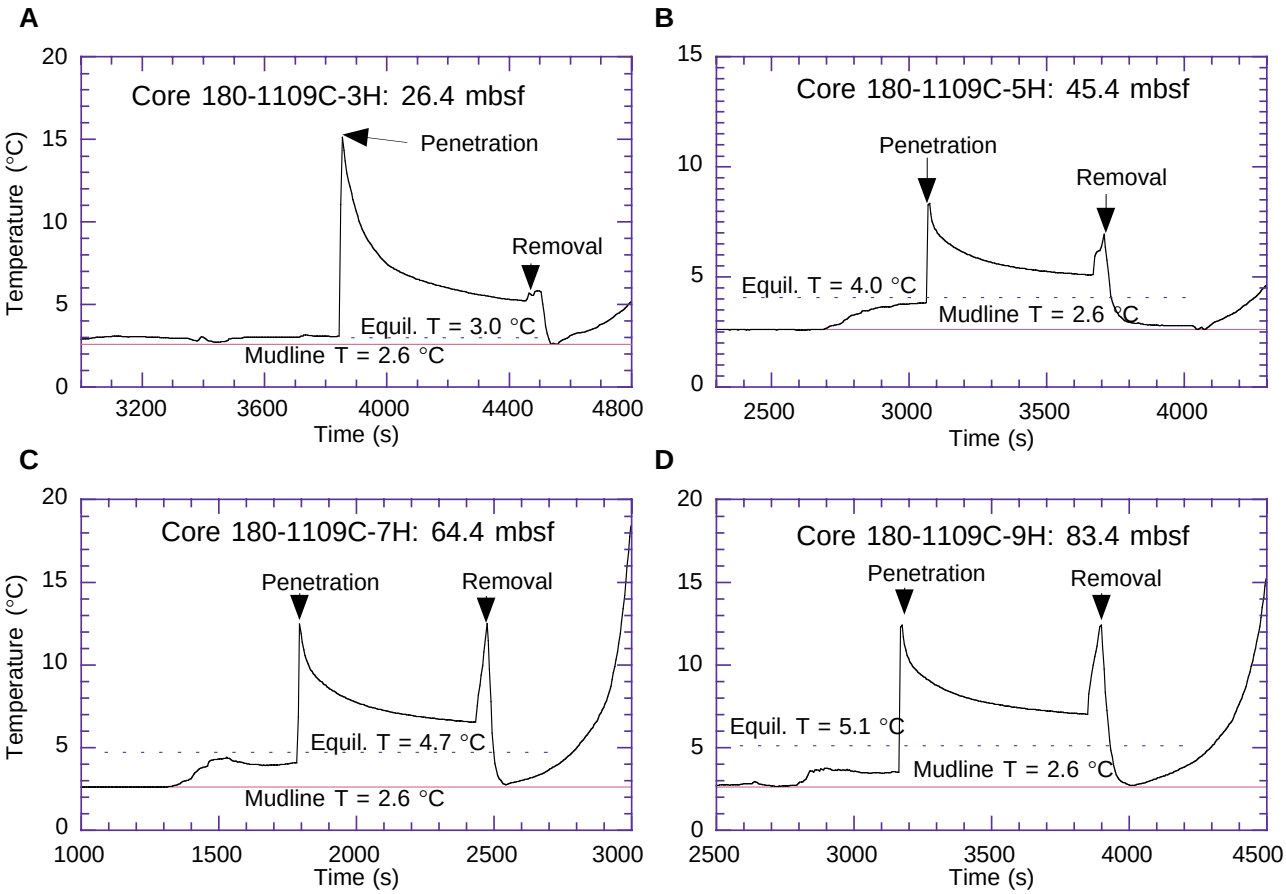

Figure F112. Temperature as a function of time for the DVTP temperature run at 170.8 mbsf. Data from the tip thermistor was used. Mudline temperature is marked by a solid line, whereas extrapolated equilibrium temperature is marked by a dashed line.

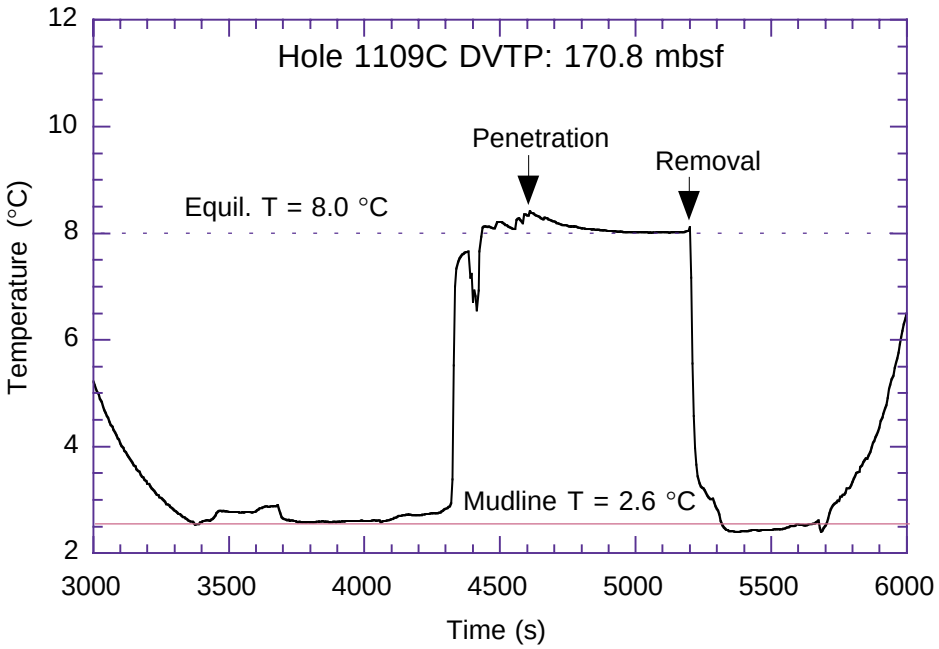

Figure F113. Estimated temperatures as a function of depth, and best-fit linear regression with intercept forced to mudline temperature. Open circles = Adara measurements. Filled circle = DVTP measurement. Computed thermal gradient is the slope of the linear regression line.

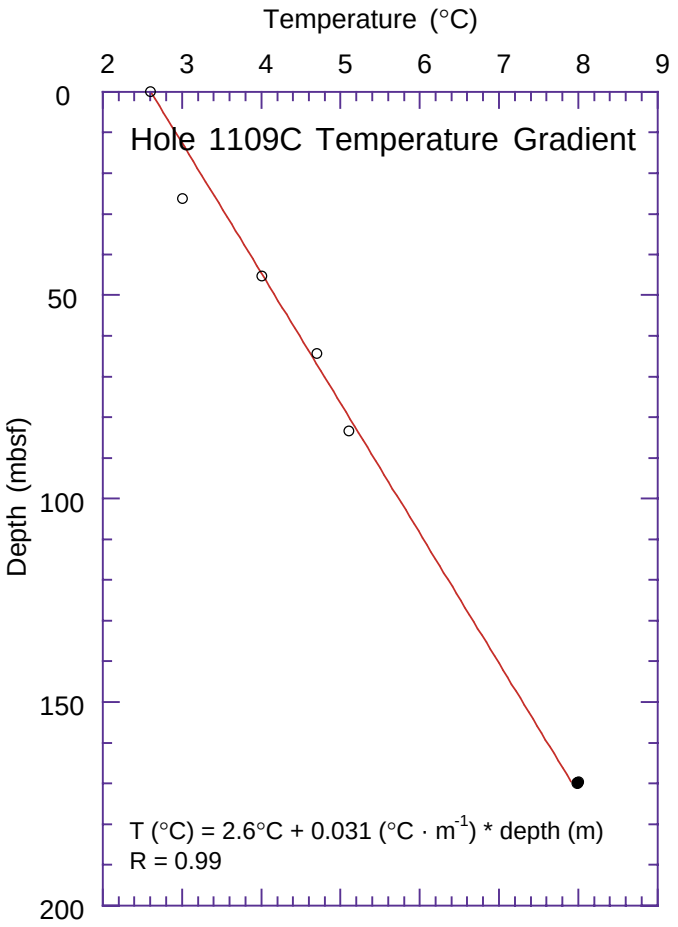

Figure F114. VSP corridor stack, repeated five times and placed between five migrated multichannel seismic (MCS) traces on both sides of Site 1109.

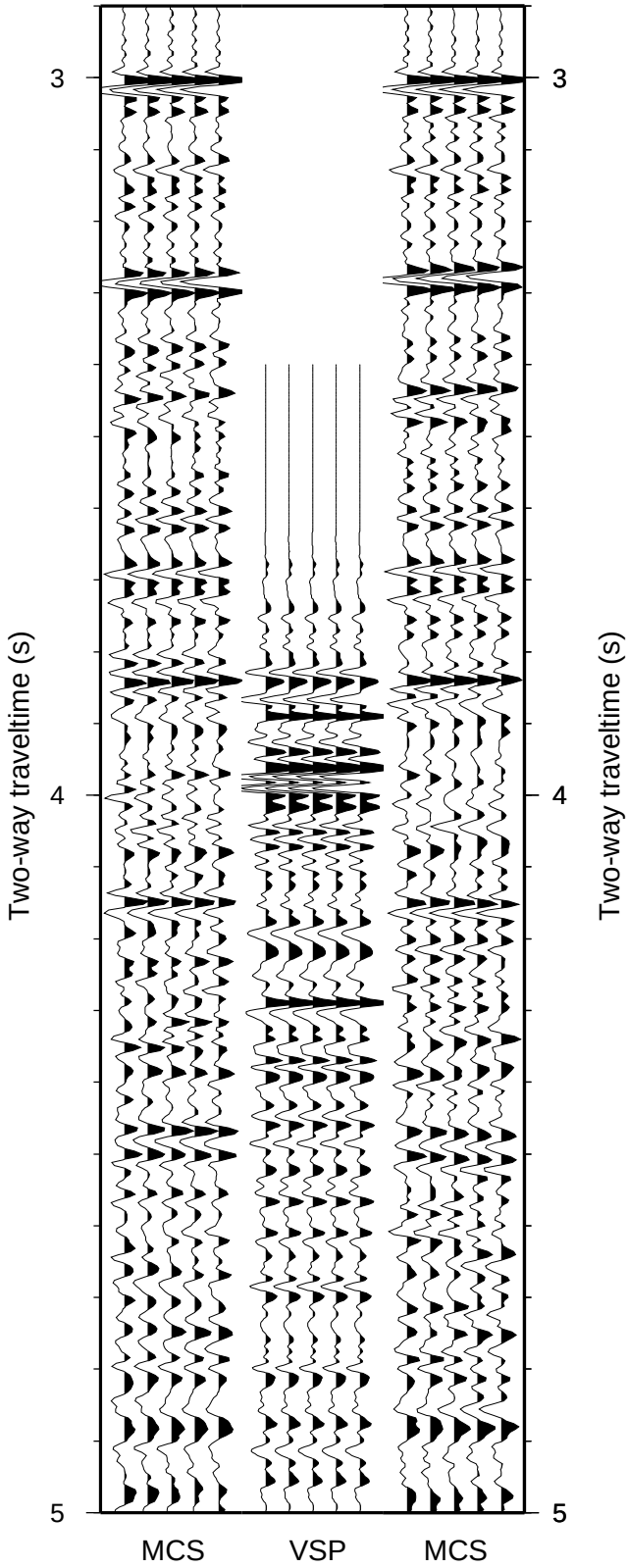

Figure F115. Depth vs. transit time for the Site 1109 VSP. The interval velocity was derived by fitting a straight line through the points and calculating the gradient.

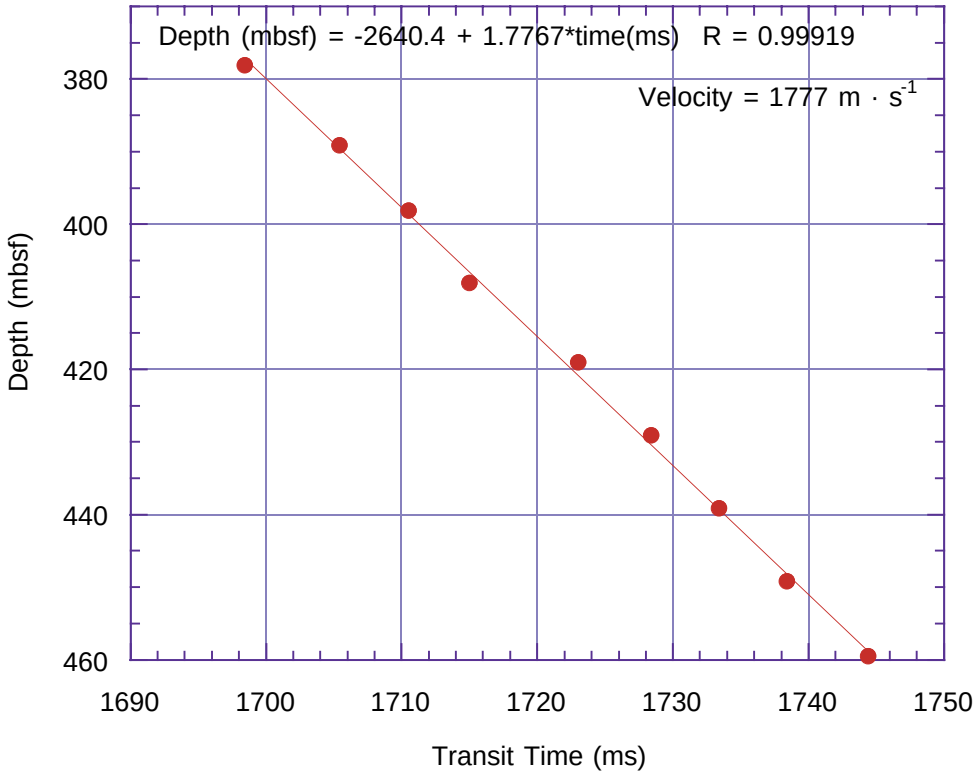

Figure F116. The velocity vs. depth function for Site 1109. Dots are sonic log velocities and crosses are from laboratory measurements. The black line defines the velocity function used.

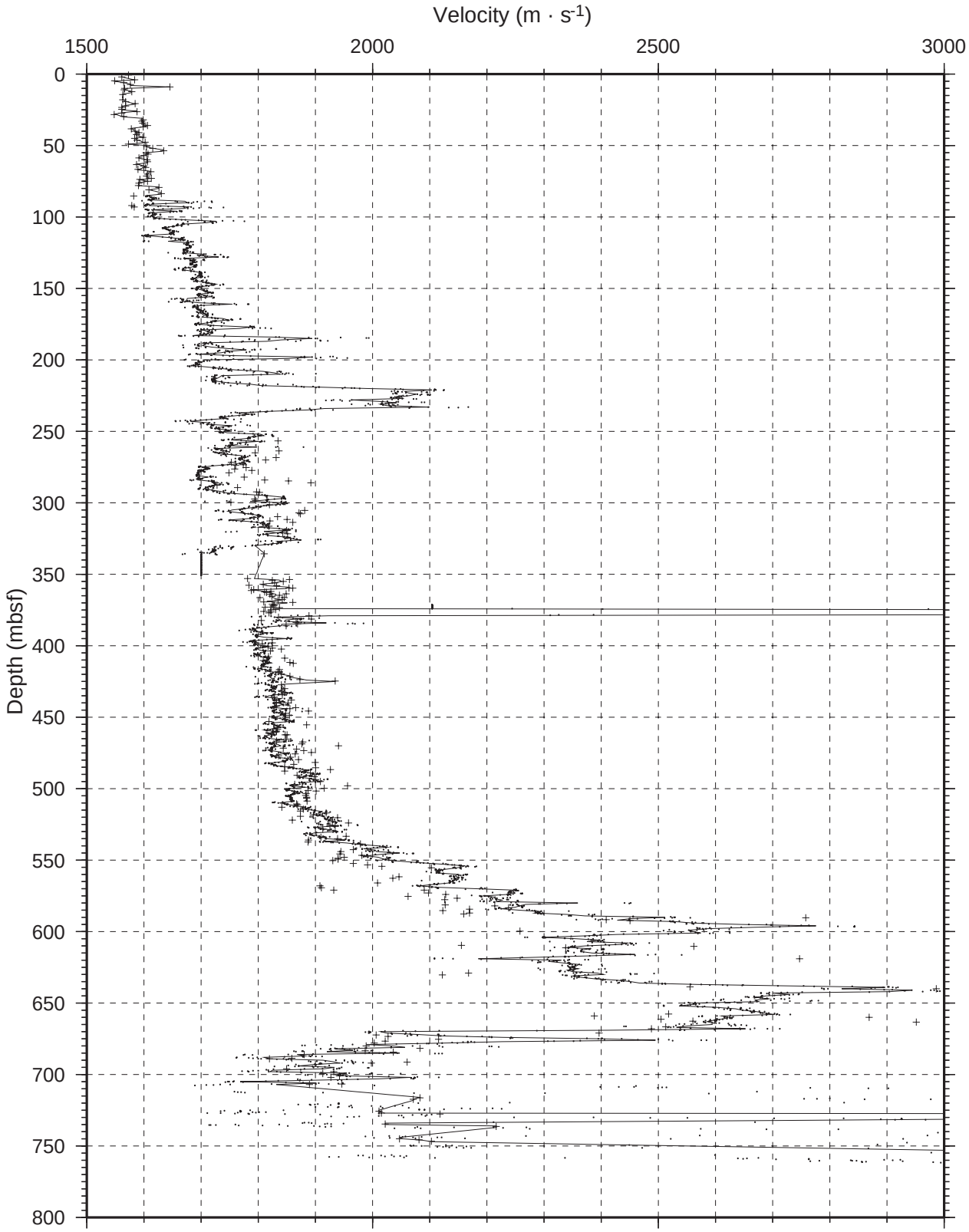

Figure F117. The density vs. depth function for Site 1109. Dots show log densities, crosses are from laboratory measurements. The black line defines the density function used.

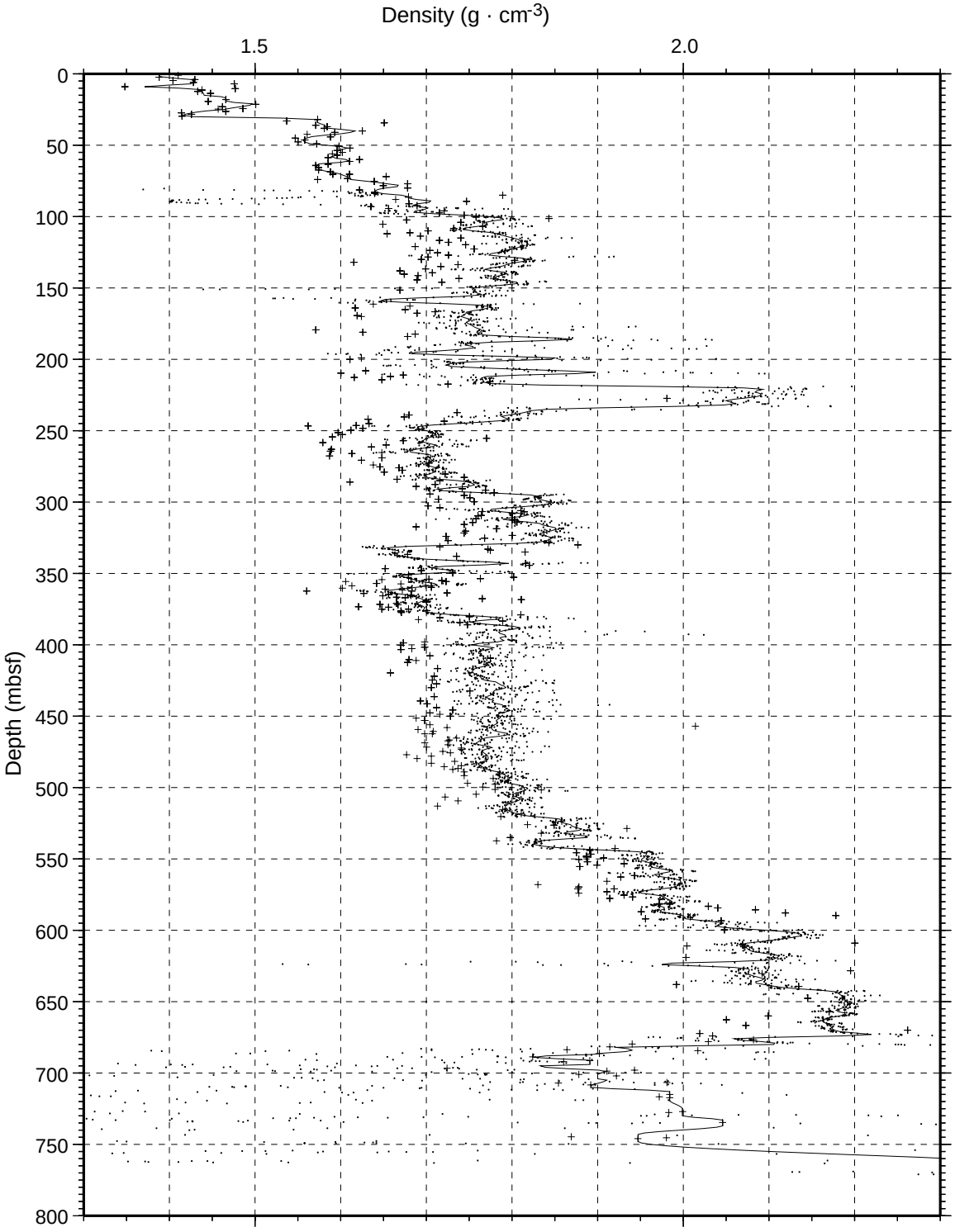

Figure F118. Depth-converted MCS data, synthetic seismic trace (syn), reflection coefficient (rc), and VSP. This compilation of data is derived from the density (blue/right) and velocity (red/left) data shown on the right.

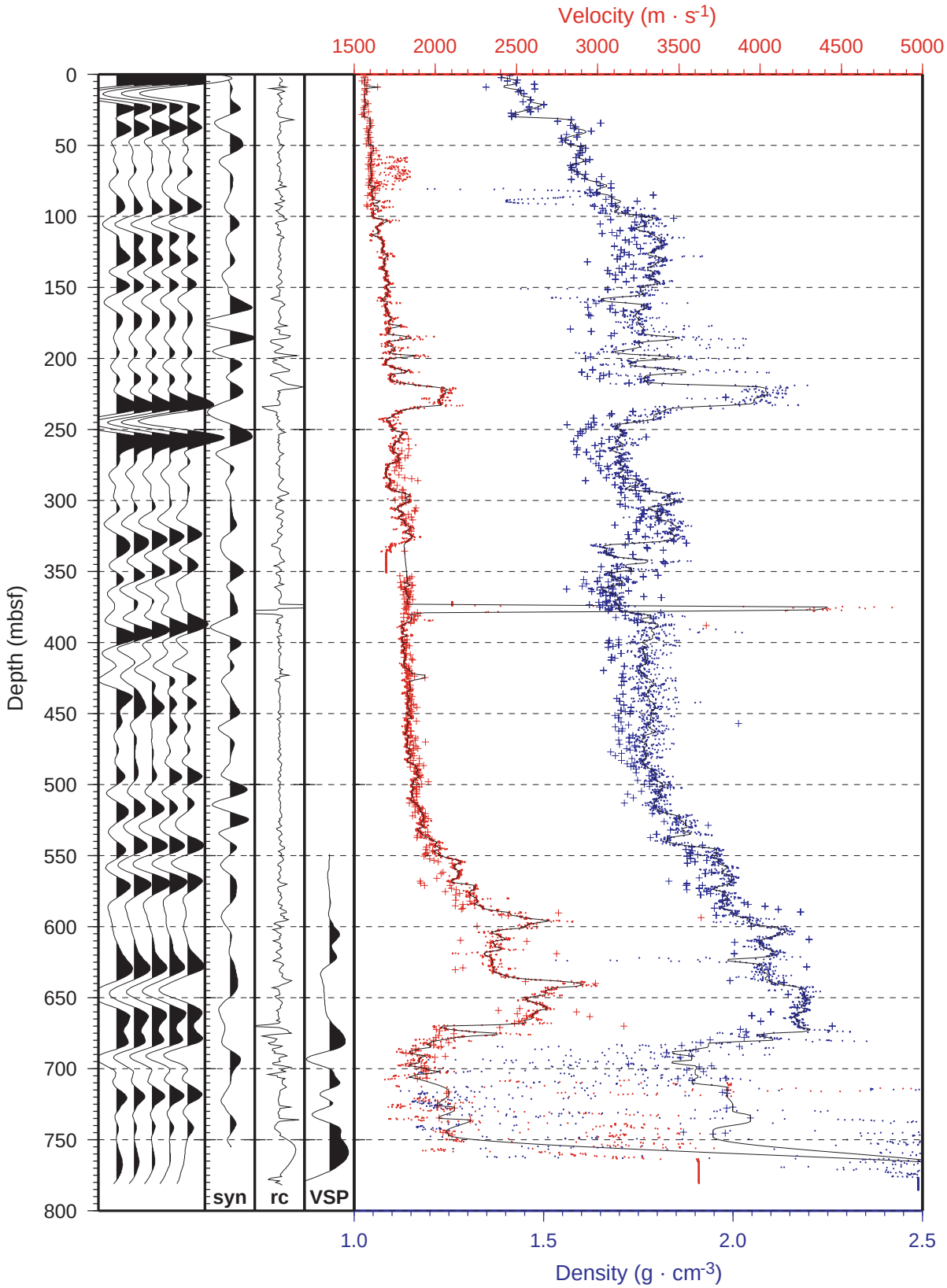

Figure F119. MCS Line EW9510–1366 cut at Site 1109. Five MCS traces have been depth converted and are displayed along side the lithostratigraphic column. Lines linking the time and depth data are spaced every 30 m. CMP = common midpoint.

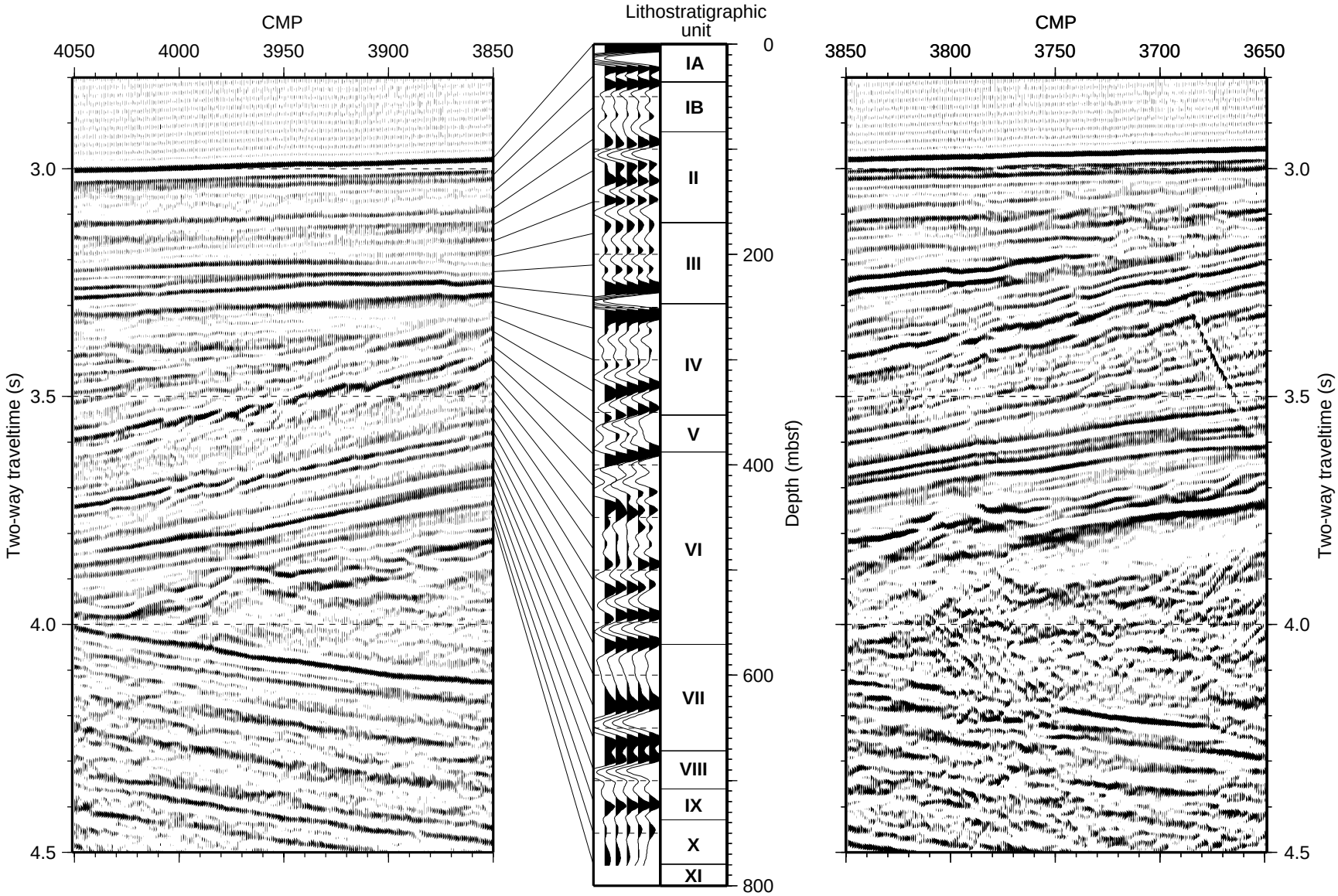

Figure F120. Correlation between Holes 1109A, 1109B, and 1109C, based on magnetic susceptibility (thin solid lines) and key beds (shaded).

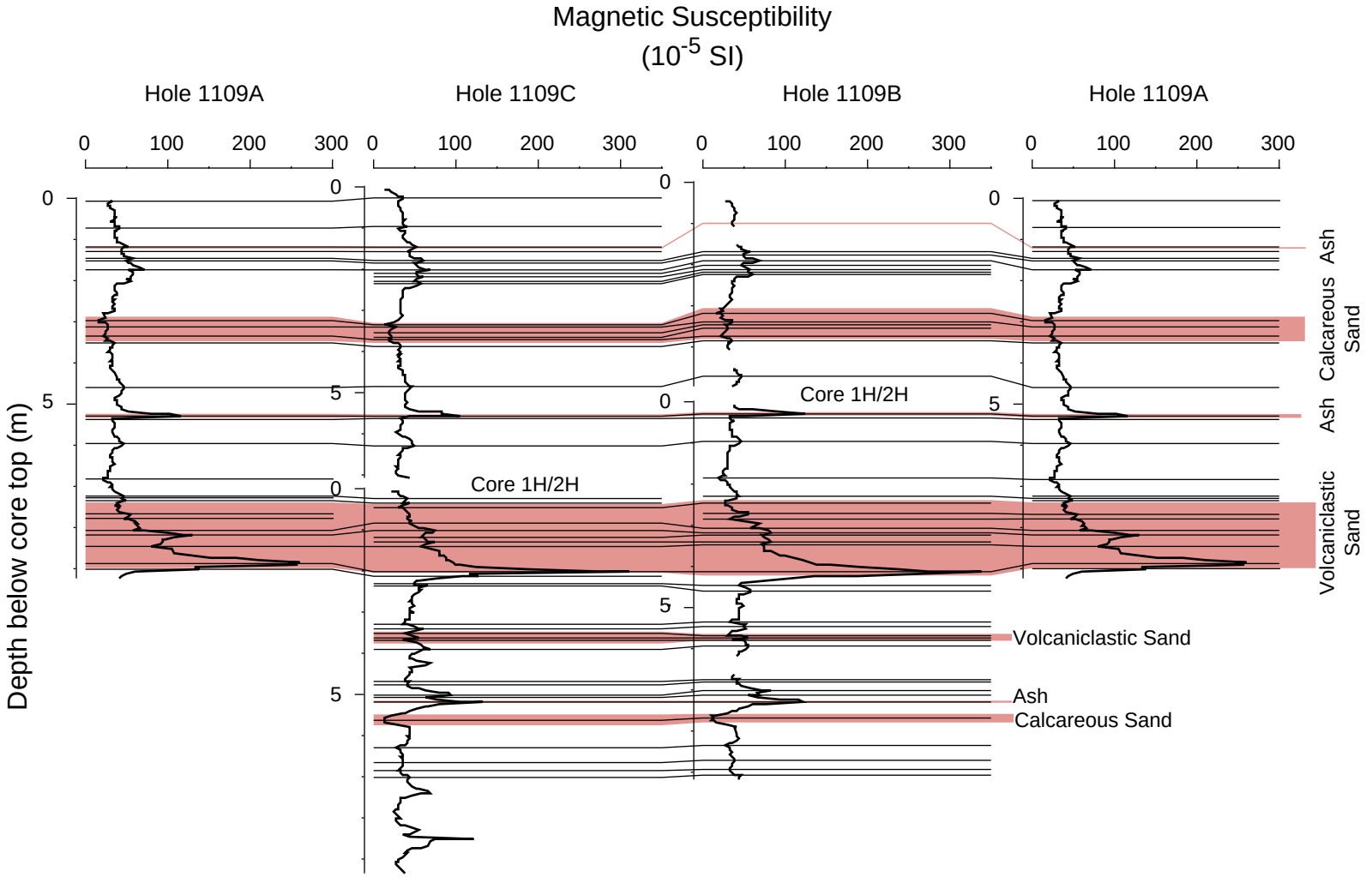

Table T1. Site 1109 coring summary. (Continued on next two pages.)

Hole 1109A

Latitude: 9°30.390′S
Longitude: 151°34.388′E
Seafloor (drill-pipe measurement from rig floor, mbrf): 2222.0
Distance between rig floor and sea level (m): 11.1
Water depth (drill-pipe measurement from sea level, m): 2210.9
Total depth (from rig floor, mbrf): 2231.50
Penetration (mbsf): 9.50
Total number of cores: 1
Total length of cored section (m): 9.50
Total core recovered (m): 9.96
Core recovery (%): 105

Core	Date (June 1998)	Time (UTC +10 hr)	Depth (mbsf)	Length cored (m)	Length recovered (m)	Recovery (%)
180-1109A-						
1H	24	1645	0-9.5	9.5	9.96	104.8
Totals:				9.5	9.96	104.8

Hole 1109B

Latitude: 9°30.396′S
Longitude: 151°34.391′E
Seafloor (drill-pipe measurement from rig floor, mbrf): 2222.2
Distance between rig floor and sea level (m): 11.1
Water depth (drill-pipe measurement from sea level, m): 2211.1
Total depth (from rig floor, mbrf): 2237.00
Penetration (mbsf): 14.80
Total number of cores: 2
Total length of cored section (m): 14.80
Total core recovered (m): 15.14
Core recovery (%): 102

Core	Date (June 1998)	Time (UTC +10 hr)	Depth (mbsf)	Length cored (m)	Length recovered (m)	Recovery (%)
180-1109B-						
1H	24	1735	0-5.3	5.3	5.25	99.6
2H	24	1820	5.3-14.8	9.5	9.86	103.8
Totals:				14.8	15.14	102.3

Hole 1109C

Latitude: 9°30.392′S
Longitude: 151°34.390′E
Seafloor (drill-pipe measurement from rig floor, mbrf): 2222.1
Distance between rig floor and sea level (m): 11.1
Water depth (drill-pipe measurement from sea level, m): 2211.0
Total depth (from rig floor, mbrf): 2597.80
Penetration (mbsf): 375.70
Total number of cores: 41
Total length of cored section (m): 375.70
Total core recovered (m): 323.11
Core recovery (%): 86

Core	Date (June 1998)	Time (UTC +10 hr)	Depth (mbsf)	Length cored (m)	Length recovered (m)	Recovery (%)
180-1109C-						
1H	24	1910	0.0-7.4	7.4	7.37	99.6
2H	24	1930	7.4-16.9	9.5	9.92	104.4
3H	24	2045	16.9-26.4	9.5	9.87	103.9
4H	24	2130	26.4-35.9	9.5	10.05	105.8
5H	24	2235	35.9-45.4	9.5	10.32	108.6
6H	24	2305	45.4-54.9	9.5	10.12	106.5
7H	25	0010	54.9-64.4	9.5	10.11	106.4
8H	24	0100	64.4-73.9	9.5	10.04	105.7

Table T1 (continued).

Core	Date (June 1998)	Time (UTC +10 hr)	Depth (mbsf)	Length cored (m)	Length recovered (m)	Recovery (%)
9H	25	0200	73.9-83.4	9.5	10.08	106.1
10H	25	0300	83.4-92.9	9.5	9.73	102.4
11H	25	0400	92.9-102.4	9.5	9.94	104.6
12X	25	0530	102.4-112.0	9.6	9.75	101.6
13X	25	0630	112.0-121.6	9.6	9.69	100.9
14X	25	0725	121.6-131.2	9.6	9.76	101.7
15X	25	0815	131.2-140.8	9.6	9.78	101.9
16X	25	0915	140.8-150.5	9.7	6.18	63.7
17X	25	1000	150.5-160.1	9.6	2.64	27.5
18X	25	1105	160.1-169.7	9.6	9.47	98.6
19X	25	1335	169.7-179.3	9.6	1.74	18.1
20X	25	1445	179.3-188.9	9.6	6.03	62.8
21X	25	1605	188.9-198.5	9.6	0.48	5.0
22X	25	1715	198.5-208.1	9.6	1.94	20.2
23X	25	1825	208.1-217.7	9.6	9.99	104.1
24X	25	2030	217.7-227.4	9.7	0.31	3.2
25X	25	2140	227.4-237.0	9.6	0.67	7.0
26X	25	2250	237.0-246.7	9.7	9.80	101.0
27X	26	0025	246.7-256.3	9.6	9.46	98.5
28X	26	0150	256.3-266.0	9.7	9.74	100.4
29X	26	0340	266.0-275.6	9.6	9.53	99.3
30X	26	0500	275.6-285.1	9.5	9.81	103.3
31X	26	0645	285.1-294.8	9.7	9.74	100.4
32X	26	0850	294.8-304.5	9.7	9.61	99.1
33X	26	1050	304.5-314.2	9.7	9.77	100.7
34X	26	1245	314.2-323.9	9.7	9.85	101.5
35X	26	1450	323.9-333.5	9.6	9.96	103.8
36X	26	1710	333.5-343.1	9.6	5.42	56.5
37X	26	1845	343.1-346.6	3.5	2.13	60.9
38X	26	2010	346.6-352.6	6.0	9.73	162.2
39X	26	2205	352.6-362.2	9.6	9.88	102.9
40X	27	0100	362.2-371.5	9.3	7.62	81.9
41X	27	0315	371.5-375.7	4.2	5.08	121.0
Totals:				375.7	323.11	86.0

Hole 1109D

Latitude: 9°30.380′S
Longitude: 151°34.355′E
Seafloor (drill-pipe measurement from rig floor, mbrf): 2222.2
Distance between rig floor and sea level (m): 11.2
Water depth (drill-pipe measurement from sea level, m): 2211.0
Total depth (from rig floor, mbrf): 3024.2
Penetration (mbsf): 802.0
Total number of cores: 51
Total length of cored section (m): 449.2
Total core recovered (m): 299.87
Core recovery (%): 67

Core	Date (1998)	Time (UTC +10 hr)	Depth (mbsf)	Length cored (m)	Length recovered (m)	Recovery (%)
180-1109D-						
		*****Drilled from 0 to 352.8 mbsf*****				
1R	28 June	0230	352.8-359.1	6.3	6.24	99.0
2R	28 June	0350	359.1-368.7	9.6	8.94	93.1
3R	28 June	0505	368.7-378.3	9.6	9.05	94.3
4R	28 June	0650	378.3-387.6	9.3	8.27	88.9
5R	28 June	0830	387.6-397.2	9.6	1.42	14.8
6R	28 June	0910	397.2-406.8	9.6	6.81	70.9
7R	28 June	1045	406.8-416.5	9.7	6.27	64.6
8R	28 June	1150	416.5-426.1	9.6	8.39	87.4
9R	28 June	1255	426.1-435.7	9.6	8.63	89.9
10R	28 June	1355	435.7-445.3	9.6	8.82	91.9
11R	28 June	1510	445.3-454.9	9.6	8.54	89.0
12R	28 June	1605	454.9-464.5	9.6	7.99	83.2
13R	28 June	1715	464.5-474.1	9.6	9.23	96.1

Table T1 (continued).

Core	Date (1998)	Time (UTC +10 hr)	Depth (mbsf)	Length cored (m)	Length recovered (m)	Recovery (%)
14R	28 June	1820	474.1-483.7	9.6	9.37	97.6
15R	28 June	1930	483.7-493.3	9.6	8.40	87.5
16R	28 June	2055	493.3-503.0	9.7	8.62	88.9
17R	28 June	2155	503.0-512.6	9.6	8.76	91.3
18R	28 June	2315	512.6-522.3	9.7	10.08	103.9
19R	29 June	0150	522.3-532.0	9.7	6.93	71.4
20R	29 June	0345	532.0-541.6	9.6	7.16	74.6
21R	29 June	0530	541.6-551.2	9.6	9.85	102.6
22R	29 June	0655	551.2-560.8	9.6	4.46	46.5
23R	29 June	0810	560.8-565.6	4.8	1.94	40.4
24R	29 June	0930	565.6-570.4	4.8	6.10	127.1
25R	29 June	1055	570.4-580.0	9.6	8.05	83.9
26R	29 June	1205	580.0-589.6	9.6	8.23	85.7
27R	29 June	1315	589.6-599.2	9.6	4.35	45.3
28R	29 June	1415	599.2-608.9	9.7	1.37	14.1
29R	29 June	1515	608.9-618.5	9.6	3.52	36.7
30R	29 June	1615	618.5-628.2	9.7	1.05	10.8
31R	29 June	1720	628.2-637.9	9.7	2.59	26.7
32R	29 June	1830	637.9-647.5	9.6	2.53	26.4
33R	29 June	2005	647.5-657.1	9.6	0.32	3.3
34R	29 June	2135	657.1-666.7	9.6	7.20	75.0
35R	29 June	2315	666.7-676.4	9.7	9.88	101.9
36R	30 June	0100	676.4-686.0	9.6	8.97	93.4
37R	30 June	0240	686.0-695.6	9.6	6.92	72.1
38R	30 June	0435	695.6-705.3	9.7	8.14	83.9
39R	30 June	0615	705.3-715.0	9.7	3.75	38.7
40R	30 June	0840	715.0-724.7	9.7	4.18	43.1
41R	30 June	1045	724.7-734.3	9.6	3.66	38.1
42R	30 June	1250	734.3-743.9	9.6	2.92	30.4
43R	30 June	1510	743.9-753.6	9.7	3.30	34.0
44R	30 June	1720	753.6-763.2	9.6	1.00	10.4
45R	30 June	2100	763.2-772.9	9.7	2.80	28.9
46R	1 July	0230	772.9-777.6	4.7	2.92	62.1
47R	1 July	0935	777.6-782.5	4.9	5.06	103.3
48R	1 July	1345	782.5-787.2	4.7	5.71	121.5
49R	1 July	1720	787.2-792.2	5.0	3.90	78.0
50R	1 July	2045	792.2-796.9	4.7	3.52	74.9
51R	1 July	0010	796.9-802.0	5.1	3.76	73.7
Cored:				449.2	299.87	66.8
Drilled:				352.8		
Total:				802.0		

Note: UTC = Universal Time Coordinated.

Table T2. Site 1109 coring summary by section. (Continued on next sixteen pages.)

Core	Date (1998)	Time (UTC +10 hr)	Core depth (mbsf) Top	Core depth (mbsf) Bottom	Length (m) Cored	Length (m) Recovered	Recovery (%)	Section	Length (m) Liner	Length (m) Curated	Section depth (mbsf) Top	Section depth (mbsf) Bottom	Catwalk samples	Comment
180-1109A														
1H	24 June	1645	0.0	9.5	9.5	9.96	104.8							
								1	1.50	1.50	0.00	1.50		
								2	1.50	1.50	1.50	3.00		
								3	1.50	1.50	3.00	4.50		
								4	1.50	1.50	4.50	6.00		
								5	1.50	1.50	6.00	7.50		
								6	1.50	1.50	7.50	9.00		
								7	0.68	0.68	9.00	9.68		
								CC	0.28	0.28	9.68	9.96	PAL	
									9.96	9.96				
				Totals:	9.5	9.96	104.8							
180-1109B														
1H	24 June	1735	0.0	5.3	5.3	5.28	99.6							
								1	1.45	1.45	0.00	1.45	IW, WROG, WRMB	
								2	1.50	1.50	1.45	2.95	IW	
								3	1.50	1.50	2.95	4.45	IW, WROG, WRMB, HS	
								4	0.55	0.55	4.45	5.00		
								CC	0.28	0.28	5.00	5.28	PAL	
									5.28	5.28				
2H	24 June	1820	5.3	14.8	9.5	9.86	103.8							
								1	1.50	1.50	5.30	6.80	IW	
								2	1.50	1.50	6.80	8.30		
								3	1.50	1.50	8.30	9.80	IW	
								4	0.80	0.80	9.80	10.60	IW	
								5	1.50	1.50	10.60	12.10	IW, WROG, WRMB, HS	
								6	1.50	1.50	12.10	13.60	IW	
								7	1.29	1.29	13.60	14.89		
								CC	0.27	0.27	14.89	15.16	PAL	
									9.86	9.86				
				Totals:	14.8	15.14	102.3							
180-1109C														
1H	24 June	1910	0.0	7.4	7.4	7.37	99.6							
								1	1.50	1.50	0.00	1.50		
								2	1.50	1.50	1.50	3.00		
								3	1.50	1.50	3.00	4.50		
								4	1.50	1.50	4.50	6.00		
								5	1.11	1.11	6.00	7.11		
								CC	0.26	0.26	7.11	7.37	PAL	
									7.37	7.37				
2H	24 June	1930	7.4	16.9	9.5	9.92	104.4							
								1	1.50	1.50	7.40	8.90		
								2	1.50	1.50	8.90	10.40		
								3	1.50	1.50	10.40	11.90		
								4	1.50	1.50	11.90	13.40		
								5	1.50	1.50	13.40	14.90		
								6	1.50	1.50	14.90	16.40		

Table T2 (continued).

Core	Date (1998)	Time (UTC +10 hr)	Core depth (mbsf) Top	Core depth (mbsf) Bottom	Length (m) Cored	Length (m) Recovered	Recovery (%)	Section	Length (m) Liner	Length (m) Curated	Section depth (mbsf) Top	Section depth (mbsf) Bottom	Catwalk samples	Comment
								7	0.78	0.78	16.40	17.18		
								CC	0.14	0.14	17.18	17.32	PAL	
									9.92	9.92				
3H	24 June	2045	16.9	26.4	9.5	9.87	103.9							Adara
								1	1.50	1.50	16.90	18.40		
								2	1.50	1.50	18.40	19.90	HS, WEL, WROG, WRMB, IW	
								3	1.50	1.50	19.90	21.40		
								4	1.50	1.50	21.40	22.90		
								5	1.50	1.50	22.90	24.40		
								6	1.50	1.50	24.40	25.90		
								7	0.68	0.68	25.90	26.58		
								CC	0.19	0.19	26.58	26.77	PAL	
									9.87	9.87				
4H	24 June	2130	26.4	35.9	9.5	10.05	105.8							
								1	1.50	1.50	26.40	27.90		
								2	1.50	1.50	27.90	29.40	HS, IW	
								3	1.50	1.50	29.40	30.90	WEL	
								4	1.50	1.50	30.90	32.40		
								5	1.50	1.50	32.40	33.90		
								6	1.50	1.50	33.90	35.40		
								7	0.74	0.74	35.40	36.14		
								CC	0.31	0.31	36.14	36.45	PAL	
									10.05	10.05				
5H	24 June	2235	35.9	45.4	9.5	10.32	108.6							Adara
								1	1.50	1.50	35.90	37.40		
								2	1.50	1.50	37.40	38.90		
								3	1.50	1.50	38.90	40.40	HS, IW	
								4	1.50	1.50	40.40	41.90	WEL	
								5	1.50	1.50	41.90	43.40		
								6	1.50	1.50	43.40	44.90		
								7	0.84	0.84	44.90	45.74		
								CC	0.48	0.48	45.74	46.22	PAL	
									10.32	10.32				
6H	24 June	2305	45.4	54.9	9.5	10.12	106.5							
								1	1.50	1.50	45.40	46.90		
								2	1.50	1.50	46.90	48.40		
								3	1.50	1.50	48.40	49.90	HS, IW	
								4	1.50	1.50	49.90	51.40	WEL	
								5	1.50	1.50	51.40	52.90		
								6	1.50	1.50	52.90	54.40		
								7	0.83	0.83	54.40	55.23		
								CC	0.29	0.29	55.23	55.52	PAL	
									10.12	10.12				
7H	25 June	0010	54.9	64.4	9.5	10.11	106.4							Adara
								1	1.50	1.50	54.90	56.40		
								2	1.50	1.50	56.40	57.90		
								3	1.50	1.50	57.90	59.40	IW	
								4	1.50	1.50	59.40	60.90	HS, WEL	

Table T2 (continued).

Core	Date (1998)	Time (UTC +10 hr)	Core depth (mbsf) Top	Core depth (mbsf) Bottom	Length (m) Cored	Length (m) Recovered	Recovery (%)	Section	Length (m) Liner	Length (m) Curated	Section depth (mbsf) Top	Section depth (mbsf) Bottom	Catwalk samples	Comment
								5	1.50	1.50	60.90	62.40		
								6	1.50	1.50	62.40	63.90		
								7	0.69	0.69	63.90	64.59		
								CC	0.42	0.42	64.59	65.01	PAL	
									10.11	10.11				
8H	24 June	0100	64.4	73.9	9.5	10.04	105.7							
								1	1.50	1.50	64.40	65.90		
								2	1.50	1.50	65.90	67.40		
								3	1.50	1.50	67.40	68.90	HS, IW	
								4	1.50	1.50	68.90	70.40	WEL	
								5	1.50	1.50	70.40	71.90		
								6	1.50	1.50	71.90	73.40		
								7	0.78	0.78	73.40	74.18		
								CC	0.26	0.26	74.18	74.44	PAL	
									10.04	10.04				
9H	25 June	0200	73.9	83.4	9.5	10.08	106.1							Adara
								1	1.50	1.50	73.90	75.40		
								2	1.50	1.50	75.40	76.90		
								3	1.50	1.50	76.90	78.40	HS, IW	
								4	1.50	1.50	78.40	79.90	WEL	
								5	1.50	1.50	79.90	81.40		
								6	1.50	1.50	81.40	82.90		
								7	0.71	0.71	82.90	83.61		
								CC	0.37	0.37	83.61	83.98	PAL	
									10.08	10.08				
10H	25 June	0300	83.4	92.9	9.5	9.73	102.4							
								1	1.50	1.50	83.40	84.90		
								2	1.50	1.50	84.90	86.40		
								3	1.50	1.50	86.40	87.90		
								4	1.50	1.50	87.90	89.40	HS, IW, WRMB, WROG	
								5	1.50	1.50	89.40	90.90	WEL	
								6	1.50	1.50	90.90	92.40		
								7	0.65	0.65	92.40	93.05		
								CC	0.08	0.08	93.05	93.13	PAL	
									9.73	9.73				
11H	25 June	0400	92.9	102.4	9.5	9.94	104.6							
								1	1.50	1.50	92.90	94.40		
								2	1.50	1.50	94.40	95.90		
								3	1.50	1.50	95.90	97.40	IW	
								4	1.50	1.50	97.40	98.90	HS, WRSCR	
								5	1.50	1.50	98.90	100.40		
								6	1.00	1.00	100.40	101.40		
								7	1.18	1.18	101.40	102.58		
								CC	0.26	0.26	102.58	102.84	PAL	
									9.94	9.94				
12X	25 June	0530	102.4	112.0	9.6	9.75	101.6							
								1	1.50	1.50	102.40	103.90		
								2	1.50	1.50	103.90	105.40	HS	

Table T2 (continued).

Core	Date (1998)	Time (UTC +10 hr)	Core depth (mbsf) Top	Core depth (mbsf) Bottom	Length (m) Cored	Length (m) Recovered	Recovery (%)	Section	Length (m) Liner	Length (m) Curated	Section depth (mbsf) Top	Section depth (mbsf) Bottom	Catwalk samples	Comment
								3	1.50	1.50	105.40	106.90	IW	
								4	1.50	1.50	106.90	108.40	WEL	
								5	1.50	1.50	108.40	109.90		
								6	1.50	1.50	109.90	111.40		
								7	0.44	0.44	111.40	111.84		
								CC	0.31	0.31	111.84	112.15	PAL	
									9.75	9.75				
13X	25 June	0630	112.0	121.6	9.6	9.69	100.9							
								1	1.50	1.50	112.00	113.50		
								2	1.50	1.50	113.50	115.00		
								3	1.50	1.50	115.00	116.50	IW	
								4	1.50	1.50	116.50	118.00	HS	
								5	1.50	1.50	118.00	119.50		
								6	1.50	1.50	119.50	121.00		
								7	0.40	0.40	121.00	121.40		
								CC	0.29	0.29	121.40	121.69	PAL	
									9.69	9.69				
14X	25 June	0725	121.6	131.2	9.6	9.76	101.7							
								1	1.50	1.50	121.60	123.10		
								2	1.50	1.50	123.10	124.60	HS	
								3	1.50	1.50	124.60	126.10	IW	
								4	1.50	1.50	126.10	127.60	WEL	
								5	1.50	1.50	127.60	129.10		
								6	1.50	1.50	129.10	130.60		
								7	0.42	0.42	130.60	131.02		
								CC	0.34	0.34	131.02	131.36	PAL	
									9.76	9.76				
15X	25 June	0815	131.2	140.8	9.6	9.78	101.9							
								1	1.47	1.47	131.20	132.67		
								2	1.50	1.50	132.67	134.17		
								3	1.50	1.50	134.17	135.67	IW	
								4	1.50	1.50	135.67	137.17	HS	
								5	1.50	1.50	137.17	138.67		
								6	1.50	1.50	138.67	140.17		
								7	0.51	0.51	140.17	140.68		
								CC	0.30	0.30	140.68	140.98	PAL	
									9.78	9.78				
16X	25 June	0915	140.8	150.5	9.7	6.18	63.7							
								1	1.50	1.50	140.80	142.30		
								2	1.50	1.50	142.30	143.80		
								3	1.50	1.50	143.80	145.30	HS, IW	
								4	1.35	1.35	145.30	146.65	WEL	
								CC	0.33	0.33	146.65	146.98		
									6.18	6.18				
17X	25 June	1000	150.5	160.1	9.6	2.64	27.5							
								1	1.50	1.50	150.50	152.00	IW	
								2	0.80	0.80	152.00	152.80	HS	

Table T2 (continued).

Core	Date (1998)	Time (UTC +10 hr)	Core depth (mbsf) Top	Core depth (mbsf) Bottom	Length (m) Cored	Length (m) Recovered	Recovery (%)	Section	Length (m) Liner	Length (m) Curated	Section depth (mbsf) Top	Section depth (mbsf) Bottom	Catwalk samples	Comment
								CC	0.34	0.34	152.80	153.14	PAL	
									2.64	2.64				
18X	25 June	1105	160.1	169.7	9.6	9.47	98.6							
								1	1.50	1.50	160.10	161.60		
								2	1.50	1.50	161.60	163.10		
								3	1.50	1.50	163.10	164.60	IW, WRMB, WROG, HS	
								4	1.20	1.20	164.60	165.80	WEL	
								5	1.50	1.50	165.80	167.30		
								6	1.50	1.50	167.30	168.80		
								7	0.63	0.63	168.80	169.43		
								CC	0.14	0.14	169.43	169.57	PAL	
									9.47	9.47				
19X	25 June	1335	169.7	179.3	9.6	1.74	18.1							
								1	1.43	1.43	169.70	171.13	HS	
								CC	0.31	0.31	171.13	171.44	PAL	
									1.74	1.74				
20X	25 June	1445	179.3	188.9	9.6	6.03	62.8							
								1	1.50	1.50	179.30	180.80	HS, IW	
								2	1.50	1.50	180.80	182.30	WEL	
								3	1.50	1.50	182.30	183.80		
								4	1.16	1.16	183.80	184.96		
								CC	0.37	0.37	184.96	185.33	PAL	
									6.03	6.03				
21X	25 June	1605	188.9	198.5	9.6	0.48	5.0							
								CC	0.48	0.48	188.90	189.38	PAL, HS	
									0.48	0.48				
22X	25 June	1715	198.5	208.1	9.6	1.94	20.2							
								1	0.80	0.80	198.50	199.30		
								2	0.78	0.78	199.30	200.08	HS, WEL	
								CC	0.36	0.36	200.08	200.44	PAL	
									1.94	1.94				
23X	25 June	1825	208.1	217.7	9.6	9.99	104.1							
								1	1.50	1.50	208.10	209.60		
								2	1.50	1.50	209.60	211.10		
								3	1.00	1.00	211.10	212.10		
								4	0.65	0.65	212.10	212.75	IW, WRSCR	
								5	1.50	1.50	212.75	214.25	HS	
								6	1.50	1.50	214.25	215.75		
								7	1.50	1.50	215.75	217.25		
								8	0.33	0.33	217.25	217.58		
								CC	0.51	0.51	217.58	218.09	PAL	
									9.99	9.99				
24X	25 June	2030	217.7	227.4	9.7	0.31	3.2							
								CC	0.31	0.31	217.70	218.01	PAL, HS	
									0.31	0.31				
25X	25 June	2140	227.4	237.0	9.6	0.67	7.0							
								1	0.35	0.35	227.40	227.75	HS	
								CC	0.32	0.32	227.75	228.07	PAL	
									0.67	0.67				

Table T2 (continued).

Core	Date (1998)	Time (UTC +10 hr)	Core depth (mbsf) Top	Core depth (mbsf) Bottom	Length (m) Cored	Length (m) Recovered	Recovery (%)	Section	Length (m) Liner	Length (m) Curated	Section depth (mbsf) Top	Section depth (mbsf) Bottom	Catwalk samples	Comment
26X	25 June	2250	237.0	246.7	9.7	9.80	101.0							
								1	1.45	1.45	237.00	238.45	IW, WRMB, WROG	
								2	1.50	1.50	238.45	239.95	HS, WEL	
								3	1.50	1.50	239.95	241.45		
								4	1.50	1.50	241.45	242.95		
								5	1.50	1.50	242.95	244.45		
								6	1.50	1.50	244.45	245.95		
								7	0.50	0.50	245.95	246.45		
								CC	0.35	0.35	246.45	246.80	PAL	
									9.80	9.80				
27X	25 June	0025	246.7	256.3	9.6	9.46	98.5							
								1	1.50	1.50	246.70	248.20		
								2	1.50	1.50	248.20	249.70	IW	
								3	1.50	1.50	249.70	251.20	HS	
								4	1.50	1.50	251.20	252.70		
								5	1.50	1.50	252.70	254.20		
								6	1.00	1.00	254.20	255.20		
								7	0.69	0.69	255.20	255.89		
								CC	0.27	0.27	255.89	256.16	PAL	
									9.46	9.46				
28X	26 June	0150	256.3	266.0	9.7	9.74	100.4							
								1	1.50	1.50	256.30	257.80		
								2	1.50	1.50	257.80	259.30		
								3	1.50	1.50	259.30	260.80		
								4	1.50	1.50	260.80	262.30	HS, IW	
								5	1.50	1.50	262.30	263.80	WEL	
								6	1.50	1.50	263.80	265.30		
								7	0.44	0.44	265.30	265.74		
								CC	0.30	0.30	265.74	266.04	PAL	
									9.74	9.74				
29X	26 June	0340	266.0	275.6	9.6	9.53	99.3							
								1	1.50	1.50	266.00	267.50		
								2	1.50	1.50	267.50	269.00		
								3	1.50	1.50	269.00	270.50	IW	
								4	1.50	1.50	270.50	272.00	HS	
								5	1.50	1.50	272.00	273.50		
								6	1.50	1.50	273.50	275.00		
								7	0.41	0.41	275.00	275.41		
								CC	0.12	0.12	275.41	275.53	PAL	
									9.53	9.53				
30X	26 June	0500	275.6	285.1	9.5	9.81	103.3							
								1	1.50	1.50	275.60	277.10	IW	
								2	1.50	1.50	277.10	278.60	WEL	
								3	1.50	1.50	278.60	280.10	HS	
								4	1.50	1.50	280.10	281.60		
								5	1.50	1.50	281.60	283.10		
								6	1.50	1.50	283.10	284.60		
								7	0.47	0.47	284.60	285.07		

Table T2 (continued).

Core	Date (1998)	Time (UTC +10 hr)	Core depth (mbsf) Top	Core depth (mbsf) Bottom	Length (m) Cored	Length (m) Recovered	Recovery (%)	Section	Length (m) Liner	Length (m) Curated	Section depth (mbsf) Top	Section depth (mbsf) Bottom	Catwalk samples	Comment
								CC	0.34	0.34	285.07	285.41	PAL	
									9.81	9.81				
31X	26 June	0645	285.1	294.8	9.7	9.74	100.4							
								1	1.50	1.50	285.10	286.60		
								2	1.50	1.50	286.60	288.10		
								3	1.50	1.50	288.10	289.60	IW	
								4	1.50	1.50	289.60	291.10	HS	
								5	1.50	1.50	291.10	292.60		
								6	1.50	1.50	292.60	294.10		Void 142-150 cm
								7	0.40	0.40	294.10	294.50		
								CC	0.34	0.34	294.50	294.84	PAL	
									9.74	9.74				
32X	26 June	0850	294.8	304.5	9.7	9.61	99.1							
								1	1.50	1.50	294.80	296.30		
								2	1.50	1.50	296.30	297.80		
								3	1.50	1.50	297.80	299.30	HS, IW	
								4	1.50	1.50	299.30	300.80	WEL	
								5	1.50	1.50	300.80	302.30		
								6	1.30	1.30	302.30	303.60	WRSCR	
								7	0.61	0.61	303.60	304.21		
								CC	0.20	0.20	304.21	304.41	PAL	
									9.61	9.61				
33X	26 June	1050	304.5	314.2	9.7	9.77	100.7							
								1	1.50	1.50	304.50	306.00		
								2	1.50	1.50	306.00	307.50		
								3	1.50	1.50	307.50	309.00		
								4	1.50	1.50	309.00	310.50	HS, IW, WROG, WRMB	
								5	1.50	1.50	310.50	312.00		
								6	1.50	1.50	312.00	313.50		
								7	0.41	0.41	313.50	313.91		
								CC	0.36	0.36	313.91	314.27	PAL	
									9.77	9.77				
34X	26 June	1245	314.2	323.9	9.7	9.85	101.5							
								1	1.50	1.50	314.20	315.70		
								2	1.50	1.50	315.70	317.20	IW, WEL	
								3	1.50	1.50	317.20	318.70	HS	
								4	1.50	1.50	318.70	320.20		
								5	1.50	1.50	320.20	321.70		
								6	1.50	1.50	321.70	323.20		
								7	0.45	0.45	323.20	323.65		
								CC	0.40	0.40	323.65	324.05	PAL	
									9.85	9.85				
35X	26 June	1450	323.9	333.5	9.6	9.96	103.8							
								1	1.50	1.50	323.90	325.40		
								2	1.50	1.50	325.40	326.90		
								3	1.50	1.50	326.90	328.40	IW	
								4	1.50	1.50	328.40	329.90	HS	
								5	1.50	1.50	329.90	331.40		

Table T2 (continued).

Core	Date (1998)	Time (UTC +10 hr)	Core depth (mbsf) Top	Core depth (mbsf) Bottom	Length (m) Cored	Length (m) Recovered	Recovery (%)	Section	Length (m) Liner	Length (m) Curated	Section depth (mbsf) Top	Section depth (mbsf) Bottom	Catwalk samples	Comment
								6	1.50	1.50	331.40	332.90		
								7	0.48	0.48	332.90	333.38		
								CC	0.48	0.48	333.38	333.86	PAL	
									9.96	9.96				
36X	26 June	1710	333.5	343.1	9.6	5.42	56.5							
								1	1.50	1.50	333.50	335.00	IW	
								2	1.50	1.50	335.00	336.50	HS, WEL	
								3	1.50	1.50	336.50	338.00		
								4	0.56	0.56	338.00	338.56		
								CC	0.36	0.36	338.56	338.92	PAL	
									5.42	5.42				
37X	26 June	1845	343.1	346.6	3.5	2.13	60.9							
								1	1.20	1.20	343.10	344.30		
								2	0.50	0.50	344.30	344.80	HS	
								CC	0.43	0.43	344.80	345.23	PAL	
									2.13	2.13				
38X	26 June	2010	346.6	352.6	6.0	9.73	162.2							
								1	1.50	1.50	346.60	348.10		
								2	1.50	1.50	348.10	349.60		
								3	1.50	1.50	349.60	351.10		
								4	1.50	1.50	351.10	352.60	IW	
								5	1.50	1.50	352.60	354.10	HS, WEL	
								6	1.50	1.50	354.10	355.60		
								7	0.44	0.44	355.60	356.04		
								CC	0.29	0.29	356.04	356.33	PAL	
									9.73	9.73				
39X	26 June	2205	352.6	362.2	9.6	9.88	102.9							
								1	1.50	1.50	352.60	354.10		
								2	1.50	1.50	354.10	355.60		
								3	1.50	1.50	355.60	357.10	IW	
								4	1.50	1.50	357.10	358.60	HS	
								5	1.50	1.50	358.60	360.10		
								6	1.50	1.50	360.10	361.60		
								7	0.43	0.43	361.60	362.03		
								CC	0.45	0.45	362.03	362.48	PAL	
									9.88	9.88				
40X	27 June	0100	362.2	371.5	9.3	7.62	81.9							
								1	1.50	1.50	362.20	363.70		
								2	1.50	1.50	363.70	365.20		
								3	1.50	1.50	365.20	366.70	HS, IW, WRMB, WROG	
								4	1.50	1.50	366.70	368.20	WEL	
								5	1.38	1.38	368.20	369.58		
								CC	0.24	0.24	369.58	369.82	PAL	
									7.62	7.62				
41X	27 June	0315	371.5	375.7	4.2	5.08	121.0							
								1	1.50	1.50	371.50	373.00		
								2	1.50	1.50	373.00	374.50	IW	
								3	1.20	1.20	374.50	375.70	HS	

Table T2 (continued).

Core	Date (1998)	Time (UTC +10 hr)	Core depth (mbsf) Top	Core depth (mbsf) Bottom	Length (m) Cored	Length (m) Recovered	Recovery (%)	Section	Length (m) Liner	Length (m) Curated	Section depth (mbsf) Top	Section depth (mbsf) Bottom	Catwalk samples	Comment
								4	0.53	0.53	375.70	376.23		
								CC	0.35	0.35	376.23	376.58	PAL	
									5.08	5.08				
				Totals:	375.7	323.11	86.0							
180-1109D														
Drilled from 0.0 to 352.8 mbsf														
1R	28 June	0230	352.8	359.1	6.3	6.24	99.0							
								1	1.50	1.50	352.80	354.30		
								2	1.50	1.50	354.30	355.80	WEL	
								3	1.50	1.50	355.80	357.30		
								4	1.38	1.38	357.30	358.68		
								CC	0.36	0.36	358.68	359.04	PAL	
									6.24	6.24				
2R	28 June	0350	359.1	368.7	9.6	8.94	93.1							
								1	1.31	1.31	359.10	360.41		
								2	1.40	1.40	360.41	361.81		
								3	1.02	1.02	361.81	362.83		
								4	1.05	1.05	362.83	363.88		
								5	1.04	1.04	363.88	364.92		
								6	1.06	1.06	364.92	365.98	IW	
								7	1.46	1.46	365.98	367.44		
								8	0.41	0.41	367.44	367.85		
								CC	0.19	0.19	367.85	368.04	PAL	
									8.94	8.94				
3R	28 June	0505	368.7	378.3	9.6	9.05	94.3							
								1	1.50	1.50	368.70	370.20		
								2	1.49	1.49	370.20	371.69	WEL	
								3	1.10	1.10	371.69	372.79		
								4	1.35	1.35	372.79	374.14		
								5	1.22	1.22	374.14	375.36		
								6	1.39	1.39	375.36	376.75		
								7	0.66	0.66	376.75	377.41		
								CC	0.34	0.34	377.41	377.75	PAL	
									9.05	9.05				
4R	28 June	0650	378.3	387.6	9.3	8.27	88.9							
								1	1.10	1.10	378.30	379.40		
								2	1.20	1.20	379.40	380.60		
								3	1.06	1.06	380.60	381.66	IW	
								4	1.11	1.11	381.66	382.77	HS	
								5	1.25	1.25	382.77	384.02	WRSCR	
								6	1.51	1.51	384.02	385.53		
								7	0.60	0.60	385.53	386.13		
								CC	0.44	0.44	386.13	386.57	PAL	
									8.27	8.27				
5R	28 June	0830	387.6	397.2	9.6	1.42	14.8							
								1	0.99	0.99	387.60	388.59	HS	
								CC	0.43	0.43	388.59	389.02	PAL	
									1.42	1.42				

Table T2 (continued).

Core	Date (1998)	Time (UTC +10 hr)	Core depth (mbsf) Top	Core depth (mbsf) Bottom	Length (m) Cored	Length (m) Recovered	Recovery (%)	Section	Length (m) Liner	Length (m) Curated	Section depth (mbsf) Top	Section depth (mbsf) Bottom	Catwalk samples	Comment
6R	28 June	0910	397.2	406.8	9.6	6.81	70.9							
								1	1.42	1.42	397.20	398.62		
								2	1.44	1.44	398.62	400.06		
								3	1.07	1.07	400.06	401.13	HS, IW	
								4	0.92	0.92	401.13	402.05	WEL	
								5	0.79	0.79	402.05	402.84		
								6	0.93	0.93	402.84	403.77		
								CC	0.24	0.24	403.77	404.01	PAL	
									6.81	6.81				
7R	28 June	1045	406.8	416.5	9.7	6.17	63.6							
								1	1.50	1.50	406.80	408.30		
								2	1.24	1.24	408.30	409.54		
								3	1.30	1.30	409.54	410.84	IW	
								4	1.36	1.36	410.84	412.20	HS	
								5	0.62	0.62	412.20	412.82		
								CC	0.25	0.25	412.82	413.07	PAL	
									6.27	6.27				
8R	28 June	1150	416.5	426.1	9.6	8.39	87.4							
								1	1.44	1.44	416.50	417.94		
								2	0.98	0.98	417.94	418.92		
								3	1.51	1.51	418.92	420.43	IW	
								4	1.19	1.19	420.43	421.62	HS, WEL	
								5	1.51	1.51	421.62	423.13		
								6	0.75	0.75	423.13	423.88		
								7	0.83	0.83	423.88	424.71		
								CC	0.18	0.18	424.71	424.89	PAL	
									8.39	8.39				
9R	28 June	1255	426.1	435.7	9.6	8.63	89.9							
								1	1.50	1.50	426.10	427.60		
								2	1.45	1.45	427.60	429.05		
								3	1.11	1.11	429.05	430.16	IW	
								4	1.36	1.36	430.16	431.52	HS	
								5	1.45	1.45	431.52	432.97		
								6	1.50	1.50	432.97	434.47		
								CC	0.26	0.26	434.47	434.73	PAL	
									8.63	8.63				
10R	28 June	1355	435.7	445.3	9.6	8.82	91.9							
								1	1.34	1.34	435.70	437.04		
								2	1.41	1.41	437.04	438.45	WROG, WRMB, IW	
								3	1.29	1.29	438.45	439.74	WEL	
								4	1.40	1.40	439.74	441.14	HS	
								5	1.26	1.26	441.14	442.40		
								6	0.96	0.96	442.40	443.36		
								7	1.04	1.04	443.36	444.40		
								CC	0.12	0.12	444.40	444.52	PAL	
									8.82	8.82				
11R	28 June	1510	445.3	454.9	9.6	8.54	89.0							
								1	1.38	1.38	445.30	446.68		

Table T2 (continued).

Core	Date (1998)	Time (UTC +10 hr)	Core depth (mbsf) Top	Core depth (mbsf) Bottom	Length (m) Cored	Length (m) Recovered	Recovery (%)	Section	Length (m) Liner	Length (m) Curated	Section depth (mbsf) Top	Section depth (mbsf) Bottom	Catwalk samples	Comment
								2	1.37	1.37	446.68	448.05		
								3	1.32	1.32	448.05	449.37	IW	
								4	1.37	1.37	449.37	450.74	HS	
								5	1.46	1.46	450.74	452.20		
								6	1.37	1.37	452.20	453.57		
								CC	0.27	0.27	453.57	453.84	PAL	
									8.54	8.54				
12R	28 June	1605	454.9	464.5	9.6	7.99	83.2							
								1	1.35	1.35	454.90	456.25		
								2	1.50	1.50	456.25	457.75		
								3	1.11	1.11	457.75	458.86		
								4	1.30	1.30	458.86	460.16	HS, IW	
								5	1.14	1.14	460.16	461.30	WEL	
								6	1.00	1.00	461.30	462.30		
								7	0.59	0.59	462.30	462.89	PAL	
									7.99	7.99				
13R	28 June	1715	464.5	474.1	9.6	9.23	96.1							
								1	1.39	1.39	464.50	465.89		
								2	1.26	1.26	465.89	467.15		
								3	0.89	0.89	467.15	468.04	IW	
								4	1.16	1.16	468.04	469.20	HS	
								5	1.44	1.44	469.20	470.64		
								6	1.33	1.33	470.64	471.97		
								7	0.90	0.90	471.97	472.87		
								8	0.70	0.70	472.87	473.57		
								CC	0.16	0.16	473.57	473.73	PAL	
									9.23	9.23				
14R	28 June	1820	474.1	483.7	9.6	9.37	97.6							
								1	1.32	1.32	474.10	475.42		
								2	1.34	1.34	475.42	476.76		
								3	1.20	1.20	476.76	477.96		
								4	1.46	1.46	477.96	479.42	IW	
								5	1.50	1.50	479.42	480.92	HS, WEL	
								6	1.50	1.50	480.92	482.42		
								7	0.88	0.88	482.42	483.30		
								CC	0.17	0.17	483.30	483.47	PAL	
									9.37	9.37				
15R	28 June	1930	483.7	493.3	9.6	8.40	87.5							
								1	1.46	1.46	483.70	485.16		
								2	0.88	0.88	485.16	486.04	WRSCR	
								3	1.28	1.28	486.04	487.32		
								4	1.50	1.50	487.32	488.82	HS	
								5	1.50	1.50	488.82	490.32		
								6	0.86	0.86	490.32	491.18		
								7	0.70	0.70	491.18	491.88		
								CC	0.22	0.22	491.88	492.10	PAL	
									8.40	8.40				

Table T2 (continued).

Core	Date (1998)	Time (UTC +10 hr)	Core depth (mbsf) Top	Core depth (mbsf) Bottom	Length (m) Cored	Length (m) Recovered	Recovery (%)	Section	Length (m) Liner	Length (m) Curated	Section depth (mbsf) Top	Section depth (mbsf) Bottom	Catwalk samples	Comment
16R	28 June	2055	493.3	503.0	9.7	8.62	88.9							
								1	1.50	1.50	493.30	494.80		
								2	1.00	1.00	494.80	495.80		
								3	1.46	1.46	495.80	497.26		
								4	1.27	1.27	497.26	498.53		
								5	1.30	1.30	498.53	499.83	IW	
								6	1.40	1.49	499.83	501.32	HS, WEL	
								7	0.29	0.29	501.32	501.61		
								CC	0.40	0.40	501.61	502.01	PAL	
									8.62	8.71				
17R	28 June	2155	503.0	512.6	9.6	8.76	91.3							
								1	1.08	1.08	503.00	504.08		
								2	1.13	1.13	504.08	505.21		
								3	1.45	1.45	505.21	506.66		
								4	1.47	1.47	506.66	508.13	HS	
								5	1.24	1.24	508.13	509.37		
								6	1.50	1.50	509.37	510.87		
								7	0.88	0.88	510.87	511.75		
								CC	0.01	0.01	511.75	511.76	PAL	
									8.76	8.76				
18R	28 June	2315	512.6	522.3	9.7	10.08	103.9							
								1	1.50	1.50	512.60	514.10		
								2	1.31	1.31	514.10	515.41		
								3	1.11	1.11	515.41	516.52		
								4	1.30	1.30	516.52	517.82	HS, IW, WROG, WRMB	
								5	1.09	1.09	517.82	518.91	WEL	
								6	1.50	1.50	518.91	520.41		
								7	1.50	1.50	520.41	521.91		
								8	0.39	0.39	521.91	522.30		
								CC	0.38	0.38	522.30	522.68	PAL	
									10.08	10.08				
19R	29 June	0150	522.3	532.0	9.7	6.93	71.4							
								1	1.50	1.50	522.30	523.80		
								2	1.19	1.19	523.80	524.99	HS	
								3	1.37	1.37	524.99	526.36		
								4	1.43	1.43	526.36	527.79		
								5	1.02	1.02	527.79	528.81		
								CC	0.42	0.42	528.81	529.23	PAL	
									6.93	6.93				
20R	29 June	0345	532.0	541.6	9.6	7.16	74.6							
								1	1.44	1.44	532.00	533.44		
								2	1.34	1.34	533.44	534.78		
								3	0.75	0.75	534.78	535.53	IW	
								4	1.47	1.47	535.53	537.00	HS, WEL	
								5	1.08	1.08	537.00	538.08		
								6	0.84	0.84	538.08	538.92		
								CC	0.24	0.24	538.92	539.16	PAL	
									7.16	7.16				

Table T2 (continued).

Core	Date (1998)	Time (UTC +10 hr)	Core depth (mbsf) Top	Core depth (mbsf) Bottom	Length (m) Cored	Length (m) Recovered	Recovery (%)	Section	Length (m) Liner	Length (m) Curated	Section depth (mbsf) Top	Section depth (mbsf) Bottom	Catwalk samples	Comment
21R	29 June	0530	541.6	551.2	9.6	9.85	102.6							
								1	1.51	1.51	541.60	543.11		
								2	1.53	1.53	543.11	544.64		
								3	1.42	1.42	544.64	546.06		
								4	1.34	1.34	546.06	547.40		
								5	0.90	0.90	547.40	548.30	HS	
								6	0.70	0.70	548.30	549.00		
								7	1.30	1.30	549.00	550.30		
								8	0.92	0.92	550.30	551.22		
								CC	0.23	0.23	551.22	551.45	PAL	
									9.85	9.85				
22R	29 June	0655	551.2	560.8	9.6	4.46	46.5							
								1	1.34	1.34	551.20	552.54	IW	
								2	1.20	1.20	552.54	553.74	HS, WEL	
								3	0.91	0.91	553.74	554.65		
								4	0.99	0.99	554.65	555.64		
								CC	0.02	0.02	555.64	555.66	PAL	
									4.46	4.46				
23R	29 June	0810	560.8	565.6	4.8	1.94	40.4							
								1	1.50	1.50	560.80	562.30		
								2	0.41	0.41	562.30	562.71	HS	
								CC	0.03	0.03	562.71	562.74	PAL	
									1.94	1.94				
24R	29 June	0930	565.6	570.4	4.8	6.10	127.1							
								1	1.44	1.44	565.60	567.04		
								2	1.48	1.48	567.04	568.52	HS, IW	
								3	1.43	1.43	568.52	569.95		
								4	1.24	1.24	569.95	571.19		
								CC	0.51	0.51	571.19	571.70	PAL	
									6.10	6.10				
25R	29 June	1055	570.4	580.0	9.6	8.05	83.9							
								1	1.44	1.44	570.40	571.84		
								2	1.29	1.29	571.84	573.13		
								3	1.50	1.50	573.13	574.63		
								4	1.50	1.50	574.63	576.13		
								5	1.34	1.34	576.13	577.47	HS	
								6	0.95	0.95	577.47	578.42		
								CC	0.03	0.03	578.42	578.45	PAL	All to paleontology lab
									8.05	8.05				
26R	29 June	1205	580.0	589.6	9.6	8.23	85.7							
								1	1.46	1.46	580.00	581.46		
								2	1.21	1.21	581.46	582.67	WEL	
								3	1.26	1.26	582.67	583.93	HS, IW, WROG, WRMB	
								4	1.11	1.11	583.93	585.04		
								5	1.35	1.35	585.04	586.39		
								6	1.04	1.04	586.39	587.43		
								7	0.72	0.72	587.43	588.15		
								CC	0.08	0.08	588.15	588.23	PAL	
									8.23	8.23				

Table T2 (continued).

Core	Date (1998)	Time (UTC +10 hr)	Core depth (mbsf) Top	Core depth (mbsf) Bottom	Length (m) Cored	Length (m) Recovered	Recovery (%)	Section	Length (m) Liner	Length (m) Curated	Section depth (mbsf) Top	Section depth (mbsf) Bottom	Catwalk samples	Comment
27R	29 June	1315	589.6	599.2	9.6	4.35	45.3							
								1	1.10	1.10	589.60	590.70	HS, WRSCR	
								2	1.30	1.30	590.70	592.00		
								3	1.09	1.09	592.00	593.09		
								4	0.69	0.69	593.09	593.78		
								CC	0.17	0.17	593.78	593.95	PAL	
									4.35	4.35				
28R	29 June	1415	599.2	608.9	9.7	1.37	14.1							
								1	1.24	1.24	599.20	600.44	HS	
								CC	0.13	0.13	600.44	600.57	PAL	
									1.37	1.37				
29R	29 June	1515	608.9	618.5	9.6	2.52	26.3							
								1	1.03	1.03	608.90	609.93		
								2	1.03	1.03	609.93	610.96	IW	
								3	1.30	1.30	610.96	612.26	HS	
								CC	0.16	0.16	612.26	612.42	PAL	
									2.52	2.52				
30R	29 June	1615	618.5	628.2	9.7	1.05	10.8							
								1	0.90	0.90	618.50	619.40	HS	
								CC	0.15	0.15	619.40	619.55	PAL	
									1.05	1.05				
31R	29 June	1720	628.2	637.9	9.7	2.59	26.7							
								1	1.40	1.40	628.20	629.60	IW	
								2	1.17	1.17	629.60	630.77	HS, WEL	
								CC	0.02	0.02	630.77	630.79	PAL	
									2.59	2.59				
32R	29 June	1830	637.9	647.5	9.6	2.53	26.4							
								1	1.41	1.41	637.90	639.31		
								2	1.11	1.11	639.31	640.42	HS	
								CC	0.01	0.01	640.42	640.43	PAL	
									2.53	2.53				
33R	29 June	2005	647.5	657.1	9.6	0.32	3.3							
								1	0.29	0.29	647.50	647.79	HS	
								CC	0.03	0.03	647.79	647.82	PAL	All to paleontology lab
									0.32	0.32				
34R	29 June	2135	657.1	666.7	9.6	7.20	75.0							
								1	1.38	1.38	657.10	658.48		
								2	1.33	1.33	658.48	659.81		
								3	1.33	1.33	659.81	661.14	IW, WRMB, WROG	
								4	1.24	1.24	661.14	662.38	HS, WEL	
								5	0.79	0.79	662.38	663.17		
								6	0.81	0.81	663.17	663.98		
								CC	0.32	0.32	663.98	664.30	PAL	
									7.20	7.20				
35R	29 June	2315	666.7	676.4	9.7	9.88	101.9							
								1	1.12	1.12	666.70	667.82	HS	
								2	1.29	1.29	667.82	669.11		
								3	0.99	0.99	669.11	670.10		

Table T2 (continued).

Core	Date (1998)	Time (UTC +10 hr)	Core depth (mbsf) Top	Core depth (mbsf) Bottom	Length (m) Cored	Length (m) Recovered	Recovery (%)	Section	Length (m) Liner	Length (m) Curated	Section depth (mbsf) Top	Section depth (mbsf) Bottom	Catwalk samples	Comment
								4	1.50	1.50	670.10	671.60		
								5	1.25	1.25	671.60	672.85		
								6	0.96	0.96	672.85	673.81		
								7	1.05	1.05	673.81	674.86		
								8	1.46	1.46	674.86	676.32		
								CC	0.26	0.26	676.32	676.58	PAL	
									9.88	9.88				
36R	30 June	0100	676.4	686.0	9.6	8.97	93.4							
								1	1.50	1.50	676.40	677.90		
								2	1.50	1.50	677.90	679.40	IW	
								3	1.50	1.50	679.40	680.90	WEL, HS	
								4	1.50	1.50	680.90	682.40		
								5	1.50	1.50	682.40	683.90		
								6	1.07	1.07	683.90	684.97		
								CC	0.40	0.40	684.97	685.37	PAL	
									8.97	8.97				
37R	30 June	0240	686.0	695.6	9.6	6.92	72.1							
								1	1.48	1.48	686.00	687.48		
								2	1.48	1.48	687.48	688.96		
								3	1.50	1.50	688.96	690.46	HS	
								4	1.27	1.27	690.46	691.73		
								5	0.97	0.97	691.73	692.70		
								CC	0.22	0.22	692.70	692.92	PAL	
									6.92	6.92				
38R	30 June	0435	695.6	705.3	9.7	8.14	83.9							
								1	1.38	1.38	695.60	696.98		
								2	1.32	1.32	696.98	698.30	WRSCR	
								3	1.46	1.46	698.30	699.76		
								4	1.50	1.50	699.76	701.26	HS	
								5	1.50	1.50	701.26	702.76	HS, WEL	
								6	0.40	0.40	702.76	703.16		
								CC	0.58	0.58	703.16	703.74	PAL	
									8.14	8.14				
39R	30 June	0615	705.3	715.0	9.7	3.75	38.7							
								1	1.31	1.31	705.30	706.61		
								2	1.43	1.43	706.61	708.04		
								3	0.83	0.83	708.04	708.87	HS	
								CC	0.18	0.18	708.87	709.05	PAL	Trace to paleontology lab
									3.75	3.75				
40R	30 June	0840	715.0	724.7	9.7	4.18	43.1							
								1	1.26	1.26	715.00	716.26		
								2	0.39	0.39	716.26	716.65	HS, IW	
								3	1.50	1.50	716.65	718.15	WEL	
								4	0.75	0.75	718.15	718.90		
								CC	0.28	0.28	718.90	719.18	PAL	
									4.18	4.18				
41R	30 June	1045	724.7	734.3	9.6	3.66	38.1							
								1	1.50	1.50	724.70	726.20		

Table T2 (continued).

Core	Date (1998)	Time (UTC +10 hr)	Core depth (mbsf) Top	Core depth (mbsf) Bottom	Length (m) Cored	Length (m) Recovered	Recovery (%)	Section	Length (m) Liner	Length (m) Curated	Section depth (mbsf) Top	Section depth (mbsf) Bottom	Catwalk samples	Comment
								2	1.08	1.08	726.20	727.28	HS	
								3	0.89	0.89	727.28	728.17		
								CC	0.19	0.19	728.17	728.36	PAL	Trace to paleontology lab
									3.66	3.66				
42R	30 June	1250	734.3	743.9	9.6	2.92	30.4							
								1	1.50	1.50	734.30	735.80		
								2	1.02	1.02	735.80	736.82	HS	
								CC	0.40	0.40	736.82	737.22	PAL	
									2.92	2.92				
43R	30 June	1510	743.9	753.6	9.7	3.30	34.0							
								1	1.02	1.02	743.90	744.92		
								2	0.89	0.89	744.92	745.81	HS, IW	
								3	1.25	1.25	745.81	747.06	PAL, WEL	
								CC	0.14	0.14	747.06	747.20		
									3.30	3.17				
44R	30 June	1720	753.6	763.2	9.6	1.00	10.4							
								1	1.00	1.40	753.60	755.00		
									1.00	1.40				
45R	30 June	2100	763.2	772.9	9.7	2.80	28.9							
								1	1.50	1.50	763.20	764.70		
								2	1.30	1.45	764.70	766.15		
								3	0.00	0.89	766.15	767.04		
									2.80	3.84				
46R	1 July	0230	772.9	777.6	4.7	2.92	62.1							
								1	1.00	1.33	772.90	774.23		
								2	1.00	1.50	774.23	775.73		
								3	0.92	0.45	775.73	776.18		
									2.92	3.28				
47R	1 July	0935	777.6	782.5	4.9	5.06	103.3							
								1	1.06	1.12	777.60	778.72		
								2	0.96	1.41	778.72	780.13		
								3	1.42	1.14	780.13	781.27		
								4	1.50	1.44	781.27	782.71		
								5	0.12	0.28	782.71	782.99		
									5.06	5.39				
48R	1 July	1345	782.5	787.2	4.7	5.71	121.5							
								1	1.01	1.03	782.50	783.53		
								2	1.39	1.44	783.53	784.97		
								3	1.34	1.50	784.97	786.47		
								4	0.99	1.10	786.47	787.57		
								5	0.58	0.89	787.57	788.46		
								6	0.40	0.00				
									5.71	5.96				
49R	1 July	1720	787.2	792.2	5.0	3.90	78.0							
								1	1.09	1.10	787.20	788.30		
								2	0.90	1.45	788.30	789.75		
								3	0.96	1.44	789.75	791.19		
								4	0.95	0.00				
									3.90	3.99				

Table T2 (continued).

Core	Date (1998)	Time (UTC +10 hr)	Core depth (mbsf) Top	Core depth (mbsf) Bottom	Length (m) Cored	Length (m) Recovered	Recovery (%)	Section	Length (m) Liner	Length (m) Curated	Section depth (mbsf) Top	Section depth (mbsf) Bottom	Catwalk samples	Comment
50R	1 July	2045	792.2	796.9	4.7	3.52	74.9							
								1	1.50	1.50	792.20	793.70		
								2	1.50	1.20	793.70	794.90		
								3	0.52	1.05	794.90	795.95		
									3.52	3.75				
51R	1 July	0010	796.9	802.0	5.1	3.76	73.7							
								1	1.26	0.91	796.90	797.81		
								2	1.50	1.19	797.81	799.00		
								3	0.64	1.39	799.00	800.39		
								4	0.36	0.69	800.39	801.08		
									3.76	4.18				
				Cored:	449.2	299.87	66.8							
				Drilled:	352.8									
				Total:	802.0									

Note: PAL = paleontology; IW = interstitial water; WROG = whole round organic geochemistry; WRMB = whole round microbiology; HS = headspace; WEL = Wellsbury microbiology; WRSCR = whole round Screaton.

Table T3. Results of X-ray diffraction analysis of bulk fine-grained sediments, Site 1109 thin sections. (Continued on next page.)

Core, section, interval (cm)	Description	XRD identification: major (minor) minerals
180-1109C-		
1H-1, 131-132	Silty clay	Calcite (quartz, plagioclase)
1H-4, 64.5-67	Calcareous silt	Calcite (quartz, plagioclase)
2H-4, 129-130	Calcareous clay	Calcite (aragonite)
3H-2, 87-88	Calcareous clay	Calcite (Mg-Calcite?)
4H-2, 105-106	Calcareous silty clay	Calcite (quartz, plagioclase)
5H-6, 58-59	Clay	Calcite (quartz, plagioclase)
6H-7, 5.5-6.6	Clayey silt	Calcite (quartz, plagioclase)
7H-5, 89-90	Clayey silt	Calcite (quartz, plagioclase)
10H-2, 42-43	Very fine sand to silt	Plagioclase, quartz, C/S? (chlorite, augite, amphibole, pyrite?)
11H-2, 104-105	Silty sand	Calcite, quartz, plagioclase, augite, C/S? (chlorite, amphibole)
12X-7, 25-26	Clay	C/S?, chlorite, quartz, plagioclase, calcite, augite (illite, amphibole)
13X-6, 117-118	Clay	C/S?, calcite, quartz, plagioclase, augite, chlorite (illite, amphibole)
14X-6, 142-143	Silty clay	Calcite, quartz, plagioclase, C/S? (chlorite, augite, amphibole, illite)
15X-6, 58-59	Clayey silt	Calcite, quartz, plagioclase, C/S? (chlorite, augite, amphibole, illite)
16X-3, 77-78	Sandy silt	Quartz, calcite, plagioclase, C/S? (chlorite, illite, augite, amphibole)
18X-4, 88-89	Sandy silt	C/S?, calcite, plagioclase, quartz, K-feldspar, augite (illite, amphibole)
19X-1, 120.5-121.5	Silty clay	Quartz, plagioclase, calcite, C/S? (illite, augite, amphibole)
20X-4, 88-89	Sandy silty clay	Calcite, plagioclase, quartz (C/S?, chlorite, augite, amphibole)
21X-CC-25-26	Clayey silt	Plagioclase, quartz, calcite (augite, C/S?, chlorite)
22X-1, 29.5-31	Fine sand	Plagioclase, calcite, quartz, C/S? (amphibole, augite, chlorite, illite)
23X-3, 32-33	Clayey silt	Calcite (plagioclase, quartz, C/S?, chlorite, amphibole, augite)
24X-CC, 11-12	Sand	Plagioclase, quartz, augite (amphibole, C/S?)
26X-3, 25-26	Clayey silt	Calcite, plagioclase, quartz (augite, C/S?, chlorite, sudoite?, amphibole)
27X-5, 115-116	Silty clay	Calcite (plagioclase, quartz, illite)
28X-4, 34-35	Clayey silt	Calcite, plagioclase (quartz, illite)
29X-3, 5-6	Sandy silt	Calcite (plagioclase, quartz)
29X-3, 39-40	Silty sand	Calcite, plagioclase (quartz)
30X-2, 33-34	Silty clay	Calcite, plagioclase (quartz, augite)
31X-3, 17-18	Sandy silt	Plagioclase, calcite, quartz, augite (chlorite, illite, amphibole)
32X-3, 107-108	Sandy silty clay	Calcite, quartz, plagioclase (chlorite, augite)
33X-6, 115-116	Sandy silty clay	Calcite, plagioclase, quartz (augite, chlorite, illite, I/V?, I/S?)
34X-2, 87-88	Clayey silt	Calcite, plagioclase, quartz (illite, augite, smectite?)
35X-6, 64.5-65	Silty clay	Calcite (quartz, plagioclase)
37X-2, 43.5-44.5	Calcareous clay	Calcite (quartz, plagioclase, smectite?))
38X-3, 53-54	Clayey silt	Calcite, plagioclase (quartz, illite, amphibole, chlorite, smectite?)
39X-6, 78-79	Silty clay	Plagioclase, cristobalite, calcite, amphibole (quartz, illite)
40X-4, 45.5-47	Silty clay	Calcite, K-feldspar, plagioclase, quartz (illite, amphibole, augite)
41X-2, 32-33	Sandy silty clay	Calcite, plagioclase, quartz (smectite?, illite, amphibole)
180-1109D-		
2R-3, 39.5-42.5	Silty sandy claystone	Calcite, plagioclase, quartz (illite, chlorite, smectite?)
3R-6, 83-85	Clayey siltstone	Calcite, plagioclase, quartz (illite, amphibole, smectite?)
4R-4, 69-71	Clayey siltstone	Calcite, plagioclase, quartz (chlorite, smectite?, illite, amphibole)
5R-1, 60-61	Sandy silty claystone	Calcite, K-feldspar, plagioclase, quartz (chlorite, smectite?, illite)
6R-1, 39.5-41.5	Clayey siltstone	Calcite, plagioclase, quartz (chlorite, smectite?, illite, amphibole)
7R-3, 15-17	Calcareous claystone	Calcite, plagioclase, quartz (illite)
9R-3, 100-101	Clayey siltstone	Calcite, plagioclase, quartz (illite)
10R-1, 22.5-26	Clayey siltstone	Calcite, plagioclase, quartz (illite)
11R-3, 58-59	Silty claystone	Calcite, plagioclase, quartz (illite, amphibole)
12R-7, 10-11	Silty claystone	Calcite, plagioclase, quartz (illite, amphibole)
13R-3, 13.5-15.5	Siltstone	Calcite, plagioclase, quartz (illite, amphibole)
14R-2, 20-22	Silty claystone	Calcite, plagioclase, quartz (illite, amphibole)
15R-1, 81-82	Silty claystone	Calcite, plagioclase, quartz (illite, amphibole)
16R-1, 83-84	Silty sandstone	Calcite, quartz, plagioclase, aragonite, illite, amphibole (chlorite)
17R-3, 74-76.5	Siltstone	Calcite, plagioclase, quartz, amphibole, illite
18R-2, 12-14	Calcareous silty claystone	Calcite, plagioclase, quartz, illite (amphibole)
19R-2, 19-21	Calcareous clayey siltstone	Calcite, quartz (plagioclase, illite)
20R-4, 36-37	Calcareous silty claystone	Calcite, plagioclase, quartz (illite, augite)
21R-4, 66-68	Calcareous silty claystone	Calcite, plagioclase, quartz (illite, amphibole)
22R-1, 62-63	Claystone	Plagioclase, illite (mica)
22R-3, 59-60.5	Calcareous sandy siltstone	Calcite, quartz, plagioclase (illite, chlorite, amphibole)
23R-2, 33-34	Calcareous silty claystone	Calcite, plagioclase, quartz (illite)
24R-3, 70-71	Sandy siltstone	Plagioclase, calcite, quartz (illite)
25R-4, 78.5-79.5	Calcareous sandstone	Calcite, hornblende, quartz, plagioclase (illite)
26R-2, 36-38	Calcareous silty sandstone	Calcite, quartz, plagioclase (illite)
27R-1, 58-59	Packstone-grainstone	Calcite, aragonite, plagioclase (quartz, illite)
28R-1, 84-87	Packstone-grainstone	Calcite, plagioclase (quartz, amphibole, illite)

Table T3 (continued).

Core, section, interval (cm)	Description	XRD identification: major (minor) minerals
29R-1, 47-49	Packstone-grainstone	Plagioclase, calcite, quartz (illite, amphibole)
30R-1, 47-49	Packstone	Plagioclase, calcite, mica/illite, amphibole
31R-1, 77-79	Packstone-grainstone	Plagioclase, calcite, amphibole, quartz, illite
32R-2, 62-63	Packstone	Calcite (plagioclase)
35R-2, 103-103.5	Silty clay	Calcite, pyroxene, plagioclase, quartz (chlorite, illite)
35R-8, 55.5-57.5	Clayey siltstone	Calcite, plagioclase, quartz (pyroxene, amphibole, illite)
36R-6, 34-35	Calcareous clayey siltstone	Pyroxene, calcite, plagioclase (smectite?, illite)
37R-2, 97-98	Sandy siltstone	Plagioclase, quartz (illite, amphibole)
38R-6, 17-17.5	Sandstone	Mg-calcite, plagioclase, quartz
39R-3, 22-24	Volcaniclastic sand	Pyroxene, plagioclase, K-feldspar
40R-1, 57-58	Silty clay, rich in limonite	Goethite, plagioclase (smectite?)
41R-3, 69-71	Clayey siltstone	Plagioclase (albite), smectite
42R-2, 90-91	Clayey siltstone	Plagioclase (quartz, smectite?)
43R-1, 62-63	Silty claystone (highly altered)	Smectite (various types)
43R-2, 66-68	Clayey siltstone (highly altered)	Smectite (various types)

Note: C/S = chlorite-smectite mixed layer; I/V = illite-vermiculite; I/S = illite-smectite mixed layer.

Table T4. Shipboard major element analyses of dolerite by X-ray fluorescence.

Core, section, interval (cm)	SiO_2	TiO_2	Al_2O_3	Fe_2O_3	MnO	MgO	CaO	Na_2O	K_2O	P_2O_5	Total	LOI	Fe_2O_3/MgO
Upper unit													
180-1109D-													
46R-1, 104-106	51.56	1.45	14.51	12.74	0.19	6.14	12.68	1.73	0.12	0.12	101.2	1.55	2.08
	50.84	1.43	14.48	12.74	0.19	6.10	12.60	1.74	0.11	0.11	100.3	1.55	2.09
47R-3, 104-107	51.24	1.43	14.58	12.72	0.18	6.30	12.69	1.76	0.08	0.12	101.1	1.25	2.02
	51.39	1.38	14.64	12.63	0.18	6.36	12.54	1.68	0.08	0.11	101.0	1.25	1.99
48R-3, 98-100	51.41	1.33	14.57	12.43	0.19	6.84	12.40	1.65	0.11	0.11	101.4	1.26	1.82
	51.01	1.33	14.45	12.45	0.19	6.84	12.34	1.62	0.11	0.11	100.4	1.26	1.82
49R-2, 103-106	50.74	1.31	15.53	12.08	0.19	6.99	12.74	1.63	0.10	0.11	101.1	2.01	1.73
	50.72	1.31	15.55	12.20	0.19	7.02	12.43	1.68	0.10	0.10	101.3	2.01	1.74
50R-1, 10-12	51.04	1.31	14.75	12.50	0.19	7.00	12.24	1.60	0.09	0.10	100.8	1.64	1.79
	51.21	1.30	14.88	12.53	0.18	7.03	12.32	1.58	0.09	0.10	101.2	1.64	1.78
51R-1, 48-51	51.48	1.33	14.81	12.43	0.19	7.49	12.09	1.55	0.11	0.10	101.6	1.74	1.66
	51.53	1.33	14.78	12.33	0.18	7.54	12.10	1.58	0.11	0.10	101.6	1.74	1.64
Lower unit													
180-1109D-													
51R-4, 51-54	51.58	1.43	15.45	11.41	0.18	7.08	12.60	1.92	0.19	0.11	101.9	2.67	1.61
	51.17	1.43	15.32	11.45	0.18	7.04	12.48	1.92	0.14	0.11	101.3	2.67	1.63
	51.73	1.42	15.38	11.37	0.18	7.11	12.52	1.99	0.14	0.11	102.0	2.67	1.60

Notes: LOI = loss on ignition. All values are in weight percent.

Table T5. Shipboard trace element analyses of dolerite by X-ray fluorescence.

Core, section, interval (cm)	Depth (mbsf)	Nb	Zr	Y	Sr	Rb	Zn	Cu	Ni	Cr	V	Ce	Ba
Upper unit													
180-1109D-													
46R-1, 104-106	773.95	4	75	25	141	3	82	144	79	316	307	7	0
		3	71	22	142	2	83	142	78	331	311	13	0
		4	72	21	141	1	82	142	78	337	310	11	0
47R-3, 104-107	781.19	4	75	25	139	3	80	141	81	339	311	11	2
		4	72	22	138	1	82	142	79	347	314	13	0
		4	72	22	139	1	81	140	82	351	314	10	0
48R-3, 98-100	785.98	4	72	25	132	3	86	131	88	393	294	5	15
		5	69	21	133	1	86	131	90	401	303	13	22
49R-2, 103-106	789.35	3	71	24	135	3	85	143	99	411	284	6	5
		4	66	20	133	0	84	143	96	429	290	16	13
50R-1, 10-12	792.31	4	70	23	138	4	83	134	113	358	286	12	13
		4	67	20	138	1	84	133	114	363	282	12	12
51R-1, 48-51	797.40	4	70	23	130	3	83	133	113	358	282	10	9
		4	66	20	131	1	83	133	113	363	293	8	13
Lower unit													
180-1109D-													
51R-4, 51-54	800.92	4	71	20	145	0	85	153	102	358	328	11	7
		4	70	20	145	1	85	151	102	355	331	10	0

Note: All values are in parts per million.

Table T6. Range chart showing the distribution of selected calcareous nannofossil species. **A.** Holes 1109A, 1109B, and 1109C. (Continued on next two pages.)

Core, section, interval (cm)	Depth (mbsf)	Abundance	Preservation	*Braarudosphaera bigelowii*	*Calcidiscus leptoporus*	*Calcidiscus macintyrei*	*Ceratolithus cristatus*	*Ceratolithus rugosus*	*Coccolithus pelagicus*	*Dictyococcites productus*	*Discoaster asymmetricus*	*Discoaster blackstockae*	*Discoaster brouweri*	*Discoaster pentaradiatus*	*Discoaster surculus*	*Discoaster tamalis*	*Discoaster variabilis*	*Emiliania huxleyi*	*Gephyrocapsa oceanica*	*Gephyrocapsa omega*	*Helicosphaera carteri*	*Helicosphaera sellii*	*Pseudoemiliania lacunosa*	*Reticulofenestra minutula*	*Sphenolithus abies*
180-1109A-																									
1H-CC, 25-28	9.93	A	VG		C													C	A		C				
180-1109B-																									
1H-CC, 26-28	5.26	A	VG		F													C	A						
2H-CC, 24-27	15.13	A	G		C													C	A		F				
180-1109C-																									
1H-CC, 23-26	7.34	A	VG		F		R		F									F	C	F	C				
2H-CC, 8-10	17.26	A	G															R							
2H-CC, 11-14	17.29	A	G		C													C	A		C				
3H-1, 95-97	17.85	A	VG																C	F					
3H-CC, 16-19	26.74	A	G		F														C		F				
4H-1, 95-97.5	27.35																						r		
4H-3, 18-19	29.58																						r		
4H-4, 104.5-105.5	31.95																						R		
4H-4, 142.5-143.5	32.33																			R			F		
4H-CC, 28-31	36.42	A	G																	F			C		
5H-1, 95-96	36.85	A	G		F														R				R	C	
5H-5, 95-96	42.85	A	M		F														C		F		F	C	
5H-6, 95-96	44.35	C	M		F														F		F			C	
5H-CC, 45-48	46.19	A	G		C	R			F													F	C		
6H-1, 95-97	46.35					R																			
6H-3, 95-97	49.35																								
6H-6, 95-97	53.85												R												
6H-CC, 26-29	55.49	A	G			R	R						F									F	C		
7H-CC, 39-42	64.98	A	G	C	C								R								C		A	F	
8H-CC, 23-26	74.41	A	VG		F	R							R								F	F	C		
9H-1, 95-97.5	74.85	F	M									R	R												
9H-CC, 34-37	83.95	C	M										R									F	C		
10H-5, 41-43	89.81	F	M																						
10H-CC, 5-8	93.10	C	M																						
11H-CC, 23-26	102.81	F	M				R			F														C	
12X-CC, 28-31	112.12	C	M										R				R								
13X-3, 19-20	115.19	F	M																						
13X-CC, 26-29	121.66	A	M		F								R									F	C		
14X-CC, 31-34	131.33				R					F												F		C	
15X-CC, 26-30	140.94	A	G																						
17X-CC, 30-34	153.10	R	P																						
18X-CC, 10-14	169.53	A	M			R							R	R								F			
19X-CC, 28-31	171.41	C	M		F				F												F	F	C		
20X-1, 78-80	180.08	F	M										R												
20X-CC, 34-37	185.30	C	M		F																R	R	F		
21X-CC, 45-48	189.35	B																							
22X-1, 67-70.5	199.17																								
22X-CC, 33-36	200.41	C	M										R								F				
23X-1, 41-43	208.51												R												
23X-5, 95-97	213.70												R	R											
23X-7, 52-54	216.27												R	R											
23X-CC, 48-51	218.06	C	M		C	R			F												C	F	C		
24X-CC, 28-31	217.98	F	M		R				R												R		R		
25X-CC, 28-31	228.03	B																							
26X-1, 95-97	237.95																								
26X-3, 119-121	241.14													R											
26X-6, 79-81	245.24												R	R											
26X-CC, 32-35	246.77	A	G		C	R			R		R		F	F							F	F	F		
27X-CC, 24-27	256.13												F	R											
28X-CC, 27-30	266.01	F	M										R												
29X-CC, 9-12	275.50	C	M										F	R											
30X-CC, 31-34	285.38	C	G										R	F											
31X-CC, 31-34	294.81	F	M										F	F											
32X-CC, 15-20	304.36	C	G										C	C	R										

Table T6 (continued).

Core, section, interval (cm)	Depth (mbsf)	Abundance	Preservation	*Braarudosphaera bigelowii*	*Calcidiscus leptoporus*	*Calcidiscus macintyrei*	*Ceratolithus cristatus*	*Ceratolithus rugosus*	*Coccolithus pelagicus*	*Dictyococcites productus*	*Discoaster asymmetricus*	*Discoaster blackstockae*	*Discoaster brouweri*	*Discoaster pentaradiatus*	*Discoaster surculus*	*Discoaster tamalis*	*Discoaster variabilis*	*Emiliania huxleyi*	*Gephyrocapsa oceanica*	*Gephyrocapsa omega*	*Helicosphaera carteri*	*Helicosphaera sellii*	*Pseudoemiliania lacunosa*	*Reticulofenestra minutula*	*Sphenolithus abies*
33X-CC, 32-36	314.23	A	G		F				R		R		C	C							F				
34X-CC, 37-40	324.02	A	G										F	C											
35X-CC, 45-48	333.83	A	G		F	R					R		C	F		R					F				
36X-CC, 33-36	338.89	A	M		F	R			R				C	F							F	R			
37X-1, 93-95.5	344.03																								R
37X-CC, 40-43	345.20	B																							
38X-CC, 26-29	356.30	A	G		F	R			F		R		F	F	R						F	R	F		
39X-CC, 40-43	362.43	A	G		F	R			R		R		F	F	R	R					F		F		
40X-CC, 21-24	369.79	C	G					R			R		C	C		R									F
41X-CC, 32-35	376.55												C	C	R										R

Notes: Abundance (number specimens of a species per field-of-view): D = dominant (>100); A = abundant (10–100); C = common (1–10); F = few (1 per 10 fields of view); R = rare (<1 per 10 fields of view); B = barren; T = trace (<1 per transect of slide). Preservation: VG = very good; G = good; M = moderate; P = poor. Distribution: C = common; F = few; R = rare; r = reworked.

Table T6 (continued). B. Hole 1109D.

Core, section, interval (cm)	Depth (mbsf)	Abundance	Preservation	*Braarudosphaera bigelowii*	*Calcidiscus leptoporus*	*Calcidiscus macintyrei*	*Ceratolithus armatus*	*Ceratolithus rugosus*	*Coccolithus pelagicus*	*Discoaster asymmetricus*	*Discoaster brouweri*	*Discoaster pentaradiatus*	*Discoaster surculus*	*Discoaster tamalis*	*Discoaster variabilis*	*Helicosphaera carteri*	*Helicosphaera sellii*	*Pseudoemiliania lacunosa*	*Reticulofenestra pseudoumbilicus*	*Reticulofenestra minuta*	*Reticulofenestra minutula*	*Sphenolithus abies*
180-1109D-																						
1R-CC, 33-36	359.01	A	VG		R	R			R	C	F		R	R		C	R				A	R
2R-1, 94.5-97	360.05	A	G							R	F	F							R			R
2R-CC, 15-19	368.00	C	G		R	R		R	R	F	F	F			R	F	F	F			C	R
3R-CC, 31-34	377.72	A	VG		R	R				R	F	R	R		R	F	R	R	R		C	R
4R-1, 96-98	379.26	A	G				R	R			F	F	R					R				R
4R-CC 40-44	386.53	C	G		R	R			F		F	F			R	F	R		R		C	F
5R-CC, 40-43	388.99	A	G	R	R	R	R		R	R	F		R		R	F			R		C	F
6R-1, 82-84.5	398.02	A	M							R				R				C				R
6R-CC, 21-24	403.98	C	M		R	R			R	R	F	R	R		R	F			R		C	F
7R-CC, 22-25	413.04	A	G		F	R		R	R		F	C	R	R		F			R			
8R-CC, 15-18	424.86	C	G		F	R		R	F	R	F	R	R			F			R			
9R-1, 80-82	426.90	A	M																			R
9R-CC, 23-26	434.70	A	M		F				R		F	R				F			R			
10R-CC, 9-12	444.49	C	M		R	R			R		F	F		R		F			R			
11R-CC, 22-27	453.79	C	M		F						F	F	R			C						
12R-7, 58-59	462.88	C	M		F	R			F		R	F				C	R		R			
13R-CC, 14-16	473.71	C	M		F	R			R		R	F				C	R					
14R-CC, 15-17	483.45	C	M		F					R		F		R		C	R		R			
15R-CC, 20-22	492.08	C	M		F	F			C	R	R	F	R			C	R		R			
16R-5, 95-97	499.48																					F
16R-CC, 37-4	501.98	C	G		C	F				R	F	F	R	R		F	R		R			
17R-CC, 0-1	511.75	C	M		F							F	R			C	F					
18R-CC, 36-38	522.66	C	G		F	R			F		R	C		R		C			R			
19R-CC, 40-42	529.21	C	M		R	R			R	R	F	F			R	F	R	R	R		C	C
20R-CC, 21-24	539.13	A	M		R	F			F		F	R			R	F	R	R			A	F
21R-CC, 17-23	551.39	C	M		R	R		R	R	R	F	R	R		R	F					C	F
22R-CC, 0-2	555.64	C	M			R	R	R	R	R	F	R			R	F			R		C	
23R-1, 95-96	561.75	A	G																			
23R-2, 21-22	562.51	A	G																			
23R-CC, 0-3	562.71	C	M			R		R	R		F	R			R	R			R		C	
24R-CC, 47-51	571.66	A	M			R			R	R	R	R			R	F	R		F			
25R-CC, 0-3	578.42	C	M			R		R			F	R			R	R					C	
26R-CC, 5-8	588.20	C	M		R			R								F			F			
27R-CC,14-17	593.92	F	P								R											
28R-CC, 10-13	600.54	F	P					R											R			
29R-CC, 13-16	612.39	C	M		F			R								F			R			
30R-CC, 13-15	619.53	C	M		F											F			F			
31R-CC, 0-2	630.77	C	M		P											F			F			
32R-CC, 0-1	640.42	F	M													R						
33R-CC, 0-3	647.79	F	P													R			R			
34R-CC, 31-32	664.29	C	P					R											R			
35R-CC, 24-26	676.56	C	P																R			
36R-CC, 37-40	685.34	R	P			R			R		R	R									R	
37R-CC, 18-22	692.88	T	P																	R		
38R-CC, 55-58	703.71	B																				
39R-CC, 17-18	709.04	B																				
40R-CC, 25-28	719.15	B																				
41R-CC, 18-19	728.35	B																				
42R-CC, 32-34	737.14	B																				
43R-3, 0-1	745.81	B																				
43R-3 0-1	745.81	B																				

Notes: Abundance (number specimens of a species per field-of-view): D = dominant (>100); A = abundant (10–100); C = common (1–10); F = few (1 per 10 fields of view); R = rare (<1 per 10 fields of view); B = barren; T = trace (<1 per transect of slide). Preservation: VG = very good; G = good; M = moderate; P = poor. Distribution: C = common; F = few; R = rare.

Table T7. Range chart showing the distribution of planktonic foraminifers, Holes 1109A, 1109C, and 1109D. (Continued on next page.)

Core, section, interval (cm)	Depth (mbsf)	Abundance	Preservation	*Bolliella adamsi*	*Bolliella calida*	*Dentoglobigerina altispira*	*Dentoglobigerina globosa*	*Globigerinella siphonifera*	*Globigerinoides conglobatus*	*Globigerinoides extremus*	*Globigerinoides fistulosus*	*Globigerinoides obliquus*	*Globigerinoides quadrilobatus*	*Globigerinoides ruber*	*Globigerinoides ruber* (pink)	*Globigerinoides sacculifer*	*Globigerinoides trilobus*	*Globorotalia crassaformis*	*Globorotalia margaritae*	*Globorotalia menardii*	*Globorotalia multicamerata*	*Globorotalia scitula*	*Globorotalia tosaensis*	*Globorotalia truncatulinoides*	*Globorotalia tumida*	*Globorotalia tumida flexuosa*	*Globorotalia ungulata*	*Neogloboquadrina acostaensis*	*Neogloboquadrina dutertrei*	*Neogloboquadrina humerosa*	*Orbulina universa*	*Pulleniatina obliquiloculata*	*Pulleniatina praecursor*	*Pulleniatina primalis*	*Pulleniatina spectabilis*	*Sphaeroidinella dehiscens*	*Sphaeroidinella dehiscens* s.l.	*Sphaeroidinellopsis paenedehiscens*	*Sphaeroidinellopsis seminulina*	*Sphaeroidinellopsis subdehiscens*	*Zeaglobigerina rubescens*
180-1109A-																																							
1H-CC, 25-28	9.93	A	VG		R			C	F				C	A	R	C		F		F		R		C		R	R		A		R	C			R				A
180-1109C-																																								
1H-CC, 23-26	7.34	A	VG	R				C	C				A	A		A		F		C		R			F	F	F		A		F	C							A
2H-CC, 11-14	17.29	A	VG		R			C	C				A	A	C	A		F		C				R	F	F			A		R	C			R				C
3H-CC, 16-19	26.74	C	M					F	F				C	C	F	F		C		F				C	F	R			C		R	C			R				F
4H-CC, 28-31	36.42	A	G					C	F				C	A	R	C		F				R	C	C		F	R		A	C	R	C			R				
5H-CC, 45-48	46.19	A	VG						A		A							A						R	A				A			A			A				
6H-CC, 26-29	55.49	A	VG						A		A					A		A					C	R	A							A			A				
7H-CC, 39-42	64.98	A	VG								A					A		C						C	A							A			A				
8H-CC, 23-26	74.41	A	VG								A							A					A	F	A							A							
9H-CC, 34-37	83.95	A	VG															A					A	C	A										A				
10H-CC, 5-8	93.10	A	VG											A		A							A	C	A				A			A							
11H-CC, 23-26	102.81	A	VG						A							A							A	C	A				A			A			A				
12X-CC, 28-31	112.12	A	VG											A									A	F	A				A			A			A				
13X-CC, 26-29	121.66	A	VG						A														A	F	A				A			A			A				
14X-CC, 31-34	131.33	A	VG						A		R			A									A	F	A				A			A			A				
15X-CC, 26-30	140.94	A	VG						A					A									A	F	A				A						A				
16X-CC, 37-40	501.98	R	P																					F	R										R				
18X-CC, 10-14	169.53	A	VG						A									A					A	F	A				A			A			A				
19X-CC, 28-31	171.41	C	G						R				C	A				R		R			C	F	R			R	R	F	R	C			R				
20X-CC, 34-37	185.30	R	M											R			R			R						R						R			R				
21X-CC, 45-48	189.35	R	M											R			R																						
24X-CC, 28-31	217.98	F	M								R		F	F		F		R		F					F							F			R				
26X-CC, 32-35	246.77	A	M							A	F		A	A		F	A	F		C		R	R	R	F		R		A	F	F				F				
27X-CC, 24-27	256.13	A	VG															F					F	R	A							A			A				
28X-CC, 27-30	266.01	A	VG								F							A					A	R	A			A				A			A				
29X-CC, 9-12	275.50	A	VG															A					A	R	A			A				A			A				
30X-CC, 31-34	285.38	A	VG								C							A						R	A			A				A			A				
31X-CC, 31-34	294.81	A	VG								C							A					A		A			A				A			A				
32X-CC, 15-20	304.36	A	VG								A							A					A		A			A				A			A				
33X-CC, 32-36	314.23	A	VG								C							A					R		A			A				A			A				
34X-CC, 37-40	324.02	A	G					F			F		A	A		A	A	R		C	R		F		F			A		C	F	F			F	F			
35X-CC, 45-48	333.83	C	M			F	F	F	F	F	F		A	A		A	A	R		C		R	R		F		F		C	R		C			R				
36X-CC, 33-36	338.89	F	M			R				R	R		F	F		R				F					R														
37X-CC, 40-43	345.20	R	M											R						R																			
38X-CC, 26-29	356.30	A	VG				R		F	A			A	A			A	F		C	R		F		F	F		C		C			F			F	F			
39X-CC, 40-43	362.43	A	VG			A												A					C		A										A				
40X-CC, 21-24	369.79	A	VG			A												C							A							A			A				
41X-CC, 32-35	376.55	A	G			A					R							R							A							C			A				
180-1109D-																																							
1R-CC, 33-36	359.01	A	VG			C												C					C		A				A		C				A				
2R-CC, 15-19	368.00	A	VG			A												C							A						C				C				
3R-CC, 31-34	377.72	A	VG			A												A							A						A	A			A				
4R-CC, 40-44	386.53	A	VG															F							A						A	C			A				
5R-CC, 40-43	388.99	A	G															C							A				C			C			C				
6R-CC, 21-24	403.98	A	VG															C							C				A		C	C			F				
7R-CC, 22-25	413.04	A	VG															C							A				C						C				
8R-CC, 15-18	424.86	F	M			F				R			F	F			F	R		R					R	F		F			R		F		R	R			
9R-CC, 23-26	434.70	F	M				R		R				R	F		F	F	R		R						R		R			R		R							
10R-CC, 9-12	444.49	F	M			R	F		R	F			F	F		F		R	R	R					F	R		F			R	F			R	R			
11R-CC, 22-27	453.79	C	M			F	C		F	C			C	C		F	C	F		F					F	F		C		C			F		R	R			
12R-7, 58-59	462.88	F	M			R							F	F		F	F	R		R					R					F						R			
13R-CC, 14-16	473.71	C	M			F	F		F	C			C	C		C	C	R		F					F					F			F		R				
14R-CC, 15-17	483.45	F	M			R	F			F			F	F		F				F					R	R				F	R		F			F			
15R-CC, 20-22	492.08	C	M			F	F			C			C	C		F	C	R		F						F				F	R		F			F	R	F	
16R-CC, 37-40	501.98	C	G			C	C			C			C	C		C	C	F		F						F		F			C		F			R	F		F	

Table T7 (continued).

Core, section, interval (cm)	Depth (mbsf)	Abundance	Preservation	*Bolliella adamsi*	*Bolliella calida*	*Dentoglobigerina altispira*	*Dentoglobigerina globosa*	*Globigerinella siphonifera*	*Globigerinoides conglobatus*	*Globigerinoides extremus*	*Globigerinoides fistulosus*	*Globigerinoides obliquus*	*Globigerinoides quadrilobatus*	*Globigerinoides ruber*	*Globigerinoides ruber* (pink)	*Globigerinoides sacculifer*	*Globigerinoides trilobus*	*Globorotalia crassaformis*	*Globorotalia margaritae*	*Globorotalia menardii*	*Globorotalia multicamerata*	*Globorotalia scitula*	*Globorotalia tosaensis*	*Globorotalia truncatulinoides*	*Globorotalia tumida*	*Globorotalia tumida flexuosa*	*Globorotalia ungulata*	*Neogloboquadrina acostaensis*	*Neogloboquadrina dutertrei*	*Neogloboquadrina humerosa*	*Orbulina universa*	*Pulleniatina obliquiloculata*	*Pulleniatina praecursor*	*Pulleniatina primalis*	*Pulleniatina spectabilis*	*Sphaeroidinella dehiscens*	*Sphaeroidinella dehiscens* s.l.	*Sphaeroidinellopsis paenedehiscens*	*Sphaeroidinellopsis seminulina*	*Sphaeroidinellopsis subdehiscens*	*Zeaglobigerina rubescens*
17R-CC, 0-1	511.75	C	M							C			C	C		F	C	R	R	F					F	F			C	R		F					R	R	R
18R-CC, 36-38	522.66	A	G			F	F		R	C			A			C	A	R	R	F					F	F		C									F		F
19R-CC, 40-42	529.21	A	VG			A								A				F							A	C			A		C	A					F		
20R-CC, 21-24	539.13	C	VG															R		A					A	R			A		R	R			R		F		
21R-CC, 17-23	551.39	A	VG			A														A					C	C			A			F					C		A
22R-CC, 0-2	555.64	A	VG																R	A					A	C			A		F	A			C		C		
23R-CC, 0-3	562.71	A	VG																	A					A	C					F	C	C				A		A
24R-CC, 47-51	571.66	A	VG																F	A					C	C			A		F			R	C		C	F	A
25R-CC, 0-3	578.42	F	P			F				R		R				R	F			R									F				F					R	
26R-CC, 5-8	588.20	A	M			C	C	R		A		A				C	A		F	F		R			F	F		F	C	R			F						R
27R-CC, 14-17	593.92	R	P														R																						
28R-CC, 10-13	600.54	F	P														F								R															
29R-CC, 13-16	612.39	R	P				R					R					R								R				R				R							
30R-CC, 13-15	619.53	F	P			R	R			F		R				R	F			R										R			R							
31R-CC, 0-2	630.77	F	P				R	R	R	F			F				F			R									F	R									R	
32R-CC, 0-1	640.42	R	P					R		R							R													R										
33R-CC, 0-3	647.79	R	P				R	R									R													R										
34R-CC, 31-32	664.29	F	P					R				R	R				R																							

Notes: Abundance (number of specimens per field of view): D = dominant (>10); A = abundant (2–9); C = common (lower range of abundant); F = few (0.5–1.0); R = rare (1–3 per tray); P = present (1 per 2–3 trays); B = barren. Preservation: VG = very good; G = good; M = moderate; P = poor.

Table T8. Tensor tool orientation data for cores, Hole 1109C.

Core	Inclination angle (°)	Mean MTF (°)
180-1109C-		
3H*	5.2	325.0
4H*	1.6	40.8
5H*	3.3	333.2
6H*	2.0	242.3
7H*	2.0	301.4
8H*	2.7	259.5
9H*	1.0	127.5
10H	0.7	239.1
11H	0.6	141.4

Notes: The inclination angle is the drift of the z-axis of the core from true vertical. The orientation parameter (MTF) is the angle in degrees between magnetic north and the double line (+x direction) marked on the center of the working half of the core. * = the mean MTF reflects a wide range of scatter in the averaged values. The local declination anomaly is 8°E.

Table T9. Polarity zonation in Holes 1109C and 1109D shown in Figure F66C, p.156.

Normal zone	Depth (mbsf)	Reversed zone	Depth (mbsf)	Mixed zone	Depth (mbsf)
N1	0-36	R1	36-48	M1	213-255
N2	48-54	R2	54-70.5	M2	266-269
N3	70.5-74	R3	74-213	M3	342-353
N4	290-331	R4	255-266	M4	698-715
N5	353-358	R5	269-290		
N6	384.5-470	R6	331-342		
N7	587-698	R7	358-384.5		
N8	715-750	R8	470-587		

Table T10. Interstitial water geochemistry, Site 1109.

Core, section, interval (cm)	Depth (mbsf)	pH	Alkalinity (mM)	Salinity	Cl (T) (mM)	Cl (IC) (mM)	SO_4 (mM)	Na (mM)	K (mM)	Mg (mM)	Ca (mM)	Li (µM)	NH_4 (µM)	Sr (µM)	SiO_2 (µM)	Ca/Mg
180-1109B-																
1H-1, 35-40	0.35	7.92	3.415	35	550	555	28.1	475	11.4	51.5	11.9	25	39	89	392	0.23
1H-2, 145-150	2.90	7.92	3.584	35	554	558	29.3	497	11.9	54.4	11.5	24	67	89	485	0.21
1H-3, 145-150	4.40	7.90	3.542	35	552	553	28.5	481	12.4	50.7	10.3	24	77	92	487	0.20
2H-1, 145-150	6.75	7.86	3.634	35	550	554	27.6	492	11.7	52.0	10.3	24	75	93	502	0.20
2H-3, 145-150	9.75	7.93	3.511	35	551	553	27.8	491	13.4	52.3	10.7	25	131	88	475	0.21
2H-4, 75-80	10.55	7.92	3.353	35	552	555	27.6	480	13.7	50.9	11.0	25	81	95	494	0.22
2H-5, 145-150	12.05	7.88	3.565	35	552	558	27.8	487	12.2	51.8	10.1	24	349	100	523	0.19
2H-6, 145-150	13.55	7.90	3.520	35	549	559	28.0	473	12.2	51.2	10.1	23	148	95	497	0.20
180-1109C-																
3H-2, 145-150	19.85	7.92	4.527	35	547	560	26.4	486	13.6	51.7	10.2	22	249	124	538	0.20
4H-2, 145150	29.35	8.00	4.816	34	548	564	23.3	480	13.0	49.3	8.3	23	608	145	504	0.17
5H-3, 145-150	40.35	7.93	5.922	34	561	572	18.4	483	12.7	46.0	6.2	21	918	170	535	0.13
6H-3, 145-150	49.85	8.05	6.330	34	559	571	15.6	487	11.8	43.2	5.4	21	1089	178	509	0.13
7H-3, 145-150	59.35	8.05	6.451	33	556	569	12.7	486	13.1	40.0	4.2	20	1277	175	498	0.10
8H-3, 145-150	68.85	8.03	7.285	33	557	576	10.2	488	12.7	38.6	4.0	18	1484	161	516	0.10
9H-3, 145-150	78.35	8.11	7.879	32	556	573	8.6	492	11.9	38.7	3.3	17	1623	148	511	0.08
10H-4, 115-120	89.05	8.11	9.665	32	557	570	6.1	489	11.5	37.7	2.6	14	1719	104	523	0.07
11H-3, 145-150	97.35	8.41	12.886	32	555	577	3.0	478	10.3	34.3	1.7	12	1863	79	417	0.05
12X-3, 145-150	106.85	8.28	13.476	32	557	572	0.0	480	10.2	34.5	1.7	11	2085	69		0.05
13X-3, 145-150	116.45	8.34	11.338	32	561	580	2.5	470	10.5	35.5	2.1	11	2145	71	408	0.06
14X-3, 145-150	126.05	8.23	9.807	32	558	579	1.8	481	10.0	35.2	2.0	12	2140	82	485	0.06
15X-3, 145-150	135.62	8.21	9.482	32	560	581	1.6	486	10.8	38.3	2.7	13	2054	84	494	0.07
16X-3, 145-150	145.25	5.30	8.991	32	561	586	2.0	463	8.7	38.3	4.3	15	2045	79	448	0.11
17X-1, 145-150	151.95	8.23	7.644	32	560	584	3.9	481	8.6	38.0	3.2	18	2097	87	413	0.08
18X-3, 115-120	164.25	8.11	5.874	32	556	586	3.3	448	8.5	36.1	3.4	18	2108	99	411	0.09
20X-1, 140-150	180.70	8.31	4.304	32	560	559	2.4	479	7.6	37.0	4.8	19	1965	112	334	0.13
23X-4, 33-43	212.43	8.35	4.183	32	559	559	2.1	463	8.2	37.4	5.1	19	1871	127	268	0.14
26X-1, 140-145	238.40	8.29	3.599	32	563	566	2.2	455	7.3	39.2	5.9	18	1608	135	327	0.15
27X-2, 140-150	249.60	8.23	3.096	32	563	561	0.0	469	8.2	39.8	6.4	17	1626	142	397	0.16
28X-4, 140-150	262.20	8.05	3.330	32	566	564	1.5	469	8.1	42.2	8.3	19	1496	140	455	0.20
29X-3, 140-150	270.40	8.05	3.010	32	563	571	0.0	463	6.8	39.0	7.6	21	1453	143	461	0.20
30X-1, 140-150	277.00	8.18	3.030	32	563	569	0.5	464	6.6	40.3	8.3	21	1398	144	413	0.21
31X-3, 140-150	289.50	8.28	2.548	32	567	568	1.5	466	6.4	40.6	8.9	23	1384	129	334	0.22
32X-3, 140-150	299.20	8.26	2.406	32	566	562	4.5	456	6.3	41.8	9.8	24	1341	121	266	0.24
33X-4, 115-120	310.15	8.27	2.401	32	556	569	1.7	458	6.2	40.1	11.2	24	1323	117	310	0.28
34X-2, 140-150	317.10	8.48	2.033	32	567	572	0.0	464	8.4	40.7	9.8	26	1466	120	246	0.24
35X-3, 140-150	328.30	8.18	2.230	32	569	572	0.5	465	7.7	41.0	9.4	27	1314	125	288	0.23
36X-1, 140-150	334.90	8.47	1.143	32	569	568	0.0	467	7.7	41.8	9.8	27	1558	125	145	0.24
38X-4, 140-150	352.50	8.36	1.551	32	564	562	0.0	461	8.6	37.1	8.6	27	1799	131	211	0.23
39X-3, 140-150	357.00	8.38	2.174	32	564	583	1.7	458	8.8	37.4	8.5	27	1641	137	387	0.23
40X-3, 110-120	366.30	8.08	3.658	32	564	573	1.3	468	8.6	38.6	8.8	28	1487	150	628	0.23
41X-2, 140-150	374.40	7.88	5.085	32	561	570	3.3	459	8.6	38.6	9.2	30	1719	171	803	0.24
180-1109D-																
2R-6, 96-106	365.88	8.32	3.491	32	562	557	0.0	441	9.2	38.2	8.4	28	1555	153	571	0.22
4R-3, 96-106	381.56	8.20	4.513	32	562	554	0.0	436	9.7	37.7	8.4	31	1692	161	724	0.22
6R-3, 97-107	401.03	8.20	4.257	32	559	554	2.5	441	10.7	36.9	8.1	36	1878	182	641	0.22
7R-3, 120-130	410.74	8.27	4.172	31	558	553	0.0	439	11.1	35.8	7.4	38	1867	186	586	0.21
8R-3, 141-151	420.33	8.39	3.474	31	560	556	0.1	446	11.9	35.2	7.2	40	1981	186	520	0.20
9R-3, 101-111	430.06	8.23	5.282	31	555	558	0.1	444	12.3	36.4	7.7	43	1974	202	650	0.21
10R-2, 131-141	438.35	8.18	4.408	31	558	557	2.7	443	11.3	35.5	7.2	45	1987	201	660	0.20
11R-3, 122-132	449.27	8.06	5.248	31	558	554	0.9	440	11.1	36.2	7.6	47	2101	217	676	0.21
12R-4, 120-130	460.06	8.11	4.592	31	561	562	0.0	445	11.2	34.6	7.2	49	2165	233	680	0.21
13R-3, 79-89	467.94	8.14	3.588	31	562	554	3.3	448	11.3	35.5	7.2	48	2172	238	597	0.20
14R-4, 136-146	479.32	8.36	5.062	32	558	553	0.0	445	11.2	34.7	9.3	50	2106	251	595	0.27
16R-5, 120-130	499.73	8.25	3.650	32	560	555	0.3	444	10.1	35.6	8.2	54	2147	302	669	0.23
18R-4, 120-130	517.72	8.26	3.546	32	559	556	0.0	440	9.1	35.5	8.5	65	2243	335	399	0.24
20R-3, 65-75	535.43	8.32	3.891	32	560	558	0.0	433	8.4	37.7	10.6	75	2142	422	474	0.28
22R-1, 124-134	552.44	8.34	1.961	32	559	556	0.0	433	6.9	36.9	11.6	83	2197	550	169	0.31
24R-2, 135-148	568.39	8.47	1.039	32	562	558	0.0	439	5.7	36.4	12.9	86	2190	724	136	0.36
26R-3, 30-40	582.97	8.59	0.979	32	564	562	0.0	435	4.6	35.9	16.6	85	2120	867	145	0.46
29R-2, 93-103	610.86	8.65	0.647	33	578	570	0.0	423	2.9	34.6	27.5	68	1792	1082	112	0.80
31R-1, 130-140	629.50	8.82	0.796	33	576	574	0.0	424	2.3	37.0	31.3	60	1844	1396	171	0.85
34R-3, 123-133	661.04	8.36	0.578	34	579	577	0.4	408	2.1	37.7	37.6	64	1441	1708	105	1.00
36R-2, 140-150	679.30	8.74	1.176	34	577	569	0.0	420	1.8	31.1	45.3	68	1030	1252	149	1.46
38R-4, 140-150	701.16	8.52	1.449	34	572	567	0.0	415	1.7	24.4	54.3	53	998	957	213	2.22
40R-2, 29-39	716.55	8.54	0.997	34	562	559	0.0	399	1.5	18.2	61.4	17	736	831	156	3.38
43R-2, 82-89	745.74			31	522	512	1.2	370	1.1	11.0	67.3	10		471	211	6.11

Notes: Cl (T) = chloride by titration, Cl (IC) = chloride by ion chromatography. Blank spaces = not detected.

Table T11. Summary of diagenetic reactions occurring in sediments, Site 1109.

Process	Effect of interstitial water geochemistry	Remarks
Microbial oxidation of organic matter	SO_4^{2-} decreases; alkalinity and NH_4^+ increase	SO_4^{2-} depletion by 100 mbsf, strong alkalinity, and NH_4^+ maximum at 100 mbsf; secondary maxima 400–500 mbsf
Carbonate reactions		
Dissolution	Ca, Sr, and alkalinity increase	Occurs with recrystallization in Units I and II; within Unit VIII provides important Sr source
Precipitation	Ca and alkalinity decrease	Unit VII (calcite cementation)
Leaching and weathering of ash layers and dispersed volcanic minerals (feldspars and plagioclase)	K, Li, SiO_2 and NH_4^+ increase; Mg decreases	0–150 mbsf (Units I and II), glass dissolution; Si release more important than from biogenic source; precipitation of Mg-rich smectite in Units VIII and IX
Extended weathering of volcanics, detrital clays, and silicate precipitation	Si, K, and alkalinity decrease; Li increases	Uptake of K by illitization; transformation of chlorite/smectite interlayer clays; Li excluded during precipitation of silicates below 400 mbsf

Table T12. Composition of headspace gas in sediments, Site 1109. (Continued on next page.)

Core, section, interval (cm)	Depth (mbsf)	C_1	C_2	C_2=	C_3
180-1109C-					
1H-3, 0-5	2.95	448	2		1
2H-5, 0-5	10.60	4			
3H-2, 0-5	18.40	3			
4H-2, 0-5	27.90	3			
5H-3, 0-5	38.90	3			
6H-3, 0-5	48.40	3			
7H-4, 0-5	59.40	3			
8H-3, 0-5	67.40	13			
9H-3, 0-5	76.90	3			
10H-4, 0-5	87.90	3			
11H-4, 0-5	97.40	2			
12X-2, 0-5	103.90	572			
13X-4, 0-5	116.50	4,807			
14X-2, 0-5	123.10	6,682			
15X-4, 0-5	135.67	6,545			
16X-3, 0-5	143.80	7,038	1		
17X-2, 0-5	152.00	7,920	1		
18X-3, 0-5	163.10	17,295	2		
19X-1, 0-5	169.70	6,601	1		
20X-1, 0-5	179.30	4,680			
21X-CC, 0-2	188.90	29,292	3		
22X-2, 0-2	199.30	6,501	1		
23X-5, 0-2	212.75	3,206			
24X-CC, 0-2	217.70	123			
25X-1, 33-35	227.73	5,563	1		
26X-2, 0-5	238.45	5,198	1		
27X-3, 0-5	249.70	10,514	1		
28X-4, 0-5	260.80	13,210	1		
29X-4, 0-5	270.50	10,931	1		
30X-3, 0-5	278.60	21,509	2		
31X-4, 0-2	289.60	10,189	1		
32X-3, 0-2	297.80	8,531	1		
33X-4, 0-2	309.00	7,363	1		
34X-3, 0-2	317.20	9,975	2		
35X-4, 0-2	328.40	5,384	1		
36X-2, 0-2	335.00	5,914	1		
37X-2, 0-5	344.30	2,344			
38X-5, 0-5	352.60	3,763	1		
39X-4, 0-5	357.10	5,113	1		
40X-3, 0-2	365.20	2,839	1		
41X-3, 0-2	374.50	3,481	1		
180-1109D-					
4R-4, 0-2	381.66	3,168	1		
5R-1, 0-1	387.60	1,348			
6R-3, 0-2	400.06	1,544			
7R-4, 0-2	410.84	2,303	1		
8R-4, 0-2	420.43	2,970	1		
9R-4, 0-2	430.16	1,828	1		
10R-4, 0-2	439.74	2,110	1		
11R-4, 0-2	449.37	3,142	1		
12R-4, 118-120	460.04	2,639	1		
13R-4, 0-2	468.04	3,589	2		
14R-5, 0-2	479.42	4,749	2		
15R-4, 0-2	487.32	4,535	2		
16R-6, 0-2	499.83	6,181	3		
17R-4, 0-2	506.66	4,984	2		
18R-4, 0-2	516.52	3,977	2		
19R-2, 0-2	523.80	4,996	2		
20R-4, 0-2	535.53	4,797	2		
21R-5, 0-2	547.40	4,196	2		
22R-2, 0-1	552.54	5,552	3		
23R-2, 0-2	562.30	3,821	2		
24R-2, 146-148	568.50	3,303	2		
25R-5, 0-2	576.13	4,335	2		
26R-3, 40-42	583.07	4,079	2		
27R-1, 0-2	589.60	2,968	2		

Table T12 (continued).

Core, section, interval (cm)	Depth (mbsf)	C_1	C_2	C_2=	C_3
28R-1, 123-124	600.43	2,037	1		
29R-3, 0-2	610.96	1,742	1		
30R-1, 0-2	618.50	1,287	1		
31R-2, 0-2	629.60	2,248	2		
32R-2, 109-111	640.40	1,008	1	1	
33R-1, 27-29	647.77	816	1		
34R-4, 0-2	661.14	115			
35R-1, 0-2	666.70	225			
36R-3, 0-2	679.40	116			
37R-3, 0-2	688.96	129			
38R-5, 0-2	701.26	169			
39R-3, 0-2	708.04	82			
40R-2, 37-39	716.63	6			
41R-2, 0-2	726.20	4			
42R-2, 0-2	735.80	4			
43R-2, 0-2	744.92	3			

Notes: All concentrations are reported in parts per million by volume. Blanks indicate values below detection limit.

Table T13. Carbon, calcium carbonate, nitrogen, and sulfur contents of sediments, Site 1109. (Continued on next page.)

Core, section, interval (cm)	Depth (mbsf)	Inorganic carbon (wt%)	$CaCO_3$ (wt%)	Organic carbon (wt%)	Total nitrogen (wt%)	C/N	Total sulfur (wt%)
180-1109C-							
1H-1, 13-14	0.13	6.29	52.38	0.44	0.02	22	
1H-5, 72-73.5	6.72	6.79	56.55	0.46	0.07	7	0.15
2H-5, 106-107	14.46	6.88	57.30	0.52	0.06	9	
3H-1, 12-13	17.02	8.22	68.47	0.22			
3H-5, 39-40	23.29	6.67	55.57	0.51	0.05	10	
3H-7, 6.5-7	25.97	5.67	47.21	0.03			
4H-1, 73-74.5	27.13	5.92	49.33	0.66		13	0.29
4H-4, 108.5-109.5	31.99	7.79	64.86	0.15			
5H-2, 8-9	37.48	7.10	59.18	0.30			
5H-5, 5-6	41.95	6.82	56.81	0.10			
6H-1, 4.5-5.5	45.44	7.42	61.77	0.30			
6H-7, 9-10	54.49	5.54	46.14	0.29			
7H-1, 75-76	55.65	5.92	49.32	0.27			0.07
7H-5, 66-67	61.56	6.64	55.28	0.39			
8H-5, 68-69	71.08	5.86	48.82	0.23			
9H-4, 19-20	78.59	6.39	53.23	0.24			
9H-5, 92-93	80.82	5.03	41.89	0.15			
10H-2, 44-45	85.34	0.34	2.84	0.48	0.02	24	
11H-2, 106-106.5	95.46	1.01	8.42	0.90	0.03	30	
12X-7, 24-25	111.64	1.27	10.55	0.57	0.03	19	
13X-6, 119-120	120.69	1.58	13.19	0.54	0.03	18	
14X-1, 88-89	122.48	1.08	8.98	0.82	0.03	27	
14X-6, 140-141	130.50	2.81	23.41	0.44			
15X-1, 56.5-57.5	131.76	3.73	31.07	0.50			
15X-6, 59-60	139.26	3.06	25.52	0.35			
16X-3, 79-80	144.59	1.13	9.39	0.69			
17X-CC, 11-12	152.91	0.36	2.96	0.15			
18X-1, 73-74	160.83	10.02	83.50	0.67			
19X-1, 115-116	170.85	0.91	7.59	0.31			
20X-3, 102-103	183.32	2.07	17.26	0.33			
20X-4, 88-89	184.68	2.23	18.61	0.48			
21X-CC, 27.5-29	189.18	0.46	3.80	0.18			
22X-1, 28-29	198.78	1.19	9.89	0.36			
23X-5, 42-43	213.17	3.16	26.30	0.50			
24X-CC, 12-13	217.82	0.68	5.64	2.73	0.04	68	
26X-3, 25-26	240.20	1.47	12.22	0.69	0.01	69	
27X-5, 117-119	253.87	4.68	38.95	0.14			
28X-4, 37-38	261.17	3.88	32.31	0.15			
29X-3, 40-41	269.40	5.85	48.71	0.36			
30X-2, 35-36	277.45	3.25	27.06	0.15			0.07
31X-3, 18-19	288.28	1.04	8.67	0.07			0.45
32X-3, 108-109	298.88	2.68	22.33	0.22	0.03	7	
33X-6, 117-120	313.17	1.79	14.93	0.39	0.03	13	0.20
34X-2, 86-87	316.56	1.54	12.83	0.35	0.03	12	0.28
34X-4, 30-31	319.00	3.91	32.60	0.33			0.22
35X-6, 64.5-65	332.05	3.66	30.52	0.27	0.05	5	0.19
35X-6, 67-68	332.07	3.72	30.98	0.35	0.03	12	0.22
37X-2, 45-46	344.75	3.93	32.77	0.40	0.05	8	0.29
38X-3, 54-55	350.14	3.78	31.47	0.42	0.04	11	0.29
39X-3, 56-57	356.16	3.57	29.72	0.39			0.30
40X-2, 55-57	364.25	2.83	23.54	0.49	0.04	12	0.45
40X-4, 63-64.5	367.33	3.07	25.60	0.40	0.04	10	0.47
41X-2, 30-31	373.30	2.70	22.48	0.45	0.04	11	0.30
180-1109D-							
1R-1, 72-73	353.52	3.80	31.65	0.55	0.04	14	0.44
2R-3, 43-45	362.24	2.52	20.97	0.38	0.03	13	0.29
3R-6, 83-85	376.19	2.51	20.88	0.30	0.03	10	0.22
4R-4, 69-71	382.35	3.18	26.52	0.44	0.05	9	0.44
5R-1, 60-61	388.20	3.48	29.02	0.52	0.05	10	0.51
6R-1, 41.5-42	397.61	3.05	25.38	0.40	0.05	8	0.32
7R-3, 15-17	409.69	3.03	25.26	0.58	0.07	8	0.61
8R-5, 79-80	422.41	2.13	17.77	0.14	0.04	3	0.32
9R-3, 99-100	430.04	2.59	21.61	0.40	0.05	8	0.35
10R-1, 22-23	435.92	2.84	23.62	0.39	0.05	8	0.33
10R-4, 55-56	440.29	2.98	24.82	0.35	0.05	7	0.32

Table T13 (continued).

Core, section, interval (cm)	Depth (mbsf)	Inorganic carbon (wt%)	$CaCO_3$ (wt%)	Organic carbon (wt%)	Total nitrogen (wt%)	C/N	Total sulfur (wt%)
11R-3, 58-59	448.63	2.92	24.33	0.58	0.05	12	0.82
12R-7, 9-10	462.39	3.04	25.28	0.50	0.06	8	0.58
13R-3, 13-15	467.28	2.34	19.48	0.26	0.04	7	0.29
14R-2, 20-22	475.62	3.51	29.24	0.42	0.05	8	0.43
15R-1, 80-81	484.50	3.14	26.17	0.61	0.07	9	0.54
16R-1, 83-84	494.13	3.15	26.20	0.32	0.04	8	
17R-3, 74-76.5	505.95	2.90	24.13	0.53	0.04	13	0.55
18R-2, 12-14	514.22	3.15	26.27	0.41	0.05	8	0.45
19R-2, 19-21	523.99	4.28	35.62	0.41	0.08	5	
20R-4, 37-38	535.90	3.10	25.84	0.39	0.11	4	
21R-4, 66-68	546.72	4.47	37.24	0.28	0.07	4	
22R-3, 59-60.5	554.33	3.90	32.52	0.48	0.10	5	0.38
23R-2, 33-34	562.63	4.51	37.58	0.49	0.10	5	0.58
24R-3, 70-71	569.22	4.06	33.84	0.41	0.11	4	
25R-4, 79.5-80.5	575.42	5.08	42.28	0.38	0.10	4	0.07
26R-2, 36-38	581.82	5.35	44.60	0.26	0.05	5	
27R-1, 59-60	590.19	6.24	51.95	0.18	0.03	6	
28R-1, 84-87	600.04	4.47	37.27	0.10	0.02	5	
29R-1, 47-49	609.37	2.11	17.58	0.25	0.03	8	
30R-1, 47-49	618.97	2.85	23.78	0.13	0.07	2	
31R-1, 77-79	628.97	3.16	26.35	0.17	0.03	6	
32R-2, 62-63	639.93	9.01	75.08	0.51	0.02	25	
34R-1, 68-70	657.78	6.59	54.86	1.57	0.03	52	
35R-5, 103-103.5	672.63	3.21	26.73	0.70	0.10	7	0.07
36R-6, 34-35	684.24	3.61	30.10	0.63	0.10	6	0.80
37R-1, 10-11	686.10	7.87	65.58	0.41	0.04	10	
37R-5, 15-16	691.88	0.22	1.79	0.96	0.01	96	1.74
38R-1, 130-131	696.90	0.04	0.37	43.81	0.72	61	6.73
38R-2, 82-83	697.80	0.03	0.26	13.95	0.42	33	7.77
38R-6, 14-15	702.90	7.44	61.96	1.10	0.03	37	
39R-3, 24-26	708.28	0.04	0.33	0.12			
40R-3, 59-61	717.24	0.03	0.22				
41R-3, 69-70	727.97	0.03	0.25		0.03	0	
42R-2, 89-90	736.69	0.03	0.22				
43R-2, 66-68	745.58	0.02	0.18				

Note: Blanks indicate values below detection limit, except for C/N ratio where blanks indicate an undefined value.

Table T14. Total bacterial populations and numbers of dividing and divided cells in sediments, Site 1109.

Hole	Depth (mbsf)	Total bacterial population (log cells/cm^3)	Dividing and divided cells (log cells/cm^3)
180-1109B-			
1H-1,0-1	0.00	8.515	7.523
1H-2,0-1	1.45	7.734	6.691
1H-3,0-1	2.95	7.406	6.418
1H-4,0-1	4.45	7.343	6.504
2H-5,0-1	10.60	7.205	6.299
180-1109C-			
3H-2, 0-5	18.40	7.352	6.516
4H-3, 0-1	29.40	7.112	6.173
5H-4, 0-1	40.40	7.123	6.005
6H-4, 0-1	49.90	6.910	6.031
7H-4, 0-5	59.40	6.760	5.753
8H-4, 0-5	68.90	6.687	5.358
9H-4, 0-5	78.40	6.833	5.805
10H-5, 0-5	89.40	6.632	5.494
12X-4, 0-5	106.90	6.751	5.457
14X-4, 0-1	126.10	6.965	5.974
16X-4, 0-1	145.30	6.484	5.183
18X-4, 0-1	164.60	6.599	5.532
20X-2, 1-2	180.81	6.421	5.318
22X-2, 0-1	199.30	6.665	5.167
26X-2, 0-1	238.45	6.411	4.855
28X-5, 0-1	262.30	6.341	5.111
30X-2, 0-2	277.10	6.474	4.983
32X-4, 0-1	299.30	6.399	5.296
34X-2, 149-150	317.19	6.392	5.174
36X-2, 0-1	335.00	6.551	5.189
38X-5, 0-1	352.60	6.594	5.400
40X-4, 0-1	366.70	6.594	5.272
180-1109D-			
1R-2, 0-1	354.30	6.591	5.558
3R-2, 0-1	370.20	6.625	5.245
6R-4, 0-1	401.13	6.434	4.916
8R-4, 0-1	420.43	6.424	4.918
10R-3, 0-1	438.45	6.651	4.903
12R-5, 0-1	460.16	6.642	5.739
14R-5, 0-1	479.42	6.577	5.107
16R-6, 0-1	499.83	6.610	5.507
20R-4, 0-1	535.53	6.340	5.273
22R-2, 0-1	552.54	6.412	4.810
26R-2, 120-121	582.66	5.875	4.671
31R-2, 0-1	629.20	5.902	4.726
34R-4, 0-1	661.14	6.288	5.233
36R-3, 0-1	679.40	6.031	5.186
38R-5, 0-1	701.26	6.248	5.327
40R-3, 0-1	716.65	5.744	4.540
43R-3, 0-1	745.80	6.092	5.031

Table T15. Index properties measured in cores, Site 1109. (Continued on next seven pages. See table note.)

Leg	Site	Hole	Core	Type	Section	Top (cm)	Bottom (cm)	Depth (mbsf)	Water content (bulk)	Water content (dry)	Bulk density (g·cm^{-3})	Dry density (g·cm^{-3})	Grain density (g·cm^{-3})	Porosity (%)	Void ratio
180	1109	B	1	H	1	88.0	90.0	0.88	55.7	126.0	1.410	0.624	2.683	76.7	3.30
180	1109	B	1	H	2	88.0	90.0	2.33	57.7	136.6	1.388	0.587	2.698	78.3	3.60
180	1109	B	1	H	3	101.0	103.0	3.96	54.0	117.2	1.430	0.658	2.673	75.4	3.06
180	1109	B	1	H	4	27.0	29.0	4.72	56.7	130.9	1.404	0.608	2.726	77.7	3.48
180	1109	B	2	H	1	63.0	65.0	5.93	54.8	121.1	1.428	0.646	2.731	76.4	3.23
180	1109	B	2	H	2	31.0	33.0	7.11	50.4	101.5	1.476	0.733	2.677	72.6	2.65
180	1109	B	2	H	3	63.0	65.0	8.93	58.4	140.4	1.348	0.561	2.429	76.9	3.33
180	1109	B	2	H	4	63.0	65.0	10.43	50.4	101.7	1.477	0.732	2.684	72.7	2.67
180	1109	B	2	H	5	77.0	79.0	11.37	52.2	109.2	1.438	0.687	2.574	73.3	2.75
180	1109	B	2	H	6	26.0	28.0	12.36	53.1	113.3	1.433	0.672	2.620	74.4	2.90
180	1109	B	2	H	7	1.0	3.0	13.61	53.0	112.6	1.448	0.681	2.714	74.9	2.98
180	1109	C	3	H	1	107.0	109.0	17.97	51.2	105.0	1.466	0.715	2.683	73.3	2.75
180	1109	C	3	H	2	80.0	82.0	19.20	53.5	115.3	1.445	0.671	2.749	75.6	3.10
180	1109	C	3	H	3	147.0	149.0	21.37	49.7	98.8	1.501	0.755	2.782	72.8	2.68
180	1109	C	3	H	4	147.0	149.0	22.87	52.3	109.8	1.462	0.697	2.754	74.7	2.95
180	1109	C	3	H	5	147.0	149.0	24.37	50.1	100.4	1.486	0.742	2.717	72.7	2.66
180	1109	C	3	H	7	28.0	30.0	26.18	50.7	102.8	1.466	0.723	2.637	72.6	2.65
180	1109	C	4	H	1	79.0	81.0	27.19	55.6	125.3	1.414	0.628	2.703	76.8	3.31
180	1109	C	4	H	2	52.5	54.5	28.42	54.5	119.7	1.426	0.649	2.691	75.9	3.15
180	1109	C	4	H	3	28.0	30.0	29.68	55.8	126.3	1.415	0.625	2.731	77.1	3.37
180	1109	C	4	H	4	95.5	97.5	31.85	44.5	80.3	1.573	0.873	2.761	68.4	2.17
180	1109	C	4	H	5	62.0	64.0	33.02	46.4	86.5	1.537	0.824	2.714	69.6	2.29
180	1109	C	4	H	6	58.5	60.5	34.49	40.3	67.5	1.651	0.986	2.814	65.0	1.86
180	1109	C	4	H	7	44.5	46.5	35.85	45.0	81.9	1.571	0.864	2.795	69.1	2.24
180	1109	C	5	H	1	104.5	106.5	36.94	43.4	76.6	1.584	0.897	2.727	67.1	2.04
180	1109	C	5	H	2	76.0	78.0	38.16	43.9	78.1	1.581	0.887	2.747	67.7	2.10
180	1109	C	5	H	3	98.0	100.0	39.88	41.2	70.0	1.625	0.956	2.756	65.3	1.88
180	1109	C	5	H	4	44.5	47.5	40.85	43.3	76.5	1.593	0.903	2.772	67.4	2.07
180	1109	C	5	H	6	76.0	78.0	44.16	43.1	75.9	1.588	0.903	2.730	66.9	2.02
180	1109	C	5	H	7	21.0	23.0	45.11	45.3	83.0	1.547	0.845	2.683	68.5	2.17
180	1109	C	6	H	1	89.5	91.5	46.29	44.9	81.6	1.558	0.858	2.710	68.3	2.16
180	1109	C	6	H	2	90.0	92.0	47.80	44.8	81.3	1.550	0.855	2.662	67.9	2.11
180	1109	C	6	H	3	59.0	61.0	48.99	43.2	76.1	1.572	0.893	2.653	66.3	1.97
180	1109	C	6	H	4	68.5	70.5	50.58	40.6	68.4	1.598	0.949	2.594	63.4	1.73
180	1109	C	6	H	5	69.0	71.0	52.09	40.6	68.3	1.611	0.957	2.647	63.8	1.77
180	1109	C	6	H	6	82.0	84.0	53.72	42.2	73.1	1.596	0.922	2.697	65.8	1.93
180	1109	C	6	H	7	46.0	48.0	54.86	40.8	69.0	1.602	0.948	2.622	63.9	1.77
180	1109	C	7	H	2	49.0	51.0	56.89	41.1	69.7	1.596	0.941	2.615	64.0	1.78
180	1109	C	7	H	3	64.0	66.0	58.54	42.1	72.7	1.585	0.918	2.633	65.1	1.87
180	1109	C	7	H	4	65.0	67.0	60.05	39.0	64.0	1.622	0.989	2.589	61.8	1.62
180	1109	C	7	H	5	49.0	51.0	61.39	40.6	68.4	1.610	0.956	2.645	63.9	1.77
180	1109	C	7	H	6	97.0	99.0	63.37	42.3	73.4	1.585	0.914	2.652	65.5	1.90
180	1109	C	7	H	7	26.0	28.0	64.16	44.0	78.6	1.571	0.880	2.711	67.6	2.08
180	1109	C	8	H	1	138.0	140.0	65.78	43.9	78.3	1.574	0.883	2.717	67.5	2.08
180	1109	C	8	H	2	138.0	140.0	67.28	44.1	78.9	1.574	0.880	2.731	67.8	2.10
180	1109	C	8	H	3	138.0	140.0	68.78	43.2	76.0	1.588	0.902	2.733	67.0	2.03

Table T15 (continued).

Leg	Site	Hole	Core	Type	Section	Top (cm)	Bottom (cm)	Depth (mbsf)	Water content (bulk)	Water content (dry)	Bulk density (g·cm^{-3})	Dry density (g·cm^{-3})	Grain density (g·cm^{-3})	Porosity (%)	Void ratio
180	1109	C	8	H	4	138.0	140.0	70.28	41.1	69.7	1.610	0.949	2.680	64.6	1.83
180	1109	C	8	H	5	9.0	11.0	70.49	43.0	75.4	1.591	0.907	2.734	66.8	2.01
180	1109	C	8	H	6	9.0	11.0	71.99	39.6	65.6	1.653	0.998	2.768	63.9	1.77
180	1109	C	8	H	7	9.0	11.0	73.49	41.7	71.6	1.608	0.937	2.717	65.5	1.90
180	1109	C	9	H	1	7.0	9.0	73.97	44.3	79.7	1.573	0.875	2.744	68.1	2.14
180	1109	C	9	H	2	7.0	9.0	75.47	38.9	63.6	1.639	1.002	2.654	62.2	1.65
180	1109	C	9	H	3	7.0	9.0	76.97	36.6	57.7	1.678	1.064	2.655	59.9	1.50
180	1109	C	9	H	4	7.0	9.0	78.47	38.9	63.7	1.650	1.008	2.702	62.7	1.68
180	1109	C	9	H	5	7.0	9.0	79.97	37.3	59.5	1.678	1.052	2.708	61.1	1.57
180	1109	C	9	H	6	7.0	9.0	81.47	41.2	70.1	1.622	0.954	2.746	65.3	1.88
180	1109	C	9	H	7	7.0	9.0	82.97	39.5	65.2	1.640	0.992	2.699	63.2	1.72
180	1109	C	10	H	1	29.0	31.0	83.69	39.4	64.9	1.640	0.994	2.690	63.0	1.71
180	1109	C	10	H	2	7.0	9.0	84.97	31.3	45.6	1.789	1.229	2.711	54.7	1.21
180	1109	C	10	H	3	7.0	9.0	86.47	37.6	60.2	1.679	1.048	2.731	61.6	1.61
180	1109	C	10	H	5	7.0	9.0	89.47	33.5	50.4	1.747	1.161	2.713	57.2	1.34
180	1109	C	10	H	6	7.0	9.0	90.97	36.8	58.2	1.680	1.062	2.677	60.3	1.52
180	1109	C	10	H	7	7.0	9.0	92.47	36.0	56.3	1.689	1.080	2.662	59.4	1.46
180	1109	C	11	H	1	8.0	10.0	92.98	39.5	65.2	1.635	0.990	2.676	63.0	1.70
180	1109	C	11	H	2	8.0	10.0	94.48	38.5	62.7	1.656	1.017	2.701	62.3	1.66
180	1109	C	11	H	3	6.0	8.0	95.96	35.1	54.2	1.721	1.117	2.727	59.1	1.44
180	1109	C	11	H	4	6.0	8.0	97.46	35.0	53.9	1.715	1.115	2.695	58.6	1.42
180	1109	C	11	H	5	6.0	8.0	98.96	33.8	51.1	1.744	1.154	2.721	57.6	1.36
180	1109	C	11	H	6	6.0	8.0	100.46	32.8	48.7	1.758	1.182	2.702	56.2	1.29
180	1109	C	11	H	7	6.0	8.0	101.46	30.5	43.9	1.843	1.280	2.839	54.9	1.22
180	1109	C	12	X	1	3.0	5.0	102.43	37.4	59.8	1.677	1.050	2.712	61.3	1.58
180	1109	C	12	X	2	3.0	5.0	103.93	32.7	48.6	1.740	1.171	2.637	55.6	1.25
180	1109	C	12	X	3	3.0	5.0	105.43	38.0	61.3	1.649	1.023	2.634	61.2	1.58
180	1109	C	12	X	4	3.0	5.0	106.93	32.7	48.5	1.766	1.189	2.725	56.4	1.29
180	1109	C	12	X	5	3.0	5.0	108.43	34.4	52.4	1.732	1.137	2.715	58.1	1.39
180	1109	C	12	X	6	3.0	5.0	109.93	36.0	56.3	1.702	1.089	2.716	59.9	1.49
180	1109	C	12	X	7	3.0	5.0	111.43	37.0	58.8	1.681	1.059	2.699	60.8	1.55
180	1109	C	13	X	1	6.0	8.0	112.06	38.4	62.4	1.654	1.019	2.687	62.1	1.64
180	1109	C	13	X	2	6.0	8.0	113.56	36.9	58.4	1.693	1.069	2.737	60.9	1.56
180	1109	C	13	X	3	6.0	8.0	115.06	34.3	52.2	1.740	1.143	2.738	58.2	1.40
180	1109	C	13	X	4	6.0	8.0	116.56	35.3	54.7	1.715	1.109	2.716	59.2	1.45
180	1109	C	13	X	5	6.0	8.0	118.06	34.9	53.7	1.726	1.123	2.730	58.9	1.43
180	1109	C	13	X	6	6.0	8.0	119.56	33.8	51.0	1.746	1.156	2.729	57.6	1.36
180	1109	C	13	X	7	6.0	8.0	121.06	36.5	57.4	1.687	1.072	2.682	60.0	1.50
180	1109	C	14	X	1	107.5	109.5	122.68	32.4	47.9	1.756	1.187	2.672	55.6	1.25
180	1109	C	14	X	2	48.5	50.5	123.58	36.0	56.3	1.704	1.090	2.723	60.0	1.50
180	1109	C	14	X	3	80.0	82.0	125.40	35.8	55.8	1.713	1.099	2.743	59.9	1.50
180	1109	C	14	X	4	78.5	80.5	126.89	33.7	50.9	1.726	1.144	2.651	56.9	1.32
180	1109	C	14	X	5	69.0	71.0	128.29	35.8	55.8	1.702	1.093	2.699	59.5	1.47
180	1109	C	14	X	6	98.0	100.0	130.08	34.4	52.4	1.694	1.111	2.578	56.9	1.32
180	1109	C	14	X	7	19.0	21.0	130.79	30.4	43.6	1.803	1.256	2.699	53.5	1.15
180	1109	C	15	X	1	81.5	83.5	132.01	41.6	71.1	1.615	0.944	2.740	65.6	1.90
180	1109	C	15	X	2	87.0	89.0	133.54	33.3	49.8	1.737	1.160	2.660	56.4	1.29
180	1109	C	15	X	3	98.0	100.0	135.15	34.9	53.7	1.717	1.118	2.697	58.6	1.41

Table T15 (continued).

Leg	Site	Hole	Core	Type	Section	Top (cm)	Bottom (cm)	Depth (mbsf)	Water content (bulk)	Water content (dry)	Bulk density ($g \cdot cm^{-3}$)	Dry density ($g \cdot cm^{-3}$)	Grain density ($g \cdot cm^{-3}$)	Porosity (%)	Void ratio
180	1109	C	15	X	4	84.0	86.0	136.51	35.5	55.1	1.699	1.096	2.669	58.9	1.44
180	1109	C	15	X	5	80.0	82.0	137.97	37.1	58.9	1.669	1.050	2.656	60.5	1.53
180	1109	C	15	X	6	69.5	71.5	139.37	34.9	53.7	1.707	1.111	2.659	58.2	1.39
180	1109	C	15	X	7	30.0	32.0	140.47	37.3	59.5	1.674	1.049	2.687	60.9	1.56
180	1109	C	16	X	1	66.5	68.5	141.46	36.1	56.4	1.690	1.081	2.672	59.6	1.47
180	1109	C	16	X	2	116.5	118.5	143.46	33.9	51.2	1.738	1.149	2.703	57.5	1.35
180	1109	C	16	X	3	62.0	64.0	144.42	36.2	56.7	1.689	1.078	2.675	59.7	1.48
180	1109	C	16	X	4	78.0	80.0	146.08	35.0	53.8	1.718	1.117	2.707	58.7	1.42
180	1109	C	17	X	1	99.5	101.5	151.49	37.8	60.9	1.669	1.038	2.708	61.7	1.61
180	1109	C	18	X	3	97.0	99.0	164.07	41.3	70.4	1.617	0.949	2.730	65.2	1.88
180	1109	C	18	X	4	56.0	58.0	165.16	37.5	60.1	1.675	1.046	2.708	61.4	1.59
180	1109	C	18	X	5	87.0	89.0	166.67	35.9	56.0	1.710	1.096	2.735	59.9	1.50
180	1109	C	18	X	6	35.5	37.5	167.65	36.6	57.8	1.689	1.070	2.704	60.4	1.53
180	1109	C	18	X	7	37.0	39.0	169.17	40.8	69.0	1.619	0.959	2.704	64.5	1.82
180	1109	C	20	X	1	8.0	10.0	179.38	44.1	79.0	1.571	0.878	2.721	67.7	2.10
180	1109	C	20	X	2	8.0	10.0	180.88	40.9	69.2	1.626	0.961	2.741	64.9	1.85
180	1109	C	20	X	3	8.0	10.0	182.38	37.1	59.0	1.687	1.061	2.728	61.1	1.57
180	1109	C	20	X	4	8.0	10.0	183.88	37.0	58.7	1.678	1.058	2.683	60.6	1.54
180	1109	C	22	X	1	65.0	67.0	199.15	39.4	65.1	1.624	0.984	2.625	62.5	1.67
180	1109	C	22	X	2	65.0	67.0	199.95	41.4	70.8	1.611	0.943	2.710	65.2	1.87
180	1109	C	23	X	1	4.0	6.0	208.14	40.2	67.3	1.629	0.974	2.704	64.0	1.78
180	1109	C	23	X	2	4.0	6.0	209.64	41.5	70.9	1.600	0.937	2.662	64.8	1.84
180	1109	C	23	X	3	4.0	6.0	211.14	37.8	60.7	1.673	1.041	2.719	61.7	1.61
180	1109	C	23	X	4	4.0	6.0	212.14	38.4	62.2	1.658	1.022	2.696	62.1	1.64
180	1109	C	23	X	5	4.0	6.0	212.79	40.6	68.4	1.616	0.960	2.674	64.1	1.79
180	1109	C	23	X	6	4.0	6.0	214.29	38.3	62.0	1.648	1.018	2.650	61.6	1.60
180	1109	C	23	X	7	4.0	6.0	215.79	30.4	43.7	1.774	1.234	2.610	52.7	1.12
180	1109	C	23	X	8	4.0	6.0	217.29	33.5	50.4	1.725	1.147	2.634	56.4	1.30
180	1109	C	25	X	1	4.0	6.0	227.44	23.2	30.2	1.981	1.521	2.759	44.9	0.81
180	1109	C	26	X	1	39.0	41.0	237.39	34.0	51.5	1.736	1.146	2.702	57.6	1.36
180	1109	C	26	X	2	39.0	41.0	238.84	36.7	57.9	1.680	1.064	2.670	60.1	1.51
180	1109	C	26	X	3	39.0	41.0	240.34	36.9	58.5	1.674	1.056	2.665	60.4	1.52
180	1109	C	26	X	4	39.0	41.0	241.84	40.1	67.1	1.632	0.977	2.714	64.0	1.78
180	1109	C	26	X	5	39.0	41.0	243.34	35.0	53.8	1.721	1.119	2.718	58.8	1.43
180	1109	C	26	X	6	39.0	41.0	244.84	40.1	67.0	1.633	0.978	2.716	64.0	1.78
180	1109	C	26	X	7	39.0	41.0	246.34	41.4	70.6	1.618	0.948	2.739	65.4	1.89
180	1109	C	27	X	1	5.0	7.0	246.75	45.0	81.8	1.562	0.859	2.739	68.6	2.19
180	1109	C	27	X	2	5.0	7.0	248.25	39.6	65.6	1.626	0.982	2.645	62.9	1.69
180	1109	C	27	X	3	5.0	7.0	249.75	40.0	66.6	1.612	0.968	2.611	62.9	1.70
180	1109	C	27	X	4	5.0	7.0	251.25	42.2	73.0	1.597	0.924	2.700	65.8	1.92
180	1109	C	27	X	5	5.0	7.0	252.75	41.0	69.4	1.602	0.946	2.630	64.0	1.78
180	1109	C	27	X	6	5.0	7.0	254.25	42.8	74.9	1.590	0.909	2.710	66.5	1.98
180	1109	C	27	X	7	5.0	7.0	255.25	30.8	44.5	1.770	1.225	2.620	53.2	1.14
180	1109	C	28	X	1	54.5	56.5	256.85	37.8	60.7	1.673	1.041	2.718	61.7	1.61
180	1109	C	28	X	2	54.5	56.5	258.35	42.7	74.4	1.579	0.905	2.647	65.8	1.92
180	1109	C	28	X	3	54.5	56.5	259.85	38.2	61.8	1.653	1.022	2.664	61.6	1.61
180	1109	C	28	X	4	54.5	56.5	261.35	39.2	64.4	1.636	0.995	2.659	62.6	1.67
180	1109	C	28	X	5	54.5	56.5	262.85	40.6	68.5	1.589	0.943	2.552	63.1	1.71

Table T15 (continued).

Leg	Site	Hole	Core	Type	Section	Top (cm)	Bottom (cm)	Depth (mbsf)	Water content (bulk)	Water content (dry)	Bulk density ($g \cdot cm^{-3}$)	Dry density ($g \cdot cm^{-3}$)	Grain density ($g \cdot cm^{-3}$)	Porosity (%)	Void ratio
180	1109	C	28	X	6	54.5	56.5	264.35	41.5	70.9	1.588	0.929	2.606	64.3	1.81
180	1109	C	29	X	1	10.0	12.0	266.10	38.8	63.3	1.613	0.988	2.536	61.1	1.57
180	1109	C	29	X	2	10.0	12.0	267.60	41.6	71.1	1.587	0.927	2.604	64.4	1.81
180	1109	C	29	X	3	10.0	12.0	269.10	39.1	64.3	1.648	1.003	2.709	63.0	1.70
180	1109	C	29	X	4	10.0	12.0	270.60	39.6	65.5	1.624	0.981	2.635	62.8	1.69
180	1109	C	29	X	5	55.5	57.5	272.55	33.6	50.5	1.703	1.132	2.562	55.8	1.26
180	1109	C	29	X	7	25.0	27.0	275.25	38.6	62.8	1.646	1.011	2.660	62.0	1.63
180	1109	C	30	X	1	42.0	44.0	276.02	37.4	59.7	1.668	1.044	2.672	60.9	1.56
180	1109	C	30	X	2	50.0	52.0	277.60	36.1	56.4	1.672	1.069	2.601	58.9	1.43
180	1109	C	30	X	3	49.0	51.0	279.09	38.1	61.5	1.651	1.023	2.649	61.4	1.59
180	1109	C	30	X	4	22.5	24.5	280.33	33.3	50.0	1.722	1.148	2.614	56.1	1.28
180	1109	C	30	X	5	107.0	109.0	282.67	32.8	48.8	1.744	1.172	2.653	55.8	1.27
180	1109	C	30	X	6	81.0	83.0	283.91	36.9	58.5	1.666	1.052	2.631	60.0	1.50
180	1109	C	30	X	7	27.5	29.5	284.87	34.0	51.5	1.716	1.132	2.631	57.0	1.32
180	1109	C	31	X	1	101.0	103.0	286.11	40.5	68.1	1.611	0.958	2.646	63.8	1.76
180	1109	C	31	X	2	112.0	114.0	287.72	34.4	52.5	1.710	1.121	2.636	57.5	1.35
180	1109	C	31	X	3	91.0	93.0	289.01	35.6	55.2	1.688	1.087	2.630	58.7	1.42
180	1109	C	31	X	4	94.0	96.0	290.54	32.9	49.1	1.742	1.168	2.656	56.0	1.28
180	1109	C	31	X	5	70.0	72.0	291.80	31.2	45.3	1.769	1.218	2.637	53.8	1.17
180	1109	C	31	X	6	58.0	60.0	293.18	31.4	45.7	1.779	1.221	2.683	54.5	1.20
180	1109	C	31	X	7	10.0	12.0	294.20	35.2	54.4	1.704	1.103	2.666	58.6	1.42
180	1109	C	32	X	1	58.0	60.0	295.38	31.7	46.5	1.744	1.191	2.593	54.1	1.18
180	1109	C	32	X	2	84.0	86.0	297.14	31.3	45.6	1.751	1.202	2.590	53.6	1.15
180	1109	C	32	X	3	32.0	34.0	298.12	33.8	51.1	1.714	1.134	2.613	56.6	1.31
180	1109	C	32	X	4	27.0	29.0	299.57	30.8	44.5	1.756	1.216	2.575	52.8	1.12
180	1109	C	32	X	6	40.0	42.0	302.70	34.9	53.6	1.702	1.108	2.638	58.0	1.38
180	1109	C	32	X	7	50.0	52.0	304.10	33.3	50.0	1.716	1.144	2.590	55.8	1.26
180	1109	C	33	X	1	147.0	149.0	305.97	29.4	41.7	1.810	1.278	2.663	52.0	1.08
180	1109	C	33	X	2	67.0	69.0	306.67	31.7	46.4	1.765	1.206	2.657	54.6	1.20
180	1109	C	33	X	2	83.0	85.0	306.83	29.1	41.1	1.814	1.286	2.657	51.6	1.07
180	1109	C	33	X	3	65.0	67.0	308.15	29.7	42.3	1.800	1.266	2.649	52.2	1.09
180	1109	C	33	X	4	40.0	42.0	309.40	32.2	47.6	1.764	1.195	2.690	55.6	1.25
180	1109	C	33	X	4	68.0	70.0	309.68	31.6	46.1	1.760	1.205	2.634	54.3	1.19
180	1109	C	33	X	5	112.0	114.0	311.62	31.7	46.4	1.758	1.201	2.635	54.4	1.19
180	1109	C	33	X	6	30.0	32.0	312.30	29.6	42.0	1.803	1.269	2.650	52.1	1.09
180	1109	C	33	X	6	38.0	40.0	312.38	30.1	43.1	1.800	1.258	2.674	53.0	1.13
180	1109	C	33	X	7	35.0	37.0	313.85	29.1	41.0	1.806	1.281	2.627	51.2	1.05
180	1109	C	34	X	1	4.0	6.0	314.24	31.6	46.2	1.754	1.199	2.614	54.1	1.18
180	1109	C	34	X	2	4.0	6.0	315.74	34.0	51.5	1.744	1.151	2.736	57.9	1.38
180	1109	C	34	X	3	4.0	6.0	317.24	35.3	54.5	1.688	1.092	2.613	58.2	1.39
180	1109	C	34	X	4	4.0	6.0	318.74	30.9	44.7	1.782	1.231	2.663	53.8	1.16
180	1109	C	34	X	5	4.0	6.0	320.24	33.0	49.2	1.746	1.170	2.674	56.3	1.29
180	1109	C	34	X	6	4.0	6.0	321.74	32.2	47.5	1.744	1.182	2.618	54.8	1.21
180	1109	C	34	X	7	4.0	6.0	323.24	29.5	41.8	1.800	1.270	2.635	51.8	1.08
180	1109	C	35	X	1	7.0	9.0	323.97	33.3	50.0	1.723	1.149	2.616	56.1	1.28
180	1109	C	35	X	2	7.0	9.0	325.47	31.6	46.2	1.768	1.210	2.660	54.5	1.20
180	1109	C	35	X	3	7.0	9.0	326.97	32.9	49.0	1.725	1.158	2.594	55.4	1.24
180	1109	C	35	X	4	7.0	9.0	328.47	27.9	38.7	1.843	1.329	2.669	50.2	1.01

Table T15 (continued).

Leg	Site	Hole	Core	Type	Section	Top (cm)	Bottom (cm)	Depth (mbsf)	Water content (bulk)	Water content (dry)	Bulk density (g·cm^{-3})	Dry density (g·cm^{-3})	Grain density (g·cm^{-3})	Porosity (%)	Void ratio
180	1109	C	35	X	5	7.0	9.0	329.97	27.1	37.1	1.877	1.369	2.717	49.6	0.99
180	1109	C	35	X	6	7.0	9.0	331.47	34.5	52.6	1.716	1.125	2.662	57.8	1.37
180	1109	C	35	X	7	7.0	9.0	332.97	30.5	43.9	1.772	1.232	2.608	52.8	1.12
180	1109	C	36	X	1	8.0	10.0	333.58	30.6	44.1	1.775	1.231	2.624	53.1	1.13
180	1109	C	36	X	2	8.0	10.0	335.08	29.9	42.7	1.815	1.272	2.709	53.1	1.13
180	1109	C	36	X	3	6.0	8.0	336.56	34.7	53.2	1.678	1.096	2.544	56.9	1.32
180	1109	C	36	X	4	5.0	7.0	338.05	33.6	50.5	1.735	1.153	2.672	56.9	1.32
180	1109	C	37	X	1	5.0	7.0	343.15	29.9	42.7	1.816	1.273	2.712	53.1	1.13
180	1109	C	37	X	2	5.0	7.0	344.35	29.4	41.6	1.820	1.285	2.692	52.2	1.09
180	1109	C	38	X	1	14.0	16.0	346.74	37.1	59.1	1.652	1.038	2.590	59.9	1.49
180	1109	C	38	X	2	2.0	4.0	348.12	35.2	54.4	1.694	1.098	2.630	58.3	1.40
180	1109	C	38	X	3	2.0	4.0	349.62	33.6	50.6	1.731	1.149	2.661	56.8	1.32
180	1109	C	38	X	4	2.0	4.0	351.12	36.5	57.5	1.679	1.066	2.655	59.8	1.49
180	1109	C	38	X	5	5.0	7.0	352.65	30.7	44.3	1.802	1.249	2.714	54.0	1.17
180	1109	C	38	X	6	5.0	7.0	354.15	34.5	52.6	1.703	1.116	2.613	57.3	1.34
180	1109	C	38	X	7	5.0	7.0	355.65	34.3	52.1	1.723	1.132	2.673	57.6	1.36
180	1109	C	40	X	1	18.5	20.5	362.39	36.2	56.8	1.683	1.073	2.652	59.5	1.47
180	1109	C	40	X	2	20.0	22.0	363.90	39.2	64.5	1.627	0.989	2.625	62.3	1.65
180	1109	C	40	X	3	21.5	23.5	365.42	36.4	57.2	1.682	1.070	2.660	59.8	1.49
180	1109	C	40	X	4	21.0	23.0	366.91	35.6	55.2	1.675	1.079	2.581	58.2	1.39
180	1109	C	40	X	5	21.0	23.0	368.41	28.6	40.1	1.811	1.292	2.618	50.6	1.03
180	1109	C	41	X	1	41.0	43.0	371.91	36.9	58.4	1.667	1.053	2.632	60.0	1.50
180	1109	C	41	X	2	41.0	43.0	373.41	39.2	64.4	1.621	0.986	2.594	62.0	1.63
180	1109	C	41	X	3	40.5	42.5	374.90	38.3	62.0	1.648	1.017	2.649	61.6	1.60
180	1109	C	41	X	4	32.0	34.0	376.02	35.2	54.3	1.700	1.102	2.652	58.5	1.41
180	1109	D	1	R	1	80.0	82.0	353.60	31.2	45.4	1.763	1.212	2.622	53.8	1.16
180	1109	D	1	R	2	79.0	81.0	355.09	34.3	52.1	1.718	1.130	2.658	57.5	1.35
180	1109	D	1	R	3	118.0	120.0	356.98	38.6	62.7	1.642	1.009	2.642	61.8	1.62
180	1109	D	2	R	1	47.0	49.0	359.57	35.2	54.3	1.706	1.106	2.673	58.6	1.42
180	1109	D	2	R	2	48.0	50.0	360.89	38.2	61.8	1.652	1.021	2.663	61.7	1.61
180	1109	D	2	R	3	50.0	52.0	362.31	39.0	64.0	1.560	0.951	2.344	59.4	1.46
180	1109	D	2	R	4	76.0	78.0	363.59	33.4	50.1	1.724	1.148	2.623	56.2	1.29
180	1109	D	2	R	5	68.0	70.0	364.56	37.8	60.8	1.656	1.030	2.649	61.1	1.57
180	1109	D	2	R	6	79.0	81.0	365.71	38.2	61.7	1.649	1.020	2.647	61.5	1.60
180	1109	D	2	R	7	68.0	70.0	366.66	37.2	59.3	1.665	1.045	2.650	60.6	1.54
180	1109	D	2	R	8	38.0	40.0	367.82	35.3	54.6	1.765	1.142	2.916	60.9	1.56
180	1109	D	3	R	1	114.0	116.0	369.84	34.8	53.4	1.700	1.108	2.626	57.8	1.37
180	1109	D	3	R	2	70.0	72.0	370.90	37.4	59.7	1.665	1.042	2.656	60.8	1.55
180	1109	D	3	R	3	9.0	11.0	371.78	38.5	62.5	1.646	1.013	2.653	61.8	1.62
180	1109	D	3	R	4	72.0	74.0	373.51	37.5	59.9	1.656	1.036	2.629	60.6	1.54
180	1109	D	3	R	5	78.0	80.0	374.92	35.8	55.8	1.679	1.078	2.609	58.7	1.42
180	1109	D	3	R	6	89.0	91.0	376.25	36.8	58.3	1.670	1.055	2.641	60.0	1.50
180	1109	D	3	R	7	44.0	46.0	377.19	36.6	57.8	1.671	1.059	2.632	59.8	1.49
180	1109	D	4	R	1	54.0	56.0	378.84	29.0	40.9	1.810	1.285	2.640	51.3	1.05
180	1109	D	4	R	2	105.0	107.0	380.45	31.5	46.0	1.750	1.199	2.600	53.9	1.17
180	1109	D	4	R	3	40.0	42.0	381.00	33.7	50.7	1.716	1.139	2.613	56.4	1.30
180	1109	D	4	R	5	65.0	67.0	383.42	31.1	45.1	1.789	1.233	2.699	54.3	1.19
180	1109	D	4	R	6	46.0	48.0	384.48	32.3	47.8	1.739	1.177	2.611	54.9	1.22

Table T15 (continued).

Leg	Site	Hole	Core	Type	Section	Top (cm)	Bottom (cm)	Depth (mbsf)	Water content (bulk)	Water content (dry)	Bulk density ($g \cdot cm^{-3}$)	Dry density ($g \cdot cm^{-3}$)	Grain density ($g \cdot cm^{-3}$)	Porosity (%)	Void ratio
180	1109	D	4	R	7	46.0	48.0	385.99	32.4	48.0	1.748	1.181	2.648	55.4	1.24
180	1109	D	6	R	2	19.0	21.0	398.81	36.5	57.5	1.673	1.062	2.630	59.6	1.48
180	1109	D	6	R	3	39.0	41.0	400.45	36.8	58.1	1.670	1.056	2.638	60.0	1.50
180	1109	D	6	R	4	67.0	69.0	401.80	35.5	55.0	1.698	1.095	2.660	58.8	1.43
180	1109	D	6	R	5	68.0	70.0	402.73	36.5	57.5	1.683	1.069	2.675	60.0	1.50
180	1109	D	6	R	6	62.0	64.0	403.46	37.0	58.7	1.670	1.052	2.651	60.3	1.52
180	1109	D	7	R	1	76.0	78.0	407.56	35.1	54.0	1.704	1.107	2.658	58.4	1.40
180	1109	D	7	R	2	98.0	100.0	409.28	30.5	43.8	1.775	1.234	2.615	52.8	1.12
180	1109	D	7	R	3	89.0	91.0	410.43	36.1	56.5	1.680	1.073	2.632	59.2	1.45
180	1109	D	7	R	5	29.0	31.0	412.49	36.3	57.1	1.678	1.068	2.640	59.5	1.47
180	1109	D	8	R	1	18.0	20.0	416.68	34.6	52.8	1.713	1.121	2.658	57.8	1.37
180	1109	D	8	R	3	70.0	72.0	419.62	37.2	59.3	1.658	1.041	2.622	60.3	1.52
180	1109	D	8	R	5	42.0	44.0	422.04	34.0	51.6	1.709	1.128	2.610	56.8	1.31
180	1109	D	8	R	7	70.0	72.0	424.58	35.2	54.4	1.707	1.105	2.678	58.7	1.42
180	1109	D	9	R	1	125.0	127.0	427.35	34.0	51.5	1.712	1.130	2.616	56.8	1.31
180	1109	D	9	R	3	94.0	96.0	429.99	34.9	53.6	1.706	1.111	2.654	58.2	1.39
180	1109	D	9	R	5	73.0	75.0	432.25	31.6	46.1	1.751	1.199	2.605	54.0	1.17
180	1109	D	10	R	1	49.0	51.0	436.19	35.2	54.3	1.709	1.108	2.685	58.7	1.42
180	1109	D	10	R	3	84.0	86.0	439.29	35.6	55.3	1.693	1.090	2.651	58.9	1.43
180	1109	D	10	R	5	4.0	6.0	441.18	35.4	54.7	1.701	1.100	2.665	58.7	1.42
180	1109	D	10	R	7	70.0	72.0	444.06	34.6	52.9	1.712	1.120	2.656	57.8	1.37
180	1109	D	11	R	1	51.0	53.0	445.81	33.4	50.2	1.731	1.153	2.650	56.5	1.30
180	1109	D	11	R	2	83.0	85.0	447.51	34.7	53.1	1.704	1.113	2.632	57.7	1.37
180	1109	D	11	R	4	55.0	57.0	449.92	33.6	50.7	1.728	1.147	2.652	56.7	1.31
180	1109	D	11	R	6	75.0	77.0	452.95	35.5	55.1	1.698	1.095	2.664	58.9	1.43
180	1109	D	19	R	4	6.0	8.0	526.42	28.2	39.2	1.849	1.328	2.703	50.9	1.04
180	1109	D	20	R	3	31.0	33.0	535.09	29.8	42.5	1.798	1.262	2.650	52.4	1.10
180	1109	D	21	R	1	91.0	93.0	542.51	25.1	33.5	1.920	1.438	2.717	47.1	0.89
180	1109	D	21	R	2	76.0	78.0	543.87	25.8	34.8	1.891	1.404	2.681	47.6	0.91
180	1109	D	21	R	3	96.5	98.5	545.60	26.1	35.2	1.875	1.386	2.651	47.7	0.91
180	1109	D	21	R	4	71.0	73.0	546.77	25.6	34.4	1.892	1.408	2.670	47.2	0.90
180	1109	D	21	R	5	61.0	63.0	548.01	26.1	35.2	1.887	1.396	2.685	48.0	0.92
180	1109	D	21	R	6	41.0	43.0	548.71	26.1	35.3	1.887	1.395	2.684	48.0	0.92
180	1109	D	21	R	7	21.0	23.0	549.21	25.5	34.2	1.907	1.421	2.702	47.4	0.90
180	1109	D	21	R	8	2.0	4.0	550.32	26.2	35.4	1.878	1.386	2.666	48.0	0.92
180	1109	D	22	R	1	93.0	95.0	552.13	25.9	34.9	1.888	1.399	2.678	47.8	0.91
180	1109	D	22	R	2	88.0	90.0	553.42	24.2	31.9	1.931	1.464	2.693	45.6	0.84
180	1109	D	22	R	3	63.0	65.0	554.37	25.1	33.5	1.899	1.422	2.661	46.6	0.87
180	1109	D	22	R	4	79.0	81.0	555.44	26.6	36.1	1.879	1.380	2.691	48.7	0.95
180	1109	D	23	R	1	86.5	88.5	561.66	23.9	31.3	1.943	1.479	2.703	45.3	0.83
180	1109	D	23	R	2	28.0	30.0	562.58	24.2	31.9	1.927	1.461	2.681	45.5	0.84
180	1109	D	24	R	3	121.5	123.5	569.73	26.6	36.2	1.878	1.379	2.690	48.7	0.95
180	1109	D	24	R	4	101.5	103.5	570.97	26.3	35.6	1.877	1.384	2.669	48.1	0.93
180	1109	D	25	R	1	51.0	53.0	570.91	24.5	32.4	1.919	1.449	2.680	45.9	0.85
180	1109	D	25	R	2	127.0	129.0	573.11	24.9	33.1	1.911	1.436	2.679	46.4	0.87
180	1109	D	25	R	4	75.0	77.0	575.38	24.2	31.9	1.931	1.464	2.693	45.6	0.84
180	1109	D	25	R	5	60.0	62.0	576.73	23.6	31.0	1.941	1.482	2.685	44.8	0.81
180	1109	D	25	R	6	4.0	6.0	577.51	24.9	33.1	1.914	1.438	2.689	46.5	0.87

Table T15 (continued).

Leg	Site	Hole	Core	Type	Section	Top (cm)	Bottom (cm)	Depth (mbsf)	Water content (bulk)	Water content (dry)	Bulk density ($g \cdot cm^{-3}$)	Dry density ($g \cdot cm^{-3}$)	Grain density ($g \cdot cm^{-3}$)	Porosity (%)	Void ratio
180	1109	D	26	R	1	126.0	128.0	581.26	21.9	28.1	1.972	1.539	2.664	42.2	0.73
180	1109	D	26	R	2	32.0	34.0	581.78	22.3	28.7	1.984	1.542	2.713	43.2	0.76
180	1109	D	26	R	3	49.0	51.0	583.16	22.2	28.6	2.029	1.578	2.822	44.1	0.79
180	1109	D	26	R	4	36.0	38.0	584.29	21.6	27.6	2.040	1.598	2.810	43.1	0.76
180	1109	D	26	R	5	47.0	49.0	585.51	19.6	24.4	2.084	1.675	2.789	40.0	0.67
180	1109	D	26	R	6	60.0	62.0	586.99	23.0	29.9	1.951	1.502	2.675	43.8	0.78
180	1109	D	26	R	7	40.0	42.0	587.83	16.2	19.3	2.119	1.776	2.671	33.5	0.50
180	1109	D	27	R	1	15.0	17.0	589.75	15.1	17.8	2.178	1.850	2.724	32.1	0.47
180	1109	D	27	R	3	14.0	16.0	592.14	21.5	27.3	1.956	1.536	2.603	41.0	0.70
180	1109	D	27	R	4	17.0	19.0	593.26	20.3	25.4	2.044	1.630	2.738	40.5	0.68
180	1109	D	28	R	1	39.0	41.0	599.59	19.5	24.2	2.048	1.649	2.704	39.0	0.64
180	1109	D	29	R	1	3.0	5.0	608.93	12.0	13.6	2.200	1.937	2.608	25.7	0.35
180	1109	D	29	R	2	4.0	6.0	609.97	18.4	22.6	2.069	1.687	2.689	37.3	0.59
180	1109	D	29	R	3	4.0	6.0	611.00	19.3	23.9	2.004	1.617	2.599	37.8	0.61
180	1109	D	30	R	1	56.0	58.0	619.06	20.8	26.3	2.003	1.587	2.675	40.7	0.69
180	1109	D	31	R	1	17.0	19.0	628.37	14.4	16.8	2.195	1.880	2.716	30.8	0.45
180	1109	D	32	R	1	10.0	12.0	638.00	19.1	23.6	1.992	1.612	2.562	37.1	0.59
180	1109	D	32	R	2	15.0	17.0	639.46	16.1	19.2	2.135	1.792	2.697	33.6	0.51
180	1109	D	33	R	1	14.0	16.0	647.64	16.2	19.3	2.145	1.798	2.720	33.9	0.51
180	1109	D	34	R	1	2.0	4.0	657.12	17.1	20.6	2.170	1.800	2.820	36.2	0.57
180	1109	D	34	R	3	7.0	9.0	659.88	17.2	20.8	2.099	1.737	2.688	35.4	0.55
180	1109	D	34	R	5	18.0	20.0	662.56	17.5	21.3	2.050	1.691	2.605	35.1	0.54
180	1109	D	35	R	1	9.0	11.0	666.79	16.6	19.9	2.073	1.729	2.605	33.6	0.51
180	1109	D	35	R	3	77.0	79.0	669.88	12.4	14.2	2.262	1.982	2.729	27.4	0.38
180	1109	D	35	R	5	86.0	88.0	672.46	20.3	25.4	2.019	1.610	2.681	40.0	0.67
180	1109	D	35	R	7	4.0	6.0	673.85	21.5	27.4	2.034	1.597	2.787	42.7	0.75
180	1109	D	36	R	1	27.5	29.5	676.67	20.3	25.5	2.082	1.659	2.826	41.3	0.70
180	1109	D	36	R	2	15.0	17.0	678.05	21.7	27.7	2.029	1.588	2.787	43.0	0.76
180	1109	D	36	R	3	40.0	42.0	679.80	22.5	29.1	1.940	1.503	2.621	42.7	0.74
180	1109	D	36	R	4	60.0	62.0	681.50	24.6	32.7	1.914	1.443	2.673	46.0	0.85
180	1109	D	36	R	5	110.0	112.0	683.50	25.8	34.7	1.864	1.384	2.607	46.9	0.88
180	1109	D	36	R	6	42.0	44.0	684.32	20.4	25.6	2.017	1.605	2.683	40.2	0.67
180	1109	D	37	R	1	40.5	42.5	686.41	25.6	34.3	1.902	1.415	2.695	47.5	0.90
180	1109	D	37	R	2	126.5	128.5	688.74	27.1	37.2	1.824	1.330	2.571	48.3	0.93
180	1109	D	37	R	4	98.0	100.0	691.44	24.8	33.0	1.891	1.422	2.625	45.8	0.85
180	1109	D	37	R	5	38.5	40.5	692.11	25.0	33.3	1.860	1.395	2.554	45.4	0.83
180	1109	D	38	R	1	94.0	96.0	696.54	28.7	40.3	1.724	1.229	2.379	48.4	0.94
180	1109	D	38	R	2	102.5	104.5	698.01	26.5	36.1	1.943	1.427	2.873	50.3	1.01
180	1109	D	38	R	3	37.5	39.5	698.67	25.3	33.9	1.911	1.427	2.704	47.2	0.89
180	1109	D	38	R	4	129.5	131.5	701.05	25.7	34.6	1.878	1.395	2.640	47.2	0.89
180	1109	D	38	R	5	65.5	67.5	701.91	24.0	31.6	1.922	1.461	2.659	45.1	0.82
180	1109	D	39	R	2	29.0	31.0	706.90	26.9	36.7	1.854	1.356	2.640	48.6	0.95
180	1109	D	39	R	3	31.0	33.0	708.35	26.5	36.1	1.892	1.390	2.727	49.0	0.96
180	1109	D	40	R	1	9.0	11.0	715.09	25.2	33.7	1.984	1.484	2.900	48.8	0.95
180	1109	D	40	R	2	24.0	26.0	716.50	22.6	29.3	1.972	1.525	2.704	43.6	0.77
180	1109	D	40	R	3	52.0	54.0	717.17	23.1	30.0	1.984	1.526	2.761	44.7	0.81
180	1109	D	41	R	2	80.0	82.0	727.00	26.0	35.1	1.999	1.480	3.005	50.8	1.03
180	1109	D	41	R	3	50.0	52.0	727.78	23.0	29.8	1.983	1.527	2.752	44.5	0.80

Table T15 (continued).

Leg	Site	Hole	Core	Type	Section	Top (cm)	Bottom (cm)	Depth (mbsf)	Water content (bulk)	Water content (dry)	Bulk density ($g \cdot cm^{-3}$)	Dry density ($g \cdot cm^{-3}$)	Grain density ($g \cdot cm^{-3}$)	Porosity (%)	Void ratio
180	1109	D	41	R	3	82.0	84.0	728.10	0.5	0.5	2.803	2.789	2.828	1.4	0.01
180	1109	D	42	R	1	41.0	43.0	734.71	20.4	25.6	2.046	1.628	2.749	40.8	0.69
180	1109	D	43	R	1	91.0	93.0	744.81	23.4	30.6	1.869	1.431	2.501	42.8	0.75
180	1109	D	43	R	2	54.0	56.0	745.46	22.6	29.1	1.980	1.533	2.719	43.6	0.77
180	1109	D	43	R	3	8.0	10.0	745.89	23.3	30.3	1.947	1.494	2.679	44.2	0.79

Note: This table is also available in ASCII format in the **TABLES** directory.

Table T16. Longitudinal (z) and transverse (x and y) velocities for cores, Site 1109. (Continued on next six pages. See table note.)

Leg	Site	Hole	Core	Type	Section	Top (cm)	Bottom (cm)	Depth (mbsf)	x-velocity ($m \cdot s^{-1}$)	y-velocity ($m \cdot s^{-1}$)	z-velocity ($m \cdot s^{-1}$)
180	1109	B	1	H	1	77.2	77.2	0.77		1530.321	1532.622
180	1109	B	1	H	2	52.5	52.5	1.98		1526.300	1521.108
180	1109	B	1	H	3	101.8	101.8	3.97		1559.075	1544.038
180	1109	B	1	H	4	27.6	27.6	4.73		1506.506	1508.588
180	1109	B	2	H	1	62.6	62.6	5.93		1527.638	1524.437
180	1109	B	2	H	2	59.6	59.6	7.40		1522.299	1536.544
180	1109	B	2	H	3	81.5	81.5	9.12		766.389	1605.246
180	1109	B	2	H	4	34.6	34.6	10.15		1527.638	1526.442
180	1109	B	2	H	5	35.8	35.8	10.96		1523.630	1525.105
180	1109	B	2	H	6	36.2	36.2	12.46		1550.750	1538.580
180	1109	B	2	H	7	65.1	65.1	14.25		1506.506	1523.104
180	1109	C	3	H	1	109.0	109.0	17.99		1556.429	
180	1109	C	3	H	1	110.3	110.3	18.00			1523.104
180	1109	C	3	H	2	81.9	81.9	19.22		1513.047	1527.781
180	1109	C	3	H	3	84.3	84.3	20.74		1533.014	1544.723
180	1109	C	3	H	4	84.3	84.3	22.24		1526.300	1527.781
180	1109	C	3	H	5	46.7	46.7	23.37		1519.644	1521.108
180	1109	C	3	H	6	19.8	19.8	24.60			1521.108
180	1109	C	3	H	6	19.8	19.8	25.00		1526.300	
180	1109	C	3	H	7	28.9	28.9	26.19		1533.014	1548.156
180	1109	C	4	H	1	80.0	80.0	27.20		1506.506	1521.108
180	1109	C	4	H	2	55.0	55.0	28.45		1501.314	1507.935
180	1109	C	4	H	3	28.8	28.8	29.69		1504.230	1524.804
180	1109	C	4	H	4	97.8	97.8	31.88		1545.249	1558.549
180	1109	C	4	H	5	62.9	62.9	33.03		1566.081	1556.459
180	1109	C	4	H	6	59.4	59.4	34.49	1614.340	1533.014	1557.852
180	1109	C	4	H	7	45.3	45.3	35.85	1627.805	1554.901	1566.260
180	1109	C	5	H	1	105.8	105.8	36.96	1622.581	1534.364	1558.549
180	1109	C	5	H	2	19.0	19.0	37.59	1606.524		
180	1109	C	5	H	2	78.9	78.9	38.19		1526.300	1537.901
180	1109	C	5	H	3	93.9	93.9	39.84		1537.071	1544.723
180	1109	C	5	H	3	98.7	98.7	39.89	1631.126		
180	1109	C	5	H	4	48.8	48.8	40.89		1535.716	1551.605
180	1109	C	5	H	4	56.6	56.6	40.97	1624.870		
180	1109	C	5	H	5	56.8	56.8	42.47	1606.019		
180	1109	C	5	H	5	48.1	48.1	42.38		1519.644	1546.781
180	1109	C	5	H	6	79.3	79.3	44.19		1538.428	1557.852
180	1109	C	5	H	6	87.7	87.7	44.28	1611.909		
180	1109	C	5	H	7	21.8	21.8	45.12		1531.666	1543.354
180	1109	C	5	H	7	30.1	30.1	45.20	1590.700		
180	1109	C	6	H	1	87.6	87.6	46.28		1538.563	1548.156
180	1109	C	6	H	1	96.6	96.6	46.37	1593.701		
180	1109	C	6	H	2	93.2	93.2	47.83		1553.515	1562.045
180	1109	C	6	H	2	100.4	100.4	47.90	1606.446		
180	1109	C	6	H	3	61.4	61.4	49.01		1522.299	1533.162
180	1109	C	6	H	3	70.3	70.3	49.10	1603.337		
180	1109	C	6	H	4	69.1	69.1	50.59		1539.787	1564.852
180	1109	C	6	H	4	77.9	77.9	50.68	1631.557		
180	1109	C	6	H	5	67.2	67.2	52.07		1559.075	1575.471
180	1109	C	6	H	5	75.7	75.7	52.16	1628.127		
180	1109	C	6	H	6	81.2	81.2	53.71		1545.249	1594.223
180	1109	C	6	H	6	89.1	89.1	53.79	1623.349		
180	1109	C	6	H	7	44.4	44.4	54.84		1535.716	1564.149
180	1109	C	6	H	7	52.9	52.9	54.93	1618.928		
180	1109	C	7	H	1	101.7	101.7	55.92		1543.880	1566.964
180	1109	C	7	H	1	110.0	110.0	56.00	1605.277		
180	1109	C	7	H	2	47.9	47.9	56.88	1606.720	1549.371	1559.247
180	1109	C	7	H	3	67.6	67.6	58.58		1542.513	1551.605
180	1109	C	7	H	3	75.6	75.6	58.66	1595.291		
180	1109	C	7	H	4	67.6	67.6	60.08		1542.513	1565.556
180	1109	C	7	H	4	78.6	78.6	60.19	1632.596		
180	1109	C	7	H	5	48.1	48.1	61.38	1607.537	1547.995	1566.260
180	1109	C	7	H	6	99.6	99.6	63.40	1592.365	1547.239	1547.468
180	1109	C	7	H	7	29.3	29.3	64.19	1610.430	1561.450	1559.945
180	1109	C	8	H	1	88.2	88.2	65.28	1603.789	1542.513	1562.745
180	1109	C	8	H	2	87.3	87.3	66.77	1607.804	1564.675	1549.534
180	1109	C	8	H	3	81.3	81.3	68.21	1634.404	1552.131	1571.915
180	1109	C	8	H	4	96.6	96.6	69.87		1522.965	1566.260

Table T16 (continued).

Leg	Site	Hole	Core	Type	Section	Top (cm)	Bottom (cm)	Depth (mbsf)	x-velocity ($m \cdot s^{-1}$)	y-velocity ($m \cdot s^{-1}$)	z-velocity ($m \cdot s^{-1}$)
180	1109	C	8	H	4	97.0	97.0	69.87	1606.814		
180	1109	C	8	H	5	99.6	99.6	71.40	1609.519	1567.278	1564.852
180	1109	C	8	H	6	110.1	110.1	73.00	1612.247	1554.277	1572.625
180	1109	C	8	H	7	30.8	30.8	73.71	1629.546	1556.290	1552.989
180	1109	C	9	H	1	114.1	114.1	75.04	1641.062	1575.711	1566.260
180	1109	C	9	H	2	101.7	101.7	76.42	1584.120	1554.901	1551.605
180	1109	C	9	H	3	103.2	103.2	77.93	1612.156	1556.290	1550.224
180	1109	C	9	H	4	103.3	103.3	79.43	1630.217	1581.718	1586.235
180	1109	C	9	H	5	105.1	105.1	80.95	1623.893	1550.750	1569.082
180	1109	C	9	H	6	117.1	117.1	82.57	1635.735		
180	1109	C	10	H	1	37.4	37.4	83.77		1575.070	1590.219
180	1109	C	9	H	7	57.8	57.8	83.48	1662.322		
180	1109	C	10	H	1	45.6	45.6	83.86	1675.317		
180	1109	C	10	H	2	25.4	25.4	85.15	1630.382		
180	1109	C	10	H	2	27.2	27.2	85.17		1559.075	1541.714
180	1109	C	10	H	3	118.9	118.9	87.59	1650.675		
180	1109	C	10	H	4	69.7	69.7	88.60	1631.831		
180	1109	C	10	H	5	26.4	26.4	89.66	1647.449		
180	1109	C	10	H	6	124.2	124.2	92.14		1547.995	1538.580
180	1109	C	10	H	6	133.0	133.0	92.23	1610.925		
180	1109	C	10	H	7	52.2	52.2	92.92	1613.395		
180	1109	C	11	H	1	139.3	139.3	94.29	1656.360		
180	1109	C	10	H	7	52.5	52.5	92.93		1538.428	1542.875
180	1109	C	11	H	2	139.0	139.0	95.79	1661.939		
180	1109	C	11	H	3	127.8	127.8	97.18	1664.003		
180	1109	C	11	H	4	115.1	115.1	98.55	1637.393		
180	1109	C	11	H	5	129.1	129.1	100.19	1653.901		
180	1109	C	11	H	6	90.2	90.2	101.30	1655.001		
180	1109	C	11	H	7	109.0	109.0	102.49	1645.222		
180	1109	C	12	X	1	133.5	133.5	103.74	1625.669		
180	1109	C	12	X	2	132.5	132.5	105.23	1640.910		
180	1109	C	12	X	3	135.0	135.0	106.75	1616.332		
180	1109	C	12	X	4	135.4	135.4	108.25	1634.327		
180	1109	C	12	X	5	131.6	131.6	109.72	1651.627		
180	1109	C	12	X	6	134.9	134.9	111.25	1629.079		
180	1109	C	12	X	7	24.8	24.8	111.65	1655.656		
180	1109	C	13	X	1	131.6	131.6	113.32	1639.224		
180	1109	C	13	X	2	132.7	132.7	114.83	1634.627		
180	1109	C	13	X	3	127.3	127.3	116.27	1659.502		
180	1109	C	13	X	4	133.9	133.9	117.84	1688.255		
180	1109	C	13	X	5	135.3	135.3	119.35	1647.349		
180	1109	C	13	X	6	128.7	128.7	120.79	1639.626		
180	1109	C	14	X	2	51.0	51.0	123.61	1585.386		
180	1109	C	14	X	5	72.3	72.3	128.32	1357.515		
180	1109	C	14	X	6	93.7	93.7	130.04	1648.401		
180	1109	C	15	X	1	84.5	84.5	132.05	1624.656		
180	1109	C	15	X	2	90.5	90.5	133.58	1597.497		
180	1109	C	15	X	3	96.3	96.3	135.13	1576.498		
180	1109	C	15	X	4	82.0	82.0	136.49	1632.100		
180	1109	C	17	X	2	39.7	39.7	152.40	1656.198		
180	1109	C	18	X	1	113.5	113.5	161.24	1699.478		
180	1109	C	18	X	2	112.8	112.8	162.73	1770.954		
180	1109	C	18	X	3	97.5	97.5	164.08	1701.465		
180	1109	C	18	X	4	57.0	57.0	165.17	1730.829		
180	1109	C	18	X	5	87.0	87.0	166.67	1767.703		
180	1109	C	18	X	6	34.5	34.5	167.65	1782.529		
180	1109	C	18	X	7	37.0	37.0	169.17	1704.514		
180	1109	C	20	X	1	59.4	59.4	179.89	1747.504		
180	1109	C	20	X	2	86.6	86.6	181.67	1644.294		
180	1109	C	20	X	4	97.0	97.0	184.77	1770.387		
180	1109	C	22	X	1	65.0	65.0	199.15	1696.135		
180	1109	C	22	X	2	21.3	21.3	199.51	1717.925		
180	1109	C	23	X	1	127.3	127.3	209.37	1677.546		
180	1109	C	23	X	3	19.4	19.4	211.29	1586.028		
180	1109	C	23	X	4	27.2	27.2	212.37	1623.998		
180	1109	C	23	X	5	81.7	81.7	213.57	1627.374		
180	1109	C	23	X	6	59.3	59.3	214.84	1688.620		
180	1109	C	23	X	7	53.4	53.4	216.28	1589.433		
180	1109	C	26	X	1	64.3	64.3	237.64	1836.891		

Table T16 (continued).

Leg	Site	Hole	Core	Type	Section	Top (cm)	Bottom (cm)	Depth (mbsf)	x-velocity ($m \cdot s^{-1}$)	y-velocity ($m \cdot s^{-1}$)	z-velocity ($m \cdot s^{-1}$)
180	1109	C	26	X	2	94.3	94.3	239.39	1833.900		
180	1109	C	26	X	3	98.0	98.0	240.93	1698.872		
180	1109	C	26	X	4	107.8	107.8	242.53	1694.641		
180	1109	C	26	X	5	96.1	96.1	243.91	1676.603		
180	1109	C	26	X	6	31.2	31.2	244.76	1686.761		
180	1109	C	26	X	6	120.2	120.2	245.65	1701.536		
180	1109	C	27	X	1	37.7	37.7	247.08	1727.302		
180	1109	C	27	X	2	72.0	72.0	248.92	1700.627		
180	1109	C	27	X	3	84.4	84.4	250.54	1676.310		
180	1109	C	27	X	4	111.1	111.1	252.31	1723.271		
180	1109	C	27	X	5	121.6	121.6	253.92	1720.056		
180	1109	C	27	X	6	28.8	28.8	254.49	1708.232		
180	1109	C	27	X	7	55.4	55.4	255.75	1771.609		
180	1109	C	28	X	1	30.0	30.0	256.60	1792.172	1806.156	1794.960
180	1109	C	28	X	2	33.8	33.8	258.14	1723.710		
180	1109	C	28	X	3	64.3	64.3	259.94	1621.484		
180	1109	C	28	X	4	70.1	70.1	261.50	1651.389		
180	1109	C	28	X	5	126.0	126.0	263.56	1771.828	1775.455	1796.645
180	1109	C	28	X	6	129.0	129.0	265.09	1730.170	1728.825	1754.207
180	1109	C	28	X	7	27.5	27.5	265.58	1685.018		
180	1109	C	29	X	1	70.5	70.5	266.71	1742.602		
180	1109	C	29	X	2	94.0	94.0	268.44	1746.316	1769.762	1791.531
180	1109	C	29	X	3	94.0	94.0	269.94	1714.405	1738.636	1773.056
180	1109	C	29	X	4	127.5	127.5	271.78	1694.845	1715.437	1712.971
180	1109	C	29	X	5	139.0	139.0	273.39	1705.987	1726.339	1733.797
180	1109	C	29	X	6	14.5	14.5	273.65	1694.845	1702.266	1720.368
180	1109	C	29	X	7	23.0	23.0	275.23	1696.625	1708.788	1738.770
180	1109	C	30	X	1	85.0	85.0	276.45	1693.941	1704.712	1718.724
180	1109	C	30	X	2	38.0	38.0	277.48	1712.640	1706.343	1749.123
180	1109	C	30	X	3	32.0	32.0	278.92	1709.375	1705.573	1708.788
180	1109	C	30	X	4	79.5	79.5	280.90	1673.366		
180	1109	C	30	X	5	36.0	36.0	281.96	1708.039	1704.712	1735.455
180	1109	C	30	X	6	99.5	99.5	284.10	1783.401	1784.932	1771.092
180	1109	C	30	X	7	11.0	11.0	284.71	1767.152	1797.727	1813.073
180	1109	C	31	X	1	91.0	91.0	286.01	1843.240	1798.375	1852.051
180	1109	C	31	X	2	117.0	117.0	287.77	1684.004	1698.175	1688.312
180	1109	C	31	X	3	133.0	133.0	289.43	1738.764	1737.738	1724.052
180	1109	C	31	X	4	90.0	90.0	290.50	1757.371	1759.969	
180	1109	C	31	X	5	117.5	117.5	292.28	1812.361	1792.388	1757.121
180	1109	C	31	X	6	22.0	22.0	292.82	1750.807	1758.807	1762.178
180	1109	C	31	X	7	21.1	21.1	294.31	1761.677		
180	1109	C	32	X	1	63.1	63.1	295.43	1618.374		
180	1109	C	32	X	2	87.0	87.0	297.17	1773.038	1768.077	1754.137
180	1109	C	32	X	3	38.5	38.5	298.19	1751.222	1743.273	1755.341
180	1109	C	32	X	4	22.3	22.3	299.52	1733.746	1725.723	1712.249
180	1109	C	32	X	5	61.5	61.5	301.42	1779.168	1762.178	1779.704
180	1109	C	32	X	6	43.5	43.5	302.74	1702.263		
180	1109	C	32	X	6	50.7	50.7	302.81	1677.873		
180	1109	C	33	X	1	96.0	96.0	305.46	1842.657	1859.578	1841.457
180	1109	C	33	X	2	93.0	93.0	306.93	1816.673	1822.780	1831.502
180	1109	C	33	X	3	25.5	25.5	307.76	1853.222	1852.476	1834.118
180	1109	C	33	X	4	58.0	58.0	309.58	1810.525	1829.757	1794.103
180	1109	C	33	X	5	118.0	118.0	311.68	1808.946	1824.525	1810.479
180	1109	C	33	X	6	56.0	56.0	312.56	2137.299	1778.004	1780.554
180	1109	C	33	X	7	27.5	27.5	313.78	1806.348	1828.013	1820.164
180	1109	C	34	X	1	105.5	105.5	315.26	1830.290	1856.915	
180	1109	C	34	X	2	70.0	70.0	316.40	1774.104	1784.804	1778.854
180	1109	C	34	X	3	38.5	38.5	317.59	1793.549	1808.750	
180	1109	C	34	X	4	48.0	48.0	319.18	1799.126	1826.269	1809.614
180	1109	C	34	X	5	84.0	84.0	321.04	1814.941	1833.539	1802.674
180	1109	C	34	X	6	12.0	12.0	321.82	1815.920	1842.337	1811.344
180	1109	C	34	X	7	15.4	15.4	323.35	1783.262		
180	1109	C	35	X	1	114.7	114.7	325.05	1661.563		
180	1109	C	35	X	2	106.8	106.8	326.47	1723.191		
180	1109	C	35	X	3	110.4	110.4	328.00	1708.058		
180	1109	C	35	X	4	115.7	115.7	329.56	1789.065		
180	1109	C	35	X	5	98.1	98.1	330.88	1706.686		
180	1109	C	35	X	6	89.3	89.3	332.29	1687.609		
180	1109	C	35	X	7	17.9	17.9	333.08	1703.816		

Table T16 (continued).

Leg	Site	Hole	Core	Type	Section	Top (cm)	Bottom (cm)	Depth (mbsf)	x-velocity ($m \cdot s^{-1}$)	y-velocity ($m \cdot s^{-1}$)	z-velocity ($m \cdot s^{-1}$)
180	1109	C	36	X	1	67.8	67.8	334.18	1660.272		
180	1109	C	36	X	2	75.0	75.0	335.75	1828.442		1770.264
180	1109	C	36	X	3	89.4	89.4	337.39	1651.512		
180	1109	C	36	X	4	25.4	25.4	338.25	1713.923		
180	1109	C	37	X	1	22.5	22.5	343.33	1786.150		
180	1109	C	37	X	1	97.0	97.0	344.07	1798.380		
180	1109	C	38	X	1	48.3	48.3	347.08	1735.760		
180	1109	C	38	X	2	61.7	61.7	348.72	1656.849		
180	1109	C	38	X	3	59.1	59.1	350.19	1634.700		
180	1109	C	38	X	4	55.3	55.3	351.65	1628.075		
180	1109	C	38	X	5	100.2	100.2	353.60	1631.286		
180	1109	C	38	X	6	79.6	79.6	354.90	1759.637		
180	1109	C	38	X	7	16.5	16.5	355.77	1692.089		
180	1109	C	39	X	1	50.0	50.0	353.10	1763.083	1770.605	1741.256
180	1109	C	39	X	2	23.0	23.0	354.33	1819.410	1813.073	1784.804
180	1109	C	39	X	3	47.0	47.0	356.07	1797.908	1819.990	1789.053
180	1109	C	39	X	4	48.0	48.0	357.58	1741.124	1756.644	1744.108
180	1109	C	39	X	5	110.0	110.0	359.70	1856.963	1848.416	1813.556
180	1109	C	39	X	6	41.0	41.0	360.51	1766.438	1776.504	1752.465
180	1109	C	39	X	7	35.0	35.0	361.95	1790.405	1806.103	1782.403
180	1109	C	40	X	1	35.0	35.0	362.55	1787.788	1812.104	1774.824
180	1109	C	40	X	2	30.0	30.0	364.00	1812.233	1739.055	1780.554
180	1109	C	40	X	3	106.0	106.0	366.26	1795.534	1806.103	1763.020
180	1109	C	40	X	4	131.0	131.0	368.01	1800.094	1798.402	1794.960
180	1109	C	40	X	5	117.5	117.5	369.38	1781.724	1789.053	1769.762
180	1109	C	41	X	1	29.0	29.0	371.79	1774.672	1818.260	1788.102
180	1109	C	41	X	2	7.5	7.5	373.08	1795.989	1788.203	1772.291
180	1109	C	41	X	3	10.0	10.0	374.60	1818.019	1830.630	1790.753
180	1109	C	41	X	4	42.5	42.5	376.13	1784.541	1790.943	1769.762
180	1109	D	1	R	1	72.0	72.0	353.52	1846.399	1853.774	1814.550
180	1109	D	1	R	2	73.0	73.0	355.03	1812.271	1831.229	1803.502
180	1109	D	1	R	3	114.0	114.0	356.94	1778.877	1793.303	1768.606
180	1109	D	1	R	4	86.0	86.0	358.16	1794.295	1807.818	1792.453
180	1109	D	2	R	1	53.0	53.0	359.63	1840.779	1828.313	1820.544
180	1109	D	2	R	2	94.0	94.0	361.35	1758.014	1746.416	1747.662
180	1109	D	2	R	3	65.0	65.0	362.46	1790.931	1792.421	1771.255
180	1109	D	2	R	4	82.0	82.0	363.65	1801.153	1809.245	1808.511
180	1109	D	2	R	5	73.0	73.0	364.61	1787.680	1810.806	1796.862
180	1109	D	2	R	6	55.0	55.0	365.47	1785.583	1809.409	1783.885
180	1109	D	2	R	7	30.0	30.0	366.28	1818.572	1822.430	1805.579
180	1109	D	2	R	8	36.0	36.0	367.80	1824.715	1802.505	1801.817
180	1109	D	3	R	1	111.0	111.0	369.81	1801.979	1812.961	1820.676
180	1109	D	3	R	2	78.0	78.0	370.98	1772.577	1782.403	1784.804
180	1109	D	3	R	3	14.5	14.5	371.84	1765.219	1788.203	1786.655
180	1109	D	3	R	4	56.0	56.0	373.35	1774.861	1784.804	1796.674
180	1109	D	3	R	5	85.0	85.0	374.99	1762.816	1764.706	1782.403
180	1109	D	3	R	6	84.0	84.0	376.20	2100.977	1781.404	1782.254
180	1109	D	3	R	7	41.0	41.0	377.16	1773.567	1789.186	1779.131
180	1109	D	4	R	1	60.5	60.5	378.91	1858.386	1863.774	1848.762
180	1109	D	4	R	2	60.5	60.5	380.01	1785.982	1800.618	1795.311
180	1109	D	4	R	3	58.0	58.0	381.18	1813.676	1804.053	1852.998
180	1109	D	4	R	4	71.0	71.0	382.37	1781.575	1788.334	1765.496
180	1109	D	4	R	5	78.0	78.0	383.55	1819.944	1823.703	1826.004
180	1109	D	4	R	6	52.0	52.0	384.54	1839.600	1846.736	1828.611
180	1109	D	4	R	7	43.0	43.0	385.96	1818.465	1830.925	1808.547
180	1109	D	5	R	1	43.0	43.0	388.03	3731.163	3912.643	3629.642
180	1109	D	6	R	1	87.0	87.0	398.07	1804.643	1817.554	1784.868
180	1109	D	6	R	2	16.5	16.5	398.79	1799.108	1794.128	1766.980
180	1109	D	6	R	3	36.0	36.0	400.42	1817.244	1809.041	1777.068
180	1109	D	6	R	4	65.0	65.0	401.78	1789.636	1790.931	1784.686
180	1109	D	6	R	5	43.0	43.0	402.48	1823.549	1826.722	1800.447
180	1109	D	6	R	6	67.0	67.0	403.51	1801.177	1785.714	1781.192
180	1109	D	7	R	1	72.0	72.0	407.52	1815.803	1810.597	1778.098
180	1109	D	7	R	2	40.0	40.0	408.70	1755.288	1799.589	1806.269
180	1109	D	7	R	3	85.0	85.0	410.39	1819.529	1817.868	1769.114
180	1109	D	7	R	4	88.0	88.0	411.72	1823.229	1899.064	1815.215
180	1109	D	7	R	5	25.0	25.0	412.45	1819.614	1836.148	1821.481
180	1109	D	8	R	1	23.0	23.0	416.73	1825.152	1819.834	1797.196
180	1109	D	8	R	2	6.0	6.0	418.00	1800.799	1841.945	1794.502

Table T16 (continued).

Leg	Site	Hole	Core	Type	Section	Top (cm)	Bottom (cm)	Depth (mbsf)	x-velocity ($m \cdot s^{-1}$)	y-velocity ($m \cdot s^{-1}$)	z-velocity ($m \cdot s^{-1}$)
180	1109	D	8	R	3	81.0	81.0	419.73	1813.605	1803.868	1800.698
180	1109	D	8	R	4	84.0	84.0	421.27	1889.712	1861.020	1815.182
180	1109	D	8	R	5	20.0	20.0	421.82	1843.067	1810.434	
180	1109	D	8	R	6	61.0	61.0	423.74	1868.548	1859.252	1832.552
180	1109	D	8	R	7	80.0	80.0	424.68	1842.898	1897.731	1894.800
180	1109	D	9	R	1	136.0	136.0	427.46	1809.840	1820.854	1800.753
180	1109	D	9	R	2	22.0	22.0	427.82	1880.691	1844.077	
180	1109	D	9	R	3	98.0	98.0	430.03	1828.582	1864.557	1806.243
180	1109	D	9	R	4	130.0	130.0	431.46	1813.100	1831.010	1800.273
180	1109	D	9	R	5	113.0	113.0	432.65	1861.107	1888.143	1806.243
180	1109	D	9	R	6	146.0	146.0	434.43	1815.697	1851.302	1802.336
180	1109	D	10	R	1	41.5	41.5	436.12	1795.800	1807.686	1788.102
180	1109	D	10	R	2	85.0	85.0	437.89	1818.110	1819.596	1817.711
180	1109	D	10	R	3	126.0	126.0	439.71	1823.853	1822.835	1792.453
180	1109	D	10	R	4	39.0	39.0	440.13	1832.149	1831.795	1812.317
180	1109	D	10	R	5	112.0	112.0	442.26	1828.045	1829.776	1791.462
180	1109	D	10	R	6	89.0	89.0	443.29	1846.130	1852.635	1825.362
180	1109	D	10	R	7	79.0	79.0	444.15	1826.644	1825.740	1815.122
180	1109	D	11	R	1	48.0	48.0	445.78	1822.705	1829.757	1847.759
180	1109	D	11	R	2	80.0	80.0	447.48	1841.779	1855.279	1807.818
180	1109	D	11	R	3	59.0	59.0	448.64	1833.801	1834.118	1814.898
180	1109	D	11	R	4	60.0	60.0	449.97	1821.728	1831.219	1806.766
180	1109	D	11	R	5	65.0	65.0	451.39	1838.955	1845.790	1806.766
180	1109	D	11	R	6	73.0	73.0	452.93	1801.465	1812.317	1779.032
180	1109	D	12	R	1	53.0	53.0	455.43	1844.500	1839.351	1844.584
180	1109	D	12	R	2	102.0	102.0	457.27	1839.454	1845.331	1792.660
180	1109	D	12	R	3	58.0	58.0	458.33	1837.978	1843.712	1793.653
180	1109	D	12	R	4	72.0	72.0	459.58	1852.320	1832.669	1791.957
180	1109	D	12	R	5	31.0	31.0	460.47	1820.604	1828.932	1790.969
180	1109	D	12	R	6	91.5	91.5	462.22	1855.139	1855.417	1806.960
180	1109	D	12	R	7	10.0	10.0	462.40	1844.200	1841.095	1810.829
180	1109	D	13	R	1	76.0	76.0	465.26	1832.497	1848.416	1808.474
180	1109	D	13	R	2	79.0	79.0	466.68	1819.192	1824.874	1791.957
180	1109	D	13	R	3	14.0	14.0	467.29	1835.898	1846.466	1837.913
180	1109	D	13	R	4	58.0	58.0	468.62	1840.864	1855.279	1835.863
180	1109	D	13	R	5	64.0	64.0	469.84	1915.326	1918.509	1900.054
180	1109	D	13	R	6	93.0	93.0	471.57	1847.366	1862.814	1803.349
180	1109	D	13	R	7	21.0	21.0	472.18	1883.567	1898.439	1827.473
180	1109	D	13	R	8	41.5	41.5	473.29	1835.800	1836.433	1839.615
180	1109	D	14	R	1	71.0	71.0	474.81	1847.295	1875.111	1853.153
180	1109	D	14	R	2	22.0	22.0	475.64	1884.764	1882.656	1824.616
180	1109	D	14	R	3	14.0	14.0	476.90	1826.938	1831.219	1795.505
180	1109	D	14	R	4	15.0	15.0	478.11	1847.425	1858.423	1816.618
180	1109	D	14	R	5	9.0	9.0	479.51	1899.092	1866.266	1830.349
180	1109	D	14	R	6	75.0	75.0	481.67	1887.451	1889.862	1859.686
180	1109	D	14	R	7	49.0	49.0	482.91	1848.543		1821.779
180	1109	D	15	R	1	105.0	105.0	484.75	1822.860	1836.735	1805.911
180	1109	D	15	R	2	21.0	21.0	485.37	1848.538	2255.459	1860.465
180	1109	D	15	R	3	70.0	70.0	486.74	1981.132	1874.221	1885.878
180	1109	D	15	R	4	27.0	27.0	487.59	1843.237	1847.005	1806.296
180	1109	D	15	R	5	28.0	28.0	489.10	1858.291	1884.981	1851.396
180	1109	D	15	R	6	51.0	51.0	490.83	1895.751	1888.570	1827.742
180	1109	D	15	R	7	43.0	43.0	491.61	1899.410	1904.030	1857.544
180	1109	D	16	R	1	47.0	47.0	493.77	1875.437	1892.671	1860.074
180	1109	D	16	R	2	21.0	21.0	495.01	1851.216	1865.738	1868.384
180	1109	D	16	R	3	127.0	127.0	497.07	1850.821	1861.721	1823.601
180	1109	D	16	R	4	90.0	90.0	498.16	1872.610	1896.552	1916.455
180	1109	D	16	R	5	109.0	109.0	499.62	1877.729	1871.686	1875.221
180	1109	D	16	R	6	143.0	143.0	501.26	1853.151	1868.103	1847.067
180	1109	D	16	R	7	23.0	23.0	501.55	1871.278	1888.274	1860.935
180	1109	D	17	R	1	24.0	24.0	503.24	1875.382	1875.333	1843.439
180	1109	D	17	R	2	52.0	52.0	504.60	1868.308	1870.114	1842.840
180	1109	D	17	R	3	75.0	75.0	505.96	1888.610	1892.062	1844.779
180	1109	D	17	R	4	17.0	17.0	506.83	1905.324	1908.383	1844.643
180	1109	D	17	R	5	61.0	61.0	508.74	1888.269	1893.953	1845.790
180	1109	D	17	R	6	123.0	123.0	510.60	1893.756	1898.974	1827.173
180	1109	D	17	R	7	59.0	59.0	511.46	1873.197	1865.619	1828.339
180	1109	D	18	R	1	27.0	27.0	512.87	1851.752	1803.684	1801.126
180	1109	D	18	R	2	14.0	14.0	514.24	1870.178	1876.880	1838.452

Table T16 (continued).

Leg	Site	Hole	Core	Type	Section	Top (cm)	Bottom (cm)	Depth (mbsf)	x-velocity ($m \cdot s^{-1}$)	y-velocity ($m \cdot s^{-1}$)	z-velocity ($m \cdot s^{-1}$)
180	1109	D	18	R	3	13.5	13.5	515.55	1853.156	1871.231	1833.391
180	1109	D	18	R	4	61.0	61.0	517.13	1908.582	1937.408	1878.998
180	1109	D	18	R	5	50.0	50.0	518.32	1909.751	1919.247	1856.293
180	1109	D	18	R	6	27.0	27.0	519.18	1873.454	1902.115	1833.679
180	1109	D	18	R	7	7.0	7.0	520.48	1908.018	1937.408	1899.155
180	1109	D	18	R	8	3.0	3.0	521.94	1836.335	1856.792	1819.748
180	1109	D	19	R	1	21.0	21.0	522.51	1910.797	1920.296	1889.364
180	1109	D	19	R	2	20.0	20.0	524.00	1936.027	1949.293	1917.734
180	1109	D	19	R	3	89.0	89.0	525.88	1901.063	1927.678	1885.035
180	1109	D	19	R	4	11.0	11.0	526.47	1889.170	1945.308	1894.493
180	1109	D	19	R	5	70.0	70.0	528.49	1917.213	1928.591	1873.013
180	1109	D	20	R	1	129.0	129.0	533.29	1962.388	1941.149	1913.988
180	1109	D	20	R	2	58.0	58.0	534.02	1927.379	1926.664	1869.573
180	1109	D	20	R	3	29.0	29.0	535.07	1921.543	1956.240	1899.155
180	1109	D	20	R	4	37.0	37.0	535.90	1882.006	1898.974	1848.283
180	1109	D	20	R	5	40.0	40.0	537.40	1884.190	1888.968	1847.067
180	1109	D	20	R	6	59.0	59.0	538.67	2012.405	2012.230	1938.382
180	1109	D	21	R	1	101.5	101.5	542.62	1968.471	1958.055	1926.530
180	1109	D	21	R	2	81.5	81.5	543.93	1955.279	1968.025	1904.848
180	1109	D	21	R	3	102.0	102.0	545.66	1970.809	1968.931	1903.302
180	1109	D	21	R	4	67.5	67.5	546.74	1986.937	1995.074	1941.622
180	1109	D	21	R	5	66.0	66.0	548.06	1981.662	1969.811	1910.641
180	1109	D	21	R	6	38.5	38.5	548.69	1973.729	1950.723	1899.512
180	1109	D	21	R	7	18.0	18.0	549.18	1958.109	1950.677	1899.512
180	1109	D	21	R	8	6.0	6.0	550.36	1942.652	1936.256	1890.068
180	1109	D	22	R	1	103.5	103.5	552.24	1972.018	1956.158	1925.885
180	1109	D	22	R	2	93.0	93.0	553.47	2026.609	1996.983	1950.950
180	1109	D	22	R	3	60.0	60.0	554.34	2017.144	1992.224	1976.374
180	1109	D	22	R	4	77.0	77.0	555.42	2074.958	2055.556	2062.684
180	1109	D	23	R	1	76.0	76.0	561.56	1996.922	2000.000	2006.318
180	1109	D	23	R	2	32.5	32.5	562.63	2012.293	2002.665	1995.530
180	1109	D	24	R	1	23.5	23.5	565.84	1992.811	1994.121	1968.989
180	1109	D	24	R	2	90.0	90.0	567.94	1859.484	1884.150	1868.311
180	1109	D	24	R	3	72.0	72.0	569.24	1870.489	1869.109	1870.160
180	1109	D	24	R	4	104.5	104.5	571.00	1941.293	1942.225	1892.212
180	1109	D	25	R	1	48.5	48.5	570.89	2058.319	2073.506	2050.238
180	1109	D	25	R	2	121.0	121.0	573.05	2124.941	2053.128	2057.991
180	1109	D	25	R	3	84.0	84.0	573.97	2124.226	2096.614	2087.999
180	1109	D	25	R	4	79.5	79.5	575.43	2063.704	2042.077	2021.827
180	1109	D	25	R	5	64.0	64.0	576.77	2131.257	2111.144	2107.570
180	1109	D	25	R	6	9.0	9.0	577.56	2094.315	2090.423	2086.466
180	1109	D	26	R	1	121.5	121.5	581.22	2078.960	2092.629	2087.008
180	1109	D	26	R	2	61.5	61.5	582.08	2143.668	2151.354	2173.373
180	1109	D	26	R	3	61.5	61.5	583.29	2127.843	2154.775	2198.136
180	1109	D	26	R	4	32.5	32.5	584.26	2104.512	2131.496	2129.470
180	1109	D	26	R	5	42.0	42.0	585.46		2050.655	2082.589
180	1109	D	26	R	6	56.0	56.0	586.95	2148.784	2151.354	2129.854
180	1109	D	26	R	7	36.5	36.5	587.80	2092.957	2083.292	2119.259
180	1109	D	27	R	1	58.0	58.0	590.18	3051.165	3075.240	2717.896
180	1109	D	27	R	2	84.0	84.0	591.54	3101.473	2588.062	2368.657
180	1109	D	27	R	3	45.0	45.0	592.45	2359.900	2434.552	2409.998
180	1109	D	27	R	4	55.0	55.0	593.64	3728.781	4006.785	3597.571
180	1109	D	28	R	1	52.0	52.0	599.72	2221.755	2205.412	2217.596
180	1109	D	29	R	1	91.5	91.5	609.82	2139.212	2117.971	2115.541
180	1109	D	29	R	2	52.0	52.0	610.45	2928.514	3038.412	2521.969
180	1109	D	29	R	3	36.5	36.5	611.33	2204.605	2294.956	2298.246
180	1109	D	30	R	1	38.0	38.0	618.88	2803.384	3005.969	2707.267
180	1109	D	31	R	1	78.0	78.0	628.98	2099.248	2125.864	2128.158
180	1109	D	31	R	2	72.0	72.0	630.32	2087.890	2101.246	2082.176
180	1109	D	32	R	1	80.0	80.0	638.70	2552.060	2597.099	2515.410
180	1109	D	32	R	2	64.0	64.0	639.95	2901.189	2887.439	2946.590
180	1109	D	33	R	1	10.1	10.1	647.60	2634.930		
180	1109	D	34	R	1	69.0	69.0	657.79	2548.021	2543.269	2478.001
180	1109	D	34	R	2	49.0	49.0	658.97	2472.112	2422.503	2348.097
180	1109	D	34	R	3	25.0	25.0	660.06	2752.413		2828.404
180	1109	D	34	R	4	14.0	14.0	661.28	2635.831	2571.289	2464.311
180	1109	D	34	R	5	41.0	41.0	662.79	2559.508	2448.412	2520.296
180	1109	D	34	R	6	24.5	24.5	663.42	3184.147	3294.888	2911.619
180	1109	D	35	R	1	7.0	7.0	666.77	2518.299	2583.374	2472.992

Table T16 (continued).

Leg	Site	Hole	Core	Type	Section	Top (cm)	Bottom (cm)	Depth (mbsf)	x-velocity ($m \cdot s^{-1}$)	y-velocity ($m \cdot s^{-1}$)	z-velocity ($m \cdot s^{-1}$)
180	1109	D	35	R	2	33.0	33.0	668.15	2776.877	2593.948	2448.133
180	1109	D	35	R	3	81.0	81.0	669.92	3459.788	3717.157	3120.189
180	1109	D	35	R	4	75.0	75.0	670.85	2252.442	2254.168	2356.603
180	1109	D	35	R	5	82.0	82.0	672.42	2059.196	2072.667	1966.092
180	1109	D	35	R	6	47.0	47.0	673.32	2105.936	2111.399	1986.749
180	1109	D	35	R	7	89.8	89.8	674.71	2124.993		
180	1109	D	35	R	8	56.0	56.0	675.42	2182.192	2167.559	2075.324
180	1109	D	36	R	1	25.0	25.0	676.65	2018.756	2018.900	1981.948
180	1109	D	36	R	2	19.5	19.5	678.10	2032.917	2031.551	1962.625
180	1109	D	36	R	3	45.0	45.0	679.85	2015.511	2001.699	1948.704
180	1109	D	36	R	4	64.0	64.0	681.54	1989.317	1912.558	2043.094
180	1109	D	36	R	5	108.0	108.0	683.48	2065.626	2124.850	1947.407
180	1109	D	36	R	6	46.0	46.0	684.36	2070.375	2074.052	1996.051
180	1109	D	37	R	1	16.5	16.5	686.17	1984.305	1982.083	1840.437
180	1109	D	37	R	2	123.5	123.5	688.72	1877.546	1876.517	1818.696
180	1109	D	37	R	3	2.0	2.0	688.98	1857.697	1876.988	1779.994
180	1109	D	37	R	4	96.0	96.0	691.42	2000.702	1986.599	2020.096
180	1109	D	37	R	5	36.5	36.5	692.10	1973.640	1970.993	1958.287
180	1109	D	38	R	1	33.0	33.0	695.93	1869.316	1881.030	1809.491
180	1109	D	38	R	2	109.0	109.0	698.07	1869.869	1805.413	1892.255
180	1109	D	38	R	3	109.0	109.0	699.39	1894.037	1901.219	1872.552
180	1109	D	38	R	4	134.0	134.0	701.10	1973.957	1964.616	1902.311
180	1109	D	38	R	5	62.0	62.0	701.88	1954.362	1958.907	1886.877
180	1109	D	39	R	1	123.0	123.0	706.53	1946.696	1949.935	1906.403
180	1109	D	39	R	2	33.0	33.0	706.94	1928.071	1936.432	1849.375
180	1109	D	39	R	3	33.0	33.0	708.37	2003.882	1997.926	
180	1109	D	40	R	1	76.7	76.7	715.77	1938.574		
180	1109	D	40	R	2	19.5	19.5	716.46	2083.096	2091.134	2042.709
180	1109	D	40	R	3	60.0	60.0	717.25	2060.785	2051.382	2031.611
180	1109	D	40	R	4	57.3	57.3	718.72	1876.868		
180	1109	D	41	R	1	101.0	101.0	725.71	2045.654	2033.604	1971.091
180	1109	D	41	R	2	74.0	74.0	726.94	2015.966	2009.319	1975.528
180	1109	D	41	R	3	43.0	43.0	727.71	2112.837	2121.578	2077.743
180	1109	D	41	R	3	81.0	81.0	728.09	6033.732	6098.398	6003.937
180	1109	D	42	R	1	25.0	25.0	734.55	2003.709	2009.279	1982.445
180	1109	D	42	R	2	66.0	66.0	736.46	2217.177	2197.585	2176.640
180	1109	D	43	R	1	96.0	96.0	744.86	2026.641	2049.354	2007.178
180	1109	D	43	R	2	67.5	67.5	745.60	2082.587	2099.105	2041.289
180	1109	D	43	R	3	72.0	72.0	746.53	2090.023	2100.732	2063.244
180	1109	D	46	R	1	19.0	19.0	773.09	5964.567	6003.948	5945.343
180	1109	D	46	R	2	37.0	37.0	774.60	5885.444	5953.709	5956.498
180	1109	D	46	R	3	18.0	18.0	775.91	6046.951	6020.869	6038.003
180	1109	D	47	R	1	85.0	85.0	778.45	5942.747		5730.742
180	1109	D	47	R	2	108.0	108.0	779.80	5685.055		5109.101
180	1109	D	47	R	3	35.0	35.0	780.48	5897.220		5283.434
180	1109	D	47	R	4	76.0	76.0	782.03			5283.434
180	1109	D	47	R	4	110.0	110.0	782.37	5733.728		
180	1109	D	47	R	5	12.0	12.0	782.83			5351.499
180	1109	D	47	R	5	12.0	12.0	782.83			5436.152

Notes: This table is also available in ASCII format in the **TABLES** directory. Blanks indicate not measured.

Table T17. Thermal conductivity values in cores, Site 1109. (Continued on next eleven pages. See table note.)

Leg	Site	Hole	Core	Type	Section	Top interval (cm)	Bottom interval (cm)	Top depth (mbsf)	Bottom depth (mbsf)	Middle depth (mbsf)	Thermal conductivity ($W \cdot m^{-1} \cdot °C^{-1}$)	Thermal conductivity average ($W \cdot m^{-1} \cdot °C^{-1}$)
180	1109	A	1	H	1	75.0	75.0	0.75	0.75	0.75	0.58	
180	1109	A	1	H	1	75.0	75.0	0.75	0.75	0.75	0.84	
180	1109	A	1	H	1	75.0	75.0	0.75	0.75	0.75	0.85	0.76
180	1109	A	1	H	3	75.0	75.0	3.75	3.75	3.75	0.79	
180	1109	A	1	H	3	75.0	75.0	3.75	3.75	3.75	0.77	0.78
180	1109	A	1	H	5	75.0	75.0	6.75	6.75	6.75	0.92	
180	1109	A	1	H	5	75.0	75.0	6.75	6.75	6.75	0.91	0.92
180	1109	A	1	H	7	15.0	15.0	9.15	9.15	9.15	0.86	
180	1109	A	1	H	7	15.0	15.0	9.15	9.15	9.15	0.86	0.86
180	1109	A	1	H	1	37.5	37.5	0.38	0.38	0.38	0.92	
180	1109	A	1	H	1	37.5	37.5	0.38	0.38	0.38	0.91	0.92
180	1109	A	1	H	3	57.0	57.0	3.57	3.57	3.57	0.89	0.89
180	1109	B	2	H	2	75.0	75.0	7.55	7.55	7.55	0.80	
180	1109	B	2	H	2	75.0	75.0	7.55	7.55	7.55	0.80	0.80
180	1109	B	2	H	4	75.0	75.0	10.55	10.55	10.55	0.76	
180	1109	B	2	H	4	75.0	75.0	10.55	10.55	10.55	0.76	0.76
180	1109	B	2	H	6	75.0	75.0	12.85	12.85	12.85	0.90	
180	1109	B	2	H	6	75.0	75.0	12.85	12.85	12.85	0.89	
180	1109	B	2	H	6	75.0	75.0	12.85	12.85	12.85	0.89	0.89
180	1109	C	1	H	2	75.0	75.0	2.25	2.25	2.25	0.84	
180	1109	C	1	H	2	75.0	75.0	2.25	2.25	2.25	0.88	0.86
180	1109	C	1	H	4	75.0	75.0	5.25	5.25	5.25	0.78	
180	1109	C	1	H	4	75.0	75.0	5.25	5.25	5.25	0.87	0.83
180	1109	C	2	H	2	75.0	75.0	9.65	9.65	9.65	0.92	
180	1109	C	2	H	2	75.0	75.0	9.65	9.65	9.65	0.89	0.91
180	1109	C	2	H	4	75.0	75.0	12.65	12.65	12.65	0.91	
180	1109	C	2	H	4	75.0	75.0	12.65	12.65	12.65	0.89	0.90
180	1109	C	2	H	6	75.0	75.0	15.65	15.65	15.65	0.93	
180	1109	C	2	H	6	75.0	75.0	15.65	15.65	15.65	0.96	0.94
180	1109	C	3	H	2	77.0	77.0	19.17	19.17	19.17	0.86	
180	1109	C	3	H	2	77.0	77.0	19.17	19.17	19.17	0.84	0.85
180	1109	C	3	H	6	75.0	75.0	25.15	25.15	25.15	0.96	
180	1109	C	3	H	6	75.0	75.0	25.15	25.15	25.15	0.96	0.96
180	1109	C	3	H	4	75.0	75.0	22.15	22.15	22.15	0.94	
180	1109	C	3	H	4	75.0	75.0	22.15	22.15	22.15	0.90	0.92
180	1109	C	4	H	2	75.0	75.0	28.65	28.65	28.65	0.85	
180	1109	C	4	H	2	75.0	75.0	28.65	28.65	28.65	0.85	0.85
180	1109	C	4	H	4	75.0	75.0	31.65	31.65	31.65	0.99	
180	1109	C	4	H	4	75.0	75.0	31.65	31.65	31.65	0.96	0.98
180	1109	C	4	H	6	75.0	75.0	34.65	34.65	34.65	1.01	
180	1109	C	4	H	6	75.0	75.0	34.65	34.65	34.65	1.01	1.01
180	1109	C	5	H	2	75.0	75.0	38.15	38.15	38.15	0.98	
180	1109	C	5	H	2	75.0	75.0	38.15	38.15	38.15	0.95	0.96
180	1109	C	5	H	4	75.0	75.0	41.15	41.15	41.15	0.96	
180	1109	C	5	H	4	75.0	75.0	41.15	41.15	41.15	0.92	0.94
180	1109	C	5	H	6	75.0	75.0	44.15	44.15	44.15	1.00	
180	1109	C	5	H	6	75.0	75.0	44.15	44.15	44.15	1.01	1.00
180	1109	C	6	H	1	75.0	75.0	46.15	46.15	46.15	1.00	
180	1109	C	6	H	1	75.0	75.0	46.15	46.15	46.15	1.02	1.01
180	1109	C	6	H	3	75.0	75.0	49.15	49.15	49.15	0.92	
180	1109	C	6	H	3	75.0	75.0	49.15	49.15	49.15	0.95	0.94
180	1109	C	6	H	5	75.0	75.0	52.15	52.15	52.15	1.01	
180	1109	C	6	H	5	75.0	75.0	52.15	52.15	52.15	1.02	1.01
180	1109	C	6	H	7	41.0	41.0	54.81	54.81	54.81	1.03	
180	1109	C	6	H	7	41.0	41.0	54.81	54.81	54.81	1.04	1.03
180	1109	C	7	H	1	75.0	75.0	55.65	55.65	55.65	1.01	
180	1109	C	7	H	1	75.0	75.0	55.65	55.65	55.65	1.01	1.01
180	1109	C	7	H	3	72.0	72.0	58.62	58.62	58.62	1.00	
180	1109	C	7	H	3	72.0	72.0	58.62	58.62	58.62	0.98	0.99
180	1109	C	7	H	5	75.0	75.0	61.65	61.65	61.65	0.94	
180	1109	C	7	H	5	75.0	75.0	61.65	61.65	61.65	0.94	0.94
180	1109	C	7	H	7	34.0	34.0	64.24	64.24	64.24	1.01	
180	1109	C	7	H	7	34.0	34.0	64.24	64.24	64.24	1.03	1.02
180	1109	C	8	H	1	75.0	75.0	65.15	65.15	65.15	1.03	
180	1109	C	8	H	1	75.0	75.0	65.15	65.15	65.15	1.04	1.04
180	1109	C	8	H	3	72.0	72.0	68.12	68.12	68.12	0.98	

Table T17 (continued).

Leg	Site	Hole	Core	Type	Section	Top interval (cm)	Bottom interval (cm)	Top depth (mbsf)	Bottom depth (mbsf)	Middle depth (mbsf)	Thermal conductivity ($W \cdot m^{-1} \cdot °C^{-1}$)	Thermal conductivity average ($W \cdot m^{-1} \cdot °C^{-1}$)
180	1109	C	8	H	3	72.0	72.0	68.12	68.12	68.12	1.01	1.00
180	1109	C	8	H	5	75.0	75.0	71.15	71.15	71.15	1.00	
180	1109	C	8	H	5	75.0	75.0	71.15	71.15	71.15	0.99	1.00
180	1109	C	8	H	7	39.5	39.5	73.80	73.80	73.80	1.05	
180	1109	C	8	H	7	39.5	39.5	73.80	73.80	73.80	1.07	1.06
180	1109	C	9	H	1	75.0	75.0	74.65	74.65	74.65	1.06	
180	1109	C	9	H	1	75.0	75.0	74.65	74.65	74.65	1.04	1.05
180	1109	C	9	H	3	72.0	72.0	77.62	77.62	77.62	1.05	
180	1109	C	9	H	3	72.0	72.0	77.62	77.62	77.62	1.07	1.06
180	1109	C	9	H	5	75.0	75.0	80.65	80.65	80.65	1.09	
180	1109	C	9	H	5	75.0	75.0	80.65	80.65	80.65	1.06	1.08
180	1109	C	9	H	7	40.0	40.0	83.30	83.30	83.30	1.03	
180	1109	C	9	H	7	40.0	40.0	83.30	83.30	83.30	1.06	1.04
180	1109	C	11	H	1	75.0	75.0	93.65	93.65	93.65	1.09	
180	1109	C	11	H	1	75.0	75.0	93.65	93.65	93.65	1.11	
180	1109	C	10	H	1	75.0	75.0	84.15	84.15	84.15	1.13	
180	1109	C	10	H	1	75.0	75.0	84.15	84.15	84.15	1.14	1.12
180	1109	C	10	H	3	75.0	75.0	87.15	87.15	87.15	1.14	
180	1109	C	10	H	3	75.0	75.0	87.15	87.15	87.15	1.12	1.13
180	1109	C	10	H	5	75.0	75.0	90.15	90.15	90.15	1.03	
180	1109	C	10	H	5	75.0	75.0	90.15	90.15	90.15	1.01	1.02
180	1109	C	11	H	3	75.0	75.0	96.65	96.65	96.65	0.82	
180	1109	C	11	H	3	75.0	75.0	96.65	96.65	96.65	0.79	0.80
180	1109	C	11	H	5	75.0	75.0	99.65	99.65	99.65	0.61	
180	1109	C	11	H	5	75.0	75.0	99.65	99.65	99.65	0.49	0.55
180	1109	C	12	X	2	75.0	75.0	104.65	104.65	104.65	0.68	
180	1109	C	12	X	2	75.0	75.0	104.65	104.65	104.65	0.70	0.69
180	1109	C	12	X	5	75.0	75.0	109.15	109.15	109.15	1.18	
180	1109	C	12	X	5	75.0	75.0	109.15	109.15	109.15	1.16	1.17
180	1109	C	13	X	2	75.0	75.0	114.25	114.25	114.25	0.63	
180	1109	C	13	X	2	75.0	75.0	114.25	114.25	114.25	0.67	0.65
180	1109	C	13	X	5	75.0	75.0	118.75	118.75	118.75	1.15	
180	1109	C	13	X	5	75.0	75.0	118.75	118.75	118.75	1.10	1.12
180	1109	C	13	X	7	20.0	20.0	121.20	121.20	121.20	0.90	
180	1109	C	13	X	7	20.0	20.0	121.20	121.20	121.20	0.92	0.91
180	1109	C	14	X	2	75.0	75.0	123.85	123.85	123.85	1.20	
180	1109	C	14	X	2	75.0	75.0	123.85	123.85	123.85	1.06	1.13
180	1109	C	14	X	5	75.0	75.0	128.35	128.35	128.35	1.10	
180	1109	C	14	X	5	75.0	75.0	128.35	128.35	128.35	1.12	1.11
180	1109	C	15	X	2	75.0	75.0	133.42	133.42	133.42	0.98	
180	1109	C	15	X	2	75.0	75.0	133.42	133.42	133.42	0.97	0.98
180	1109	C	15	X	5	75.0	75.0	137.92	137.92	137.92	1.07	
180	1109	C	15	X	5	75.0	75.0	137.92	137.92	137.92	1.07	1.07
180	1109	C	16	X	2	75.0	75.0	143.05	143.05	143.05	0.88	
180	1109	C	16	X	2	75.0	75.0	143.05	143.05	143.05	0.86	0.87
180	1109	C	16	X	4	75.0	75.0	146.05	146.05	146.05	0.94	
180	1109	C	16	X	4	75.0	75.0	146.05	146.05	146.05	0.94	0.94
180	1109	C	17	X	1	35.0	35.0	150.85	150.85	150.85	0.85	
180	1109	C	17	X	1	35.0	35.0	150.85	150.85	150.85	0.84	0.84
180	1109	C	18	X	2	75.0	75.0	162.35	162.35	162.35	0.87	
180	1109	C	18	X	2	75.0	75.0	162.35	162.35	162.35	0.86	0.87
180	1109	C	18	X	5	75.0	75.0	166.55	166.55	166.55	0.89	
180	1109	C	18	X	5	75.0	75.0	166.55	166.55	166.55	0.88	0.89
180	1109	C	18	X	7	33.5	33.5	169.14	169.14	169.14	0.66	
180	1109	C	18	X	7	33.5	33.5	169.14	169.14	169.14	0.64	0.65
180	1109	C	19	X	1	75.0	75.0	170.45	170.45	170.45	1.09	
180	1109	C	19	X	1	75.0	75.0	170.45	170.45	170.45	1.10	1.10
180	1109	C	20	X	2	75.0	75.0	181.55	181.55	181.55	0.82	
180	1109	C	20	X	2	75.0	75.0	181.55	181.55	181.55	0.84	0.83
180	1109	C	20	X	4	58.0	58.0	184.38	184.38	184.38	0.97	
180	1109	C	20	X	4	58.0	58.0	184.38	184.38	184.38	1.02	1.00
180	1109	C	22	X	2	38.0	38.0	199.68	199.68	199.68	0.86	
180	1109	C	22	X	2	38.0	38.0	199.68	199.68	199.68	0.88	0.87
180	1109	C	23	X	1	75.0	75.0	208.85	208.85	208.85	0.82	
180	1109	C	23	X	1	75.0	75.0	208.85	208.85	208.85	0.84	0.83
180	1109	C	23	X	3	50.0	50.0	211.60	211.60	211.60	0.88	
180	1109	C	23	X	3	50.0	50.0	211.60	211.60	211.60	0.91	0.90

Table T17 (continued).

Leg	Site	Hole	Core	Type	Section	Top interval (cm)	Bottom interval (cm)	Top depth (mbsf)	Bottom depth (mbsf)	Middle depth (mbsf)	Thermal conductivity ($W \cdot m^{-1} \cdot °C^{-1}$)	Thermal conductivity average ($W \cdot m^{-1} \cdot °C^{-1}$)
180	1109	C	23	X	5	75.0	75.0	213.50	213.50	213.50	0.90	
180	1109	C	23	X	5	75.0	75.0	213.50	213.50	213.50	0.91	0.90
180	1109	C	23	X	7	75.0	75.0	216.50	216.50	216.50	0.72	
180	1109	C	23	X	7	75.0	75.0	216.50	216.50	216.50	0.71	0.71
180	1109	C	25	X	1	9.5	9.5	227.50	227.50	227.50	0.79	
180	1109	C	25	X	1	9.5	9.5	227.50	227.50	227.50	0.77	
180	1109	C	26	X	1	50.0	50.0	237.50	237.50	237.50	0.97	
180	1109	C	26	X	1	50.0	50.0	237.50	237.50	237.50	0.95	0.87
180	1109	C	26	X	3	75.0	75.0	240.70	240.70	240.70	0.97	
180	1109	C	26	X	3	75.0	75.0	240.70	240.70	240.70	0.90	0.94
180	1109	C	26	X	5	75.0	75.0	243.70	243.70	243.70	0.80	
180	1109	C	26	X	5	75.0	75.0	243.70	243.70	243.70	0.79	0.79
180	1109	C	26	X	7	25.0	25.0	246.20	246.20	246.20	0.96	
180	1109	C	26	X	7	25.0	25.0	246.20	246.20	246.20	1.00	0.98
180	1109	C	27	X	1	75.0	75.0	247.45	247.45	247.45	0.50	
180	1109	C	27	X	1	75.0	75.0	247.45	247.45	247.45	0.50	0.50
180	1109	C	27	X	3	80.0	80.0	250.50	250.50	250.50	0.91	
180	1109	C	27	X	3	80.0	80.0	250.50	250.50	250.50	0.90	0.90
180	1109	C	27	X	5	75.0	75.0	253.45	253.45	253.45	0.85	
180	1109	C	27	X	5	75.0	75.0	253.45	253.45	253.45	0.85	0.85
180	1109	C	27	X	7	34.5	34.5	255.55	255.55	255.55	0.90	
180	1109	C	27	X	7	34.5	34.5	255.55	255.55	255.55	0.92	0.91
180	1109	C	28	X	1	75.0	75.0	257.05	257.05	257.05	0.77	
180	1109	C	28	X	1	75.0	75.0	257.05	257.05	257.05	0.77	0.77
180	1109	C	28	X	3	75.0	75.0	260.05	260.05	260.05	0.91	
180	1109	C	28	X	3	75.0	75.0	260.05	260.05	260.05	0.97	
180	1109	C	28	X	3	75.0	75.0	260.05	260.05	260.05	1.00	0.96
180	1109	C	28	X	5	75.0	75.0	263.05	263.05	263.05	0.89	
180	1109	C	28	X	5	75.0	75.0	263.05	263.05	263.05	0.95	0.92
180	1109	C	28	X	7	30.0	30.0	265.60	265.60	265.60	0.80	
180	1109	C	28	X	7	30.0	30.0	265.60	265.60	265.60	0.81	0.80
180	1109	C	29	X	1	75.0	75.0	266.75	266.75	266.75	0.74	
180	1109	C	29	X	1	75.0	75.0	266.75	266.75	266.75	0.76	0.75
180	1109	C	29	X	3	75.0	75.0	269.75	269.75	269.75	0.70	
180	1109	C	29	X	3	75.0	75.0	269.75	269.75	269.75	0.71	0.70
180	1109	C	29	X	5	75.0	75.0	272.75	272.75	272.75	0.59	
180	1109	C	29	X	5	75.0	75.0	272.75	272.75	272.75	0.60	0.59
180	1109	C	29	X	7	20.0	20.0	275.20	275.20	275.20	0.80	
180	1109	C	29	X	7	20.0	20.0	275.20	275.20	275.20	0.82	0.81
180	1109	C	30	X	1	75.0	75.0	276.35	276.35	276.35	0.84	
180	1109	C	30	X	1	75.0	75.0	276.35	276.35	276.35	0.86	0.85
180	1109	C	30	X	3	75.0	75.0	279.35	279.35	279.35	0.81	
180	1109	C	30	X	3	75.0	75.0	279.35	279.35	279.35	0.83	0.82
180	1109	C	30	X	5	75.0	75.0	282.35	282.35	282.35	0.80	
180	1109	C	30	X	5	75.0	75.0	282.35	282.35	282.35	0.79	0.80
180	1109	C	30	X	7	20.0	20.0	284.80	284.80	284.80	1.03	
180	1109	C	30	X	7	20.0	20.0	284.80	284.80	284.80	1.02	1.03
180	1109	C	31	X	1	75.0	75.0	285.85	285.85	285.85	0.77	
180	1109	C	31	X	1	75.0	75.0	285.85	285.85	285.85	0.76	0.76
180	1109	C	31	X	3	75.0	75.0	288.85	288.85	288.85	0.71	
180	1109	C	31	X	3	75.0	75.0	288.85	288.85	288.85	0.72	0.72
180	1109	C	31	X	5	75.0	75.0	291.85	291.85	291.85	0.73	
180	1109	C	31	X	5	75.0	75.0	291.85	291.85	291.85	0.75	0.74
180	1109	C	31	X	7	20.0	20.0	294.30	294.30	294.30	0.84	
180	1109	C	31	X	7	20.0	20.0	294.30	294.30	294.30	0.84	0.84
180	1109	C	32	X	1	75.0	75.0	295.55	295.55	295.55	1.41	
180	1109	C	32	X	1	75.0	75.0	295.55	295.55	295.55	0.84	
180	1109	C	32	X	1	75.0	75.0	295.55	295.55	295.55	1.03	
180	1109	C	32	X	1	75.0	75.0	295.55	295.55	295.55	1.07	1.09
180	1109	C	32	X	3	75.0	75.0	298.55	298.55	298.55	0.79	
180	1109	C	32	X	3	75.0	75.0	298.55	298.55	298.55	0.75	0.77
180	1109	C	32	X	5	75.0	75.0	301.55	301.55	301.55	0.80	
180	1109	C	32	X	5	75.0	75.0	301.55	301.55	301.55	0.79	0.79
180	1109	C	32	X	7	30.0	30.0	303.90	303.90	303.90	0.79	
180	1109	C	32	X	7	30.0	30.0	303.90	303.90	303.90	0.81	0.80
180	1109	C	33	X	1	75.0	75.0	305.25	305.25	305.25	1.03	
180	1109	C	33	X	1	75.0	75.0	305.25	305.25	305.25	1.01	1.02

Table T17 (continued).

Leg	Site	Hole	Core	Type	Section	Top interval (cm)	Bottom interval (cm)	Top depth (mbsf)	Bottom depth (mbsf)	Middle depth (mbsf)	Thermal conductivity ($W \cdot m^{-1} \cdot °C^{-1}$)	Thermal conductivity average ($W \cdot m^{-1} \cdot °C^{-1}$)
180	1109	C	33	X	3	75.0	75.0	308.25	308.25	308.25	0.88	
180	1109	C	33	X	3	75.0	75.0	308.25	308.25	308.25	0.90	0.89
180	1109	C	33	X	5	75.0	75.0	311.25	311.25	311.25	0.82	
180	1109	C	33	X	5	75.0	75.0	311.25	311.25	311.25	0.85	0.83
180	1109	C	33	X	7	20.0	20.0	313.70	313.70	313.70	1.04	
180	1109	C	33	X	7	20.0	20.0	313.70	313.70	313.70	1.03	1.03
180	1109	C	34	X	1	75.0	75.0	314.95	314.95	314.95	0.92	
180	1109	C	34	X	1	75.0	75.0	314.95	314.95	314.95	0.93	0.93
180	1109	C	34	X	3	75.0	75.0	317.95	317.95	317.95	0.90	
180	1109	C	34	X	3	75.0	75.0	317.95	317.95	317.95	0.89	0.89
180	1109	C	34	X	5	85.0	85.0	321.05	321.05	321.05	0.96	
180	1109	C	34	X	5	85.0	85.0	321.05	321.05	321.05	0.98	0.97
180	1109	C	34	X	7	26.0	26.0	323.46	323.46	323.46	1.01	
180	1109	C	34	X	7	26.0	26.0	323.46	323.46	323.46	1.04	1.03
180	1109	C	35	X	1	75.0	75.0	324.65	324.65	324.65	0.92	
180	1109	C	35	X	1	75.0	75.0	324.65	324.65	324.65	0.89	0.90
180	1109	C	35	X	3	75.0	75.0	327.65	327.65	327.65	0.84	
180	1109	C	35	X	3	75.0	75.0	327.65	327.65	327.65	0.86	0.85
180	1109	C	35	X	5	75.0	75.0	330.65	330.65	330.65	0.88	
180	1109	C	35	X	5	75.0	75.0	330.65	330.65	330.65	0.90	0.89
180	1109	C	35	X	7	24.0	24.0	333.14	333.14	333.14	1.10	
180	1109	C	35	X	7	24.0	24.0	333.14	333.14	333.14	1.07	1.08
180	1109	C	36	X	1	75.0	75.0	334.25	334.25	334.25	0.71	
180	1109	C	36	X	1	75.0	75.0	334.25	334.25	334.25	0.73	0.72
180	1109	C	36	X	3	75.0	75.0	337.25	337.25	337.25	0.85	
180	1109	C	36	X	3	75.0	75.0	337.25	337.25	337.25	0.86	0.86
180	1109	C	37	X	1	84.0	84.0	343.94	343.94	343.94	0.87	
180	1109	C	37	X	1	84.0	84.0	343.94	343.94	343.94	0.86	
180	1109	C	38	X	1	75.0	75.0	347.35	347.35	347.35	0.92	
180	1109	C	38	X	1	75.0	75.0	347.35	347.35	347.35	0.98	0.91
180	1109	C	38	X	3	75.0	75.0	350.35	350.35	350.35	1.06	
180	1109	C	38	X	3	75.0	75.0	350.35	350.35	350.35	1.06	1.06
180	1109	C	38	X	5	76.0	76.0	353.36	353.36	353.36	0.99	
180	1109	C	38	X	5	76.0	76.0	353.36	353.36	353.36	0.99	0.99
180	1109	C	39	X	1	66.0	66.0	353.26	353.26	353.26	0.89	
180	1109	C	39	X	1	66.0	66.0	353.26	353.26	353.26	0.90	0.90
180	1109	C	38	X	7	22.0	22.0	355.82	355.82	355.82	1.05	
180	1109	C	38	X	7	22.0	22.0	355.82	355.82	355.82	1.07	1.06
180	1109	C	39	X	3	75.0	75.0	356.35	356.35	356.35	0.99	
180	1109	C	39	X	3	75.0	75.0	356.35	356.35	356.35	0.98	0.99
180	1109	C	39	X	5	75.0	75.0	359.35	359.35	359.35	0.99	
180	1109	C	39	X	5	75.0	75.0	359.35	359.35	359.35	1.01	1.00
180	1109	C	39	X	7	23.0	23.0	361.83	361.83	361.83	1.06	
180	1109	C	39	X	7	23.0	23.0	361.83	361.83	361.83	1.09	1.08
180	1109	C	40	X	1	75.0	75.0	362.95	362.95	362.95	0.75	
180	1109	C	40	X	1	75.0	75.0	362.95	362.95	362.95	0.76	0.76
180	1109	C	40	X	3	54.0	54.0	365.74	365.74	365.74	0.93	
180	1109	C	40	X	3	54.0	54.0	365.74	365.74	365.74	0.95	0.94
180	1109	C	40	X	5	69.0	69.0	368.89	368.89	368.89	1.02	
180	1109	C	40	X	5	69.0	69.0	368.89	368.89	368.89	0.99	1.00
180	1109	C	41	X	1	75.0	75.0	372.25	372.25	372.25	0.80	
180	1109	C	41	X	1	75.0	75.0	372.25	372.25	372.25	0.80	0.80
180	1109	C	41	X	3	61.0	61.0	375.11	375.11	375.11	0.87	
180	1109	C	41	X	3	61.0	61.0	375.11	375.11	375.11	0.89	0.88
180	1109	C	33	X	2	89.0	90.0	306.89	306.90	306.90	1.08	
180	1109	C	33	X	2	89.0	90.0	306.89	306.90	306.90	1.16	1.12
180	1109	C	34	X	6	9.0	11.0	321.79	321.81	321.80	1.09	
180	1109	C	34	X	6	9.0	11.0	321.79	321.81	321.80	1.09	1.09
180	1109	D	1	R	1	141.0	142.0	354.21	354.22	354.22	1.10	
180	1109	D	1	R	1	141.0	142.0	354.21	354.22	354.22	1.05	
180	1109	D	1	R	1	141.0	142.0	354.21	354.22	354.22	1.22	1.12
180	1109	D	1	R	2	75.0	77.0	355.05	355.07	355.06	1.04	
180	1109	D	1	R	2	75.0	77.0	355.05	355.07	355.06	1.07	
180	1109	D	1	R	2	75.0	77.0	355.05	355.07	355.06	1.08	1.06
180	1109	D	1	R	3	115.0	117.0	356.95	356.97	356.96	0.99	
180	1109	D	1	R	3	115.0	117.0	356.95	356.97	356.96	1.06	
180	1109	D	1	R	3	115.0	117.0	356.95	356.97	356.96	1.04	

Table T17 (continued).

Leg	Site	Hole	Core	Type	Section	Top interval (cm)	Bottom interval (cm)	Top depth (mbsf)	Bottom depth (mbsf)	Middle depth (mbsf)	Thermal conductivity ($W \cdot m^{-1} \cdot °C^{-1}$)	Thermal conductivity average ($W \cdot m^{-1} \cdot °C^{-1}$)
180	1109	D	1	R	3	115.0	117.0	356.95	356.97	356.96	1.04	1.03
180	1109	D	1	R	4	90.0	92.0	358.20	358.22	358.21	0.92	
180	1109	D	1	R	4	90.0	92.0	358.20	358.22	358.21	0.94	
180	1109	D	1	R	4	90.0	92.0	358.20	358.22	358.21	0.96	
180	1109	D	1	R	4	90.0	92.0	358.20	358.22	358.21	0.93	0.94
180	1109	D	3	R	1	112.0	113.0	369.82	369.83	369.83	0.98	
180	1109	D	3	R	1	112.0	113.0	369.82	369.83	369.83	1.03	
180	1109	D	3	R	1	112.0	113.0	369.82	369.83	369.83	1.00	
180	1109	D	3	R	1	112.0	113.0	369.82	369.83	369.83	1.06	1.02
180	1109	D	3	R	2	73.5	74.5	370.94	370.95	370.94	0.99	
180	1109	D	3	R	2	73.5	74.5	370.94	370.95	370.94	1.01	
180	1109	D	3	R	2	73.5	74.5	370.94	370.95	370.94	1.01	
180	1109	D	3	R	2	73.5	74.5	370.94	370.95	370.94	1.01	1.00
180	1109	D	3	R	3	16.0	17.0	371.85	371.86	371.86	0.99	
180	1109	D	3	R	3	16.0	17.0	371.85	371.86	371.86	1.02	
180	1109	D	3	R	3	16.0	17.0	371.85	371.86	371.86	1.05	
180	1109	D	3	R	3	16.0	17.0	371.85	371.86	371.86	1.03	1.02
180	1109	D	3	R	4	75.0	77.0	373.54	373.56	373.55	0.99	
180	1109	D	3	R	4	75.0	77.0	373.54	373.56	373.55	0.96	
180	1109	D	3	R	4	75.0	77.0	373.54	373.56	373.55	1.03	
180	1109	D	3	R	4	75.0	77.0	373.54	373.56	373.55	1.04	1.01
180	1109	D	3	R	5	82.0	84.0	374.96	374.98	374.97	0.96	
180	1109	D	3	R	5	82.0	84.0	374.96	374.98	374.97	1.01	
180	1109	D	3	R	5	82.0	84.0	374.96	374.98	374.97	1.03	
180	1109	D	3	R	5	82.0	84.0	374.96	374.98	374.97	1.00	1.00
180	1109	D	3	R	6	85.5	86.5	376.22	376.23	376.22	0.89	
180	1109	D	3	R	6	85.5	86.5	376.22	376.23	376.22	1.00	
180	1109	D	3	R	6	85.5	86.5	376.22	376.23	376.22	0.98	
180	1109	D	3	R	6	85.5	86.5	376.22	376.23	376.22	1.01	0.97
180	1109	D	3	R	7	38.0	39.0	377.13	377.14	377.14	0.91	
180	1109	D	3	R	7	38.0	39.0	377.13	377.14	377.14	1.02	
180	1109	D	3	R	7	38.0	39.0	377.13	377.14	377.14	1.03	
180	1109	D	3	R	7	38.0	39.0	377.13	377.14	377.14	1.03	1.00
180	1109	D	4	R	1	58.0	59.0	378.88	378.89	378.89	1.04	
180	1109	D	4	R	1	58.0	59.0	378.88	378.89	378.89	1.08	
180	1109	D	4	R	1	58.0	59.0	378.88	378.89	378.89	1.04	
180	1109	D	4	R	1	58.0	59.0	378.88	378.89	378.89	1.11	1.07
180	1109	D	4	R	3	45.0	46.0	381.05	381.06	381.06	0.97	
180	1109	D	4	R	3	45.0	46.0	381.05	381.06	381.06	1.03	
180	1109	D	4	R	3	45.0	46.0	381.05	381.06	381.06	1.01	
180	1109	D	4	R	3	45.0	46.0	381.05	381.06	381.06	1.02	1.01
180	1109	D	4	R	5	76.0	77.0	383.53	383.54	383.54	1.03	
180	1109	D	4	R	5	76.0	77.0	383.53	383.54	383.54	1.07	
180	1109	D	4	R	5	76.0	77.0	383.53	383.54	383.54	1.06	
180	1109	D	4	R	5	76.0	77.0	383.53	383.54	383.54	1.05	1.05
180	1109	D	5	R	1	71.0	72.0	388.31	388.32	388.32	1.39	
180	1109	D	5	R	1	71.0	72.0	388.31	388.32	388.32	1.44	
180	1109	D	5	R	1	71.0	72.0	388.31	388.32	388.32	1.34	
180	1109	D	5	R	1	71.0	72.0	388.31	388.32	388.32	1.42	1.40
180	1109	D	2	R	2	79.0	80.0	361.20	361.21	361.21	0.89	
180	1109	D	2	R	2	79.0	80.0	361.20	361.21	361.21	1.02	
180	1109	D	2	R	2	79.0	80.0	361.20	361.21	361.21	1.02	
180	1109	D	2	R	2	79.0	80.0	361.20	361.21	361.21	0.98	0.97
180	1109	D	2	R	5	74.0	75.0	364.62	364.63	364.63	0.99	
180	1109	D	2	R	5	74.0	75.0	364.62	364.63	364.63	1.00	
180	1109	D	2	R	5	74.0	75.0	364.62	364.63	364.63	1.01	
180	1109	D	2	R	5	74.0	75.0	364.62	364.63	364.63	1.00	1.00
180	1109	D	2	R	6	53.0	54.0	365.45	365.46	365.46	1.01	
180	1109	D	2	R	6	53.0	54.0	365.45	365.46	365.46	1.04	
180	1109	D	2	R	6	53.0	54.0	365.45	365.46	365.46	1.03	
180	1109	D	2	R	6	53.0	54.0	365.45	365.46	365.46	1.02	1.02
180	1109	D	6	R	1	85.0	86.0	398.05	398.06	398.06	1.01	
180	1109	D	6	R	1	85.0	86.0	398.05	398.06	398.06	1.06	
180	1109	D	6	R	1	85.0	86.0	398.05	398.06	398.06	1.05	
180	1109	D	6	R	1	85.0	86.0	398.05	398.06	398.06	1.08	1.05
180	1109	D	6	R	3	34.0	35.0	400.40	400.41	400.41	0.42	
180	1109	D	6	R	3	34.0	35.0	400.40	400.41	400.41	0.47	

Table T17 (continued).

Leg	Site	Hole	Core	Type	Section	Top interval (cm)	Bottom interval (cm)	Top depth (mbsf)	Bottom depth (mbsf)	Middle depth (mbsf)	Thermal conductivity ($W \cdot m^{-1} \cdot °C^{-1}$)	Thermal conductivity average ($W \cdot m^{-1} \cdot °C^{-1}$)
180	1109	D	6	R	3	34.0	35.0	400.40	400.41	400.41	0.47	
180	1109	D	6	R	3	34.0	35.0	400.40	400.41	400.41	0.46	0.46
180	1109	D	6	R	3	34.0	35.0	400.40	400.41	400.41	1.07	
180	1109	D	6	R	3	34.0	35.0	400.40	400.41	400.41	1.02	
180	1109	D	6	R	3	34.0	35.0	400.40	400.41	400.41	1.02	
180	1109	D	6	R	3	34.0	35.0	400.40	400.41	400.41	1.04	1.04
180	1109	D	6	R	5	41.0	42.0	402.46	402.47	402.47	0.99	
180	1109	D	6	R	5	41.0	42.0	402.46	402.47	402.47	1.04	
180	1109	D	6	R	5	41.0	42.0	402.46	402.47	402.47	1.05	
180	1109	D	6	R	5	41.0	42.0	402.46	402.47	402.47	1.08	1.04
180	1109	D	7	R	1	73.0	74.0	407.53	407.54	407.54	1.03	
180	1109	D	7	R	1	73.0	74.0	407.53	407.54	407.54	1.07	
180	1109	D	7	R	1	73.0	74.0	407.53	407.54	407.54	1.06	
180	1109	D	7	R	1	73.0	74.0	407.53	407.54	407.54	1.05	1.05
180	1109	D	7	R	3	86.0	87.0	410.40	410.41	410.41	0.96	
180	1109	D	7	R	3	86.0	87.0	410.40	410.41	410.41	1.05	
180	1109	D	7	R	3	86.0	87.0	410.40	410.41	410.41	1.03	
180	1109	D	7	R	3	86.0	87.0	410.40	410.41	410.41	1.03	1.02
180	1109	D	7	R	5	23.0	24.0	412.43	412.44	412.44	1.04	
180	1109	D	7	R	5	23.0	24.0	412.43	412.44	412.44	1.07	
180	1109	D	7	R	5	23.0	24.0	412.43	412.44	412.44	1.05	
180	1109	D	7	R	5	23.0	24.0	412.43	412.44	412.44	1.05	1.05
180	1109	D	8	R	1	24.0	25.0	416.74	416.75	416.75	0.95	
180	1109	D	8	R	1	24.0	25.0	416.74	416.75	416.75	1.05	
180	1109	D	8	R	1	24.0	25.0	416.74	416.75	416.75	1.06	
180	1109	D	8	R	1	24.0	25.0	416.74	416.75	416.75	1.06	1.03
180	1109	D	8	R	4	82.0	83.0	421.25	421.26	421.26	0.98	
180	1109	D	8	R	4	82.0	83.0	421.25	421.26	421.26	0.98	
180	1109	D	8	R	4	82.0	83.0	421.25	421.26	421.26	0.95	
180	1109	D	8	R	4	82.0	83.0	421.25	421.26	421.26	1.03	
180	1109	D	8	R	4	82.0	83.0	421.25	421.26	421.26	1.01	0.99
180	1109	D	8	R	6	34.0	35.0	423.47	423.48	423.48	0.99	
180	1109	D	8	R	6	34.0	35.0	423.47	423.48	423.48	1.03	
180	1109	D	8	R	6	34.0	35.0	423.47	423.48	423.48	1.03	
180	1109	D	8	R	6	34.0	35.0	423.47	423.48	423.48	1.04	1.02
180	1109	D	9	R	1	134.0	135.0	427.44	427.45	427.45	1.03	
180	1109	D	9	R	1	134.0	135.0	427.44	427.45	427.45	1.05	
180	1109	D	9	R	1	134.0	135.0	427.44	427.45	427.45	1.07	
180	1109	D	9	R	1	134.0	135.0	427.44	427.45	427.45	1.04	1.04
180	1109	D	9	R	3	97.0	98.0	430.02	430.03	430.03	1.02	
180	1109	D	9	R	3	97.0	98.0	430.02	430.03	430.03	1.04	
180	1109	D	9	R	3	97.0	98.0	430.02	430.03	430.03	1.06	
180	1109	D	9	R	3	97.0	98.0	430.02	430.03	430.03	1.06	1.04
180	1109	D	9	R	5	112.0	113.0	432.64	432.65	432.65	0.87	
180	1109	D	9	R	5	112.0	113.0	432.64	432.65	432.65	1.05	
180	1109	D	9	R	5	112.0	113.0	432.64	432.65	432.65	1.02	
180	1109	D	9	R	5	112.0	113.0	432.64	432.65	432.65	1.03	0.99
180	1109	D	10	R	1	44.0	45.0	436.14	436.15	436.15	1.02	
180	1109	D	10	R	1	44.0	45.0	436.14	436.15	436.15	0.99	
180	1109	D	10	R	1	44.0	45.0	436.14	436.15	436.15	1.03	
180	1109	D	10	R	1	44.0	45.0	436.14	436.15	436.15	1.02	1.01
180	1109	D	10	R	3	124.0	125.0	439.69	439.70	439.70	0.72	
180	1109	D	10	R	3	124.0	125.0	439.69	439.70	439.70	1.02	
180	1109	D	10	R	3	124.0	125.0	439.69	439.70	439.70	1.03	
180	1109	D	10	R	3	124.0	125.0	439.69	439.70	439.70	1.04	0.95
180	1109	D	10	R	5	114.0	115.0	442.28	442.29	442.29	1.04	
180	1109	D	10	R	5	114.0	115.0	442.28	442.29	442.29	1.07	
180	1109	D	10	R	5	114.0	115.0	442.28	442.29	442.29	1.03	1.05
180	1109	D	10	R	7	86.0	87.0	444.22	444.23	444.23	0.972	
180	1109	D	10	R	7	86.0	87.0	444.22	444.23	444.23	1.03	
180	1109	D	10	R	7	86.0	87.0	444.22	444.23	444.23	1.20	
180	1109	D	10	R	7	86.0	87.0	444.22	444.23	444.23	1.21	1.14
180	1109	D	11	R	1	49.0	50.0	445.79	445.80	445.80	1.04	
180	1109	D	11	R	1	49.0	50.0	445.79	445.80	445.80	1.06	
180	1109	D	11	R	1	49.0	50.0	445.79	445.80	445.80	1.05	
180	1109	D	11	R	1	49.0	50.0	445.79	445.80	445.80	1.01	1.04
180	1109	D	11	R	3	60.0	61.0	448.65	448.66	448.66	0.77	

Table T17 (continued).

Leg	Site	Hole	Core	Type	Section	Top interval (cm)	Bottom interval (cm)	Top depth (mbsf)	Bottom depth (mbsf)	Middle depth (mbsf)	Thermal conductivity ($W \cdot m^{-1} \cdot °C^{-1}$)	Thermal conductivity average ($W \cdot m^{-1} \cdot °C^{-1}$)
180	1109	D	11	R	3	60.0	61.0	448.65	448.66	448.66	1.06	
180	1109	D	11	R	3	60.0	61.0	448.65	448.66	448.66	1.06	
180	1109	D	11	R	3	60.0	61.0	448.65	448.66	448.66	1.06	1.06
180	1109	D	11	R	5	63.0	64.0	451.37	451.38	451.38	1.05	
180	1109	D	11	R	5	63.0	64.0	451.37	451.38	451.38	1.13	
180	1109	D	11	R	5	63.0	64.0	451.37	451.38	451.38	1.09	
180	1109	D	11	R	5	63.0	64.0	451.37	451.38	451.38	1.10	1.11
180	1109	D	12	R	1	54.0	55.0	455.44	455.45	455.45	1.02	
180	1109	D	12	R	1	54.0	55.0	455.44	455.45	455.45	1.11	
180	1109	D	12	R	1	54.0	55.0	455.44	455.45	455.45	1.12	
180	1109	D	12	R	1	54.0	55.0	455.44	455.45	455.45	1.09	1.10
180	1109	D	12	R	3	62.0	64.0	458.37	458.39	458.38	0.97	
180	1109	D	12	R	3	62.0	64.0	458.37	458.39	458.38	1.06	
180	1109	D	12	R	3	62.0	64.0	458.37	458.39	458.38	1.07	1.03
180	1109	D	12	R	5	33.0	35.0	460.49	460.51	460.50	0.89	
180	1109	D	12	R	5	33.0	35.0	460.49	460.51	460.50	1.05	
180	1109	D	12	R	5	33.0	35.0	460.49	460.51	460.50	1.05	
180	1109	D	12	R	5	33.0	35.0	460.49	460.51	460.50	1.08	1.02
180	1109	D	12	R	7	0.0	2.0	462.30	462.32	462.31	0.91	
180	1109	D	12	R	7	0.0	2.0	462.30	462.32	462.31	1.05	
180	1109	D	12	R	7	0.0	2.0	462.30	462.32	462.31	1.06	
180	1109	D	12	R	7	0.0	2.0	462.30	462.32	462.31	1.04	1.01
180	1109	D	13	R	1	77.0	78.0	465.27	465.28	465.28	1.06	
180	1109	D	13	R	1	77.0	78.0	465.27	465.28	465.28	1.02	
180	1109	D	13	R	1	77.0	78.0	465.27	465.28	465.28	1.10	
180	1109	D	13	R	1	77.0	78.0	465.27	465.28	465.28	1.05	1.06
180	1109	D	13	R	3	15.5	17.5	467.31	467.33	467.32	1.06	
180	1109	D	13	R	3	15.5	17.5	467.31	467.33	467.32	1.06	
180	1109	D	13	R	3	15.5	17.5	467.31	467.33	467.32	1.03	
180	1109	D	13	R	3	15.5	17.5	467.31	467.33	467.32	1.04	1.05
180	1109	D	13	R	5	66.0	67.0	469.86	469.87	469.87	1.31	
180	1109	D	13	R	5	66.0	67.0	469.86	469.87	469.87	1.33	
180	1109	D	13	R	5	66.0	67.0	469.86	469.87	469.87	1.34	
180	1109	D	13	R	5	66.0	67.0	469.86	469.87	469.87	1.37	1.34
180	1109	D	13	R	7	21.0	23.0	472.18	472.20	472.19	1.06	
180	1109	D	13	R	7	21.0	23.0	472.18	472.20	472.19	1.10	
180	1109	D	13	R	7	21.0	23.0	472.18	472.20	472.19	1.10	
180	1109	D	13	R	7	21.0	23.0	472.18	472.20	472.19	1.08	1.08
180	1109	D	14	R	1	70.0	71.0	474.80	474.81	474.81	1.05	
180	1109	D	14	R	1	70.0	71.0	474.80	474.81	474.81	1.05	
180	1109	D	14	R	1	70.0	71.0	474.80	474.81	474.81	1.06	
180	1109	D	14	R	1	70.0	71.0	474.80	474.81	474.81	1.05	1.05
180	1109	D	14	R	3	14.0	15.0	476.90	476.91	476.91	1.03	
180	1109	D	14	R	3	14.0	15.0	476.90	476.91	476.91	1.03	
180	1109	D	14	R	3	14.0	15.0	476.90	476.91	476.91	1.02	
180	1109	D	14	R	3	14.0	15.0	476.90	476.91	476.91	1.05	1.03
180	1109	D	14	R	5	6.0	7.0	479.48	479.49	479.49	1.05	
180	1109	D	14	R	5	6.0	7.0	479.48	479.49	479.49	1.07	
180	1109	D	14	R	5	6.0	7.0	479.48	479.49	479.49	1.06	
180	1109	D	14	R	5	6.0	7.0	479.48	479.49	479.49	1.06	1.06
180	1109	D	14	R	7	46.0	47.0	482.88	482.89	482.89	1.07	
180	1109	D	14	R	7	46.0	47.0	482.88	482.89	482.89	1.01	
180	1109	D	14	R	7	46.0	47.0	482.88	482.89	482.89	1.06	
180	1109	D	14	R	7	46.0	47.0	482.88	482.89	482.89	1.05	1.05
180	1109	D	15	R	1	106.0	107.0	484.76	484.77	484.77	0.99	
180	1109	D	15	R	1	106.0	107.0	484.76	484.77	484.77	1.03	
180	1109	D	15	R	1	106.0	107.0	484.76	484.77	484.77	1.11	
180	1109	D	15	R	1	106.0	107.0	484.76	484.77	484.77	1.05	1.04
180	1109	D	15	R	3	70.0	72.0	486.74	486.76	486.75	1.01	
180	1109	D	15	R	3	70.0	72.0	486.74	486.76	486.75	1.06	
180	1109	D	15	R	3	70.0	72.0	486.74	486.76	486.75	1.03	
180	1109	D	15	R	3	70.0	72.0	486.74	486.76	486.75	1.04	1.03
180	1109	D	15	R	5	28.0	30.0	489.10	489.12	489.11	0.96	
180	1109	D	15	R	5	28.0	30.0	489.10	489.12	489.11	1.02	
180	1109	D	15	R	5	28.0	30.0	489.10	489.12	489.11	1.05	
180	1109	D	15	R	5	28.0	30.0	489.10	489.12	489.11	1.06	1.02
180	1109	D	15	R	7	44.0	45.0	491.62	491.63	491.63	1.11	

Table T17 (continued).

Leg	Site	Hole	Core	Type	Section	Top interval (cm)	Bottom interval (cm)	Top depth (mbsf)	Bottom depth (mbsf)	Middle depth (mbsf)	Thermal conductivity ($W \cdot m^{-1} \cdot °C^{-1}$)	Thermal conductivity average ($W \cdot m^{-1} \cdot °C^{-1}$)
180	1109	D	15	R	7	44.0	45.0	491.62	491.63	491.63	1.10	
180	1109	D	15	R	7	44.0	45.0	491.62	491.63	491.63	1.09	
180	1109	D	15	R	7	44.0	45.0	491.62	491.63	491.63	1.13	1.11
180	1109	D	16	R	1	49.0	50.0	493.79	493.80	493.80	1.10	
180	1109	D	16	R	1	49.0	50.0	493.79	493.80	493.80	1.10	
180	1109	D	16	R	1	49.0	50.0	493.79	493.80	493.80	1.09	
180	1109	D	16	R	1	49.0	50.0	493.79	493.80	493.80	1.16	1.11
180	1109	D	16	R	3	128.0	129.0	497.08	497.09	497.09	1.08	
180	1109	D	16	R	3	128.0	129.0	497.08	497.09	497.09	1.08	
180	1109	D	16	R	3	128.0	129.0	497.08	497.09	497.09	1.09	
180	1109	D	16	R	3	128.0	129.0	497.08	497.09	497.09	1.08	1.08
180	1109	D	16	R	5	111.0	112.0	499.64	499.65	499.65	1.07	
180	1109	D	16	R	5	111.0	112.0	499.64	499.65	499.65	1.08	
180	1109	D	16	R	5	111.0	112.0	499.64	499.65	499.65	1.10	
180	1109	D	16	R	5	111.0	112.0	499.64	499.65	499.65	1.10	1.09
180	1109	D	16	R	7	21.0	22.0	501.53	501.54	501.54	1.03	
180	1109	D	16	R	7	21.0	22.0	501.53	501.54	501.54	1.10	1.06
180	1109	D	17	R	1	26.0	27.0	503.26	503.27	503.27	1.11	
180	1109	D	17	R	1	26.0	27.0	503.26	503.27	503.27	1.13	
180	1109	D	17	R	1	26.0	27.0	503.26	503.27	503.27	1.14	
180	1109	D	17	R	1	26.0	27.0	503.26	503.27	503.27	1.14	1.13
180	1109	D	17	R	3	77.0	78.0	505.98	505.99	505.99	1.03	
180	1109	D	17	R	3	77.0	78.0	505.98	505.99	505.99	1.08	
180	1109	D	17	R	3	77.0	78.0	505.98	505.99	505.99	1.09	
180	1109	D	17	R	3	77.0	78.0	505.98	505.99	505.99	1.09	1.07
180	1109	D	17	R	5	62.0	63.0	508.75	508.76	508.76	1.06	
180	1109	D	17	R	5	62.0	63.0	508.75	508.76	508.76	1.06	
180	1109	D	17	R	5	62.0	63.0	508.75	508.76	508.76	1.08	
180	1109	D	17	R	5	62.0	63.0	508.75	508.76	508.76	0.95	1.04
180	1109	D	18	R	1	25.0	26.0	512.85	512.86	512.86	1.06	
180	1109	D	18	R	1	25.0	26.0	512.85	512.86	512.86	1.07	
180	1109	D	18	R	1	25.0	26.0	512.85	512.86	512.86	1.09	
180	1109	D	18	R	1	25.0	26.0	512.85	512.86	512.86	1.04	1.06
180	1109	D	18	R	3	9.0	10.0	515.50	515.51	515.51	1.08	
180	1109	D	18	R	3	9.0	10.0	515.50	515.51	515.51	1.08	
180	1109	D	18	R	3	9.0	10.0	515.50	515.51	515.51	1.09	
180	1109	D	18	R	3	9.0	10.0	515.50	515.51	515.51	1.08	1.08
180	1109	D	18	R	5	48.0	49.0	518.30	518.31	518.31	1.11	
180	1109	D	18	R	5	48.0	49.0	518.30	518.31	518.31	1.16	
180	1109	D	18	R	5	48.0	49.0	518.30	518.31	518.31	1.16	
180	1109	D	18	R	5	48.0	49.0	518.30	518.31	518.31	1.11	1.14
180	1109	D	19	R	1	18.0	19.0	522.48	522.49	522.49	1.10	
180	1109	D	19	R	1	18.0	19.0	522.48	522.49	522.49	1.12	
180	1109	D	19	R	1	18.0	19.0	522.48	522.49	522.49	1.13	
180	1109	D	19	R	1	18.0	19.0	522.48	522.49	522.49	1.12	1.12
180	1109	D	19	R	3	86.0	87.0	525.85	525.86	525.86	1.14	
180	1109	D	19	R	3	86.0	87.0	525.85	525.86	525.86	1.15	
180	1109	D	19	R	3	86.0	87.0	525.85	525.86	525.86	1.12	
180	1109	D	19	R	3	86.0	87.0	525.85	525.86	525.86	1.15	1.14
180	1109	D	19	R	5	67.0	68.0	528.46	528.47	528.47	1.14	
180	1109	D	19	R	5	67.0	68.0	528.46	528.47	528.47	1.09	
180	1109	D	19	R	5	67.0	68.0	528.46	528.47	528.47	1.14	
180	1109	D	19	R	5	67.0	68.0	528.46	528.47	528.47	1.12	1.12
180	1109	D	20	R	5	38.0	39.0	537.38	537.39	537.39	1.09	
180	1109	D	20	R	5	38.0	39.0	537.38	537.39	537.39	1.13	
180	1109	D	20	R	5	38.0	39.0	537.38	537.39	537.39	1.13	
180	1109	D	20	R	5	38.0	39.0	537.38	537.39	537.39	1.12	1.12
180	1109	D	20	R	3	30.0	31.0	535.08	535.09	535.09	1.06	
180	1109	D	20	R	3	30.0	31.0	535.08	535.09	535.09	1.08	
180	1109	D	20	R	3	30.0	31.0	535.08	535.09	535.09	1.09	
180	1109	D	20	R	3	30.0	31.0	535.08	535.09	535.09	1.06	1.07
180	1109	D	20	R	1	134.0	136.0	533.34	533.36	533.35	0.88	
180	1109	D	20	R	1	134.0	136.0	533.34	533.36	533.35	1.08	
180	1109	D	20	R	1	134.0	136.0	533.34	533.36	533.35	1.07	
180	1109	D	20	R	1	134.0	136.0	533.34	533.36	533.35	1.08	1.03
180	1109	D	21	R	1	103.0	104.5	542.63	542.65	542.64	0.81	
180	1109	D	21	R	1	103.0	104.5	542.63	542.65	542.64	1.14	

Table T17 (continued).

Leg	Site	Hole	Core	Type	Section	Top interval (cm)	Bottom interval (cm)	Top depth (mbsf)	Bottom depth (mbsf)	Middle depth (mbsf)	Thermal conductivity ($W \cdot m^{-1} \cdot °C^{-1}$)	Thermal conductivity average ($W \cdot m^{-1} \cdot °C^{-1}$)
180	1109	D	21	R	1	103.0	104.5	542.63	542.65	542.64	1.12	
180	1109	D	21	R	1	103.0	104.5	542.63	542.65	542.64	1.15	1.05
180	1109	D	21	R	3	105.5	107.5	545.70	545.72	545.71	1.14	
180	1109	D	21	R	3	105.5	107.5	545.70	545.72	545.71	1.10	
180	1109	D	21	R	3	105.5	107.5	545.70	545.72	545.71	1.18	
180	1109	D	21	R	3	105.5	107.5	545.70	545.72	545.71	1.17	1.15
180	1109	D	21	R	5	64.5	65.5	548.05	548.06	548.05	1.17	
180	1109	D	21	R	5	64.5	65.5	548.05	548.06	548.05	1.13	
180	1109	D	21	R	5	64.5	65.5	548.05	548.06	548.05	1.15	
180	1109	D	21	R	5	64.5	65.5	548.05	548.06	548.05	1.17	1.15
180	1109	D	12	R	7	16.0	17.0	462.46	462.47	462.47	1.15	
180	1109	D	12	R	7	16.0	17.0	462.46	462.47	462.47	1.19	
180	1109	D	12	R	7	16.0	17.0	462.46	462.47	462.47	1.21	
180	1109	D	12	R	7	16.0	17.0	462.46	462.47	462.47	1.23	1.19
180	1109	D	22	R	1	102.5	103.0	552.23	552.23	552.23	1.06	
180	1109	D	22	R	1	102.5	103.0	552.23	552.23	552.23	1.04	
180	1109	D	22	R	1	102.5	103.0	552.23	552.23	552.23	1.05	
180	1109	D	22	R	1	102.5	103.0	552.23	552.23	552.23	1.09	1.06
180	1109	D	22	R	3	61.0	61.5	554.35	554.36	554.35	1.19	
180	1109	D	22	R	3	61.0	61.5	554.35	554.36	554.35	1.06	
180	1109	D	22	R	3	61.0	61.5	554.35	554.36	554.35	1.11	
180	1109	D	22	R	3	61.0	61.5	554.35	554.36	554.35	1.17	1.13
180	1109	D	23	R	1	78.0	79.0	561.58	561.59	561.59	1.13	
180	1109	D	23	R	1	78.0	79.0	561.58	561.59	561.59	1.22	
180	1109	D	23	R	1	78.0	79.0	561.58	561.59	561.59	1.24	
180	1109	D	23	R	1	78.0	79.0	561.58	561.59	561.59	1.23	1.21
180	1109	D	24	R	1	21.5	22.5	565.82	565.83	565.82	1.06	
180	1109	D	24	R	1	21.5	22.5	565.82	565.83	565.82	1.20	
180	1109	D	24	R	1	21.5	22.5	565.82	565.83	565.82	1.19	
180	1109	D	24	R	1	21.5	22.5	565.82	565.83	565.82	1.17	1.15
180	1109	D	24	R	3	68.0	70.0	569.20	569.22	569.21	1.05	
180	1109	D	24	R	3	68.0	70.0	569.20	569.22	569.21	1.16	
180	1109	D	24	R	3	68.0	70.0	569.20	569.22	569.21	1.16	1.12
180	1109	D	25	R	1	46.5	47.5	570.87	570.88	570.87	1.19	
180	1109	D	25	R	1	46.5	47.5	570.87	570.88	570.87	1.08	
180	1109	D	25	R	1	46.5	47.5	570.87	570.88	570.87	1.09	
180	1109	D	25	R	1	46.5	47.5	570.87	570.88	570.87	1.12	1.12
180	1109	D	25	R	3	85.0	86.0	573.98	573.99	573.99	1.23	
180	1109	D	25	R	3	85.0	86.0	573.98	573.99	573.99	1.18	
180	1109	D	25	R	3	85.0	86.0	573.98	573.99	573.99	1.14	
180	1109	D	25	R	3	85.0	86.0	573.98	573.99	573.99	1.19	1.18
180	1109	D	25	R	5	65.0	66.0	576.78	576.79	576.79	1.14	
180	1109	D	25	R	5	65.0	66.0	576.78	576.79	576.79	1.21	
180	1109	D	25	R	5	65.0	66.0	576.78	576.79	576.79	1.21	
180	1109	D	25	R	5	65.0	66.0	576.78	576.79	576.79	1.22	1.20
180	1109	D	26	R	1	123.0	124.0	581.23	581.24	581.24	1.21	
180	1109	D	26	R	1	123.0	124.0	581.23	581.24	581.24	1.23	
180	1109	D	26	R	1	123.0	124.0	581.23	581.24	581.24	1.19	
180	1109	D	26	R	1	123.0	124.0	581.23	581.24	581.24	1.23	1.22
180	1109	D	26	R	3	54.5	56.0	583.22	583.23	583.22	1.28	
180	1109	D	26	R	3	54.5	56.0	583.22	583.23	583.22	1.28	
180	1109	D	26	R	3	54.5	56.0	583.22	583.23	583.22	1.30	
180	1109	D	26	R	3	54.5	56.0	583.22	583.23	583.22	1.29	1.29
180	1109	D	26	R	5	43.0	45.0	585.47	585.49	585.48	1.15	
180	1109	D	26	R	5	43.0	45.0	585.47	585.49	585.48	1.22	
180	1109	D	26	R	5	43.0	45.0	585.47	585.49	585.48	1.23	
180	1109	D	26	R	5	43.0	45.0	585.47	585.49	585.48	1.24	1.21
180	1109	D	26	R	7	34.0	35.0	587.77	587.78	587.78	0.98	
180	1109	D	26	R	7	34.0	35.0	587.77	587.78	587.78	1.29	
180	1109	D	26	R	7	34.0	35.0	587.77	587.78	587.78	1.29	
180	1109	D	26	R	7	34.0	35.0	587.77	587.78	587.78	1.25	1.20
180	1109	D	27	R	1	56.0	57.0	590.16	590.17	590.17	1.48	
180	1109	D	27	R	1	56.0	57.0	590.16	590.17	590.17	1.52	
180	1109	D	27	R	1	56.0	57.0	590.16	590.17	590.17	1.47	
180	1109	D	27	R	1	56.0	57.0	590.16	590.17	590.17	1.45	1.48
180	1109	D	27	R	3	42.0	43.0	592.42	592.43	592.43	1.29	
180	1109	D	27	R	3	42.0	43.0	592.42	592.43	592.43	1.30	

Table T17 (continued).

Leg	Site	Hole	Core	Type	Section	Top interval (cm)	Bottom interval (cm)	Top depth (mbsf)	Bottom depth (mbsf)	Middle depth (mbsf)	Thermal conductivity ($W \cdot m^{-1} \cdot °C^{-1}$)	Thermal conductivity average ($W \cdot m^{-1} \cdot °C^{-1}$)
180	1109	D	27	R	3	42.0	43.0	592.42	592.43	592.43	1.23	
180	1109	D	27	R	3	42.0	43.0	592.42	592.43	592.43	1.30	1.28
180	1109	D	28	R	1	50.0	51.0	599.70	599.71	599.71	1.43	
180	1109	D	28	R	1	50.0	51.0	599.70	599.71	599.71	1.38	
180	1109	D	28	R	1	50.0	51.0	599.70	599.71	599.71	1.37	
180	1109	D	28	R	1	50.0	51.0	599.70	599.71	599.71	1.35	1.38
180	1109	D	29	R	3	33.0	35.0	611.29	611.31	611.30	1.24	
180	1109	D	29	R	3	33.0	35.0	611.29	611.31	611.30	1.32	
180	1109	D	29	R	3	33.0	35.0	611.29	611.31	611.30	1.33	
180	1109	D	29	R	3	33.0	35.0	611.29	611.31	611.30	1.22	1.28
180	1109	D	29	R	1	89.0	90.0	609.79	609.80	609.80	1.31	
180	1109	D	29	R	1	89.0	90.0	609.79	609.80	609.80	1.27	
180	1109	D	29	R	1	89.0	90.0	609.79	609.80	609.80	1.35	
180	1109	D	29	R	1	89.0	90.0	609.79	609.80	609.80	1.34	1.32
180	1109	D	30	R	1	34.0	36.0	618.84	618.86	618.85	1.57	
180	1109	D	30	R	1	34.0	36.0	618.84	618.86	618.85	1.59	
180	1109	D	30	R	1	34.0	36.0	618.84	618.86	618.85	1.59	
180	1109	D	30	R	1	34.0	36.0	618.84	618.86	618.85	1.60	1.58
180	1109	D	31	R	1	76.0	77.0	628.96	628.97	628.97	1.39	
180	1109	D	31	R	1	76.0	77.0	628.96	628.97	628.97	1.50	
180	1109	D	31	R	1	76.0	77.0	628.96	628.97	628.97	1.48	
180	1109	D	31	R	1	76.0	77.0	628.96	628.97	628.97	1.49	1.47
180	1109	D	32	R	1	76.0	78.0	638.66	638.68	638.67	1.32	
180	1109	D	32	R	1	76.0	78.0	638.66	638.68	638.67	1.34	
180	1109	D	32	R	1	76.0	78.0	638.66	638.68	638.67	1.33	
180	1109	D	32	R	1	76.0	78.0	638.66	638.68	638.67	1.33	1.33
180	1109	D	33	R	1	16.0	17.0	647.66	647.67	647.67	1.38	
180	1109	D	33	R	1	16.0	17.0	647.66	647.67	647.67	1.52	
180	1109	D	33	R	1	16.0	17.0	647.66	647.67	647.67	1.46	
180	1109	D	33	R	1	16.0	17.0	647.66	647.67	647.67	1.50	1.47
180	1109	D	34	R	2	50.0	52.0	658.98	659.00	658.99	1.42	
180	1109	D	34	R	2	50.0	52.0	658.98	659.00	658.99	1.42	
180	1109	D	34	R	2	50.0	52.0	658.98	659.00	658.99	1.46	
180	1109	D	34	R	2	50.0	52.0	658.98	659.00	658.99	1.45	1.44
180	1109	D	34	R	4	11.0	13.0	661.25	661.27	661.26	1.12	
180	1109	D	34	R	4	11.0	13.0	661.25	661.27	661.26	1.56	
180	1109	D	34	R	4	11.0	13.0	661.25	661.27	661.26	1.54	
180	1109	D	34	R	4	11.0	13.0	661.25	661.27	661.26	1.67	1.47
180	1109	D	34	R	6	22.0	23.0	663.39	663.40	663.40	1.50	
180	1109	D	34	R	6	22.0	23.0	663.39	663.40	663.40	1.42	
180	1109	D	34	R	6	22.0	23.0	663.39	663.40	663.40	1.48	
180	1109	D	34	R	6	22.0	23.0	663.39	663.40	663.40	1.47	
180	1109	D	34	R	6	22.0	23.0	663.39	663.40	663.40	1.48	
180	1109	D	34	R	6	22.0	23.0	663.39	663.40	663.40	1.49	1.47
180	1109	D	35	R	1	8.0	12.0	666.78	666.82	666.80	1.89	
180	1109	D	35	R	1	8.0	12.0	666.78	666.82	666.80	1.75	
180	1109	D	35	R	1	8.0	12.0	666.78	666.82	666.80	1.98	
180	1109	D	35	R	1	8.0	12.0	666.78	666.82	666.80	1.51	1.78
180	1109	D	35	R	4	72.0	74.0	670.82	670.84	670.83	1.38	
180	1109	D	35	R	4	72.0	74.0	670.82	670.84	670.83	1.33	
180	1109	D	35	R	4	72.0	74.0	670.82	670.84	670.83	1.34	
180	1109	D	35	R	4	72.0	74.0	670.82	670.84	670.83	1.38	1.36
180	1109	D	35	R	6	44.0	45.0	673.29	673.30	673.30	1.18	
180	1109	D	35	R	6	44.0	45.0	673.29	673.30	673.30	1.17	
180	1109	D	35	R	6	44.0	45.0	673.29	673.30	673.30	1.16	
180	1109	D	35	R	6	44.0	45.0	673.29	673.30	673.30	1.19	1.17
180	1109	D	36	R	1	26.0	29.0	676.66	676.69	676.68	1.14	
180	1109	D	36	R	1	26.0	29.0	676.66	676.69	676.68	1.15	
180	1109	D	36	R	1	26.0	29.0	676.66	676.69	676.68	1.16	
180	1109	D	36	R	1	26.0	29.0	676.66	676.69	676.68	1.14	1.15
180	1109	D	36	R	3	45.5	46.0	679.86	679.86	679.86	1.13	
180	1109	D	36	R	3	45.5	46.0	679.86	679.86	679.86	1.14	
180	1109	D	36	R	3	45.5	46.0	679.86	679.86	679.86	1.15	
180	1109	D	36	R	3	45.5	46.0	679.86	679.86	679.86	1.14	1.14
180	1109	D	36	R	5	109.0	110.0	683.49	683.50	683.50	1.01	
180	1109	D	36	R	5	109.0	110.0	683.49	683.50	683.50	1.05	
180	1109	D	36	R	5	109.0	110.0	683.49	683.50	683.50	1.03	1.03

Table T17 (continued).

Leg	Site	Hole	Core	Type	Section	Top interval (cm)	Bottom interval (cm)	Top depth (mbsf)	Bottom depth (mbsf)	Middle depth (mbsf)	Thermal conductivity ($W \cdot m^{-1} \cdot °C^{-1}$)	Thermal conductivity average ($W \cdot m^{-1} \cdot °C^{-1}$)
180	1109	D	37	R	1	18.0	19.0	686.18	686.19	686.19	1.04	
180	1109	D	37	R	1	18.0	19.0	686.18	686.19	686.19	1.07	
180	1109	D	37	R	1	18.0	19.0	686.18	686.19	686.19	1.06	
180	1109	D	37	R	1	18.0	19.0	686.18	686.19	686.19	1.05	1.05
180	1109	D	37	R	3	0.0	1.0	688.96	688.97	688.97	0.93	
180	1109	D	37	R	3	0.0	1.0	688.96	688.97	688.97	0.93	
180	1109	D	37	R	3	0.0	1.0	688.96	688.97	688.97	0.96	
180	1109	D	37	R	3	0.0	1.0	688.96	688.97	688.97	0.98	0.95
180	1109	D	37	R	5	34.5	35.5	692.08	692.09	692.08	1.01	
180	1109	D	37	R	5	34.5	35.5	692.08	692.09	692.08	1.07	
180	1109	D	37	R	5	34.5	35.5	692.08	692.09	692.08	1.07	
180	1109	D	37	R	5	34.5	35.5	692.08	692.09	692.08	1.05	1.05
180	1109	D	38	R	1	34.5	35.5	695.95	695.96	695.95	0.93	
180	1109	D	38	R	1	34.5	35.5	695.95	695.96	695.95	0.96	
180	1109	D	38	R	1	34.5	35.5	695.95	695.96	695.95	0.99	
180	1109	D	38	R	1	34.5	35.5	695.95	695.96	695.95	0.94	0.95
180	1109	D	38	R	3	33.0	35.0	698.63	698.65	698.64	1.06	
180	1109	D	38	R	3	33.0	35.0	698.63	698.65	698.64	1.09	
180	1109	D	38	R	3	33.0	35.0	698.63	698.65	698.64	1.10	
180	1109	D	38	R	3	33.0	35.0	698.63	698.65	698.64	1.07	1.08
180	1109	D	38	R	5	59.0	61.0	701.85	701.87	701.86	1.04	
180	1109	D	38	R	5	59.0	61.0	701.85	701.87	701.86	1.06	
180	1109	D	38	R	5	59.0	61.0	701.85	701.87	701.86	1.07	1.06
180	1109	D	46	R	1	16.5	18.0	773.07	773.08	773.07	1.56	
180	1109	D	46	R	1	16.5	18.0	773.07	773.08	773.07	1.81	
180	1109	D	46	R	1	16.5	18.0	773.07	773.08	773.07	1.43	
180	1109	D	46	R	1	16.5	18.0	773.07	773.08	773.07	1.84	1.66
180	1109	D	46	R	3	18.0	19.0	775.91	775.92	775.92	1.21	
180	1109	D	46	R	3	18.0	19.0	775.91	775.92	775.92	1.15	
180	1109	D	46	R	3	18.0	19.0	775.91	775.92	775.92	1.29	
180	1109	D	46	R	3	18.0	19.0	775.91	775.92	775.92	1.20	1.21
180	1109	D	39	R	1	58.5	59.5	705.89	705.90	705.89	0.95	
180	1109	D	39	R	1	58.5	59.5	705.89	705.90	705.89	0.99	
180	1109	D	39	R	1	58.5	59.5	705.89	705.90	705.89	0.94	0.96
180	1109	D	39	R	3	26.0	27.0	708.30	708.31	708.31	1.01	
180	1109	D	39	R	3	26.0	27.0	708.30	708.31	708.31	1.10	
180	1109	D	39	R	3	26.0	27.0	708.30	708.31	708.31	1.13	
180	1109	D	39	R	3	26.0	27.0	708.30	708.31	708.31	1.10	1.08
180	1109	D	40	R	2	21.0	22.0	716.47	716.48	716.48	1.12	
180	1109	D	40	R	2	21.0	22.0	716.47	716.48	716.48	1.07	
180	1109	D	40	R	2	21.0	22.0	716.47	716.48	716.48	1.13	
180	1109	D	40	R	2	21.0	22.0	716.47	716.48	716.48	1.08	1.10
180	1109	D	40	R	3	61.0	63.0	717.26	717.28	717.27	0.90	
180	1109	D	40	R	3	61.0	63.0	717.26	717.28	717.27	1.15	
180	1109	D	40	R	3	61.0	63.0	717.26	717.28	717.27	1.14	
180	1109	D	40	R	3	61.0	63.0	717.26	717.28	717.27	1.13	1.08
180	1109	D	41	R	2	71.0	72.0	726.91	726.92	726.92	1.07	
180	1109	D	41	R	2	71.0	72.0	726.91	726.92	726.92	1.07	
180	1109	D	41	R	2	71.0	72.0	726.91	726.92	726.92	1.07	
180	1109	D	41	R	2	71.0	72.0	726.91	726.92	726.92	1.05	1.06
180	1109	D	41	R	3	42.0	42.0	727.70	727.70	727.70	1.12	
180	1109	D	41	R	3	42.0	42.0	727.70	727.70	727.70	1.11	
180	1109	D	41	R	3	42.0	42.0	727.70	727.70	727.70	1.12	
180	1109	D	41	R	3	42.0	42.0	727.70	727.70	727.70	1.16	1.13
180	1109	D	41	R	CC	5.0	8.0	728.22	728.25	728.24	1.39	
180	1109	D	41	R	CC	5.0	8.0	728.22	728.25	728.24	1.84	
180	1109	D	41	R	CC	5.0	8.0	728.22	728.25	728.24	1.81	
180	1109	D	41	R	CC	5.0	8.0	728.22	728.25	728.24	1.75	1.70
180	1109	D	42	R	1	67.0	68.0	734.97	734.98	734.98	1.12	
180	1109	D	42	R	1	67.0	68.0	734.97	734.98	734.98	1.11	
180	1109	D	42	R	1	67.0	68.0	734.97	734.98	734.98	1.11	
180	1109	D	42	R	1	67.0	68.0	734.97	734.98	734.98	1.16	1.13
180	1109	D	43	R	1	88.0	89.0	744.78	744.79	744.79	1.09	
180	1109	D	43	R	1	88.0	89.0	744.78	744.79	744.79	1.10	
180	1109	D	43	R	1	88.0	89.0	744.78	744.79	744.79	1.14	
180	1109	D	43	R	1	88.0	89.0	744.78	744.79	744.79	1.08	1.10
180	1109	D	43	R	3	68.0	69.0	746.49	746.50	746.50	1.12	

Table T17 (continued).

Leg	Site	Hole	Core	Type	Section	Top interval (cm)	Bottom interval (cm)	Top depth (mbsf)	Bottom depth (mbsf)	Middle depth (mbsf)	Thermal conductivity ($W \cdot m^{-1} \cdot °C^{-1}$)	Thermal conductivity average ($W \cdot m^{-1} \cdot °C^{-1}$)
180	1109	D	43	R	3	68.0	69.0	746.49	746.50	746.50	1.13	
180	1109	D	43	R	3	68.0	69.0	746.49	746.50	746.50	1.08	
180	1109	D	43	R	3	68.0	69.0	746.49	746.50	746.50	1.15	1.12
180	1109	D	47	R	1	83.0	90.0	778.43	778.50	778.47	1.76	
180	1109	D	47	R	1	83.0	90.0	778.43	778.50	778.47	1.76	
180	1109	D	47	R	1	83.0	90.0	778.43	778.50	778.47	1.76	1.76
180	1109	D	47	R	3	32.0	36.0	780.45	780.49	780.47	2.09	
180	1109	D	47	R	3	32.0	36.0	780.45	780.49	780.47	2.15	
180	1109	D	47	R	3	32.0	36.0	780.45	780.49	780.47	2.05	
180	1109	D	47	R	3	32.0	36.0	780.45	780.49	780.47	1.99	2.07
180	1109	D	48	R	1	87.0	88.0	783.37	783.38	783.38	1.54	
180	1109	D	48	R	1	87.0	88.0	783.37	783.38	783.38	1.45	
180	1109	D	48	R	1	87.0	88.0	783.37	783.38	783.38	1.55	
180	1109	D	48	R	1	87.0	88.0	783.37	783.38	783.38	1.55	1.52
180	1109	D	48	R	3	100.0	101.0	785.97	785.98	785.98	1.39	
180	1109	D	48	R	3	100.0	101.0	785.97	785.98	785.98	1.40	
180	1109	D	48	R	3	100.0	101.0	785.97	785.98	785.98	1.59	
180	1109	D	48	R	3	100.0	101.0	785.97	785.98	785.98	1.62	1.50
180	1109	D	48	R	5	78.0	79.0	788.35	788.36	788.36	1.46	
180	1109	D	48	R	5	78.0	79.0	788.35	788.36	788.36	1.45	
180	1109	D	48	R	5	78.0	79.0	788.35	788.36	788.36	1.43	
180	1109	D	48	R	5	78.0	79.0	788.35	788.36	788.36	1.44	1.44
180	1109	D	49	R	1	73.0	74.0	787.93	787.94	787.94	1.47	
180	1109	D	49	R	1	73.0	74.0	787.93	787.94	787.94	1.51	
180	1109	D	49	R	1	73.0	74.0	787.93	787.94	787.94	1.51	
180	1109	D	49	R	1	73.0	74.0	787.93	787.94	787.94	1.25	1.43
180	1109	D	49	R	3	70.0	71.0	790.45	790.46	790.46	2.02	
180	1109	D	49	R	3	70.0	71.0	790.45	790.46	790.46	1.66	
180	1109	D	49	R	3	70.0	71.0	790.45	790.46	790.46	1.91	
180	1109	D	49	R	3	70.0	71.0	790.45	790.46	790.46	2.21	1.95
180	1109	D	50	R	1	45.0	50.0	792.65	792.70	792.68	0.06	
180	1109	D	50	R	1	45.0	50.0	792.65	792.70	792.68	1.76	
180	1109	D	50	R	1	45.0	50.0	792.65	792.70	792.68	1.76	
180	1109	D	50	R	1	45.0	50.0	792.65	792.70	792.68	1.73	0.91
180	1109	D	50	R	2	20.0	26.0	793.90	793.96	793.93	0.58	
180	1109	D	50	R	2	20.0	26.0	793.90	793.96	793.93	1.92	
180	1109	D	50	R	2	20.0	26.0	793.90	793.96	793.93	1.89	
180	1109	D	50	R	2	20.0	26.0	793.90	793.96	793.93	1.89	1.57
180	1109	D	50	R	3	32.0	37.0	795.22	795.27	795.25	0.77	
180	1109	D	50	R	3	32.0	37.0	795.22	795.27	795.25	1.53	
180	1109	D	50	R	3	32.0	37.0	795.22	795.27	795.25	1.49	
180	1109	D	50	R	3	32.0	37.0	795.22	795.27	795.25	1.53	1.26
180	1109	D	51	R	4	1.0	7.0	800.40	800.46	800.43	1.62	
180	1109	D	51	R	4	1.0	7.0	800.40	800.46	800.43	1.71	
180	1109	D	51	R	4	1.0	7.0	800.40	800.46	800.43	1.62	
180	1109	D	51	R	4	1.0	7.0	800.40	800.46	800.43	1.70	1.66
180	1109	D	51	R	3	92.0	96.0	799.92	799.96	799.94	0.64	
180	1109	D	51	R	3	92.0	96.0	799.92	799.96	799.94	1.80	
180	1109	D	51	R	3	92.0	96.0	799.92	799.96	799.94	1.76	
180	1109	D	51	R	3	92.0	96.0	799.92	799.96	799.94	1.71	1.48
180	1109	D	51	R	2	115.0	118.0	798.96	798.99	798.98	1.68	
180	1109	D	51	R	2	115.0	118.0	798.96	798.99	798.98	1.92	
180	1109	D	51	R	2	115.0	118.0	798.96	798.99	798.98	1.83	
180	1109	D	51	R	2	115.0	118.0	798.96	798.99	798.98	1.95	1.81
180	1109	D	51	R	1	34.0	39.0	797.24	797.29	797.27	1.68	
180	1109	D	51	R	1	34.0	39.0	797.24	797.29	797.27	1.83	
180	1109	D	51	R	1	34.0	39.0	797.24	797.29	797.27	1.82	
180	1109	D	51	R	1	34.0	39.0	797.24	797.29	797.27	1.80	
180	1109	D	51	R	1	34.0	39.0	797.24	797.29	797.27	1.78	
180	1109	D	51	R	1	34.0	39.0	797.24	797.29	797.27	1.74	
180	1109	D	51	R	1	34.0	39.0	797.24	797.29	797.27	1.77	1.80
180	1109	D	51	R	3	37.0	38.0	799.37	799.38	799.38	1.05	
180	1109	D	51	R	3	37.0	38.0	799.37	799.38	799.38	1.15	
180	1109	D	51	R	3	37.0	38.0	799.37	799.38	799.38	1.27	
180	1109	D	51	R	3	37.0	38.0	799.37	799.38	799.38	1.10	1.14

Note: This table is also available in ASCII format in the **TABLES** directory.

Table T18. Unconfined compressive strength and vane shear strength, Site 1109. (Continued on next three pages. See table note.)

Leg	Site	Hole	Core	Type	Section	Top interval (cm)	Bottom interval (cm)	Depth (mbsf)	Unconfined compressive strength (kPa)	Vane shear strength (kPa)
180	1109	B	1	H	1	78.8	78.8	0.79		10.124
180	1109	B	1	H	2	59.4	59.4	2.04		10.886
180	1109	B	1	H	3	101.8	101.8	3.97		11.974
180	1109	B	1	H	4	27.0	27.0	4.72		17.199
180	1109	B	2	H	1	61.9	61.9	5.92		14.913
180	1109	B	2	H	2	60.6	60.6	7.41		11.539
180	1109	B	2	H	3	91.4	91.4	9.21		2.395
180	1109	B	2	H	4	60.2	60.2	10.40		19.159
180	1109	B	2	H	5	36.6	36.6	10.97		13.607
180	1109	B	2	H	6	36.2	36.2	12.46		16.002
180	1109	B	2	H	7	71.3	71.3	14.31		23.078
180	1109	C	3	H	1	91.0	91.0	17.81	40.00	
180	1109	C	3	H	2	90.0	90.0	19.30	40.00	
180	1109	C	3	H	3	79.0	79.0	20.69	30.00	
180	1109	C	3	H	4	77.5	77.5	22.18	30.00	
180	1109	C	3	H	5	41.5	41.5	23.32	45.00	
180	1109	C	3	H	6	15.0	15.0	24.55	30.00	
180	1109	C	3	H	7	21.0	21.0	26.11	15.00	
180	1109	C	3	H	1	93.5	93.5	17.83		20.030
180	1109	C	3	H	2	74.9	74.9	19.15		25.581
180	1109	C	3	H	2	74.9	74.9	19.15		25.581
180	1109	C	3	H	3	84.1	84.1	20.74		11.212
180	1109	C	3	H	4	84.3	84.3	22.24		20.465
180	1109	C	3	H	5	46.6	46.6	23.37		24.384
180	1109	C	3	H	6	19.8	19.8	24.60		17.199
180	1109	C	3	H	6	19.8	19.8	24.60		17.199
180	1109	C	3	H	7	28.9	28.9	26.19		14.043
180	1109	C	4	H	1	88.0	88.0	27.28	30.00	
180	1109	C	4	H	2	46.0	46.0	28.36	25.00	
180	1109	C	4	H	3	20.0	20.0	29.60	25.00	
180	1109	C	4	H	4	107.5	107.5	31.98	80.00	
180	1109	C	4	H	5	70.0	70.0	33.10	25.00	
180	1109	C	4	H	6	55.0	55.0	34.45	60.00	
180	1109	C	4	H	7	53.0	53.0	35.93	80.00	
180	1109	C	4	H	1	78.3	78.3	27.18		13.825
180	1109	C	4	H	2	55.0	55.0	28.45		14.587
180	1109	C	4	H	3	28.8	28.8	29.69		12.083
180	1109	C	4	H	4	109.6	109.6	32.00		38.862
180	1109	C	4	H	5	62.1	62.1	33.02		15.022
180	1109	C	4	H	6	59.4	59.4	34.49		27.432
180	1109	C	4	H	7	45.2	45.2	35.85		28.194
180	1109	C	5	H	1	99.0	99.0	36.89	60.00	
180	1109	C	5	H	2	73.5	73.5	38.14	40.00	
180	1109	C	5	H	3	105.0	105.0	39.95	75.00	
180	1109	C	5	H	4	59.5	59.5	41.00	75.00	
180	1109	C	5	H	5	61.0	61.0	42.51	80.00	
180	1109	C	5	H	6	62.0	62.0	44.02	40.00	
180	1109	C	5	H	7	34.0	34.0	45.24	110.00	
180	1109	C	5	H	1	105.8	105.8	36.96		21.336
180	1109	C	5	H	2	78.9	78.9	38.19		19.703
180	1109	C	5	H	3	93.9	93.9	39.84		12.954
180	1109	C	5	H	4	48.7	48.7	40.89		20.465
180	1109	C	5	H	5	48.1	48.1	42.38		35.923
180	1109	C	5	H	5	48.1	48.1	42.38		35.923
180	1109	C	5	H	6	79.3	79.3	44.19		28.521
180	1109	C	5	H	7	21.8	21.8	45.12		24.928
180	1109	C	6	H	1	94.0	94.0	46.34	40.00	
180	1109	C	6	H	2	103.5	103.5	47.94	12.50	
180	1109	C	6	H	3	68.5	68.5	49.09	55.00	
180	1109	C	6	H	4	63.5	63.5	50.54	62.50	
180	1109	C	6	H	5	73.0	73.0	52.13	85.00	
180	1109	C	6	H	6	87.5	87.5	53.78	80.00	
180	1109	C	6	H	7	56.0	56.0	54.96	100.00	
180	1109	C	6	H	1	87.7	87.7	46.28		9.253
180	1109	C	6	H	2	93.2	93.2	47.83		15.240
180	1109	C	6	H	3	60.4	60.4	49.00		15.022

Table T18 (continued).

Leg	Site	Hole	Core	Type	Section	Top interval (cm)	Bottom interval (cm)	Depth (mbsf)	Unconfined compressive strength (kPa)	Vane shear strength (kPa)
180	1109	C	6	H	4	69.1	69.1	50.59		13.934
180	1109	C	6	H	5	67.2	67.2	52.07		51.598
180	1109	C	6	H	6	81.2	81.2	53.71		23.622
180	1109	C	6	H	7	44.4	44.4	54.84		46.918
180	1109	C	7	H	1	113.0	113.0	56.03	130.00	
180	1109	C	7	H	2	34.0	34.0	56.74	130.00	
180	1109	C	7	H	3	79.0	79.0	58.69	125.00	
180	1109	C	7	H	4	83.5	83.5	60.24	120.00	
180	1109	C	7	H	5	42.0	42.0	61.32	95.00	
180	1109	C	7	H	6	109.5	109.5	63.50	137.50	
180	1109	C	7	H	7	36.5	36.5	64.27	130.00	
180	1109	C	7	H	1	101.7	101.7	55.92		56.388
180	1109	C	7	H	2	47.9	47.9	56.88		61.722
180	1109	C	7	H	3	67.6	67.6	58.58		45.502
180	1109	C	7	H	4	67.6	67.6	60.08		47.462
180	1109	C	7	H	5	48.1	48.1	61.38		64.444
180	1109	C	7	H	6	99.6	99.6	63.40		45.720
180	1109	C	7	H	7	29.3	29.3	64.19		47.680
180	1109	C	8	H	1	25.0	25.0	64.65	87.50	
180	1109	C	8	H	2	25.0	25.0	66.15	112.50	
180	1109	C	8	H	3	25.0	25.0	67.65	100.00	
180	1109	C	8	H	4	25.0	25.0	69.15	75.00	
180	1109	C	8	H	5	25.0	25.0	70.65	90.00	
180	1109	C	8	H	6	25.0	25.0	72.15	162.50	
180	1109	C	8	H	7	25.0	25.0	73.65	125.00	
180	1109	C	8	H	1	94.6	94.6	65.35		72.390
180	1109	C	8	H	2	93.1	93.1	66.83		75.874
180	1109	C	8	H	2	87.2	87.2	66.77		81.099
180	1109	C	8	H	4	103.5	103.5	69.93		106.680
180	1109	C	8	H	5	105.9	105.9	71.46		130.730
180	1109	C	8	H	6	117.1	117.1	73.07		116.360
180	1109	C	8	H	7	38.2	38.2	73.78		90.243
180	1109	C	9	H	1	60.0	60.0	74.50	155.00	
180	1109	C	9	H	2	60.0	60.0	76.00	137.50	
180	1109	C	9	H	3	60.0	60.0	77.50	120.00	
180	1109	C	9	H	4	60.0	60.0	79.00	135.00	
180	1109	C	9	H	5	56.0	56.0	80.46	130.00	
180	1109	C	9	H	6	60.0	60.0	82.00	195.00	
180	1109	C	9	H	7	60.0	60.0	83.50	125.00	
180	1109	C	9	H	1	124.7	124.7	75.15		106.460
180	1109	C	9	H	2	111.2	111.2	76.51		117.450
180	1109	C	9	H	3	113.7	113.7	78.04		115.710
180	1109	C	9	H	4	132.4	132.4	79.72		35.596
180	1109	C	9	H	5	80.7	80.7	80.71		110.590
180	1109	C	9	H	6	130.7	130.7	82.71		155.990
180	1109	C	10	H	1	70.0	70.0	84.10	62.50	
180	1109	C	10	H	2	120.0	120.0	86.10	120.00	
180	1109	C	10	H	3	80.0	80.0	87.20	120.00	
180	1109	C	10	H	4	81.0	81.0	88.71	125.00	
180	1109	C	10	H	5	26.0	26.0	89.66	150.00	
180	1109	C	10	H	6	24.0	24.0	91.14	20.00	
180	1109	C	10	H	7	30.0	30.0	92.70	25.00	
180	1109	C	10	H	1	22.9	22.9	83.63		56.497
180	1109	C	10	H	2	39.9	39.9	85.30		85.780
180	1109	C	10	H	3	122.6	122.6	87.63		94.924
180	1109	C	10	H	4	74.9	74.9	88.65		76.745
180	1109	C	10	H	5	91.0	91.0	90.31		91.223
180	1109	C	10	H	6	140.9	140.9	92.31		22.098
180	1109	C	10	H	7	60.7	60.7	93.01		24.928
180	1109	C	11	H	1	89.0	89.0	93.79	210.00	
180	1109	C	11	H	2	92.0	92.0	95.32	190.00	
180	1109	C	11	H	3	40.0	40.0	96.30	200.00	
180	1109	C	11	H	4	64.0	64.0	98.04	187.50	
180	1109	C	11	H	5	87.0	87.0	99.77	220.00	
180	1109	C	11	H	6	73.0	73.0	101.13	225.00	
180	1109	C	11	H	7	102.0	102.0	102.42	170.00	
180	1109	C	12	X	1	20.0	20.0	102.60	125.00	

Table T18 (continued).

Leg	Site	Hole	Core	Type	Section	Top interval (cm)	Bottom interval (cm)	Depth (mbsf)	Unconfined compressive strength (kPa)	Vane shear strength (kPa)
180	1109	C	12	X	1	60.0	60.0	103.00	120.00	
180	1109	C	12	X	1	130.0	130.0	103.70	120.00	
180	1109	C	12	X	2	60.0	60.0	104.50	137.50	
180	1109	C	12	X	2	130.0	130.0	105.20	117.50	
180	1109	C	12	X	3	40.0	40.0	105.80	117.50	
180	1109	C	12	X	3	120.0	120.0	106.60	140.00	
180	1109	C	12	X	4	40.0	40.0	107.30	100.00	
180	1109	C	12	X	4	80.0	80.0	107.70	112.50	
180	1109	C	12	X	5	50.0	50.0	108.90	115.00	
180	1109	C	12	X	5	130.0	130.0	109.70	90.00	
180	1109	C	12	X	5	150.0	150.0	109.90	75.00	
180	1109	C	12	X	6	20.0	20.0	110.10	117.50	
180	1109	C	12	X	6	50.0	50.0	110.40	162.50	
180	1109	C	12	X	6	100.0	100.0	110.90	200.00	
180	1109	C	12	X	6	140.0	140.0	111.30	205.00	
180	1109	C	12	X	7	30.0	30.0	111.70	162.50	
180	1109	C	13	X	1	20.0	20.0	112.20	67.50	
180	1109	C	13	X	2	20.0	20.0	113.70	55.00	
180	1109	C	13	X	3	20.0	20.0	115.20	65.00	
180	1109	C	13	X	4	20.0	20.0	116.70	87.50	
180	1109	C	13	X	5	20.0	20.0	118.20	112.50	
180	1109	C	13	X	6	20.0	20.0	119.70	212.50	
180	1109	C	13	X	7	20.0	20.0	121.20	137.50	
180	1109	C	14	X	1	122.0	122.0	122.82	20.00	
180	1109	C	14	X	2	45.5	45.5	123.56	35.00	
180	1109	C	14	X	3	82.0	82.0	125.42	30.00	
180	1109	C	14	X	4	84.5	84.5	126.95	70.00	
180	1109	C	14	X	5	85.5	85.5	128.46	90.00	
180	1109	C	14	X	6	92.5	92.5	130.03	80.00	
180	1109	C	14	X	7	19.5	19.5	130.80	110.00	
180	1109	C	14	X	1	117.9	117.9	122.78		5.878
180	1109	C	14	X	2	51.0	51.0	123.61		20.465
180	1109	C	14	X	2	42.5	42.5	123.53		27.976
180	1109	C	14	X	3	75.5	75.5	125.36		19.268
180	1109	C	14	X	4	78.0	78.0	126.88		37.447
180	1109	C	14	X	5	72.3	72.3	128.32		40.931
180	1109	C	14	X	6	93.7	93.7	130.04		55.517
180	1109	C	14	X	7	22.8	22.8	130.83		86.106
180	1109	C	15	X	1	96.0	96.0	132.16	75.00	
180	1109	C	15	X	2	101.5	101.5	133.69	40.00	
180	1109	C	15	X	3	106.5	106.5	135.24	60.00	
180	1109	C	15	X	4	89.0	89.0	136.56	35.00	
180	1109	C	15	X	5	80.0	80.0	137.97	60.00	
180	1109	C	15	X	6	68.5	68.5	139.36	140.00	
180	1109	C	15	X	7	31.5	31.5	140.49	50.00	
180	1109	C	15	X	1	86.0	86.0	132.06		43.543
180	1109	C	15	X	2	90.5	90.5	133.57		27.868
180	1109	C	15	X	3	96.3	96.3	135.13		30.807
180	1109	C	15	X	4	82.0	82.0	136.49		32.440
180	1109	C	15	X	5	81.0	81.0	137.98		31.133
180	1109	C	15	X	6	71.6	71.6	139.39		56.279
180	1109	C	15	X	7	32.0	32.0	140.49		39.624
180	1109	C	16	X	1	58.5	58.5	141.39	62.50	
180	1109	C	16	X	2	111.0	111.0	143.41	50.00	
180	1109	C	16	X	3	61.0	61.0	144.41	70.00	
180	1109	C	16	X	4	95.0	95.0	146.25	80.00	
180	1109	C	16	X	1	65.0	65.0	141.45		22.751
180	1109	C	16	X	2	114.6	114.6	143.45		23.295
180	1109	C	16	X	3	67.3	67.3	144.47		30.154
180	1109	C	16	X	4	74.8	74.8	146.05		44.849
180	1109	C	17	X	1	107.5	107.5	151.58	25.00	
180	1109	C	17	X	2	36.5	36.5	152.37	12.50	
180	1109	C	17	X	1	101.5	101.5	151.51		14.478
180	1109	C	17	X	2	39.5	39.5	152.40		15.893
180	1109	C	18	X	1	70.6	70.6	160.81		9.471
180	1109	C	19	X	1	33.0	33.0	170.03	10.00	
180	1109	C	20	X	1	105.0	105.0	180.35	25.00	

Table T18 (continued).

Leg	Site	Hole	Core	Type	Section	Top interval (cm)	Bottom interval (cm)	Depth (mbsf)	Unconfined compressive strength (kPa)	Vane shear strength (kPa)
180	1109	C	20	X	2	115.5	115.5	181.96	60.00	
180	1109	C	20	X	3	3.0	3.0	182.33	75.00	
180	1109	C	20	X	4	37.0	37.0	184.17	75.00	
180	1109	C	20	X	1	114.1	114.1	180.44		18.615
180	1109	C	20	X	2	125.0	125.0	182.05		21.880
180	1109	C	20	X	3	119.2	119.2	183.49		19.921
180	1109	C	23	X	1	36.0	36.0	208.46	25.00	
180	1109	C	23	X	2	37.0	37.0	209.97	37.50	
180	1109	C	23	X	3	24.0	24.0	211.34	40.00	
180	1109	C	23	X	4	10.0	10.0	212.20	45.00	
180	1109	C	23	X	5	33.0	33.0	213.08	30.00	
180	1109	C	23	X	6	88.0	88.0	215.13	25.00	
180	1109	C	23	X	7	100.0	100.0	216.75	155.00	
180	1109	C	23	X	8	28.0	28.0	217.53	45.00	
180	1109	C	23	X	1	137.0	137.0	209.47		14.369
180	1109	C	23	X	2	116.8	116.8	210.77		15.349
180	1109	C	23	X	3	13.9	13.9	211.24		22.207
180	1109	C	23	X	4	21.2	21.2	212.31		11.212
180	1109	C	23	X	5	73.9	73.9	213.49		25.908
180	1109	C	23	X	6	119.0	119.0	215.44		36.141
180	1109	C	23	X	7	134.1	134.1	217.09		47.244
180	1109	C	23	X	8	16.1	16.1	217.41		38.862

Note: This table is also available in ASCII format in the **TABLES** directory.

Table T19. Summary of logging operations, Hole 1109D.

Logging			Mudline depth (mbrf)		Pipe depth (mbsf)		Logged interval (mbsf)	
Run	Tool string	Pass	Drill pipe	Wireline	Drill pipe	Wireline	Bottom	Top
1		Down	2222.2		99		786	102
1		Up	2222.2	2218.2	79	81.8	786	–68
1		Repeat	2222.2	2218.2	79	81.8	141	24
2		Up	2222.2	2219.1	79	80.0	351	82
3		Up	2222.2	2214.0	381	384.5	786	376

Table T20. Break times, transit times, depths, and interval velocities for each station occupied during the VSP experiment.

Station	Depth (mbsf)	Hydrophone break time (ms)	Geophone break time (ms)	Transit time (ms)	Interval velocity ($m \cdot s^{-1}$)
8	378.10	74.57	1773.00	1698.43	1575.93
7	389.10	74.59	1780.00	1705.41	1775.15
6	398.10	74.52	1785.00	1710.48	2212.39
5	408.10	74.00	1789.00	1715.00	1362.50
4	419.00	74.00	1797.00	1723.00	1877.32
3	429.10	74.62	1803.00	1728.38	1992.03
2	439.10	74.60	1808.00	1733.40	2020.00
1	449.20	74.60	1813.00	1738.40	1716.67
0	459.50	74.60	1819.00	1744.40	1537.78

Table T21. A comparison of VSP check-shot data with depth estimates derived from physical properties and logging measurements.

VSP depth (mbsf)	VSP TWT (ms)	VSP TWT (ms bsf)	Predicted depth (m)	Error (m)
378.1	3405.7	428.8	377.25	0.85
389.1	3419.6	442.8	390.26	–1.16
398.1	3429.8	452.9	399.65	–1.55
408.1	3438.8	461.9	407.94	0.16
419.0	3454.8	477.9	422.87	–3.87
429.1	3465.6	488.7	433.23	–4.13
439.1	3475.6	498.7	442.42	–3.32
449.2	3485.6	508.7	451.80	–2.60
459.5	3497.6	520.7	462.96	–3.46

Note: VSP two-way traveltime (TWT) is converted to two-way traveltime below seafloor (bsf) in column three for comparison to depth measurements made relative to the seafloor.

Table T22. The depths of the correlative peaks of magnetic susceptibility.

Key bed lithology	Section	Interval (cm)	Distance from core top (m)	Depth below core top (m)	Section	Interval (cm)	Distance from core top (m)	Depth below core top (m)	Section	Interval (cm)	Distance from core top (m)	Depth below core top (m)	Depth (mcd)
	Core 180-1109A-1H				Core 180-1109B-1H				Core 180-1109C-1H				
	1	8	0.08	0.08					1	28	0.28	0.28	0.28
	1	72	0.72	0.69					1	96	0.96	0.96	0.93
Ash	1	120	1.20	1.14					1	144	1.44	1.44	1.39
	1	132	1.32	1.26					2	4	1.54	1.54	1.50
	2	4	1.54	1.47	2	24	1.69	1.69	2	28	1.78	1.78	1.73
	2	8	1.58	1.51	2	28	1.73	1.73	2	36	1.86	1.86	1.78
	2	28	1.78	1.70	2	44	1.89	1.89	2	52	2.02	2.02	1.95
					2	56	2.01	2.01	2	60	2.10	2.10	
					2	64	2.09	2.09	2	68	2.18	2.18	
					2	68	2.13	2.13	2	76	2.26	2.26	
					2	76	2.21	2.21	2	84	2.34	2.34	
Calcareous sand	3	8	3.08	2.94	3	20	3.15	3.15	3	32	3.32	3.32	3.22
	3	24	3.24	3.09	3	40	3.35	3.35	3	40	3.40	3.40	3.36
					3	52	3.47	3.47	3	48	3.48	3.48	
					3	60	3.55	3.55	3	64	3.64	3.64	
	3	52	3.52	3.36	3	76	3.71	3.71	3	68	3.68	3.68	3.66
	3	68	3.68	3.51	3	88	3.83	3.83	3	88	3.88	3.88	3.82
	4	32	4.82	4.60	4	28	4.73	4.73	4	36	4.86	4.86	4.81
					Core 180-1109B-2H								
Ash	4	104	5.54	5.28	1	28	0.28	0.27	4	104	5.54	5.54	5.49
	4	112	5.62	5.36	1	36	0.36	0.35	4	112	5.62	5.62	5.57
	5	24	6.24	5.95	1	96	0.96	0.92	5	28	6.28	6.28	6.18
									Core 180-1109C-2H				
	5	116	7.16	6.83	2	40	1.90	1.83					7.07
	6	8	7.58	7.23					1	24	0.24	0.23	7.47
	6	12	7.62	7.27	2	84	2.34	2.25					7.50
	6	16	7.66	7.31					1	36	0.36	0.34	7.54
Volcaniclastic sand					2	100	2.50	2.41	1	44	0.44	0.42	7.70
	6	56	8.06	7.69	2	128	2.78	2.68					7.97
	6	64	8.14	7.76	2	144	2.94	2.83					8.08
	6	92	8.42	8.03	3	16	3.16	3.04	1	84	0.84	0.80	8.32
	6	108	8.58	8.18	3	28	3.28	3.16	1	104	1.04	1.00	8.47
					3	36	3.36	3.24	1	120	1.20	1.15	8.59
					3	52	3.52	3.39	1	136	1.36	1.30	8.74
	6	136	8.86	8.45	3	60	3.60	3.47	1	144	1.44	1.38	8.82
	7	24	9.24	8.81	3	128	4.28	4.12	2	60	2.10	2.01	9.37
	7	44	9.44	9.00					2	68	2.18	2.09	9.50
					4	12	4.62	4.45	2	92	2.42	2.32	9.73
					4	20	4.70	4.53	2	96	2.46	2.36	9.79
					5	24	5.54	5.34	3	40	3.40	3.26	10.64
					5	40	5.70	5.49	3	56	3.56	3.41	10.80
Volcaniclastic sand					5	56	5.86	5.65	3	68	3.68	3.52	10.93
					5	64	5.94	5.72	3	76	3.76	3.60	11.01
					5	68	5.98	5.76	3	80	3.80	3.64	11.05
					5	84	6.14	5.92	3	104	4.04	3.87	11.24
					6	20	7.00	6.74	4	40	4.90	4.69	12.07
					6	28	7.08	6.82	4	44	4.94	4.73	12.12
					6	48	7.28	7.01	4	72	5.22	5.00	12.35
					6	60	7.40	7.13	4	80	5.30	5.08	12.45
Ash					6	76	7.56	7.28	4	92	5.42	5.19	12.59
Calcareous sand					6	120	8.00	7.71	4	136	5.86	5.61	13.01
					7	36	8.66	8.34	5	56	6.56	6.28	13.66
					7	72	9.02	8.69	5	92	6.92	6.63	14.01
					7	92	9.22	8.88	5	112	7.12	6.82	14.20
					7	112	9.42	9.08	5	132	7.32	7.01	14.39

Notes: mcd = meters composite depth. Thin solid line and areas surrounded by thin solid line indicate key beds.